

THE UNIVERSITY *of* EDINBURGH

This thesis has been submitted in fulfilment of the requirements for a postgraduate degree (e. g. PhD, MPhil, DClinPsychol) at the University of Edinburgh. Please note the following terms and conditions of use:

- This work is protected by copyright and other intellectual property rights, which are retained by the thesis author, unless otherwise stated.
- A copy can be downloaded for personal non-commercial research or study, without prior permission or charge.
- This thesis cannot be reproduced or quoted extensively from without first obtaining permission in writing from the author.
- The content must not be changed in any way or sold commercially in any format or medium without the formal permission of the author.
- When referring to this work, full bibliographic details including the author, title, awarding institution and date of the thesis must be given.

Middle-Late Miocene palaeoceanographic development of Cyprus (E. Mediterranean) based on integrated study of $\delta^{18}O$ and $\delta^{13}C$ stable isotope records, supported by Mg/Ca palaeothermometry, nannofossil biostratigraphy, Sr isotopic dating, sedimentology and other geochemical data.

Torin Cannings

BSc (Hons) (University of Manchester)

MScR (University of Edinburgh)



Thesis submitted in fulfilment of the requirements for the degree of

Doctor of Philosophy

University of Edinburgh

2023

This thesis is dedicated to the memory of Professor Dick Kroon.

His unlimited enthusiasm fuelled this work.

Declaration

I declare that this thesis has been composed solely by myself and that it has not been submitted, in whole or in part, in any previous application for a degree. Except where stated otherwise by reference or acknowledgement, the work presented is entirely my own.

Torin Cannings

Research Statement

During my time spent working on this PhD project, I have contributed to the following articles, which have been published in peer-reviewed journals. Results from these works are cited where necessary.

Cannings, T., Balmer, E.M., Coletti, G., Ickert, R.B., Kroon, D., Raffi, I. and Robertson, A.H.F. (2020) 'Microfossil and strontium isotope chronology used to identify the controls of Miocene reefs and related facies in NW Cyprus', *Journal of the Geological Society*, 178(2). Available at: https://doi.org/10.1144/JGS2020-081.

Coletti, G., Balmer, E.M., Bialik, O.M., Cannings, T., Kroon, D., Robertson, A.H.F. and Basso, D. (2021) 'Microfacies evidence for the evolution of Miocene coral-reef environments in Cyprus', *Palaeogeography, Palaeoclimatology, Palaeoecology*, 584. Available at: https://doi.org/10.1016/j.palaeo.2021.110670.

Coletti, G., Bosio, G., Collareta, A., Malinverno, E., Bracchi, V.A., Di Celma, C., Basso, D., Stainbank, S., Spezzaferri, S., Cannings, T. and Bianucci, G. (2019) 'Biostratigraphic, evolutionary, and paleoenvironmental significance of the southernmost lepidocyclinids of the Pacific coast of South America (East Pisco Basin, southern Peru)', *Journal of South American Earth Sciences*, 96. Available at: https://doi.org/10.1016/j.jsames.2019.102372.

Funding

This project was funded by the Natural Environment Research Council (NERC) through the Edinburgh Earth, Ecology and Environment Doctoral Training Partnership (E4 DTP), led by the School of GeoSciences at the University of Edinburgh.

Abstract

Dynamic climate changes and regional tectonic convergence/collision were fundamental factors in the formation of earth, ocean and climate systems during the Middle to Late Miocene. CO_2-driven global warming of the Miocene Climatic Optimum (MCO) has been proposed as an analogue for future anthropogenic climate change. However, the nature and extent of both the MCO and the subsequent Middle to Late Miocene cooling had remained poorly constrained in the eastern Mediterranean region. This region was affected by the closure of key ocean gateways, to the Indian Ocean during the Middle Miocene and to the Atlantic Ocean during the Late Miocene. The Late Miocene isolation of Mediterranean basins culminated in dramatic seawater salinity increase and extensive evaporite formation, known as the Messinian Salinity Crisis (MSC).

The island of Cyprus exposes uplifted Cenozoic and Neogene deep-sea pelagic sedimentary rocks. These successions have not undergone deep burial diagenesis and can therefore be utilised to produce reliable geochemical records. The Lower to Upper Miocene succession at Kottaphi Hill and the Upper Miocene succession at Lapatza Hill were sampled in order to produce a composite stable isotope record (O and C), which spans the onset of the MCO to the onset of the MSC. The two successions were sampled at a vertical spacing of 5–25 cm and correlated using calcareous nannofossil biostratigraphy and stable isotope data, supported by field observations, X-ray diffraction and X-ray fluorescence data. Fine-fraction bulk rock and planktic foraminifera stable isotope records, together with trace element/Ca records, provide fresh insights into the evolution of sea surface temperature and ocean chemistry. The new data reveal how both global climate changes and the local to regional effects of ocean gateway closures affected Cyprus, and probably also the wider eastern Mediterranean during this time interval. The data also shed light on the sedimentary development related to the tectonic development of the adjacent Mesaoria Basin in Cyprus. In addition, strontium isotope dating of redeposited shallow-water carbonate material (e.g. bivalves) aids interpretation of contemporaneous Miocene reef-related facies elsewhere, in northwest Cyprus. This research demonstrates that pelagic carbonate successions such as at Kottaphi Hill can produce excellent stable isotopic records comparable to those for deep-sea cores, opening the way for comparable land-based isotopic studies elsewhere.

Lay Summary

This research focuses on the environmental and climatic conditions of the eastern Mediterranean region during the Miocene Epoch. The Miocene Epoch is a division of geological time that spanned from approximately twenty-three million years ago until five million years ago. More specifically, this research explores the oceanographic conditions of the eastern Mediterranean Sea and its predecessor, the Southern Neotethys, during the Miocene.

At the start of the Miocene, the arrangement of oceans and continents had several differences from the modern-day Earth. During the Miocene, plate tectonic movements caused mountain-building events and the closure of several ocean gateways, culminating in a world much more similar to the one we live in.

Compared to today, the Miocene was warm, but a long-term cooling trend during the Miocene resulted in temperatures closer to those of the modern Earth. By the end of the Miocene, ice sheets had formed on the Antarctic continent. This long-term cooling trend was interrupted about 17 million years ago by a period of carbon dioxide-driven global warming known as the Miocene Climatic Optimum (MCO). The MCO is an important analogue for modern (anthropogenic) climate change.

At the start of the Miocene, the Southern Neotethys was connected to the Atlantic Ocean to the west and the Indian Ocean to the east. By the middle of the Miocene, connection was lost between the Indian Ocean and the Southern Neotethys, resulting in the formation of the proto-Mediterranean Sea. At the end of the Miocene, the connection between the proto-Mediterranean Sea and the Atlantic Ocean was also lost. This isolation of the proto-Mediterranean Sea resulted in a dramatic desiccation event known as the Messinian Salinity Crisis (MSC).

The island of Cyprus provides a unique opportunity to study recently uplifted sedimentary rocks that were deposited on the sea floor during the Miocene. Chemical analyses of these rocks and the fossilised microorganisms (plankton) preserved within them provides insights into the temperature, salinity and other conditions of the sea in which these rocks were deposited. This research helps to better our understanding of past conditions in the eastern Mediterranean region during changes in ocean circulation, a greenhouse event (MCO) and an extreme desiccation event (MSC).

Acknowledgements

It's fair to say that this PhD project hasn't been plain sailing. The support and generosity of several people has helped me to overcome several obstacles, I will always be grateful to everyone who made this thesis possible.

Firstly, I would like to thank Alastair Robertson, whose supervision throughout this PhD has been more than I could ever ask for. Alastair's encyclopaedic knowledge of eastern Mediterranean geology is enviable, but it was his logic, patience and generosity that made him a perfect supervisor.

I will forever be grateful to have had the guidance and company of Dick Kroon. I was incredibly fortunate to have Dick as a supervisor. His enthusiasm for science was inspiring. Without his energy and expertise, this project would not have been possible. He is greatly missed both by those who worked closely with him, and the greater scientific community. I would also like to thank Dick's wife, Erica de Leau. Erica's generosity and friendship during such a difficult time has been phenomenal.

Dick was irreplaceable, but several great people stepped in to help me with my project following Dick's death. I would like to thank Simon Jung for joining my supervisory team and providing fantastic guidance in the final year of my PhD. Without James Barnet, the trace element analysis that forms a fundamental part of this project would not have been possible. I am extremely grateful to James for taking time the time to help me with this work. I would also like to thank James Rae and the St Andrews isotope geochemistry group for their help with the trace element analysis.

I am hugely appreciative of Ulrike Baranowski and Colin Chilcott for their help with stable isotope analyses; special thanks go to Ulrike for her additional guidance on various aspects of my thesis. I am very appreciative of Nicola Cayzer, who provided training and guidance for scanning electron microscopy. I thank Nic Odling for running my samples for XRF and XRD analysis, and Anne Kelly for running my samples for Sr isotope analysis. I am also very grateful to Isabella Raffi for training me in the methods used for calcareous nannofossil biostratigraphy at her home department in Italy. I am appreciative of my advisor Katriona Edlmann who offered support throughout my project, as well as Sophie Ramette and Stephanie Robin in the PGR office. I would like to thank the NERC and the E4DTP for funding this project and for offering support

and guidance during the COVID-19 lockdowns that prevented me from carrying out lab or fieldwork.

I would like to thank both the Island of Cyprus and the City of Edinburgh for being such beautiful places with wonderful people. I could not have picked better places to spend my time completing this PhD.

I am grateful to Mehmet Necdet for his help during fieldwork in the north of Cyprus, which was essential for this project. My thanks also go to Elizabeth Balmer and Jake Shearer for their help as field assistants during this project. I would also like to thank Elizabeth, together with Gillian McCay for countless discussions about the geology of Cyprus. I would like to thank all of my office mates and colleagues on the field trips I have taught on for helping me make so many great memories during the last four years.

Huge thanks go to my parents, my brother and the rest of my family and friends for always being so supportive and pretending to care while I bore them with information about rocks. Special thanks go to my friends who have joined me in escaping from work on hiking, climbing, cycling and skiing adventures.

Lastly, I would like to thank my wife, Erin, for putting up with me and making me smile and Bonnie for being a funny little dog who always makes me laugh. Stay weird.

Contents

Declaration 5

Research Statement 6

Funding 6

Abstract 7

Lay Summary 8

Acknowledgements 9

Contents 11

Greek and Turkish Language 18

Objectives & Rationale 19

1 Introduction 20

1.1 Key Principles 20

Palaeothermometry 20

Orbital Forcing 21

1.2 The Miocene Epoch – Global Context 23

1.2.1 Chronostratigraphy 23

1.2.2 Palaeogeography – Tectonic and Orogenic 25

1.2.3 Ocean Gateways and Circulation 30

1.2.4 Climate and Ocean Chemistry 33

Early Miocene – Slight Cooling 33

Early to Middle Miocene - Climate Optimum 34

Middle Miocene - Climate Transition 35

Late Miocene 37

1.3 Geological Context 40

1.3.1 Geological History of the Eastern Mediterranean Region 40

Palaeozoic 40

Triassic 41

Jurassic-Early Cretaceous 42

Late Cretaceous 44

Palaeocene-Eocene 45

Oligocene 47
Miocene 47
Pliocene-Pleistocene 50
1.3.2 Tectonostratigraphic Framework of Cyprus 51
The Kyrenia (Girne) Range 52
The Troodos Massif 54
The Mamonia Complex 54
Circum-Troodos Cover 55
Cretaceous – Palaeocene Circum-Troodos Cover 56
Late Cretaceous – Oligocene Sedimentary Cover of the Troodos Ophiolite and Mamonia Complex 56
Miocene Cover of the Troodos Ophiolite and Mamonia Complex 58
Pliocene-Recent Cover of the Kyrenia range, Troodos Ophiolite and Mamonia Complex 62
Age Equivalence of Miocene 'circum-Troodos' and Kyrenia Sedimentary Cover 64
2 Materials and Methods 66
2.1 Fieldwork 66
2.1.1 Site Selection 67
Kottaphi Hill 68
Kato Moni 70
Lapatza Hill 71
Marki Hill 72
Marki River 72
Pissouri Slip Road 73
Kouroulla Gorge 73
2.1.2 Sampling 74
2.2 Foraminifera 74
2.2.1 Methodology 76
2.3 Calcareous Nannofossils 77
2.3.1 Methodology 77
2.4 Strontium Isotope Dating 78

2.4.1 Methodology 79
2.5 Stable Isotopes ($\delta^{18}O$ and $\delta^{13}C$) 84
2.5.1 Bulk carbonate (fine fraction) δ18O and δ13C Methodology 87
2.5.2 Foraminifera $\delta^{18}O$ and $\delta^{13}C$ Methodology 87
2.6 Trace Element Analysis 88
2.7 X-Ray Diffraction 93
Kottaphi Hill 93
Lapatza Hill 94
2.8 X-Ray Fluorescence 95
2.9 Scanning Electron Microscopy 95
3 Stratigraphy and Sedimentology 97
3.1 Methodology 98
3.1.1 Lithology and Field Observations 98
3.1.2 Calcareous Nannofossil Biostratigraphy 98
3.1.3 XRF & XRD 98
3.1.4 Foraminifera 98
3.1.5 Strontium Isotope Analysis 99
3.1.6 Age Model 100
3.2 Results 101
3.2.1 Lithology and Field Observations 101
Kottaphi Hill 101
Lapatza Hill 111
3.2.2 Calcareous Nannofossil Biostratigraphy 117
Kottaphi Hill 117
Lapatza Hill 120
3.2.3 XRF & XRD 123
Kottaphi Hill - X-Ray Diffraction 123
Kottaphi Hill - X-Ray Fluorescence 126
Lapatza Hill-X-Ray Diffraction 135
3.2.4 Foraminifera 139

Assessment of Preservation Quality 141
3.2.5 Strontium Isotope Analysis 146
Kouroulla Gorge 146
Kottaphi Hill 147
Lapatza Hill 148
3.2.6 Age Model 150
Kottaphi Hill 150
Lapatza Hill 152
The Composite Temporal Record 156
3.3 Discussion 157
3.3.1 Kouroulla Gorge 157
3.3.2 Kottaphi Hill 159
3.3.3 Lapatza Hill 170
3.3.4 A Composite Early-Late Miocene Temporal Record 175
3.4 Summary of Key Points 178
Kouroulla Gorge 178
Kottaphi Hill 178
Lapatza Hill 178
4 Geochemical evidence for palaeotemperature changes from the composite succession 180
4.1 Methods 180
4.1.1 Oxygen stable isotope records 180
4.1.2 $\delta^{18}O_{planktic}$ Palaeothermometry 181
4.1.3 Mg/Ca Palaeothermometry 184
4.1.4 Combined $\delta^{18}O_{planktic}$ & Mg/Ca Palaeothermometry 188
4.1.5 Smoothing of data 189
4.2 Results 189
4.2.1 Oxygen stable isotope records 189
4.2.2 $\delta^{18}O_{planktic}$ Palaeothermometry 191
4.2.3 Mg/Ca Palaeothermometry 192
4.2.4 Combined $\delta^{18}O_{planktic}$ & Mg/Ca Palaeothermometry 193

4.3 Discussion 196
4.3.1 Oxygen stable isotope records 196
4.3.2 Palaeotemperature records for the composite Miocene succession 197
4.3.3 Regional to Global Comparisons 199
4.4 Summary of key points 212
5 Geochemical evidence for palaeoenvironmental changes from the new composite succession 213
5.1 Methods 213
5.1.1 Carbon stable isotopes 213
5.1.2 Trace elements 214
B/Ca 215
Na/Ca 216
Ba/Ca 216
5.1.3 $\delta^{18}O_{sw\text{-}ivc}$ 217
5.1.4 Smoothing of data 218
5.2 Results 218
5.2.1 Carbon stable isotopes 218
5.2.2 Trace elements 220
B/Ca 220
Na/Ca 221
Ba/Ca 222
5.2.3 $\delta^{18}O_{sw\text{-}ivc}$ 223
5.3 Discussion 225
5.3.1 Carbon stable isotopes 225
5.3.2 B/Ca – additional insights into carbonate chemistry 229
5.3.3 Salinity ($\delta^{18}O_{sw\text{-}ivc}$) 233
5.3.4 Additional insights into Local Hydrography 237
5.4 Summary of key points 240
6 Synthesis – Miocene palaeoceanographic evolution of Cyprus in the context of the geological development of the eastern Mediterranean region 242
6.1 Late Oligocene (Chattian) – 27.82 Ma to 23.03 Ma 246

6.2 Early Miocene (Aquitanian and Burdigalian) - 23.03 Ma to 15.97 Ma 248

6.3 Middle Miocene (Langhian and Serravallian) - 15.97 Ma to 11.63 Ma 255

6.4 Late Miocene (Tortonian and Messinian) - 11.63 Ma to 5.33 Ma 261

7 Conclusions & scope for future work 276

7.1 Summary Conclusions 276

7.2 Future Work 278

References 281

8 Appendices 319

8.1 Age and $\delta^{18}O$ and $\delta^{13}C$ (planktic and bulk) composition of samples collected at Kottaphi Hill 319

8.2 Age and $\delta^{18}O$ and $\delta^{13}C$ (planktic and bulk) composition of samples collected at Lapatza Hill 328

8.3 All measurements of the COR1D standard during planktic foraminifera analysis used in this research 334

8.4 All measurements of the COR1D standard during fine fraction analysis used in this research 339

8.5 Foraminiferal preservation and lithological information for samples collected at Kottaphi Hill . 343

8.6 Foraminiferal preservation and lithological information for samples collected at Lapatza Hill . 351

8.7 Trace element data for planktic foraminifera samples 358

8.8 All measurements of the NITS RM 8301F standard during analysis used in this research 374

8.9 Temperatures calculated from Mg/Ca and $\delta^{18}O_{planktic}$ data 377

8.10 $\delta^{18}O_{seawater}$ and $\delta^{18}O_{sw\text{-}ivc}$ calculated from Mg/Ca and $\delta^{18}O_{planktic}$ data 387

8.11 All data collected during strontium isotope analysis, including ages calculated 390

8.12 Energy dispersive X-ray spectrometry data for planktic foraminifera samples 392

8.12.1 Sample TC19 214 (cleaned and broken) 392

8.12.2 Sample TC21 426 (cleaned and broken) 394

8.12.3 Sample TC21 341 (cleaned and broken) 397

8.12.4 Sample TC21 341 (cleaned and broken) 400

8.12.5 Sample TC21 341 (uncleaned and broken) 403

8.12.6 Sample TC21 341 (uncleaned and broken) 406

8.13 X-ray Fluorescence Data for samples collected at Kottaphi Hill 409

8.14 X-ray Diffraction Data for samples collected at Kottaphi Hill 410

8.15 X-ray Diffraction Data for samples collected at Lapatza Hill 411

Greek and Turkish Language

The island of Cyprus is currently divided into two territories. The Turkish Republic of Northern Cyprus (TRNC) is the northern territory, where Turkish is the primary language used. The Republic of Cyprus (ROC) is the southern territory, where the primary language is Greek. Localities in both territories were studied in this project. In this thesis, the Greek names of lithostratigraphic units are used. Where appropriate, these names are followed by the Turkish names. For lithostratigraphic units that only have Turkish names, these names are used.

As the Greek language uses the Greek alphabet, some words have multiple spellings when written using the Latin alphabet. In this study, the most commonly used spellings of place names and lithostratigraphic units are used. For words that have multiple common spellings, both spellings are initially provided, but the most generally accepted spelling is used thereafter.

Objectives

Primary objectives

The primary objective of this research was to create and interpret palaeoceanographic records for the eastern Mediterranean region, specifically Cyprus, during the interval from the Miocene Climate Optimum (*c.* 17 Ma) and the Messinian Salinity Crisis (5.33 Ma). This includes records of past changes in temperature, salinity and biogenic processes.

Related Objectives

A related objective of this study was to assess the effects of the palaeoceanographic changes recorded on living organisms such as reef builders and plankton during the Middle to Late Miocene.

Rationale

Climatic events such as the Miocene Climate Optimum and Middle Miocene Climate Transition have been recognised in palaeoceanographic records from around the world (see Chapter 1.2.4). These events are regarded as important analogues for modern climatic changes. However, little is known about the effects of such climatic changes in the eastern Mediterranean. Together with climatic changes, the study area underwent tectonic changes, including extensive modifications of ocean circulation patterns due to the closure of several ocean gateways during the Miocene. The changes culminated in the extreme desiccation event known as the Messinian Salinity Crisis. This study examines the effects of a complex balance of climatic and tectonic controls on basin development, sedimentation and oceanography to give new insights into the history of the eastern Mediterranean region.

1 Introduction

1.1 Key Principles

A basic understanding of some key concepts related to this work is crucial in understanding this thesis and the cited background literature. This section outlines these major principles and provides references for further reading on the subjects.

Palaeothermometry

Palaeothermometry is the method of estimating past temperatures (such as sea surface temperature) with the use of an empirically calibrated proxy. In palaeoceanographic and palaeoclimate studies, palaeotemperature proxies are often based on the chemical analysis of the tests of foraminifera. Commonly used palaeotemperature proxies in palaeoceanographic studies include the $\delta^{18}O$ method and the Mg/Ca method, as used in this study; further details of these methods and their application to this work are provided in Chapter 2 and 4. Other commonly used methods for establishing Miocene palaeotemperature records include the TEX_{86} and $U^{K}_{37}{}'$ methods.

The TEX_{86} method is based on the measurement of the degree of cyclisation of membrane lipids produced by mesophilic (organisms that grow best in moderate temperatures) marine and lacustrine Thaumarchaeota (a phylum of archaea). The membrane lipids of Thaumarchaeota are composed of glycerol dialkyl glycerol tetraethers (GDGT). The relative abundance of GDGT in Thaumarchaeota membrane lipids is temperature dependent, but does not alter after the death of the organism, and thus if preserved records the temperature at which the organism was living (Schouten *et al.*, 2002, 2013; Kim *et al.*, 2008). $U^{K}_{37}{}'$ palaeothermometry is based on the measurement of the relative degree of unsaturation of alkenones in a sample.

Alkenones are long-chain ketones that are produced by Prymnesiophyceae phytoplankton (de Leeuw *et al.*, 1980). The organisms respond to temperature change by altering the types of alkenones they produce; they produce a higher relative proportion of saturated alkenones at higher temperatures (Brassell *et al.*, 1986; Müller *et al.*, 1998). Therefore, the relative degree of unsaturation of alkenones can be used to estimate the temperatures in which the alkenone-producing organisms lived (Brassell *et al.*, 1986; Müller *et al.*, 1998).

Orbital Forcing

Variations in the Earth's orbit have been a major control of the amount of solar radiation that has reached the Earth throughout its history (Milankovitch, 1941; Hays *et al.*, 1976; Berger, 1977, 1988). The control of these orbital variations on insolation on Earth is known as orbital forcing or Milankovitch cyclicity. There are three primary components of orbital forcing: eccentricity, obliquity (tilt), and precession (wobble).

Eccentricity refers to variations in the shape of the Earth's orbit. Throughout time, the shape of the Earth's orbit varies between a more elongated elliptical shape (high eccentricity) and a more circular shape (low eccentricity) (Milankovitch, 1941; Berger, 1978). High eccentricity results in a greater variation in the distance between the Earth and the Sun during an orbit, leading to a wider range of insolation levels throughout a year (Milankovitch, 1941; Hays *et al.*, 1976; Berger, 1988). Eccentricity takes place with a periodicity of 100,000 years (Berger, 1977, 1988).

Obliquity refers to variations in the angle of the Earth's axis, also known as tilt. Throughout the Earth's history, the angle of its axis has varied between 21.5° and 24.5° (Milankovitch, 1941; Berger, 1988). A higher axial tilt angle results in a greater difference in the solar radiation received by each hemisphere during summer when

the hemisphere is tilted closer to the sun, and winter when it is tilted further away from the sun (Milankovitch, 1941; Berger, 1988). Obliquity has a greater effect on higher latitude areas, as the variation in distance from the sun due to tilt is greater at the poles than at the equator (Hays *et al.*, 1976). Obliquity has a periodicity of 41,000 years (Hays *et al.*, 1976; Berger, 1977, 1988).

Precession refers to changes in the orientation of the Earth's axis throughout time. Throughout time, the Earth's axis of rotation has experienced a gradual wobble, like a slowing spinning top (Milankovitch, 1941; Berger, 1988). As this wobble happened, the timing of the seasons within Earth's orbit changed. Similar to obliquity, precession has a greater effect on higher latitude areas compared to low latitude areas (Hays *et al.*, 1976). Precession has a periodicity of 19,000 and 23,000 years (Hays *et al.*, 1976; Berger, 1977, 1988).

The interaction of these three components leads to large-scale variations in the insolation levels on Earth and has a significant impact on long-term global climate changes. Solar radiation on Earth reaches a maximum or minimum level when the maxima or minima of these three Milankovitch cycles coincide (Milankovitch, 1941; Berger, 1988). Throughout Earth's climate history, one or more of these orbital forcing mechanisms have controlled variations. Evidence of these cyclical events is well preserved in the geological record and can be used to improve our understanding of major climatic changes, and better constrain the dating of these events (Hays *et al.*, 1976; Berger, 1988; Fischer and Bottjer, 1991; De Boer and Smith, 1994; Shackleton *et al.*, 2000; Lourens *et al.*, 2005).

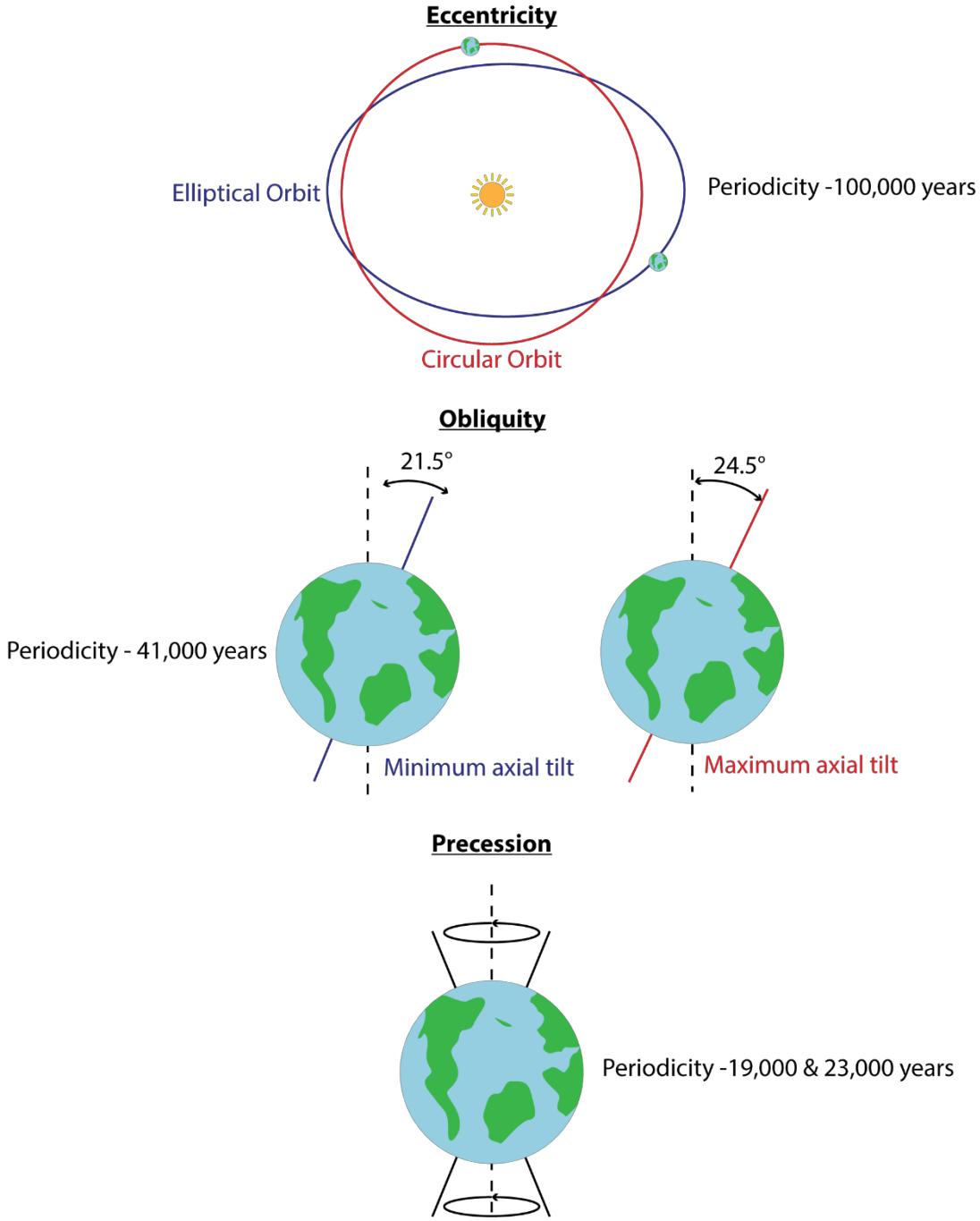


Figure 1.1 – Diagrams showing the three primary components of orbital forcing (modified from Elsom 1992; Wade 2001).

1.2 The Miocene Epoch – Global Context

1.2.1 Chronostratigraphy

The Miocene, from the Greek 'meíōn kainós' meaning 'less recent', is the first epoch of the Neogene Period. The Miocene Epoch begins at the end of the Oligocene period, at the Palaeogene-Neogene boundary (23.03 Ma). Figure 1.2.1 shows the chronology

of the Miocene Epoch including the six ages defined within the epoch. The Miocene was originally defined as a division of the Tertiary Period (*c.* 66 - 2.6 Ma) (Lyell, 1833); however, this division is now obsolete and has been replaced by the Palaeogene and Neogene periods. This thesis utilises the current International Commission on Stratigraphy timescale (Cohen *et al.*, 2013); however, cited literature may use other older timescales.

This section will focus on global environmental and geographical conditions and changes during the Miocene epoch, in order to provide context for the study area in the eastern Mediterranean/ Cyprus.

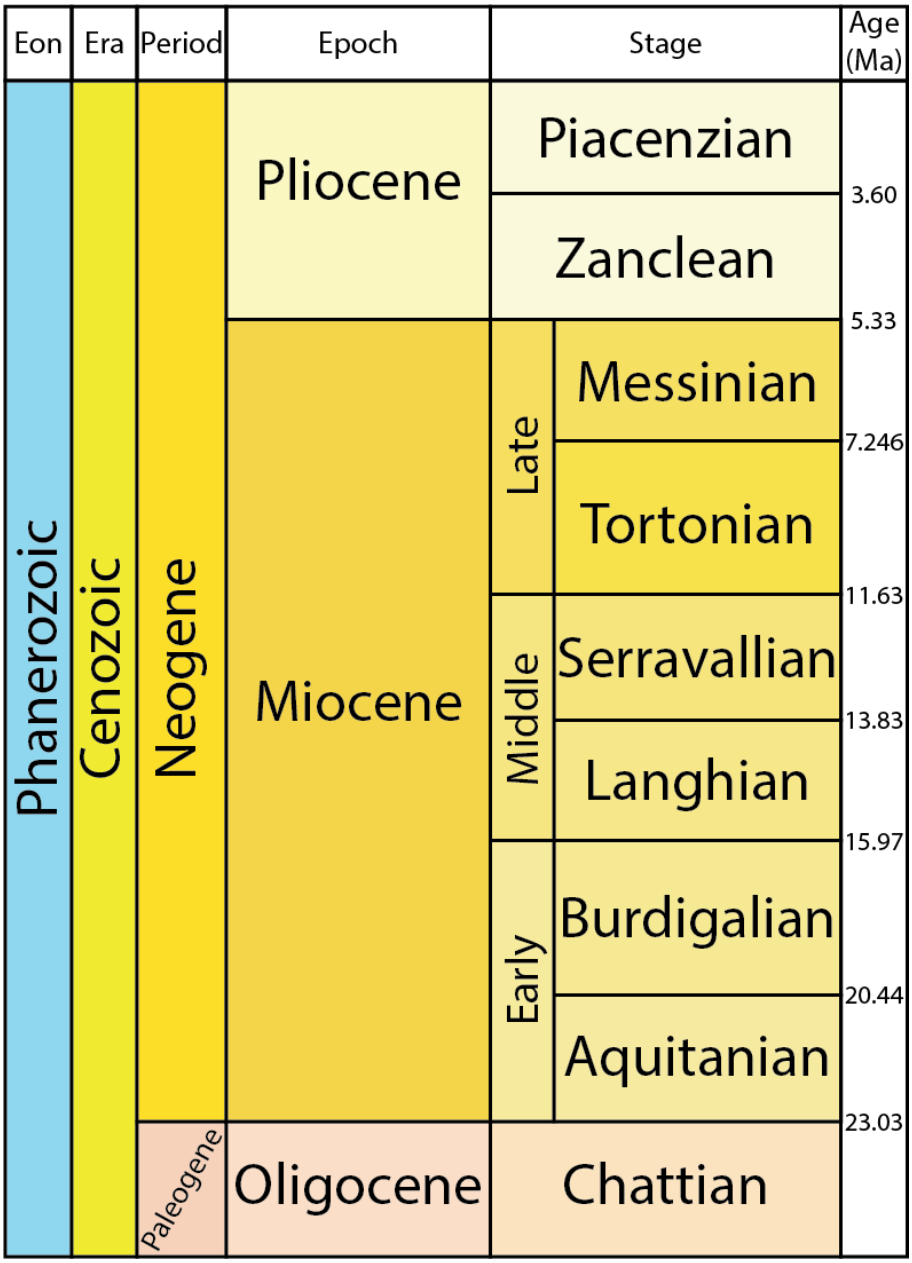


Figure 1.2.1 -The Miocene timescale (after Cohen *et al*. 2013).

1.2.2 Palaeogeography – Tectonic and Orogenic

By the beginning of the Miocene, the large-scale arrangement of the continents was broadly similar to the present day (Figure 1.2.2.1). The Miocene was an important interval with extensive mountain building and tectonic activity that shaped much of today's global geography. Such orogenic events played an important role in organising the global weather patterns (e.g. Raymo *et al.* 1988; Zheng *et al.* 2004) and fluvial systems (e.g. river channels) (e.g. Clark *et al.* 2004; Sissingh 2006), and also created

biogeographic boundaries (Harzhauser *et al.*, 2002; Glor and Warren, 2011). Below, the major orogenic developments during the Miocene are outlined, starting with those beyond the study area, and proceeding to the Mediterranean region and the eastern Mediterranean region.

In North America, large volumes (*c.* 210,000 km^3) of flood basalts erupted, forming the Columbia River Basalt Group (CRBG) during the Burdigalian (Hooper, 1982). Uplift of the Basin and Range Province began during the Late Oligocene; extension-related mountain building continued until the Late Miocene, as indicated by palaeomagnetic and structural reconstructions (Zoback and Thompson, 1978; Perkins *et al.*, 1998; Henry and Aranda-Gomez, 2000). The Rocky Mountains and Appalachian mountain chain both formed prior to the Miocene but thermochronological data reveal that both experienced additional uplift during the Miocene (Pazzaglia and Gardner, 1994; Armstrong *et al.*, 2003; Rosenberg *et al.*, 2014). In South America, palaeoaltimetric studies suggest that the Andes and Andean Plateau underwent significant uplift throughout the Miocene (Tosdal *et al.*, 1984; Ghosh *et al.*, 2006; Kober *et al.*, 2006; Garzione *et al.*, 2008). Fossil data indicates that the Orinoco River altered its course and began draining into the Atlantic Ocean rather than the Caribbean Sea due to the uplift of the Medellin Andes (Diaz De Gamero, 1996). The Amazon River was initiated as a transcontinental river and began to drain into the Atlantic during the Serravallian-Tortonian, as indicated by biostratigraphic, isotopic and sedimentological data (Dobson *et al.*, 2001; Figueiredo *et al.*, 2009)

Due to the collision of the Indian and Eurasian Plates, the uplift of the Himalaya and the Tibetan Plateau had initiated prior to the Miocene (England and Searle, 1986; Tapponnier *et al.*, 2001; Wang *et al.*, 2008, 2014). The timing of the uplift of the Himalaya and the surrounding area is presently a topic of debate; however; it is clear

that the Miocene was a key interval for mountain building in this area (e.g. Burbank *et al.* 1988; Meigs *et al.* 1995; Wang *et al.* 2013; Xu *et al.* 2013). Structural data and dating, together with herpetological phylogeographic suggest the area that makes up modern-day Tibet began to form a High Plateau as the surrounding mountains grew due to compressional uplift and sediment fill during the early-middle Miocene (England and Houseman, 1988; Coleman and Hodges, 1995; Xu *et al.*, 2021). This uplift resulted in increased clastic input to the Indus River, Ganges-Brahmaputra complex and the Bengal Fan, as indicated by sedimentological studies (Lindsay *et al.*, 1991; Clift, 2002; Rea, 2013). Modern-day drainage patterns of the Tibetan plateau were established, and the flow of the Middle Yangtze River was reversed by the end of the Miocene (Clark *et al.*, 2004). The uplift of the Himalayan region generated a strong rain shadow effect, which has been linked with the intensification of the Southern Asian Monsoon (Zhisheng *et al.*, 2001; Ding *et al.*, 2017).

Orogenesis also took place in North Africa during the Miocene. Both sedimentological and structural evidence indicate that the western flank of the Atlas Mountains was uplifted during the Burdigalian and the eastern flank was subsequently uplifted in the Tortonian (Fraissinet *et al.*, 1988; Burollet, 1991; Piqué *et al.*, 2002; Görler *et al.*, 2005). Isotopic and structural studies show that large areas of southern and eastern Africa were also uplifted during the Miocene (Partridge, 1997; Sepulchre *et al.*, 2006); uplift in western Africa has also been inferred from seismic studies (Lavier *et al.*, 2001). During the Miocene, the East African Rift extended southwestward, and the Red Sea widened (Mougenot *et al.*, 1986; Purser and Bosence, 1998; Fielding, 2001). Sedimentological evidence shows that major river systems such as the Nile River and the Zambezi Delta were established by the end of the Miocene (Said, 1982; Walford *et al.*, 2005).

In western Europe, the northward movement of the African plate and the resultant collision with the Eurasian plate had led to some uplift of the Alps prior to the Miocene (Meulenkamp and Sissingh, 2003; Jolivet *et al.*, 2006); however, modern elevations of the Alps were not reached until the Miocene. Palinspastic restorations (Frisch *et al.*, 1998) and fission track dating (Hurford *et al.*, 1991) indicate that modern-day or higher elevations were reached by the end of the Middle Miocene in the western Alps. Structural and geomorphological constructions indicate that the Central Alps reached modern-day or higher elevations during the Middle Miocene (Sharp *et al.*, 2005; Campani *et al.*, 2012). The eastern Alps remained far lower than modern elevations at least until the Middle Miocene, with major uplift taking place during the Late Miocene (Schmid *et al.*, 1996; Frisch *et al.*, 2000; Kuhlemann, 2007; Jiménez-Moreno *et al.*, 2008). Palaeomagnetic, sedimentary and structural data show that the Carpathian Mountains also underwent uplift during the Miocene, experiencing a significant period of uplift during the Middle Miocene (Kovac *et al.*, 1994; Kuhlemann *et al.*, 2001). By the Late Miocene, the Rhine and Rhone Rivers were established in the northern and western margins of the Western Alps (Kuhlemann *et al.*, 2001; Meulenkamp and Sissingh, 2003) and the palaeo-Danube River had formed to the east (Magyar *et al.*, 2013).

In the present-day eastern Mediterranean area, structural reconstructions show that the Zagros Mountains began to develop during the Middle-Late Miocene (Molinaro *et al.*, 2005). The North Anatolian Fault initiated and began to propagate westwards (Şengör *et al.*, 2005). At the boundary between the Eurasian and African Plates, the Dead Sea transform fault was active (Eyal and Reches, 1983; Steckler *et al.*, 1988; Bosworth and McClay, 2001).

Collision between the Arabian Plate and the southern margin of the Eurasian plate was initiated during the Late Eocene-Early Oligocene, and led to the formation of fold and thrust belts across eastern and central Anatolia such as the proto-Taurus mountain chain (Robertson, 1998b; Meulenkamp and Sissingh, 2003; McQuarrie and Van Hinsbergen, 2013; Aksu *et al.*, 2021). Surface uplift of the proto-Taurus mountain chain was restricted during Oligocene-Early Miocene time (Jaffey and Robertson, 2005). Sedimentological and structural evidence in the Aktoprak and Ecemiş basins (S Turkey) indicate a compressional pulse in the Middle Miocene (Jaffey and Robertson, 2005). This compressional pulse was most likely related to the collision of the Tauride and Arabian plates in eastern Turkey, and may have led to some uplift in the Taurus Mountains during the Middle Miocene (Sengor *et al.*, 1985; Robertson *et al.*, 2004; Jaffey and Robertson, 2005). During the Late Miocene, the whole Central Anatolian Plateau was uplifted; possibly due to the removal of lithospheric mantle from beneath the Anatolian plate (Meijers *et al.*, 2018a). Following the uplift of the Central Anatolian Plateau, the Taurus Mountains, at the southern margin of the plateau, underwent major uplift due to one or several mechanisms of subduction-related crustal thickening (Dilek *et al.*, 1999; Jaffey and Robertson, 2005; Meijers *et al.*, 2018a). This phase of uplift has been attributed to fore-arc shortening and subsequent regional compression during the Late Miocene (Meijers *et al.*, 2018a) and has also been linked to magmatic underplating as a result of the subduction of the African beneath the Eurasian Plate (Dilek *et al.*, 1999; Ring and Layer, 2003; Jaffey and Robertson, 2005). Surface exposure dating and fluvial incision rate calculations indicate that the Central Anatolian Plateau underwent a phase of uplift from between 8 and 5.45 Ma until 1.6 Ma. This phase resulted in *c.* 800 m of uplift, this was succeeded by rapid uplift in the Pleistocene (Schildgen *et al.*, 2012).

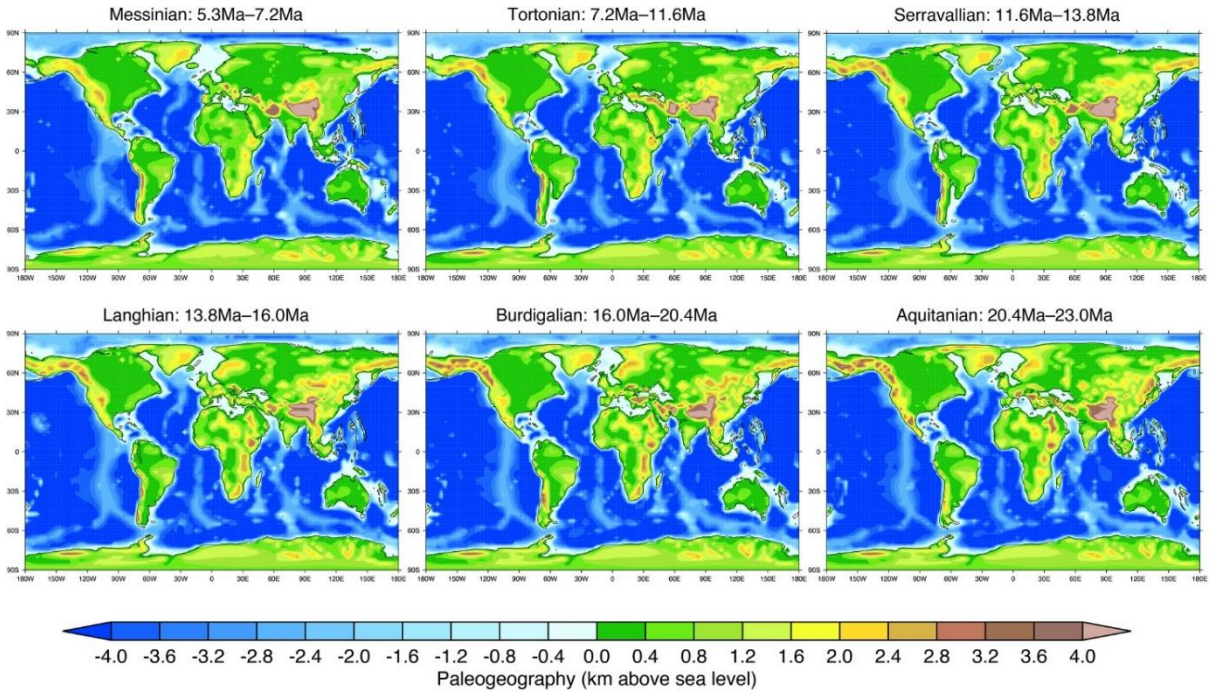


Figure 1.2.2.1 – Palaeogeographical and topographical evolution during each of the Miocene stages. Based on the reconstructions of Getech Plc (Steinthorsdottir *et al.*, 2021).

1.2.3 Ocean Gateways and Circulation

During the Miocene, the opening and closure of oceanic gateways (Figure 1.2.4.1) led to the onset of modern oceanic currents. Both the Tasmanian Passage (Australia - Antarctica) and Drake's Passage (S America – Antarctica) had opened prior to the Miocene, during the Middle-Late Palaeogene (Barker and Burrell, 1977; Lanyon *et al.*, 1993; Lawver and Gahagan, 2003). The opening of these oceanic gateways allowed the Antarctic Circumpolar Current to flow from west to east around Antarctica. Bathymetric and tectonic models indicate that this opening prevented warmer equatorial waters from reaching Antarctica and allowed the East Antarctic Ice Sheet (EAIS) to expand westwards (Nicol *et al.*, 2000; Barker and Thomas, 2004; Kennett *et al.*, 2004; Pfuhl and McCave, 2005; Scher and Martin, 2006; Lagabrielle *et al.*, 2009; Young *et al.*, 2011; Bijl *et al.*, 2013). During the Middle to Late Miocene, subsidence of the Greenland-Scotland Ridge allowed large amounts of cold Arctic deep water to

flow into the Atlantic Ocean as demonstrated by models based on bathymetric and stable isotope data (Wright, 1998; Stärz *et al.*, 2017).

In Southeast Asia, the Indonesian Gateway began to close during the latest Oligocene, limiting the connection between the Indian and Pacific Oceans. Tectonic and bathymetric reconstructions show that this gateway was closed to deep-water flow by the end of the Early Miocene (Kuhnt *et al.*, 2004). The Isthmus of Panama began to form during the Middle Miocene, restricting the tropical connection between the Atlantic and Pacific Oceans. Models based on stratigraphic, bathymetric and fossil data indicate that connectivity continued to reduce until the eventual closure of the gateway during the Pliocene (Coates *et al.*, 2004; Coates and Stallard, 2013).

In the Mediterranean area, at the beginning of the Miocene, the Southern Neotethys Ocean was connected to the Indian Ocean to the east and the Atlantic Ocean to the west. This connectivity allowed warm surface water to flow from the Indian Ocean through the Mediterranean, and then into the Atlantic Ocean. Palaeontological data suggests that connectivity through these gateways also allowed cold intermediate to deep water to flow from the Atlantic Ocean through the Southern Neotethys Ocean into the Indian Ocean (Bialik *et al.*, 2019).

During the Miocene, this ocean gateway became restricted and eventually closed as a result of collision between the Arabian platform and the Tauride continent. The exact timing of the closure of the closure of this gateway is debatable. However, geochemical (Bialik *et al.*, 2019; Torfstein and Steinberg, 2020), micropalaeontological (Torfstein and Steinberg, 2020) and geological data (Hüsing *et al.*, 2009; Torfstein and Steinberg, 2020) all indicate that a substantial closure event took place during the Early Miocene (*c.* 20 Ma). Box models based on neodymium isotope data suggest that

water mass exchange was reduced by *c.* 90% during an initial closure event at *c.* 20 Ma (Bialik *et al.*, 2019).

After the initial phase of closure, it is likely that connectivity between the Southern Neotethys and the Indian Ocean was greatly restricted, with the two basins potentially only connected by a shallow seaway (Hüsing *et al.*, 2009). It has been suggested that the final loss of connectivity between these two basins took place at *c.* 13.8 Ma as a result of a sea-level fall related to the Middle Miocene Climate Transition (MMCT) (see Chapter 1.2.4) (Bialik *et al.*, 2019). This timing for final closure is not in agreement with sedimentological data, which suggests that deposition in the shallow foreland basins, which made up this gateway, was continuous throughout the Serravalian (Hüsing *et al.*, 2009). However, geological evidence does indicate that any possible deep-marine connection was lost by the Late Miocene (*c.* 11 Ma) (Hüsing *et al.*, 2009) (See Chapter 1.3.1 for further details regarding the geological history of the eastern Mediterranean region).

Integrated studies of stable isotope and microfossil data indicate that the closure of the three above oceanic gateways during the Miocene terminated global equatorial flow and resulted in the formation of the Gulf Stream, initiating the modern ocean circulation pattern (Keller and Barron, 1983; Lyle *et al.*, 1995).

Tectonic uplift due to the northwestward migration of the African Plate during the Messinian Stage resulted in the closure of the Betic Straight and the Riffian Corridors (Weijermars, 1988; Garcés *et al.*, 1998; Krijgsman *et al.*, 1999b, 1999a; Ng *et al.*, 2021). The closure of these ocean gateways resulted in a restricted connection between the Mediterranean Sea and the Atlantic Ocean, as indicated by magnetostratigraphic and biostratigraphic data (Krijgsman *et al.*, 1999a; Flecker *et al.*,

2015). Some connection is interpreted to have remained through the Gibraltar Corridor during the Messinian Stage; such connectivity would have been required in order to supply the amount of saltwater required to form the extensive evaporite deposits within the Mediterranean basins (Krijgsman *et al.*, 2018). However, this connectivity was very limited and mostly unidirectional, with saltwater being delivered from the Atlantic Ocean to the Mediterranean Sea (Krijgsman *et al.*, 2018). This change in ocean gateway configuration resulted in the isolation of the Mediterranean Sea at *c.* 6 Ma and subsequently triggered the Messinian Salinity Crisis (MSC). During the MSC, Mediterranean sea level fell to more than 1000m lower than the open ocean (Hsü *et al.*, 1973a; Rouchy and Caruso, 2006). This dramatic sea-level fall and related hyper-aridity resulted in the deposition of thick halite and gypsum units in basins across the Mediterranean area, including Cyprus from *c.* 5.57 Ma (Hsü *et al.*, 1973b; Robertson *et al.*, 1995; Krijgsman *et al.*, 2002; Wade and Bown, 2006; Manzi *et al.*, 2016). Towards the end of the MSC, freshwater contribution increased, culminating in the development of extensive shallow brackish to freshwater lacustrine systems, known as the Lago-Mare (Krijgsman *et al.*, 1999a; Rouchy *et al.*, 2001; Rouchy and Caruso, 2006). Abrupt marine re-flooding at the beginning of the Pliocene (Zanclean Stage) terminated the Lago-Mare conditions and, thus, the MSC (Rouchy *et al.*, 2001; Blanc, 2002; Rouchy and Caruso, 2006; Garcia-Castellanos *et al.*, 2009).

1.2.4 Climate and Ocean Chemistry

Early Miocene – Slight Cooling

The Oligocene-Early Miocene boundary is notoriously difficult to identify, correlate and date globally (Shackleton *et al.*, 2000). A small Antarctic glaciation at the Oligocene-Miocene Boundary is indicated by Benthic foraminiferal $\delta^{18}O$ records (Figure 1.2.4.1). After this glaciation, conditions did not return to the relatively warm climate of the Late

Oligocene, and instead entered the cooler conditions of the Early Miocene. Benthic foraminiferal $\delta^{18}O$ and Mg/Ca records from the Pacific Ocean, suggest that the Early Miocene was a unipolar icehouse, with large-scale ice volume variations and 40-60m fluctuations in sea-level on the 1.2 Myr obliquity cycle (Miller *et al.*, 2005, 2020). Large-scale ice-volume variations persisted throughout the Oligocene and the Early Miocene with a slight cooling trend until the onset of the Miocene climate (MCO) (Miller *et al.*, 1991b; Zachos *et al.*, 2001a, 2001b; Miller *et al.*, 2005; Westerhold *et al.*, 2005; Zachos *et al.*, 2008; Miller *et al.*, 2020; Westerhold *et al.*, 2020).

Early to Middle Miocene - Climate Optimum

Multi-proxy palaeotemperature records show that the Miocene Climate Optimum (MCO) abruptly interrupted a steady multi-million-year cooling trend throughout the Miocene. The MCO is a *c.* 3 Myr greenhouse interval which began at approximately 16.9 Ma and lasted until *c.* 14.7 Ma (Zachos *et al.*, 2008; Holbourn *et al.*, 2015; Westerhold *et al.*, 2020). Warm peaks on the *c*. 400 kyr eccentricity cycle are assumed to be occurrences of an ice-free Earth during the MCO (Miller *et al.*, 2005, 2020).

The onset of the MCO is believed to have been triggered by a dramatic rise in CO_2 levels from approximately 400 ppm to 500 ppm (You *et al.*, 2009; Zhang *et al.*, 2013; Holbourn *et al.*, 2015), leading to a *c.* 4ºC rise in temperature globally (Zachos *et al.*, 2001a, 2008; Westerhold *et al.*, 2005, 2020). Organic palaeothermometry ($U^{K'}_{37}$ & TEX_{86}) indicates that North Atlantic sea surface temperatures were 10-15ºC warmer than in modern times between 17 Ma and 14.5 Ma (Super *et al.*, 2020).

The initial warming event is believed to have caused a sea-level rise of *c*. 50m, with sea-level staying relatively stable (< 20m change) throughout the MCO until the end of the warm period as indicated by stable isotope-based sea-level reconstructions

(Miller *et al.*, 2005, 2020). Similarly to other warm periods in the Earth's history, the MCO is believed to have led to an equable climate, in which there was a much smaller drop in temperature between the equator and higher latitudes compared to the Earth's recent history; this is supported by fossil evidence (Pound *et al.*, 2012).

The Middle Miocene increase in CO_2 is often attributed to the rapid eruption of the Columbia River basalt group (CRBG) (e.g. Hodell and Woodruff 1994; Foster *et al.* 2012; Reidel 2015; Kasbohm and Schoene 2018). Extensive volcanic activity took place across western North America (Hooper, 1982); biogeochemical box-models indicate these eruptions emitted an estimated 3000-4000 Gt of carbon (Armstrong McKay *et al.*, 2014). The timing of the eruption is approximately coeval with the MCO, U-Pb geochronology suggests that over 95% of the CRBG erupted between 16.7 and 15.9 Ma (Kasbohm and Schoene, 2018).

A rapid increase in $\delta^{13}C$ at *c.*16.9 Ma indicates the onset of the Monterey Event, a positive carbon-isotope excursion, which lasted until *c.* 13.5 Ma (Vincent and Berger, 1985; Holbourn *et al.*, 2007, 2015). The approximate co-occurrence of the MCO with the Monterey Event indicates that warming was coupled with a significant disruption to the global carbon cycle. The Monterey Event has been interpreted to represent an increase in biological carbon isotope fractionation under high CO_2 conditions, together with enhanced burial of organic matter on continental shelves as a result of eustatic sea-level rise (Vincent and Berger, 1985; Holbourn *et al.*, 2007; Sosdian *et al.*, 2020).

Middle Miocene - Climate Transition

The MCO was followed by the Middle Miocene Climate Transition (MMCT), which, according to $\delta^{18}O$-based sea-level reconstructions, included a dramatic, three-step, global cooling event. The first step (Mi2a) took place around 14.8 Ma with *c.* 0.7ºC of

cooling and a *c.* 30m fall in sea level; this was followed at *c.* 13.8 Ma (Mi3) by 1.2°C of cooling and a *c.* 50m sea-level fall. The final cooling step (Mi4) took place at *c.* 12.8 Ma with *c.* 1ºC cooling and a 20-30 m sea-level fall (Miller *et al.*, 2020). The final temperature decrease and sea-level fall are believed to correspond to the establishment of a permanent East Antarctic Ice Sheet (EAIS) (Kennett *et al.*, 1975; Flower and Kennett, 1994; Holbourn *et al.*, 2005; Miller *et al.*, 2005, 2020; John *et al.*, 2011). Sea-level reconstructions suggest that the global mean sea level (GMSL) following the MMCT was only *c.* 12 m higher than in modern times. This dramatic cooling and sea-level fall is associated with an extinction event (Hoffman and Kitchell, 1984; Raup and Sepkoski, 1984; Torfstein and Steinberg, 2020). In the North Atlantic, the MMCT is characterised by a greater cooling at mid-latitudes than at high latitudes (*c.* 14.5 Ma), leading to a collapse in the North Atlantic SST gradient, which did not re-establish for *c.* 7 Myr (after Late Miocene cooling at high latitudes) (Super *et al.*, 2020). The gradient collapse is reportedly related to changes in the North Atlantic surface currents and deep water formation as the Earth cooled and the Arctic Gateway opened (Super *et al.*, 2020). It is unclear from the literature if the dramatic temperature changes in the North Atlantic also occurred in the eastern Mediterranean; this study sheds light on this issue.

The MMCT is believed to have been the result of a decrease in CO_2 levels following the highs of the MCO, paired with global changes in ocean circulation. This decrease in CO_2 levels is often attributed to the incorporation of CO_2 into organic material at continental margins (e.g. Monterey Formation, California, USA) (Pearson and Palmer, 2000). The increase in organic carbon burial related to the Monterey Event is believed to have driven the CO_2 drawdown (Vincent and Berger, 1985; Flower and Kennett, 1993, 1994; Sosdian *et al.*, 2020). Resultant increases in Antarctic bottom water and

North Atlantic deep-water production, as well as a reduction in saline water movement from the Indian Ocean to the Southern Ocean (Flower and Kennett, 1994), lead to changes in ocean circulation on a global scale, resulting in further cooling. A reduction in carbonate deposition is recorded globally between *c.* 12 Ma and *c.* 9 Ma (Mayer *et al.*, 1986; Lyle *et al.*, 1995) with a dramatic period of reduced carbonate deposition between *c.* 11.5 Ma and *c.* 10 Ma (Rouchy *et al.*, 2000; Diester-Haass *et al.*, 2004; Lübbers *et al.*, 2019). This interval is sometimes referred to as the Miocene Carbonate Crash (Lyle *et al.*, 1995). This carbonate crash has been related to ocean circulation changes as a result of the closure of the Panama Gateway (Lyle *et al.*, 1995), changes in nutrient storage (Lyle *et al.*, 2019) and chemical weathering processes (Lübbers *et al.*, 2019).

Late Miocene

Following the MMCT, foraminiferal $\delta^{18}O$ records indicate that temperatures remained cool. Global temperature and sea level fluctuated on the 1.2 Myr obliquity cycle as they did in the Early Miocene; however, fluctuations took place at a smaller magnitude (< 1ºC & *c.* 20 m) (Miller *et al.*, 2005, 2020; De Vleeschouwer *et al.*, 2017). High latitudes continued to cool throughout the Late Miocene as the Earth transitioned from an eccentricity-modulated precession to an obliquity-driven signal due to the existence of a stable East Antarctic Ice Sheet (EAIS), as indicated by SST reconstructions (Super *et al.*, 2020). Positive feedbacks such as ice-albedo, resulted in the development of a dynamic Arctic Ice sheet during the Late Miocene (De Vleeschouwer *et al.*, 2017). The 41-kyr obliquity cycle controlled some very minor sea-level fluctuations throughout the Late Miocene, although sea level is believed to have remained relatively stable during this time (De Vleeschouwer *et al.*, 2017; Miller *et al.*, 2020). Organic palaeothermometry (TEX_{86}) of samples from northern Italy (Monte dei

Corvi) indicate that the western Mediterranean region was significantly warmer than present at the start of the Late Miocene, and cooled dramatically at *c.* 8 Ma (Tzanova *et al.*, 2015). High aridity in the Mediterranean region during this time has been linked to the formation of the Sahara desert in North Africa (Zhang *et al.*, 2014). However, carbon and oxygen isotope data from Miocene lacustrine carbonates in the Kangal Basin (central Turkey) suggest that climate remained relatively stable in the Anatolian region during the Messinian Salinity Crisis (Meijers *et al.*, 2018b, 2020).

The Late Miocene Carbon Isotope Shift (LMCIS) is a *c.*1 ‰ decrease in benthic foraminiferal $\delta^{13}C$ from *c.* 7.2 to *c.* 7 Ma, probably due to a decrease in marine organic carbon burial rates. The LMCIS has been linked to the intensification of global cooling and the Asian winter monsoon during the Late Miocene (Holbourn *et al.*, 2018). The nature of the LCMIS is currently a topic of debate; it may be related to ocean circulation, atmospheric circulation, or a combination of other factors such as redistribution of nutrients, changes in photosynthetic pathways and terrestrial weathering (Dickens and Owen, 1999; Diester-Haass *et al.*, 2005; Holbourn *et al.*, 2015; Tzanova *et al.*, 2015; Herbert *et al.*, 2016; Lyle *et al.*, 2019). Biogenic blooms preserved in the fossil record have also been related to the LMCIS; the timing of the LMCIS coincides with the onset of the Late Miocene-Early Pliocene Biogenic Bloom (Dickens and Owen, 1999; Diester-Haass *et al.*, 2004, 2005).

Eustatic sea-level fall was previously inferred to be a cause of the loss of connection between the Atlantic Ocean and the proto-Mediterranean Sea, leading to the MSC (Hsü *et al.*, 1973b; Ryan, 1973; Adams *et al.*, 1977; Hsü, 1978). However, it is now believed that there was no major global sea-level change during this time. Benthic foraminiferal $\delta^{18}O$ records indicate that sea-level was relatively stable during this time (Miller *et al.*, 2020). The 400-kyr eccentricity cycle may have controlled the exact

timing of isolation, but is not believed to have been the driving force behind the event (Krijgsman *et al.*, 1999a). Climatic controls have been linked to changes in conditions and the onset of different phases of the MSC (such as evaporate deposition and Lago-Mare conditions), as well as the eventual reflooding of the Mediterranean basin (Rouchy and Caruso 2006).

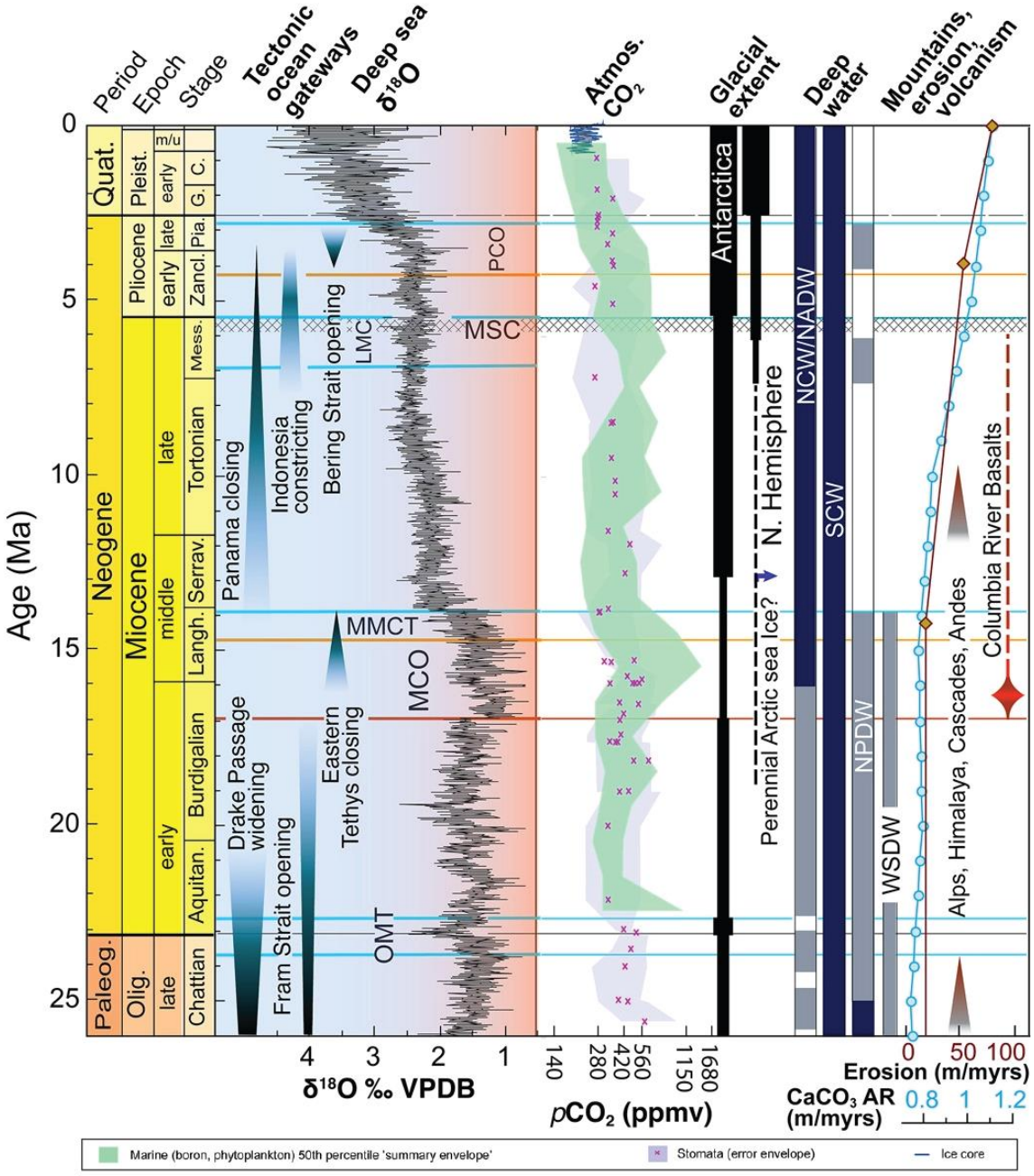


Figure 1.2.4.1 – Summary diagram of Miocene climatic, oceanic and tectonic changes. Adapted from Steinthorsdottir *et al*. 2020. Deep-water masses: NCW, Northern Component Water; NADW, North Atlantic Deep Water; AABW, Antarctic Bottom Water; NPDW, North Pacific Deep Water; TISW, Tethys Indian Ocean

Saline Water, (= Warm Saline Deep Water). Global erosion estimate (brown diamonds); Wilkinson (2005). CaCO3 AR = marine biogenic carbonate accumulation rate, Opdyke and Wilkinson (1988). LMC, Late Miocene Cooling; LMCIS, Late Miocene Carbon Isotope Shift; MCO, Miocene Climatic Optimum; MMCT, Middle Miocene Climatic Transition; MSC, Messinian Salinity Crisis; OMT, Oligocene–Miocene Transition; PCO, Pliocene Climatic Optimum. The Monterey Event = a *c.* 3.4 Myr-long positive $\delta^{13}C$ excursion indicative of an intense perturbation of the carbon cycle.

1.3 **Geological Context**

This section focuses on the geological history and tectonostratigraphic framework for the eastern Mediterranean region, with a specific focus on providing context for the deposition of sedimentary rocks in Cyprus during the Miocene.

1.3.1 Geological History of the Eastern Mediterranean Region

The island of Cyprus lies in the eastern Mediterranean region and makes up part of the Alpine-Mediterranean tectonic belt, a convergent orogenic belt, where the African, Arabian and Anatolian plates meet (Figure 1.3.1.6). The complex geological setting of Cyprus is illustrated by the present-day northward-dipping subduction zone around 50km south of Cyprus, where the African Plate dips beneath the Eurasian Plate. The formation of the Alpine-Mediterranean belt is related to the closure of the Neotethys Ocean (Dewey and Bird, 1970; Smith, 1971; Dewey *et al.*, 1973). The Neotethys Ocean is the most southerly in a series of Tethyan oceans and formed during the subduction of the Palaeotethys during the Mesozoic (Robertson *et al.*, 1991). At present, Cyprus sits in the eastern Mediterranean Sea. The Mediterranean Sea developed from the Southern Neotethys, a Neotethyan basin with a dynamic geological history from Late Palaeozoic to Recent times.

Palaeozoic

Prior to the Late Permian, the easternmost Mediterranean region formed the northern part of the Gondwanan continental margin (Garfunkel and Derin, 1984; Robertson and

Woodcock, 1986). By the Early to Late Permian, the region underwent rifting resulting in a broad marine transgression, leading to the formation of Permian shallow-marine limestones in the Kyrenia Range (Robertson, 1998b). Pulsed rifting began in the Southern Neotethys during the Late Permian, resulting in a period of ocean spreading and continental break-up that lasted until the Late Triassic (Carnian - Norian) (Robertson *et al.*, 2012a; Chen *et al.*, 2018; Robertson *et al.*, 2020; Chen *et al.*, 2022).

Triassic

Early-Mid Triassic rifting was associated with the formation of 'within plate' alkaline lavas such as those represented within the Dhiarizos Group of the Mamonia Complex in SW Cyprus (Robertson and Woodcock, 1979). During the Late Triassic, continental breakup commenced, associated with seafloor spreading and the eruption of Mid-Ocean Ridge basalts type lavas (Robertson, 1998b). The breakup of the Gondwanan margin resulted in the formation of a number of rifted microcontinents (e.g. the Mamonia complex in southwest Cyprus) separated by interconnected ocean basins (Robertson and Dixon, 1984; Şengör *et al.*, 1984). The Southern Neotethyan Ocean and the İzmir–Ankara–Erzincan Ocean ("Northern Neotethys") are recognised as the two major Neotethyan basins which formed between Gondwana and Eurasia during the Triassic (Robertson *et al.*, 2012a) (Figure 1.3.1.1).

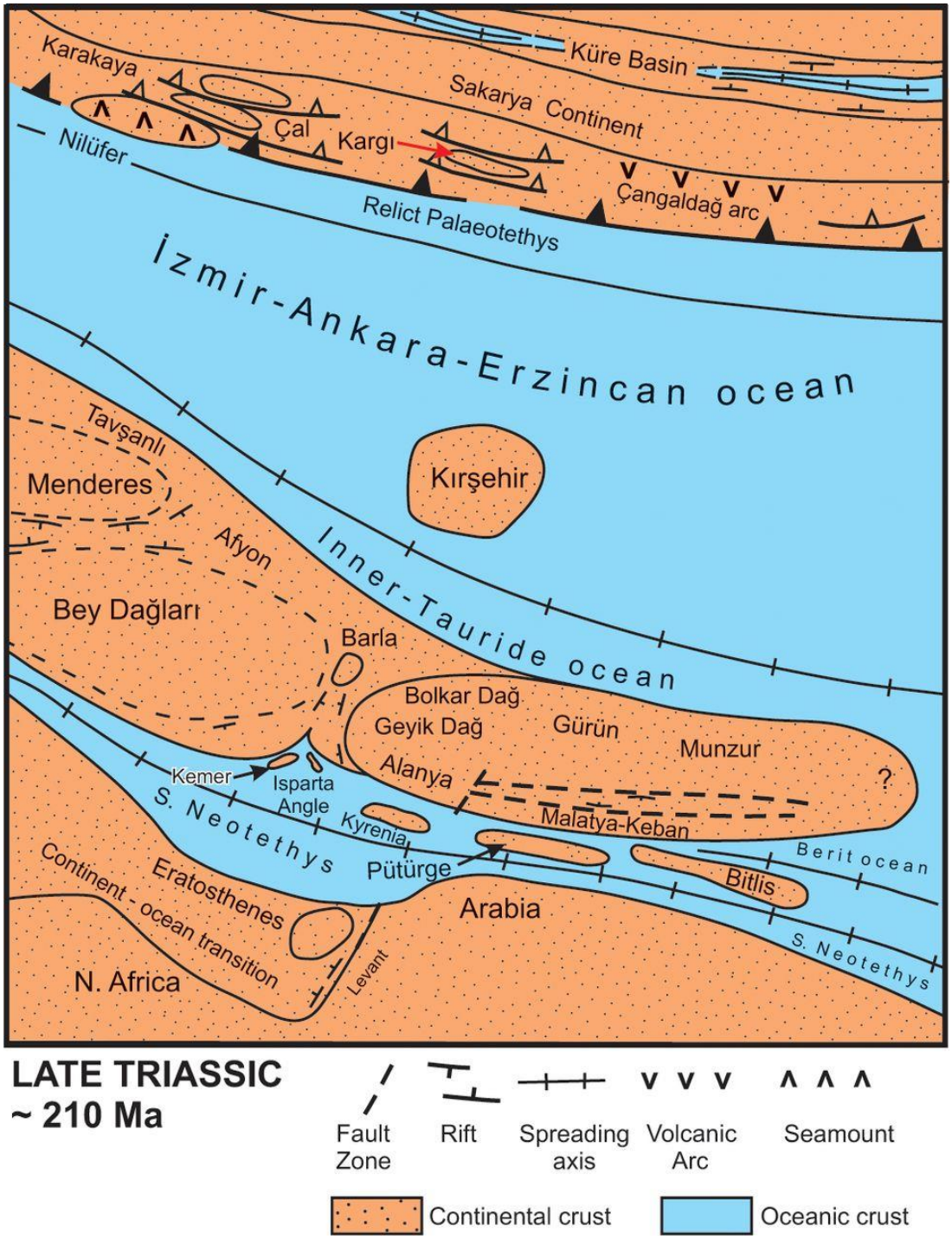


Figure 1.3.1.1 – Palaeogeographic reconstruction of the Neotethys area in the Late Triassic (Robertson et al. 2012).

Jurassic-Early Cretaceous

The Southern Neotethyan basins underwent passive subsidence during the Early-Mid Jurassic. A further pulse of rifting led to a second phase of spreading during the Late Jurassic - Early Cretaceous, with the Southern Neotethys reaching its maximum width

during the Early Cretaceous (Figure 1.3.1.2). The development of carbonate platforms and the deposition of deep-water sediments along the Neotethyan passive margins record this subsidence (Robertson, 1998b).

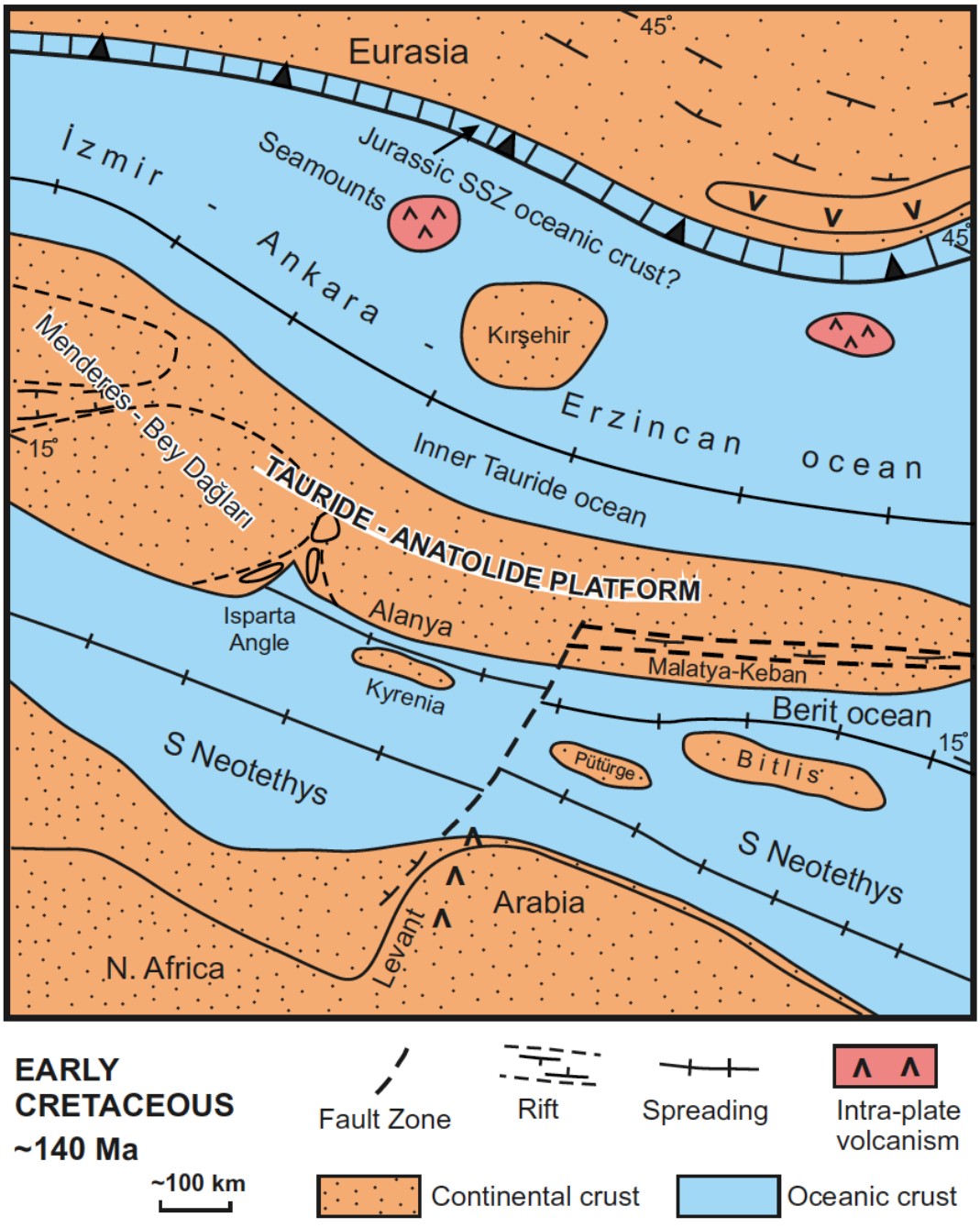


Figure 1.3.1.2 – Palaeogeographic reconstruction of the Neotethys area in the Early Cretaceous (Robertson et al. 2012).

Late Cretaceous

During the Late Cretaceous, plate convergence took place as the African Plate drifted northwards relative to the Eurasian Plate (Livermore and Smith, 1985; Savostin *et al.*, 1986) (Figure 1.3.1.3). This convergence was associated with the formation of ophiolites by supra-subduction zone spreading within several Neotethyan basins. Including the Southern Neotethys (e.g. the Troodos ophiolite, Cyprus, the Antalya and Hatay ophiolites, Turkey) (Pearce *et al.*, 1984; Robertson, 2000; Parlak *et al.*, 2009; Pearce and Robinson, 2010; Robertson *et al.*, 2012a, 2016b) and the İzmir–Ankara–Erzincan Ocean (e.g. the Lycian and Mersin Ophiolites) (Özgül, 1984; Andrew and Robertson, 2002; Göncüoglu *et al.*, 2003; Parlak and Robertson, 2004).

Due to the northward subduction of ocean basins, localised arc-type magmatism took place on the northern margins of the Southern Neotethyan basins, leading to the development of various magmatic arcs including the Kyrenia Range of Northern Cyprus (Robertson *et al.*, 2012b; Chen and Robertson, 2019).

Between the Late Campanian and the Early Eocene, the Troodos microplate rotated by *c.* 90º anti-clockwise related to the continued convergence of the African and Eurasian plates (Moores and Vine, 1971; Clube and Robertson, 1986; Allerton and Vine, 1987; Morris, 1996; Robertson, 1998b; Inwood *et al.*, 2009). During the Latest Cretaceous, the Troodos Massif and the Mamonia Complex were juxtaposed along arcuate high-angle serpentinite cored fault lineaments (Robertson and Woodcock, 1979; Swarbrick, 1980; Morris *et al.*, 1998; Bailey *et al.*, 2000b). The Maastrichtian Kathikas Formation (Swarbrick and Naylor, 1980) and the Maastrichtian to Oligocene Lefkara Formation (Robertson and Hudson, 1973; Robertson, 1976) were deposited on top of the newly amalgamated terranes.

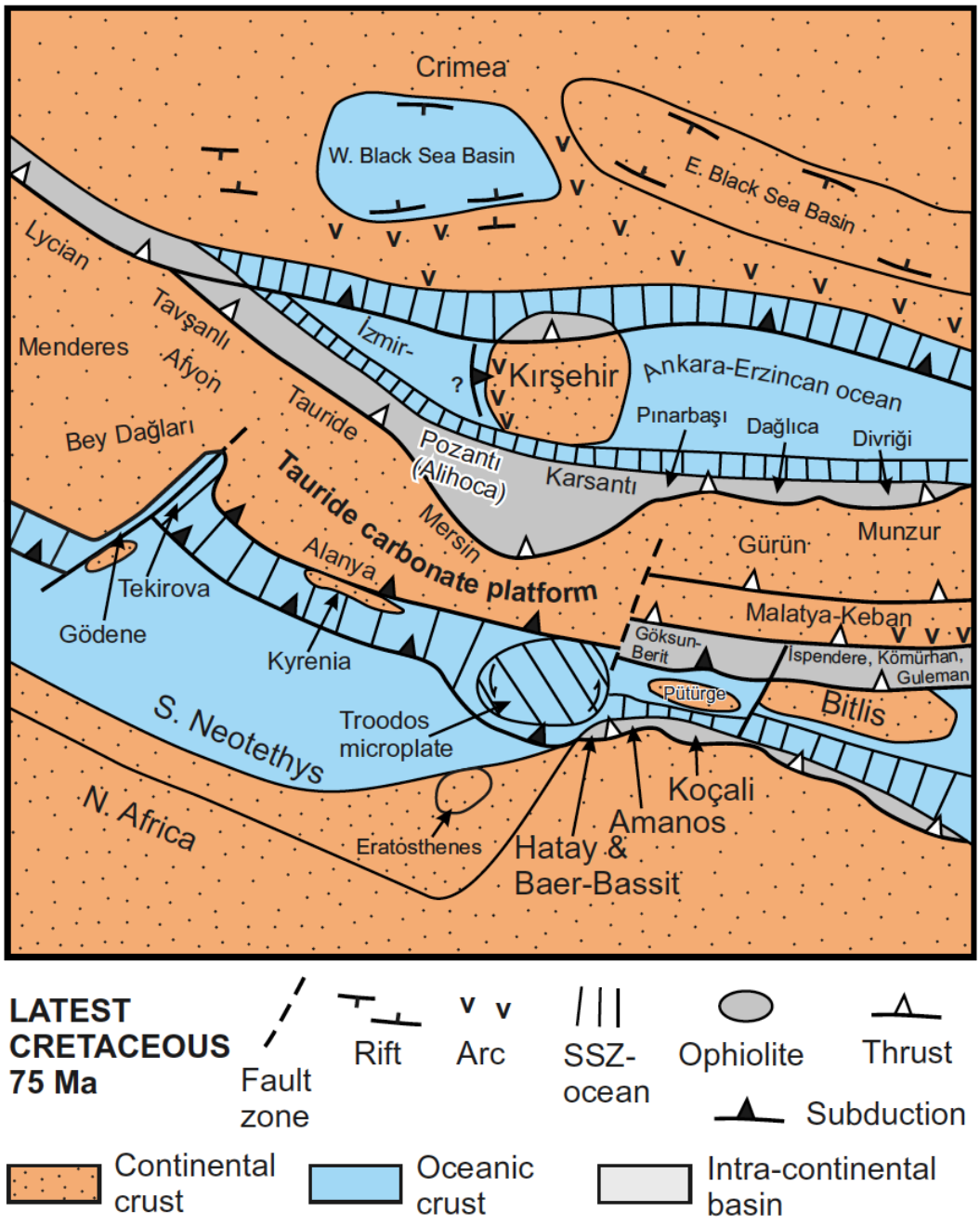


Figure 1.3.1.3 – Palaeogeographic reconstruction of the Neotethys area in the Latest Cretaceous (Robertson et al. 2012).

Palaeocene-Eocene

Kinematic reconstructions suggest that the Palaeocene-Eocene convergence of the African and Eurasian plates took place in a pulsed manner, possibly pausing completely during the earliest Cenozoic (Savostin *et al.*, 1986). The African-Eurasia convergence resulted in the closure of several Southern Neotethyan ocean basins

leading to rapid subsidence of the Kyrenia Range and subduction-related volcanism in a deep-water basinal setting (Robertson, 1998b; Robertson *et al.*, 2012a). By the Mid-Eocene the İzmir– Ankara–Erzincan Ocean had closed (Şengör and Yilmaz, 1981), whilst the Southern Neotethys remained open and continued to undergo northward subduction (Robertson *et al.*, 2016b) (Figure 1.3.1.4).

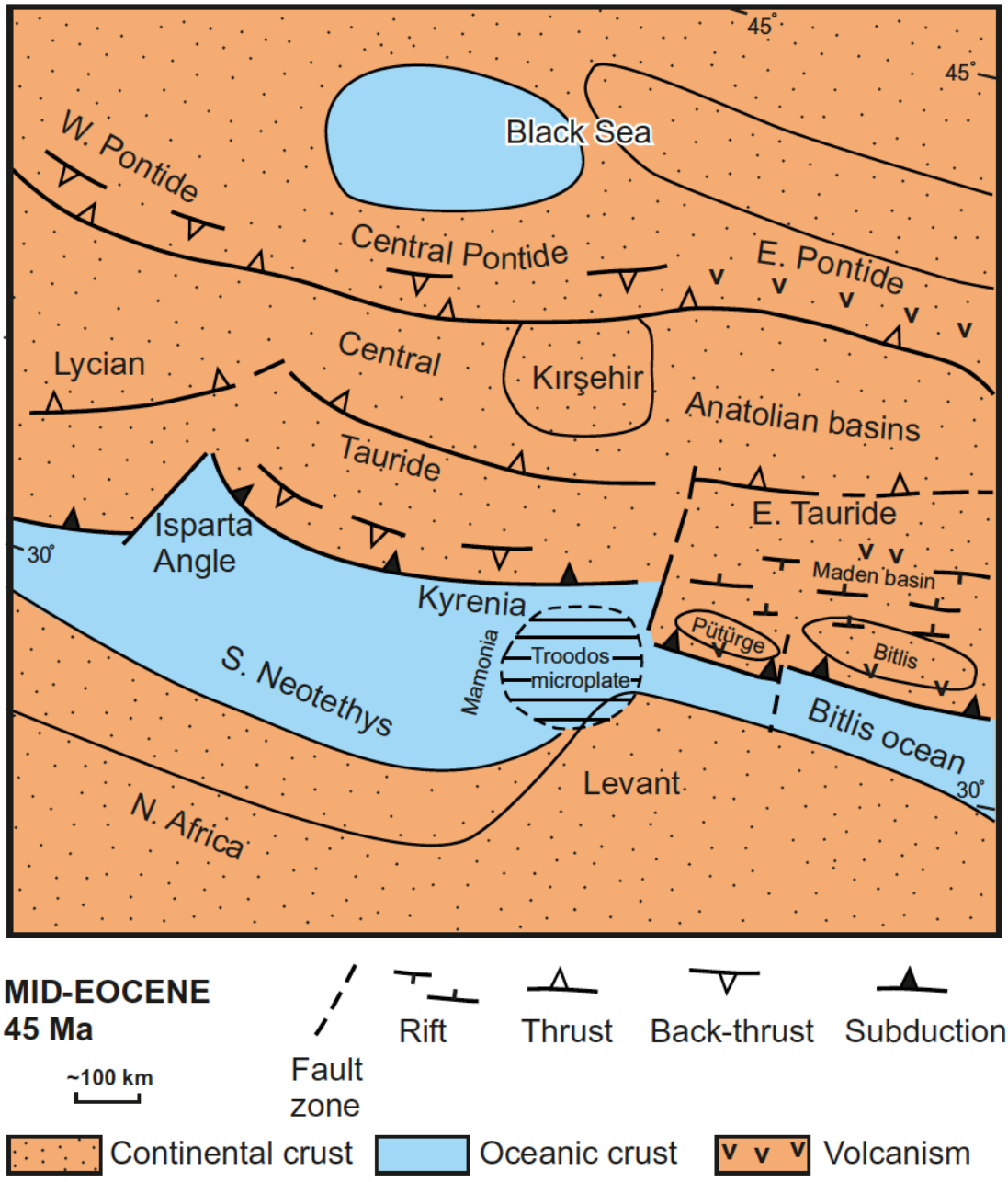


Figure 1.3.1.4 – Palaeogeographic reconstruction of the Neotethys area in the Mid-Eocene (Robertson et al. 2012).

During the Late Eocene, the African-Eurasia convergence culminated in the amalgamation of the Troodos Massif and the Kyrenia Range. Deepwater pelagic carbonate deposition (Lefkara Formation) continued on top of the Troodos Massif and the Mamonia Complex basement during this time (Robertson, 1976; Kähler and Stow, 1998; Miguez-Salas and Rodríguez-Tovar, 2019b). Pelagic carbonates also accumulated in the Kyrenia Range during the Palaeocene (Ayios Nikolaos (Yamaçköy) Formation) (Baroz, 1979; Robertson and Woodcock, 1986; McCay and Robertson, 2012).

Oligocene

During the Oligocene, the northward subduction of the Southern Neotethys continued. The ocean was reduced in size but remained open in the area that now makes up the easternmost Mediterranean. Pelagic carbonates continued to accumulate on the Troodos Massif and the Mamonia Complex. At the same time, siliciclastic turbidity deposits formed in the Kyrenia Range (Robertson, 1998b; McCay and Robertson, 2012).

Miocene

At the start of the Miocene, the Southern Neotethys was further reduced in aerial extent, due to the subduction of the African and Eurasian plates. Deep marine connection between the Southern Neotethys and the Indian Ocean remained through the eastern Tethys gateway (Bitlis Ocean) (Hüsing *et al.*, 2009). Deep marine sedimentation continued in the remnant Southern Neotethys Ocean, although the basin shallowed.

From the Early Miocene, the Troodos Massif was located on the over-riding plate a northward-dipping subduction zone located to the south of Cyprus (Robertson, 1998b).

Slab roll-back at the Cyprus Trench led to the extension of the Mesaoria (Mesarya) basin between the Kyrenia Range and the Troodos Massif (Kinnaird and Robertson, 2013; McCay and Robertson, 2013). Uplift related to the formation of this subduction zone resulted in a phase of varied localised faulting and local relative sea-level fall, leading to the deposition of hemipelagic carbonates and the growth of localised coral reefs (Robertson, 1977a, 1990; Follows, 1990; Follows *et al.*, 1996; Cannings *et al.*, 2020).

Localised compression took place in southern Cyprus during the Early Miocene, with subsequent extension during the Middle to Late Miocene. The Polis graben formed in northwestern Cyprus during the Mid-Late Miocene associated with major extensional faulting in north and northwestern Cyprus (Payne, 1995; Payne and Robertson, 1995).

During the Aquitanian (*c.*20 Ma), continental collision between the Eurasian and Arabian plates began along the Bitlis thrust zone, with the Bitlis Ocean eventually closing before the end of the Burdigalian (*c.*16 Ma) (Okay *et al.*, 2010) (Figure 1.3.1.5). Despite the closure of the Bitlis Ocean in the Early Miocene, Mid-Miocene deep marine connectivity between the Southern Neotethys and the Indian Ocean was possible through the Kahramanmaraş Basin (Hüsing *et al.*, 2009), although most studies infer that only shallow water connectivity remained following the Early Miocene (Goff *et al.*, 1995; Taylforth *et al.*, 2014). Any possible deep-marine connection between the Southern Neotethys and the Indian Ocean terminated by the Late Miocene (*c.*11 Ma) (Hüsing *et al.*, 2009). The Mediterranean Sea, as a remnant of the Southern Neotethys, was reduced to the present-day eastern Mediterranean basin by the Tortonian and was by then completely isolated from the Indian Ocean, but open to the Atlantic Ocean in the western Mediterranean.

The relative motion between the African and Eurasian Plates changed from north-south to northwest-southeast during the Middle-Late Miocene time (Le Pichon *et al.*, 1979; Jolivet and Faccenna, 2000; Nocquet and Calais, 2004; Jolivet *et al.*, 2006). This change in plate motion relates to the opening of the Red Sea, as well as to the closure of the Betic Straight and the Riffian Corridor leading to a loss of connection between the Atlantic Ocean and the proto-Mediterranean Sea. This isolation of the Mediterranean Sea led to the Messinian Salinity Crisis and the deposition of thick halite and gypsum units in deep basins across the Mediterranean area, including Cyprus (Hsü *et al.*, 1973b; Robertson *et al.*, 1995; Krijgsman *et al.*, 2002; Wade and Bown, 2006; Manzi *et al.*, 2016).

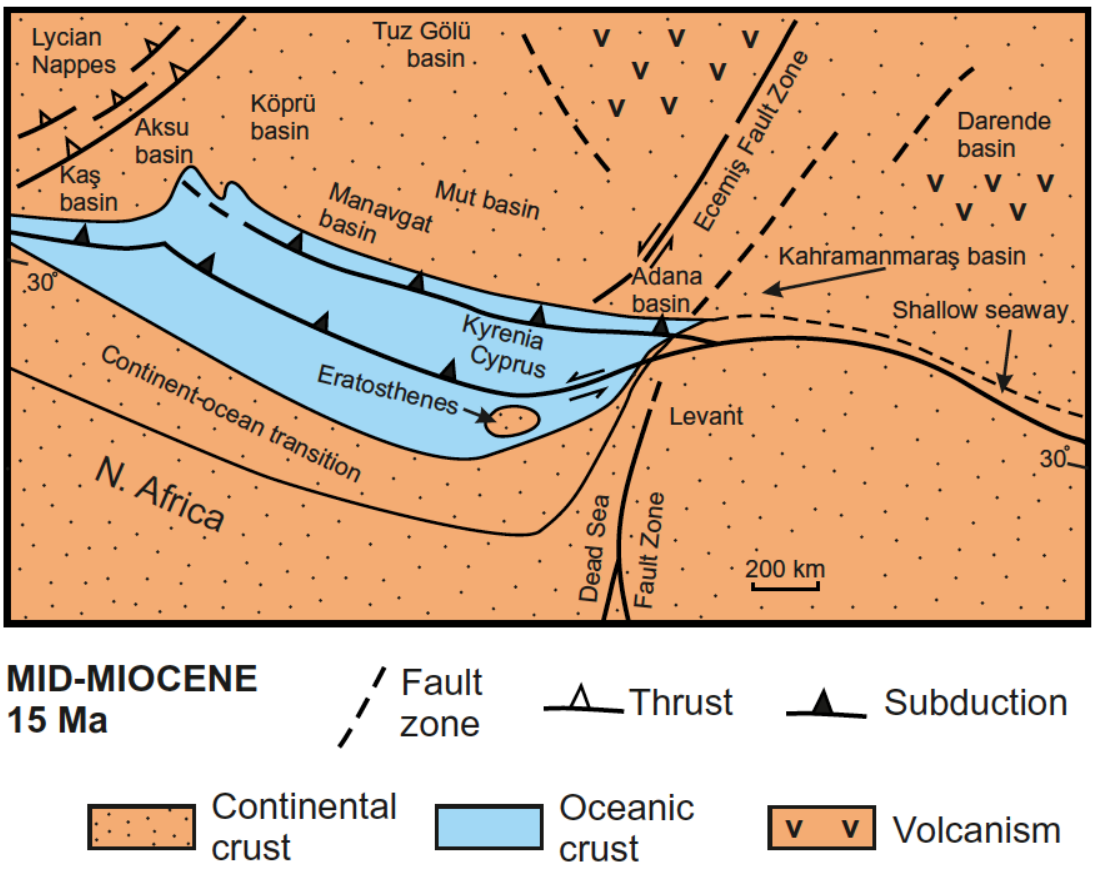


Figure 1.3.1.5 – Palaeogeographic reconstruction of the Neotethys area in the Mid Miocene (Robertson *et al.* 2012).

Pliocene-Pleistocene

Renewed connection between the Atlantic Ocean and the Mediterranean Sea led to the refilling of the Mediterranean Basins. This event marks the end of the Messinian Salinity Crisis and the start of the Pliocene, sometimes referred to as the Zanclean Flood (Garcia-Castellanos *et al.*, 2009).

The African Plate continued to converge northwards with the Eurasian Plate, leading to collision between the Eratosthenes Seamount with the Cyprus Trench to the south of Cyprus. This collision resulted in the rapid uplift of the Kyrenia Range and Troodos Massif (Robertson, 1977a, 1998d, 1998c; Poole and Robertson, 1998; Kinnaird *et al.*, 2011; Palamakumbura and Robertson, 2016, 2018). Ultramafic rocks in the overriding slab underwent serpentinite diapirism, resulting in the updoming of the Troodos

ophiolite (Poole *et al.*, 1990; Robertson, 1990; Poole and Robertson, 1991; Robertson, 1998b, 2000; Morag *et al.*, 2016; Evans *et al.*, 2021).

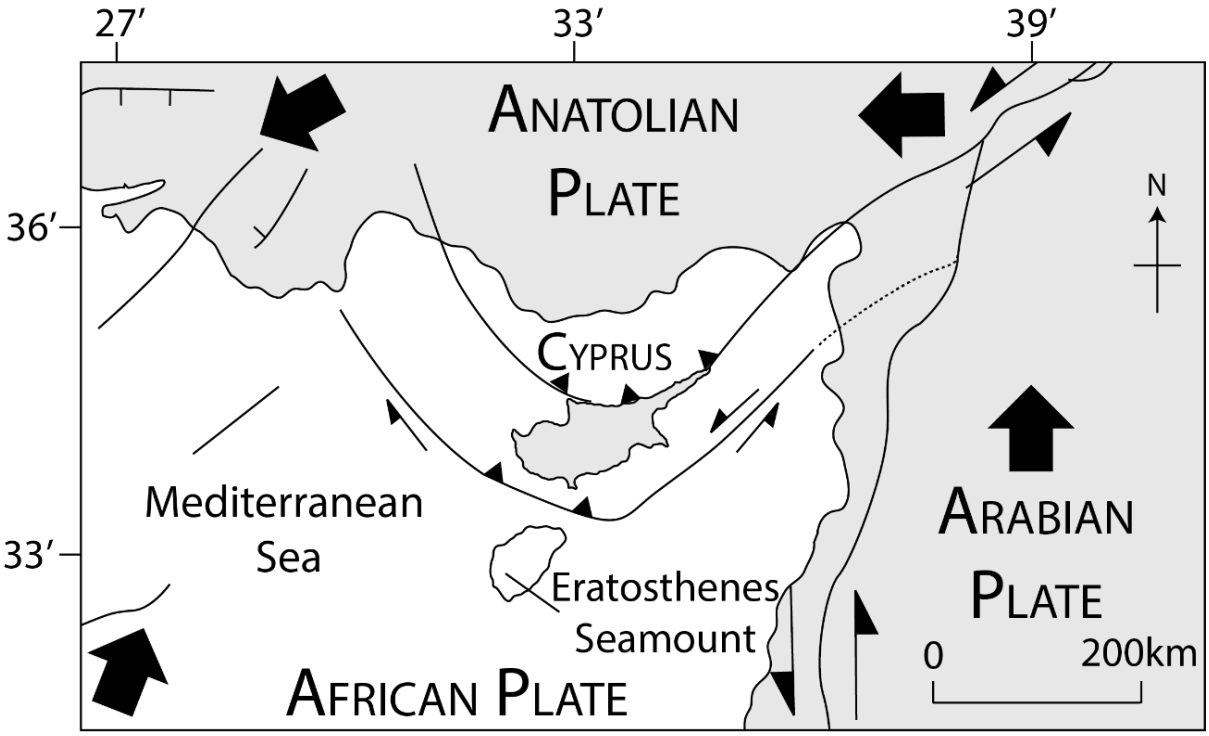


Figure 1.3.1.6 – Overview map showing the tectonic setting of Cyprus in the modern eastern Mediterranean (modified from Follows and Robertson 1990, Robertson et al. 1991 and Payne 1995).

1.3.2 Tectonostratigraphic Framework of Cyprus

The island of Cyprus is composed of three distinct geological units (terranes), each of which has a unique geological history. The Kyrenia (Girne) range in the north (Robertson and Woodcock, 1986; Robertson, 1990), the Troodos Ophiolite (Gass and Masson-Smith, 1963; Moores and Vine, 1971) in the island's centre, and the Mamonia Complex in the west (Lapierre, 1972; Robertson and Woodcock, 1979; Robertson, 1990; Robertson and Xenophontos, 1993) (Figure 1.3.2.1). The main topographic highs on Cyprus today indicate the approximate configuration of these litho-tectonic assemblages (terranes), with the Kyrenia (Girne) Range in the north, the Troodos Massif in the centre and the Akamas peninsula in the west (made up of the Mamonia Complex and Troodos ophiolite). The Troodos Massif is fringed by the circum-Troodos

sedimentary cover, a varied sedimentary and siliciclastic sequence which also overlies the Mamonia Complex in some places (Robertson, 1977a).

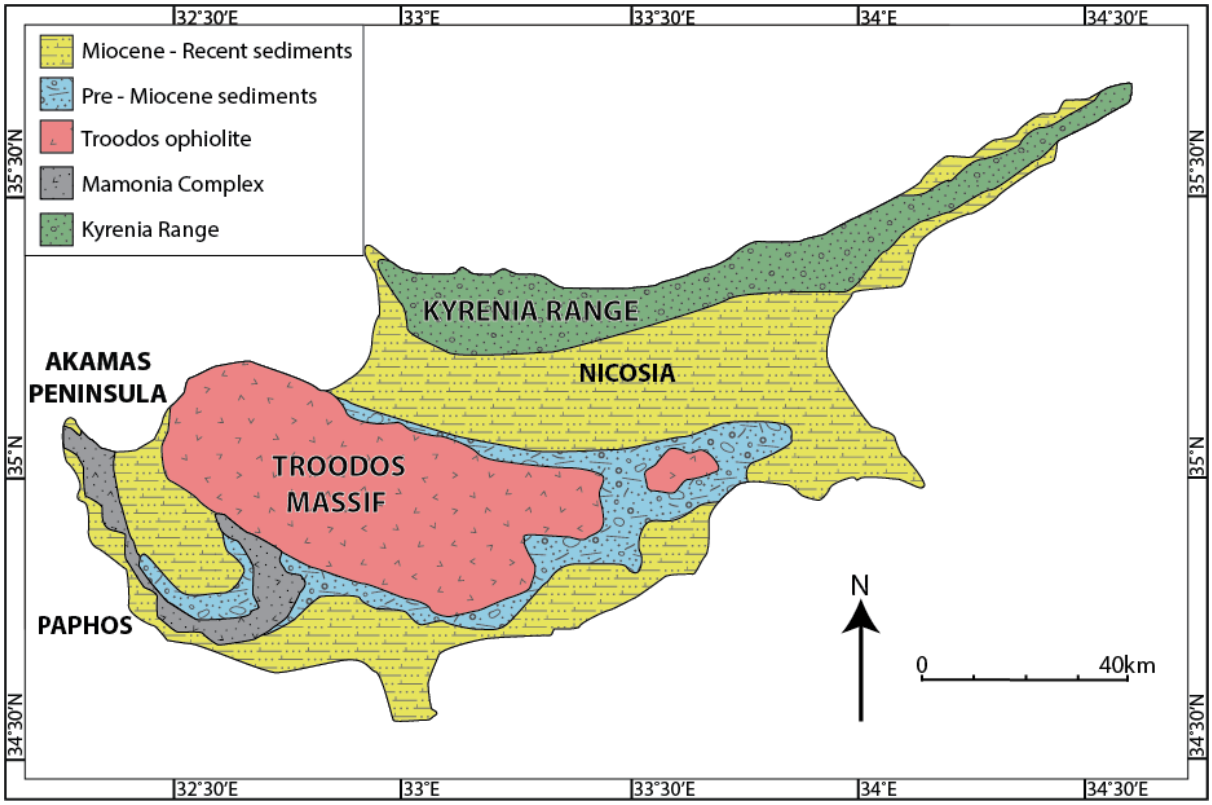


Figure 1.3.2.1 – A simplified geological map of Cyprus showing the three 'terranes' that make up the island of Cyprus (After Follows 1990).

The Kyrenia (Girne) Range

The Kyrenia (Girne) range is a narrow arcuate belt, which is several kilometres in width, spanning the northernmost coast of the island. The Mesozoic – Cenozoic sedimentary rocks of the Kyrenia range are divided into four main successions. These successions are separated by major unconformities, which represent distinct notable deformation events (Robertson and Woodcock, 1986; McCay *et al.*, 2013).

The Trypa (Tripa) Group is a *c.* 700m succession of Late Triassic-Cretaceous, mainly shallow-water platform carbonates. During the Late Cretaceous, this unit underwent brecciation, recrystallization and greenschist-grade metamorphosis (Ducloz, 1972; Robertson and Woodcock, 1986; Robertson *et al.*, 2012b).

The Lapithos (Lapta) Group unconformably overlies the Trypa Group. The Lapithos Group is a *c.*1500m thick Late Cretaceous (Campian)-Middle Eocene sequence of redeposited volcanic sediments, carbonate breccias, pelagic carbonates, basic volcanic rocks and calcareous sandstones. This succession was deformed and metamorphosed during the Late Eocene. Together with the Trypa Group. The Lapithos Group forms the axis of the Kyrenia Range in the east (Ducloz, 1972; Robertson and Woodcock, 1986; Robertson *et al.*, 2012b, 2014; McCay *et al.*, 2013; Chen *et al.*, 2022).

The Kythrea (Değirmenlik) Group unconformably overlies the Lapithos Group. The Kythrea Group is a Late Eocene-Late Miocene succession of variably deformed non-marine to relatively deep marine conglomerates, sandstones and mudstones (Robertson *et al.*, 2014; Chen *et al.*, 2022). This succession underwent uplift and subsequent deformation during the Late Miocene-Early Pliocene (McCay, 2011; McCay *et al.*, 2013).

The Mesaoria (Mesarya) Group is a Pliocene-Pleistocene succession of conglomerates, sandstones and marls. An unconformity of Messinian age separates the Mesaoria Group from the underlying Kythrea Group (McCay, 2011; McCay and Robertson, 2013; McCay *et al.*, 2013). Additional information on the Mesaoria Group is also included in the 'circum-Troodos' cover section of this introduction. The tectonically controlled deposition of Pleistocene-aged terraces in the Kyrenia Range provides insights into the uplift history of the Kyrenia Range during the Pleistocene (Palamakumbura and Robertson, 2016; Palamakumbura *et al.*, 2016a, 2016b). Pliocene-Pleistocene sedimentary successions in the Mesaoria Basin illustrate the development and infill of a basin located between two tectonically active lineaments (the Troodos Massif and Kyrenia Range) (Palamakumbura and Robertson, 2018).

The Troodos Massif

The Troodos Massif is exposed in central and southern Cyprus. It comprises the Troodos Ophiolite and its sedimentary cover. The ophiolite consists of serpentinized upper mantle harzburgite, overlain by layered ultramafic-mafic cumulates, layered and massive gabbros, local plagiogranite, sheeted dolerite dykes and basaltic pillow lavas (Gass and Masson-Smith, 1963; Moores and Vine, 1971; Allerton and Vine, 1987; Robertson and Xenophontos, 1993; Mackenzie *et al.*, 2006). The Troodos Ophiolite formed by supra-subduction zone spreading during the Late Cretaceous, c. 91 Ma (Kidd and Cann, 1974; Schmincke *et al.*, 1983; Mukasa and Ludden, 1987; Pearce and Robinson, 2010; Morag *et al.*, 2016).

The Mamonia Complex

The Mamonia Complex is a structurally complex litho-tectonic assemblage, which is exposed in western Cyprus; it represents remnants of a rifted passive margin and marginal ocean crust of the Southern Neotethys. The Mamonia Complex comprises broken formations and melanges containing sedimentary, volcanic and locally metamorphosed rocks (Swarbrick, 1980).

The volcanic and metasedimentary Dhiarizos Group represents the Late Triassic ocean floor, seamounts and atolls. The Dharizos Group is composed of alkaline-tholeiitic pillows lavas, mid-ocean ridge basalts and volcanic breccias in addition to recrystallized algae and coral-rich boundstones, coquina (shell detrital) limestones, with both carbonate and radiolarian mudstones (Malpas *et al.*, 1992; Lapierre *et al.*, 2007).

The Agios Photios Group is composed of a sequence of Middle-Upper Triassic quartzose turbidites that are interbedded with deepwater carbonate mudstone and

limestone. The Agios Photios Group also includes Jurassic radiolarian mudstones and reworked carbonates followed by Lower Cretaceous quartzarenite mudflows (Robertson and Woodcock, 1979; Torley and Robertson, 2018).

The Agia Varvara Group comprises amphibolite, metapelite, metachert and marble. This unit is interpreted to represent a metamorphosed equivalent of the Dhiarizos Group (Swarbrick, 1980; Robertson and Woodcock, 1986; Malpas *et al.*, 1992; Bailey *et al.*, 2000b). The metamorphic history of the Agia Varvara Group provides key insights into the process of amalgamation of the Troodos ophiolite with the Mamonia Complex (Swarbrick and Naylor, 1980; Malpas *et al.*, 1992; Bailey *et al.*, 2000b).

Circum-Troodos Cover

The Troodos ophiolite is covered by a thick (200-1000m) sequence of sedimentary rocks, which accumulated from the Late Cretaceous (92-85 Ma) to recent times (Robertson and Hudson, 1974; Robertson, 1977a; Robertson and Xenophontos, 1993; Gass *et al.*, 1994). This sequence has been the subject of numerous studies investigating the palaeoclimatic and oceanographic history of the eastern Mediterranean region (Read, 1993; Robertson and Xenophontos, 1993; Davies, 2001; Robertson *et al.*, 2009, 2019; Coletti *et al.*, 2019b), the tectonic evolution of the eastern Mediterranean region (Robertson, 1990, 2000; Robertson *et al.*, 1991, 2009) and uplift history of the Troodos ophiolite (Robertson and Xenophontos, 1993; Kinnaird and Robertson, 2013; Palamakumbura and Robertson, 2018; Balmer *et al.*, 2019; Murray and Robertson, 2020). The Circum-Troodos cover has significant spatial and temporal irregularities due to the uneven topography of the underlying Troodos ophiolite and the amalgamation of the Troodos ophiolite with the Mamonia Complex.

Cretaceous – Palaeocene Circum-Troodos Cover

The Perapedhi Formation is an Upper Cretaceous (92-90 Ma) succession of metalliferous Iron and manganese-rich, hydrothermal sediments (umbers), manganese-rich shales and mudstones (Robertson and Hudson, 1973; Robertson, 1975; Boyle and Robertson, 1984). Together with the Kanaviou Formation and the Kathikas Melange, the Perapedhi Formation represents the first phase of *in situ* sedimentation on top of the newly created, topographically irregular ocean floor of the Troodos ophiolite. The Campanian-Maastrichtian-age Kannaviou Formation comprises bentonitic clays with volcaniclastic sandstones and siltstones (Lapierre, 1975; Robertson, 1977b; Urquhart and Banner, 1994; Gilbert and Robertson, 2013; Chen and Robertson, 2019).

Late Cretaceous – Oligocene Sedimentary Cover of the Troodos Ophiolite and Mamonia Complex

The Kathikas Formation overlies both the Kannaviou Formation (Circum-Troodos cover) and the Agios Photios Group (Mamonia Complex). The Kathikas Formation is formed of poorly sorted submarine debris-flow deposits up to several hundred metres thick. These debris-flow units contain deformed and fragmented Mamonia Complex-derived clasts along with rare clasts of Troodos ophiolite material (Swarbrick and Naylor, 1980). A red/purple silt matrix supports these debris flow units. The contact between the Mamonia Complex and the Kathikas Formation is gradational in some places (Swarbrick and Naylor, 1980; Swarbrick and Robertson, 1980). Interbeds of Late Maastrichtian-Early Palaeocene age chalks occur within the debris flow units in some localities (Swarbrick and Naylor, 1980; Urquhart and Banner, 1994; Lord *et al.*, 2000).

The Lefkara Formation is a Cretaceous to Oligocene-aged sequence of deep-water pelagic carbonates (Mantis, 1970; Robertson and Hudson, 1973; Robertson, 1976; Kähler and Stow, 1998; Lord *et al.*, 2000). The nature of the contact between the Lefkara Formation and the underlying Kathikas Melange is complex and is the subject of ongoing PhD research by Elizabeth Balmer. It is separated into four members, each representing a different depositional environment.

The Lower Marl Member is Maastrichtian (Late Cretaceous) to Early Eocene in age. This member is mainly pinkish marls and white chalky marls, very rare chert beds are occasionally present. The Lower Marl Member has vast thickness irregularities (*c.* 25-100m) and is laterally discontinuous (Kähler and Stow, 1998).

The Chalk and Chert Member is a Lower to Middle Eocene succession of regularly bedded chalks and marls of varying carbonate content, together with common interbeds of chert and silicified micrite (Robertson, 1977c). The unit has a maximum thickness of *c.* 300m. Incomplete Bouma sequences are indicated by sedimentary structures within this unit, indicating turbiditic deposition. The frequency of these calciturbidite deposits increases in the upper part of the unit (Robertson, 1976; Kähler and Stow, 1998; BouDagher-Fadel and Lord, 2006).

The Massive Chalk Member is an Upper Eocene to Uppermost Oligocene unit of variable thickness (*c.*70-250m). Thick beds of massive chalks dominate this unit, occasional marly chalk beds also occur, and chert is completely absent (Robertson, 1976).

The Upper Eocene to uppermost Oligocene Upper Marl Member is a succession of thinly bedded marls and chalky marls with a variable thickness of up to 200m. Fossil contourites are preserved in this unit, indicating reworking due to the persistent action

of bottom water currents (Kähler and Stow, 1998; Stow *et al.*, 2002; Miguez-Salas and Rodríguez-Tovar, 2019a; Hüneke *et al.*, 2021; Hernández-Molina *et al.*, 2022). Chert is absent from this unit (Robertson, 1976). In western Cyprus, calcarenites rich in large benthic foraminifera and shell fragments are exposed in small patch-like outcrops. These benthic foraminifera indicate an Early Chattian (Late Oligocene) age (Cannings *et al.*, 2020).

Miocene Cover of the Troodos Ophiolite and Mamonia Complex

The Miocene-aged Pakhna Formation stratigraphically overlies the Lefkara Formation. Due to the spatial irregularity and lateral discontinuity of the Lefkara Formation, the contact between the Pakhna Formation and the Lefkara Formation is complex and lacks uniformity (Bagnall, 1960; Pantazis, 1967; Eaton and Robertson, 1993; Read, 1993). The Pakhna Formation generally lies directly above the 'Upper Marls' of the Lefkara Formation. However, the localised absence of all or some of the Lefkara Formation means that in some places the Pakhna Formation sits unconformably on top of the stratigraphically lower Members of the Lefkara Formation, or directly on top of the Mamonia Complex Basement (Eaton and Robertson, 1993; BouDagher-Fadel and Lord, 2006). The nature of this contact is the subject of ongoing PhD research (by Elizabeth Balmer) outside of the scope of this project. The Paknha Formation is of variable thickness (*c.* 350-1200 m) (Follows, 1990; Eaton and Robertson, 1993; BouDagher-Fadel and Lord, 2006).

The Pakhna Formation is an Early-Late Miocene-aged unit of pelagic/hemipelagic sediments together with turbiditic and shallow-water carbonates. The Pakhna Formation also includes debris-flow deposits containing reworked Palaeogene and Neogene carbonates and locally, rare material from the Troodos ophiolite and Mamonia Complex Basement (Eaton and Robertson, 1993; BouDagher-Fadel and

Lord, 2006). The change in depositional environments from the deeper water Lefkara Formation to the shallower Pakhna Formation may be related to regional collision, and has been linked to tectonic instability and uplift during the Miocene (Robertson, 1977a, 1998a; Robertson *et al.*, 2009). The Pakhna Formation is composed of the 'undifferentiated Pakhna Formation' and the reef-related Terra and Koronia Members.

Nannofossil ooze (chalk) and planktic foraminifer-rich calcareous mudstones (marls) as well as bioclastic limestones and conglomerates form the undifferentiated Pakhna Formation. The chalks of the undifferentiated Pakhna Formation are off-white to buff in colour, and show cyclical alteration of darker (buff coloured), more consolidated bands and lighter (off-white) less consolidated bands. This cyclical alteration is also present in the calcareous mudstones of the Pakhna Formation, which are off-white to pinkish in colour. Fine parallel laminations and fining upwards occur within calcareous mudstone and chalk beds. In general, stratigraphically lower sections of the unit preserve more chalk deposits, with increased calcareous mudstone deposition higher up, indicating shallowing upwards in the succession (Eaton and Robertson, 1993; Cannings *et al.*, 2020). Due to the irregular sea floor topography and the presence of localised sub-basins, chalk and calcareous mudstones of the Pakhna Formation were deposited synchronously in different localities. These chalks and calcareous mudstones are the lithologies sampled for the Kottaphi Hill succession studied in this project. Further details on the changes in deposition from chalk to calcareous mud facies are provided in Chapter 3.

In some areas (e.g. the Polis graben area), reworked chalk clasts are found within the calcareous mudstones of the Pakhna Formation. Interbeds of organic-rich calcareous mudstones with a fining upwards sequence are present in Late Miocene deposits within Pakhna Formation, these are interpreted to represent sapropels (Davies, 2001;

Smith and Gale, 2009; Cannings *et al.*, 2020; Athanasiou *et al.*, 2021; Bialik *et al.*, 2022).

The undifferentiated Pakhna Formation also includes debris-flow deposits. These debris-flow deposits are preserved as off-white polymictic conglomerates, which preserve coral material, together with algae, echinoderms and bivalve shell fragments (Follows, 1990; Payne, 1995; Follows *et al.*, 1996; Cannings *et al.*, 2020). This conglomerate is typically interbedded with calcareous mudstones.

An Upper Miocene calcarenite is exposed as patch-like deposits in some localities. This calcarenite is rich in benthic foraminifera and lacks sedimentary structures or bedding (Follows, 1990; Follows *et al.*, 1996; Cannings *et al.*, 2020). This facies is thought to be related to the Late Miocene reef growth phase associated with the Koronia Member and thus is included as part of the Koronia Member by some authors (Follows, 1990).

Two reef-related members are contained within the Paknha Formation. The Terra Member is the stratigraphically lowermost of these units. The basal contact of the Terra Member is the subject of ongoing PhD research outside of the scope of this study, by Elizabeth Balmer. In some places, the Terra Member is overlain by reworked Lefkara Member Material, however, the Terra Member is generally assumed to lie stratigraphically above Oligocene Lefkara Formation chalk (Eaton and Robertson, 1993; Follows *et al.*, 1996; BouDagher-Fadel and Lord, 2006). The undifferentiated Pakhna Formation bounds the Terra Member, both at its top and laterally. The Terra Member is composed of framestones, which display high levels of algal and coral biodiversity (Follows, 1990; Follows *et al.*, 1996; Coletti *et al.*, 2021). The best-preserved examples of Terra Member reef material are in the SE of Cyprus at Cape

Greco (Follows, 1990, 1992; Follows *et al.*, 1996), where the Terra Member is thought to have grown on a stable platform, with little tectonic activity. The reef facies Terra Member in SE Cyprus is associated with a benthic foraminifera-rich calcarenite facies, interpreted as foraminiferal shoals surrounding the reef. The Terra Member is also exposed in the Polis graben area of western Cyprus, where it is preserved as localized *in situ* reef material, together with more widespread exposures of reworked shallow water carbonate material. Benthic foraminiferal biostratigraphy indicates that the Terra Member is the same age in south-eastern and western Cyprus. (Follows *et al.*, 1996). The Terra Member is not present on the northern Margin of the Troodos Ophiolite (e.g. Kottaphi Hill).

The Koronia Member is the younger of the two reef-related members of the Pakhna Formation. On the northern margin of the Troodos Massif the Koronia Member is exposed as discontinuous fringing reefs, believed to have grown on faulted blocks (Follows, 1990; Follows *et al.*, 1996). At Happy Valley in southern Cyprus, the Koronia Member is also exposed as large detached blocks. In western Cyprus, the Koronia Member is exposed mainly as reef talus material with localised outcrops of *in situ* reef material at high elevations. The Koronia Member contains a reef facies that is almost entirely composed of Poritid coral. Laminar poritids provide binding material, while both ramose forms and massive forms provide a framework (Follows, 1990; Coletti *et al.*, 2021). The off-reef facies of the Koronia Member is composed of rhodolith-dominated packstones, calcarenites and chalks containing scattered bivalve and poritid fragments (Follows, 1990). Deposits of Koronia Member-derived talus material also contain clasts of bioclastic calcarenite. On the east flank of the Polis graben, the Koronia Member talus includes clasts of ophiolitic material (e.g. basalt and serpentinite) (Follows, 1990; Follows *et al.*, 1996). The uppermost exposures of the

Koronia Member have been karstified and have a network of fissures on their karstified surfaces; these are interpreted as neptunian dykes and are infilled by material from the Pliocene Nicosia Formation (Cannings *et al.*, 2020).

The Kalavasos Formation is the youngest Miocene unit within the 'circum-Troodos' cover and overlies the uppermost Pakhna Formation. The onset of the Messinian Salinity Crisis (MSC) controlled the deposition of the Messinian-aged Kalavasos Formation. The Kalavasos Formation contains three units, which represent different phases of the salinity crisis. The pre-evaporitic unit is composed of cyclical alterations of chalk and gypsum, indicating that increased salinity and evaporate deposition interrupted chalk deposition during this period. The evaporitic unit contains exclusively evaporitic rocks, with several varieties of gypsum facies represented (Robertson *et al.*, 1995). The post-evaporitic unit is only preserved in southwest Cyprus and is a succession of marls, conglomerates, carbonates and palaeosols dated to the latest Messinian. The post-evaporitic unit is recognised as a 'Lago Mare' succession and represents sediments deposited in brackish and freshwater environments directly preceding the 'reflooding' of evaporitic basins (Orszag-Sperber *et al.*, 1989, 2009; Rouchy *et al.*, 2001).

Pliocene-Recent Cover of the Kyrenia range, Troodos Ophiolite and Mamonia Complex

The Mesaoria (Mesarya) Group is a Pliocene-Pleistocene Succession of conglomerates, sandstones and marls. An unconformity of Messinian age separates the Mesaoria (Mesarya) Group from the underlying Kythrea (Değirmenlik) Group (Baroz, 1979; McCay, 2011; McCay and Robertson, 2013; McCay *et al.*, 2013). The Nicosia (Lefkoşa) Formation was deposited across Cyprus during the Pliocene and is included in both the 'circum-Troodos' and Kyrenia sedimentary cover. The Nicosia

(Lefkoşa) Formation is composed of marls, chalks, mudstones, sandstones, bioclastic limestones and conglomerates (McCallum and Robertson, 1995b, 1995a; Robertson *et al.*, 2009; Kinnaird *et al.*, 2011; Palamakumbura and Robertson, 2018; Balmer *et al.*, 2019). The Nicosia (Lefkoşa) Formation is overlain by the Athalassa (Gürpınar) Formation; a Pliocene to Pleistocene aged unit, which is dominated by calcarenite and calcirudite, this is in turn overlain by a Pleistocene aged fanglomerate sequence (Palamakumbura *et al.*, 2016a; Palamakumbura and Robertson, 2018). Well-developed marine and non-marine terraces of Pliocene to Pleistocene age are preserved across the island of Cyprus and have been the subject of numerous studies on the uplift of the Troodos ophiolite (Kinnaird *et al.*, 2011; Palamakumbura *et al.*, 2016a; Murray and Robertson, 2020). Climatic changes during the Pleistocene also influenced the formation of these terraces and the development of Pleistocene-aged river channels (Main *et al.*, 2016; Murray and Robertson, 2020).

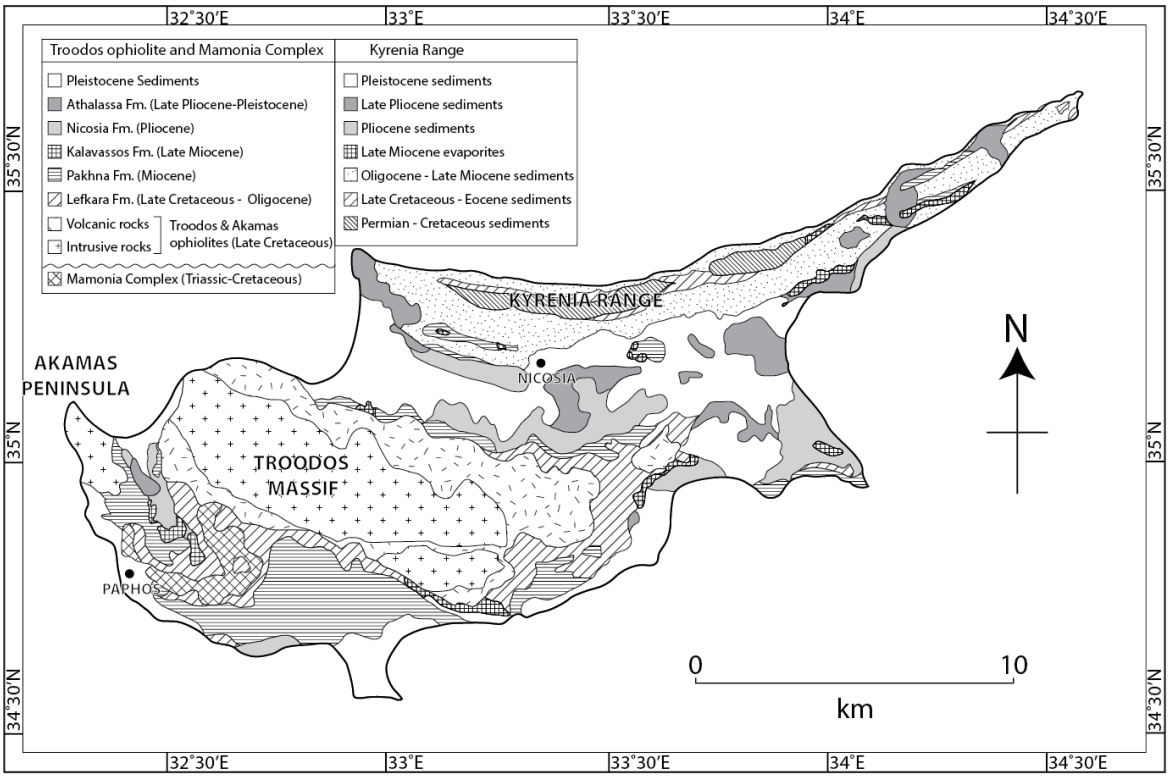


Figure 1.3.2.2 - Outline geological map of Cyprus showing the Troodos Massif, Mamonia Complex and Kyrenia Range as well as their sedimentary cover (modified from Kinnaird et al. 2011).

Age Equivalence of Miocene 'circum-Troodos' and Kyrenia Sedimentary Cover

This thesis concentrates on the Miocene-aged sedimentary rocks of Cyprus. Samples used in this study were taken from hemipelagic and pelagic sediments belonging to both the 'circum-Troodos' Miocene cover and the Kyrenia cover. The Miocene-aged hemipelagic and pelagic sediments of the 'circum-Troodos' cover in southern Cyprus belong to the undifferentiated Pakhna Formation. The Early-Middle Miocene aged rocks of the Kythrea (Degirmenlik) Group in northern Cyprus mainly originated from a siliciclastic system. These units were deposited as part of a trench or foreland basin along the northern margin of the southern Neotethys (McCay, 2011; McCay *et al.*, 2013). The controls on the deposition of these units are complex and not relevant to this research; therefore, these units are not extensively detailed in this thesis.

The deposition of the Late Miocene units with the Kythrea (Degirmenlik) Group can be related to regional-global scale climate and oceanographic changes. The Kythrea (Degirmenlik) Group includes hemipelagic sediment capped by evaporitic gypsum. The mudstones and marls of the Tortonian (Late Miocene) age Yılmazköy Formation are overlain by the finer-grained sediments of the Tortonian-Lower Messinian Yazılıtepe Formation, which are in turn capped by the evaporitic gypsum of the Messinian Lapatza (Mermertepe) Formation (Hakyemez *et al.*, 2000; McCay, 2011; McCay *et al.*, 2013). The Late Miocene hemipelagic sediments of the Kythrea (Degirmenlik) Group have much higher terrigenous mud content relative to the Late Miocene hemipelagic sediment of the Pakhna Member in southern Cyprus. Early Messinian aged bedded manganese deposits occur in the Yazılıtepe Formation, the deposition of these Manganese layers is related to cyclical redox changes prior to the Messinian salinity crisis (Robertson *et al.*, 2019). The gypsum deposits of the Lapatza (Mermertepe) Formation are associated with the Messinian Salinity Crisis and

therefore can be correlated with the Kalavasos Formation in southern Cyprus. It should be noted that there are no reef-related units in the Miocene-aged cover of the Kyrenia Range.

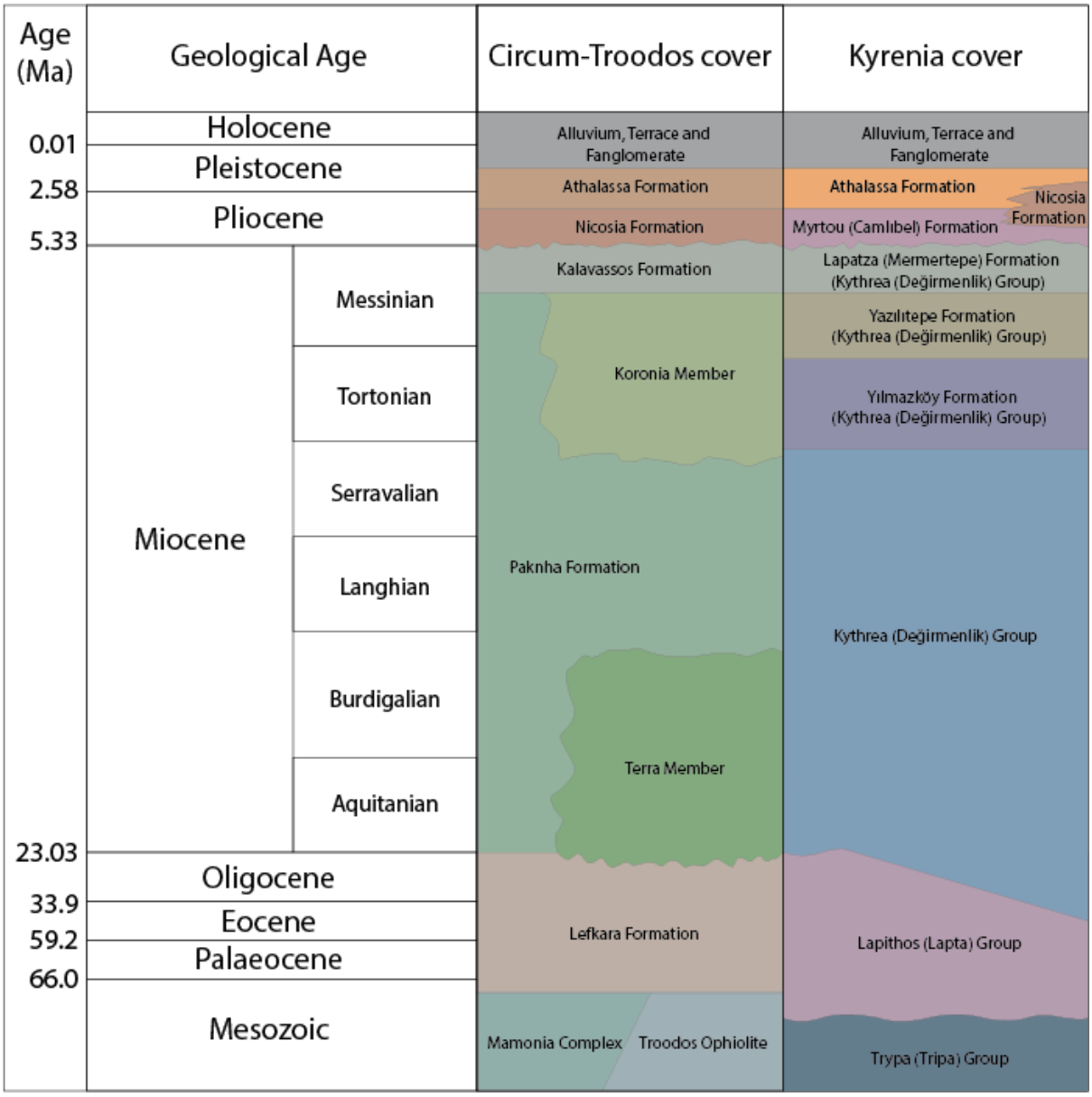


Figure 1.3.2.3 – Simplified stratigraphic sections for the 'circum-Troodos' and 'circum-Kyrenia' sediment cover (after Harrison et al., 2004, Follows 1990 and Cannings *et al*. 2020).

2 Materials and Methods

This is a data-based research project and a fundamental component of this study was the collection of data through fieldwork and sample analyses. This section outlines the methods used in order to create the primary dataset on which this study is based. Further analytical methods used to process and interpret these data, such as proxies, are detailed in the relevant chapters later in this thesis.

2.1 **Fieldwork**

This study utilises samples collected from pelagic/hemipelagic sediment outcrops. This is in contrast to the majority of palaeoceanographic studies, which commonly utilise pelagic/hemipelagic sediment samples collected through ocean drilling. The main objective of fieldwork for this project was to collect a continuous sequence of samples covering the whole time interval of interest (*c.*17.50 to 5.33 Ma) which could be used for geochemical analysis.

Fieldwork for this study comprised high-resolution logging and sampling of pelagic and hemipelagic sedimentary rock successions on the island of Cyprus. Initial fieldwork took place during the autumn of 2019, this fieldwork was carried out with the assistance of Elizabeth Balmer, Prof. Alastair Robertson and Prof. Dick Kroon. Further fieldwork was planned for spring 2020; however, this had to be significantly delayed due to the Coronavirus disease 2019 (COVID-19) pandemic and subsequent global travel restrictions. The required fieldwork was eventually completed during the autumn of 2021 (with the assistance of Jacob Shearer) and the spring of 2022 (with the assistance of Elizabeth Balmer), once travel restrictions eased.

2.1.1 Site Selection

In order to ensure that the collected samples provided a continuous record of the target time interval (Chapter 1), several exposures across the island of Cyprus were selected for logging and sampling. This included a combination of previously studied localities and some new successions that were sampled and logged for the first time during this study. Approximate ages were available for previously studied exposures, while the likely age range of new exposures could only be estimated through field observations such as lithological correlation. Samples from the new successions were later dated using calcareous nannofossil biostratigraphy (see Chapter 2.3). The suitability of the samples for geochemical analyses was also known for some previously studied successions, but this was uncertain for the new successions. For this reason, suitable successions that had previously been dated were preferred in the first instance.

Following fieldwork and preliminary dating of the successions sampled, the Kottaphi Hill Succession and the Lapatza Hill Succession were taken together to produce a ‘composite succession’ spanning the target time interval. For this reason, samples collected at other sites described were not used in this research project, although they are described in this thesis with the aim of assisting with site selection for any future palaeoceanographic studies in the area. Samples from Kouroulla Gorge were used for the purpose of dating fossil material contained within previously identified (Cannings *et al.*, 2020) debris-flow units.

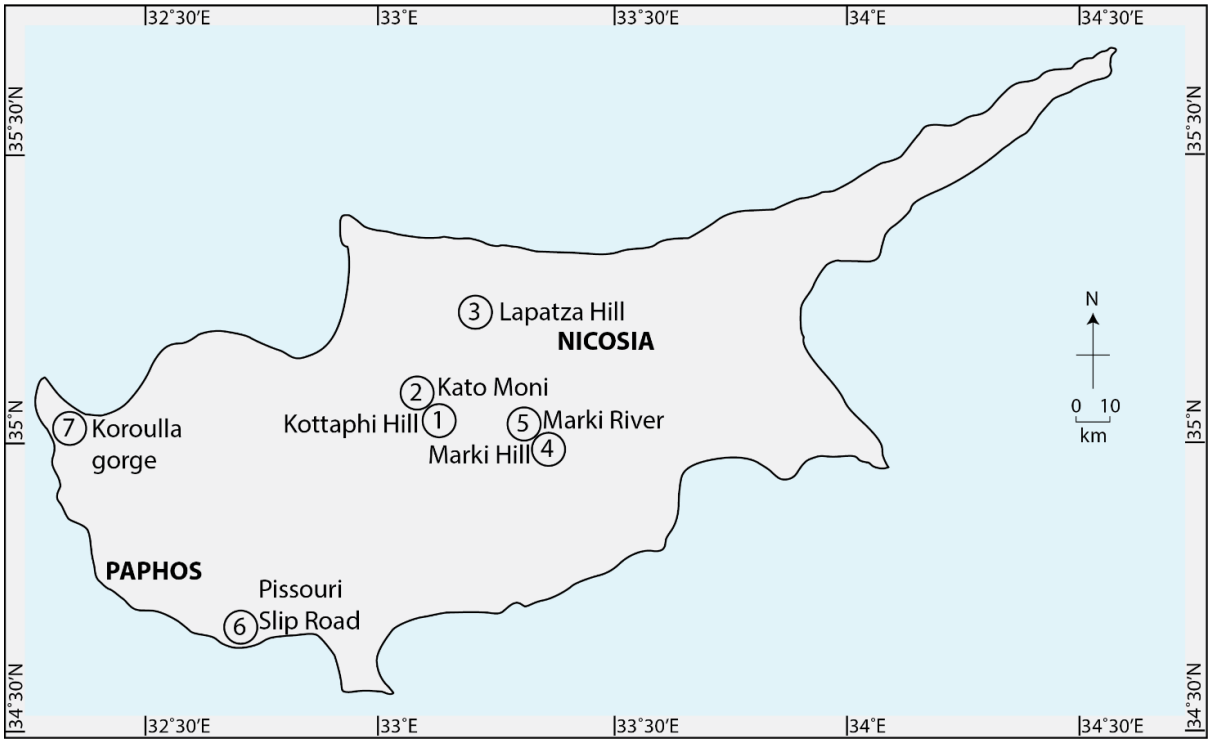


Figure 2.1.1.1 – Map showing the locations of field sites described above within Cyprus: (1) Kottaphi Hill; (2) Kato Moni; (3) Lapatza Hill; (4) Marki Hill; (5) Marki River; (6) Pissouri Slip Road; (7) Kouroulla Gorge.

Kottaphi Hill

Kottaphi Hill (Κοτάφι, Kotaphi or Kottafi) (35° 2’50.40” N 33° 9’13.60” E) is located to the north of Agrokipia (Αγροκηπιά) village (Nicosia District) on the northern margin of the Troodos Massif (Figure 2.1.1.1). Kottaphi Hill is a classic succession for the Miocene Pakhna Formation (Mantis, 1972) of Cyprus and has been the subject of several previous studies (Follows *et al.*, 1996; Davies, 2001; Penttila, 2014; Athanasiou *et al.*, 2021; Coletti *et al.*, 2021). The Miocene succession (Figure 2.1.1.2) begins with *c.* 60m of cyclically bedded chalk and marl couplets assigned to the undifferentiated Pakhna Formation. The pelagic-hemiplegic succession is overlain by bioclastic limestones, which are capped by a neritic-carbonate-debris-rich conglomerate, assigned to the Koronia Member of the Pakhna Formation (Follows, 1990, 1992).

Davies (2001) logged and sampled the succession at a low resolution (> 20 cm) relative to this study, with the aim of examining the roles of climate versus tectonics as controls on sedimentation in Cyprus during the Miocene. The succession was dated as Burdigalian to Tortonian using calcareous nannofossil biostratigraphy supported by low-resolution carbon and oxygen stable isotope records. Davies (2001) identified a well-cemented trace-fossil-rich manganese and iron-rich layer roughly halfway up the succession, and concluded that this represented a hardground. Based on spectral analysis, Davies (2001) suggested that the chalk-marl-couplet cyclicity at Kottaphi Hill was controlled by regional to global changes in climate and sea level, related to Milankovitch cyclicity. Davies (2001) also identified the Monterey Excursion in their $\delta^{13}C$ record and linked a positive $\delta^{18}O$ trend from 13 to 14 Ma with the closure of the Mediterranean. The closure of the Mediterranean from the Indian Ocean had previously been suggested as a reason for a positive $\delta^{18}O$ trend in a Miocene stable isotope record from Malta (Jacobs *et al.*, 1996). Davies (2001) remarked that future work should aim to increase the resolution of sampling and extend the record in order to improve the understanding of the relationship between local sedimentation and global events.

Penttila (2014) built on the work of Davies (2001) using calcareous nannofossil biostratigraphy and strontium isotope dating alongside foraminiferal abundance and some X-ray diffraction analysis. This study identified an incoming of feldspar and clay-rich lithic fragments at *c.* 10.6 Ma and suggested that this indicated that the Troodos Massif had emerged above the seafloor by this time. Penttila (2014) also identified ‘ghost sapropels’ (less than 2% total organic carbon) towards the top of the succession.

Athanasiou *et al.* (2021) collected samples from a 42.1 m succession at the base of Kottaphi Hill. The samples collected were subjected to calcareous nannofossil, pollen and palynomorph, $\delta^{13}C$ and $\delta^{18}O$ and total organic carbon analysis. Athanasiou *et al.* (2021) inferred that the organic carbon-rich layers at Kottaphi Hill were deposited in warm oligotrophic seawater, with strong water column stratification and further suggested that these layers represent the precursors to sapropels. Athanasiou *et al.* (2021) also identified the Mi3–Mi5 events (Miller *et al.*, 1991a, 2020) and CM5–CM7 episodes (Woodruff and Savin, 1985, 1991) in their $\delta^{13}C$ and $\delta^{18}O$ stable isotope record. Pollen and palynomorph analysis indicated that land nearby was densely vegetated before *c.* 14.5 Ma. After *c.* 13 Ma, a more open landscape hosting high rates of nearby soil erosion were inferred.



Figure 2.1.1.2 – Photograph showing the Kottaphi Hill succession (left) with the first interval of high-resolution sampling indicated (right).

Kato Moni

The Middle Miocene Kato Moni (Κάτω Μονή) succession (35° 3’59.20” N 33° 6’14.10” E) (Figure 2.1.1.1), studied by Davies (2001) and Penttila (2014) was selected as a potential site for detailed logging and sampling. However, this outcrop has degraded and field observations indicated that samples collected here would not be suitable for

geochemical analyses. This succession is also bound by faults and has a small age range in comparison with the Kottaphi Hill succession.

Lapatza Hill

Lapatza Hill (Lapatza Vouno) (35°14’44.70” N 33° 8’35.80” E) (Figure 2.1.1.1) was first studied by Henson *et al.* (1949) and is the type locality for the Lapatza (Mermetepe) Formation. Recently, manganese-rich layers were noted in the pre-evaporitic succession underlying the gypsum which caps Lapatza Hill (Robertson *et al.*, 2019). Although this succession had not previously been dated, the gypsum which caps Lapatza Hill was assumed with a high level of confidence, to be of Mid-Late Messinian age (McCay *et al.*, 2013; Varol and Atalar, 2017; Artiaga *et al.*, 2021). Therefore, the *c.* 60m pelagic/hemipelagic succession that underlies this gypsum (Figure 2.1.1.3) was inferred to be of late Miocene age. Prof. Alastair Robertson carried out ‘reconnaissance sampling’ of this succession together with Dr Mehmet Necdet prior to this PhD project. These samples enabled the suitability of the succession to be examined prior to fieldwork. Samples from the ‘reconnaissance sampling’ hosted well-preserved planktic foraminiferal assemblages and therefore indicated that this succession is suitable for geochemical analysis.

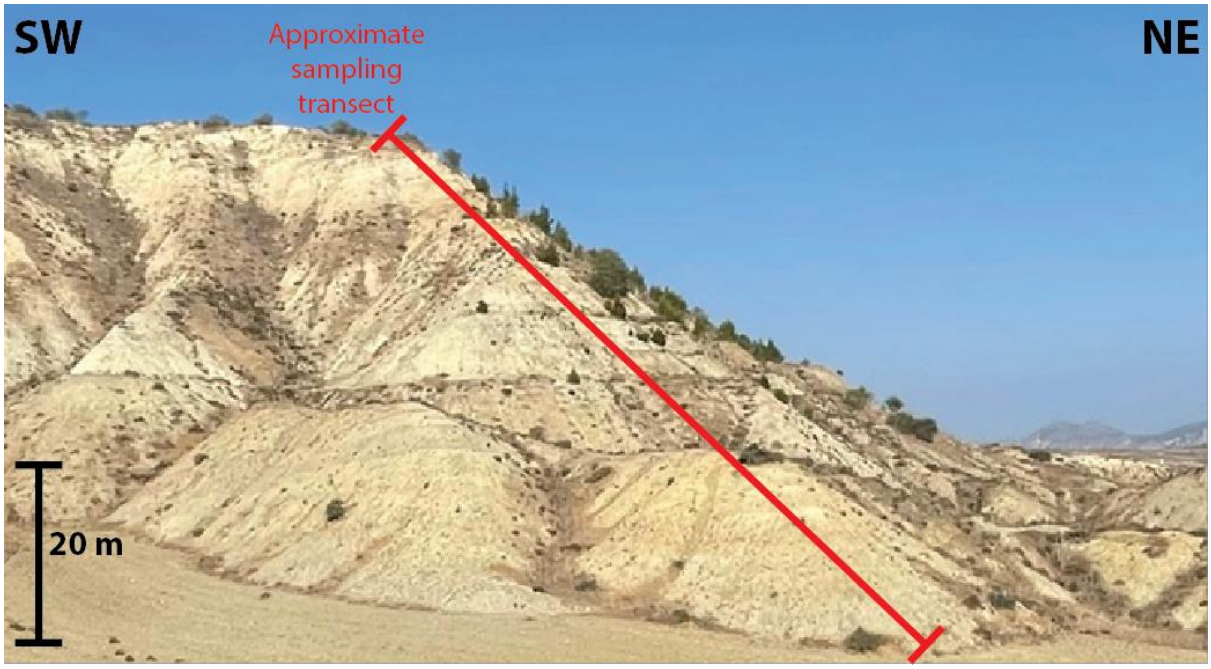


Figure 2.1.1.3 – Photograph of the sampled succession at Lapatza Hill with the approximate sampling transect indicated (red).

Marki Hill

Two new successions, one *c.* 30m and one *c.* 75m in height, on a hill between the Marki (Μαρκί or Margi) and Kotsiatis (Κοτσιάτης) villages (35° 0'57.30" N 33°20'39.00" E) (Figure 2.1.1.1) were sampled at a low resolution (*c.* 5 m intervals) in order to examine the age and suitability of samples from this locality for geochemical analysis. These successions were chosen for 'reconnaissance sampling' as they appeared to be continuous and lithologically similar to the uppermost sediments at Kottaphi Hill. Initial calcareous nannofossil biostratigraphy revealed extensive reworking in this succession; therefore, the samples collected at Marki Hill were not studied further.

Marki River

A new succession along the river bank at Marki Hill (35° 1'38.30" N 33°19'47.30" E) (Figure 2.1.1.1) was also subjected to 'reconnaissance sampling' at a *c.* 5 m interval as suggested by the lithological similarity to the uppermost sediments at Kottaphi Hill. Initial calcareous nannofossil biostratigraphy again revealed extensive reworking in

this succession; therefore, the samples collected at Marki River were not studied further either.

Pissouri Slip Road

The unsuitability of the above sections hinted that a gap in the combined age range of the Kottaphi Hill and Lapatza Hill successions might exist. In order to ensure that no gap in the record was present between the top of the Kottaphi Hill succession and the base of the Lapatza Hill succession, a roadcut section (34°40'24.68" N 32°39'56.59" E) (Figure 2.1.1.1) close to Pissouri (Πισσούρι) in southern Cyprus was subject to moderate resolution sampling and logging. There are no other suitable successions on the northern Troodos Margin. This succession is located on the sliproad of the A6 motorway at junction 41A, stratigraphically below the 'Pissouri Motorway Section' studied by Krijgsman *et al.* (2002). The base of the 'Pissouri Motorway Section' (Krijgsman *et al.*, 2002) and, therefore, the top of this succession was dated at *c.* 7.5 Ma using calcareous nannofossil biostratigraphy. This succession would only be subject to analysis if required in order to ensure a complete record with no time gaps.

Kouroulla Gorge

A secondary objective of this research was to better constrain the dating of debris-flow deposits containing Miocene reef material in the northwest of Cyprus (Akamas Peninsula). This new dating built on the work of Cannings *et al.* (2020), in which the timing of debris-flow deposition was dated but not the age of the material within the debris-flow deposits. Dating of the material within these debris-flow deposits would allow us to distinguish whether these debris-flows represent contemporaneous reworking of living reef-material or instead redeposition of reef-material that was already dead. Such dating would allow us to better constrain the timing of the end of Early Miocene reef growth (Terra Member) in Cyprus and examine the relationship

between the termination of reef growth and local to global scale events such as tectonic and climatic changes.

Several samples of fossilised coral material and oyster shell material were collected from Kouroulla Gorge (35° 0’57.50” N 32°22’3.80” E) (Figure 2.1.1.1). Logging and description of this succession were carried out previously as part of my own MScR project (Cannings, 2018; Cannings *et al.*, 2020).

2.1.2 Sampling

Samples were collected by hand, using a geological hammer and chisel to dig and collect a fresh sample that was unlikely to have been affected by surface processes. For some successions a shovel was used to dig a trench and take samples; this was necessary for successions with large amounts of loose sediment cover, especially those exposed on poorly consolidated, shallow-angle slopes (such as Lapatza Hill). The samples were collected at short intervals to ensure that high-resolution geochemical records could be obtained. The sampling resolution varied for each locality based on the time interval covered and the inferred sedimentation rate. Sedimentary logs detailing changes in lithology, sedimentary features and the presence of fossils were made for all successions during sample collection (see Chapter 3.2.1).

2.2 **Foraminifera**

Foraminifera are a group of amoeboid protists that make up a major proportion of the marine benthos and zooplankton, both in the modern oceans and in the fossil record. The majority of foraminifera secrete a calcareous test (shell) which protects their cytoplasm (Banner, 1982; Sen Gupta, 2003). The tests of foraminifera are abundant, geographically widespread and readily preserved throughout the fossil record and

have, therefore, been extensively utilised for biostratigraphic, paleoceanographic and palaeoclimatological studies (e.g. Chappell and Shackleton, 1986; Elderfield and Ganssen, 2000; Wade *et al.*, 2011), including in Cyprus (Davies, 2001; Kouwenhoven *et al.*, 2006; Cannings *et al.*, 2020).

The planktic *Praeorbulina-Orbulina* lineage Figure 2.1.2.1) (Blow, 1956; Pearson *et al.*, 1997; Aze *et al.*, 2011; Spezzaferri *et al.*, 2015) is used for geochemical analysis in this study. This ancestral lineage contains several species that are common in Miocene hemipelagic sediments. This lineage contains foraminiferal species which are present throughout the target interval and are not known to have any variation in vital effects, depth habitat or symbiotic association (Pearson *et al.*, 1997).

Foraminifer samples were categorised based on the level of preservation, as shown in Table 2.1.2.1. Scanning electron microscope images of foraminifera from a range of levels of preservation are shown in Chapter 3.2.4. Foraminifera with the best possible preservation levels were used for geochemical analyses, poorly and very poorly preserved samples were not used for any analyses.

Preservation	Category	Description
0	Very poorly preserved	Heavily overgrown, test structure is difficult to identify
1	Poorly Preserved	Hard frosted - 75% of test structure easily visible
2	Moderately well preserved	Mild frosting with some hard frosted patches - at least 90% of test structure visible
3	Well Preserved	Mild frosting - test wall texture still clearly visible all over but some frosting or overgrowth is present.
4	Very well preserved	Very mild frosting - test wall texture is still easily visible, negligible crystal overgrowth or frosting.
5	Exceptionally well Preserved	Perfectly clean - test wall structure can be easily identified and frosting or crystal overgrowth is completely absent.

Table 2.1.2.1 – Table showing the categories and criteria used to examine the preservation quality of foraminifera samples.

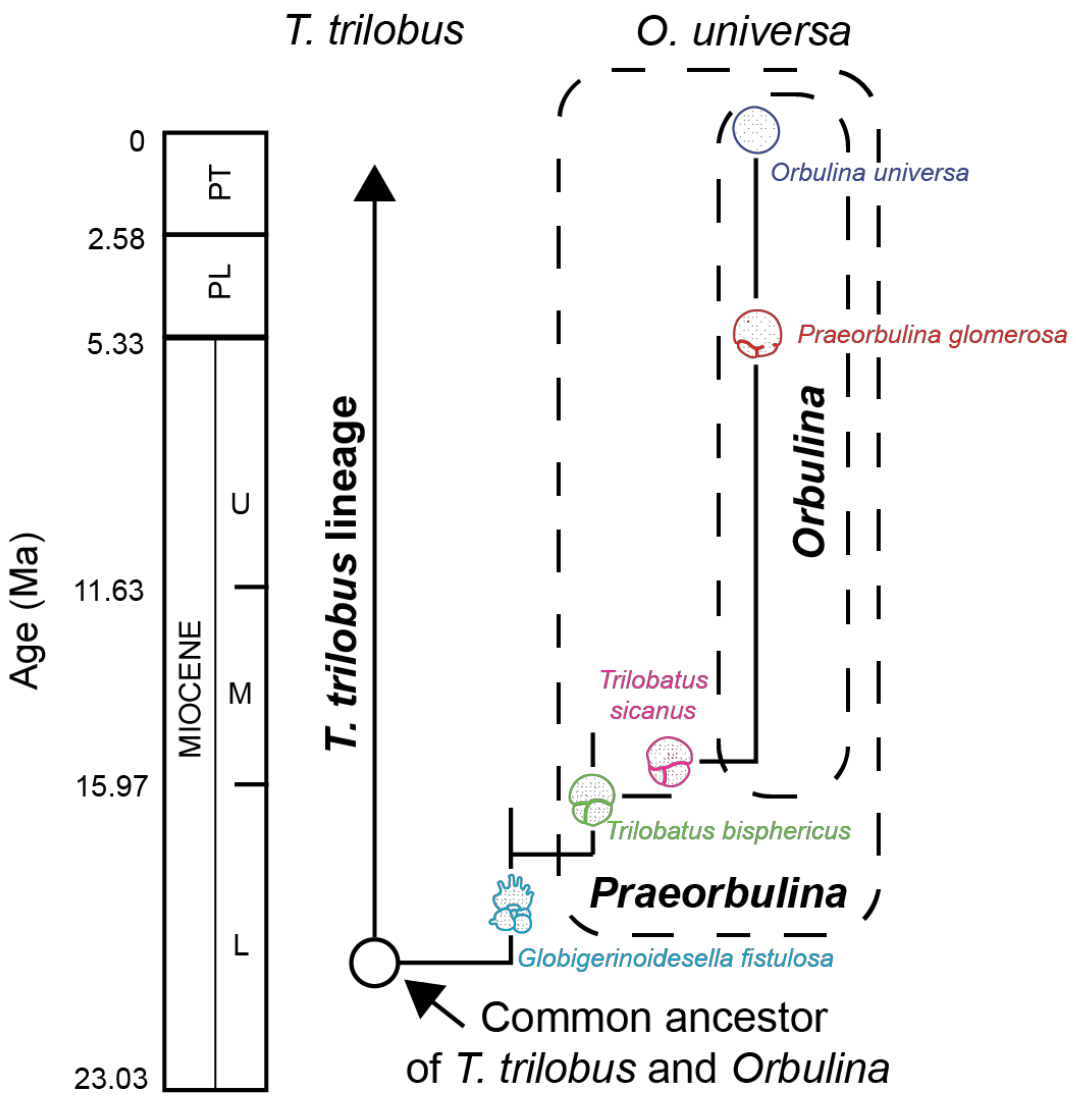


Figure 2.1.2.1 – Simplified stratophyletic polygeny showing the relationship between species within the *Praeorbulina-Orbulina* lineage (modified from Spezzaferri *et al*., 2015).

2.2.1 Methodology

All of the samples were washed using a 32 µm sieve to remove fine clay and silt fractions. Samples which were not easily broken up by wet sieving were soaked in Milli-Q water and placed on a shaker plate for 90 minutes before being washed again over a 32 µm sieve. This process was repeated up to 3 times for the most resistant samples. The foraminiferal samples were then dried in an oven at 30°C and dry sieved into size fractions for foraminiferal picking. The main use of the foraminiferal samples

in this study was for trace element and stable isotope geochemical analysis. However, the species assemblages in the samples were also examined for biostratigraphic and environmental interpretations in order to support data collected through other methods.

2.3 Calcareous Nannofossils

Calcareous nannofossils are a group of microfossils that are abundant in marine sediments throughout the geological record (from at least *c.* 220 Ma). Calcareous nannofossils are produced by calcareous nannoplankton, a diverse group of microorganisms which produce biomineralized calcite skeletons. Their abundance throughout the geological record, geographical distribution and rapid evolution of have made them one of the most powerful tools for the biostratigraphic dating of marine carbonate sediments (Agnini *et al.*, 2017). Calcareous nannofossil biostratigraphy is one of the most established methods of dating Neogene sediments globally and has been used successfully in Cyprus in several previous studies (Morse, 1996; McCay *et al.*, 2013; Robertson *et al.*, 2019; Cannings *et al.*, 2020).

2.3.1 Methodology

Calcareous nannofossils were identified using smear slides prepared using the standard smear method (Backman and Shackleton, 1983; Bown and Young, 1998), and then examined with a light microscope at a magnification of ×1000–1250. The calcareous nannofossil biostratigraphy used here is based on Backman *et al.* (2012). The biostratigraphy of Backman *et al.* (2012) is consistent with commonly used ‘up to date’ geological timescales (e.g. Cohen *et al.*, 2013; Gradstein, 2020). Species diversity within nannofossil assemblages was also used as an indicator of environmental setting, especially salinity (Wade and Bown, 2006).

2.4 **Strontium Isotope Dating**

Strontium isotope dating has also been used for the dating of Neogene carbonate sediments in Cyprus (McCay *et al.*, 2013; Penttila, 2014; Cannings *et al.*, 2020) and in many other areas. Strontium isotope stratigraphy is a well-established dating technique, as demonstrated in the 1980s (Elderfield, 1986). The technique is based on the gradual change of the ratio of $^{87}Sr/^{86}Sr$ in seawater throughout time. Initially, this change was attributed to the decay of rubidium (^{87}Rb to ^{87}Sr) (Wickman, 1948). However Rb decay as a cause is unlikely, as Rb has a low decay rate and both seawater and biogenic carbonates contain negligible amounts of Rb relative to Sr. These factors also mean that Rb contamination is unlikely to have any effect on the dating of biogenic carbonate samples of Miocene to recent age.

Three factors are known to contribute to the change in the $^{87}Sr/^{86}Sr$ ratio of seawater throughout time: 1. The $^{87}Sr/^{86}Sr$ ratio of seawater decreases due to hydrothermal activity (Brass, 1975); 2. The $^{87}Sr/^{86}Sr$ ratio of seawater increases with increased sediment input (Brass, 1975); and 3. Changes in the $^{87}Sr/^{86}Sr$ ratio of seawater are buffered by carbonate dissolution (Palmer and Elderfield, 1985; Hodell and Woodruff, 1994). The technique is reliant on the assumption that at any given time the world's oceans are homogenous (i.e. well mixed) in terms of $^{87}Sr/^{86}Sr$ ratio. Ocean mixing rates (≈103 years) are short relative to the rates of Sr isotope fluctuation (≈106 years), indicating that homogeneity is likely (McArthur *et al.*, 2012).

Organisms such as foraminifera construct their tests with the same $^{87}Sr/^{86}Sr$ ratio as the seawater they live in. They incorporate Sr dissolved in seawater into their tests with no selective fractionation. This ratio does not change over time; therefore, the $^{87}Sr/^{86}Sr$ ratio in foraminiferal tests is the same as the ratio that the organisms lived in (Elderfield, 1986). This means that the $^{87}Sr/^{86}Sr$ of a foraminifera test is indicative of

age when matched to an empirical calibration of seawater $^{87}Sr/^{86}Sr$ changes (e.g. McArthur *et al.*, 2001).

The $^{87}Sr/^{86}Sr$ ratio of seawater has been increasing gradually since the Jurassic and began to rise more rapidly throughout the Cenozoic, with a dramatic increase during the Early Miocene (Brass, 1975; McArthur *et al.*, 2001). It is likely that both continental collision (Richter *et al.*, 1992) and increased glacial erosion (Hodell and Woodruff, 1994; Oslick *et al.*, 1994) resulted in the rapid rise in the $^{87}Sr/^{86}Sr$ ratio during this time period. This rapid increase allows for high resolution dating of Cenozoic-aged samples, and an especially high-resolution for samples of Early Miocene age.

The isolation of the Mediterranean during the Messinian Salinity Crisis (MSC) is believed to have caused anomalous $^{87}Sr/^{86}Sr$ ratios during the Messinian, and therefore samples of this age cannot be reliably dated using this method (Flecker and Ellam, 1999, 2006; Flecker *et al.*, 2002).

2.4.1 Methodology

Five Samples of planktic foraminifera from the *Praeorbulina-Orbulina* lineage from the Kottaphi Hill succession, and 5 samples of planktic foraminifera from the *Praeorbulina-Orbulina* lineage from the Lapatza Hill succession were dated using the strontium (Sr) isotope method. These 10 planktic foraminiferal samples were analysed in order to further constrain the dating of the chosen composite succession that had been dated by biostratigraphic methods. Foraminiferal specimens were picked from the 355–400 μm size fraction, then crushed between two glass slides and transferred to clean vials. In order to ensure that all the clay had been removed from the foraminiferal tests, samples underwent further ultrasonic cleaning following crushing. This step of

ultrasonic cleaning was repeated seven times for each sample. Each sample was ultrasonicated for fifteen seconds per round at this stage.

Two well-preserved oyster shells (*Ostrea Sp.*) and one piece of scleractinian coral from the genus *Faviidae*, that were collected from debris-flow units at Kouroulla Gorge, were also selected for dating using the Sr isotope method. Samples were cut to provide a clean internal surface for sample extraction by microdrilling. One sample of dark foliated calcite and one sample of light chalky calcite material were microdrilled from each oyster shell. One sample of the well-preserved material from the coral sample was microdrilled in order to produce a clean, powdered sample.

Strontium Isotope Analysis was carried out at the Scottish Universities Environmental Research Centre by Anne Kelly. Carbonate samples (~25 µg) were weighed into PFA vials and leached in ammonium acetate to remove groundwater salts and displace contaminant strontium on exchangeable sites (Bailey *et al.*, 2000a). The remaining material was rinsed twice in deionised water and then dissolved in dilute HCl (prepared by sub-boiling distillation in PFA (Mattinson, 1972). Strontium was separated from matrix elements using strontium-specific resin (Horwitz *et al.*, 1991; Philip Horwitz *et al.*, 1992), following a nitric acid extraction chemical procedure (adapted from Pin *et al.* 1994), in which samples are loaded in 8 molar (M) HNO3, cleaned in sequential steps of 8M HNO3 and 3M HNO3, and strontium eluted in 0.01 M HNO3. After ion exchange chemistry, the samples were loaded onto purified Re filaments in a Ta-emitter solution (Birck, 1986). Total procedural blanks yielded values of better than 350 pg, which are negligible relative to the amount of sample run (> 1µg).

The isotopic analyses were made on a VG-Sector-54 thermal ionization mass spectrometer using a three-cycle dynamic multicollector routine and an exponential

mass fractionation correction relative to $^{86}Sr/^{88}Sr$ = 0.1194 (Nier, 1938; Steiger and Jäger, 1977; Moore *et al.*, 1982; Hans *et al.*, 2013). Filaments were slowly heated to 2.4 A, focussing and filament current was adjusted to achieve a stable 1E-11 A ion beam on 88Sr. Analyses are typically run for 15 blocks of 10 cycles (150 ratios), for approximately 1.5 hours. Rubidium interferences were monitored but were negligible. Repeated measurements of reference material NBS987 at similar run conditions during the period over which these analyses were made yielded a value of 0.710266 (+/-0.000007 2SD, n=10), within an uncertainty of the convention value of 0.71026 for the reference material, and indicates that the measurement repeatability is close to with the within-run uncertainty.

Strontium isotopic ages were calculated using the LOWESS Sr isotope Look-Up Table (Version 4: 08/04) (McArthur *et al.*, 2001; McArthur and Howarth, 2004).

The total combined errors were then calculated from a combination of the uncertainties of the Sr isotopic analyses, and the error (upper and lower age range) of the LOWESS Sr isotope Look-Up Table (Version 4: 08/04) (McArthur *et al.*, 2001; McArthur and Howarth, 2004). This timescale is consistent with commonly used ‘up to date’ geological timescales (e.g. Cohen *et al.*, 2013; Gradstein, 2020). Total combined error age ranges were calculated by combining 2 standard deviations of the analytical error, with the empirical error of the LOWESS “look-up table” to find the largest error range (McCay *et al.*, 2013). A maximum age was obtained by subtracting 2σ (standard deviation) from the mean isotopic value and finding the age for this value on the ‘upper age limit curve’ of the LOWESS Sr Curve. A minimum age was obtained by adding 2σ (standard deviation) to the mean isotopic value and finding the age for this value on the ‘lower age limit curve’ of the LOWESS Sr Curve. Results from strontium isotope dating are presented and discussed in Chapter 3.

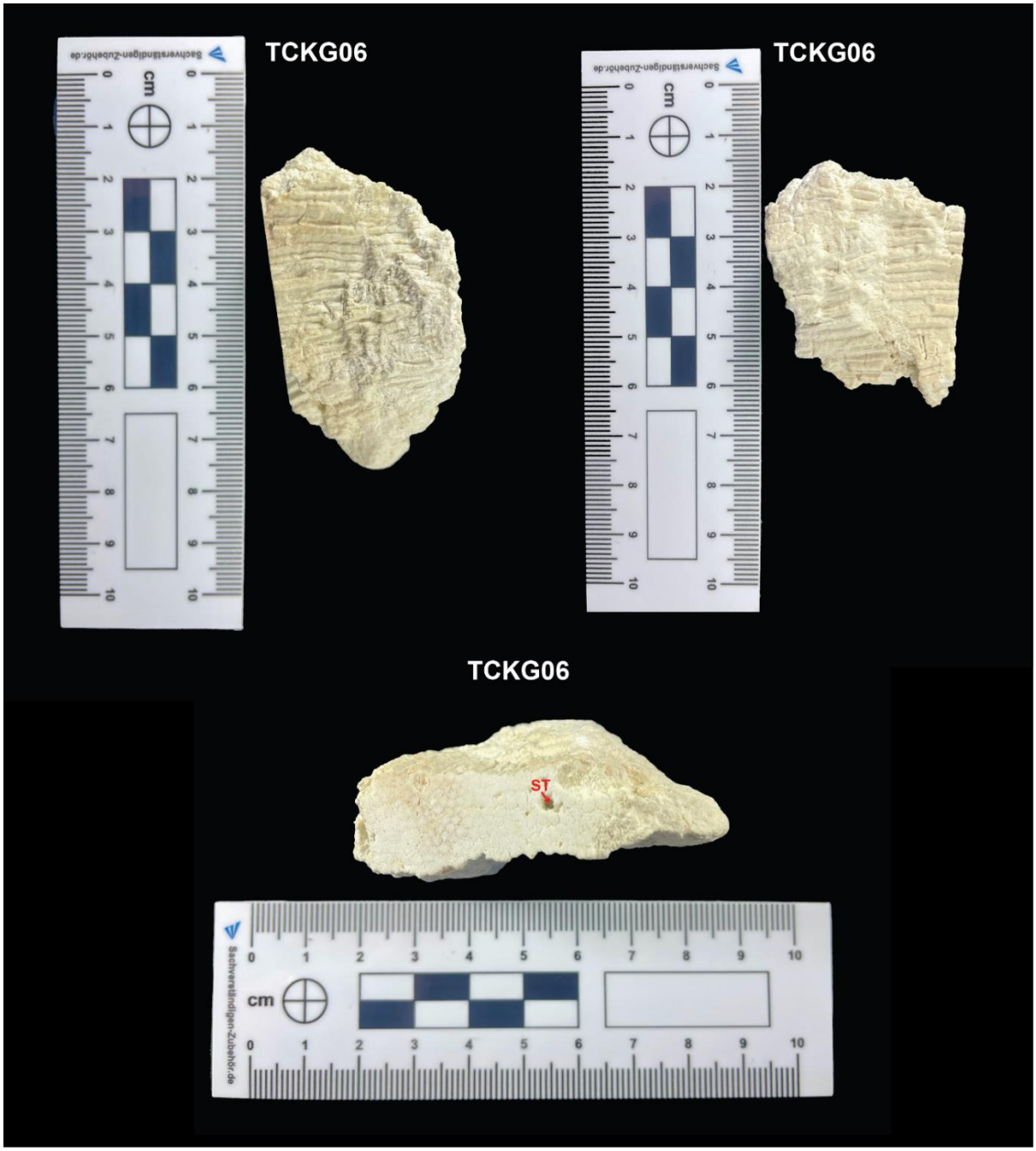


Figure 2.4.1.1 – Images of the *Faviidae sp*. sample (TCKG06) analysed for strontium isotope dating. Images show the outer and internal structures of the sample. ST= Sample Taken.

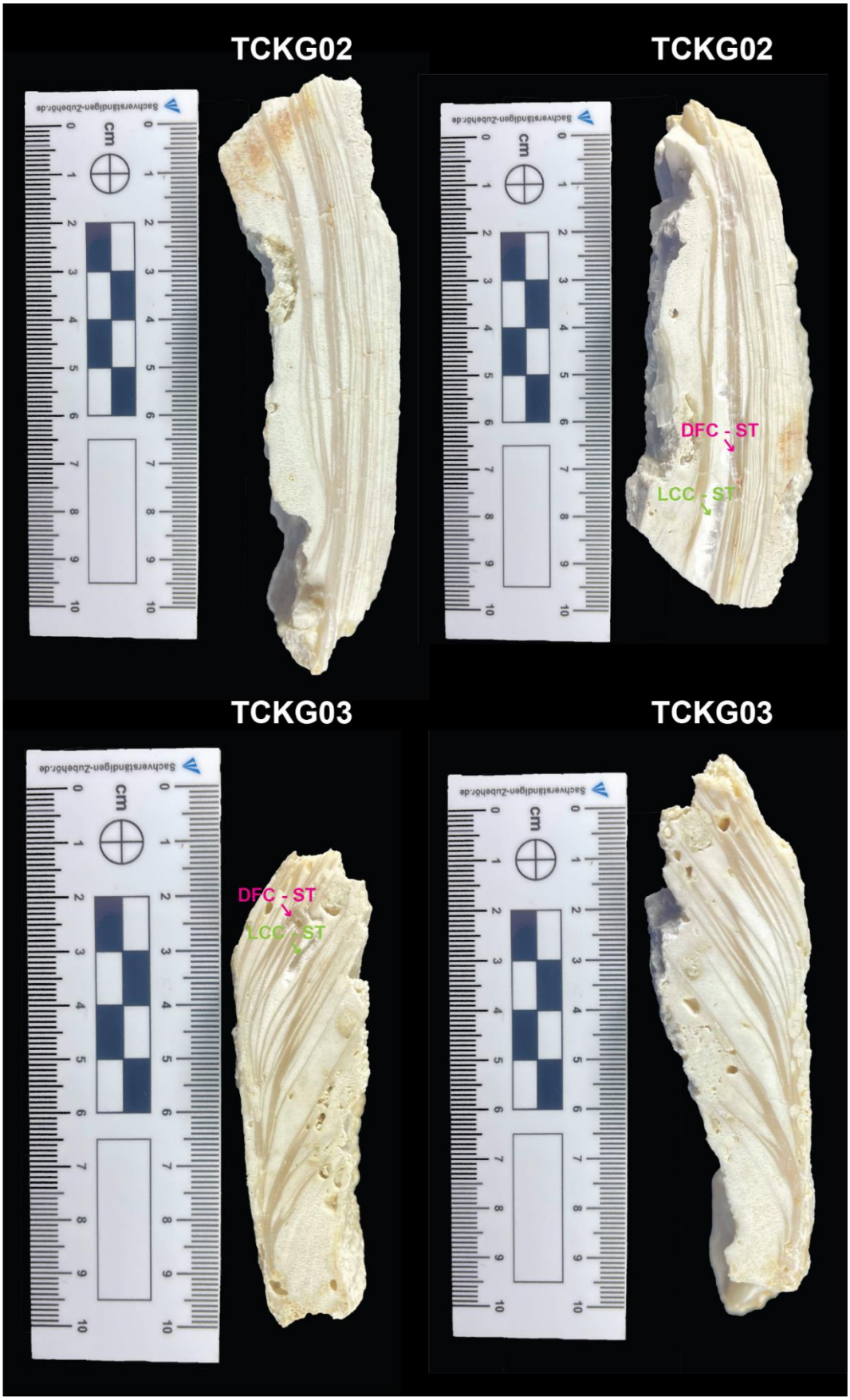


Figure 2.4.1.2 – Images of the *Ostrea sp.* samples (TCKG02 and TCKG03) analysed for strontium isotope dating. DFC-ST = dark foliated calcite – sample taken, LCC- ST light chalky calcite –sample taken.

2.5 **Stable Isotopes ($\delta^{18}O$ and $\delta^{13}C$)**

The measurement of oxygen and carbon stable isotope signals in calcareous foraminiferal tests and bulk carbonate sedimentary rocks is one of the most well-established palaeoclimatological and palaeoceanographic research methods (e.g. Pearson, 2012)

Oxygen stable isotope analysis measures the ratio of the two stable isotopes of oxygen (^{18}O and ^{16}O) in a sample; this ratio is known as $\delta^{18}O$. The $\delta^{18}O$ notation gives the ratio of ^{18}O to ^{16}O relative to an international standard with a concentration unit of per mil (‰). This is shown in the equation below:

$$\boldsymbol{\delta^{18}O = \left[\frac{(^{18}O/^{16}O)sample - (^{18}O/^{16}O)\ standard}{(^{18}O/^{16}O)standard}\right] \times 1000} \qquad \textbf{[Eq. 2.4.1.1]}$$

In this study, the values are stated in relation to the Vienna Pee Dee Belemnite (VPDB) scale (Hut, 1987).

The $\delta^{18}O$ of biogenic carbonate material varies due to five main factors: the isotopic composition of water, temperature, mineral phase, diagenesis and vital effects. Where the influence of four of these factors is known or can be estimated, the influence of the remaining factor can be calculated/approximated (Shackleton, 1967; Shackleton and Opdyke, 1973; Prentice and Matthews, 1991). In this work, the main aim is to reconstruct sea temperature. Further information on the calculation of palaeotemperature and other interpretations from $\delta^{18}O$ is provided in Chapter 4.1.1.

Carbon stable isotope analysis is similar to oxygen stable isotope analysis; however, the ratio ($\delta^{13}C$) between stable carbon isotopes (^{13}C and ^{12}C) is primarily influenced by biological factors (i.e. primary productivity) rather than environmental factors (Kennett and Shackleton, 1975; Shackleton *et al.*, 1983). By understanding the

productivity of an ecosystem at a past point in time, we can better understand the way in which living organisms are altering the environment they live in (further information on the use of $\delta^{13}C$ as a palaeoenvironmental proxy is provided in Chapter 5.1.1.

The $\delta^{13}C$ notation gives the ratio of ^{13}C to ^{12}C relative to a standard (in this case VPDB) with a concentration unit of per mil (‰), as shown in the equation below:

$$\boldsymbol{\delta^{13}C} = \left[\frac{(^{13}C/^{12}C)sample - (^{13}C/^{12}C)standard}{(^{13}C/^{12}C)standard}\right] \times \mathbf{1000} \qquad \textbf{[Eq. 2.4.1.2]}$$

Both a bulk carbonate (fine fraction (<63 um)) and a planktic foraminiferal stable isotope record are presented in this thesis from Kottaphi Hill and Lapatza Hill (see Chapter 2.1.1). The creation of both bulk carbonate (fine fraction) and planktic foraminiferal records allows for the most complete isotope record possible for the target time interval, reducing the number of gaps in the record to a minimum.

A bulk carbonate (fine fraction) stable isotope record mostly measures the calcareous nannofossil component of a sample, with some contribution of calcite from foraminifera and other sources (Reghellin *et al.*, 2015, 2019). As bulk carbonate stable isotope records reflect the average composition of the whole (or in this case the whole fine fraction) of a sample, they can be viewed as an insight into overall changes in temperature and ocean chemistry over time (Bramlette and Riede, 1954; Anderson and Cole, 1975; Vincent and Berger, 1981; Luciani *et al.*, 2016; Reghellin *et al.*, 2019). Research on the Late Miocene-Recent of the eastern equatorial Pacific has revealed that bulk carbonate samples primarily record mixed layer conditions (Reghellin *et al.*, 2015).

Bulk carbonate and planktic foraminiferal records can differ due to varied vital effects in the biogenic components (Anderson and Cole, 1975; Reghellin *et al.*, 2015). A

planktic foraminiferal sample contains only one biogenic component, whereas a bulk carbonate sample contains multiple biogenic components. The depth of habitat of the major biogenic components of a sample within the water column, is the major control on temperature at the time of biomineralization, and therefore has an effect on the composition and $\delta^{18}O$ of a sample (Mulitza *et al.*, 1997; Rohling *et al.*, 2004; Friedrich *et al.*, 2012; Reghellin *et al.*, 2019). The water depth at which an organism lives can also affect the $\delta^{13}C$ of its test due to the changing $\delta^{13}C$ gradient through the water column (Mulitza *et al.*, 1997; Rohling *et al.*, 2004; Friedrich *et al.*, 2012). The calcification depths of a given species of planktic foraminifera can be interpreted from the behaviour of modern foraminifera from the same (or closely related) species (Rohling *et al.*, 2004; Birch *et al.*, 2013). The impact of vital effects on the stable isotope ratio of foraminiferal calcite for a given species can also be estimated from extant species (Birch *et al.*, 2013). As the biogenic components of a bulk carbonate record are not quantified, these two factors remain partially unknown for bulk carbonate stable isotope records. It has been documented that carbonate dissolution and secondary diagenetic effects preferentially affect certain microfossil types (Berger, 1970; Bé *et al.*, 1975; Thunell and Honjo, 1981). As the bulk carbonate record is a composite of several biogenic components, it is not possible to fully understand such effects on a bulk carbonate sample. Such diagenetic effects are believed to have a more pronounced effect on $\delta^{18}O$ data than $\delta^{13}C$ data (Frank *et al.*, 1999; Luciani *et al.*, 2016).

The $\delta^{18}O$ and $\delta^{13}C$ values of foraminiferal tests reflect the isotope ratio of the ambient seawater that the organism was living in (Emiliani, 1954, 1955; Vincent and Berger, 1981). By measuring the stable isotope ratios of a single species of foraminifera we

can produce a record for which the effect of factors such as calcification depth and vital effects can be assessed.

2.5.1 Bulk carbonate (fine fraction) δ18O and δ13C Methodology

640 samples were roughly broken up and dry sieved through a 38 μm sieve, in order to collect a concentrated sample of nannofossil ooze and reduce the likelihood of terrigenous components being present in the analysed sample. These samples were then ground using a porcelain pestle and mortar to ensure a consistent/homogeneous fine powder. Next, ~ 0.5 mg of each powdered sample was weighed on a Sartorius SE 2 microbalance, into Labco 3.7 ml vials, and taken for isotopic analyses. All of the stable isotope measurements of bulk carbonate (fine fraction) samples were run in the Wolfson stable isotope ratio mass spectrometry suite at Edinburgh University on an Elementar precisION continuous flow stable isotope ratio mass spectrometer, using a Gilson autosampler equipped with an automated acidification system, heated tray and an iso FLOW system. The samples were automatically acidified with anhydrous orthophosphoric acid, with a specific gravity of 1.92 g/cm^3, within the heated tray of the autosampler at 75°C. Alongside the samples, replicate measurements of the in-house COR1D standard (0.5 mg), were run and give the instrument an analytical precision (1σ n= 196) of ~ 0.071 ‰ for $\delta^{13}C$ and ~ 0.12 ‰ for $\delta^{18}O$. COR1D is an aragonitic coral in-house standard with established $\delta^{13}C$ values of -0.648 ‰ VPDB and 4.923 ‰ VPDB, calibrated against NBS18 and NBS19. All measurements of COR1D for each run and the error calculations are shown in Appendix 8.4.

2.5.2 Foraminifera $\delta^{18}O$ and $\delta^{13}C$ Methodology

Specimens of planktic foraminifera from the *Praeorbulina-Orbulina* lineage were picked from the 355–400 μm size fraction. Prior to stable isotopic analysis,

foraminiferal tests were subject to 15 seconds of ultrasonic cleaning in Milli-Q water to remove adhering particles. This cleaning process was repeated three times for each sample. The quantity of foraminiferal specimens analysed varied based on the number of well-preserved specimens available. Between 3 and 30 well-preserved planktic foraminifera specimens were analysed per sample (analysed specimens per sample given in Appendix 8.1 and 8.2). Stable isotopic measurements of 578 foraminifera samples were conducted in the Wolfson stable isotope ratio mass spectrometry suite at the School of GeoSciences at the University of Edinburgh on a dual-inlet Thermo Electron Delta + Advantage stable isotope mass spectrometer, interfaced with a Kiel carbonate II device. Samples were reacted with anhydrous orthophosphoric acid (H_3PO_4), specific gravity 1.92g/cm^3, at 70°C for 15 minutes, with the evolved CO_2 gas collected in a liquid nitrogen coldtrap and analysed compared to a working gas. All samples were corrected using the powdered coral in-house COR1D standard, calibrated against NBS 18 and NBS19, which was run alongside the samples and expressed as parts per mil (‰) relative to Vienna Pee Dee Belemnite (VPDB). COR1D was run four times at the beginning of the run with a duplicate after every 10 samples and four runs of COR1D at the end of each run. Replicate measurements of the COR1D standard give the instrument an analytical precision (1σ n= 260) of ~ 0.05 ‰ for $\delta^{13}C$ and ~ 0.04 ‰ for $\delta^{18}O$. All measurements of COR1D for each run and the error calculations are shown in Appendix 8.3.

2.6 **Trace Element Analysis**

The analysis of trace element to calcium ratios (TE/Ca) in foraminiferal calcite has recently become one of the most popular and effective tools for interpreting past environments. Laboratory studies on cultured foraminifera provide useful calibrations for the use of TE/Ca measurements as proxies for conditions. The use of Mg/Ca as a

proxy for palaeotemperature and B/Ca as a proxy for pH-related changes in ocean carbonate chemistry are well studied and are therefore commonly utilised tools. Other studies have revealed that additional TE/Ca ratios may provide useful proxies, such as Sr/Ca for dissolved inorganic carbon (DIC) (Keul *et al.*, 2017) and U/Ca for carbonate ion concentrations (CO3 2-) (Russell *et al.*, 2004; Allen *et al.*, 2016); these techniques are however less studied and therefore such proxies are calibrated with greater uncertainty. Further research and development on the use of the TE/Ca ratios will help to constrain and calibrate additional proxies for seawater chemistry; therefore, all TE/Ca data collected during this research project is presented in this thesis for use in future research. However, only well-established TE/Ca proxies (e.g. Mg/Ca and B/Ca) are used as a means to interpret changes in temperature and ocean chemistry in this thesis. In addition, the use of Ba/Ca and Na/Ca as proxies for changes in salinity is investigated.

25 specimens of planktic foraminifera from the *Praeorbulina-Orbulina* lineage were picked from the 355–400 μm size fraction using a Leica EZ4 microscope. In order to remove adhering particles, foraminifera tests were subject to ultrasonic cleaning in Milli-Q water prior to trace element analysis. 5μl of Milli-Q water was added to each sample. The samples were then ultrasonicated for 15 seconds and Milli-Q water was then removed using a pipette. This cleaning process was repeated three times for each sample. This preparation process took place at the University of Edinburgh.

Further sample preparation was carried out in the STAiG laboratory at the University of St Andrews prior to analysis. Samples were gently crushed between two clean glass slides and transferred to clean vials. Following crushing, samples underwent further ultrasonic cleaning in order to ensure that all of the clay had been removed from the crushed foraminiferal tests. 500μl of boron-free MQ were added to the sample vials,

followed by 15 seconds of ultrasonication to shake fine-grained clay particles into suspension, so they could be removed by pipetting. This was repeated seven times to remove all of the clays from the tests. Crushing of the samples opened up the foraminiferal tests to allow contaminates to be removed from the inside of the foraminifer tests by ultrasonic cleaning. Sample crushing also exposed all surfaces of the foraminifera tests to cleaning fluids.

For selected samples, a reductive cleaning stage (Boyle and Keigwin, 1985; Yu *et al.*, 2007) was trialled in an attempt to further reduce potential Mn oxide contaminants, as indicated by high Mn/Ca ratios from the initial sample set. For this step, 100µl of hydrous hydrazine/ammonium citrate solution was added to each sample. The reductive solution was prepared by combining 62.5µl of 31M hydrous hydrazine ($NH_2NH_2H_2O$) with 500µl of 18M ammonium hydroxide (NH_4OH) and 500µl of ammonium citrate ($(NH_4)2C_6H_8O_7$). Ammonium citrate ($(NH_4)2C_6H_8O_7$) was made by adding 5 g of citric acid ($C_6H_8O_7$) to 100 ml of 18M ammonium hydroxide (NH_4OH) solution in an ice bath. Samples were then placed in a water bath at 80ºC for 15 minutes, removing every 5 minutes to ultrasonicate for 15 seconds. Next, the samples were thoroughly rinsed with Milli-Q water 3 times to ensure all reductive solutions had been removed. The results of this trial revealed that some Mg was also removed in the reductive cleaning stage. In addition, the effect of this stage on Mn/Ca ratios was negligible; therefore, reductive cleaning was deemed unnecessary and not carried out further.

Oxidative cleaning was carried out on all samples in order to remove the organic material attached to the foraminiferal tests. For oxidative cleaning (Barker *et al.*, 2003; Yu *et al.*, 2007), 250µl of an oxidative solution of buffered hydrogen peroxide (H_2O_2) solution was added to each sample. The oxidative solution was prepared by combining

3 parts hydrogen peroxide (H_2O_2) with 7 Parts 0.1M ammonium hydroxide (NH_4OH). Samples were then placed in a water bath at 80ºC for 15 minutes, removing every 5 minutes to ultrasonicate for 15 seconds. Next, samples were rinsed 3 times with Milli-Q water in order to remove any remaining oxidative solution and transferred to new clean vials.

Following transfer, samples were subject to a weak acid leach in order to remove any remaining contaminates prior to the dissolution of the samples. 250µl of 0.0005M nitric acid (HNO_5) was added to the samples and left for 20 to 30 seconds before being diluted with Milli-Q water. Samples were then rinsed three times with Milli-Q water; all of the water was then removed. Finally, samples were dissolved in a solution of 75 µL MQ and 25 µL 0.5 M HNO_3. For samples which did not fully dissolve, additional HNO_3 was added in increments of 10 µL until they fully dissolved (see Appendix 8.7 for the amount of acid used for each sample). This final acid solution with a dissolved sample was then taken for trace element analysis.

The samples were analysed on an Agilent 8900 Triple Quadrupole Inductively Coupled Plasma Mass Spectrometer (QQQ-ICP-MS) in the STAiG laboratory at the University of St Andrews. Calcium (Ca), lithium (Li), boron (B), sodium (Na), magnesium (Mg), aluminium (Al), strontium (Sr), molybdenum (Mo), cadmium (Cd), barium (Ba), uranium (U), potassium (K), manganese (Mn), iron (Fe), nickel (Ni), copper (Cu), zinc (Zn), rubidium (Rb), phosphorous (P), sulphur (S), cobalt (Co) and neodymium (Nd) were measured. A 3µl aliquot of each sample was initially diluted in 197µl HNO_3 and analysed in order to ascertain Ca concentration. Calcium concentration results were used to calculate the volumes required in order to dilute the samples and the standards to a consistent Ca matrix of 1 mM. Samples that contained anomalously high levels of Al, Fe and/or Mn were assumed to be contaminated or contain material other than

foraminiferal calcite. These samples were excluded from the results and interpretations presented in this thesis. All results from trace element analysis are presented in Appendix 8.7.

NIST RM 8301F (Stewart *et al.*, 2021) was measured throughout the run as a consistency standard. Four in-house standards (STGFrm, STGCco, STGLim and STGCrl) were also measured before and after each run for calibration purposes. Samples and consistency standards were bracketed by an in-house standard (STGFrm). The reproducibility of NIST RM 8301F across all runs is shown in Table 2.5.2.1. All measurements of NIST RM 8301F for each run are shown in Appendix 8.8.

Element	Unit	Mean (This study)	Mean (Inter lab) (Stewart et al., 2021)	STDEV	Relative STDEV
Li^{7}/Ca	µmol/mol	9.353743983	9.01	0.185752127	1.985858571
B^{11}/Ca	µmol/mol	145.2055539	138.9	2.519140376	1.734878804
Na^{23}/Ca	mmol/mol	2.986765384	3.06	0.026921772	0.901368832
Mg^{24}/Ca	mmol/mol	2.608839928	2.62	0.016094396	0.61691774
Mg^{25}/Ca	mmol/mol	2.622434541	2.62	0.020361001	0.776415985
Mg^{26}/Ca	mmol/mol	2.624786252		0.018182386	0.692718726
Al^{27}/Ca	µmol/mol	98.95952294	90.91	1.135945416	1.147888937
Sr^{88}/Ca	mmol/mol	1.338840015	1.34	0.008139124	0.607923552
Mo^{92}/Ca	µmol/mol	0.077911451	3.9	0.011043983	14.17504435
Cd^{111}/Ca	µmol/mol	0.600293948	0.58	0.021442864	3.572060728
Ba^{138}/Ca	µmol/mol	3.970839429	3.9	0.033031568	0.83185354
U^{238}/Ca	nmol/mol	67.91163765	68.7	1.490635808	2.19496372
$K^{39}H^{2}/Ca$	µmol/mol	0.319123691		1.223774339	383.4796262
$Mn^{55}H^{2}/Ca$	µmol/mol	50.87955733	49.4	0.863767214	1.697670459
$Fe^{56}H^{2}/Ca$	µmol/mol	25.00035473	25.42	1.410214803	5.640779174
$Ni^{58}H^{2}/Ca$	µmol/mol	5.628756453		0.630152372	11.1952325
$Cu^{63}H^{2}/Ca$	µmol/mol	5.597854664		0.222027297	3.966292622
$Zn^{64}H^{2}/Ca$	µmol/mol	9.102421509		0.579867729	6.370477668
$Rb^{85}H^{2}/Ca$	µmol/mol	0.079644462		0.003567912	4.479798633
$P^{31\text{-}47}O^{2}/Ca$	µmol/mol	31.15452845		0.894933391	2.872562788
$S^{32\text{-}48}O^{2}/Ca$	mmol/mol	0.070690492		0.022711496	32.12807809
$Co^{59\text{-}75}O^{2}/Ca$	µmol/mol	0.817760949		0.109614315	13.40420027
$Nd^{146\text{-}162}O^{2}/Ca$	µmol/mol	5.118908729	5.06	0.166280627	3.248360846

Table 2.5.2.1 – Table showing reproducibility data for measurements of NIST RM8301F compiled for all runs used in this study.

2.7 X-Ray Diffraction

Kottaphi Hill

Five samples from the Kottaphi Hill succession and 12 samples from Prof. Alastair Robertson's 'Reconnaissance sampling' of the Lapatza Hill succession were selected for X-ray diffraction (XRD) analysis in order to determine the mineral assemblage composition of the samples. XRD is a semiquantitative method, as the relative proportions of minerals within a sample can be estimated based on peak area and diffraction pattern intensity.

The samples were air-dried and then roughly broken up to ensure that no diagenetic features were present. Next, 1 g of fresh, unaltered sample was ground to a powder using a mortar and pestle and pressed to a pellet using a Spex® SamplePrep X-Press® Hydraulic Laboratory Pellet Press. A small particle size and planar upper surface are essential to avoid diffraction-related artefacts and ensure adequate representation of all mineral components (Bish and Reynolds, 1989). The samples were analysed using a Bruker D8 Advance Diffractometer with a Sol-x energy dispersive detector using CuKα primary radiation generated at an accelerating voltage of 40KV tube current of 40mA. CuKαII peaks were removed through electronic filtering. X-ray diffractograms were produced using the Bruker Diffrac. EVA analysis package. The phases present were identified through comparison with standard reference patterns from the International Centre for Diffraction Data (ICDD) database. The catalogue of Brown and Brindley (1980) was used to identify minerals based on d-spacings calculated from diffraction peaks.

Lapatza Hill

The 12 samples from Lapatza Hill underwent additional analysis in order to examine the clay minerals present and were, therefore, analysed using a different method to the samples from Kottaphi Hill. These samples were smeared onto 2.5cm glass specimen powder holders producing a planar upper surface. A small particle size and planar upper surface are essential to avoid diffraction-related artefacts and ensure adequate representation of all mineral components (Bish and Reynolds, 1989). These samples were then analysed using the method detailed above for the samples from Kottaphi Hill.

For clay mineral separation, samples were roughly disaggregated using a mortar and pestle. Samples were then soaked in 100ml of deionised water. Six drops of deflocculant were then added and samples were mixed and ultrasonicated for 10 minutes in order to aid the separation of clay minerals from coarse-grained particles.

Samples were left for two hours of gravity settling, after which clay particles were held in suspension, but all other sediment had accumulated at the bottom of the beaker. The liquid and clay minerals held in suspension were extracted and centrifuged for 10 minutes. Next, the supernatant liquid was extracted using a pipette. Samples were then transferred by pipette onto clean glass slides and left to air dry for 24 hours. After drying, the slides were placed onto specimen holders and analysed as detailed above in the diffractometer. The samples were saturated with ethylene glycol, using vapour treatment in order to identify expandable clay minerals. After ‘vapour treatment’, samples were analysed again in the diffractometer. The samples were then heated for 10 minutes in an oven at 400 °C and analysed again, before being heated for 10 minutes in a 500 °C oven and analysed for a final time. This four-step method of

analysis is well established in the literature (e.g. Marumo, 1986; Rawlins *et al.*, 2006; Melo *et al.*, 2008; Bergslien, 2013).

2.8 **X-Ray Fluorescence**

5 samples from the Kottaphi Hill succession were selected for X-ray fluorescence (XRF) analysis, in order to determine the major and trace-element composition of the sediments of each facies. The same procedure of pressed pellet production used for XRD analysis was followed for XRF spectrometry. The techniques used for whole rock chemical analysis by XRF spectrometry were described by Fitton *et al.* (1997) and Fitton and Godard (2004). Samples were analysed using a Phillips 1280 wavelength dispersive sequential X-ray fluorescence spectrometer at The University of Edinburgh.

2.9 **Scanning Electron Microscopy**

Scanning electron microscopy (SEM) was used in order to examine the preservation quality of planktic foraminiferal samples from the *Praeorbulina-Orbulina* lineage and to inspect the efficacy of the cleaning procedures. In addition to imaging, energy dispersive X-ray spectrometry (EDS) allowed for chemical analyses of the planktic foraminifera sample surfaces, therefore helping to determine the composition of any diagenetically altered components of the foraminiferal tests. The SEM and EDS analysis took place at the University of Edinburgh, using a Carl Zeiss SIGMA DH VP field emission scanning electron microscope and Oxford AZtec ED X-ray analysis software. Twenty-five samples at an approximately regular spacing throughout the composite section were selected for SEM analysis, imaging samples throughout the whole section allows for a full range of foraminifera species and preservation qualities to be examined. Following the cleaning procedure used for stable isotope analyses (Chapter 2.5.2), two specimens of planktic foraminifera from each selected sample were picked for analysis. In addition, additional specimens from six uncleaned

samples were selected to represent a full range of preservation standards. Finally, four cleaned and four uncleaned specimens from a sample that exhibited infill of the foraminiferal tests. For each sample, one specimen was broken to reveal internal structures and the other was left intact. The foraminifera were mounted onto carbon adhesive mounting discs and platinum coated. Images and spectra were produced at an accelerating voltage of 10 kV, an aperture size of 80 μm, and a working distance of 7 ± 1 mm.

3 Stratigraphy and Sedimentology

This chapter outlines the methods used and results produced to deliver a stratigraphic framework and age model that, in turn, provides the context for other findings from this research. Methods and results that are used to understand the geological setting of the successions sampled are also presented here. This chapter includes a discussion of the data presented within it, outlining initial interpretations based on these data. The results and the discussion of this chapter contribute to the synthesis presented in this thesis in Chapter 6.

A sound understanding of the stratigraphy of the successions sampled is essential and is the foundation of any valid palaeoceanographic interpretations. Understanding the lithostratigraphy and sedimentology of the successions is fundamental to assess the impact of global climate and environmental changes, regional palaeogeographical changes and both regional and local tectonic changes on the eastern Mediterranean basins. Multiple methods are used in combination to produce an age model that allows the results and interpretations from this study to be compared with previous research. The establishment of an age model for the individual successions studied is also necessary in order to produce a composite temporal record, allowing the recognition of long-term trends during Middle to Late Miocene time.

A secondary objective of this research is to constrain the dating of debris-flow deposits containing Miocene reef material in the northwest of Cyprus. The aim of dating the fossil material within these debris-flow units was to constrain the timing of the end of Early Miocene reef growth (Terra Member) in Cyprus, and to examine the relationship between the termination of reef growth and local to global scale events such as

tectonic and climatic changes. The data collected are presented in the results section; interpretations based on these data are presented in the discussion.

3.1 Methodology

3.1.1 Lithology and Field Observations

The collection of samples and logging of successions are described in Chapter 2.1.2.

3.1.2 Calcareous Nannofossil Biostratigraphy

The primary method of dating used in this study is calcareous nannofossil biostratigraphy. The methodology for calcareous nannofossil biostratigraphy, as used in this study, is described in Chapter 2.3.

Initially, calcareous nannofossil biostratigraphy during this work was carried out at a resolution of 25 cm for the Kottaphi Hill succession (*c.* 33 m thick). If a change in biozone was recognised between two dated samples, the samples between the dated samples were then examined in order to locate the bio-horizon. The same procedure was used for samples from the Lapatza Hill succession (*c.* 66 m thick); however, a 1 m resolution was used for the initial examination of this succession.

3.1.3 XRF & XRD

Field observations are supported by pilot-scale X-ray fluorescence (XRF) and X-ray diffraction (XRD) analysis (see Chapter 2.7 & 2.8 for methodology) in order to help understand the sedimentary settings of the successions sampled.

3.1.4 Foraminifera

The primary objective of picking foraminifera in this study is for geochemical analysis (Chapter 4 & Chapter 5). However, some initial observations of foraminiferal assemblages were made whilst examining the samples for suitability for geochemical analysis. These observations were compared to global (Wade *et al.*, 2011) and

regional (Lirer *et al.*, 2019) biostratigraphic schemes in order to ensure that no discrepancy existed between the ages indicated by calcareous nannofossils and foraminifera. Observations of foraminiferal assemblages are also useful for interpreting the depositional settings of pelagic and hemiplegic sediments in which they are preserved.

The geochemical analysis of foraminiferal tests contributes fundamental data to this study notably the chemostratigraphic use of the new $\delta^{18}O_{planktic}$ record to constrain the age model for this study. Foraminiferal tests are susceptible to geochemical alteration through recrystallization and overgrowth (Pearson *et al.*, 2001; Williams *et al.*, 2005; Pearson and Burgess, 2008; Bissett *et al.*, 2011; Pearson, 2012). Any such diagenetic alteration can be assumed to increase the uncertainty of geochemical analyses. However, recent research indicates that the impact of diagenetic alteration, such as recrystallization on geochemical analysis may, in general, be smaller than previously thought (Pearson, 2012; Kozdon *et al.*, 2013; Voigt *et al.*, 2016). Therefore, ensuring that only well-preserved foraminifera were used for geochemical analysis was essential. Scanning electron microscope (SEM) analysis was used in order to ensure that visual classifications of preservation quality in planktic foraminifera are accurate. Additionally, energy dispersive X-ray spectrometry (EDS) analysis was used in order to examine the chemical properties of any crystalline overgrowth and infill within foraminiferal tests. The methodology used for the SEM analysis is described in Chapter 2.9.

3.1.5 Strontium Isotope Analysis

Calcareous nannofossil dating is supported by strontium (Sr) isotope stratigraphy. This method is described in Chapter 2.4.

In addition to dating the main successions sampled, Sr isotope stratigraphy was also used to date biogenic material from Kourolla Gorge in the northwest of Cyprus. The aim of dating these samples was to better constrain the timing of the end of Terra Member-related reef growth (see below). Strontium isotope dating is useful in this instance as it allows for clasts of biogenic material to be dated individually, whereas other methods used in this study are only able to provide a date for the sedimentary matrix (microfossil ooze) in which these clasts are held.

3.1.6 Age Model

New age models were created during this work for both the Kottaphi Hill and Lapatza Hill successions. Calcareous nannofossil data provided the most complete chronology of the methods used, therefore these data were given priority as the primary method of dating. The calcareous nannofossil data is supported by Sr isotope dating.

A preliminary age model was created based on calcareous nannofossil biostratigraphy. Sedimentation rates were calculated based on the depth/height difference between samples identified as bio-horizons. Samples that were not biostratigraphically dated were assigned tentative ages using a linear interpolation based on the calculated sedimentation rate.

The final age model was produced using AnalySeries 2.0.8 (Paillard *et al.*, 1996). The aim of this step was to align the age model of the sections sampled in this study with pre-existing orbitally tuned records from open oceans. The new $\delta^{18}O_{planktic}$ record produced for this study (see Chapter 2.5.2 for methods) was used for this purpose and aligned to the North Atlantic $\delta^{18}O_{benthic}$ compilation record of Cramer *et al.* (2009).

For the alignment, the new $\delta^{18}O_{planktic}$ record was filtered using multiple steps (20, 60, 100 ky) of box filtering, in order to reduce ‘noise’ and only show long-term trends and

major perturbations. The preliminary age model was segmented into sections separated by key biostratigraphic tie points. These segments were then compared and aligned with the reference record. Major trends within the record were aligned with the reference record by creating tie points at the midpoints of such trends. This age modelling technique has uncertainty which is produced by a combination of uncertainties associated with calcareous nannofossil biostratigraphy, uncertainties associated with the $\delta^{18}O_{planktic}$ record of this study and the uncertainties associated with the $\delta^{18}O_{benthic}$ target record (Cramer *et al.*, 2009). The sampling resolution (number of samples per My) for the two successions used in this study is not considered high enough for astronomical tuning.

Individual age models for both the Kottaphi Hill and Lapatza Hill successions were produced using the same method. After an age model had been produced for each succession, the records were carefully compared in order to find an appropriate splice point to combine the two records. The records were then combined at this splice point to produce a composite temporal record covering the whole time interval of interest. The age models and information about the selection of the splice point are presented in Chapter 3.2.6.

3.2 **Results**

3.2.1 Lithology and Field Observations

Kottaphi Hill

The sample collection and sedimentological study for this research took place with the main objective of creating geochemical records for the Miocene Epoch. For this reason, previous research on the Kottaphi Hill succession was utilised in order to identify the interval of interest. The base of the section, which is older than the target time range (and appears more diagenetically altered than the sampled section) was

not studied in this work. The Kottaphi Hill succession detailed in this thesis begins *c.* 10 m stratigraphically below the prominent hard layer which was previously documented as a ‘hardground’ by several previous authors (Chapter 2.1.1).

A simplified stratigraphic log of the Kottaphi Hill succession sampled is shown in Figure 3.2.1.1, whereas the full, detailed stratigraphic log of the succession is shown in Figure 3.2.1.3. The succession at Kottaphi Hill was divided into facies associations (A-G) which are separated by significant changes in lithology.

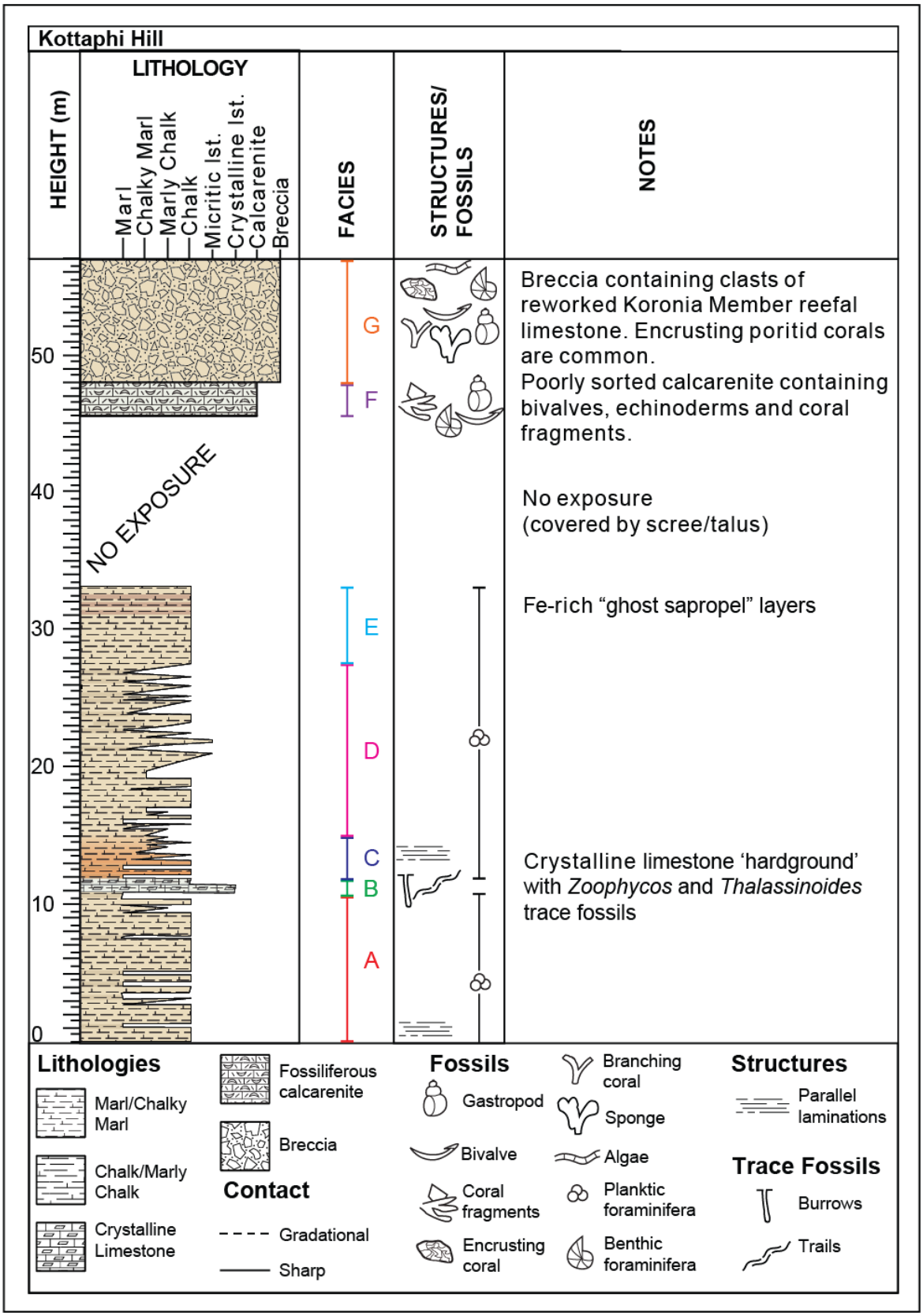


Figure 3.2.1.1 – Simplified stratigraphic log of the Kottaphi Hill succession showing the occurrence of sedimentary structures, fossils and general trend of lithological and facies changes up the section. This figure is a simplified version of Figure 3.2.1.3.

The measured succession at Kottaphi Hill begins with 10.97 m of alternating beds of light buff-coloured chalk and slightly darker buff-coloured calcareous marl (Figure 3.2.1.2B). These alternating chalk-calcareous marl beds are labelled facies A in Figure 3.2.1.1 Planktic foraminifera are abundant in both the chalk and calcareous marl layers. In the chalk beds, the planktic foraminifera are supported by a matrix of calcareous nannofossil ooze (*c.* 95%). In the calcareous marl units, planktic foraminifera are supported by a matrix of clay minerals (*c.* 25%) as well as calcareous nannofossil ooze. The calcareous marl layers are less resistant to weathering than the chalk layers. The lowermost beds preserve well-defined parallel laminations; rare vertical burrows were identified in some chalk beds but no other sedimentary features are present in this facies.

At 10.97 m, an abrupt lithological change is identified between the top of facies A and the base of facies B. Facies B represents the layer documented as a ‘hardground’ by several previous authors (see Chapter 2.1.1 & Chapter 3.3.2) (Figure 3.2.1.2C & D). In this study, this layer is interpreted to represent a firm ground, rather than a hard ground (see Chapter 3.3.2). The final calcareous marl bed of the underlying sequence (Facies A) has an irregular upper surface and laminations parallel to this irregular surface are preserved within this bed. Above, three thin layers (4-15 cm) of light grey crystalline limestone are interbedded with darker buff micritic limestone (3-10 cm thick). These beds are labelled facies B in Figure 3.2.1.1. All of the beds of this facies have distinctively irregular upper and lower surfaces. The light grey limestone is significantly harder than the other lithologies in this succession (making a metallic noise when hit with a hammer). The upper surfaces of the three hard grey limestone beds are dominated by well-preserved *Thalassinoides, Diplocraterion* and *Zoophycos* trace fossils. Dark grey, black, and reddish brown calcite crystals are also found in this

hard limestone unit together with small nodules and concretions. In the field, these nodules were inferred to be early diagenetic Manganese concretions.

The beds directly above the top of facies B have a distinct pinkish-red colour (Figure 3.2.1.2E & F). This colour gradually fades to a buff colour over *c.* 4 m of chalk-calcareous marl interbeds. These chalk and calcareous marl interbeds start at 11.3 m above the final micritic limestone layer of facies B, and are labelled as facies C (Figure 3.2.1.1). Upwards, calcareous marl beds in facies C regularly become more chalk-like and harder at their tops. In contrast to facies A, calcareous marl beds comprise the major proportion (*c.* 65%) of the beds in facies C.

At 15.09 m, the distinctive pinkish colour of facies C is no longer seen; this point marks the base of facies D (Figure 3.2.1.1). Facies D also comprises chalk and calcareous marl interbeds; however, in this facies, the chalk beds have a higher relative abundance than the calcareous marl beds. At the midpoint (*c.* 21 m) of this unit, two beds of micritic limestone are present. These beds are visually similar to the chalk beds of this facies, but are distinguished by their increased hardness and resistance to weathering. From these harder beds to the top of this unit, the calcareous marl beds exhibit a slightly darker colour and reduced resistance to weathering (Figure 3.2.1.2G).

Ten thick (30-85 cm) chalky marl beds that are interbedded with thinner (5-20 cm) marl beds span 27.79 m to 32.96 m (facies E). Several soft marl beds within this facies have a distinctive dark reddish brown colour (Figure 3.2.1.2H). In the field, these reddish brown marl layers were interpreted as oxidised “ghost” sapropels.

Facies A to E are assigned to the undifferentiated Pakhna Formation and were therefore sampled for geochemical analysis and biostratigraphic dating.

At 32.96 m, the exposure is covered by reworked debris from the above units, together with modern soil and plant material. This break in exposure ends at *c.* 45.5 m. Rare patchy exposures in this interval comprise buff to light brown coloured marl with infrequent beds of biogenic calcarenite. The calcarenite is mostly composed of fragmented bivalve shells and large benthic foraminifera; these layers were intepreted as debris-flow deposits in the field.

Above the interval of poor exposure irregular, poorly defined beds of bioclastic calcarenite are found above a poorly defined base at *c.* 45.5 m height in the succession. These calcarenite beds are assigned to Facies F (Figure 3.2.1.1). Poorly sorted bivalve shells, large benthic foraminifera and echinoderm spines, together with algal and coral fragments make up the biogenic component of these calcarenite beds. All of the biogenic material in this unit is heavily fragmentary. In the calcarenite beds, clast size ranges from < 1 mm to *c.* 5 mm in size and some beds show weak normal grading. The calcarenite is matrix-supported and separated by thin (<15 cm) clay-rich beds.

The calcarenite beds of facies F are, in turn, overlain by a massive clast-supported breccia unit labelled facies G in Figure 3.2.1.1. This unit continues for *c*. 9 m to the summit of Kottaphi Hill. Clasts in this breccia are poorly sorted. The majority of the clasts range from 2-40 cm in size; however, some large blocks (up to 3 m) are also present. A small amount of calcareous marl matrix is present, similar to the lithology of the underlying facies. Encrusting poritid corals make up the dominant proportion of the clasts, together with some branching poritid coral and poorly preserved fragmented poritid coral and calcareous algae. Calcarenite clasts consisting of bivalve fragments, gastropod shells, serpulid worm tubes, echinoderms and benthic foraminifera make up the remaining proportion of clasts in this breccia. These calcarenite clasts appear

to be of the same lithology as the underlying facies F. This facies has previously been the subject of detailed study (Follows, 1992; Coletti *et al.*, 2021), as discussed in Chapter 3.3.2.

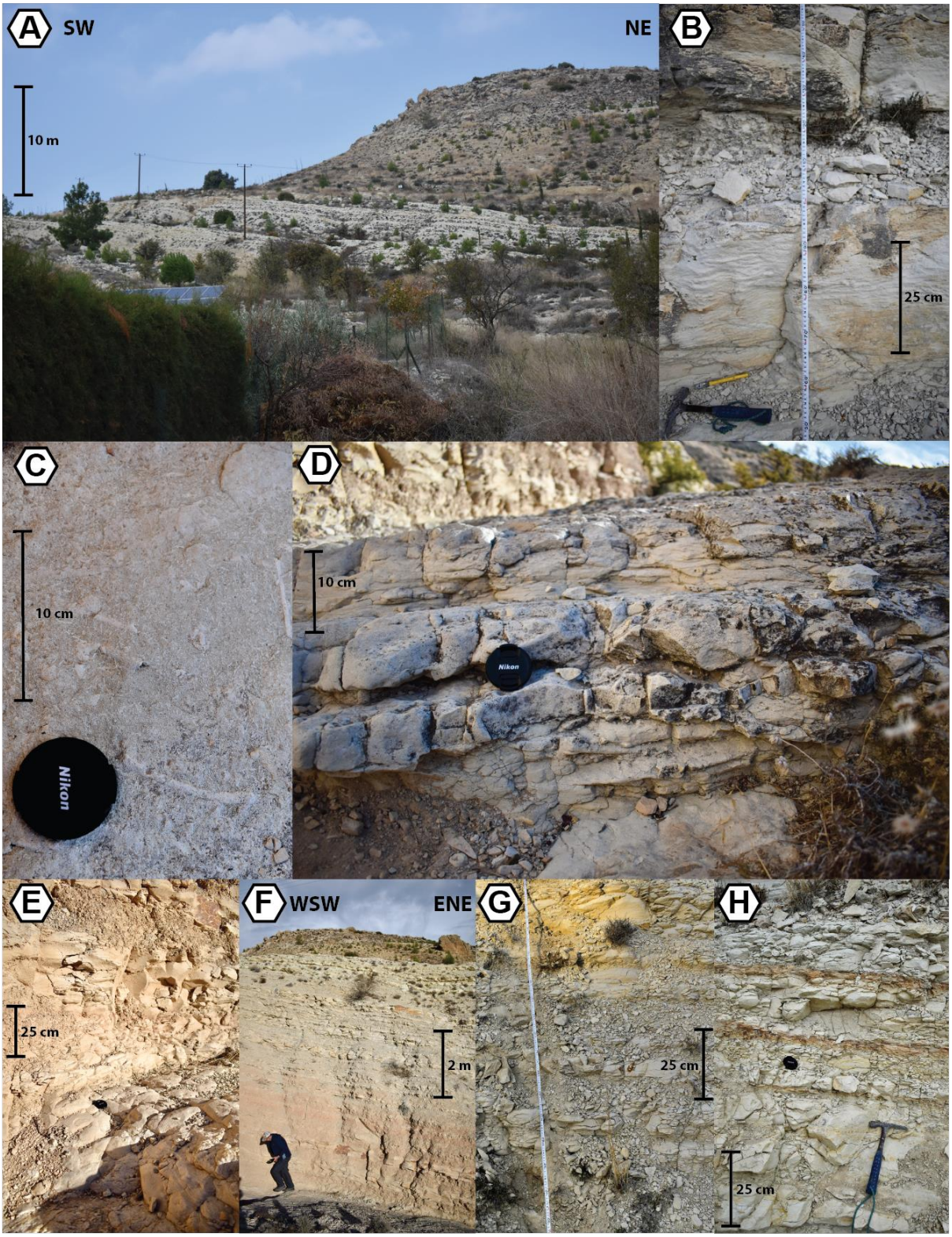
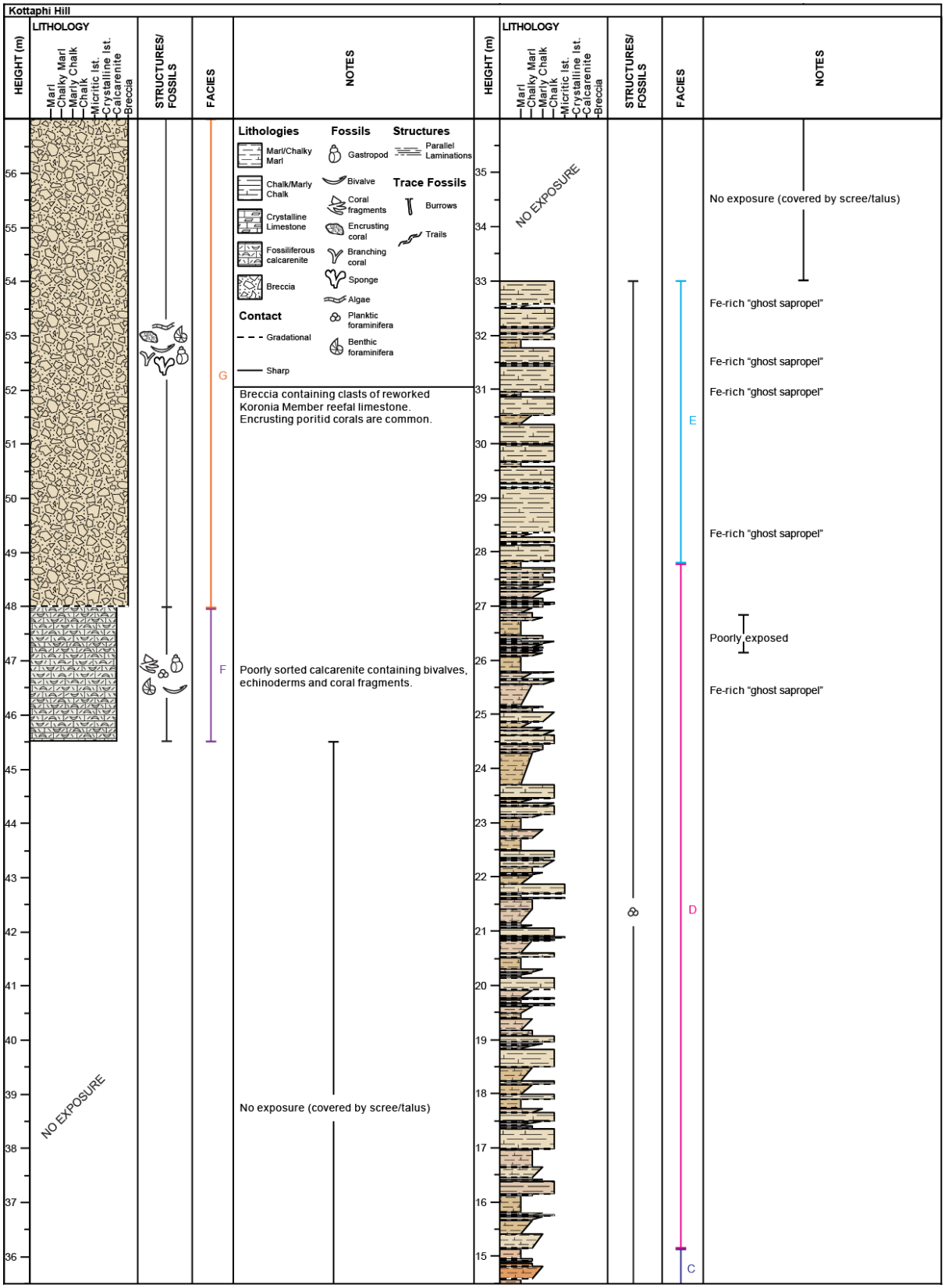


Figure 3.2.1.2 – Selected photographs of the succession sampled at Kottaphi Hill: (A) Overview of the whole succession; (B) Facies A chalk and calcareous marl; (C) *Thalassinoides* ichnofossils on the upper surface of the top bed of facies B; (D) Cross section view of facies B; (E) The transition between facies B and C; (F) Facies C, note the pinkish colour; (G) Facies D, note the darker brown layers within the marl beds; (F) Facies E, note the dark red layers.


Kottaphi Hill
HEIGHT (m)
LITHOLOGY
Marl
Chalky Marl
Marly Chalk
Chalk
Micritic lst.
Crystalline lst.
Calcarenite
Breccia
STRUCTURES/ FOSSILS
FACIES
NOTES
Lithologies
Marl/Chalky Marl
Chalk/Marly Chalk
Crystalline Limestone
Fossiliferous calcarenite
Breccia
Contact
Gradational
Sharp
Fossils
Gastropod
Bivalve
Coral fragments
Encrusting coral
Branching coral
Sponge
Algae
Planktic foraminifera
Benthic foraminifera
Structures
Parallel Laminations
Trace Fossils
Burrows
Trails
Breccia containing clasts of reworked Koronia Member reefal limestone. Encrusting poritid corals are common.
Poorly sorted calcarenite containing bivalves, echinoderms and coral fragments.
No exposure (covered by scree/talus)
NO EXPOSURE
G
F
E
D
C
No exposure (covered by scree/talus)
Fe-rich "ghost sapropel"
Fe-rich "ghost sapropel"
Fe-rich "ghost sapropel"
Fe-rich "ghost sapropel"
Poorly exposed
Fe-rich "ghost sapropel"

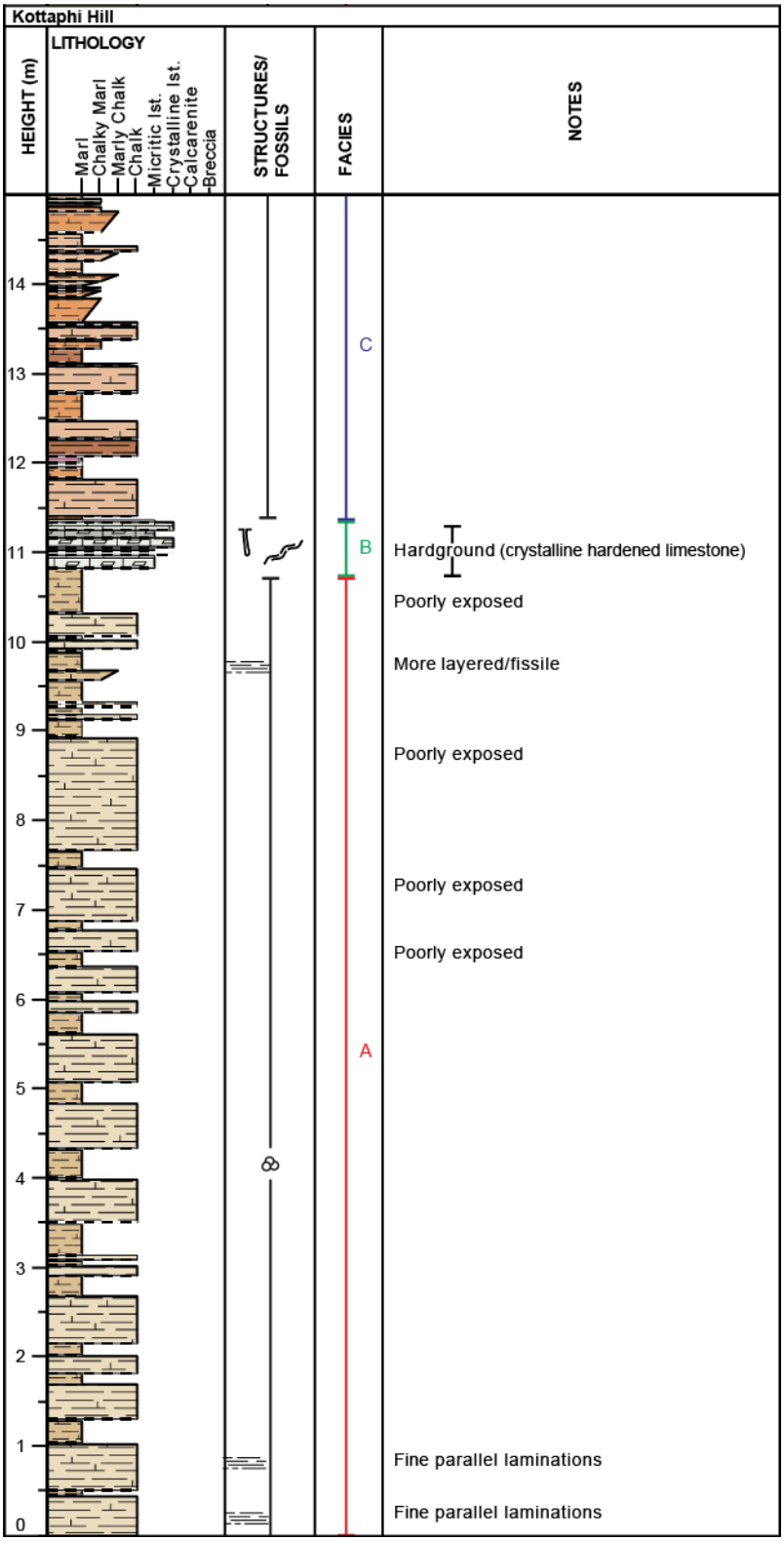


Figure 3.2.1.3 – Stratigraphic log of the Kottaphi Hill succession showing the occurrence of sedimentary structures, fossils and general trend of lithological and facies changes up the section.

Lapatza Hill

The succession studied at Lapatza Hill (Figure 3.2.1.4 & Figure 3.2.1.5) comprises a 63.1 m sequence of marl with infrequent chalky marl interbeds. This sequence is overlain by a *c.* 15 m thick sequence of fine-grained alabastrine gypsum that continues to the summit of the hill.

The majority of the sequence is composed of calcareous marl, with infrequent layers of darker brown marl, dark red marl and chalky calcareous marl. Fine parallel laminations are present throughout the succession; these laminations are more prominent towards the top of the sequence. No other notable sedimentary structures were identified.

The calcareous marls are very rich in planktic foraminifera at the base; however, at *c.* 52.5 m this abundance is reduced, especially in the softest marl beds. At *c.* 61 m, foraminifera are completely absent. Some foraminifera are found in chalky marl beds at *c.* 62 m; however, their abundance rapidly decreases towards an abrupt contact with the base of the overlying evaporate unit. No other body or trace fossils were found in this sequence.

Thin (1-5 cm) dark brown marl layers are frequent within the calcareous marl sequence. Some of these layers have dark grey dendritic patterns (related to oxidative weathering) on their upper surfaces (Figure 3.2.1.5C). These dark brown layers are often (but not exclusively) found in alternation with dark red marl layers. In such sequences, the red layers are found above the brown layers. In general, the frequency of the dark layers is irregular; however, three occurrences of regularly space darker layers are noted throughout the sequence (at *c.* 8.6 m, *c.* 10.2 m and *c.* 38.6 m). There, darker marl layers of 3-5 cm thickness are interbedded with 3-5 cm marl layers and

dark reddish marl for an interval of 50-80 cm. The origin of these darker marl layers is discussed in Chapter 3.3.3. These regularly spaced layers are harder than other dark red and dark brown marl layers in the sequence.

Towards the top of the section, infrequent layers of bright yellow fine-grained material are found together with layers of remobilised secondary gypsum. Infrequent lighter-coloured bands of chalky calcareous marl were also noted in the upper half of the sequence.

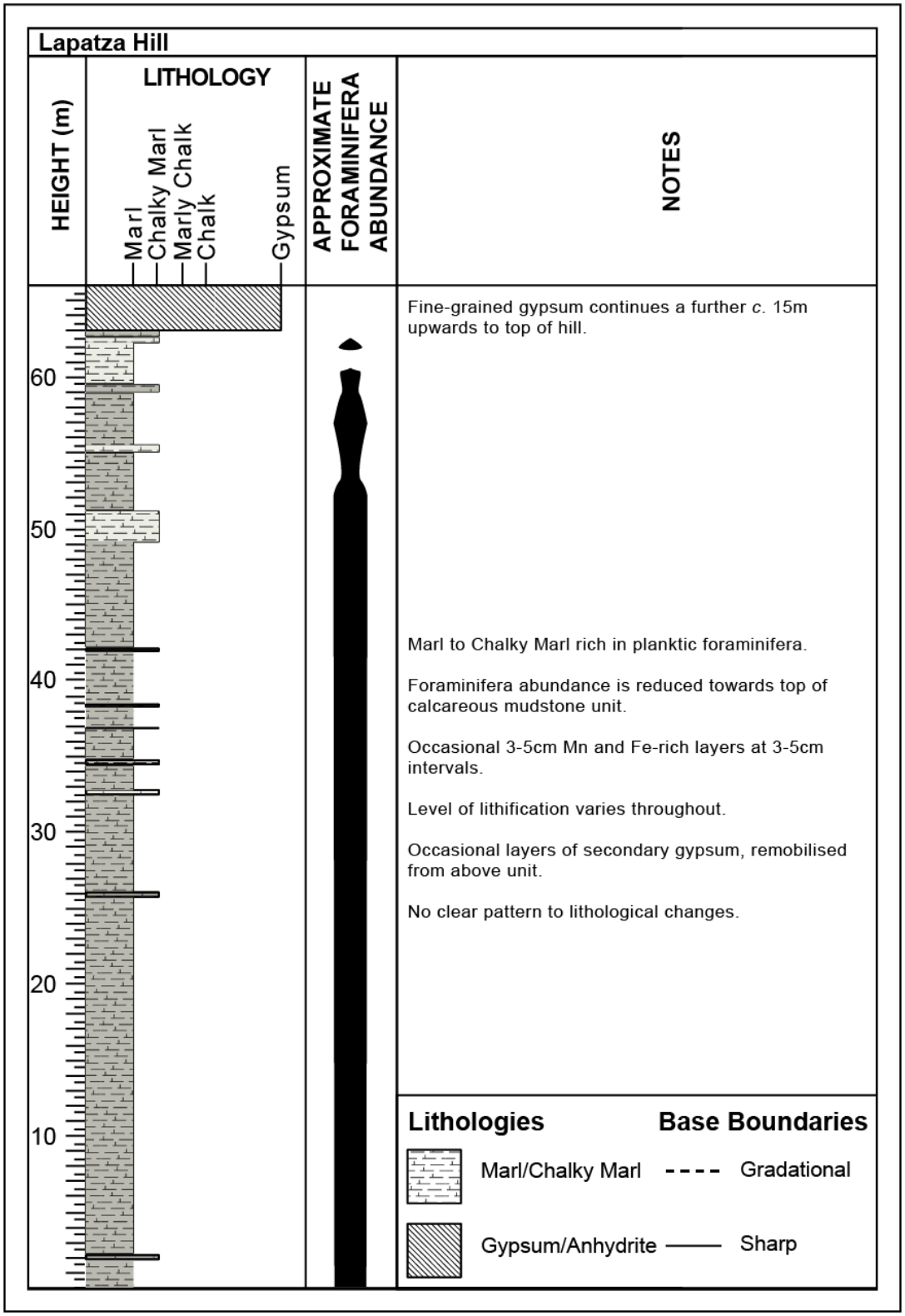


Figure 3.2.1.4 – Simplified stratigraphic log of the Lapatza Hill succession showing the approximate abundance of planktic foraminifera, and the general trend of lithological changes up the section. This figure is a simplified version of Figure 3.2.1.6.

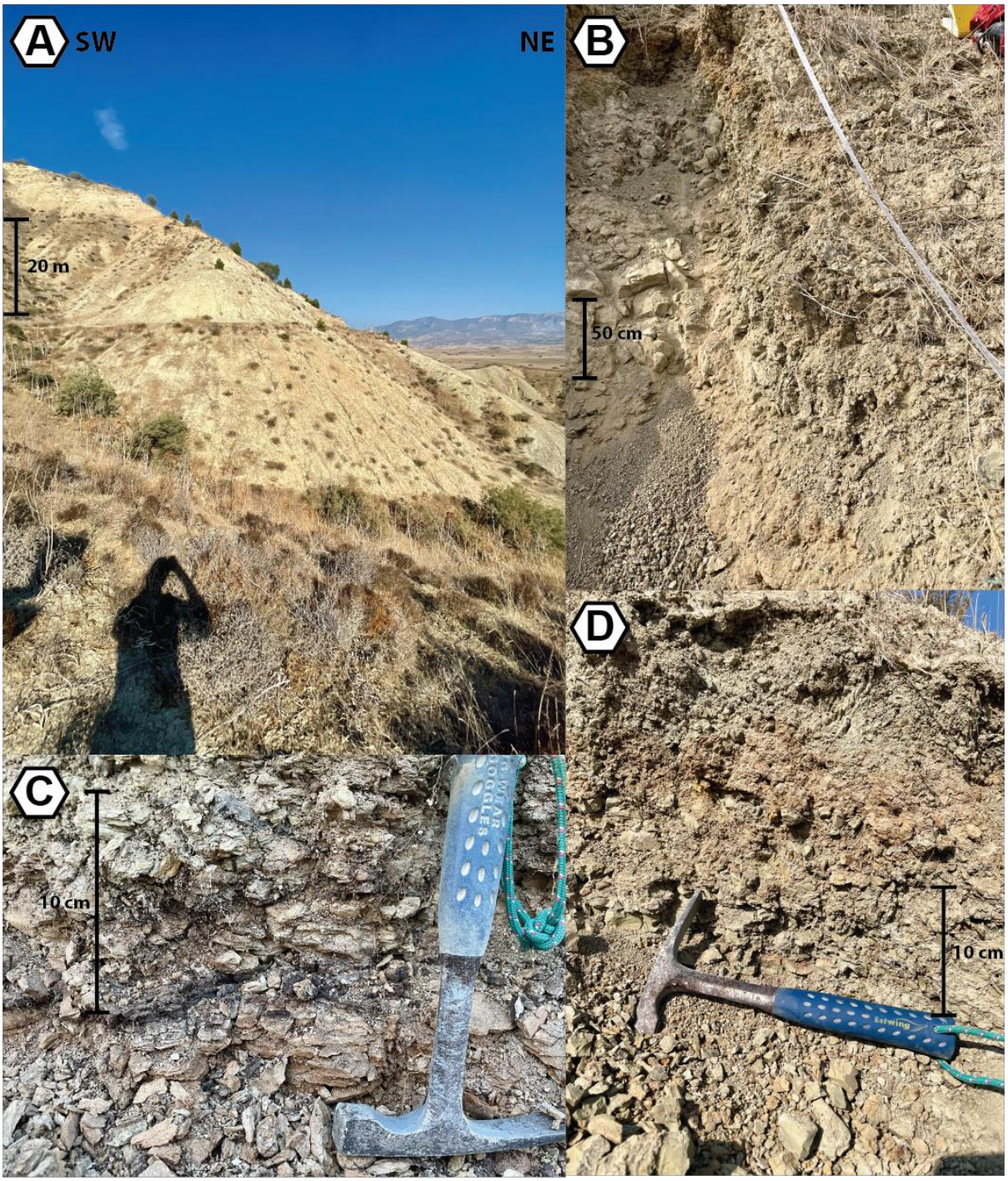
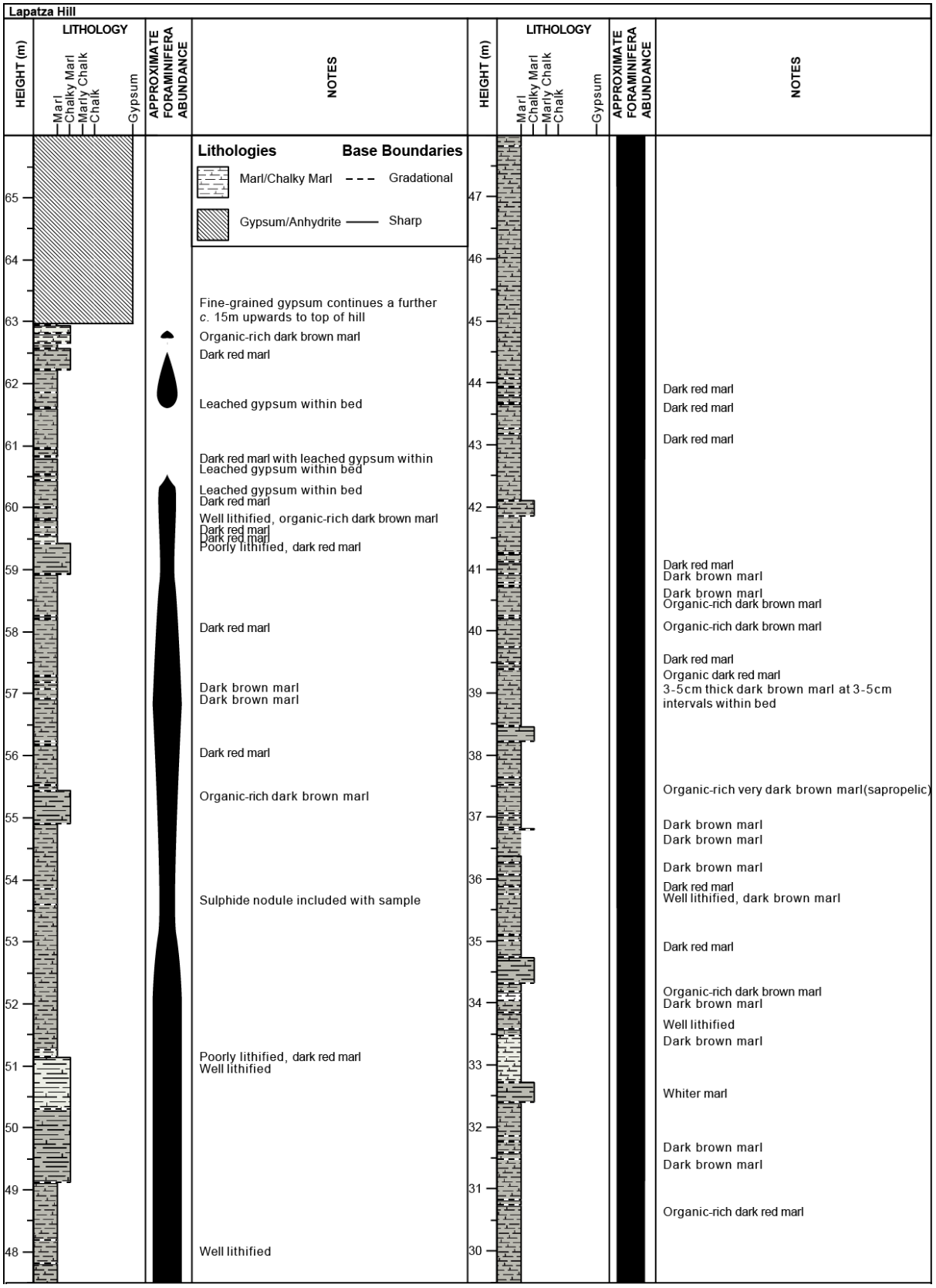


Figure 3.2.1.5 – Selected photographs of the succession sampled at Lapatza Hill: (A) Overview of the succession; (B) Example of chalky marl beds in the small trench dug for sampling at *c.* 50 m; (C) Example of a dark muddy layer at *c.* 26 m; (D) Example of muddy marl layers at *c.* 3 m.


Lapatza Hill
HEIGHT (m)
LITHOLOGY
Marl
Chalky Marl
Marly Chalk
Chalk
Gypsum
APPROXIMATE FORAMINIFERA ABUNDANCE
NOTES
Lithologies
Base Boundaries
Marl/Chalky Marl
Gradational
Gypsum/Anhydrite
Sharp
65
64
63
62
61
60
59
58
57
56
55
54
53
52
51
50
49
48
Fine-grained gypsum continues a further c. 15m upwards to top of hill
Organic-rich dark brown marl
Dark red marl
Leached gypsum within bed
Dark red marl with leached gypsum within
Leached gypsum within bed
Leached gypsum within bed
Dark red marl
Well lithified, organic-rich dark brown marl
Dark red marl
Dark red marl
Poorly lithified, dark red marl
Dark red marl
Dark brown marl
Dark brown marl
Dark red marl
Organic-rich dark brown marl
Sulphide nodule included with sample
Poorly lithified, dark red marl
Well lithified
Well lithified
47
46
45
44
43
42
41
40
39
38
37
36
35
34
33
32
31
30
Dark red marl
Dark red marl
Dark red marl
Dark red marl
Dark brown marl
Dark brown marl
Organic-rich dark brown marl
Organic-rich dark brown marl
Dark red marl
Organic dark red marl
3-5cm thick dark brown marl at 3-5cm intervals within bed
Organic-rich very dark brown marl(sapropelic)
Dark brown marl
Dark brown marl
Dark brown marl
Dark red marl
Well lithified, dark brown marl
Dark red marl
Organic-rich dark brown marl
Dark brown marl
Well lithified
Dark brown marl
Whiter marl
Dark brown marl
Dark brown marl
Organic-rich dark red marl

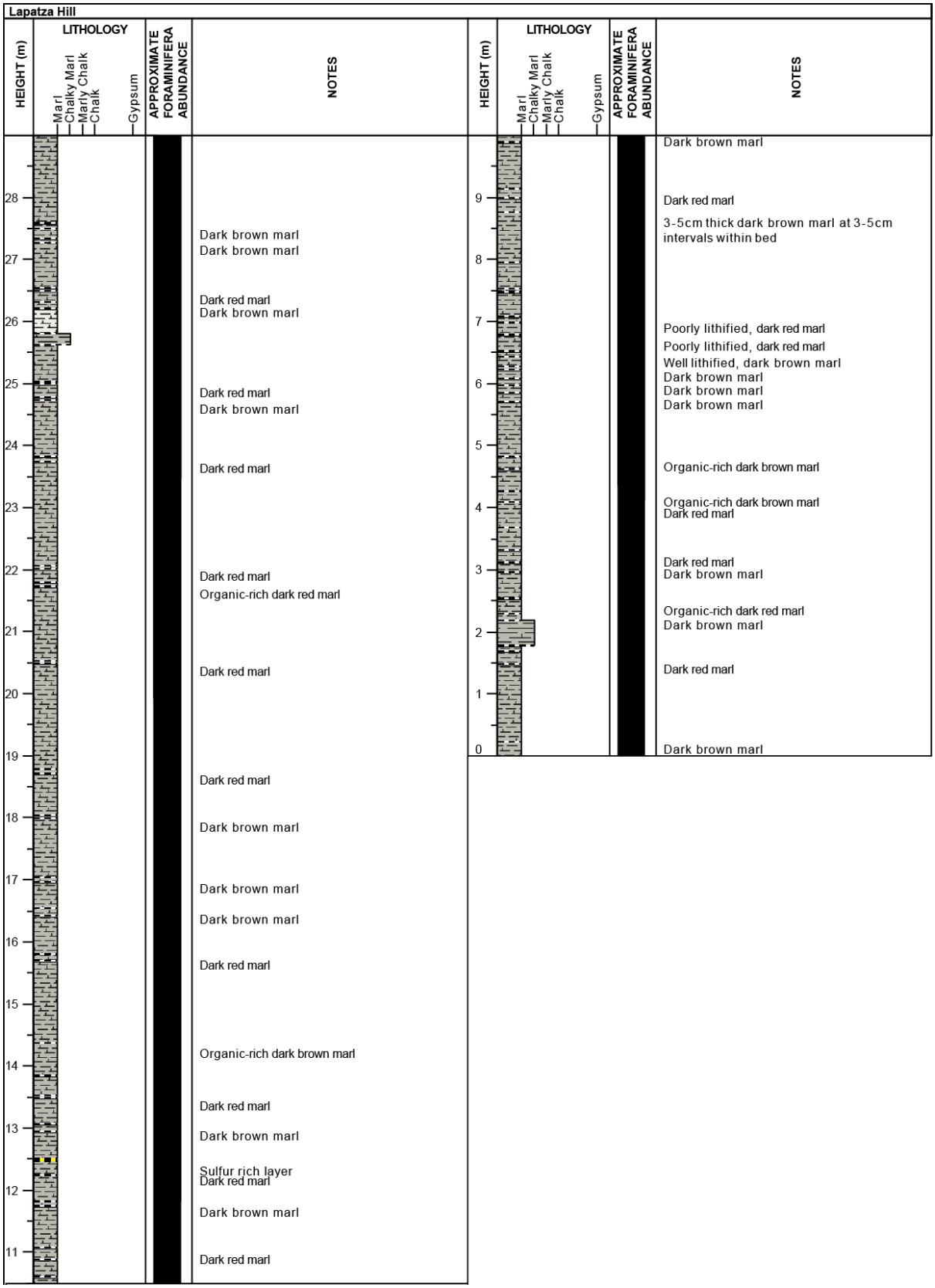


Figure 3.2.1.6 – Stratigraphic log of the Lapatza Hill succession showing the approximate abundance of planktic foraminifera, and the general trend of lithological changes up the section.

3.2.2 Calcareous Nannofossil Biostratigraphy

Kottaphi Hill

Figure 3.2.2.1 and Figure 3.2.2.2 show the ages obtained from calcareous nannofossil biostratigraphy for the samples from the Kottaphi Hill succession. According to this biostratigraphy, the base of the succession sampled at Kottaphi Hill is between 19.01 and 17.96 Ma, as indicated by the presence of *Sphenolithus belemnos* (using the biostratigraphy of Backman *et al.*, 2012). The top of the succession is slightly younger than 8.8 Ma, as indicated by an increase in the relative abundance of *Reticulofenestra pseudoumbilicus* slightly beneath the top of the succession. These dates indicate that the Kottaphi Hill succession has an average sedimentation rate (non-decompacted) of *c.* 0.25 cm/ky. Calcareous nannofossil biostratigraphy indicates the highest sedimentation rate (non-decompacted) was 0.33 cm/ky between 11.88 Ma and 11.60 Ma. The lowest sedimentation rate (non-decompacted) is indicated to have been 0.19 cm/ky between 17.75 Ma and 15.73 Ma. These non-decompacted sedimentation rates are considered useful, as there is no evidence of any deep burial of either of the successions studied.

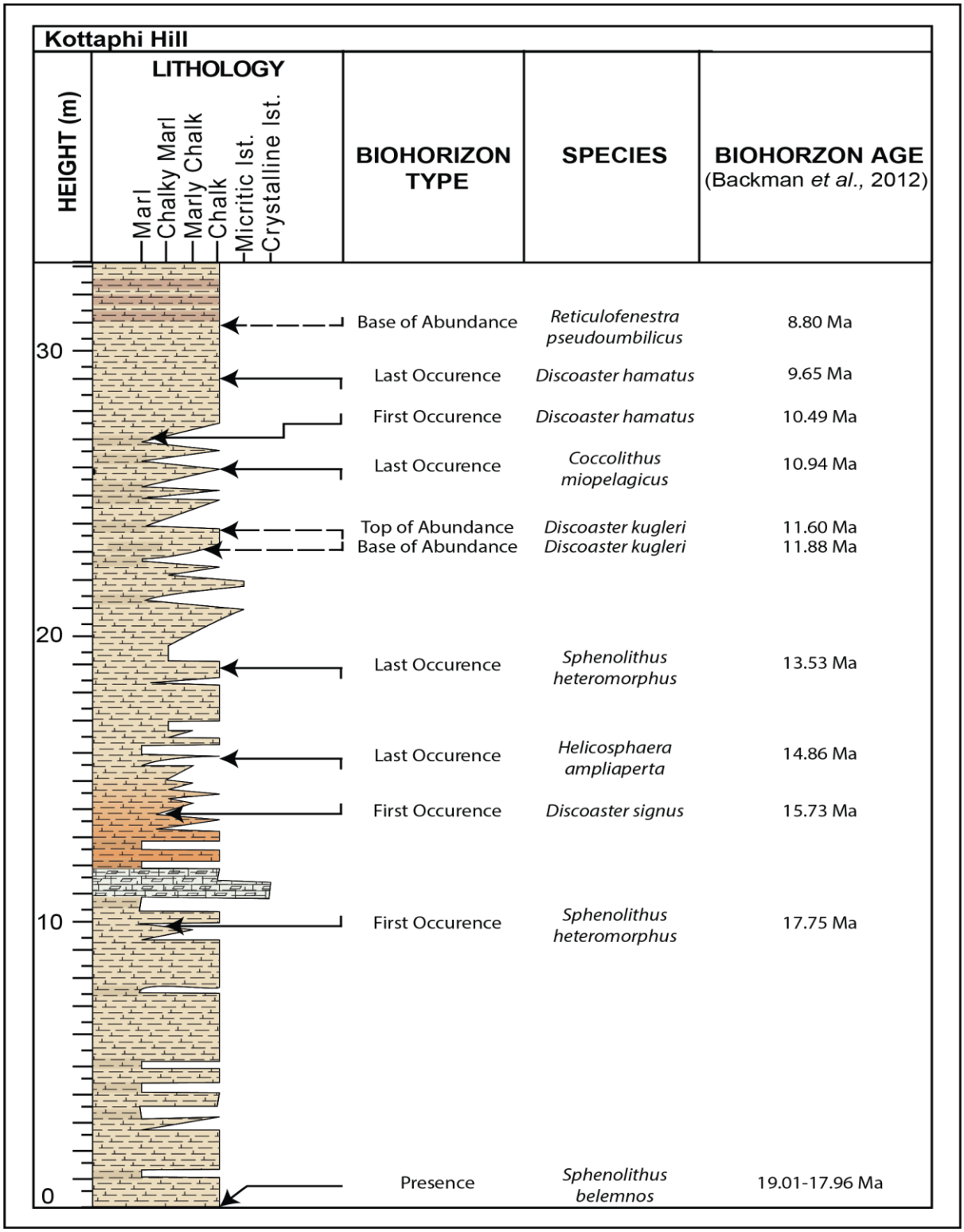


Figure 3.2.2.1 – Stratigraphic log of the succession sampled at Kottaphi Hill with the height and nature of biohorizons annotated, together with ages according to Backman *et al*. (2012). Bio-horizons based on relative abundance (Backman *et al.*, 2012) are less quantitative than other bio-horizons and are marked with a dashed line.

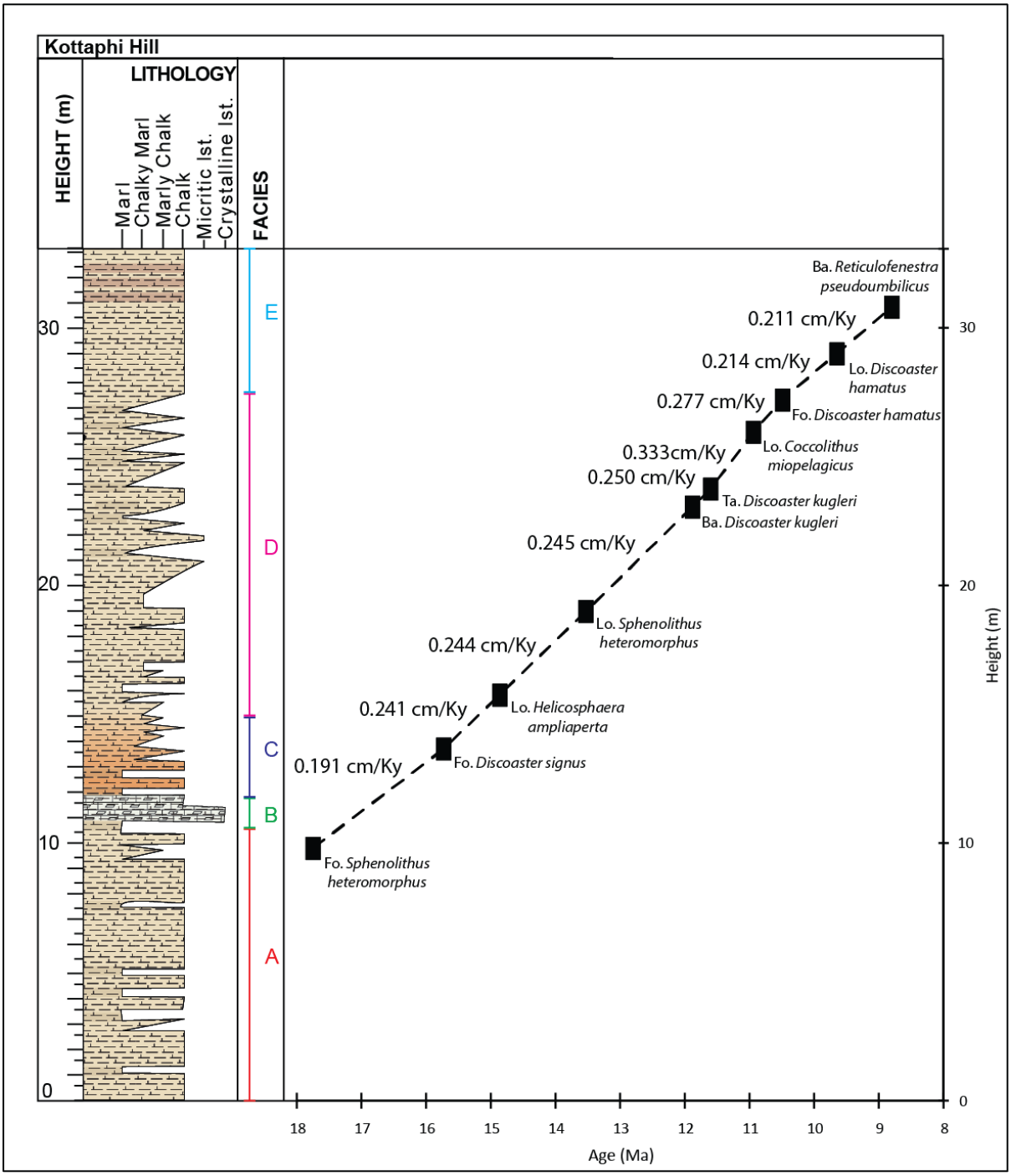


Figure 3.2.2.2 – Stratigraphic log of the succession sampled at Kottaphi Hill with height plotted against age according to Backman *et al*. (2012). The sedimentation rate between biohorizons is also annotated. Fo. = First occurrence, Lo. = Last occurrence, Ba = Base of abundance, Ta. = Top of abundance.

Lapatza Hill

Figure 3.2.2.3 and Figure 3.2.2.4 show the ages inferred from calcareous nannofossil biostratigraphy for samples from the Lapatza Hill succession. The increase in relative abundance of *Reticulofenestra pseudoumbilicus* slightly above the base of the succession indicates that the base of the succession is older than 8.8 Ma (using the biostratigraphy of Backman *et al.*, 2012). The first occurrence of *Amaurolithus primus* at *c.* 18.5m indicates an age of 7.39 Ma. These dates indicate that the Lapatza Hill succession has an average sedimentation rate (non-decompacted) of *c.* 1.01 cm/ky. Calcareous nannofossil biostratigraphy indicates that the highest sedimentation rate (non-decompacted) was 1.08 cm/ky between 8.8 Ma and 7.39 Ma. The lowest sedimentation rate (non-decompacted) is indicated to have been 0.92 cm/ky between 7.39 Ma and 7.09 Ma.

Calcareous nannofossil assemblages above 25 m high in the Lapatza Hill succession are not diagnostic of age. Samples from the upper part of the section contain a diverse calcareous nannofossil assemblage; however, age-indicative species are unfortunately absent. One notable observation from the calcareous nannofossil biostratigraphy of the Lapatza Hill succession is the absence of all calcareous nannofossils from the *Discoaster* genus above *c.* 60 m. *Discoaster spp.* specimens are abundant in samples from the lower part of the section.

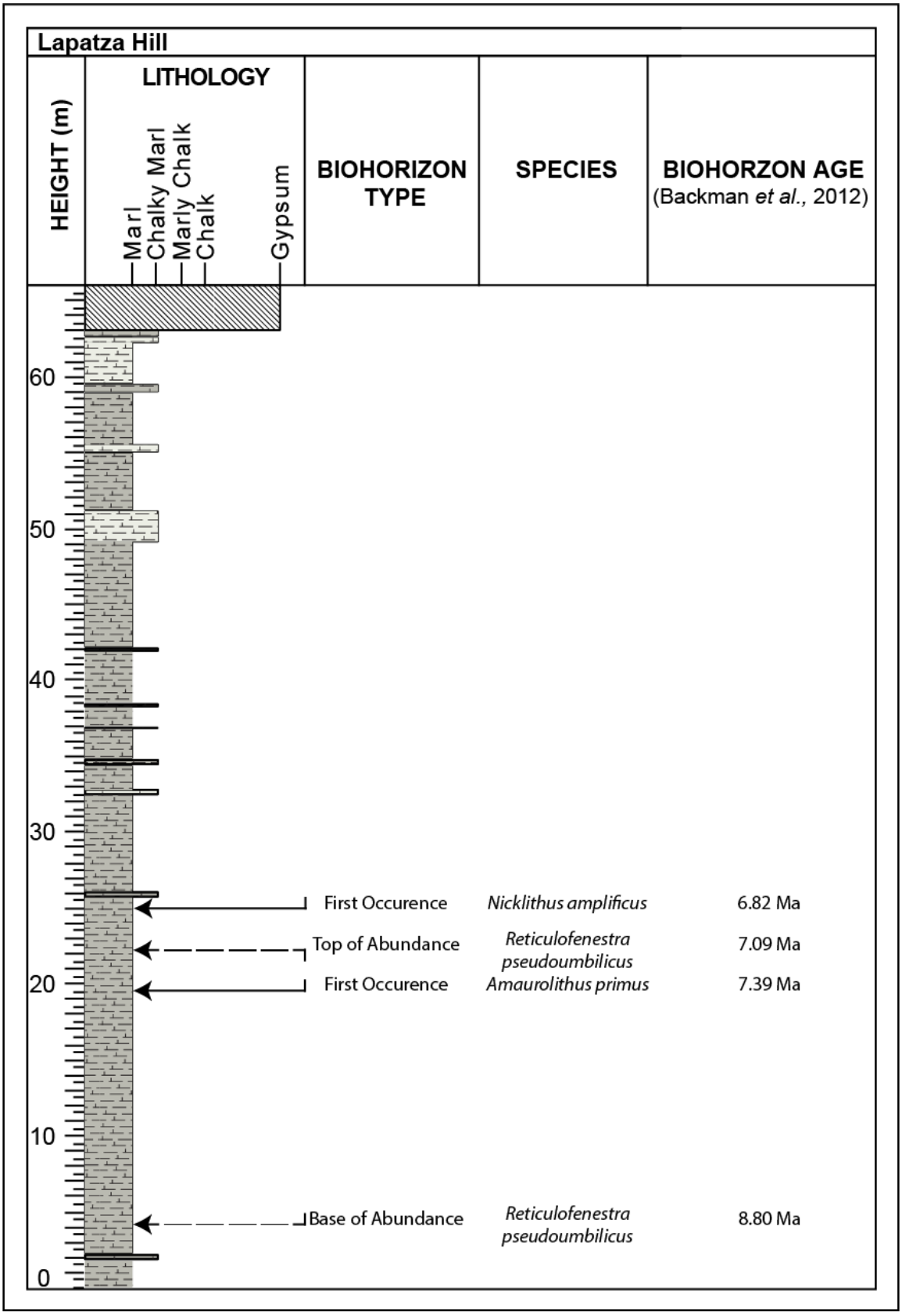


Figure 3.2.2.3 – Stratigraphic log of the succession sampled at Lapatza Hill with height and nature of bio-horizons annotated, together with the ages according to Backman *et al*. (2012). Bio-horizons based on relative abundance (Backman *et al.*, 2012) are less quantitative than other bio-horizons and are marked with a dashed line.

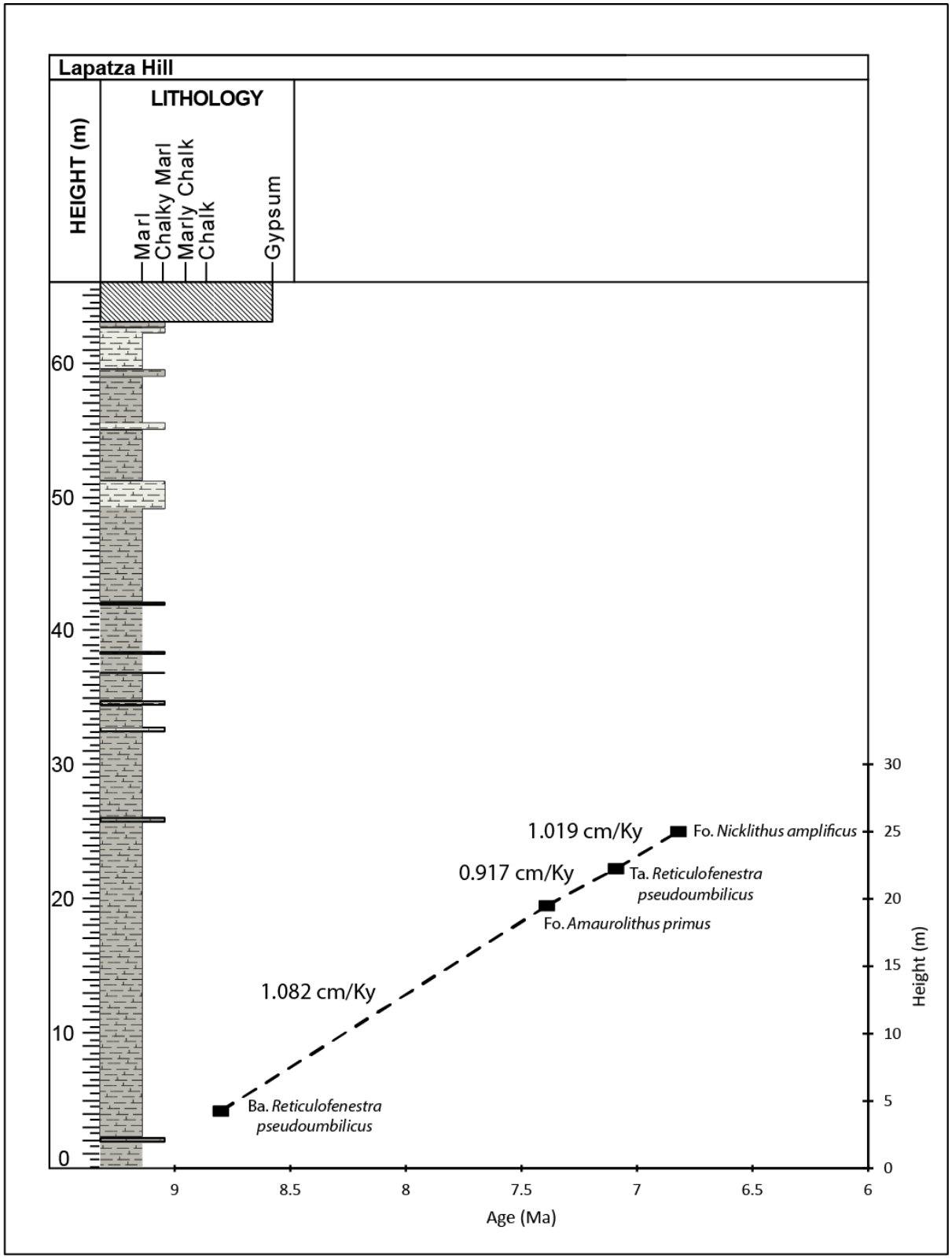


Figure 3.2.2.4 – Stratigraphic log of the succession sampled at Lapatza Hill with height plotted against age according to Backman *et al*. (2012). The sedimentation rate between bio-horizons is also annotated. Fo.= First occurrence, Lo.= Last occurrence, Ba = Base of abundance, Ta. = Top of abundance.

3.2.3 XRF & XRD

Kottaphi Hill - X-Ray Diffraction

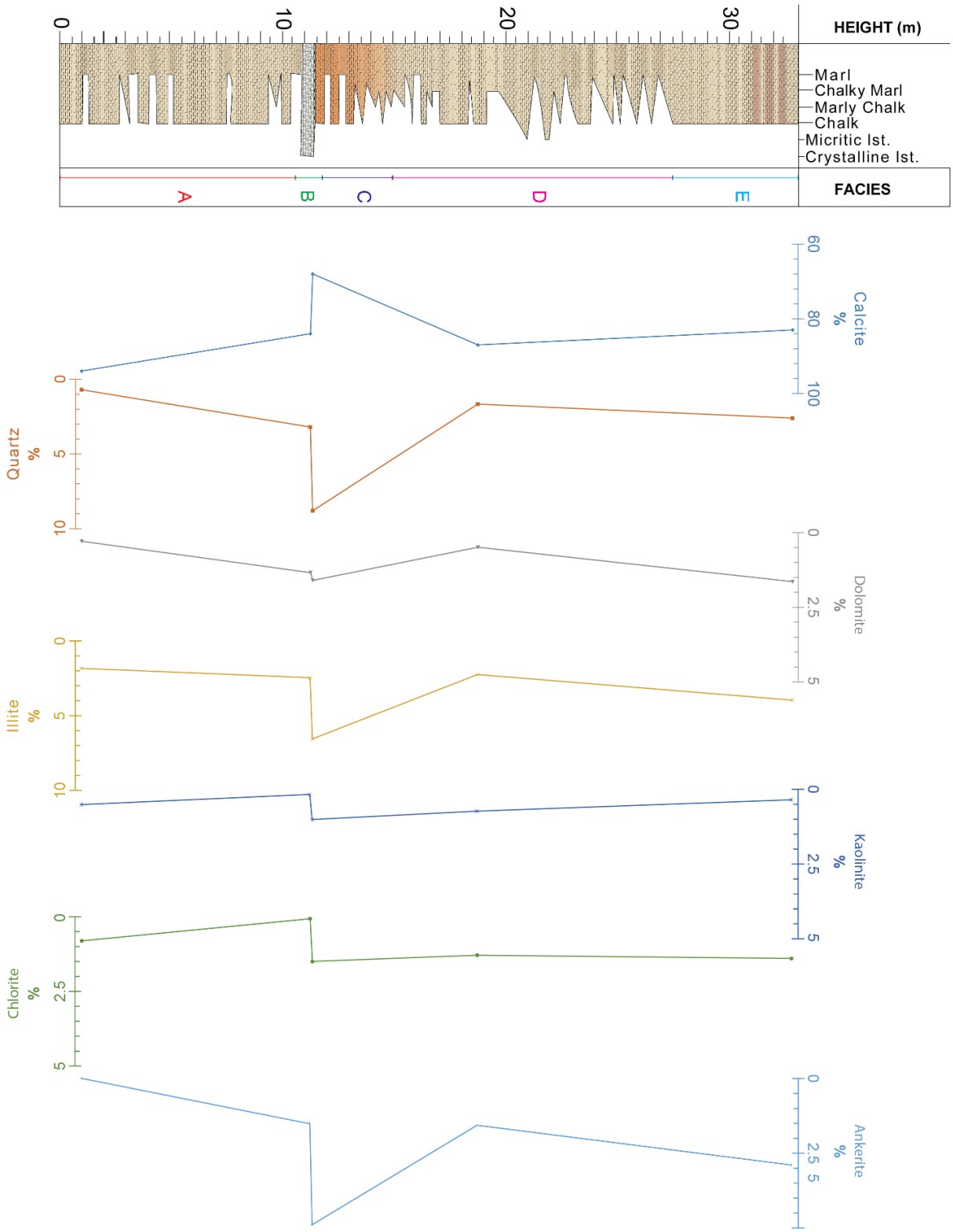


Figure 3.2.3.1 – Plots of selected XRD data for facies A to E of the Kottaphi Hill succession shown relative to the succession sampled

Height (m)	Sample Number	Lithology note	Calcite (%)	Quartz (%)	Dolomite (%)	illite_90144 (%)	Kaolinite (BISH) (%)	Chlorite IIb (%)	Ankerite Fe0.7 (%)	Aragonite (%)	Halite (%)	Rhodochrosite (%)	Gypsum (%)	Calcite Magnesian (%)	Ankerite Fe0.2 (%)	Ankerite Fe0.55 (%)
1	TC19 257	Facies A Chalk	94	0.7	0.29	1.88	0.5	0.81	BD	BD	0.23	0.16	BD	0.82	0.1	BD
11.25	TC19 246	Facies B Crystalline limestone	84	3.2	1.34	2.5	0.16	0.07	1.52	1	0.25	0.6	0.55	1.14	3.5	BD
11.35	TC19 033	Facies C Reddish Marl	68	8.8	1.6	6.6	1	1.5	4.9	BD	0.22	0.4	0.51	1.2	4	1
18.75	TC19 182	Facies D Chalk	87	1.66	0.49	2.29	0.72	1.29	1.57	1	0.13	0.47	0.3	0.91	2.2	0.52
32.85	TC19 277	Facies E Calcareous Marl	83	2.6	1.64	4	0.34	1.4	2.9	BD	0.55	0.63	0.06	0.79	1.1	0.81

Table 3.2.3.1 – Table showing the XRD data obtained for the Kottaphi Hill succession. BD = Below Detection

Facies A chalk is calcite-rich (94%), with 0.7% quartz and *c.* 3% clay minerals. Facies B recrystallized limestone is composed of 84% calcite with 3.2% quartz and *c.* 3% clay minerals. The method used for XRD analyses is discussed in Chapter 2.7. This lithology is richer in illite, dolomite, and ankerite than the underlying unit. Reddish calcareous marl from facies C is not as rich in calcite as the underlying units (68%). In this unit quartz (8.8%), dolomite (1.6%), illite (6.6%), kaolinite (1%), chlorite (1.5%) and ankerite (4.9%) account for the highest relative proportions compared to all of the other samples analysed from the succession. Facies D chalk comprises 87% calcite and 1.66% quartz. This unit is relatively rich in dolomite (0.49%), illite (2.29%), kaolinite (0.72%), chlorite (1.29%), ankerite (1.57%) in comparison with facies A chalk. Facies E calcareous marl is calcite-rich (83%) when compared to the calcareous marl of facies C. This unit is also comparatively rich in dolomite (1.64%), illite (4%), kaolinite (0.34%), chlorite (1.4%) and ankerite (2.9%). This calcareous marl is depleted in quartz (2.6%) when compared with facies C. These XRD data are discussed in Chapter 3.3.2.

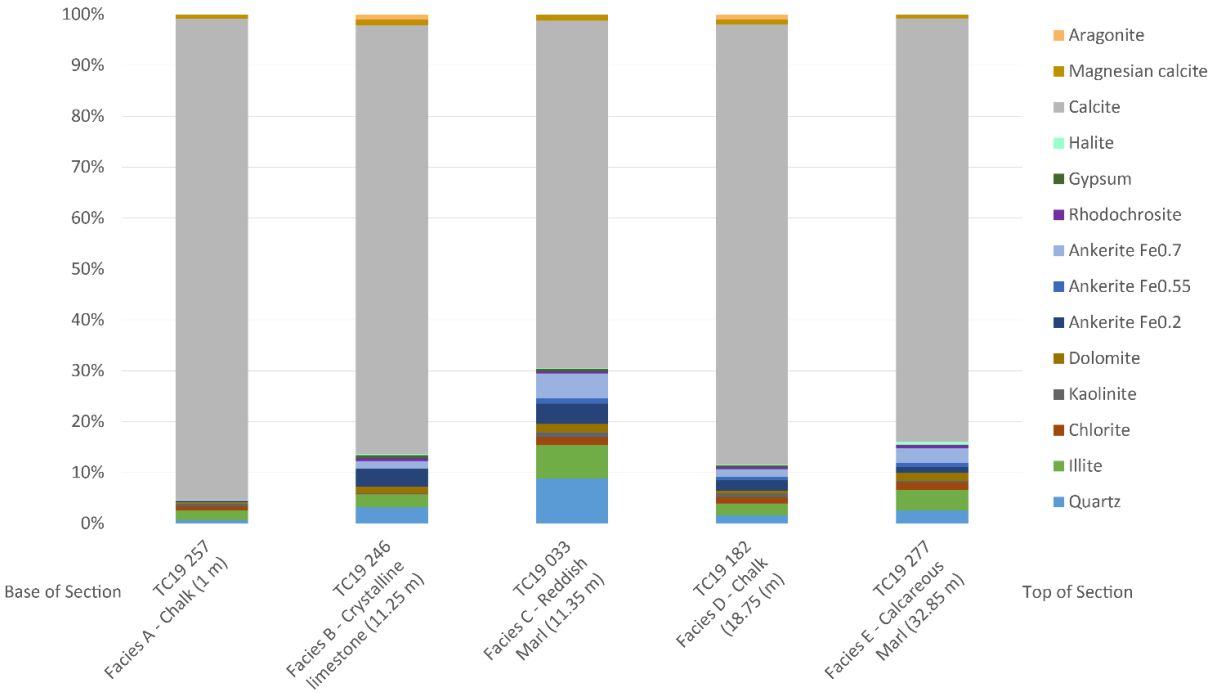


Figure 3.2.3.2 – Stacked bar graphs showing the percentages of all of the XRD data obtained for facies A to E of the Kottaphi hill succession.

Kottaphi Hill - X-Ray Fluorescence

Total values are low for the XRF data collected due to relatively high loss on ignition values (see Table 3.2.3.2); however, in this study, the data are analysed in terms of ratios (relative to other elements). Therefore, absolute values are not critical to interpretations made in this thesis. For the plots shown in Figure 3.2.3.3 measured oxides were converted to major elements using a stoichiometric oxide-to-element conversion. Moving up the section between facies A chalk and facies B crystalline limestone the most notable composition change is in the Si/Al, V/AL and Mo/Al ratios (Figure 3.2.3.3), which all show moderate decreases. The Fe/Ca and Mg/Ca ratios both show a slight increase between these facies. The most notable change in composition throughout the whole section is associated with facies C. The distinctively coloured calcareous marls of facies C have significantly elevated Ti/Ca, Fe/Ca, Mg/Ca and Si/Al ratios. A significant decrease in Ba/Al, V/Al and Mo/Al ratios is noted for this unit. Facies D chalk has a generally similar composition to facies A, although the Ba/Ca ratio of facies D is much lower. V/Al and Mo/Al are elevated in facies D compared to all other facies. Facies E calcareous marl is generally similar in elemental composition to the underlying facies D chalk; however, Fe/Ca, Mg/Ca and Si/Ca are slightly elevated. Facies E also shows a corresponding decrease in Mo/Al and V/Al ratios when compared to facies D.

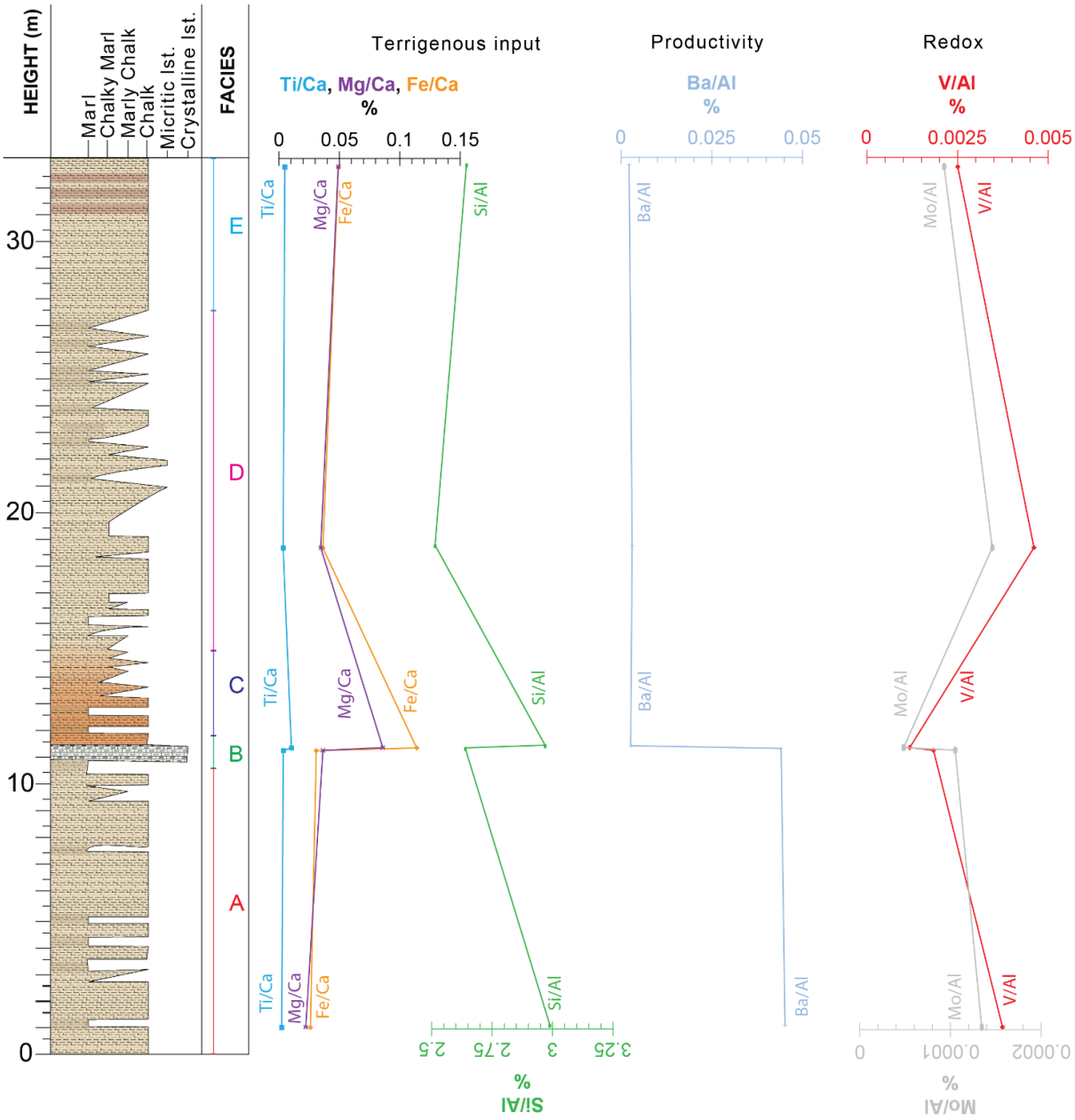


Figure 3.2.3.3 – Ratios of selected XRF data for facies A to E of the Kottaphi Hill succession shown relative to the succession sampled. Data are shown as % elemental ratios and grouped based on common indications of these elemental ratios. Ti/Ca Mg/Ca, Fe/Ca and Si/Al are grouped as indicators of terrigenous input (Arz *et al.*, 1998; Adegbie *et al.*, 2003; Jaeschke *et al.*, 2007; Govin *et al.*, 2012). Ba/Al is indicative of biological productivity (Dymond *et al.*, 1992). Mo/Al and V/Al are indicative of redox conditions (Tribovillard *et al.*, 2006; Neumeister *et al.*, 2016). Measured oxides were converted to major elements using a stoichiometric oxide-to-element conversion.

Major element variation plots (Figure 3.2.3.4) for the XRF data from the Kottaphi Hill samples all show a general positive correlation. Where element oxides lie on or near

to a straight line, they are likely to be associated with a single component (e.g. terrigenous component). The correlations in these plots indicate the presence of terrigenous components in these samples. The reddish marl sample of facies C consistently has the highest ratios of the major elements plotted compared to the other samples, indicating a larger terrigenous component in this sample relative to the others. This sample is also enriched in Fe_2O_3 relative to the other samples. This indicates that some of the Fe_2O_3 in the reddish marl is of independent origin compared to the terrigenous component (e.g. seawater precipitate) (see Chapter 3.3.2). The calcareous marl sample from facies E also appears to have a relatively high terrigenous component. The chalk of facies A consistently has the lowest proportion of the selected major elements, indicating a small terrigenous component relative to the other samples.

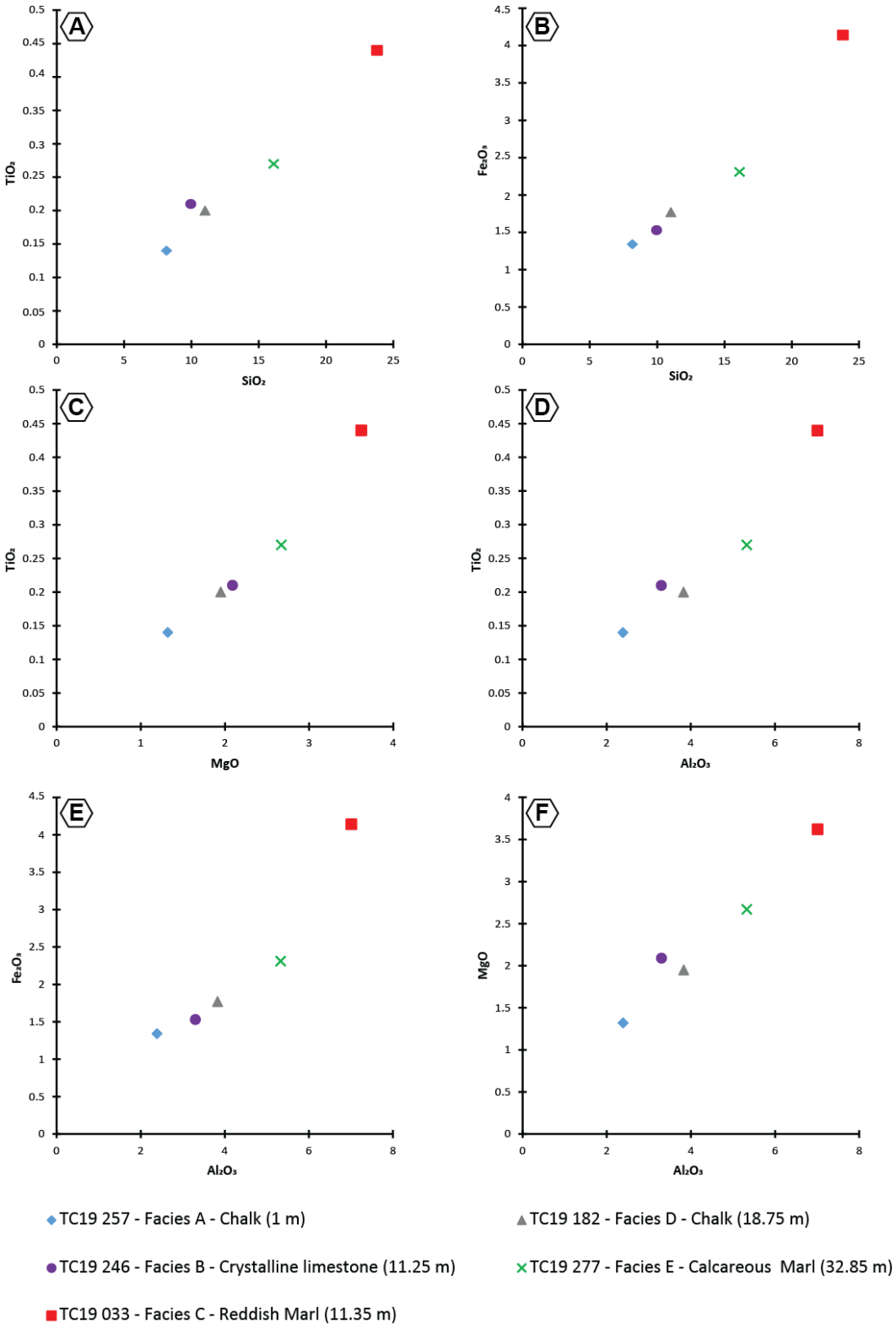


Figure 3.2.3.4 – Selected major element variation plots (After Robertson and Hudson, 1973) for the selected samples from the Kottaphi Hill succession. (A) TiO_2 v. SiO_2; (B) Fe_2O_3 v. SiO_2; (C) TiO_2 v. MgO; (D) TiO_2 v. Al_2O_3; (E) Fe_2O_3 v. Al_2O_3; (F) MgO v. Al_2O_3.

Spider plots (Figure 3.2.3.5) of the XRF data from the samples collected at Kottaphi Hill allow comparisons with other samples from elsewhere in Cyprus, which may have a similar source of terrigenous components as the Kottaphi Hill samples (although suitable data are limited).

The most notable compositional differences seen between the samples from Kottaphi Hill are in the minor and trace element compositions of the samples. Facies C appears to be enriched in both Cr and Ni compared to other samples. Facies E is relatively depleted in Y and Sc compared to other samples from Kottaphi Hill. Both PAAS and continental crust-normalized spider plots (Figure 3.2.3.5) show notable differences in composition between the Kottaphi Hill samples and the samples from the Jurassic Episkopi Formation and the Triassic Vlambouros Formation of the Mamonia Complex in southwest Cyprus (Torley and Robertson, 2018). The Episkopi Formation of the Mamonia Complex is depleted in Na_2O and MnO compared to the Kottaphi Hill samples. The Vlambouros Formation and the Episkopi Formation are both comparatively depleted in Ni and Sr but are enriched in Zr and SiO_2. The Vlambouros Formation is also comparatively depleted in Sc. There are few similarities between the Upper Pillow Lavas (UPL) of the Troodos Ophiolite (Rautenschlein *et al.*, 1985) and the Kottaphi Hill samples. The UPL sample is comparatively depleted in CaO, K_2O, Rb, Sr and Ba. Compared to the Kottaphi Hill samples, the UPL sample is enriched in Na_2O. The Kottaphi Hill samples appear to have the greatest similarity to the Cenozoic sedimentary samples from the Kyrenia Range of northern Cyprus (Trapeza, Davlos and Mia Milia Formations), although there are also differences between these samples. The Davlos Formation and Mia Milia Formation samples both have high levels of Na_2O compared to the samples from Kottaphi Hill. The sample from the Trapeza Formation also has higher levels of Na_2O albeit lower than the other Kyrenia

Range samples. The Kottaphi Hill samples have lower levels of Cr than the three samples from the Kyrenia Range.

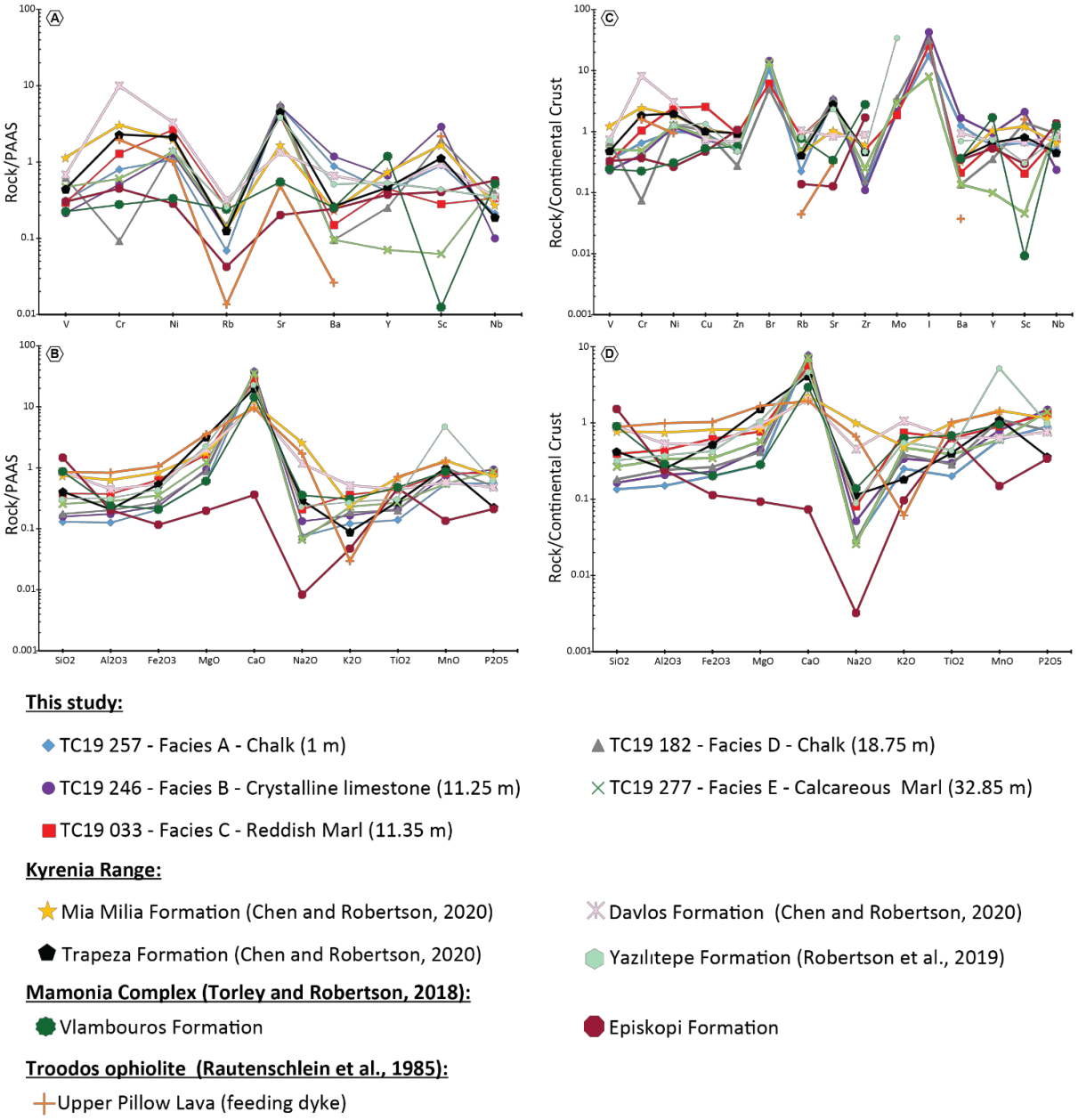


Figure 3.2.3.5 – Spider plots showing XRF data for the samples analysed from the Kottaphi Hill succession together with selected reference samples from Rautenschlein *et al.* (1985), Torley and Robertson (2018), (Robertson *et al.*, 2019) and Chen and Robertson (2020). (A) Minor and trace elements normalised to Post-Archaean Australian Shale (PAAS); (B) Major element (oxides) normalised to PAAS; (C) Minor and Trace elements normalised to upper continental crust; (D) Major element (oxides) normalized to upper continental crust. Values for PAAS are taken from Taylor and McLennan (1985). Values for upper continental crust are taken from Rudnick and Gao (2003).

The ternary plot shown in Figure 3.2.3.6 allows for further comparison between the composition of the Kottaphi Hill samples and those from the Mamonia Complex and Kyrenia Range. Unfortunately, there are no appropriate data available for the Upper Pillow Lavas of the Troodos Ophiolite for comparison. In this plot, Zr is used to indicate terrigenous input derived from felsic igneous rocks (Chen and Robertson, 2020). V and Ni are plotted in order to identify rocks with an ultramafic source; enrichment of Ni relative to V is noted in ultramafic debris (Garver and Scott, 1995; Bracciali *et al.*, 2007; Chen and Robertson, 2020). The plot shows a clear difference between the selected Mamonia Complex samples and the samples collected at Kottaphi Hill. The Mamonia Complex samples are comparatively enriched in Zr and depleted in Ni and V. The samples from Kottaphi Hill are closer in composition but still distinct from the Kyrenia Range sedimentary cover samples.

It is clear from these results that the samples collected at Kottaphi Hill are comparatively closest in composition to the reference samples from the Kyrenia Range. However, the Kottaphi Hill samples are still clearly distinct from these samples. The samples collected at Kottaphi Hill are comparatively depleted in Na_2O compared to the samples from the Kyrenia Range and the sample from the Troodos ophiolite (Figure 3.2.3.5). The Kottaphi Hill samples have very little similarity in composition with samples from the Troodos Ophiolite or the Mamonia Complex (Figure 3.2.3.5 & Figure 3.2.3.6). These XRF data are discussed in Chapter 3.3.2.

Unfortunately, no XRF data are available for the Lapatza Hill succession. However, the chemical composition is likely to be similar to the Mia Milia Formation (Figure 3.2.3.5 & Figure 3.2.3.6) which underlies the succession, sampled elsewhere in the Kyrenia Range. The composition of the Lapatza Hill samples is likely to be similar to the similarly aged marl with Mn-rich horizons (see Chapter 3.3.3) analysed from the

eastern Kyrenia Range (Yazılıtepe Formation - Figure 3.2.3.5 & Figure 3.2.3.6) (Robertson *et al.*, 2019).

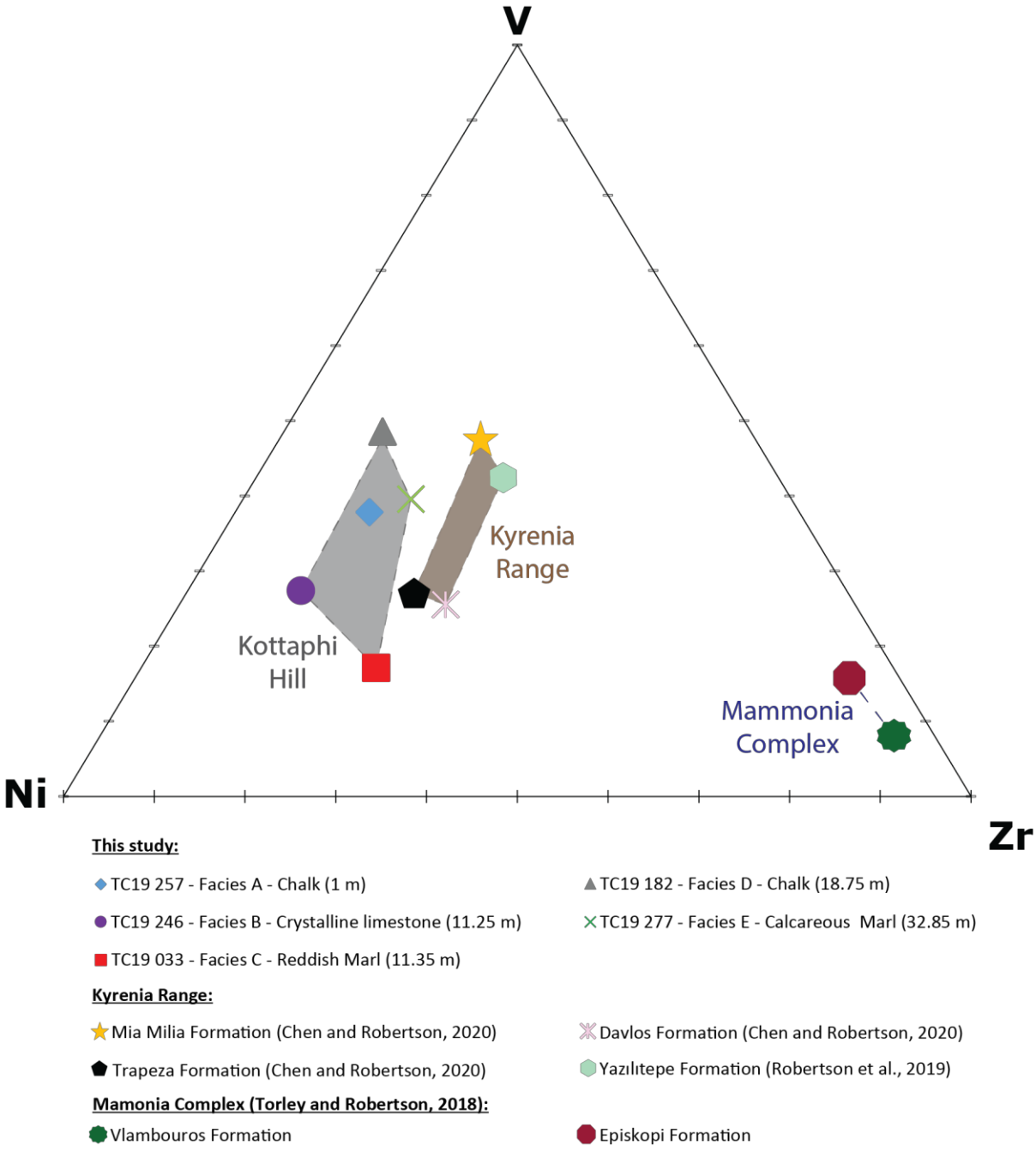


Figure 3.2.3.6 – Ternary V-Ni-Zr plot showing the Kottaphi Hill samples together with reference samples from the Kyrenia Range Cover (Robertson *et al.*, 2019; Chen and Robertson, 2020) and the Mamonia Complex (Torley and Robertson, 2018).

													(ppm)									
Height (m)	**Sample Number**	**Lithology note**	**V**	**Cr**	**Ni**	**Cu**	**Zn**	**Br**	**Rb**	**Sr**	**Zr**	**Mo**	**I**	**Ba**	**Y**	**Sc**	**Nb**					
1	TC19 257	Facies A- Chalk	47.3	87.9	59.2	25.1	34.8	9.3	11.0	1058.8	18.5	1.6	12.2	571.3	11.1	14.5	4.0					
11.25	TC19 246	Facies B - Crystalline limestone	32.1	56.0	70.4	20.1	38.4	12.8	20.6	1063.4	14.6	1.7	30.1	770.0	18.0	46.4	1.9					
11.35	TC19 033	Facies C - Reddish Marl	43.9	141.6	146.2	69.3	67.0	5.4	40.6	797.8	66.5	1.5	18.2	97.2	12.0	4.5	6.4					
18.75	TC19 182	Facies D - Chalk	93.4	10.1	78.0	27.9	19.9	4.4	23.5	1120.4	20.9	2.8	22.6	61.7	6.8	30.8	7.4					
32.85	TC19 277	Facies E - Calcareous Marl	70.7	66.3	74.9	22.4	36.7	12.0	22.4	894.8	33.0	2.4	5.6	62.2	1.9	1.0	9.5					
													%									
Height (m)	**Sample Number**	**Lithology note**	**Na_2O**	**Al_2O_3**	**CaO**	**Fe_2O_3**	**K_2O**	**MgO**	**MnO**	**P_2O_5**	**SiO_2**	**TiO_2**	**Total**	**LOI**								
1	TC19 257	Facies A- Chalk	0.09	2.39	50.3	1.34	0.45	1.32	0.06	0.09	8.16	0.14	63.34	35.48								
11.25	TC19 246	Facies B - Crystalline limestone	0.16	3.3	48.45	1.53	0.61	2.09	0.08	0.15	9.96	0.21	66.54	33.22								
11.35	TC19 033	Facies C - Reddish Marl	0.25	7.01	35.54	4.14	1.34	3.62	0.09	0.13	23.78	0.44	76.34	23.05								
18.75	TC19 182	Facies D - Chalk	0.09	3.83	47.55	1.77	0.69	1.95	0.11	0.08	11.02	0.2	67.39	32.55								
32.85	TC19 277	Facies E - Calcareous Marl	0.08	5.33	45.9	2.31	0.85	2.67	0.06	0.14	16.12	0.27	73.73	26.13								

Table 3.2.3.2 – Table showing XRF data obtained for the Kottaphi Hill succession. LOI = Loss on Ignition XRF values lower than 1% are considered less reliable.

Lapatza Hill-X-Ray Diffraction

XRD analysis of representative samples from the Lapatza Hill marl sequence gives insights into the mineralogy of the succession sampled. These data are displayed in Figure 3.2.3.8, Figure 3.2.3.7 and Table 3.2.3.3. Sampling for XRD was focussed on the lowermost and uppermost parts of the succession; the method used for XRD analyses is discussed in Chapter 2.7. The modal proportion of calcite ranges from 25.8% at 7.25 m to 78.2% at 50.75 m. The mean calcite proportion is 49.6%. In general higher calcite proportions are measured in the lighter coloured marl layers in the upper part of the succession, whereas the lowest proportions are measured in darker muds and marls in the lower part of the succession. Quartz appears to have a near inverse trend to calcite with the highest proportions of quartz (maximum 14.8% at 4.85 m) in the lower part of the succession and the lowest proportions measured in the upper part of the succession (minimum 4.2% at 60.7 m). Dolomite is measured at low levels in the lower part of the section (*c.*1.5-4%) and very low levels (0-0.3%) in the upper part of the succession. Two samples have much larger proportions of dolomite: the sample of dark muddy marl at 9.75 m contains 19.6% dolomite and the grey marl sample from 14.6 m contains 9.2% dolomite. Gypsum makes up a small (0-3%) proportion of most samples; however, dark marl at 15.95 m contains 9.1% gypsum, reddish marl at 56.8 m contains 16% gypsum and the brown marl at the base of the gypsum layer contains 26% gypsum. Samples between 7.25 m and 18.4 m contain higher proportions of illite and kaolinite (5.4-6.3% and 5.1-6.3%) than samples from the upper part of the section (2.0-5.4% and 2.0-5.4%). However, the dark mud sample at 9.75 m from this interval has much lower levels of illite (3.5%) and kaolinite (1.4%). Chlorite also makes up a larger proportion of the samples found between 7.25 m and 18.4 m (5.0-7.8%) than in the upper part of the section (1.6-3.4%). Ankerite is found

in the lower 19 m of the section (2.1-14.3%) but is absent from all but the highest sample (0.5% ankerite) from the upper part of the section. The dark mud sample at 9.75 m has the highest proportion of ankerite of the samples at 9.75%. These XRD data are discussed in Chapter 3.3.3.

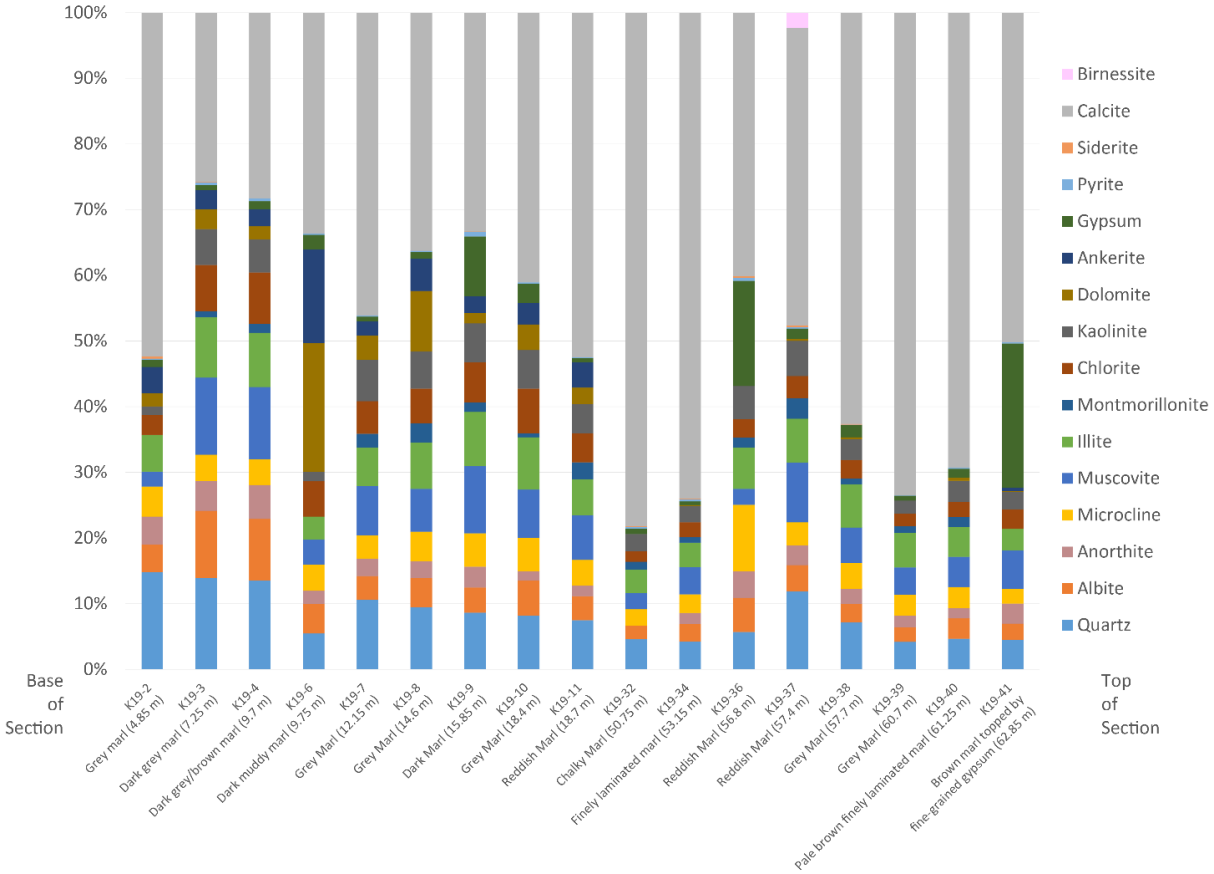


Figure 3.2.3.7 – Stacked bar graphs showing the percentages of all of the XRD data obtained for the Lapatza Hill succession.

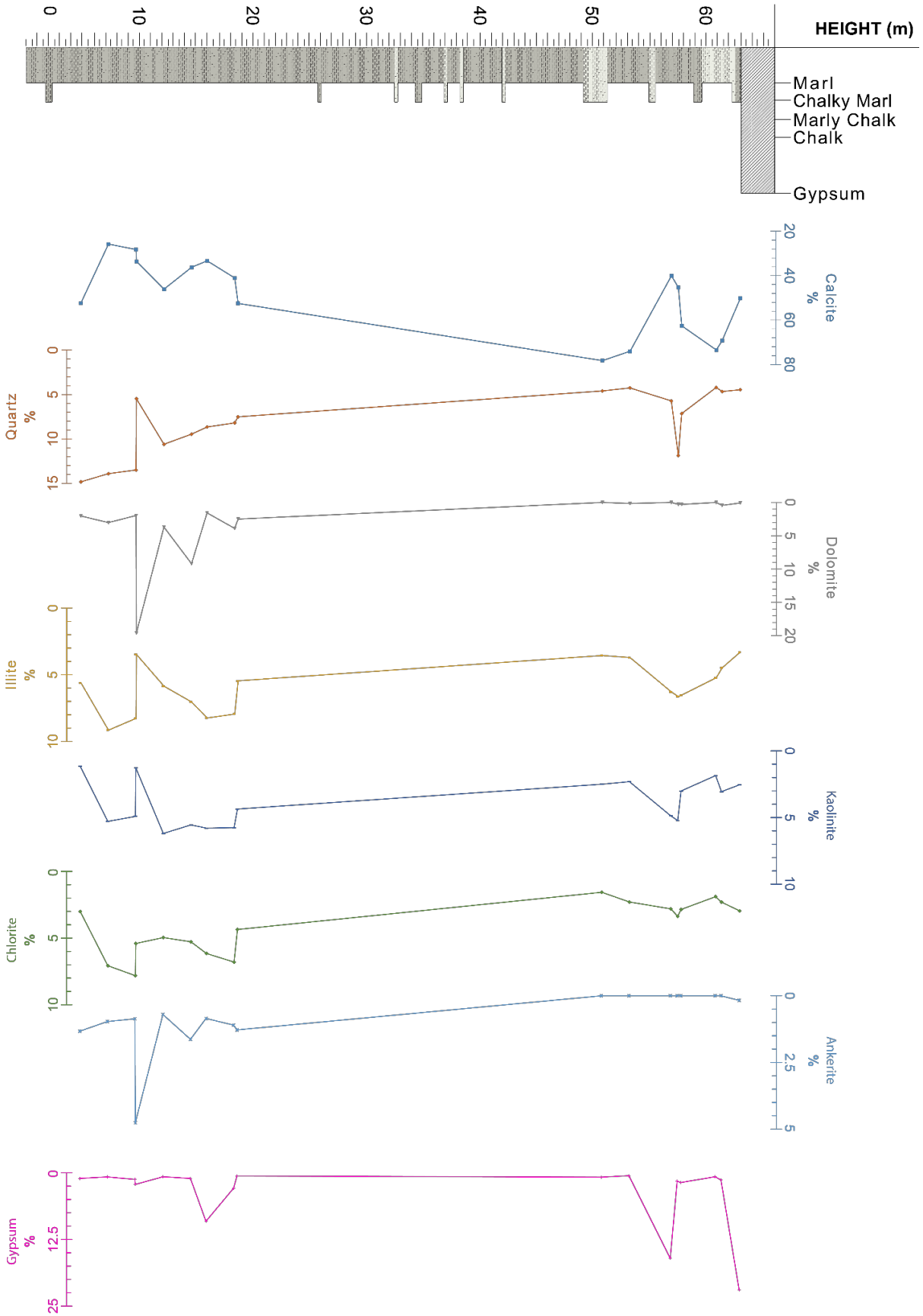


Figure 3.2.3.8 – XRD plots of selected samples from facies A to E of the Lapatza Hill succession shown, relative to the succession sampled.

Height (m)	Sample Number	Lithology note	Calcite (%)	Quartz (%)	Dolomite (%)	illite_90144 (%)	Kaolinite (BISH) (%)	Chlorite IIb (%)	Siderite (%)	Gypsum (%)	Microcline maximum (%)	Muscovite 2 m1 (%)	Ankerite Fe0.55 (%)	Pyrite (%)	Albite (%)	Anorthite (%)	Montmorillonite (%)	Birnessite(%)
4.85	K19-2	Grey marl	52.36	14.82	2.03	5.63	1.30	3.00	0.32	1.05	4.59	2.24	3.98	0.22	4.17	4.28	BD	ND
7.25	K19-3	Dark grey marl	25.79	13.90	3.04	9.18	5.43	7.07	0.07	0.78	4.01	11.71	2.90	0.40	10.24	4.56	0.93	ND
9.7	K19-4	Dark grey/brown marl	28.28	13.49	1.97	8.29	5.06	7.81	BD	1.23	3.93	10.96	2.59	0.45	9.43	5.17	1.34	ND
9.75	K19-6	Dark muddy marl	33.61	5.46	19.60	3.50	1.41	5.40	BD	2.19	3.95	3.81	14.30	0.23	4.50	2.03	BD	ND
12.15	K19-7	Grey Marl	46.07	10.59	3.70	5.89	6.34	4.96	BD	0.75	3.53	7.52	2.10	0.21	3.62	2.66	2.08	ND
14.6	K19-8	Grey Marl	36.27	9.45	9.19	7.06	5.69	5.28	BD	1.04	4.57	6.48	4.90	0.18	4.46	2.51	2.93	ND
15.95	K19-9	Dark Marl	33.33	8.65	1.57	8.27	5.94	6.15	0.01	9.09	5.09	10.22	2.55	0.75	3.79	3.20	1.38	ND
18.4	K19-10	Grey Marl	41.07	8.18	3.90	7.97	5.90	6.80	BD	2.91	5.13	7.33	3.30	0.20	5.32	1.41	0.59	BD
18.7	K19-11	Reddish Marl	52.51	7.50	2.50	5.48	4.50	4.35	BD	0.60	3.94	6.81	3.84	0.14	3.66	1.57	2.59	BD
50.75	K19-32	Chalky Marl	78.25	4.59	BD	3.58	2.64	1.56	0.08	0.82	2.49	2.44	BD	0.24	2.09	BD	1.21	ND
53.15	K19-34	Finely laminated marl	74.03	4.25	0.16	3.74	2.45	2.29	0.02	0.55	2.83	4.13	BD	0.37	2.62	1.71	0.84	ND
56.8	K19-36	Reddish Marl	40.10	5.71	BD	6.32	5.01	2.81	0.27	16.04	10.13	2.41	BD	0.46	5.21	4.01	1.52	BD
57.4	K19-37	Reddish Marl	45.27	11.87	0.29	6.66	5.36	3.36	0.28	1.56	3.51	9.12	BD	0.23	3.95	3.03	3.14	2.35
57.7	K19-38	Grey Marl	62.61	7.14	0.30	6.54	3.15	2.85	0.12	1.84	3.93	5.37	BD	0.07	2.87	2.30	0.91	BD
60.7	K19-39	Grey Marl	73.45	4.20	BD	5.25	1.99	1.89	BD	0.73	3.15	4.20	BD	0.10	2.20	1.78	1.05	BD
61.25	K19-40	Pale brown finely laminated marl	69.24	4.66	0.46	4.51	3.20	2.30	BD	1.35	3.25	4.60	BD	0.21	3.11	1.54	1.58	BD
62.85	K19-41	Brown marl topped by base of fine-grained gypsum	50.21	4.45	0.08	3.32	2.68	2.96	BD	21.97	2.28	5.79	0.52	0.18	2.53	3.04	BD	BD

Table 3.2.3.3 – Table showing all XRD data obtained for the Lapatza Hill succession. BD = Below Detection, ND = No Data.

3.2.4 Foraminifera

Foraminifera were examined with a light microscope before being picked for geochemical analysis. The preservation quality of foraminiferal tests was assessed optically and later these optical assessments were tested with a scanning electron microscope.

Samples from facies A of Kottaphi Hill show poor preservation. The level of preservation does not allow for the identification of individual foraminiferal species. Foraminifera are not preserved in the crystalline limestone of facies B. Very rare planktic foraminifera are preserved in the darker buff micritic limestone interbeds.

Samples from facies C contain an assemblage of moderately to well-preserved foraminifera allowing for the identification of individual species. Planktic foraminifera are common in this assemblage, whereas benthic foraminifera are very rare. *Trilobatus trilobus* dominates this assemblage. *Trilobatus sacculifer, Globoquadrina dehiscens, Globigerinita glutinata, Globigerinoides obliquus* are also present in this assemblage. Less common occurrences of *Globigerina bulloides* and *Dentoglobigerina altispira* are noted. Very rare benthic foraminifera are also present in these samples, of which *Uvigerina spp.* are most common, and *Cibicidoides spp.* are also present.

Facies D also contains a well-preserved assemblage which is dominated by planktic foraminifera. Foraminifera from the *Praeorbulina* genus (*Praeorbulina glomerosa*, *Praeorbulina circularis* and *Praeorbulina curva*) dominate samples from the lower part of the facies. Species from the *Orbulina* genus (*Orbulina suturalis* and *Orbulina universa*) dominate the upper part of the facies. This transition appears to be gradual and few other changes in the assemblage are noted throughout the facies.

Dentoglobigerina altispira is common, *Globigerina bulloides, Trilobatus sacculifer, Globigerinita glutinata, Trilobatus trilobus, Globoquadrina dehiscens* are also present. Benthic foraminifera are rare, but also noted; *Lenticulina spp., Bolivina spp*., *Cibicidoides spp. and. Uvigerina spp.* are all present.

A well-preserved planktic foraminiferal assemblage is also noted in facies E. This assemblage is dominated by planktic foraminifera from the *Orbulina* genus. *Orbulina universa* is most abundant; *Orbulina suturalis* is also abundant. *Neogloboquadrina acostaensis* and *Globorotalia menardii* are common. *Globigerina bulloides*, *Globorotalia scitula, Trilobatus sacculifer, Globigerinita glutinata* and *Trilobatus trilobus* are also present. *Elphidium spp., Lenticulina spp., Bolivina spp*., *Cibicidoides spp.* and *Uvigerina spp.* are all present, but rare.

The identification of foraminiferal assemblages in the uppermost facies (F and G) at Kottaphi Hill was outside of the scope of this research.

Although changes in the overall abundances of foraminifera within the samples from Lapatza Hill are noted (Figure 3.2.1.4), no striking changes in the assemblage are noted. The foraminiferal assemblages from Lapatza Hill are dominated by *Orbulina universa; Orbulina suturalis* is abundant; *Globigerinoides obliquus* and *Neogloboquadrina acostaensis* are common. *Globigerina bulloides*, *Globorotalia scitula, Trilobatus sacculifer, Globigerinita glutinata* and *Trilobatus trilobus* are also present. Very rare benthic foraminifera from the *Cibicidoides* and *Uvigerina* genera are present in some samples below 21 m. *Uvigerina* is present in some samples above 21 m; however, no benthic foraminifera are identified from samples above 32 m.

Assessment of Preservation Quality

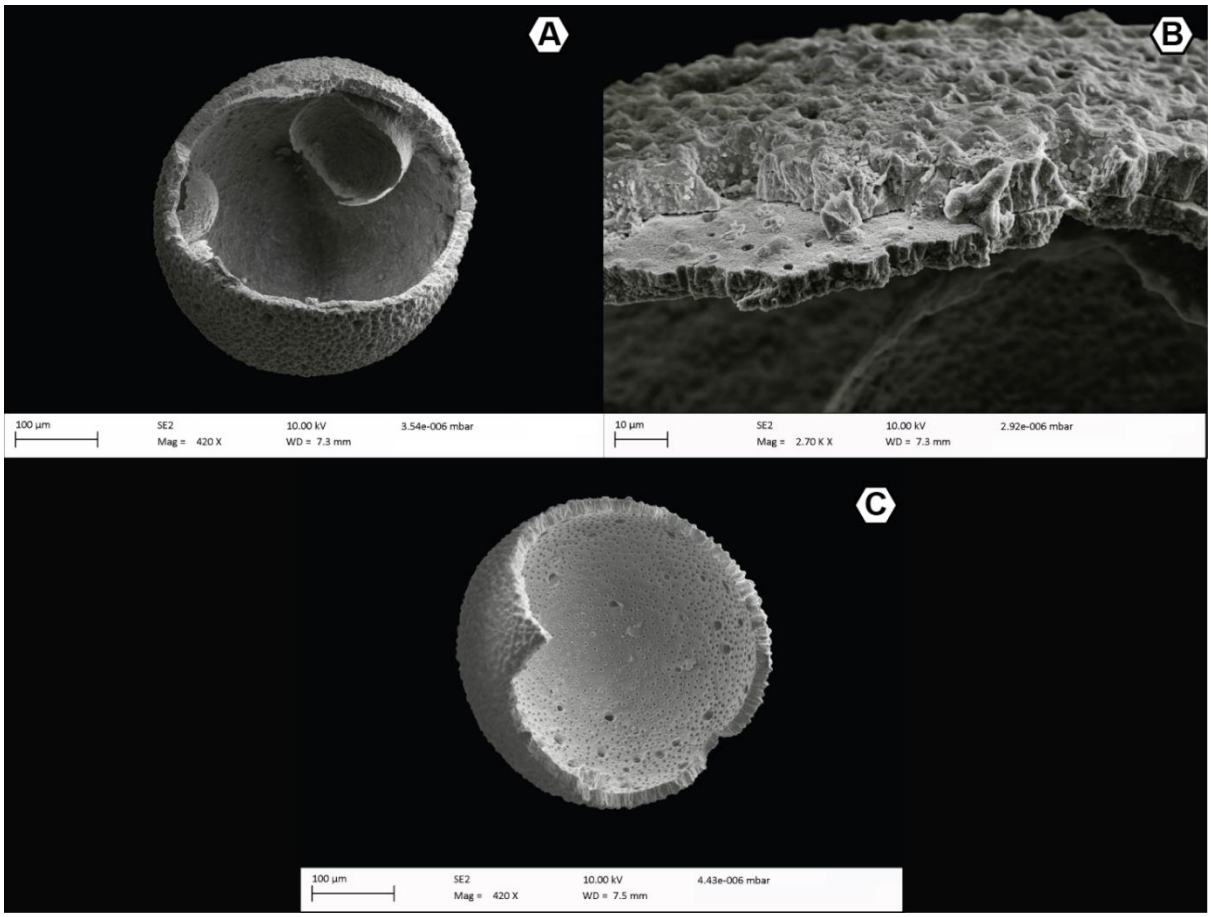


Figure 3.2.4.1 – Scanning electron micrographs of foraminifera classified as well preserved: (A) *Orbulina universa* from sample TC21466; (B) High magnification image of the test wall structure of *Orbulina universa* from sample TC21466; (C) *Orbulina universa* from sample TC21391.

Well-preserved foraminifera were prioritised and picked for all forms of analysis where possible to help ensure that primary biogenic calcite from foraminiferal tests was analysed rather than any diagenetic material (See Chapter 2.5). SEM images show exceptional preservation in samples of foraminifera classified as well preserved (Figure 3.2.4.1). Sample TC21466 (Figure 3.2.4.1A & B) exhibits exceptional preservation of the test wall structure. This exceptional preservation retains the inner calcite layer and the outer calcite layer of the outer chamber of the foraminiferal test. The contact between these two layers was the location of the primary organic membrane layer during life (Spero, 1988). Sample TC21391 (Figure 3.2.4.1C) exhibits

well-preserved test wall structures and pore structures. The internal chambers were removed from this specimen in order to examine the internal structure of the final chamber. Diagenetic features such as crystal overgrowth, recrystallization or infill are absent from these tests.

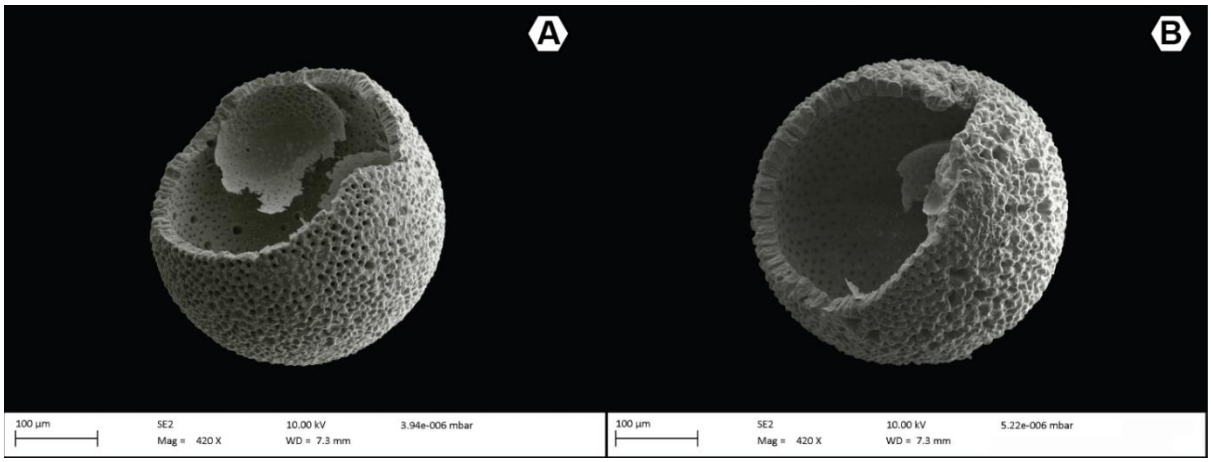


Figure 3.2.4.2 – Scanning electron micrographs of foraminifera classified as moderately well preserved: (A) *Orbulina universa* from sample TC21471; (B) *Orbulina universa* from sample TC21310.

Figure 3.2.4.2 shows SEM images of foraminifera that were categorised as moderately well preserved. Foraminiferal tests of this preservation quality were only used where well-preserved specimens were completely absent. The *Orbulina universa* specimen from sample TC21471 shows an exceptionally well-preserved example of a specimen categorised as well-preserved whereas the specimen from samples TC21310 shows the lowest level of preservation classified as moderately well preserved.

The specimen shown in Figure 3.2.4.2A shows well-preserved pore structures in the test wall, and no clear signs of alteration in the test wall itself. However, some signs of a thin diagenetic coating are noted on the outer layer of the final chamber of this specimen. The internal chambers in this specimen are partially dissolved.

Figure 3.2.4.2B shows a specimen where the pore structure of the test wall is still preserved and no clear signs of recrystallization are seen in the test wall itself.

However, in this specimen, a thicker diagenetic coating is noted on the outside of the final chamber and internal chambers are mostly dissolved.

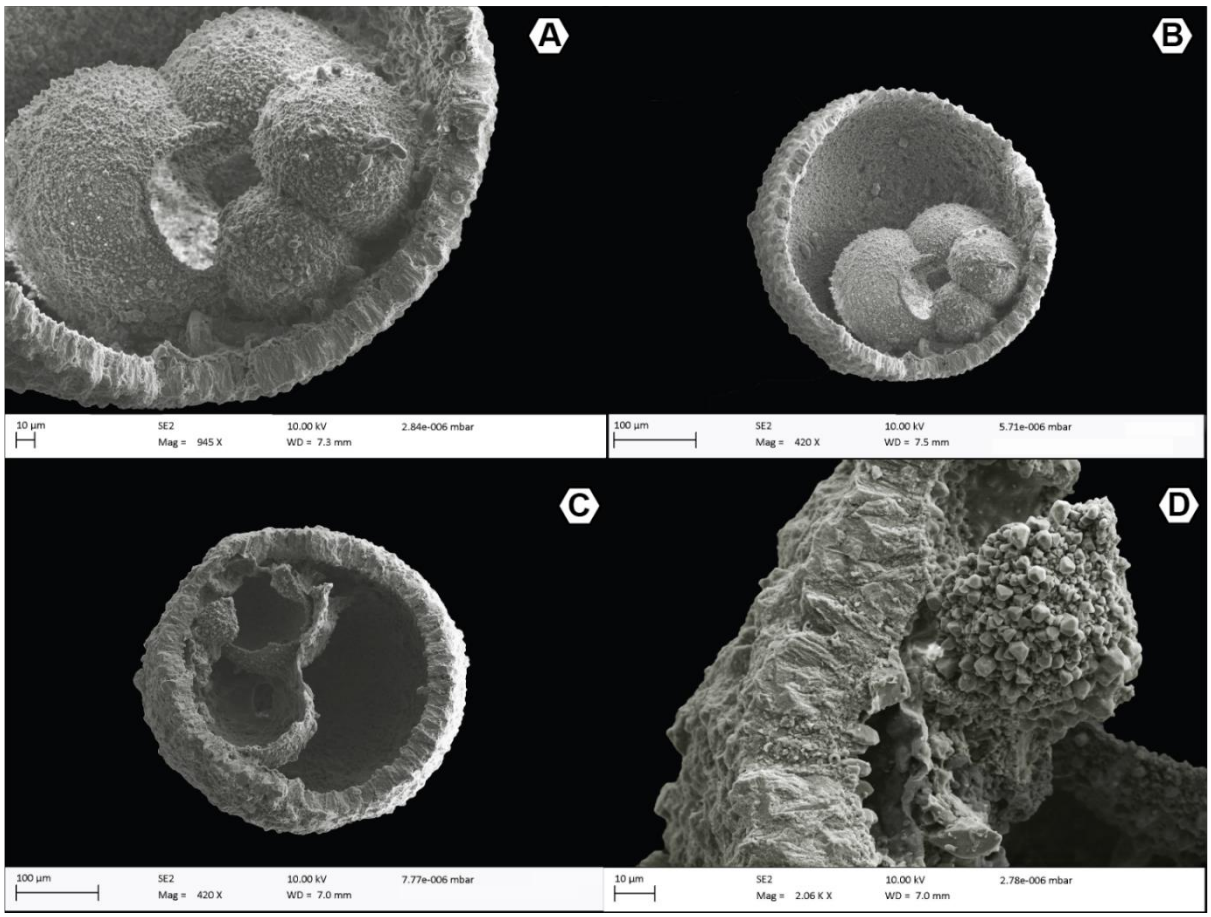


Figure 3.2.4.3 – Scanning electron micrographs of foraminifera classified as poorly preserved: (A) High magnification image of the test wall structure of *Orbulina universa* from sample TC21175; (B) *Orbulina universa* from sample TC21175 (C) *Orbulina suturalis* from sample TC19241; (D) High magnification image of the test wall structure of *Orbulina suturalis* from sample TC1924.

Samples that were categorised as poorly preserved were not selected for geochemical analysis. Figure 3.2.4.3A & B show a planktic foraminiferal specimen which has signs of recrystallisation of the test wall of the final chamber and diagenetic coating on the outer surface of earlier chambers. Figure 3.2.4.3C & D show a specimen of planktic foraminifera with clear diagenetic alteration of the outer chamber test wall and a thick diagenetic coating on the final chamber. This specimen also exhibits crystal overgrowth in an internal early chamber.

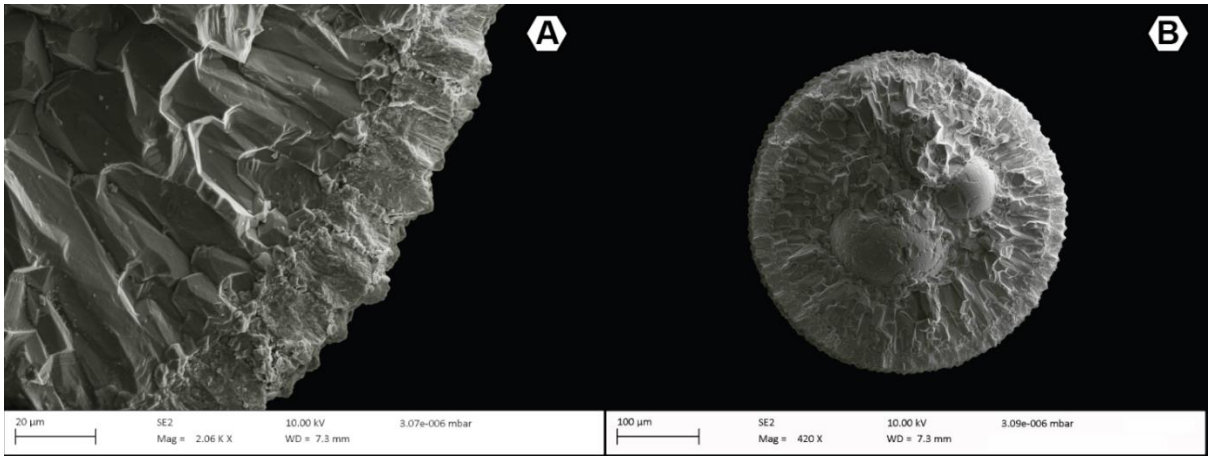


Figure 3.2.4.4 – Scanning electron micrographs of foraminifera classified as very poorly preserved: (A) High magnification image of *Orbulina universa* from sample TC21341; (B) *Orbulina universa* from sample TC21341.

Some samples contain foraminifera that have been completely infilled by crystalline diagenetic material. These samples were not used for any geochemical analysis. Figure 3.2.4.4A & B show a specimen of *Orbulina universa* which has crystalline infill; the test wall structure is altered but still preserved as are internal early chambers.

Foraminiferal tests which showed infill and diagenetic features were subject to EDS analysis; these data are shown in Appendix.8.12.

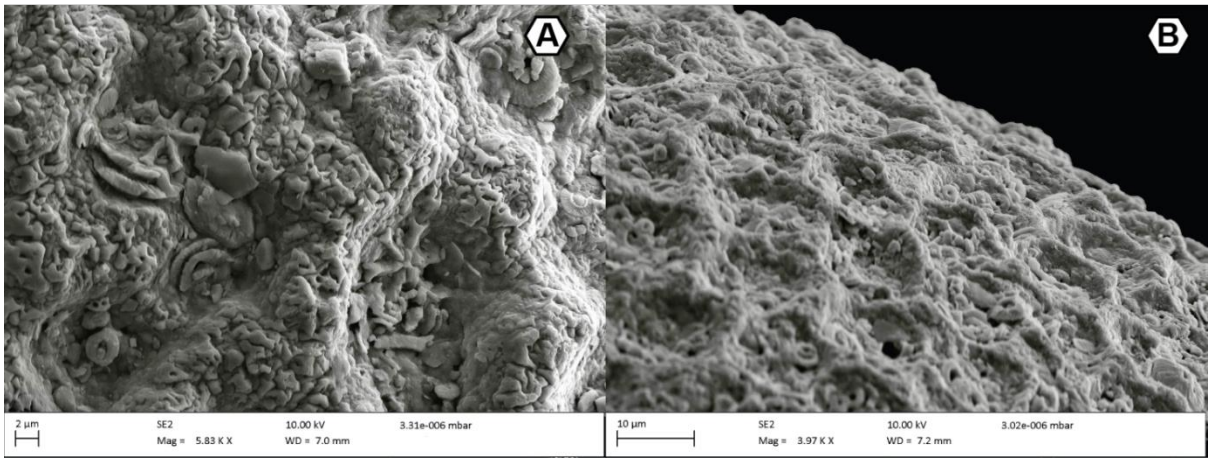


Figure 3.2.4.5 – Scanning electron micrographs of *Orbulina universa* final chamber outer surface showing the efficacy of ultrasonic cleaning protocol: (A) Uncleaned test from sample TC21341; (B) Cleaned test from sample TC21341

SEM imaging also allows some examinations of the efficacy of ultrasonic cleaning. Figure 3.2.4.5A shows the outer surface of the final chamber of an uncleaned test. Abundant calcareous nannofossils including coccoliths and discoasters are visible. Figure 3.2.4.5B shows the outer surface of the final chamber of a test which underwent ultrasonic cleaning as described in Chapter 2.5.2. Although some calcareous nannofossil material is still present, the number of nannofossils present is reduced compared to the test shown in Figure 3.2.4.5A.

3.2.5 Strontium Isotope Analysis

Kouroulla Gorge

Sr isotope analysis of light chalky calcite material from sample TCKG02 from Kouroulla Gorge (see Chapter 2.1.1) gives an isotopic ratio of 0.708221, which indicates an age of 23.63 Ma with an error range of 23.33 Ma to 23.93 Ma (late Chattian). In addition, a ratio of 0.708182 for dark foliated calcite material from the same sample indicates an age of 24.37 Ma, with an error range of 24.07 Ma to 24.72 Ma (Figure 3.2.5.1). A ratio of 0.708256 for light chalky calcite material from sample TCKG03 also gives a younger age (22.96 Ma with an error range of 22.71 Ma to 23.24 Ma), compared to 0.708133 for the dark foliated calcite (25.62 Ma with an error range of 25.16 Ma to 26.1 Ma) (Figure 3.2.5.1). The discrepancy between the ages calculated for the different materials within the same sample is problematic and is discussed in Chapter 3.3.1.

A ratio of 0.708461 for the *Faviidae sp.* coral clast sample from Kouroulla Gorge indicates a Sr isotope age of 19.68 Ma, with an error range of 19.5 Ma to 19.86 Ma (Figure 3.2.5.1).

TC Sample Number	Sample Type	87Sr/86Sr	SRM897 2 σ abs	87Sr/86Sr - SRM897 2 σ abs	87Sr/86Sr + SRM897 2 σ abs	Age (from LOOKUP Table)	Min Age (+)	Max Age (-)
TCKG02 - Light	Oyster Shell	0.708221	0.000007	0.708214	0.708228	23.63	23.33	23.93
TCKG02 - Dark	Oyster Shell	0.708182	0.000007	0.708175	0.708189	24.37	24.07	24.72
TCKG03 - Light	Oyster Shell	0.708256	0.000007	0.708249	0.708263	22.96	22.71	23.24
TCKG03 - Dark	Oyster Shell	0.708133	0.000007	0.708126	0.70814	25.62	25.16	26.1
TCKG06	Coral	0.708461	0.000007	0.708454	0.708468	19.68	19.5	19.86

Table 3.2.5.1 – Table showing strontium isotope data and calculated ages (see Chapter 2.4) for the samples from Kouroulla Gorge.

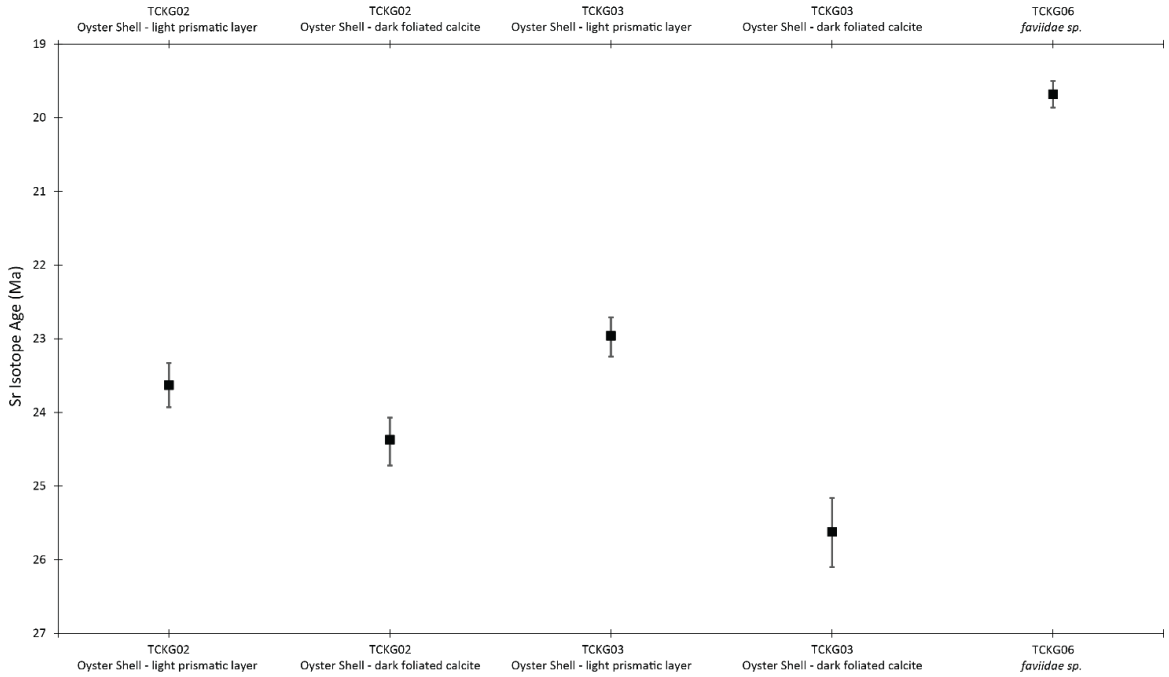


Figure 3.2.5.1 – Sr age data for biogenic clast samples from Kouroulla Gorge plotted against absolute age. The determined age and the total combined error are shown for each sample.

Kottaphi Hill

Sr isotope dating indicates that the succession at Kottaphi Hill above the crystalline limestone of facies B (Figure 3.2.1.1) ranges from 16.22 Ma (with an error range of 16.01 Ma to 16.46 Ma) to 7.25 Ma (with an error range of 6.86 Ma to 7.82 Ma) (Figure 3.2.5.2). These Sr isotope ages indicate that these sediments remain orientated in the order they were deposited (i.e. not reworked) with an average sedimentation rate (non-decompacted) of 0.27 cm/ky.

Sample Number	Height (m)	87Sr/86Sr	SRM897 2 σ abs	87Sr/86Sr - SRM897 2 σ abs	87Sr/86Sr + SRM897 2 σ abs	Age (from LOOKUP Table)	Min Age (+)	Max Age (-)
TC19040	21.65	0.708706	0.000007	0.708699	0.708713	16.22	16.01	16.46
TC19136	15.825	0.708784	0.000007	0.708777	0.708791	14.92	14.48	15.21
TC21006	10.55	0.708827	0.000007	0.70882	0.708834	12.45	11.76	13.03
TC21115	5.275	0.70892	0.000007	0.708913	0.708927	8.84	7.85	9.43
TC21191	0	0.708948	0.000007	0.708941	0.708955	7.25	6.86	7.82

Table 3.2.5.2 – Table showing strontium isotope data and calculated ages (see Chapter 2.4) for the samples from Kottaphi Hill.

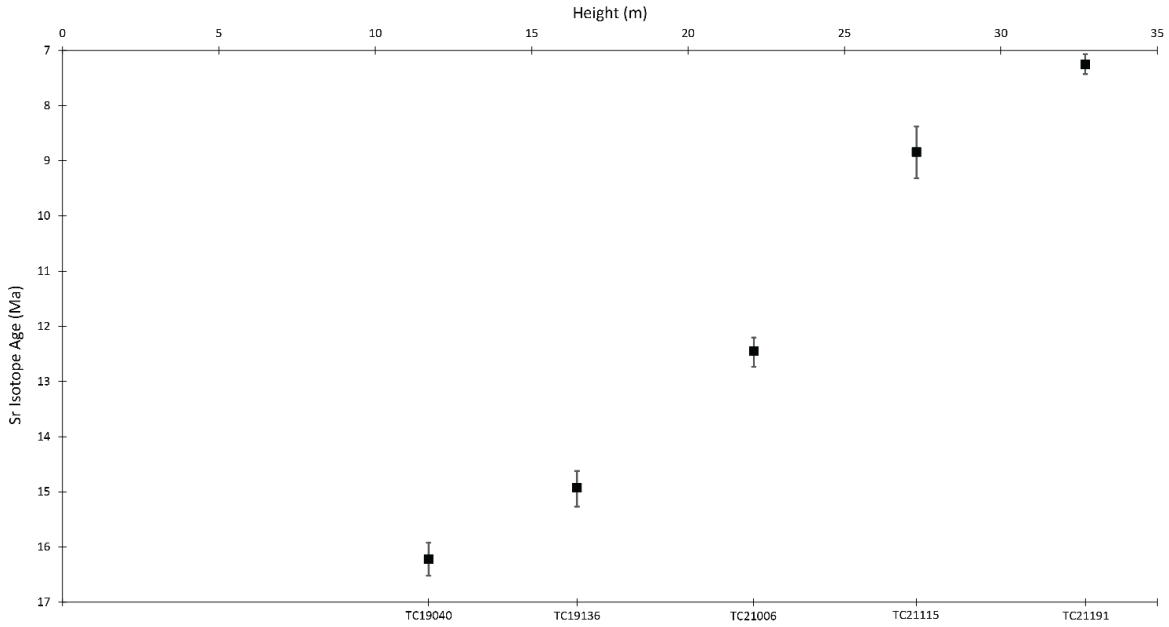


Figure 3.2.5.2 – Sr age data for planktic foraminiferal samples from Kottaphi Hill plotted against absolute age. The determined age and the total combined error are shown for each sample.

Lapatza Hill

Sr isotope data for the Lapatza Hill succession indicate an age range of 11.45 Ma (with an error range of 10.9 Ma to 12.24 Ma) to 5.44 Ma (with an error range of 5.139 Ma to 5.66 Ma) (Figure 3.2.5.3). However, the oldest age given (lowest $^{87}Sr/^{86}Sr$) is for sample TC22 330, which was taken from a height of 31.5 m whilst younger ages are assigned to samples both above and below this. This would indicate, either that the height of the samples up the section does not correlate with their age, or that the ages determined are not true ages for the timing of biomineralization of these planktic foraminifer samples. Additionally, sample TC22 470, taken from a height of 62.75 m has a strontium isotopic value (0.709241) which is not compatible for dating with the LOWESS Sr isotope Look-Up Table (Version 4: 08/04) (McArthur *et al.*, 2001; McArthur and Howarth, 2004). This suggests that the Sr isotope value measured for this sample is not a ratio that has ever existed in global seawater.

The results of Sr isotope dating for the Lapatza Hill samples are problematic and are discussed in Chapter 3.3.3.

Sample Number	Height (m)	87Sr/86Sr	SRM897 2 σ abs	87Sr/86Sr - SRM897 2 σ abs	87Sr/86Sr + SRM897 2 σ abs	Age (from LOOKUP Table)	Min Age (+)	Max Age (-)
TC22203	62.75	0.70901	0.000007	0.709003	0.709017	5.71	5.5	5.89
TC22264	47.0625	0.709022	0.000007	0.709015	0.709029	5.44	5.139	5.66
TC22330	31.375	0.708845	0.000007	0.708838	0.708852	11.45	10.9	12.24
TC22399	15.6875	0.708989	0.000007	0.708982	0.708996	6.07	5.92	6.25
TC22470	0	0.709241	0.000007	0.709234	0.709248	N/A	N/A	N/A

Table 3.2.5.3 – Table showing strontium isotope data and calculated ages (see Chapter 2.4) for the samples from Lapatza Hill.

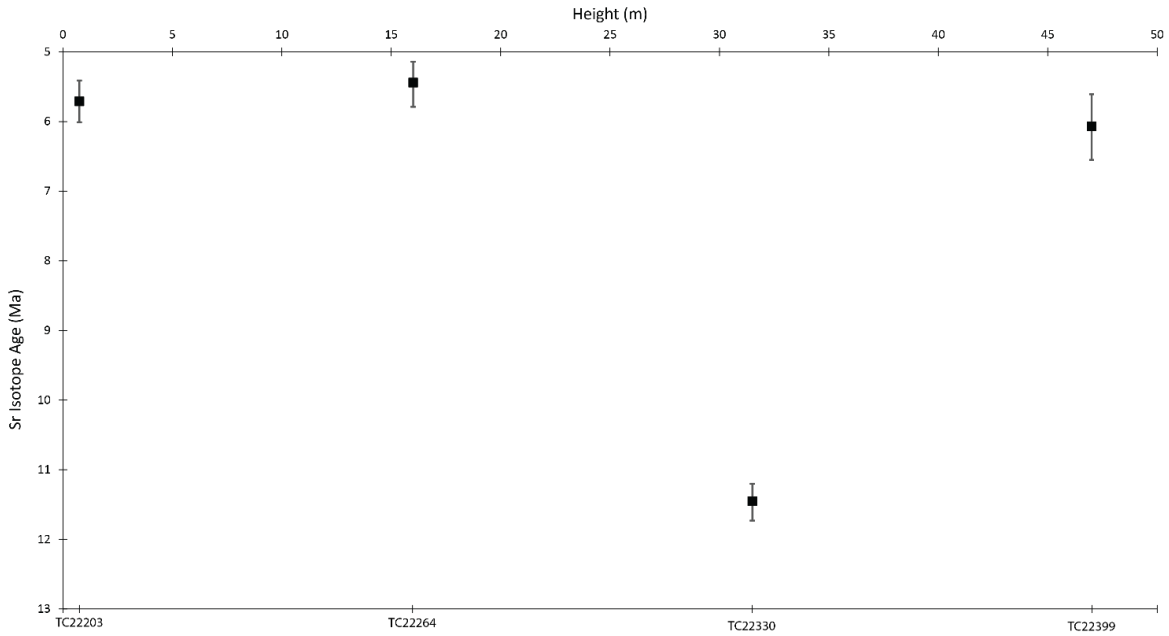


Figure 3.2.5.3 – Sr age data for planktic foraminiferal samples from Lapatza Hill plotted against absolute age. The determined age and the total combined error are shown for each sample.

3.2.6 Age Model

Kottaphi Hill

A new age model for the Kottaphi Hill succession is key to providing a temporal context for data presented and discussed in this thesis. The age model for the Kottaphi Hill succession is presented below.

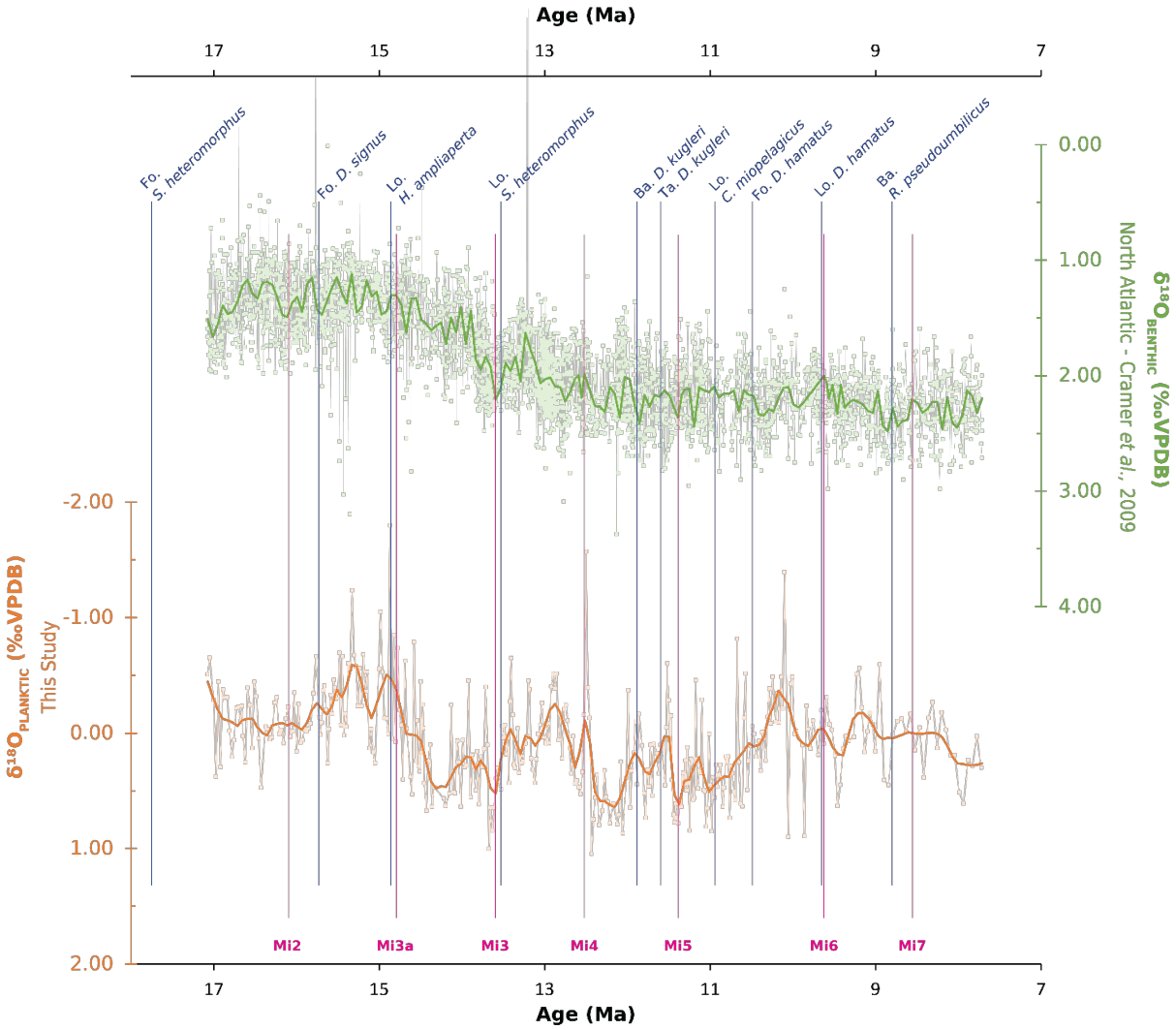


Figure 3.2.6.1 – Graph showing the final adjusted age model for the Kottaphi Hill succession (see Chapter 3.1.6). The Kottaphi Hill $\delta^{18}O_{PLANKTIC}$ record is shown relative to the reference $\delta^{18}O_{BENTHIC}$ record of Cramer *et al.* (2009). Biohorizons used for calcareous nannofossil biostratigraphy are also shown, together with the Miocene oxygen isotope events of Miller *et al.* (1991) and Miller *et al.* (2020). Fine lines plot the measured $\delta^{18}O$ values. Bold lines show the $\delta^{18}O$ smoothed by a locally weighted function over 60 kyr.

The new age model for Kottaphi Hill indicates that the succession sampled spans from 18.96 Ma (Burdigalian) to 7.72 Ma (Tortonian). The new age model is shown in Figure 3.2.6.1, relative to the reference curve with which it was tuned (Cramer *et al.*, 2009); biohorizons used for calcareous nannofossil biostratigraphy are also shown, together with Miocene oxygen isotope events (Miller *et al.*, 1991a, 2020). Figure 3.2.6.2 shows the new age model relative to the height in the succession sampled and, therefore, highlights changes in the sedimentation rate. Although some minor changes in sedimentation rate are calculated from the succession, only one major sedimentation rate change is confirmed. From the base of the succession to 10.97 m (17.15 Ma), an average sedimentation rate of 0.805 cm/ky is calculated. A slower sedimentation rate (0.245 cm/ky) is calculated between 10.97 m (17.15 Ma) and the top of the succession sampled.

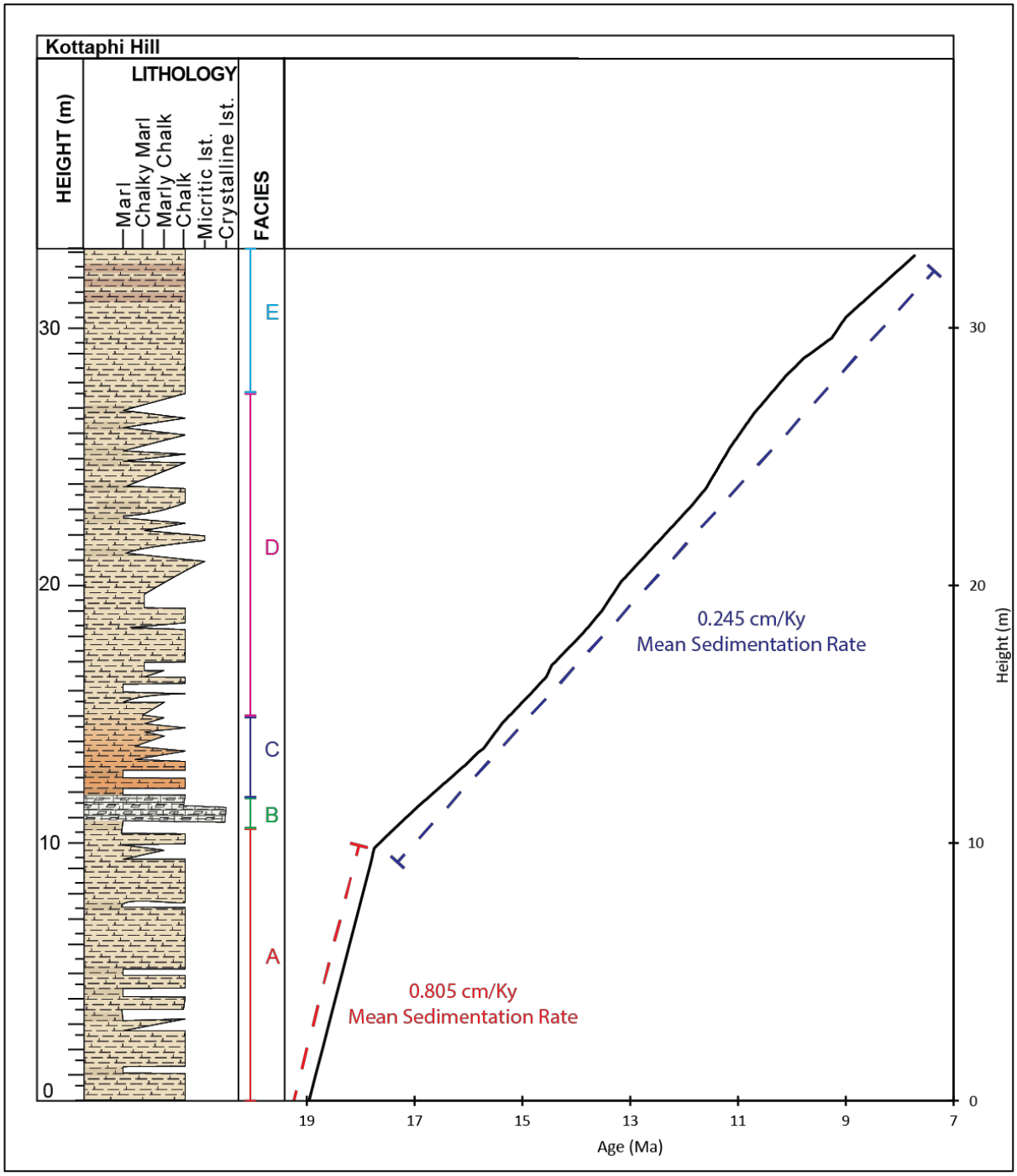


Figure 3.2.6.2 – Plot of Age (Ma) versus Height (m) for the Kottaphi Hill succession shown relative to the simplified stratigraphic column of the succession. Average sedimentation rates are shown for two intervals of the succession.

Lapatza Hill

In order to provide context for the data presented and discussed in this thesis, an age model was produced for the Lapatza Hill succession. This age model is presented below.

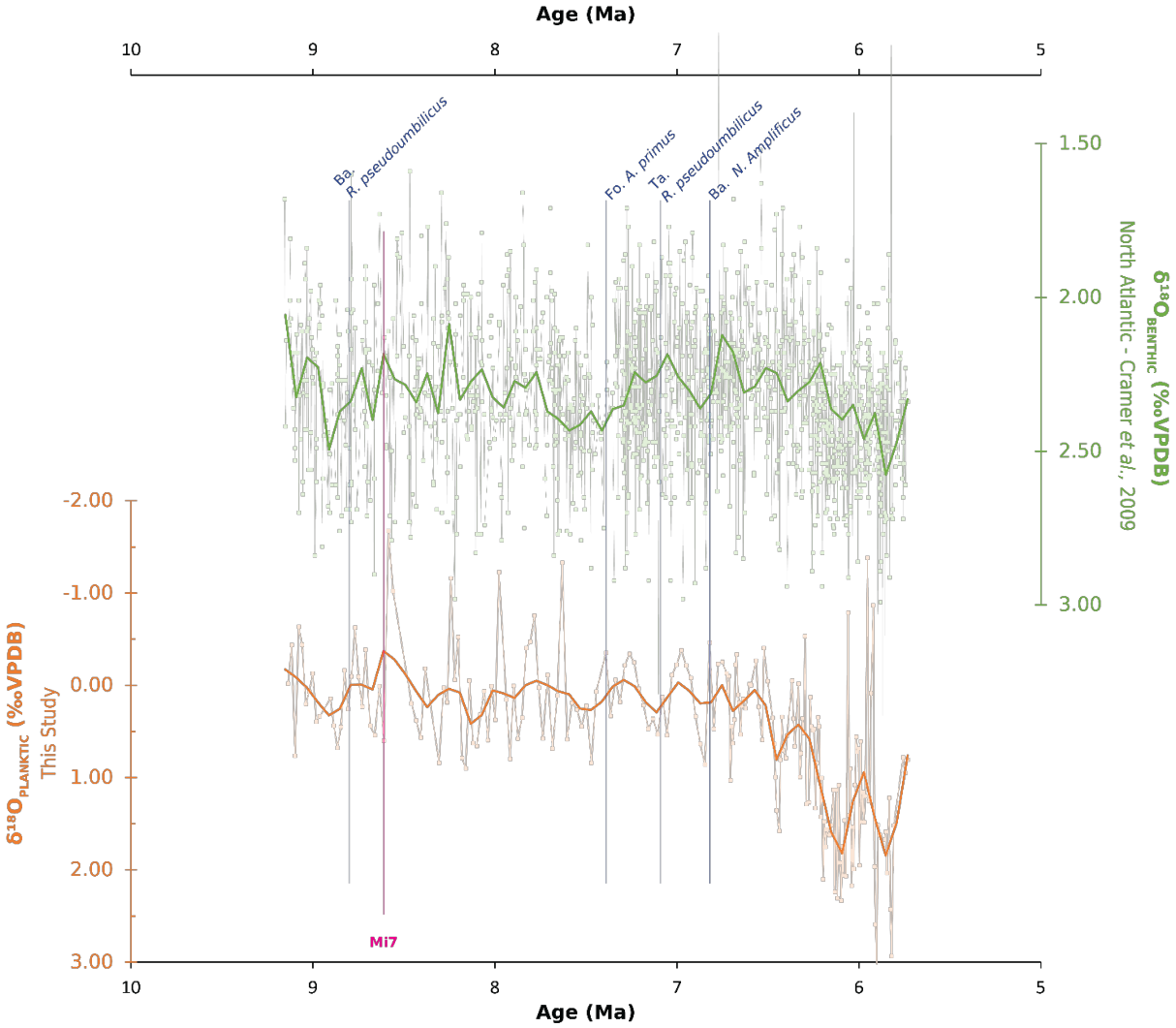


Figure 3.2.6.3 – Graph showing the final adjusted age model for the Lapatza Hill succession (see Chapter 3.1.6). The Lapatza Hill $\delta^{18}O_{PLANKTIC}$ record is shown relative to the reference $\delta^{18}O_{BENTHIC}$ record of Cramer *et al.* (2009). Biohorizons used for calcareous nannofossil biostratigraphy are also shown, together with the Miocene oxygen isotope events of Miller *et al.* (1991). Fine lines plot the measured $\delta^{18}O$ values. Bold lines show the $\delta^{18}O$ smoothed by a locally weighted function over 60 kyr.

The succession sampled at Lapatza Hill spans 9.14 Ma (Tortonian) to 5.74 Ma (Messinian) as indicated by the new age model new age model. Figure 3.2.6.3 shows the new age model relative to the reference curve which it was tuned with (Cramer *et al.*, 2009). Bio-horizons used for calcareous nannofossil biostratigraphy are also shown, together with Miocene oxygen isotope events (Miller *et al.*, 1991a). The new age model is shown relative to the height of the succession sampled in Figure 3.2.6.4. One distinct change in the sedimentation rate is noted in Figure 3.2.6.4. From the base

of the succession to 25 m (6.82 Ma) an average sedimentation rate of 1.099 cm/ky is calculated, with little variation from this mean. From 25 m (6.82 Ma) to the top of the succession, an increase in sedimentation rate (3.627 cm/ky) is noted.

2

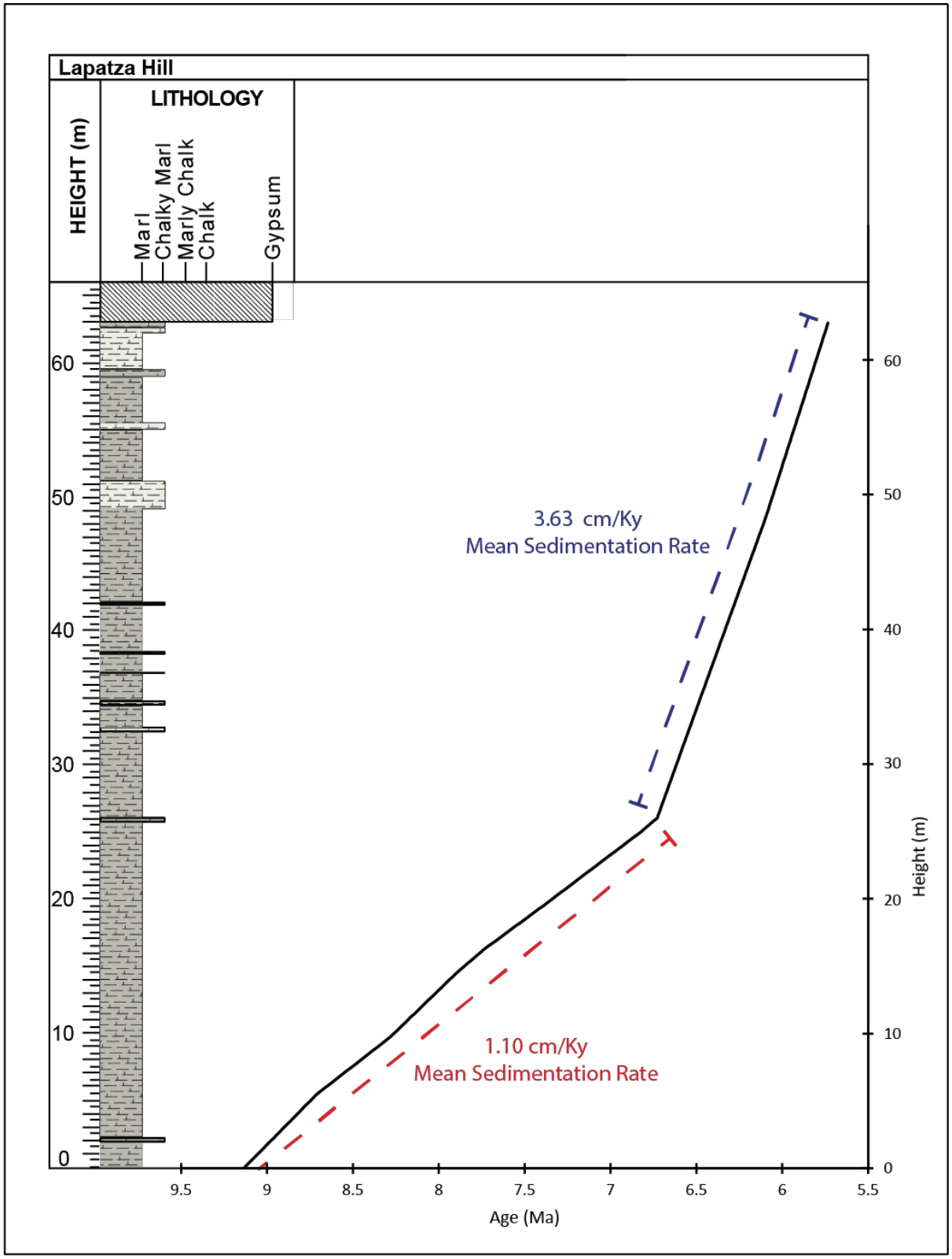


Figure 3.2.6.4 – Plot of Age (Ma) versus Height (m) for the Lapatza Hill succession shown relative to the simplified stratigraphic column of the succession. Average sedimentation rates are shown for two intervals of the succession.

The Composite Temporal Record

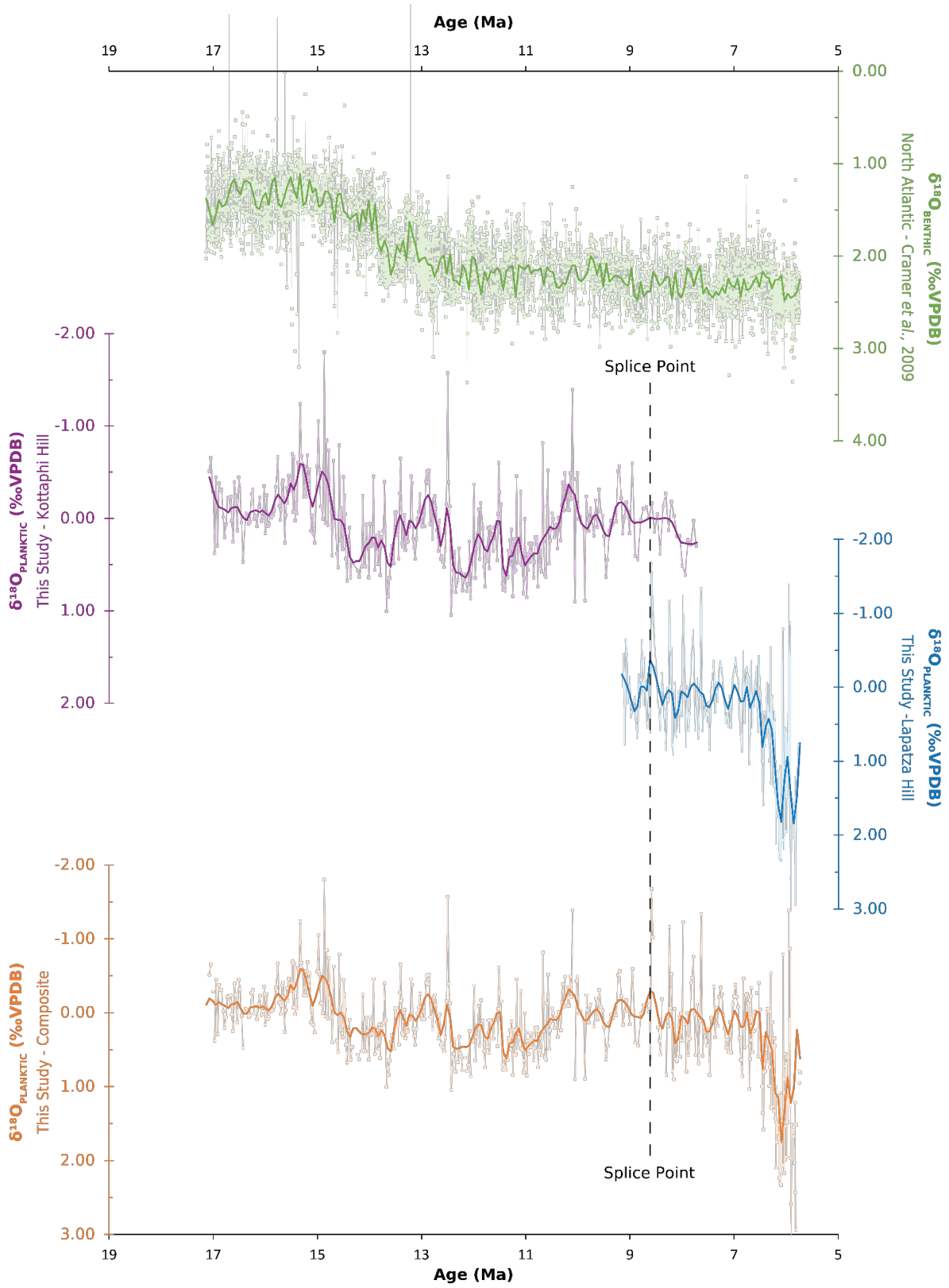


Figure 3.2.6.5 – Graph showing the $\delta^{18}O_{planktic}$ record for the adjusted age model for the composite temporal record from the Kottaphi Hill and Lapatza Hill successions. Both the Kottaphi Hill and Lapatza Hill successions are shown relative to the composite record and reference $\delta^{18}O_{benthic}$ record of Cramer *et al.*

(2009). The splice point (see text for explanation) at which the two records are combined to form a composite record is also shown. Fine lines plot the measured $\delta^{18}O$ values. Bold lines show the $\delta^{18}O$ smoothed by a locally weighted function over 60 Kyr.

The two succession sampled were combined to produce a composite temporal record (Figure 3.2.6.5). A composite temporal record allows for the examination of changes in climatic and environmental conditions throughout the whole time interval of interest. A small peak (heavier $\delta^{18}O$ values) in $\delta^{18}O_{planktic}$ is noted in both records at 8.60 Ma. This point (8.60 Ma) was selected as the splice point to combine the two records due to the similarity in $\delta^{18}O_{planktic}$, $\delta^{18}O_{bulk}$, $\delta^{13}C_{planktic}$ and $\delta^{13}C_{bulk}$ trends and values at this point. This combined 'composite record' provides a *c.* 13.2 My record from 18.95 Ma (Burdigalian) to 5.74 Ma (Messinian). The composite record covers the whole interval of interest from the onset of the Miocene Climate Optimum to the onset of the Messinian Salinity Crisis.

3.3 **Discussion**

This discussion section consolidates the results presented earlier in this chapter with reference to relevant previous research. A comprehensive synthesis and discussion of the data presented in this chapter, together with the information presented in Chapters 4 and 5, is presented in Chapter 6.

3.3.1 Kouroulla Gorge

Both oyster shell samples showed intrashell variation in Sr isotope ratio between the dark foliated and light chalky calcite layers. This apparent discrepancy indicates that one of these layers does not retain the true Sr isotopic value of seawater when bio-mineralisation took place. The difference between ages calculated for each layer is far longer than the lifespan of an Oyster and there is no overlap in error range.

Compositional ($\delta^{18}O$ and $\delta^{13}C$) differences between the dark foliated and light chalky layers of fossil oysters have been noted previously. These differences are attributed to the fact that the chalky calcite layer is secreted over a wider range of environmental conditions (Steuber, 1999; Brigaud *et al.*, 2008; Sælen *et al.*, 2016). However, the Sr isotope ratio of seawater does not undergo such extensive localised or temporal change (within the lifespan of an oyster) (Elderfield, 1986; McArthur *et al.*, 2001, 2012). An alternative hypothesis for this variation in composition between the layers of the oyster shells is that the chalky calcite layers are highly susceptible to diagenetic alteration, mainly due to their high porosity (Chinzei, 1995; Pons and Vicens, 2008). Preferential diagenetic alteration of the chalky layers is the most likely reason for intrashell compositional differences seen in this study; therefore, the data from the dark foliated calcite layers is used in order to date the oyster shells from Kouroulla Gorge.

The intrashell variation found in this study highlights the importance of careful selection of material for geochemical analysis.

The dark foliated calcite layers of oyster shells gave strontium isotope ages of 25.62 Ma (error range of 25.16 Ma to 26.1 Ma) and 24.37 Ma (error range of 24.07 Ma to 24.72 Ma). These new ages support the existence of a shallow-water carbonate shelf in NW Cyprus during the Late Oligocene (Chattian). This material must have been redeposited during the Miocene (see Chapter 2.1.1). The existence of a Late Oligocene shallow-water carbonate shelf in NW Cyprus has recently been suggested, based on the biostratigraphic dating of benthic foraminifera-rich calcarenites (Cannings, 2018; Cannings *et al.*, 2020).

The *Faviidae sp.* coral clast from Kouroulla Gorge is dated at 19.68 Ma with an error range of 19.5 Ma to 19.86 Ma. This Early Miocene age indicates that this coral belongs to the Terra Member reef.

These new age data indicate that the debris-flow units at Kouroulla Gorge (see Chapter 2.1.1) redeposited biogenic material of mixed provenance and age. The dated material that was redeposited during these debris-flow events is significantly older than the age previously given for the debris-flow units themselves based on the dating of the matrix sediment (Cannings, 2018; Cannings *et al.*, 2020). Therefore, these debris-flows did not deposit reef-related material that had been living close to the time of debris-flow deposition. These findings indicate that it is unlikely that debris-flow deposition and the termination of reef growth had the same trigger (Chapter 0 & 6.2).

3.3.2 Kottaphi Hill

The new age model for Kottaphi Hill indicates that the succession sampled spans *c.* 11 Ma from 18.96 Ma (Burdigalian) to 7.72 Ma (Tortonian). Sr isotope dating of samples from Kottaphi Hill is in agreement with calcareous nannofossil dating and field observations. The ages of samples produced by the age model are within the error range calculated with Sr isotope analysis. The foraminiferal assemblages identified in each facies of the Kottaphi Hill succession are in agreement with the dating produced with the age model.

Facies A at Kottaphi Hill ranges from 18.96 Ma to 17.25 Ma, with a mean sedimentation rate of 0.81 cm/ky. The chalk-marl couplets (each spanning *c.* 0.1 Ma) in this interval are interpreted to represent eccentricity-forced orbital cycles. This interpretation is in agreement with spectral analysis of the succession, which revealed distinguishable peaks in power spectra which are characteristic of orbital cyclicity

(Davies, 2001). The higher relative proportion of terrigenous material in the marl layers is a result of increased weathering and erosion on land, possibly as a result of eccentricity-forced climatic changes. The poor preservation of foraminifera within this facies may indicate that the lower part of the succession underwent some early-diagenesis. However, there is no evidence of deep burial or extensive diagenetic alteration. The poor preservation of foraminifera in this facies makes interpretation of depositional depth difficult. This facies has the smallest terrigenous component of any of the analysed facies (as indicated by XRF). The high proportion of carbonate material relative to terrigenous material (as indicated by XRF and XRD) indicates that these sediments were deposited far enough away from land to be free of dominant terrestrial influence. The lack of any sedimentary structure other than parallel laminations and rare burrows indicates a low-energy environment. Facies A is interpreted to represent deep marine sediments.

The irregular crystalline limestone of facies B in which the trace fossils are preserved is interpreted to represent a firm ground, previous authors have described this layer as a marine hardground (see Chapter 2.1.1). A marine hardground is a horizon that has undergone syn-depositional cementation on, or near, the seafloor (Christ *et al.*, 2015). However, the absence of borings and encrusting organisms preserved in this harder layer mean that it is more accurately described as a firm ground. The interpretation that this layer has undergone some cementation is supported by the increased proportions of magnesian calcite and ankerite, which are interpreted to have formed cements. The crystalline limestone beds were initially deposited as pelagic or hemipelagic sediments and later underwent cementation and were hardened on the seafloor. This cementation must have taken place during an interval of very low sedimentation rates. The presence of the softer micritic limestone interbeds indicates

that the low sedimentation intervals were interrupted by a return to a more normal depositional setting. The softer interbeds also indicate that cementation was limited to a relatively thin (4-15 cm) upper layer of sediments. The whole of facies B represents a condensed section, where sedimentation rates were low overall. Despite showing signs of cementation, this facies does not have any significant differences in composition to the other facies in the succession. XRD indicates relatively high levels of dolomite and magnesian calcite in facies B, these minerals may constitute some of the cement which has hardened this unit. Magnesium enrichment has been shown to correlate with sea floor lithification in firm ground and hardground layers (Allouc, 1990; Christ *et al.*, 2015). However, XRF analysis indicates that facies B is not significantly enriched in Mg compared to other facies at Kottaphi Hill. Therefore, the lack of significant Mg enrichment in facies B is in agreement with the interpretation that this facies does not represent a fully formed hardground layer.

The presence of *Thalassinoides* and *Zoophycos* trace fossils in facies B is indicative of the low energy *Zoophycos* ichnofacies; this is typical of continental slope to abyssal depositional environments (Seilacher, 1967). *Zoophycos* ichnofossils are associated with the bioturbation of soft or loose sediment, indicating that the beds in which they are preserved were initially soft and became lithified after the trace fossils had formed. However, *Diplocraterion* ichnofossils are more common in continental shelf settings but may also occur in dewatered sediments such as firm grounds (Seilacher, 1967).

Facies C was deposited between 16.97 Ma and 14.80 Ma. This facies comprises chalk and calcareous marl interbeds which are interpreted as orbitally forced (eccentricity driven) chalk marl couplets, as indicated by spectral analysis (Davies, 2001) (see above). This facies has a larger terrigenous component and smaller carbonate component than the underlying units, as supported by the relatively high levels of illite

and quartz reported from XRD analyses. The distinctive red colour of facies C is attributed to the high levels of Fe in the sediment, as indicated by XRF analysis (Table 3.2.3.2). Increased Al, Mg, K, Ti, Ba and Si are attributed to an increased terrestrial input in these units.

The provenance of the increased terrestrial input in facies C is debatable. The Troodos ophiolite is not believed to have become exposed until later than *c.* 16.97 Ma when these sediments were deposited (Kinnaird *et al.*, 2011). XRF analyses also show few similarities between the composition of this facies and the Upper Pillow Lavas of the Troodos ophiolite, meaning that a Troodos ophiolite source for this terrigenous input is unlikely. However, high levels of Cr and Ni in this facies suggest an ultramafic source for some of the terrigenous component (Garver and Scott, 1995; Bracciali *et al.*, 2007; Chen and Robertson, 2020). Previous research (Penttila, 2014) suggests that the first occurrences of Troodos ophiolite-derived material are represented by feldspar and clay-rich lithic fragments in facies D, which overlies facies C. Sedimentological studies also indicate that at this time most of the Troodos Ophiolite remained covered by the deep-marine sediments of the Lefkara Formation (Follows and Robertson, 1990; Eaton and Robertson, 1993).

It is also possible that some of the terrigenous material found in facies C represents enhanced weathering followed by fluvial run-off from continental land masses bordering the eastern Mediterranean. Enhanced weathering may be expected during the extreme climate conditions of the Miocene Climate Optimum (MCO), during which this facies was deposited. The large terrigenous component in this facies could also be interpreted to represent a period of dust flux and therefore this facies could indicate the presence of a nearby desert-like environment in the latest Middle Miocene. However, modern nearby deserts such as the Arabian Desert and the Sahara Desert

did not form until later than this time (deMenocal, 2004; Vaks *et al.*, 2013; Zhang *et al.*, 2014). It is possible that the eastern Mediterranean region experienced arid conditions during the MCO, which could have resulted in increased dust flux. It is also possible that some of the terrigenous component in facies C has come from a distal fluvial source, such as runoff from the North African Continent.

XRF analyses indicate some similarities between the composition of this facies and samples from the Kyrenia Range (notably the coeval Trapeza Formation). It is possible that the terrigenous component in this facies (or some of it) is from the same source as the terrigenous component of the Kyrenia Range samples. The samples from Kottaphi Hill have relatively low levels of Na_2O compared to samples from the Kyrenia Range; this indicates some differences in the provenance of the terrigenous components. It is likely that this facies at Kottaphi Hill received terrigenous input from several sources, one or several of which were probably shared with the coeval Kyrenia Range sediments. The majority of the terrigenous components in the Kyrenia Range sediments come from the Tauride allochthons in southeastern Turkey, followed by transport to the eastern Mediterranean Sea (McCay, 2011; McCay and Robertson, 2012; Chen, 2018; Chen *et al.*, 2022).

In summary, possible sources of terrigenous components, especially in facies C, include fluvial runoff and/or dust from nearby continents such as North Africa and southeastern Turkey as recorded in coeval sediments from the Kyrenia Range. A more complete database of the chemical compositions of all of the potential sources would be required to fully identify the provenance of the terrestrial input (especially for facies C) and relate this to regional to global scale tectonic and environmental changes.

As well as a comparatively large terrigenous component, major element variation plots also indicate that facies C received Fe_2O_3 enrichment from an additional independent source. This is likely a result of precipitation from enriched seawater during a time of deposition in a strongly oxidising environment, as expected during the MCO.

The presence of very rare foraminifera from the genus *Uvigerina* indicates that these sediments were deposited at outer-shelf to upper slope depths (Pekar and Kominz, 2001; Drinia *et al.*, 2016). *Uvigerina spp.* have previously been used as an indicator of sediment-starved environments and suboxic conditions (0.3 to 1.5 ml/l oxygen content) (Corliss, 1991; Kaminski *et al.*, 2002; Drinia *et al.*, 2003) and may indicate oxygen deficiency at the depth of deposition. Low sedimentation rates inferred from the presence of *Uvigerina spp.* are in agreement with the very low sedimentation rates (*c.* 0.25 cm/ky) calculated for this succession.

Facies D is interpreted to represent a similar depositional environment to the underlying facies C, but with little to no input of the Fe-rich terrigenous material noted in facies C. The higher relative proportion of chalk beds relative to marl beds indicates a long-term climate that was more favourable to chalk deposition (i.e. high carbonate productivity and reduced weathering/erosion). The phases of marl deposition are again likely to represent orbitally forced periods of increased terrestrial weathering. XRF analysis indicates that facies D has a smaller terrigenous component than the underlying facies C. However, the chalk of facies D does contain more terrigenous material than the chalk of facies A. Facies D was deposited from 14.80 Ma to 10.25 Ma. Facies D has relatively low levels of Cr and Zr as well as high levels of V compared to the other facies at Kottaphi Hill. For this reason, facies D is less likely to share a terrigenous input source with the Kyrenia Range sediments. It is unclear where the terrigenous component of facies D was derived from; however, it is unlikely to be from

the Mamonia Complex (SW Cyprus), the Kyrenia Range or the Troodos Ophiolite according to the compositional comparisons made based on XRF data. The small terrigenous component in facies D is likely to be from a more remote source, such as runoff from the North African Continent.

The presence of *Uvigerina spp.* together with *Lenticulina spp.,* and *Bolivina spp*. in facies D suggest a depositional environment with low sedimentation rates and low oxygen levels such as an upper shelf to bathyal environment (Corliss, 1991; Aharon and Sen Gupta, 1994; Katz and Miller, 1996; Kaminski *et al.*, 2002; Drinia *et al.*, 2003). The infrequent darker marl layers found within this facies are interpreted to be organic-rich layers; this interpretation is consistent with the oxygen minimum zone conditions indicated by the benthic foraminiferal assemblage and high V/Al and Mo/Al ratios (Tribovillard *et al*., 2006; Neumeister *et al*., 2016) obtained by XRF analysis (Figure 3.2.3.3). This facies includes two micritic limestone layers that are more resistant to weathering but not significantly altered or hardened. The partial hardening of these beds was potentially the result of dewatering and compaction. The hardened micritic limestone beds are interpreted to represent a firmground (Christ *et al.*, 2015). Firmgrounds have been identified in Miocene successions from various locations in the Mediterranean region (e.g. Thrana and Talbot, 2006; Moissette *et al.*, 2018; Marred *et al.*, 2022). However, the documented absence of trace fossils in these specific horizons means that little can be inferred about the environmental setting in which the firmground formed. The lack of complete cementation and absence of trace fossils in these firmground beds suggest that these layers may represent a shorter-lived or less intense period of sediment starvation than the facies B firm ground layers. Previous work (Penttila, 2014) has indicated that the upper part of this facies contains

the first occurrence of material derived from the Troodos Ophiolite in the Pakhna Formation, based on the presence of feldspar and clay-rich lithic fragments.

Facies E was deposited between 10.25 Ma and 7.72 Ma. The facies is distinguished by the presence of softer dark mudstone/marl layers. These organic-rich dark layers are interpreted to be related to the formation of sapropels; this is consistent with the common interpretation of increased freshwater nutrient input leading to oxygen stratification (Rohling, 1994; Emeis *et al.*, 2000; Casford *et al.*, 2003; De Lange *et al.*, 2008). Sapropels are noted across the eastern Mediterranean region during the Middle-Late Miocene (Nijenhuis *et al.*, 1996; Taylforth *et al.*, 2014), and are believed to form in relation to the onset of the North African Monsoon. The relatively high abundance of Mn and Fe carbonate minerals (ankerite and rhodochrosite) is consistent with elevated Fe & Mn reported from sapropel-bearing rocks (Neumann *et al.*, 2002; Rutten and de Lange, 2003; Reitz *et al.*, 2006). However, the layers found at Kottaphi Hill lack the characteristic darkness of sapropels and have lower organic content (<2% total organic carbon) than true sapropels (Penttila, 2014). Previous work has suggested that the organic-rich layers at Kottaphi Hill represent an organic-rich precursor to sapropelic layers (Athanasiou *et al.*, 2021). However, it is also possible that these layers represent sapropels which have been modified by postdepositional oxidation, sometimes known as ‘ghost sapropels’ (Higgs *et al.*, 1994; Kroon *et al.*, 1998; Penttila, 2014). The presence of *Uvigerina spp.* together with *Lenticulina spp.,* and Bolivina spp., suggests a similar outer shelf to bathyal depositional environment to the one suggested for facies D. *Elphidium spp.* is indicative of neritic to shallow marine settings. The deep water, low oxygen conditions implied by the other benthic foraminifera in this assemblage and the organic-rich layers indicate that this facies was not deposited in a shallow water or neritic environment. The presence of

Elphidium spp. may, therefore, indicate that increased organic material was being transported to the outer shelf from shallower sites during this interval.

Facies A-E comprise the succession sampled at Kottaphi Hill. XRF analyses indicate that the differences in composition between these facies are mainly in the terrigenous fraction (as indicated by major element plots; see Figure 3.2.3.4). As discussed above, the available XRF data do not allow a single source of terrigenous input to be identified. It is likely that these facies (especially facies C) received mixed terrigenous input from several sources (e.g. southeastern Turkey, North Africa). Enrichment in Ni relative to V in the samples from Kottaphi Hill suggests that some (ophiolitic) ultramafic debris is present within these samples. The Troodos ophiolite is not a likely source of this material; previous research indicates that the ophiolite was not unroofed until the late Miocene (Follows and Robertson, 1990; Eaton and Robertson, 1993; Penttila, 2014), and clear compositional differences are noted between the samples from Kottaphi Hill and the Troodos Ophiolite (see 3.2.3). It is likely that ultramafic debris in the samples from Kottaphi Hill has a shared provenance with the ultramafic debris found in samples from the Kyrenia range, which originated in the Tauride allochthons (McCay and Robertson, 2012; Chen *et al.*, 2022). The close proximity to the Kyrenia Range (several kilometres) compared to the further distance to other possible sources, such as North Africa (several hundred kilometres) also makes a shared source with the Kyrenia Range sediments more likely.

The differences in terrigenous fraction composition between the samples analysed are likely to be due to changes in the relative terrigenous inputs from these sources. Such changes in the relative inputs from each source may be influenced by changes in ocean circulation, tectonics, climate, depositional pathways or a combination of

factors. Further data from both within and outside the study area are required to constrain better the provenance of potentially varied terrigenous components.

An interval of 12.5 metres of little to no exposure is found above facies E. The interval is covered by redeposited material from the above units, together with modern vegetation. Rare patchy exposures in this interval contain marl with calcarenite debris-flow units. Consistent with a shallower setting than the underlying facies. The presence of vegetation and lack of exposure could indicate that these rocks are less resistant to weathering than the underlying units; i.e. marl with considerably less chalk than the underlying facies. Chalk beds are more resistant to weathering than marl beds and therefore are less likely to host vegetative overgrowth. An interval of marl beds in this section of limited exposure is consistent with a shallower depositional environment than the facies beneath. This is in agreement with the change in depositional depth noted between the pelagic sediments beneath and the shallow water facies found above the interval of no exposure.

Facies F is located above the interval of no exposure. The much larger (but variable) clast size and irregular bedding of this facies indicate that the material has been deposited during higher energy events than the units below. The fossil assemblage of this facies has previously been the subject of an in-depth study; the presence of both deep water and oligotrophic-zone-dwelling organisms indicates an outer shelf setting which received a relatively high input of shallower water material (Coletti *et al.*, 2021). The large benthic foraminifera and fragmented coralline algae, together with larger clasts and blocks in this facies are interpreted to represent material that was transported downslope from the lowermost photic zone to the outer shelf.

The fossil assemblage of facies G has also been subject to recent detailed study (Coletti *et al.*, 2021). This facies is composed of reworked Koronia Member coral-reef facies. The fossil assemblage of the Koronia Member coral-reef indicates a shallow neritic environment with a water depth of <15 m (Follows, 1990, 1992; Follows and Robertson, 1990; Coletti *et al.*, 2021). This coral-reef facies material is preserved as clasts which range up to several metres in size within a poorly sorted talus breccia. Although the reef material has been reworked, the size of clasts (up to several metres) indicates that it is unlikely that it has travelled a great distance; therefore this facies is interpreted to represent locally redeposited reef talus. It is likely that this talus was transported from a nearby *in situ* reef deposit, such as the one noted on Kreatos Hill, above Mitsero Mine *c.* 1km to the East of Kottaphi Hill (Follows and Robertson, 1990; Follows *et al.*, 1996).

The Miocene Kottaphi Hill succession is interpreted to represent an overall shallowing-upward sequence. The lower facies (A-E) represent low energy, outer shelf to bathyal depositional environments with relatively low sedimentation rates. The interval of no exposure is inferred to represent a period of transition towards a higher energy environment with increased terrigenous input. Facies F represents a higher energy environment than the underlying facies (A-E) but still represents a depositional environment at depth (outer shelf). Facies G represents a reworked shallow-water neritic facies and likely the lowest relative sea level of the succession. This long-term shallowing sequence is interpreted to be controlled by uplift related to regional tectonics (Follows, 1990; Follows and Robertson, 1990; Follows *et al.*, 1996; Kinnaird *et al.*, 2011); Smaller fluctuations in relative sea level also took place during this time due to orbital forcing (Davies, 2001).

3.3.3 Lapatza Hill

The Lapatza Hill succession was deposited from 9.14 Ma (Tortonian) to 5.74 Ma (Messinian). The marl and chalky marl succession at Lapatza Hill has relatively few marked changes in lithology, fossil assemblage or sedimentary structure throughout. The high relative abundance of planktic foraminifera and very rare occurrence of benthic foraminifera from the *Cibicidoides* and *Uvigerina* genera at the base of Lapatza Hill indicate an upper shelf to bathyal depositional setting. After 7.23 Ma (*c.* 21 m), the abundance of benthic foraminifera further reduced, and only very rare *Uvigerina spp.* are noted. Reduced species diversity of benthic foraminifera has been noted during this time interval in northern Italy. Anoxic conditions and increased salinity may have controlled these abundance changes (Kouwenhoven *et al.*, 1999). After 6.56 Ma (*c.* 32 m), benthic foraminifera are completely absent from the samples from Lapatza Hill; this indicates that conditions were no longer habitable for benthic foraminifera. Several factors may have led to uninhabitable bottom waters; relative sea-level rise may have resulted in the sea floor becoming deeper than the depth habitats of the benthic foraminifera concerned. A more likely scenario is that stratification of seawater in the basin resulted in bottom water conditions which were uninhabitable due to high salinity or dysoxia. This stratification model has previously been suggested for northern Cyprus during the Late Miocene (Robertson *et al.*, 2019). The reduction in abundance and complete absence of planktic foraminifera during some intervals near the top of the succession are interpreted to represent periods where the basin became isolated and may have experienced increased salinity. This is supported by the absence of calcareous nannofossils from the *Discoaster* genus. The absence of Discoasters in the late Messinian samples has been reported from elsewhere in Cyprus, and is related to salinity and fluctuations in nutrient supply (Wade and Bown, 2006).

Sampling of the Lapatza Hill succession for XRD analysis focussed on the background sediments; therefore, darker marl layers were avoided. However, one sample indicated the presence of birnessite. Similar dark marl layers have been noted in a comparable sequence in northeast Cyprus; these layers have been shown to be invariably enriched in manganese oxide (birnessite) (Robertson *et al.*, 2019). Therefore, the dark brown marl layers at Lapatza Hill are interpreted as manganese oxide-rich (birnessite) deposits. In northeast Cyprus, these layers have been interpreted to represent cyclical redox changes which were associated with the input of manganese from land, likely from local exposure in the Kyrenia Range. These inferred redox changes are believed to represent periods of basin isolation which resulted in anoxic bottom waters rich in dissolved manganese, followed by oxidation, which caused the manganese to precipitate out as discrete manganese oxide layers (Robertson *et al.*, 2019). The occurrence of these layers throughout the Lapatza Hill succession indicates that the conditions required for their formation (i.e. supply of manganese enrichment) existed, at least periodically, for at least *c.* 3 Ma. In some instances, the dark brown marl layers are found in association with dark red layers; these are interpreted to represent iron oxide-rich layers. The reason why these iron-rich and manganese-rich layers were deposited separately is unclear, but may represent periodic oxygenation of bottom waters. Some of these metalliferous marl layers are partially lithified and are interpreted to represent indurated metal-rich layers.

The age model indicates that the sedimentation rate increased for the upper part of the Lapatza Hill succession (3.627 cm/ky) compared to the lower part of the basin (1.099 cm/ky). This increase in sedimentation rate reflects an increase in sediment and nutrient supply as indicated by microfossil assemblage examinations.

The Lapatza Hill succession has a relatively large terrigenous component, especially near to the base of the section. Higher proportions of quartz, illite, kaolinite, chlorite, microcline, muscovite, albite and anorthite are found at the bottom of the section; these minerals mainly have a terrigenous source. Higher relative proportions of calcite are found at the top of the succession. This high sediment flux can be related to nearby tectonism. Suture tightening and thrusting took place during the Late Miocene due to compression between the Arabian Platform and the Tauride continent (Robertson *et al.*, 2004; McCay, 2011). This compressional phase has been related to Late Miocene high-concentration turbidity current deposition throughout northern Cyprus. These turbidites formed as a result of increased sediment input from the Tauride allochthons in southeastern Turkey (McCay, 2011; McCay and Robertson, 2012). Although no such turbidity current deposits are found in the Lapatza Hill succession, it is likely that the Late Miocene increase in sediment input from the Tauride allochthons would have also resulted in increased sedimentation in an adjacent deep basin. The Lapatza Hill succession comprises the upper part of the Kythrea (Değirmenlik) Group succession. The upper Kythrea (Değirmenlik) Group is dominated by mudrocks, which overlie a thick sequence of turbidite deposits (McCay, 2011; McCay and Robertson, 2012). This transition from turbidite deposits to mudrocks is interpreted to represent the waning of the source of turbidite deposits (Tauride allochthons) leading to the deposition of lower energy hemipelagic gravity deposits as seen at Lapatza Hill.

Estimates of changes in relative sea level and depth are difficult for the Lapatza Hill deposit due to the low abundance of benthic foraminifera and the absence of large-scale changes in lithology or sedimentary facies.

Fine-grained yellow material is interpreted to represent sulphur-bearing deposits. These deposits are found in association with gypsum at irregular intervals throughout

the succession. These gypsum layers form secondary veins composed of selenitic gypsum that formed through the remobilization of the primary gypsum deposit which caps the hill.

Sr isotope dating of the samples from Lapatza Hill produced unexpected results. Sedimentological study of the succession did not uncover any evidence of large-scale reworking of material or any evidence of deformation or overturning of the strata. The most likely explanation for the non-correlation between age and sample height at Lapatza Hill is that the Sr isotope values of the planktic foraminifera samples analysed do not reflect the Sr isotope value of global seawater at the time of biomineralization. The incompatible Sr isotope ratio of TC22 470 also indicates that the $^{87}Sr/^{86}Sr$ of these planktic foraminifera samples does not reflect the global seawater $^{87}Sr/^{86}Sr$ at this time. Although localized reworking of planktic foraminifera samples cannot be completely discounted, this is unlikely to have produced such anomalous results. Reworking is not indicated by any other methods (e.g. field observations, stable isotope analysis, calcareous nannofossil biostratigraphy or trace element analysis; see above, Chapter 4 and Chapter 5).

There are two likely causes of these anomalous results: (1) The samples may have been diagenetically altered in a way that resulted in anomalous $^{87}Sr/^{86}Sr$ ratios; (2) the $^{87}Sr/^{86}Sr$ of the seawater in which biomineralization took place was dramatically different from that of the open ocean.

It is possible that the cyclical redox changes that resulted in the formation of metalliferous marl layers also resulted in alterations to the composition of foraminiferal tests during these times. However, it is unclear if such conditions could have had an effect on the Sr isotope composition of foraminiferal tests that were deposited on the

seafloor during these times. Whilst diagenetic alteration is a possibility, no such diagenetic alteration is noted to have caused anomalous results in other geochemical analyses of planktic foraminifera samples from Lapatza Hill (i.e. stable isotope and trace element analyses; see Chapter 4 and Chapter 5). Samples analysed were carefully examined prior to their analysis, and no visual signs of diagenetic alteration were noted. Samples close to metalliferous marl layers were not selected for Sr isotope analysis.

Anomalous $^{87}Sr/^{86}Sr$ values have been previously documented for samples of Messinian age and are interpreted as a result of the onset of the Messinian Salinity Crisis (MSC). It has been suggested that anomalous results in pre-evaporitic sequences in southern Turkey are a result of local variation in $^{87}Sr/^{86}Sr$ due to the isolation of Mediterranean basins prior to the Messinian Salinity Crisis (Flecker and Ellam, 1999, 2006; Flecker *et al.*, 2002). Therefore, although the analysis of Sr isotopes was not a success for dating samples from Lapatza Hill, the Sr isotope data may help to illustrate the history of isolation of the eastern Mediterranean basins and the onset of the MSC.

Although anomalous results may be expected for samples close to the onset of evaporite deposition (such as TC22 470), the anomalous $^{87}Sr/^{86}Sr$ values for all of the samples in this succession suggest that the onset of the MSC led to changes in the local $^{87}Sr/^{86}Sr$ of seawater several million years before the deposition of evaporites. The age model produced in this study suggests that the lowermost sample used for Sr isotope analysis (TC22 203) was deposited at 9.078 Ma; this would indicate that local changes in seawater chemistry had begun at least *c*. 3.35 My prior to evaporite deposition (*c.* 5.73 Ma). Sr isotope analysis from the Manavgat Basin in southern Turkey has also revealed a localised change in $^{87}Sr/^{86}Sr$ from *c.* 3 My prior to evaporite

deposition (Flecker and Ellam, 1999); this is also not assumed to be diagenetic and is supported by modelling (Flecker *et al.*, 2002). However, the Manavgat Basin is a marginal basin where the relative control of continental weathering and runoff is assumed to be greater. There is no obvious evidence for shallowing upwards in the Lapatza Hill succession beneath the Messinian evaporites; therefore, the Lapatza Hill succession is not believed to represent a marginal setting at any time prior to evaporite deposition.

On the other hand, changes in the nannofossil assemblage for samples from Lapatza Hill mostly correlate with the sequence of changes in the open ocean (until *c.* 6.8 Ma); therefore, some connectivity should have been retained between eastern Mediterranean basins and the open ocean. It is likely that changes in local $^{87}Sr/^{86}Sr$ reflect changes in the balance of controls on local $^{87}Sr/^{86}Sr$ seawater composition; i.e. a shift in the balance between ocean input and local changes in the hydrological cycle, as inferred from previous modelling of $^{87}Sr/^{86}Sr$ ratios in Mediterranean basins during the Late Miocene (Flecker *et al.*, 2002). Modelling studies indicate that the closure of the eastern gateway of the southern Neotethys resulted in significant alterations to the hydrological cycle in the eastern Mediterranean, with evaporation exceeding freshwater input (Karami *et al.*, 2009).

3.3.4 A Composite Early-Late Miocene Temporal Record

By combining the Kottaphi Hill and Lapatza Hill successions, a composite temporal record for the latest Early Miocene to the Late Miocene can be constructed (e.g. Figure 3.2.6.5). As this composite temporal record combines data from two successions sampled, care should be taken when making interpretations based on a composite succession. Whilst these two successions are both composed of deep-water

sediments, marked environmental differences are noted between the two successions.

The Kottaphi Hill succession represents a shallowing upward sequence. Most of the succession sampled is believed to have been deposited in an upper slope to outer shelf environment. Depth interpretations of the Lapatza Hill succession are difficult; the succession is believed to represent a bathyal environment. There is no evidence for shallowing upwards in the succession sampled at Lapatza Hill. The Lapatza Hill succession formed under conditions of much higher sediment input than the Kottaphi Hill succession, as reflected in the much higher sedimentation rates calculated for the Lapatza Hill succession. Therefore, although the Lapatza Hill succession is thought to have been deposited in a deeper setting, it underwent more influence from processes on land (i.e. detrital terrigenous input from deposition in the Kyrenia Range).

Local to regional-scale tectonic changes and related sea level changes, together with eustatic sea level changes, significantly influenced the depositional environments of both successions. For the Kottaphi Hill succession these depth changes were mostly the result of the early uplift of the adjacent Troodos Ophiolite, which resulted in the shallowing-upward sequence. The tectonic controls on the Lapatza Hill succession are more complex. High sediment supply in this depositional setting was a result of regional tectonics, related to compression between the Arabian platform and the Tauride continent (McCay, 2011; McCay and Robertson, 2012).

This tectonism is likely to have also resulted in changes in relative sea level for the sediments deposited in the Lapatza Hill succession. These tectonic changes are also likely to have influenced basin isolation, as indicated by Sr isotope data. These periods of isolation indicate that the Lapatza Hill succession formed in a unique setting; the

manganese and iron deposits noted in the succession and fossil assemblage also support this. Isolation from open oceans was a crucial part in the development of the succession deposited at Lapatza Hill. Isolation up to and including the Messinian Salinity Crisis (MSC) had an effect on ocean chemistry, this is likely to be preserved in geochemical records. Local basin isolation together with Mediterranean-wide isolation is also related to the dramatic sea level fall at the end of the succession related to the MSC.

Both successions preserve largely unaltered pelagic-hemipelagic sediments which contain well-preserved planktic foraminifera. In the Kottaphi Hill succession, an exception to this favourable preservation is noted in the heavily cemented beds of the carbonate firm ground (facies B). Some parts of the Lapatza Hill succession are affected by the deposition of remobilized gypsum in the form of selenitic gypsum veins. Additional care must be taken when conducting geochemical analyses of samples that may be affected by secondary diagenesis.

3.4 Summary of Key Points

Kouroulla Gorge

- The oyster shell material contained within debris-flow deposits at Kouroulla Gorge represents Late Oligocene shallow water material which was redeposited by debris-flow processes during the Middle Miocene.
- Early Miocene coral was also redeposited by these debris-flow events during the Middle Miocene.

Kottaphi Hill

- Pelagic sediments with variable amounts and sources of terrigenous input were deposited between 18.96 Ma (Burdigalian) and 7.72 Ma (Tortonian) at Kottaphi Hill.
- The rate of sedimentation from 18.96 Ma to 7.72 Ma at Kottaphi Hill was very low. A period of remarkably low sedimentation rate (17.25 to 16.97 Ma) is evidenced by the presence of a marine firm ground.
- The pelagic sediments of the succession sampled are overlain by reworked shallow water material, consistent with a ‘shallowing-upwards’ sequence, which is interpreted as a result of the uplift of the Troodos ophiolite.

Lapatza Hill

- Hemipelagic sediments at Lapatza Hill were deposited between 9.14 Ma (Tortonian) and 5.74 Ma (Messinian). The deposition of these sediments shortly preceded the deposition of evaporites related to the Messinian salinity crisis.
- The presence of manganese oxide-rich marl layers throughout the succession is interpreted to indicate partial or periodic isolation of the basin, resulting in fluctuating redox conditions.

- Changes to the abundance and assemblage composition of planktic and benthic foraminifera as well as calcareous nannofossils, are interpreted to represent partial isolation of the basin, resulting in environmental changes e.g. nutrient supply fluctuations and/or increased salinity.

4 Geochemical evidence for palaeotemperature changes from the composite succession

The purpose of this chapter is to outline the methods used to produce a sea temperature record and to present and interpret the results obtained. As highlighted in Chapter 1.2.4, the Miocene was a time of extensive global climate changes. In this study, both Mg/Ca and $\delta^{18}O_{planktic}$ palaeotemperature records were produced; these records are presented in this chapter. An improved method which utilises a combination of both $\delta^{18}O_{planktic}$ and Mg/Ca palaeotemperature calculations in order to produce a high-resolution temperature record is also presented. A better understanding of the extent of Miocene climate events, and the oceanographic response to such changes, is of growing interest, especially in regions where the Miocene climate has not been studied extensively, such as the E Mediterranean region.

4.1 Methods

4.1.1 Oxygen stable isotope records

The methods used for oxygen stable isotopic analysis of fine fraction bulk samples and planktic foraminifera samples are described in Chapter 2.5.

Although empirically calibrated calculations (see Chapter 4.1.2) must be used to interpret numerical palaeotemperature information, measured oxygen stable isotope data can be useful to gain a basic understanding of temperature changes. This is especially applicable to stable isotope records based on the analysis of bulk fine fraction samples, which are not suitable for high-resolution temperature calibrations (Chapter 2.5). In this study, the $\delta^{18}O_{finefraction}$ record is more complete and covers a broader time interval than the $\delta^{18}O_{planktic}$ record. This is due to the unsuitability of some

planktic foraminifera samples for stable isotope analysis resulting from the absence or poor preservation of the foraminifera (Chapter 3.2.4). The $\delta^{18}O_{finefraction}$ record can be utilised for limited interpretation of temperature trends for time intervals not covered by the $\delta^{18}O_{planktic}$ record. Palaeotemperature interpretations based on $\delta^{18}O_{finefraction}$ data have a greater uncertainty than interpretations based on $\delta^{18}O_{planktic}$ data (See Chapter 2.5). It should be noted that fine fraction samples might also be affected by diagenetic factors that resulted in the poor preservation of foraminifera, further adding to the uncertainty of interpretations based on $\delta^{18}O_{finefraction}$ measurements alone.

4.1.2 $\delta^{18}O_{planktic}$ Palaeothermometry

The methodology used to analyse the oxygen stable isotopic composition of planktic foraminifera is described in Chapter 2.5.2. In this study, planktic foraminifera from the *Praeorbulina-Orbulina* lineage were subjected to stable isotope analysis; the stable isotopic composition of foraminifera from this lineage analysed in this study is referred to as $\delta^{18}O_{planktic}$.

The stable oxygen isotopic composition of marine carbonate material ($\delta^{18}O_c$) is one of the best-established methods of palaeotemperature calculation (Shackleton and Opdyke, 1973; Zachos *et al.*, 2001a; Grossman, 2012; Pearson, 2012; Wright, 2013; Westerhold *et al.*, 2020; Gaskell and Hull, 2023). Foraminifera are amongst the most commonly utilised sources of marine carbonate in the production of such temperature records. This extensive use is due to the success in producing geochemical records through analysis of foraminiferal calcite in view of their abundance throughout the fossil record and widespread geographical abundance (Kucera, 2007; Pearson, 2012; Wright, 2013).

As described in Chapter 2.5, the $\delta^{18}O$ composition of foraminiferal calcite varies due to the isotopic composition of water, temperature, mineral phase, diagenesis and vital effects (Shackleton, 1967; Shackleton and Opdyke, 1973; Prentice and Matthews, 1991). As only foraminifera tests which have no evidence of diagenetic alteration were analysed, diagenesis and diagenetic effects on the mineral phase should not be a control of the $\delta^{18}O_{planktic}$ record presented in this thesis. Analysis took place from a narrow size fraction (355–400 μm); this helped to ensure that the specimens analysed were of a similar test composition and represent a similar phase in their life cycle, therefore limiting the effects of gametogenic calcite and algal symbiont isotopic signatures. By using a constrained size fraction from a lineage of foraminifera, which has no known change in test composition or depth habitat (Pearson *et al.*, 1997), the effects of mineral phase and vital effects are also constrained. The role of vital effects, such as species-specific response to temperature change is accounted for by the use of species-specific, empirically calibrated palaeotemperature calibrations. Therefore, the only two remaining factors which could have an effect on the calculated $\delta^{18}O_{planktic}$ palaeotemperature calculations are the isotopic composition of seawater ($\delta^{18}O_{sw}$) and the seawater temperature, which is the control desired for measurement. For this reason, calculations of palaeotemperature from $\delta^{18}O$ of foraminiferal calcite must include an estimation of $\delta^{18}O_{sw}$.

In the modern ocean, $\delta^{18}O_{sw}$ in surface waters varies with latitude; therefore, previous studies often used a $\delta^{18}O_{sw}$ estimate based on the palaeolatitude of the sample site, often incorporating an ice volume correction (Zachos *et al.*, 1994; Hollis *et al.*, 2019). However, modelling studies predict that a stable $\delta^{18}O_{sw}$ is unlikely over extended time periods, and latitudinal variations may have been altered for warm periods when the hydrological cycle was reorganised (Zhou *et al.*, 2008; Tindall *et al.*, 2010; Roberts *et*

al., 2011; Zhu *et al.*, 2020). Therefore, proxy (e.g. Steinke *et al.*, 2010; Brand *et al.*, 2013) and model-based $\delta^{18}O_{sw}$ estimates are becoming increasingly popular (Zachos *et al.*, 2001a; Westerhold *et al.*, 2020; Gaskell and Hull, 2023). In this study, $\delta^{18}O_{sw}$ estimates were calculated with the use of an additional palaeotemperature proxy, which is independently calibrated and not related to $\delta^{18}O_{sw}$. This is one of several benefits of a multi-proxy approach as discussed in Chapter 4.1.4.

Numerous previous studies have proposed calibrations for the calculation of palaeotemperature based on the $\delta^{18}O$ values of the test of *Orbulina universa*; these calibrations come from studies based on sediment core samples (e.g. Farmer *et al.*, 2007), plankton tow samples (e.g. Bouvier-Soumagnac and Duplessy, 1985) and lab-cultured foraminifera samples (e.g. Bemis *et al.*, 1998). Calibrations for calculating temperature from biogenic calcite are based on the equation below (Bemis *et al.*, 1998):

$$\boldsymbol{T = a - b(\delta^{18}O_c - \delta^{18}O_{sw})} \qquad \textbf{[Eq. 4.1.2.1]}$$

In this equation the experimental variable *a* represents the temperature in °C at which $\delta^{18}O_c$ and $\delta^{18}O_{sw}$ are in equilibrium; *b* represents the slope of the equation. The calibrations used in this study are presented in Table 4.1.2.1. As described in Chapter 2.5, convention dictates that $\delta^{18}O_c$ values are recorded as ‰ VDPB; however, $\delta^{18}O_{sw}$ values are conventionally recorded relative to a different standard reference material; i.e. Vienna Standard Mean Ocean Water (VSMOW). It is therefore important to incorporate a conversion (Brand *et al.*, 2014) to VPDB when dealing with $\delta^{18}O_{sw}$ which are given in units of ‰ VSMOW.

Reference	Light Level	a	b	Method	Temperature yielded
Bemis *et al.,* (1998)	High Light (HL)	14.9	4.80	Culture	*In situ*

Bemis *et al.,* (1998)	Low Light (LL)	16.5	4.80	Culture	*In situ*
Bemis *et al.,* (1998)	HL & LL Mean	15.7	4.80	Culture	*In situ*
Bouvier-Soumagnac and Duplessy (1985)	Non-Specific	15.4	4.81	Plankton tow regression	*In situ*
Farmer et al. (2007)	Non-Specific	16.4	5.11	Core-top regression	*In situ (annual mean)*

Table 4.1.2.1 - $\delta^{18}O$ temperature calibrations for equation 4.1.1 as used in this study. See Gaskell and Hull (2023) for a comprehensive list of previously published $\delta^{18}O$ temperature calibrations.

4.1.3 Mg/Ca Palaeothermometry

Mg/Ca data used for Mg/Ca palaeothermometry in this study were collected during the trace elemental analysis of planktic foraminifera from the *Praeorbulina-Orbulina* lineage. The methodology used in this analysis is described in Chapter 2.6

Mg/Ca palaeothermometry is based on the principle that the substitution of Mg^{2+} into biogenic calcite has a strong temperature dependency (Nürnberg *et al.*, 1996; Elderfield and Ganssen, 2000; Anand *et al.*, 2003). Experiments on cultured foraminifera (Nürnberg *et al.*, 1996; Lea *et al.*, 1999; Russell *et al.*, 2004; Kisakürek *et al.*, 2008; Hönisch *et al.*, 2013; Allen *et al.*, 2016; Evans *et al.*, 2016), supported by core top (Delaney *et al.*, 1985; Lea *et al.*, 1999; Dekens *et al.*, 2002; Anand *et al.*, 2003; McConnell and Thunell, 2005), and sediment trap (Delaney *et al.*, 1985; Nürnberg *et al.*, 1996; Rosenthal *et al.*, 1997; Elderfield and Ganssen, 2000; Dekens *et al.*, 2002; Lear *et al.*, 2002; Rathmann *et al.*, 2004) studies, have revealed an exponential positive relationship between the ratio of Mg to Ca and calcification temperature in foraminiferal calcite. This relationship results in an increase of *c.* 6% in Mg/Ca ratios per 1 °C in *Orbulina universa* (Lea *et al.*, 1999; Anand *et al.*, 2003; Russell *et al.*, 2004; Gray and Evans, 2019).

Species-specific variations in the relationship between Mg/Ca ratios and temperature have been observed in living foraminifera. Therefore, calibrations for calculating

calcification temperature from the Mg/Ca ratios of foraminiferal calcite are specific to the species or genera analysed. In this study, specimens from the *Praeorbulina-Orbulina* lineage were analysed. *O.universa* is one of the most studied extant species of foraminifera, and therefore has well-constrained calibrations from laboratory culture experiments (Lea *et al.*, 1999; Anand *et al.*, 2003; Russell *et al.*, 2004; Gray and Evans, 2019). As there is no known difference in depth habitat, test composition or algal symbiont relationship between species in the *Praeorbulina-Orbulina* lineage (Pearson *et al.*, 1997), calculations calibrated with living *O. universa* specimens are used for all of the samples in this study including samples of other species from the *Praeorbulina-Orbulina* lineage.

A major strength of Mg/Ca palaeothermometry is that it can be carried out on foraminiferal test samples, as is the standard for $\delta^{18}O$-based palaeothermometry, but is independent of $\delta^{18}O_{sw}$. The Mg/Ca palaeothermometer does have some limitations, however. Most of these can be accounted for by the careful use of specific calibrations. Mg/Ca ratios in foraminiferal calcite are not purely a function of temperature; the Mg/Ca composition of seawater is an important control, and laboratory culture experiments have also shown that both salinity and seawater carbonate chemistry (pH) are secondary controls on the incorporation of Mg into foraminiferal calcite.

A relatively modest salinity influence (~3.6% per PSU) on the Mg/Ca ratio of foraminiferal calcite is supported by lab culture (e.g. Nürnberg *et al.*, 1996; Hönisch *et al.*, 2013) and sediment trap studies (Gray *et al.*, 2018). Studies of planktic foraminifera in high salinity environments have revealed that extremely high Mg/Ca ratios reported from field studies (Ferguson *et al.*, 2008; Mathien-Blard and Bassinot, 2009; Arbuszewski *et al.*, 2010) are likely to be due to the overgrowth of secondary high-Mg calcite, rather than increased Mg uptake into foraminiferal calcite (Hoogakker *et al.*,

2009; Schmidt and Spero, 2011). Therefore, careful sample examination and selection can help to ensure such secondary salinity effects are not a component of Mg/Ca-derived palaeotemperatures.

Variations in seawater carbonate chemistry (pH) have a larger control on Mg/Ca ratios in foraminiferal calcite (−5 to −9% per 0.1 pH) (Russell *et al.*, 2004; Evans *et al.*, 2016; Gray *et al.*, 2018; Gray and Evans, 2019). However, seawater pH variations generally take place at relatively low magnitudes (±0.05 pH units) (Gray and Evans, 2019), and therefore do not have a great effect on the Mg/Ca ratio of foraminiferal calcite. A 0.03 pH decrease is indicated globally during the time interval covered by the Mg/Ca record in this study (Zeebe and Tyrrell, 2019).

Recent Mg/Ca palaeotemperature calibrations (e.g. Gray and Evans, 2019) seek to correct for the effects of both salinity and seawater carbonate chemistry (pH); however, it is difficult to reconstruct accurate records of salinity and seawater carbonate chemistry (pH) throughout geological history, resulting in some uncertainty in this method. Typically, estimates of atmospheric CO_2 are used to estimate pH changes; recently, boron isotope analysis has been used to improve constraints on seawater pH changes throughout a sampled time interval (Gray and Evans, 2019). The calibration calculation of Gray and Evans (2019) gives a combined temperature uncertainty of ±0.8 °C (2σ) as a result of a salinity uncertainty of ±1 PSU (2σ) and a pH uncertainty of ±0.05 (2σ). This uncertainty increases to *c.*±1.5 °C (2σ) as a result of temperature calibration uncertainties.

It is also suggested that seawater Mg/Ca ($Mg/Ca_{seawater}$) variation due to changes in the rate of oceanic crust formation, dolomite precipitation and the Mg/Ca composition of terrigenous input may have some effect on long-term Mg/Ca records (Evans and

Müller, 2012). $Mg/Ca_{seawater}$ variation can be corrected for when calculating temperatures with Mg/Ca palaeothermometry by integrating an estimate of $Mg/Ca_{seawater}$ into calculations. Proxy-based studies (Lowenstein *et al.*, 2001; Horita *et al.*, 2002; Dickson, 2004; Coggon *et al.*, 2010) and modelling studies (Stanley and Hardie, 1998; Berner, 2004; Demicco *et al.*, 2005) have sought to produce records of $Mg/Ca_{seawater}$ variation through geological history. A *c.* 2.5 mol/mol increase in $Mg/Ca_{seawater}$ is indicated between the Oligocene and the Pliocene. However, $Mg/Ca_{seawater}$ records for the Miocene remain poorly constrained, resulting in some uncertainty for Mg/Ca palaeotemperatures for the Miocene.

No records are available for the pH or salinity in the eastern Mediterranean region during the Miocene; therefore, modern measurements of these variables are used in Mg/Ca palaeotemperature calculations presented in this study. The upper 150m of the modern eastern Mediterranean Sea has a pH of 8.21 and a salinity of 38.8 PSU (Techtmann *et al.*, 2015). The accuracy of temperature calculations made in this study could be improved in the future by the development of methods and future research to constrain pH, salinity and $Mg/Ca_{seawater}$ for the eastern Mediterranean region during the Miocene.

Analyses of *O. universa* in laboratory culture experiments have revealed that this species has Mg/Ca heterogeneity across its test (Eggins *et al.*, 2004). The discovery of this intratest Mg/Ca heterogeneity in *O. universa* and other species of planktic foraminifera led to concerns about their suitability for accurate Mg/Ca palaeothermometry (Eggins *et al.*, 2004; Sadekov *et al.*, 2008, 2009). However, this heterogeneity is thought to be a natural component of day/night test growth (Eggins *et al.*, 2004; Spero *et al.*, 2015). Laboratory culture studies have revealed that both day and night calcite growth exhibits a similar Mg incorporation response to temperature

change (Schmidt and Spero, 2011; Spero *et al.*, 2015). Mg/Ca palaeothermometry in this study is based on the analyses of multiple (25) dissolved whole tests per sample; therefore, the Mg/Ca ratios measured are representative of the average intratest composition of several tests. The calibrations used for calculating palaeotemperature from Mg/Ca ratios are also based on the measurement of an averaged intratest Mg/Ca composition from a suite of tests (Lea *et al.*, 1999; Anand *et al.*, 2003; Russell *et al.*, 2004; Schmidt and Spero, 2011; Gray and Evans, 2019). Therefore, the occurrence of intratest Mg/Ca heterogeneity should not be a concern for the use of *O. universa* for Mg/Ca palaeothermometry.

4.1.4 Combined $\delta^{18}O_{planktic}$ & Mg/Ca Palaeothermometry

The analysis of oxygen stable isotopes in this study was carried out at a significantly higher resolution than the trace element analyses. Therefore, the $\delta^{18}O_{planktic}$ palaeotemperature presented is able to track temperature changes at a higher resolution than the Mg/Ca record presented in this study. However, as discussed in Chapter 4.1.2, $\delta^{18}O_{planktic}$ palaeothermometry requires an estimation of $\delta^{18}O_{sw}$. In this study, $\delta^{18}O_{sw}$ is estimated by using Mg/Ca palaeotemperature in order to quantify the temperature component of $\delta^{18}O_{planktic}$ measurements, and therefore produce a $\delta^{18}O_{sw}$ estimate that is specific to the location and age of the sample. A $\delta^{18}O_{sw}$ estimate for samples which were not subject to trace element analysis (and thus do not have Mg/Ca derived palaeotemperatures) is produced by using a linear interpolation between the samples that were subjected to trace element analysis. This method of interpolation assumes a consistent rate of change in $\delta^{18}O_{sw}$ between measured samples. This does not take into account the fact that extreme Mg/Ca values might reflect variations that take place on a timescale that is smaller than the Mg/Ca sampling resolution. A rearranged version of the equation used to calculate

palaeotemperature from $\delta^{18}O_{planktic}$ measurements (Bemis *et al.*, 1998) is used in order to estimate $\delta^{18}O_{sw}$ using Mg/Ca derived palaeotemperatures (MgT), as shown below:

$$\delta^{18}O_{sw} = \frac{-MgT + a - b(\delta^{18}O_c)}{b} \qquad \textit{[Eq. 4.1.4.1]}$$

Estimates of $\delta^{18}O_{sw}$ using this equation have a unit of ‰ VDPB and, therefore, no conversion from ‰ VSMOW to ‰ VDPB is required.

4.1.5 Smoothing of data

In order to allow long-term trends in geochemical and temperature records to be identified, smoothed data are shown in figures (bold lines) together with measured values (thin lines with box markers). These data were smoothed using a nonparametric LOESS (locally estimated scatterplot smoothing) quadratic regression (Cleveland, 1979; Cleveland and Devlin, 1988) with a locally weighted function equivalent to 60 kyr.

4.2 Results

4.2.1 Oxygen stable isotope records

Figure 4.2.1.1 shows the $\delta^{18}O_{planktic}$ and $\delta^{18}O_{finefraction}$ records for the composite temporal record and allows for comparison between the two methods. Both records appear to show a generally similar trend for the Kottaphi Hill succession. Although the $\delta^{18}O_{planktic}$ record appears to have more variability than the $\delta^{18}O_{finefraction}$ record, the two records display peaks and troughs in approximate synchronicity. Prior to the start of the $\delta^{18}O_{planktic}$ record, the $\delta^{18}O_{finefraction}$ record shows a very gradual decrease in $\delta^{18}O$ (lighter $\delta^{18}O$ values).

The two records show a striking divergence at the splice point (the beginning of the Lapatza Hill succession) (Figure 4.2.1.1). While the $\delta^{18}O_{planktic}$ record for Lapatza Hill

continues at a similar $\delta^{18}O$ value to the Kottaphi Hill succession, the $\delta^{18}O_{finefraction}$ record exhibits a dramatic (*c.* 6.0 ‰ VDPB) offset between the two successions. The $\delta^{18}O_{finefraction}$ time series also records increased variability in $\delta^{18}O$ values for the Lapatza Hill succession than the Kottaphi Hill succession. The two records show discrete trends for the Lapatza Hill succession. However, both records do show the highest (heaviest) $\delta^{18}O$ values for the Lapatza Hill succession at *c.* 6 Ma.

Chapter 4.3.1 includes an examination of the potential causes of the divergence between the $\delta^{18}O_{planktic}$ and $\delta^{18}O_{finefraction}$ records and the apparent offset in $\delta^{18}O_{finefraction}$ between the two successions sampled. An offset in $\delta^{13}C_{finefraction}$ values at the splice point is also noted (Chapter 5.3.1). The offsets noted for fine fraction stable isotope records at the splice point between the two successions are related to the lithological differences between the two successions. Such lithological differences between the two successions, as well as the settings in which the successions were deposited and the relationship of each succession sampled to the underlying and overlying strata are discussed in Chapter 3.3.

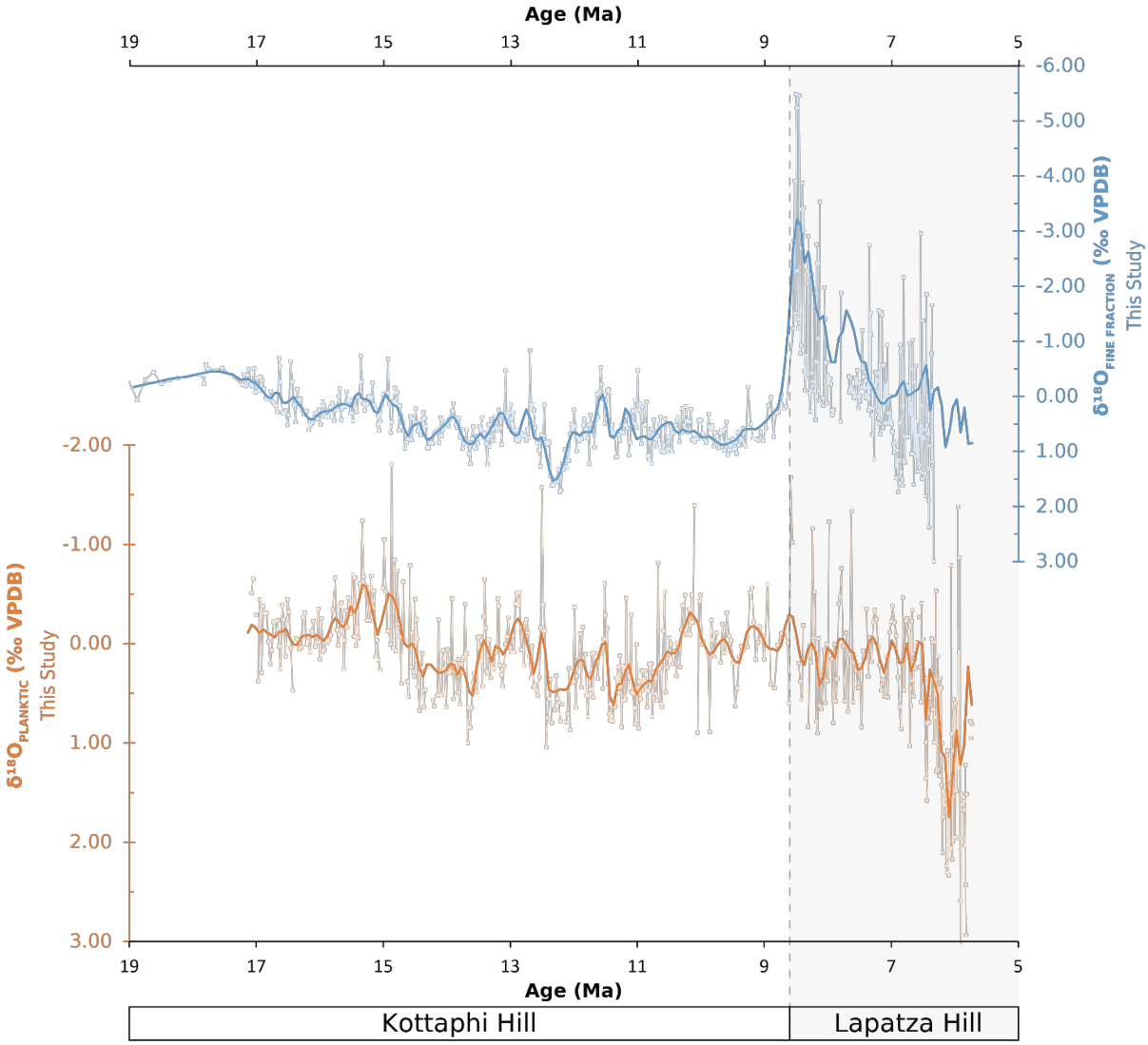


Figure 4.2.1.1 – Plot of $\delta^{18}O_{planktic}$ (orange) and $\delta^{18}O_{finefraction}$ (blue) versus age for the composite temporal record. Measurements are shown relative to VDPB. All measured data are shown with a thin line and box markers; bold lines show these $\delta^{18}O$ data smoothed by a locally weighted function over 60 kyr (see Chapter 4.1.5).

4.2.2 $\delta^{18}O_{planktic}$ Palaeothermometry

Figure 4.2.2.1 shows calculated palaeotemperatures based on the measurement of $\delta^{18}O$ for samples of planktic foraminifera from the *Praeorbulina-Orbulina* lineage. A maximum temperature of 27.4 °C is calculated for 14.86 Ma (Langhian). The lowest temperature calculated is 4.69 °C at 5.90 Ma (Messinian). These temperature calculations are discussed and compared to other methods in Chapter 4.3.2.

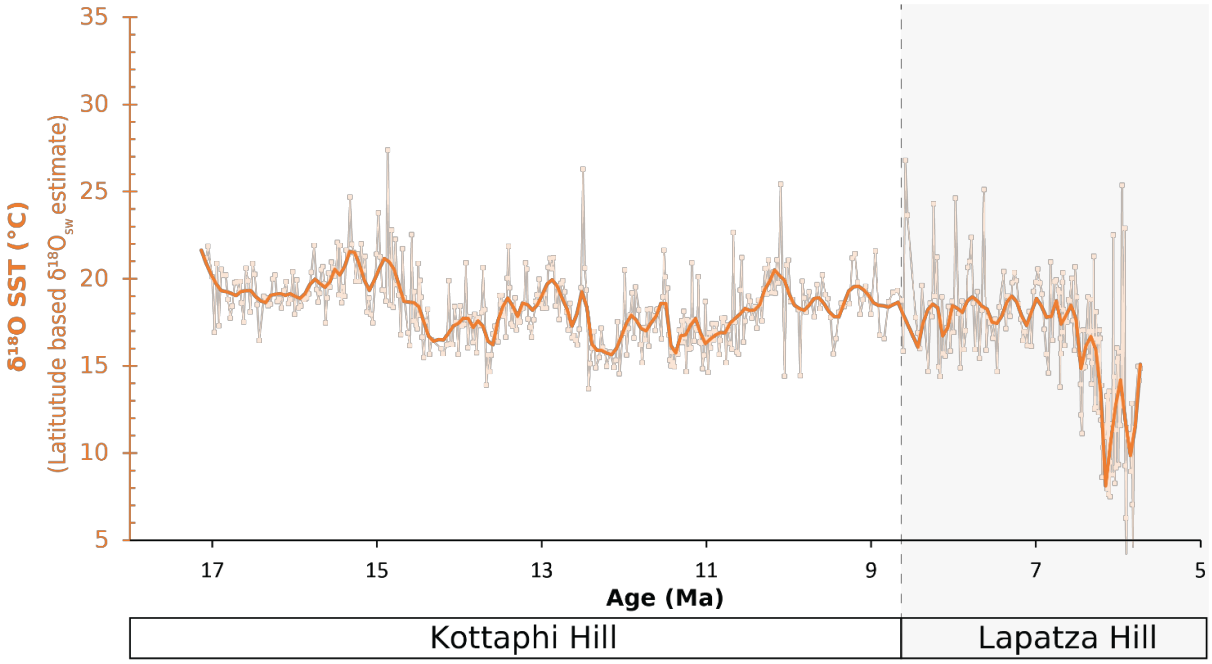


Figure 4.2.2.1 - Plot of temperature versus age for the composite temporal record. Temperatures are calculated from $\delta^{18}O_{planktic}$ measurements using the calibration calculation of Bemis *et al*. (1999) for *O. universa* in mean light intensity conditions. This calculation used a latitude-based $\delta^{18}O_{sw}$ estimate from Zachos *et al*. (1994). Both smoothed and calculated data are shown, as in Figure 4.2.2.1 (see Chapter 4.1.5).

4.2.3 Mg/Ca Palaeothermometry

Figure 4.2.3.1 shows measured Mg/Ca ratios and calculated palaeotemperatures based on the Mg/Ca data for samples of planktic foraminifera from the *Praeorbulina-Orbulina* lineage. A maximum temperature of 27.55 °C is calculated for 12.98 Ma. This corresponds to the maximum measured Mg/Ca of 13.28 mmol/mol. The lowest temperature calculated is 14.59 °C at 5.90 Ma, corresponding to the minimum measure Mg/Ca of 5.02 mmol/mol. These temperature calculations are discussed together with other methods in Chapter 4.3.2.

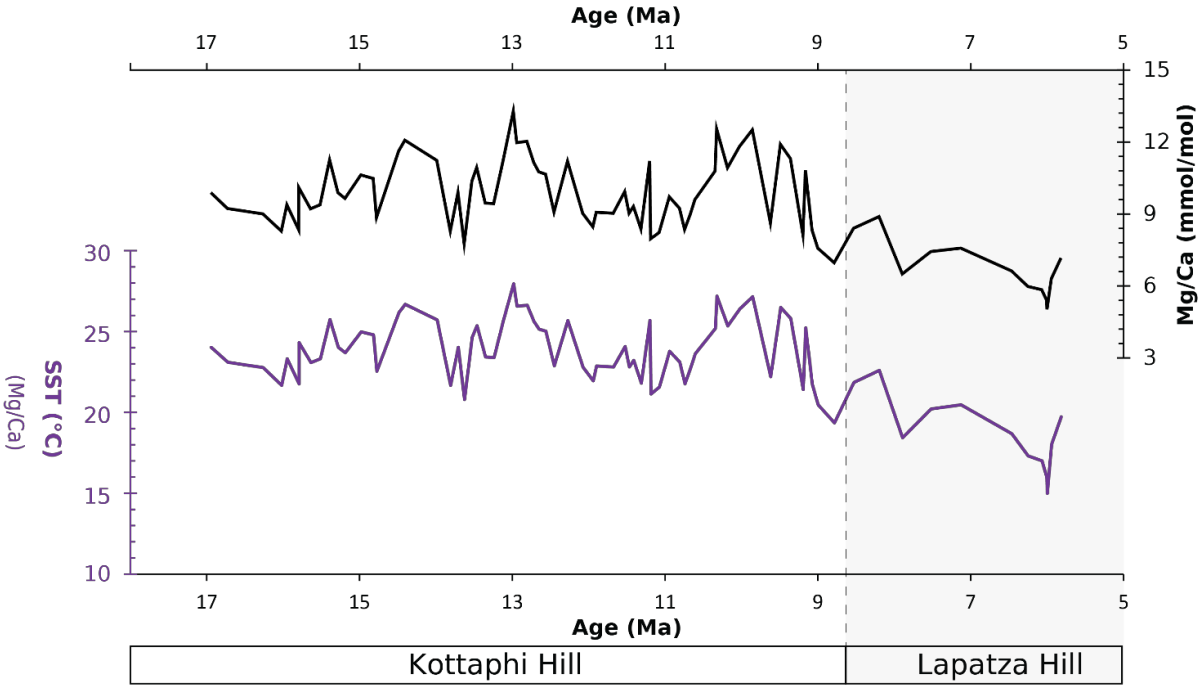


Figure 4.2.3.1 - Plot of temperature versus age for the composite temporal record. Temperatures are calculated from Mg/Ca measurements using the calibration calculation of Gray and Evans (2019) for *O. universa* (purple). Measured Mg/Ca ratios are also shown in mmol/mol (black).

4.2.4 Combined $\delta^{18}O_{planktic}$ & Mg/Ca Palaeothermometry

In order to adjust the $\delta^{18}O_{planktic}$ temperature calculations for the effects of local changes in $\delta^{18}O_{sw}$ first the approximate local $\delta^{18}O_{sw}$ must be calculated. The local evolution of $\delta^{18}O_{sw}$ calculated using the $\delta^{18}O_{planktic}$ and Mg/Ca data produced in this study is presented in Figure 4.2.4.1. To be compared to other published $\delta^{18}O_{sw}$ data, it may be necessary to convert these data to measurements relative to VSMOW (Brand *et al.*, 2014) (See Appendix 8.10 for $\delta^{18}O_{sw}$ data relative to VSMOW). Stable isotope measurements presented in this thesis were made relative to VPDB; therefore, all stable isotope data in this study are presented relative to VPDB. The calculated $\delta^{18}O_{sw}$ (Figure 4.2.4.1) has a maximum value of 3.52 ‰ (VDPB) and a minimum of 0.29 ‰ (VDPB). The mean of the calculated $\delta^{18}O_{sw}$ values is 1.45 ‰ (VDPB). Throughout the record, some cyclicity on a scale of *c.* 100 Myr is observed; however, the overall trends can be observed from the smoothed record.

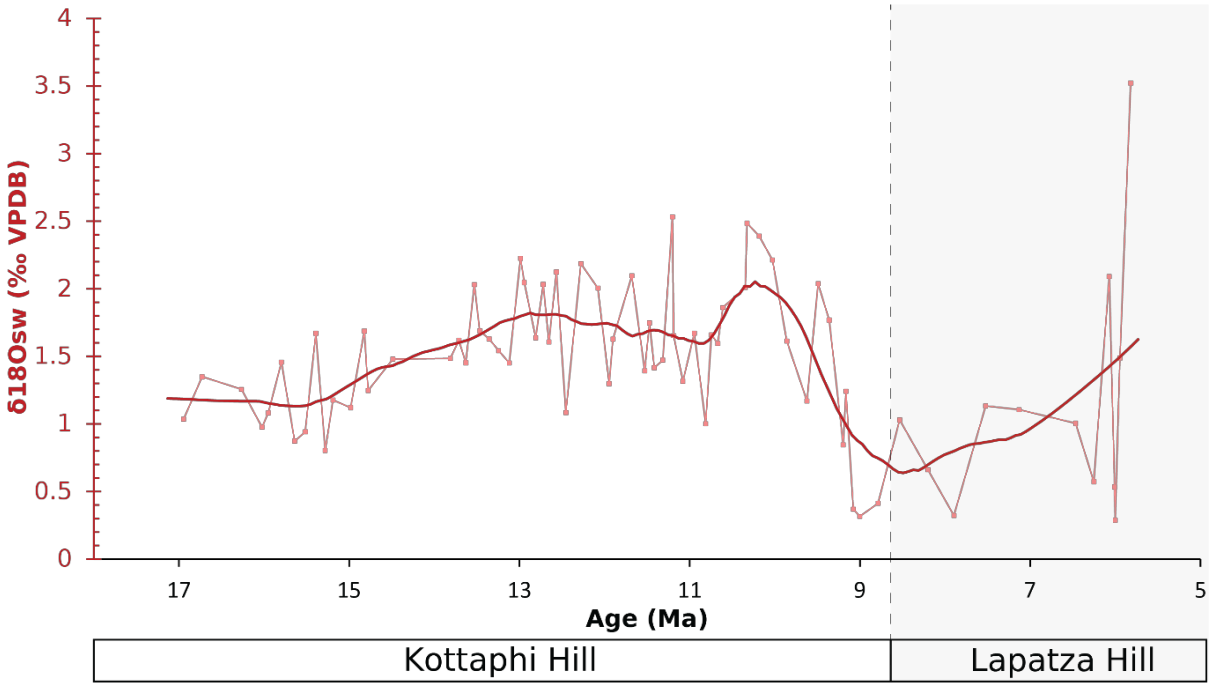


Figure 4.2.4.1 – Plot of estimated local $\delta^{18}O_{sw}$ versus age for the composite temporal record. $\delta^{18}O_{sw}$ is calculated from the Mg/Ca and $\delta^{18}O_{planktic}$ measurements made in this study. Both smoothed and calculated data are shown, as in Figure 4.2.2.1 (see Chapter 4.1.5). Note; these data are shown relative to VPDB, as used in temperature calculations and measurements of foraminiferal calcite in this study. Other published $\delta^{18}O_{sw}$ data may be shown relative to VSMOW.

The results of the $\delta^{18}O_{planktic}$ palaeotemperature calculations using the local $\delta^{18}O_{sw}$ calculations are shown in Figure 4.2.4.2. The maximum temperature calculated using this adjusted calibration is 34.24 °C at 10.09 Ma (Tortonian). A minimum temperature of 9.14 °C was calculated at 5.99 Ma (Messinian).

Although the magnitude of change and the absolute temperature values differ in these three temperature calculations, they all show the same general trend of temperature change throughout the sampled successions. The general trend of temperature change can be divided into several time intervals of general cooling, warming, or stable temperatures. From the start of the record (*c.* 17.08 Ma) to *c.* 13 Ma, there is no clear overall increase or decrease in temperature trend (Figure 4.2.4.2). This interval is punctuated by warm periods (*c.* 3-5°C warming) at *c.* 15.4 Ma (Langhian), *c.* 14.9 Ma

(Langhian) and *c.* 13 Ma (Serravallian). From *c.* 13 Ma (Serravallian) to *c.* 6.6 Ma (Messinian), a gradual cooling trend (*c.* 3 °C) is apparent. This cooling trend is interrupted by an extremely warm period at *c.* 10.2 Ma (Tortonian). Cooling continued, but appears to have happened at a faster rate (*c.* 4°C) from *c.* 6.6 Ma to *c.* 6 Ma. From *c.* 6 Ma until the end of the record (*c.* 5.73 Ma), temperatures appear to increase rapidly by *c.* 8°C.

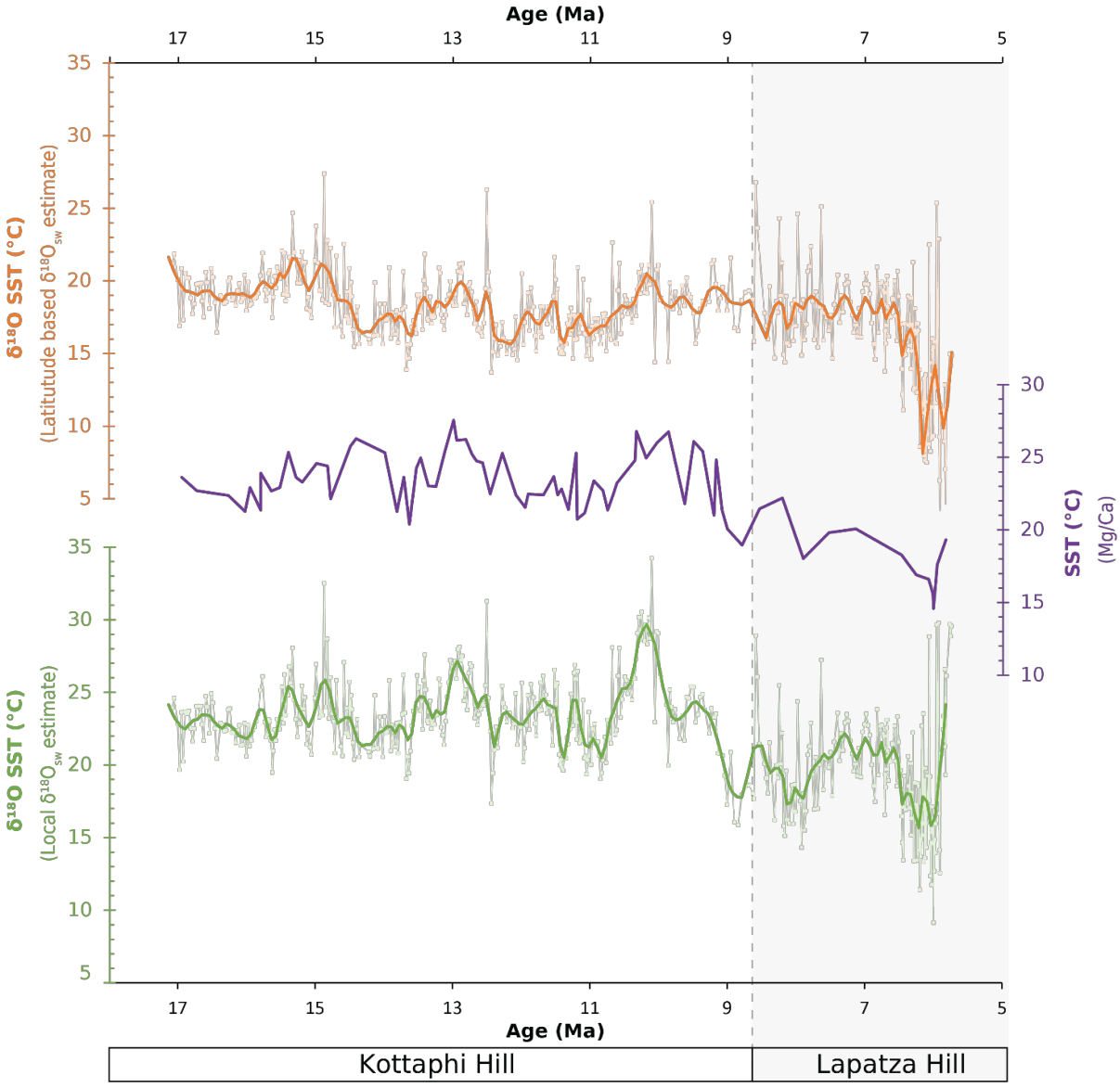


Figure 4.2.4.2 - Plot of temperature versus age for the composite temporal record. Showing temperatures calculated from $\delta^{18}O_{planktic}$ using the local estimation of $\delta^{18}O_{sw}$ (green), Mg/Ca (purple) (Figure 4.2.3.1) and $\delta^{18}O_{planktic}$ using a latitude-based $\delta^{18}O_{sw}$ estimation (orange) (Figure 4.2.2.1). Both smoothed and calculated data are shown, as in Figure 4.2.2.1 (see Chapter 4.1.5).

4.3 Discussion

4.3.1 Oxygen stable isotope records

The $\delta^{18}O_{finefraction}$ record (Figure 4.2.1.1) shows a dramatic offset towards much lighter $\delta^{18}O$ values at the splice point between the Kottaphi Hill succession and the Lapatza Hill succession. Following this offset, the $\delta^{18}O_{finefraction}$ record continues to show a different trend to the $\delta^{18}O_{planktic}$ record for the same sample set.

As discussed in Chapter 2.5, interpretations based on $\delta^{18}O_{finefraction}$ measurements cannot be as well constrained as those based on $\delta^{18}O_{planktic}$ measurements, because the exact composition of these fine fraction bulk samples is unknown. Lithological observations and geochemical data indicate that the samples from the Lapatza Hill succession have a larger terrigenous component compared to the samples from the Kottaphi Hill succession (Chapter 3.3) It is, therefore, very likely that the isotopic signal of the terrigenous component is measured together with the signal of the biogenic carbonate when analysing fine fraction bulk samples from the Lapatza Hill succession. In contrast, for the Kottaphi Hill succession, the $\delta^{18}O_{finefraction}$ record is mainly influenced by the biogenic carbonate material; as evidenced by the similarity between the $\delta^{18}O_{finefraction}$ record and the $\delta^{18}O_{planktic}$ record (Figure 4.2.1.1). Lithological differences between the two successions, as well as the settings in which the successions were deposited and the relationship of each succession sampled to the underlying and overlying strata are discussed in Chapter 3.3.

The distinct offset towards much lighter $\delta^{18}O$ values at the splice point is followed by a gradual trend towards heavier values. This trend indicates some compositional change in the fine fraction bulk samples moving up the Lapatza Hill succession. Further chemical analysis of bulk fine fraction samples at a high resolution would be necessary to infer the possible cause of this apparent trend in the $\delta^{18}O_{finefraction}$ record.

This, therefore, means that the $\delta^{18}O_{finefraction}$ record for Lapatza Hill is not a suitable dataset for interpreting climatic changes. The $\delta^{18}O_{planktic}$ record for Lapatza Hill is relatively complete and, therefore, there is little need for any interpretation based on the $\delta^{18}O_{finefraction}$ record. However, $\delta^{18}O_{finefraction}$ measurements of samples from Kottaphi Hill appear to be controlled by the stable isotopic composition of biogenic calcite. Therefore, the Kottaphi Hill $\delta^{18}O_{finefraction}$ record can be used for some interpretation of temperature changes. This is especially useful for the interval from *c.* 19 Ma to *c.* 17 Ma where planktic foraminifera are absent or poorly preserved.

The $\delta^{18}O_{finefraction}$ record (Figure 4.2.1.1) shows a *c.* 0.3 ‰ decrease for the interval from *c.* 19 Ma to *c.* 17 Ma. Later in the record a *c.* 0.3 ‰ decrease in $\delta^{18}O_{finefraction}$ represents a *c.* 2°C increase in temperature, as calculated by the combined Mg/Ca and $\delta^{18}O_{planktic}$ method (Chapter 4.2.4). An offset in $\delta^{13}C_{finefraction}$ values at the splice point is also noted (Chapter 5.3.1)

4.3.2 Palaeotemperature records for the composite Miocene succession

Three palaeotemperature records are presented in this thesis (Figure 4.2.4.2), two of which rely on single proxies ($\delta^{18}O$ and Mg/Ca) and one of which combines these two proxies. The ranges of temperatures calculated together with the mean temperature values are shown in Table 4.3.2.1.

Temperature Calibration Method	Maximum Temperature (°C)	Minimum Temperature (°C)	Mean Temperature (°C)	Temperature Range (°C)
$\delta18O_{planktic}$ (Latitude estimate $\delta18O_{sw}$)	27.83	4.69	18.03	23.14
Mg/Ca	27.55	14.59	22.69	12.96
$\delta18O_{planktic}$ (Local estimate $\delta18O_{sw}$)	34.24	9.14	22.04	25.10

Table 4.3.2.1 – Table showing maximum, minimum mean and range of temperatures calculated using different calibration methods in this study.

Maximum temperatures for both single proxy calculations are close (0.27 °C difference). The $\delta 18O_{planktic}$ only method gives a lower minimum temperature (9.90 °C difference) than the Mg/Ca calculation. The mean of the Mg/Ca temperature calculations is higher (4.65 °C difference) than the mean of the $\delta 18O_{planktic}$ only temperature calculations. The $\delta 18O_{planktic}$ only temperatures have a much larger range (10.18°C difference) than the Mg/Ca temperature calculations. The difference in resolution of the analysed samples probably has some impact on these temperature differences. The higher resolution $\delta 18O_{planktic}$ record represents more individual time intervals and therefore has a higher probability of recording extreme temperature events, assuming that these events were short-lived.

The multi-proxy method ($\delta 18O_{planktic}$ using Mg/Ca-based $\delta 18O_{sw}$ estimate) records a higher maximum temperature than either of the two other methods. The mean and minimum values for this combined proxy method lie between the two single proxy methods, but are closer to the Mg/Ca values. This is expected as the Mg/Ca method is used as a true temperature value in this calibration and $\delta 18O_{planktic}$ temperature estimates are adjusted to align with Mg/Ca temperature estimates. The temperature range provided by this combined method is the largest of the three methods; this shows that this combined method records the extreme temperature intervals recorded by the $\delta 18O_{planktic}$ method, which are not recorded by the Mg/Ca method.

The use of this combined method seeks to avoid uncertainties in the $\delta 18O_{planktic}$ -method which are due to the unknown $\delta 18O_{sw}$ values. However, this method is not free of uncertainty. Salinity is a control of Mg/Ca in foraminiferal calcite (Chapter 4.1.3) and is poorly constrained for these Mg/Ca palaeotemperature calculations. As discussed in Chapter 1.2.3, the Miocene is known to be a time of extensive change in ocean circulation for the E Mediterranean region and, therefore, changes in salinity

during this interval are possible. However, the effect of salinity as a control on the Mg/Ca proxy (Gray and Evans, 2019) is less than for $\delta^{18}O$ palaeothermometry (Groeneveld *et al.*, 2008; Pearson, 2012); therefore, Mg/Ca derived palaeotemperature calculations are generally considered less dependent on salinity and more accurate than $\delta^{18}O$ palaeothermometry. Changes in salinity during the Miocene are further discussed in Chapter 5.3.3. The multi-proxy temperature record which combines Mg/Ca and $\delta^{18}O$ measurements to provide a palaeotemperature record is considered to have the best combination of accuracy and resolution and is, therefore, used in this thesis for interpretations of the climate history of the eastern Mediterranean region during the Miocene.

4.3.3 Regional to Global Comparisons

One of the main motives for the production of this Miocene palaeotemperature record for Cyprus was the potential to compare and contrast the climatic changes inferred for Cyprus with global to regional scale climatic changes, as identified by previous research.

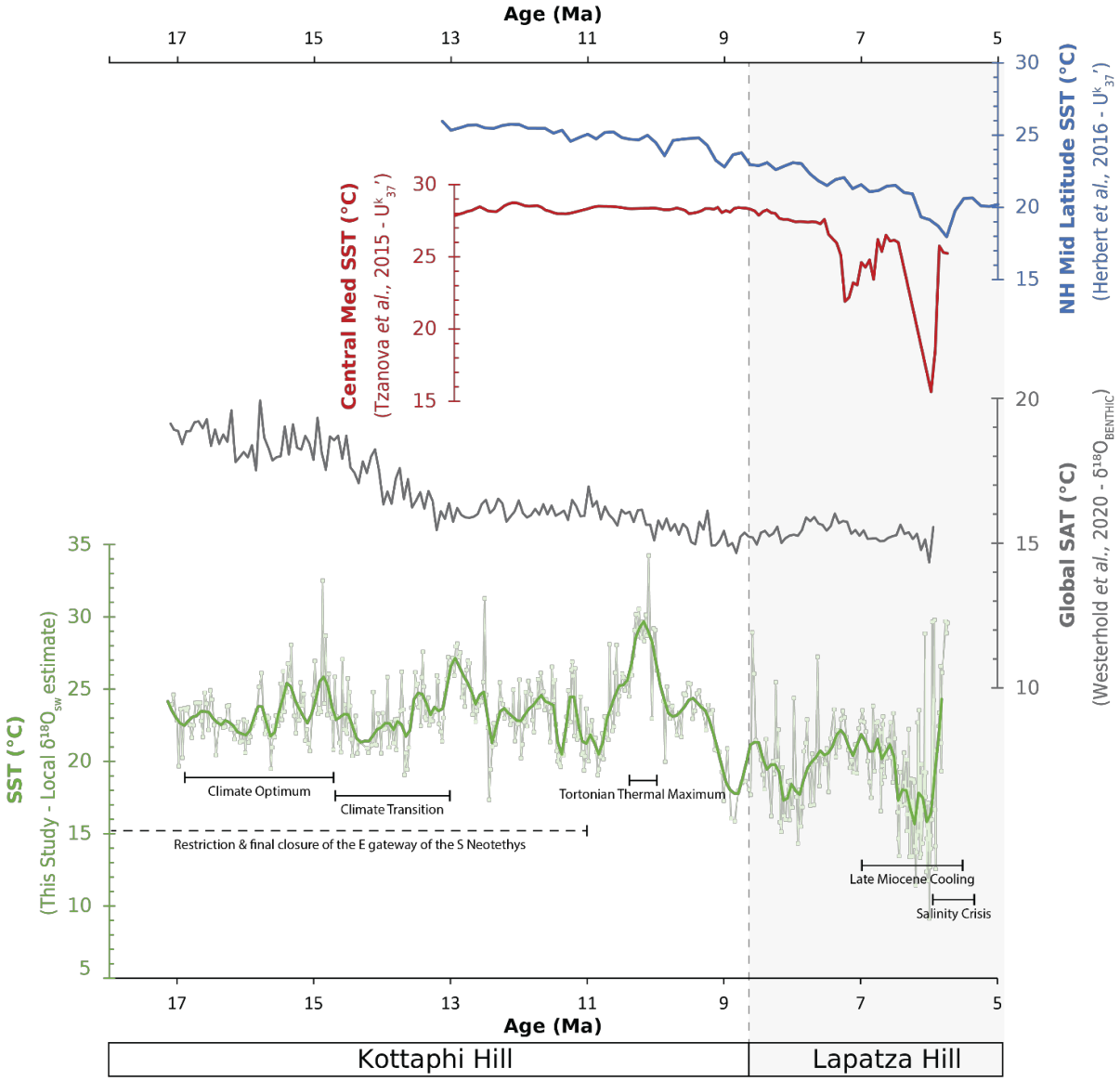


Figure 4.3.3.1 - Plot of temperature versus age for the composite temporal record. Showing temperatures calculated from $\delta^{18}O_{planktic}$ using the local estimation of $\delta^{18}O_{sw}$ (green) (Figure 4.2.4.2). Both smoothed and calculated data are shown, as in Figure 4.2.2.1 (see Chapter 4.1.5). The Global Surface Air Temperature (SAT) record (calculated from $\delta^{18}O_{benthic}$ data) of Westerhold *et al.* (2020) (grey), together with the U^{K}_{37}' based SST (Sea Surface Temperature) records of Tzanova *et al.* (2015) (central Mediterranean - red) and Herbert *et al.* (2016) (Northern Hemisphere compilation stack - blue) are shown for comparison. The timing of several global to regional scale climatic and ocean circulation changes are also annotated: (1) The Miocene Climate Optimum (Zachos *et al.*, 2008; Holbourn *et al.*, 2015; Westerhold *et al.*, 2020); (2) Restriction (from *c.* 20 Ma) and closure of the eastern gateway of the Southern Neotethys (see Chapter 1.2.3) (Hüsing *et al.*, 2009; Bialik *et al.*, 2019); (3) The Miocene Climate Transition (Holbourn *et al.*, 2005; Westerhold *et al.*, 2020); (4) The Tortonian Thermal Maximum (Westerhold *et al.*, 2020); (5) Late Miocene Cooling (Herbert *et al.*, 2016); (6) The Messinian Salinity Crisis (Krijgsman *et al.*, 1999a).

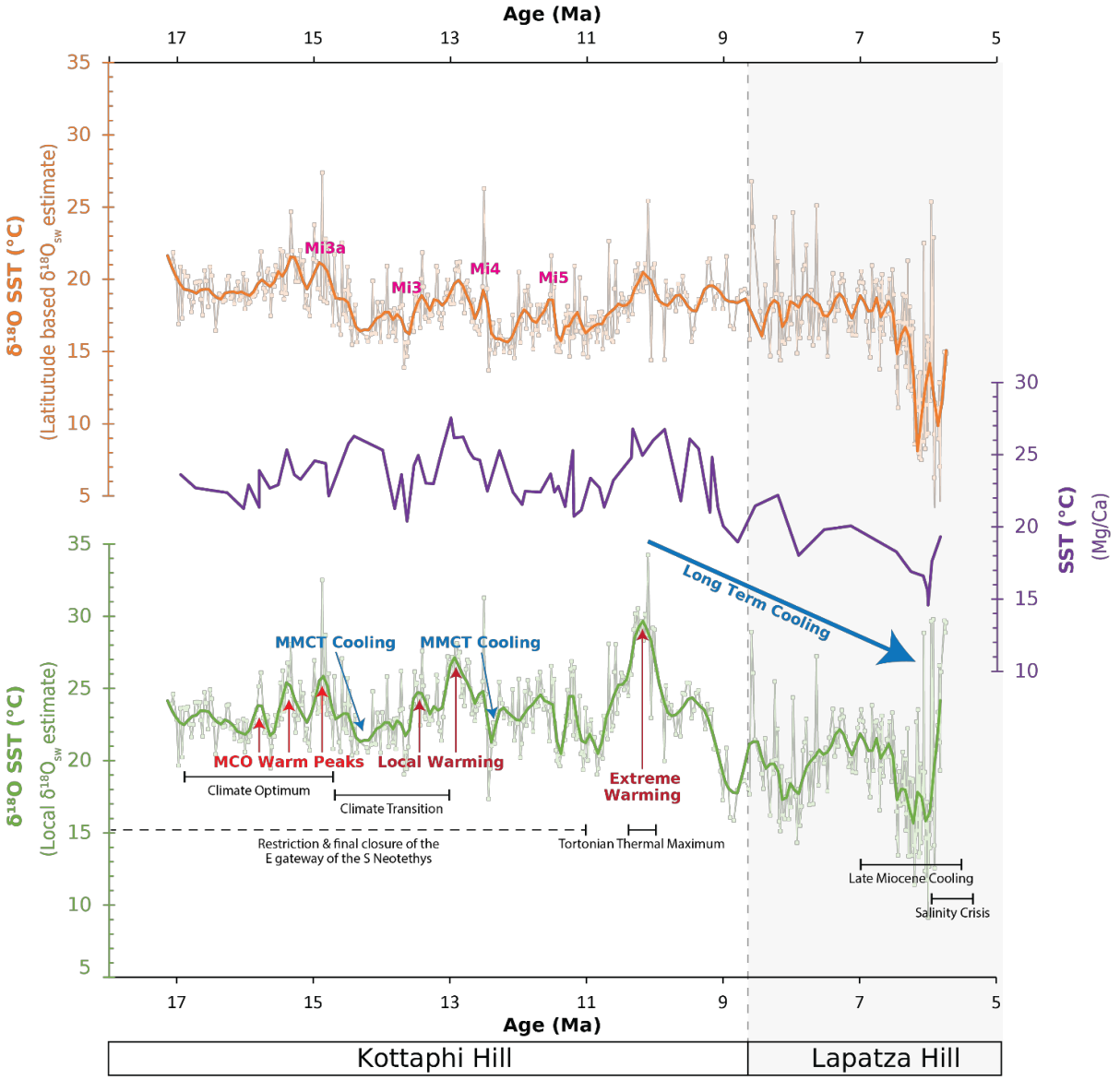


Figure 4.3.3.2 - Plot of temperature versus age for the composite temporal record. Showing temperatures calculated from $\delta^{18}O_{planktic}$ using the local estimation of $\delta^{18}O_{sw}$ (green), Mg/Ca (purple) (Figure 4.2.3.1) and $\delta^{18}O_{planktic}$ using a latitude-based $\delta^{18}O_{sw}$ estimation (orange) (Figure 4.2.2.1). Both smoothed and calculated data are shown, as in Figure 4.2.2.1 (see Chapter 4.1.5). The events and trends discussed in this chapter are annotated. Miocene oxygen isotope events of Miller *et al*. (1999) and Miller *et al.* (2020) are annotated in pink. The timing of several global to regional scale climatic and ocean circulation changes are also annotated as in Figure 4.3.3.1.

A trend towards lighter $\delta^{18}O_{finefraction}$ values indicates some warming in the lowermost part of the Kottaphi Hill succession between 18.96 Ma and 17.08 Ma (Figure 4.2.1.1) (as discussed in 4.3.1). The new palaeotemperature record begins at 17.08 Ma and allows for more direct comparison with records from elsewhere. The apparent warming

from 18.96 Ma and 17.08 Ma is followed by a warm period from 17.08 Ma to 14.78 Ma (*c.* 23.35°C average) (Figure 4.3.3.2). Palaeotemperature reconstructions for surface air temperature (SAT) (Westerhold *et al.*, 2020) also record high temperatures during this interval; this warm interval can be correlated to the Miocene Climate Optimum (See Chapter 1.2.4). The Global SAT record shown in Figure 4.3.3.1 is derived from $\delta^{18}O_{benthic}$ records and, therefore, shows less variability than records based on the measurement of planktic organisms.

An average SST of 23.35°C for the MCO interval is *c.* 3.1°C warmer than modern average temperatures for the region (Techtmann *et al.*, 2015). Global temperatures during the MCO are reported to have been 4-8°C warmer than modern-day temperatures (Goldner *et al.*, 2014). $U^{K}_{37}{}'$ & TEX_{86} data (see Chapter 1.1) indicate that the North Atlantic was 10-15ºC warmer than in modern times between 17 Ma and 14.5 Ma (Super *et al.*, 2020). Therefore, average temperatures from the Cyprus record are lower than expected for this interval. However, the highest temperature calculated during this interval is 32.5°C at 14.87 Ma; this is 12.3°C warmer than the modern day (Techtmann *et al.*, 2015). A warm interval (25.9°C) at *c.* 14.85 Ma is present in a TEX_{86} palaeotemperature record from the North Atlantic (Super *et al.*, 2020). Therefore, it appears that although temperatures were high during the MCO in the eastern Mediterranean region, the average temperatures may not have been as high as has been suggested for other regions. Eastern Mediterranean temperatures did, however, reach extreme peaks during this interval (Figure 4.3.3.2), which correspond to high temperatures recorded elsewhere (Figure 4.3.3.1).

In Cyprus, intervals of extremely high temperatures punctuated this warm period (Figure 4.3.3.1 & Figure 4.3.3.2). The three most prominent of these warm periods took place at *c.* 15.7 Ma, *c.* 15.3 Ma and *c.* 14.9 Ma, suggesting an approximate 400

kyr cyclicity. Warm peaks on the *c*. 400-kyr eccentricity cycle are also present in palaeotemperature records from the Pacific Ocean. These intervals are assumed to be occurrences of an ice-free Earth during the MCO, and may have been the most recent ice-free periods in Earth's history (Miller *et al.*, 2005, 2020).

At 14.78 Ma, a dramatic fall in temperature is recorded in the Cyprus palaeotemperature record (Figure 4.3.3.3). This *c*. 4.5°C SST fall between 14.78 Ma and 14.31 Ma corresponds to the first step of the Middle Miocene Climate Transition (MMCT) (see Chapter 1.2.4). This cooling step is correlated with a Mi3a global $\delta^{18}O$ event (Miller *et al.*, 1991b, 2020). This cooling was followed by a *c.* 1°C increase to more stable temperatures until *c*. 13.7 Ma when another dramatic cooling event took place. The temperature of 19.06°C is colder than any calculated temperatures for older samples in the succession. Cooling at *c.* 13.7 Ma corresponds to the second step of the MMCT and the Mi3 $\delta^{18}O$ event (Miller *et al.*, 1991b, 2020). The calculated temperatures then abruptly rose to a high of 27.58°C at 13.4 Ma (Figure 4.3.3.3). This rise was followed by a steady fall to 21.38°C at 13.1 Ma, which, in turn, was followed by a rise to 28.14°C at 12.8 Ma. Open-ocean temperature records show slight warming and relatively stable temperature following the first two cooling steps of the MMCT (Zachos *et al.*, 1994; Miller *et al.*, 2020; Westerhold *et al.*, 2020) (Figure 4.3.3.1), rather than warming at the magnitude calculated in the Cyprus record. The distinct warming between 13.7 Ma and 12.8 Ma (Figure 4.3.3.1) could indicate that during this interval, the E Mediterranean region was decoupled from global climate changes. As discussed in Chapter 1.2.3 the oceanic gateway between the Southern Neotethys and the Indian Ocean was dramatically restricted after *c.* 20 Ma. Isolation from the open ocean to the east might explain why the palaeotemperature record from the eastern Mediterranean does not show the same trend as open ocean records. Geochemical data (neodymium

isotopes) indicate that the final closure of the seaway took place at *c.* 13.8 Ma (Bialik *et al.*, 2019), however geological data indicates that connection through this ocean gateway lasted until *c.* 11 Ma (Hüsing *et al.*, 2009). This warming trend is recorded in both the independent $\delta^{18}O$ and Mg/Ca palaeotemperature records as well as the combined method record. It should be noted, however, that the highest magnitude warming is recorded by the Mg/Ca method.

A rapid cooling trend is recorded between 12.8 Ma and 12.42 Ma (Figure 4.3.3.3). This cooling was coeval with the final step of the MMCT and the Mi4 $\delta^{18}O$ event (Miller *et al.*, 1991b, 2020). This cooling marked an apparent realignment of eastern Mediterranean and global climate changes. At 12.43 Ma, a temperature of 17.35°C is the coldest temperature recorded in the Early to Middle Miocene part of the record.

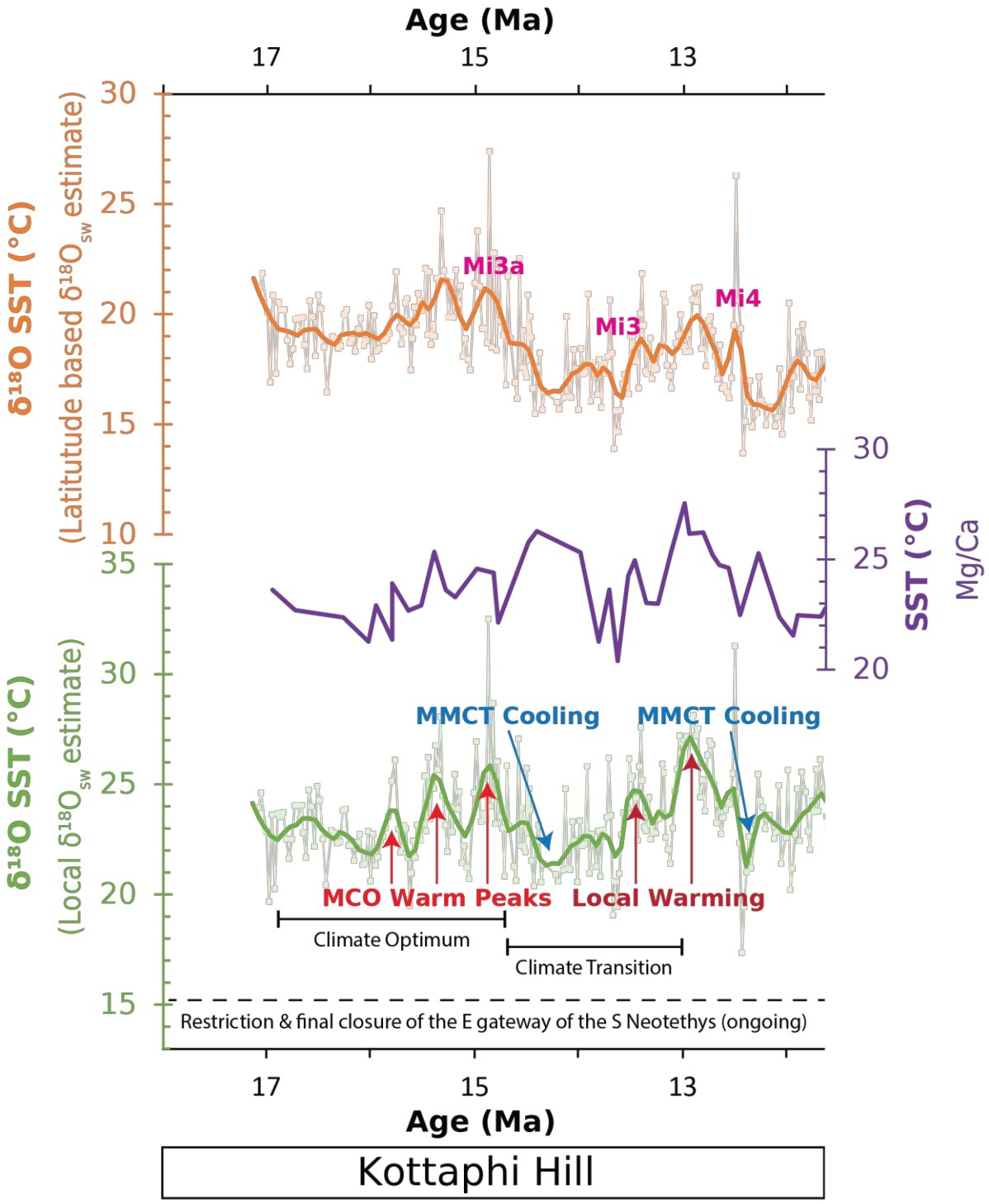


Figure 4.3.3.3 – Plot of temperature versus age for the Early to Middle Miocene of the composite temporal record with the events and trends discussed annotated. This figure is an adaptation of Figure 4.3.3.2 and has been edited to focus on the Early to Middle Miocene time.

Following the cooling event between 12.8 Ma and 12.42 Ma, temperatures rebound by *c.* 2°C and remain relatively stable until *c.* 11.2 Ma. This period is punctuated by a

cold period at *c.* 12 Ma, followed by a pronounced cold excursion at 11.4 Ma, which corresponds to the Mi5 $\delta^{18}O$ event (Miller *et al.*, 1991b) (Figure 4.3.3.4).

After *c.* 11.2 Ma, another dramatic cooling event is recorded, culminating in low temperatures of 19.05°C at 10.85 Ma (Figure 4.3.3.4). This cooling event was, in turn, followed by a dramatic warming event at *c.* 10.8 Ma. A coeval warming event preceded by fast cooling is noted in a $\delta^{18}O_{benthic}$ record from the Western Pacific Ocean; this corresponds to peak insolation during eccentricity maxima (100 and 400 kyr) (Holbourn *et al.*, 2013). The warming event recorded in the Western Pacific Ocean was transient and ended after <100kyr. This transient warming event is known as the Tortonian Thermal Maximum and is also reported in global temperature compilations (Westerhold *et al.*, 2020). However, the coeval warming event recorded in the eastern Mediterranean continued until *c.* 10.2 Ma, with a peak temperature of 34.24°C (Figure 4.3.3.4). Both this warming event and the prior cooling event appear to have taken place at a greater magnitude in the eastern Mediterranean than is recorded in global records, which, during this interval, are mostly based on deep-sea cores from the Pacific Ocean (Westerhold *et al.*, 2020) (Figure 4.3.3.1). An approximately coeval interval of warming between *c.* 11 Ma and *c.* 10 Ma is noted in Mg/Ca palaeotemperature records from the Equatorial Atlantic Ocean (Lear *et al.*, 2003). This interval of *c.* 3°C warming for bottom water temperatures is not recorded in the Pacific Ocean (Lear *et al.*, 2003). The palaeotemperature record presented in this study therefore suggests that by this time period, temperature changes in the Southern Neotethys reflect those seen in the Atlantic Ocean rather than the Pacific Ocean. This is consistent with limited connectivity between the Southern Neotethys and the Indian Ocean to the east at this time.

This time interval of discrepancy between Atlantic Ocean and Pacific Ocean temperatures is interpreted to be related to the formation of North Atlantic Deep Water (NADW) during the Serravallian (Lear *et al.*, 2003). The formation of proto-NADW is interpreted to have taken place at *c.* 12 Ma, resulting in cooling in the Atlantic Ocean until *c.* 11 Ma when the flow of proto-NADW ceased and the Atlantic Ocean warmed to temperatures similar to those recorded in the Pacific Ocean (Lear *et al.*, 2003). Temperatures in the eastern Mediterranean region followed the pattern of those recorded in the Atlantic Ocean. A coeval period of anomalously high precipitation (rainfall) is interpreted from the ecophysiological study of samples across central and eastern Europe; this has been related to the constriction of the Central American Seaway, which affected the northward heat transport, resulting in an enhanced hydrological cycle in Europe (Böhme *et al.*, 2008).

Analyses of deep-sea cores revealed that the North Atlantic SST gradient collapsed after the beginning of the MMCT (*c.* 14.8 Ma) and did not recover until *c.* 7 Ma. Changes in ocean circulation patterns following the MMCT are suggested to be the cause of this rearrangement of the SST gradient between the middle and high-latitude North Atlantic (Super *et al.*, 2020). It is likely that the apparent decoupling between global and regional-local SSTs in the E Mediterranean was also related to changes in ocean circulation patterns. These findings emphasise that changes in ocean circulation patterns were a fundamental control on SSTs during the period after the MMCT. During this interval, temperature discrepancies are recorded between the Atlantic and Pacific Oceans and the collapse of latitude-related SST gradients is recorded in the North Atlantic (Lear *et al.*, 2003; Super *et al.*, 2020). It is, therefore, apparent that this was a time of extensive variation and disequilibrium both between and within the two major ocean basins. Therefore, ‘global’ temperature records are not

likely to reflect temperature changes seen across all locations during this interval and could be biased towards the sites of sample selection used for the global compilation records.

The extreme warming, which culminated at *c.* 10.2 Ma, was followed by two distinct steps of rapid cooling (Figure 4.3.3.4). This cooling is concurrent with stepwise cooling reported from the Western Pacific at *c.* 9.9 Ma and *c.* 9 Ma, which has been related to Antarctic glacial expansion (Holbourn *et al.*, 2013). This stepped cooling appears to mark the beginning of a general cooling trend between *c.* 10 Ma and *c.* 6 Ma, which was punctuated by a phase of intense cooling at *c.* 8 Ma and culminated in extreme cooling between *c.* 7 Ma and *c.* 6 Ma.

Two temperature peaks are noted at *c.* 8.5 Ma and *c.* 7.3 Ma (Figure 4.3.3.4); the 1.2 Myr spacing of these two peaks is consistent with coeval sea-level fluctuations which were apparently controlled by the 1.2 Myr obliquity cycle (Miller *et al.*, 2005, 2020; De Vleeschouwer *et al.*, 2017).

A compilation (stacked) $U^{K}_{37'}$ palaeotemperature record for several Northern Hemisphere mid-latitude (30°–50° N) sites also records a long-term cooling trend between *c.* 10 Ma and *c.* 6 Ma, which has been related to the acceleration of Antarctic glaciation (Figure 4.3.3.1) (Herbert *et al.*, 2022). These records show cooling throughout the Late Miocene with an intense interval of cooling from *c.* 7 Ma and *c.* 6 Ma, termed 'Late Miocene Cooling' (LMC) (Herbert *et al.*, 2016). The LMC is recognised in $U^{K}_{37'}$ palaeotemperature records for high, mid and tropical latitudes in both hemispheres for both the Atlantic and Pacific oceans (Herbert *et al.*, 2016; Tanner *et al.*, 2020). A lack of continental ice has been suggested as a reason for the absence of the LMC in benthic records (Herbert *et al.*, 2022). Up to 14°C of cooling is indicated

during this interval, in this study; this is a larger temperature change than is recorded in palaeotemperature records for the Northern Hemisphere mid-latitude compilation (*c.* 4.5) or the Northern Hemisphere high latitude compilation, where the largest temperature fall (*c.* 5.5°C) is recorded (Herbert *et al.*, 2016) (Figure 4.3.3.1).

A *c.* 11°C temperature drop associated with the LMC is reported from a coeval sediment sequence in the central Mediterranean (Tzanova *et al.*, 2015) (Figure 4.3.3.1). It is, therefore, apparent that LMC-associated cooling took place at a high intensity across the Southern Neotethys. However, the long-term Late Miocene cooling trend shown in the Cyprus composite record and the Northern Hemisphere mid-latitude $U^{K}_{37'}$ palaeotemperature record (Herbert *et al.*, 2016) are not present in the central Mediterranean $U^{K}_{37'}$ palaeotemperature record (Tzanova *et al.*, 2015). The temperatures calculated following the Tortonian Thermal Maximum in the Cyprus composite temporal record are lower than those recorded for a coeval succession in the central Mediterranean, where temperatures apparently remained high until *c.* 7.5 Ma (Tzanova *et al.*, 2015). It appears that Late Miocene temperature changes in the eastern Mediterranean region were closely related to global temperature changes (as seen in Northern Hemisphere Compilations), whilst the central Mediterranean exhibits a unique temperature history for this interval. However, during the LMC, records from both the eastern and central Mediterranean regions record extreme cooling at a similar magnitude (*c.* 11-14°C). This extreme transient cooling event took place during a time of longer-term cooling and aridity intensification, related to the formation of the Sahara Desert (Zhang *et al.*, 2014; Tzanova *et al.*, 2015).

Both the eastern and central Mediterranean records show a rapid rebound to pre-LMC temperatures directly after maximum cooling (Figure 4.3.3.1). However, caution should be taken in the interpretation of this apparent ‘warming’ event as extensive

changes in the hydrological cycle related to the Messinian Salinity Crisis are inferred during this time interval. It is likely that, during this interval, high salinity levels were an important control on $\delta^{18}O$ and Mg/Ca in foraminiferal calcite. Increased salinity is known to result in higher $\delta^{18}O_{seawater}$ and Mg/Ca values which would result in the calculation of higher temperatures.

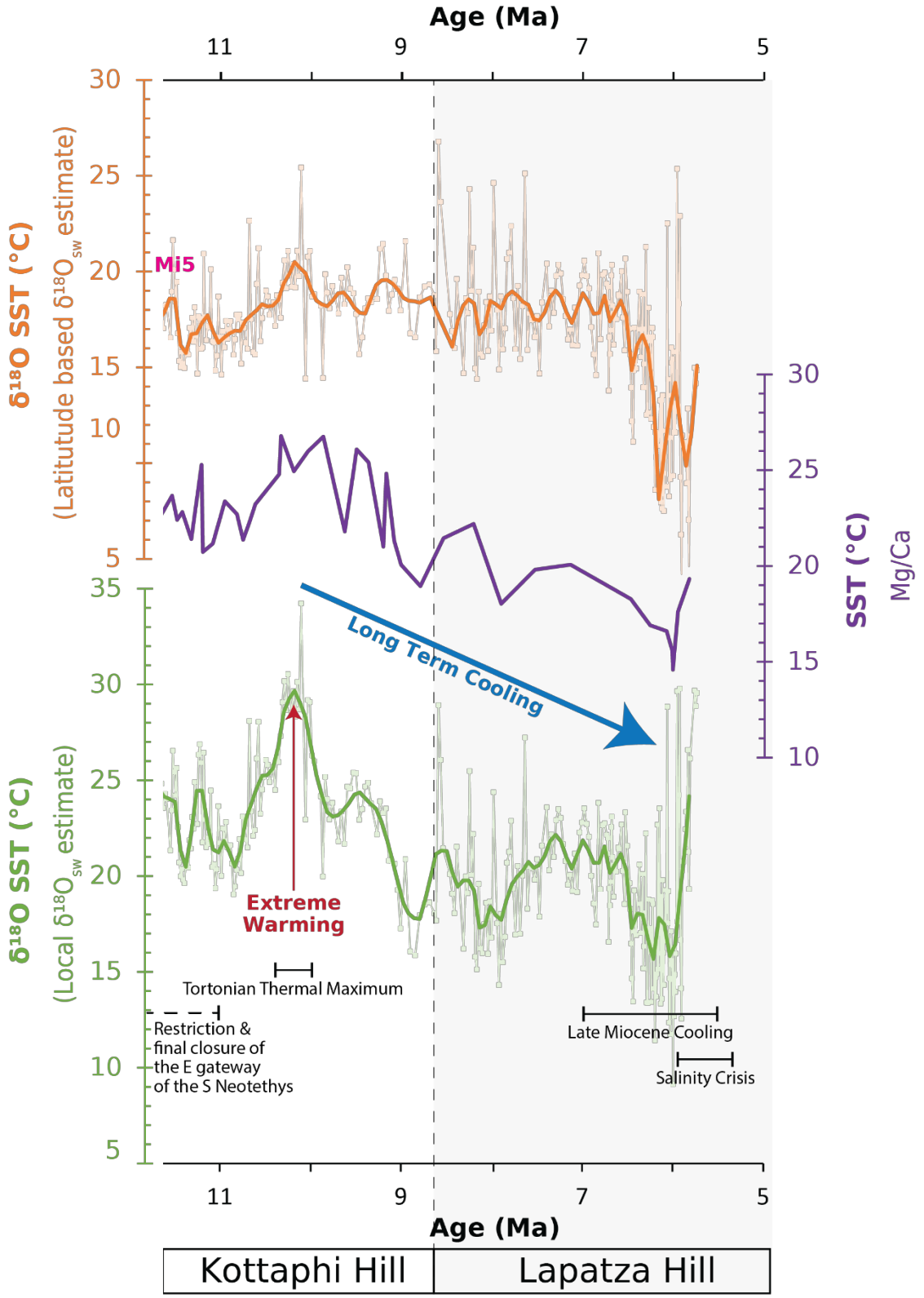


Figure 4.3.3.4 – Plot of temperature versus age for the Late Miocene of the composite temporal record with the events and trends discussed annotated. This figure is an adaptation of Figure 4.3.3.2 and has been edited to focus on the Late Miocene time.

4.4 **Summary of key points**

- The Miocene Climate Optimum resulted in peak temperatures *c.* 12 °C warmer than the modern day in the eastern Mediterranean region. This was followed by dramatic cooling related to the Middle Miocene Climate Transition (MMCT).
- A period of relatively high temperatures appears to have followed the initial cooling step of the MMCT. This was followed by further cooling, after which extremely high temperatures were not recorded until the Tortonian Thermal Maximum.
- The new palaeotemperature record indicates extremely high temperatures during the Tortonian Thermal Maximum (*c.* 10.2 Ma) in the eastern Mediterranean region.
- A long-term cooling trend follows the Tortonian Thermal Maximum (*c.* 10.2 Ma) until *c.* 6 Ma.
- Up to 14°C of cooling was recorded between *c.* 7 Ma and *c.* 6 Ma. This corresponds with globally reported ‘Late Miocene Cooling’.

5 Geochemical evidence for palaeoenvironmental changes from the new composite succession

Both global and regional changes in ocean chemistry are well documented during the Miocene (see Chapter 1.2.4). In this chapter, the new geochemical records produced during this study are examined in order to reveal how global to regional events affected the successions sampled in Cyprus and to identify the presence of any unique (local) events that may have taken place. Examination of changes in ocean chemistry during this period also gives insights into the timing of regional tectonic and climatic events, which controlled ocean chemistry. Aside from the $\delta^{13}C_{finefraction}$ analyses, all of the analyses discussed in this chapter were carried out on planktic foraminifera from the *Praeorbulina-Orbulina* lineage. Therefore, the seawater chemistry data and interpretations presented during this chapter relate to the ocean surface mixed layer (25–50 m) where these foraminifera lived (Birch *et al.*, 2013). Additional trace element data from the analysis of planktic foraminiferal samples are shown in Appendix 8.7.

5.1 Methods

5.1.1 Carbon stable isotopes

The methods used for carbon stable isotopic analysis of fine fraction bulk samples and planktic foraminifera samples are described in Chapter 2.5.

The balance of controls on the $\delta^{13}C$ composition of marine carbonates is more complex than for $\delta^{18}O$, and therefore no direct proxy calibrations (such as temperature calibrations used for $\delta^{18}O$) for $\delta^{13}C$ are used in this study. However, $\delta^{13}C$ remains a useful tool for interpreting ocean chemistry changes which are often related to biological processes. $\delta^{13}C$ in foraminiferal calcite is influenced by the isotopic composition of dissolved inorganic carbon (DIC) in the water body where

biomineralization took place. The isotopic composition of DIC is influenced by a variety of geological factors, such as the burial of carbonate or organic material, weathering, metamorphosis, and volcanism. The $\delta^{13}C$ values of seawater, and therefore, foraminiferal calcite, are influenced by photosynthetic pathways, photosynthetic fractionation, seawater mixing and air-sea gas exchange. For this reason, $\delta^{13}C$ has been used as an indicator of changes in various processes in palaeoceanographic records, such as biological productivity (Woodruff and Savin, 1985), ocean circulation (Bulian *et al.*, 2022), sea-level (Woodruff and Savin, 1985; Mutti *et al.*, 1997) and light intensity (Spero and Williams, 1988). Global carbon isotope shifts in the Miocene (see Chapter 1.2.4) have been linked to changes in the hydrological cycle (Holbourn *et al.*, 2015, 2018), nutrient cycling (Hodell *et al.*, 1994; Dickens and Owen, 1999; Diester-Haass *et al.*, 2005; Holbourn *et al.*, 2018; Lübbers *et al.*, 2019), and changes in photosynthetic pathways in plants (Cerling *et al.*, 1997; Diester-Haass *et al.*, 2006; Tzanova *et al.*, 2015; Herbert *et al.*, 2016).

5.1.2 Trace elements

Interpretations concerning local-to-global scale changes in ocean chemistry can be made by examining TE/Ca ratios in foraminiferal calcite. In this study, planktic foraminifera from the *Praeorbulina-Orbulina* lineage were used for trace element analysis. The methodology used in this analysis is described in Chapter 2.6. It is important to note that numerous biological and oceanographic factors control the incorporation of trace elements into foraminiferal calcite (Allen *et al.*, 2016). Therefore, indications of environmental changes from the measurement of trace elements in foraminiferal calcite may differ from those utilised when analysing bulk rock samples that may contain additional non-biogenic constituents.

B/Ca

The ratio of boron (B) to calcium (Ca) in foraminiferal calcite is one of the most well-established methods for gaining knowledge of carbonate chemistry in past environments. Boron is almost exclusively present in seawater as either boric acid ($B(OH)_3$) or borate ($B(OH)_4^-$) (Hemming and Hanson, 1992). Early studies found that the ratio of boric acid to borate in modern seawater is largely dependent on pH, suggesting that borate is the dominant species in high-pH seawater (Hershey *et al.*, 1986; Hemming and Hanson, 1992). Therefore, foraminiferal B/Ca ratios were believed to reflect borate/bicarbonate ($B(OH)_4^-$) /HCO_3^-) ratios in seawater and could be an effective proxy for palaeo-seawater pH (Hemming and Hanson, 1992; Hemming *et al.*, 1995; Allen *et al.*, 2011; He *et al.*, 2013; Henehan *et al.*, 2013, 2015). Recent studies have suggested that the B/Ca ratio in foraminiferal calcite reflects the ratio of borate to dissolved inorganic carbon ($B(OH)_4^-$/DIC) in seawater rather than the ratio of borate/bicarbonate (($B(OH)_4^-$)/HCO_3^-) (Haynes *et al.*, 2017).

Further studies have indicated that salinity, nutrient concentrations, DIC, boron concentrations in seawater, temperature and test growth all may exert some control on the B/Ca composition of foraminiferal calcite (Wara *et al.*, 2003; Hönisch and Hemming, 2004; Allen *et al.*, 2011, 2012; Henehan *et al.*, 2013, 2015; Naik and Naidu, 2014; Haynes *et al.*, 2017). Awareness of the possible effects of these additional controls is especially important for studies on potentially isolated basins, where salinity, nutrient conditions and freshwater inputs may vary more than in open ocean settings. B/Ca ratios can also be affected by post-depositional dissolution of foraminiferal calcite which can preferentially remove boron-enriched calcite (Coadic *et al.*, 2013). With awareness of these possible complications, the B/Ca proxy has been successfully utilised to understand better the carbonate chemistry in past oceans. This

method has been successfully used on Miocene samples from elsewhere in the eastern Mediterranean (Badger *et al.*, 2013; Antonarakou *et al.*, 2019; Zammit, 2022), but has never been applied to samples from Cyprus before.

Na/Ca

The ratio of sodium (Na) to calcium (Ca) in foraminiferal calcite has been suggested as a proxy for past changes in seawater salinity. This potential proxy is based on relationships observed in laboratory culture studies (e.g. Wit *et al.*, 2013). However, recent studies have indicated that the controls on the incorporation of Na into foraminiferal calcite are complex, leading to uncertainty about the potential of Na/Ca as a salinity proxy for fossil foraminifera (Gray *et al.*, 2023). The Lapatza Hill succession used in this study provides an excellent opportunity to investigate how this potential salinity proxy could have recorded the onset of the Messinian Salinity Crisis. Na/Ca data can also be compared to the local $\delta^{18}O_{seawater}$ (See Chapter 5.1.3) data calculated in this study, which is an independent proxy for changes in salinity. Na/Ca has also recently been suggested as a proxy for seawater calcium concentration (Zhou *et al.*, 2021).

Ba/Ca

The ratio of barium (Ba) to calcium (Ca) in foraminiferal calcite has been suggested as a proxy for salinity. The Ba/Ca salinity proxy is based on the principle that the Ba^{2+} content of river water is higher than in seawater (Hönisch *et al.*, 2011; Bahr *et al.*, 2013; Evans *et al.*, 2015; Groeneveld *et al.*, 2018). This means that this proxy is more accurately described as a proxy for continental run-off and is only suitable for enclosed basins where freshwater input from river runoff is the main control on salinity. Ba/Ca has been used as a proxy for continental run-off and the effects of such run-off on salinity for Messinian successions in the western and central Mediterranean (Sprovieri

et al., 2008; Mancini *et al.*, 2020). Ba/Ca is examined as a possible continental run-off and thus salinity proxy and is compared to the local $\delta^{18}O_{seawater}$ (See Chapter 5.1.3) data calculated in this study.

5.1.3 $\delta^{18}O_{sw\text{-}ivc}$

$\delta^{18}O$ values of foraminiferal calcite ($\delta^{18}O_{planktic}$ in this study) are controlled by temperature (T), local hydrography (E-P), and ice volume (IVC) (Shackleton, 1967, 1974; Waelbroeck *et al.*, 2002; Pearson, 2012) as shown in the equation below:

$$\boldsymbol{\delta^{18}O_{planktic} = \Delta\delta^{18}O_{T} + \Delta\delta^{18}O_{E-P} + \Delta\delta^{18}O_{ivc}} \qquad \textbf{[Eq. 5.1.3.1]}$$

Therefore, by correcting for the contributions of ice volume (IVC) and temperature (T), past records of local hydrography can be determined. The $\delta^{18}O_{planktic}$ record in this study was corrected for temperature (T) using the Mg/Ca-based temperature calculations in order to calculate $\delta^{18}O_{seawater}$ (see Chapter 4.2.4). By correcting the $\delta^{18}O_{seawater}$ record for the ice volume contribution (IVC) the effects of local hydrography (E-P) could be examined. This is often referred to as $\delta^{18}O_{seawater}$ minus ice volume contribution ($\delta^{18}O_{sw\text{-}ivc}$), and is commonly used as a proxy for changes in salinity (Groeneveld *et al.*, 2008, 2018; Riethdorf *et al.*, 2013; Saraswat *et al.*, 2019; Farmer *et al.*, 2023; Nuber *et al.*, 2023). In this study, the record of Miller *et al.* (2020) is used to calculate and correct for ice volume contributions. The equation for the calculation of $\delta^{18}O_{sw\text{-}ivc}$ is shown below:

$$\boldsymbol{\delta^{18}O_{sw-ivc} = \delta^{18}O_{planktic} - \Delta\delta^{18}O_{T} - \delta^{18}O_{ivc}} \qquad \textbf{[Eq. 5.1.3.2]}$$

Some previous studies equate changes in $\delta^{18}O_{sw\text{-}ivc}$ to salinity changes measured in practical salinity units (PSU) (Groeneveld *et al.*, 2008, 2018; Saraswat *et al.*, 2019). A

1.0 ‰ change in $\delta^{18}O_{sw\text{-}ivc}$ is indicated to be equivalent to a 3-4 PSU salinity change in the modern Indian Ocean (Delaygue *et al.*, 2001). However, in this study, the $\delta^{18}O_{sw\text{-}ivc}$ data are used as a method to interpret local hydrography and salinity trends and changes rather than as an attempt to calculate PSU values. As discussed in Chapter 4.2.4, there are limitations and uncertainties associated with both the $\delta^{18}O$ and Mg/Ca methods, which may lead to inaccurate or misleading PSU values. There have also been significant changes in ocean circulation and climate in the Mediterranean region since the Miocene, meaning that the region is not suitable for the extrapolation of salinity changes measured in PSU from modern PSU values based on changes in $\delta^{18}O_{sw\text{-}ivc}$.

5.1.4 Smoothing of data

In order to allow long-term trends in geochemical records to be identified, smoothed data are shown in figures (bold lines) together with measured values (thin lines with box markers). These data were smoothed using a nonparametric LOESS (locally estimated scatterplot smoothing) quadratic regression (Cleveland, 1979; Cleveland and Devlin, 1988) with a locally weighted function equivalent to 60 kyr.

5.2 **Results**

5.2.1 Carbon stable isotopes

The $\delta^{13}C$ data collected for the composite temporal record are shown in Figure 5.2.1.1. For the Kottaphi Hill succession, the two records follow a similar trend, although, the $\delta^{13}C_{planktic}$ record shows a greater amount of variability than the $\delta^{13}C_{finefraction}$ record. The $\delta^{13}C_{planktic}$ values record an event of steep increase (heavier values) in $\delta^{13}C$ at *c.* 14.6 Ma, as recorded in the $\delta^{13}C_{finefraction}$ record. Both records show a significant shift towards lighter values at the splice point between the Kottaphi Hill and Lapatza Hill records. In the $\delta^{13}C_{planktic}$ record, shortly after this shift, values return to a similar level

(1-2 ‰) as in the Kottaphi Hill succession. The shift in $\delta^{13}C$ is more dramatic (*c.* 4.5 ‰) in the $\delta^{13}C_{finefraction}$ and values do not return to a similar level as in the Kottaphi Hill succession but instead remain lower. Following the splice point, the $\delta^{13}C_{planktic}$ and $\delta^{13}C_{finefraction}$ records show discrete trends. The $\delta^{13}C_{planktic}$ values record a second shift to lighter $\delta^{13}C$ values at *c.* 7.6 Ma, which was followed by continued a 'saw-tooth stepped' decrease until *c.* 6.5 Ma when values steeply increased, before once again decreasing until the end of the record. In the $\delta^{13}C_{finefraction}$ record, values continued to decrease following the negative shift at the splice point until *c.* 8.5 Ma when values began to increase before rapidly increasing to *c.* 0.00 ‰ at *c.* 7 Ma. $\delta^{13}C_{finefraction}$ values steadily decreased from *c.* 6.9 Ma until the end of the record. These results are related to a similar offset noted in the $\delta^{18}O_{finefraction}$ record and are related to differences in lithology and depositional environment between the two successions sampled as discussed in Chapter 5.3.1.

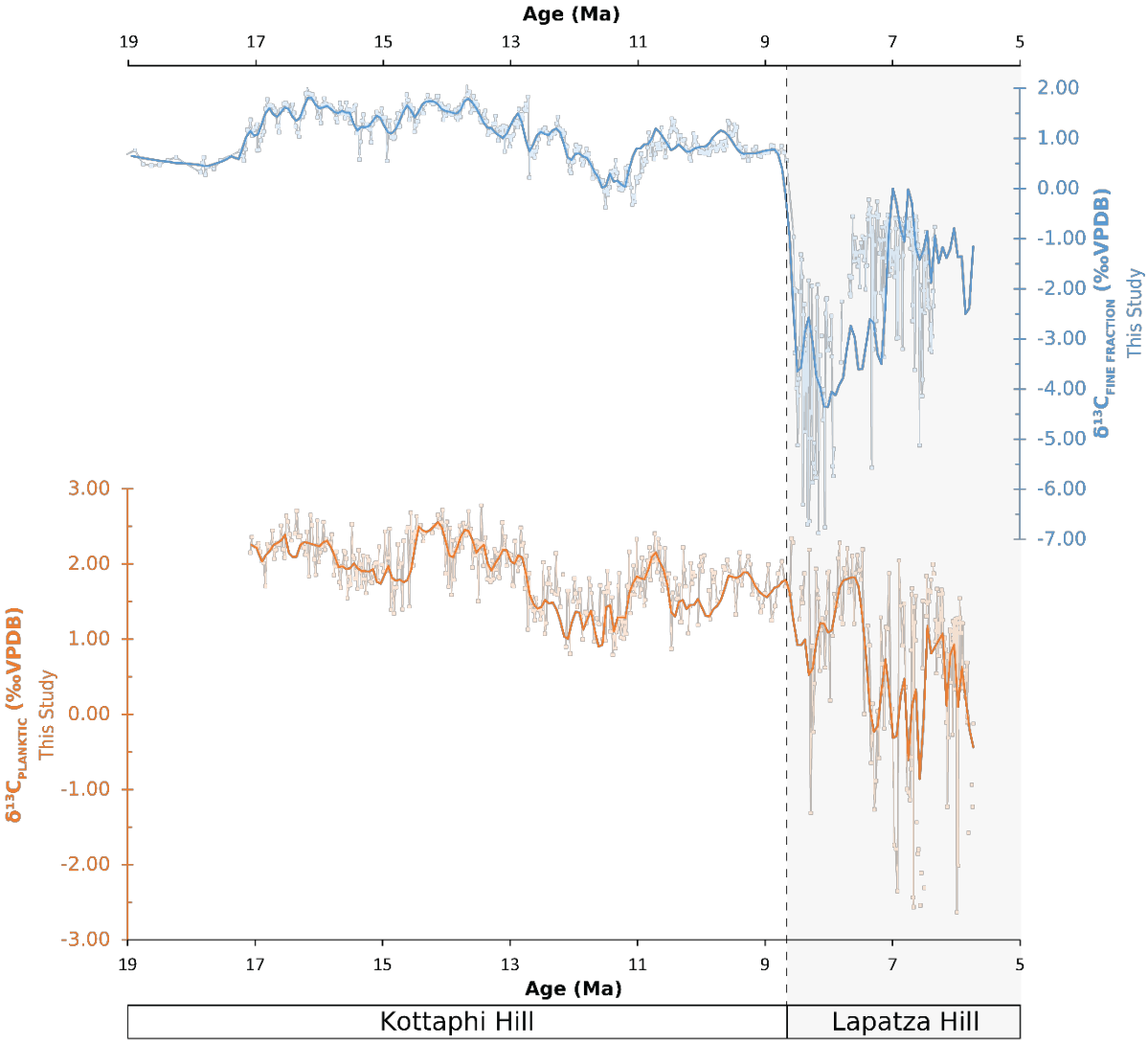


Figure 5.2.1.1 – Plot of $\delta^{13}C_{planktic}$ (orange) and $\delta^{13}C_{finefraction}$ (blue) versus age for the composite temporal record. Measurements are shown relative to VDPB. All of the measured data are shown with box markers connected by a thin line; bold lines show these data smoothed by a locally weighted function over 60 kyr (see Chapter 5.1.4).

5.2.2 Trace elements

B/Ca

The B/Ca record begins with a gradually increasing trend from *c.* 47 to 58 µmol/mol at the start of the record (*c.* 17 Ma) to 56 to 66 µmol/mol at *c.* 13 Ma (Figure 5.2.2.1). After *c.* 13 Ma the B/Ca ratios fell rapidly to a minimum of 44.8 µmol/mol at 11.95 Ma. Between 11.95 Ma and *c.* 9.6 Ma, the B/Ca ratio increased at a fast rate to *c.* 82 µmol/mol. The B/Ca ratios then show a very gradual decrease until the end of the record (5.82 Ma); however, the measured values

exhibit far greater variability (25 µmol/mol range) for this part of the composite temporal record.

From *c.* 16.2 Ma to *c.* 14.8 Ma, the B/Ca values appear to vary, with some cyclicity at a periodicity of *c.* 0.4 Ma. Between 13.7 Ma and 12.6 Ma values appear to vary with a cyclical pattern with a spacing of *c.* 0.22 Ma. A cyclical pattern is also present in the B/Ca record between 11.7 Ma and 10.75 Ma, when the cycles have a spacing of *c.* 0.19 Ma. However, the sample resolution is not high enough to distinguish if these are true cyclical patterns.

There is no clear offset in the B/Ca values at the splice point between the two successions sampled.

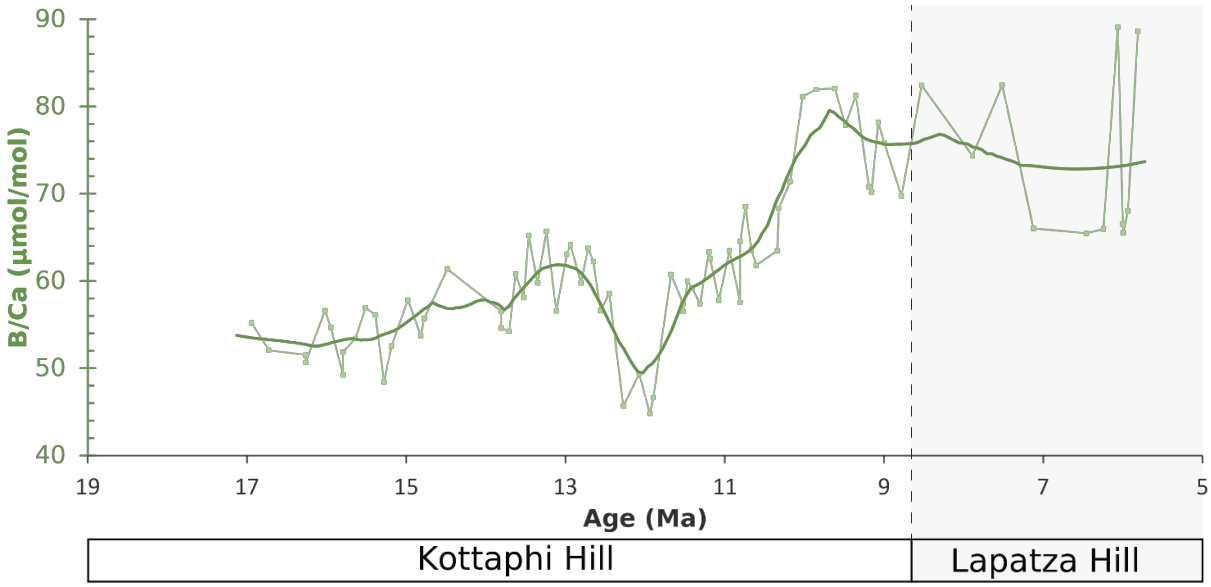


Figure 5.2.2.1 - Plot of B/Ca versus age for the composite temporal record. Both smoothed and calculated data are shown, as in Figure 5.2.1.1 (see Chapter 5.1.4).

Na/Ca

Na/Ca measurements show a gradual increase from the start of the record (*c.* 3.2 mmol/mol at *c.* 17 Ma) to *c.* 12.7 Ma (*c.* 4.2 mmol/mol) (Figure 5.2.2.2). The Na/Ca ratio then fell to a low of 2.96 mmol/mol at 12.28 Ma. The Na/Ca values then show a gradually increasing trend until the end of the record (5.82 Ma). This gradual

increasing trend is interrupted by a small decrease in Na/Ca from 11.2 to 10.7 Ma. A short excursion to lower Na/Ca values (3.68 mmol/mol) is also recorded at 9.16 Ma. Two excursions to high Na/Ca values are recorded at 9.08 Ma (4.86 mmol/mol) and 8.53 Ma (4.96 mmol/mol).

The Na/Ca record shows a cyclical pattern with a spacing of c. 0.22 Ma between 13.7 Ma and 12.6 Ma. Between 11.7 Ma and 10.75 Ma, apparent cycles have a spacing of c. 0.19 Ma. However, the sample resolution is not high enough to distinguish if these are true cyclical patterns.

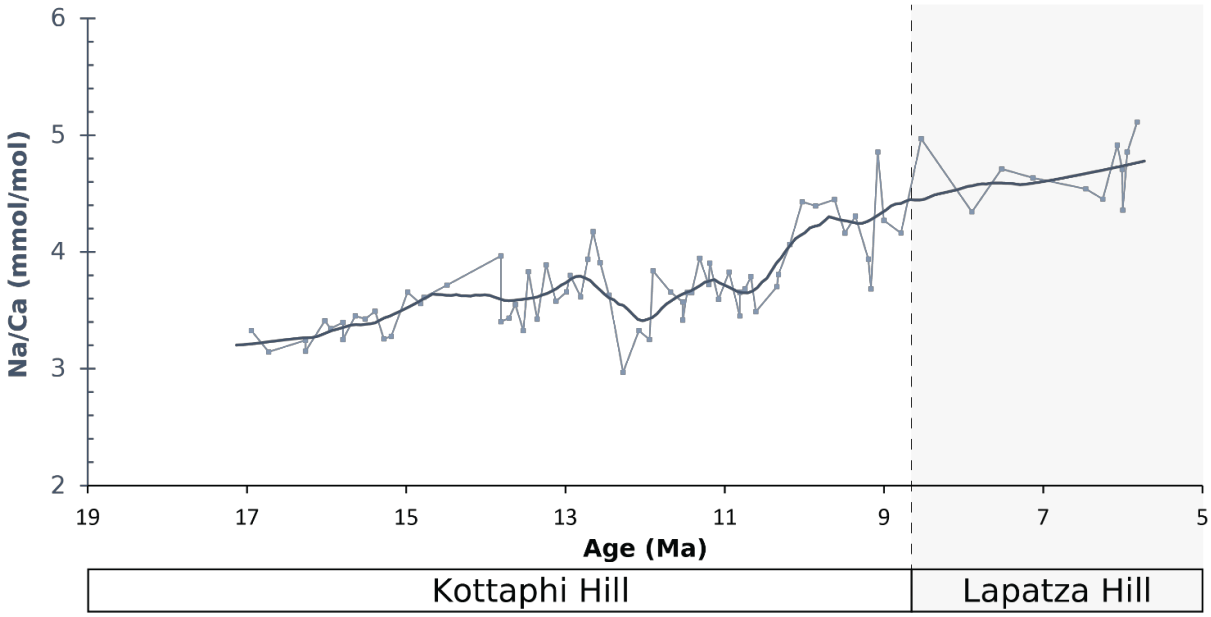


Figure 5.2.2.2 - Plot of Na/Ca versus age for the composite temporal record. Both smoothed and calculated data are shown, as in Figure 5.2.1.1 (see Chapter 5.1.4).

Ba/Ca

The ratio of barium to calcium shows a small decrease from the beginning of the Kottaphi Hill succession (*c.* 17 Ma) to *c.* 16 Ma (Figure 5.2.2.3). After this, the Ba/Ca record remains stable at between *c.* 1 and *c.* 3 µmol/mol from *c.* 16 Ma to *c.* 11 Ma. At *c.* 11 Ma, a steep increase in Ba/Ca is measured, with a peak of 4.85 µmol/mol at 10.67 Ma. A second peak in Ba/Ca is recorded at 9.86 Ma, when values reached 3.76

μmol/mol. After *c.* 9.2 Ma, the variability of measured values increased greatly, resulting in an increase in the smoothed Ba/Ca record. The minimum values during this period of high variability remained in a similar range (*c.* 1 and *c.* 3 μmol/mol) to the stable parts of the record; however, the peaks during this part of the record reached 8.99 μmol/mol at 9.08 Ma and 12.11 μmol/mol at 8.79 Ma. It appears that some offset to lower values is present between the end of the Kottaphi Hill succession and the start of the Lapatza Hill succession. However, the extent of this offset is difficult to decipher due to the high variability in measurements from the uppermost part of the Kottaphi Hill succession. The Ba/Ca record for the Lapatza Hill succession begins with a decrease in Ba/Ca values from 8.53 Ma (8.81 μmol/mol) to 7.90 Ma (6.66 μmol/mol). From 7.90 Ma to the end of the record (5.82 Ma), the Ba/Ca values increased rapidly.

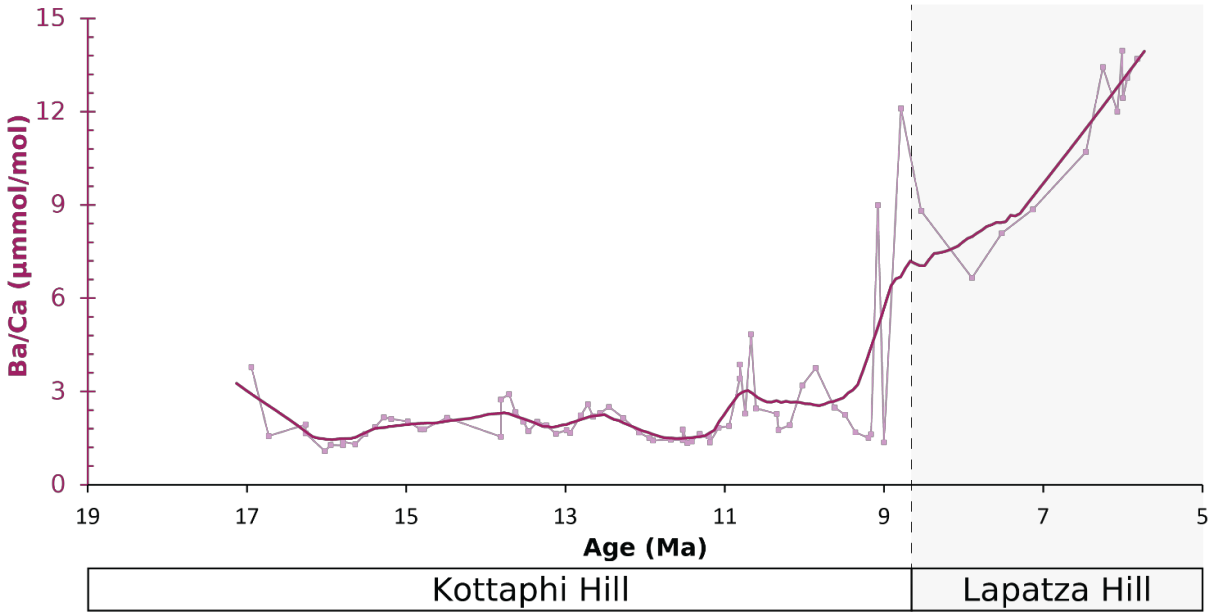


Figure 5.2.2.3 - Plot of Ba/Ca versus age for the composite temporal record. Both smoothed and calculated data are shown, as in Figure 5.2.1.1 (see Chapter 5.1.4).

5.2.3 $\delta^{18}O_{sw\text{-}ivc}$

The $\delta^{18}O_{sw\text{-}ivc}$ record is relatively stable with some small variations (*c.* 0.25 ‰ to c. -0.3 ‰) between the start of the record (*c.* 17 Ma) and *c.* 15.2 Ma (Figure 5.2.3.1). At

14.98 Ma the calculated $\delta^{18}O_{sw\text{-}ivc}$ fell to -0.86 ‰. $\delta^{18}O_{sw\text{-}ivc}$ values then increased, with a peak of 1.05 ‰ at 13.53 Ma, before falling to -0.22 ‰ at 12.80 Ma. Calculated values then rose, with two peaks at 12.57 Ma (0.53 ‰) and 12.08 Ma (0.54 ‰). The calculated $\delta^{18}O_{sw\text{-}ivc}$ values then fell again to -0.27 at 11.90 Ma. Values remained low until a fast increase in $\delta^{18}O_{sw\text{-}ivc}$ at *c.* 11.5 Ma. The calculated $\delta^{18}O_{sw\text{-}ivc}$ values then show a gradual decrease until *c.* 8.2 Ma. After 8.2 Ma, the $\delta^{18}O_{sw\text{-}ivc}$ values increased steadily until the end of the record (5.82 Ma).

Although there is a change in trend (from decreasing to increasing $\delta^{18}O_{sw\text{-}ivc}$ values) after the splice point between the two successions sampled, there is no clear offset between the two records. A weak cyclical pattern can be recognised throughout the $\delta^{18}O_{sw\text{-}ivc}$ record for the Kottaphi Hill succession, with a spacing of *c.* 0.4 Ma. There is no clear pattern other than the increasing trend in $\delta^{18}O_{sw\text{-}ivc}$ values for the Lapatza Hill succession.

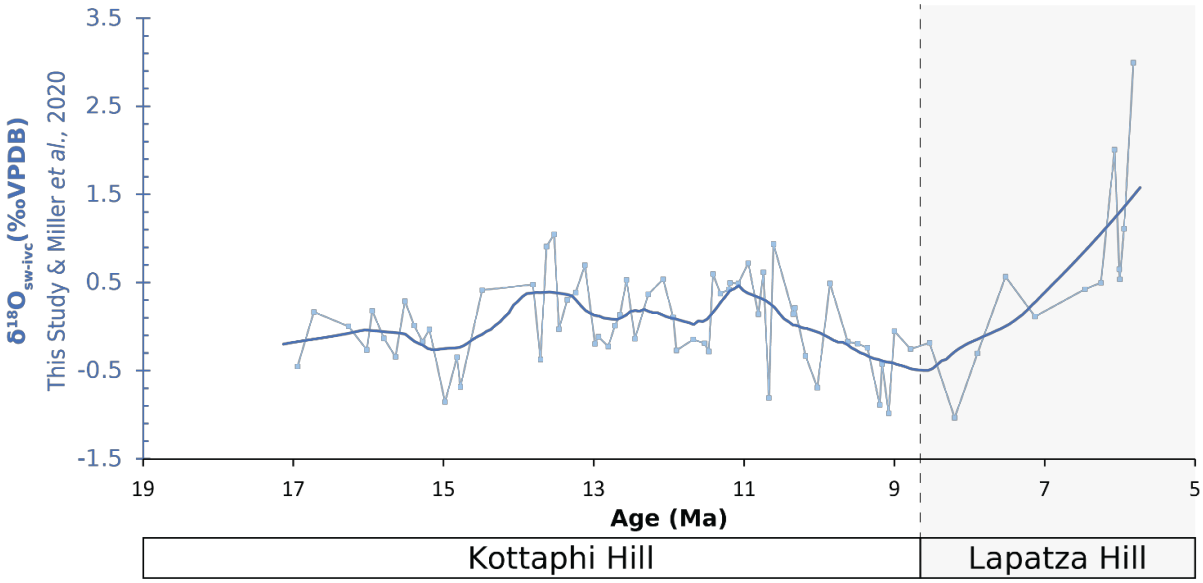


Figure 5.2.3.1 - Plot of calculated $\delta^{18}O_{sw\text{-}ivc}$ versus age for the composite temporal record. Note – these data are shown relative to VPDB as is used in temperature calculations and measurements of foraminiferal calcite in this study. Other published $\delta^{18}O_{sw}$ data may be shown relative to VSMOW. Both smoothed and calculated data are shown, as in Figure 5.2.1.1 (see Chapter 5.1.4).

5.3 Discussion

5.3.1 Carbon stable isotopes

The $\delta^{13}C_{finefraction}$ record shows a dramatic offset (*c.* 4.5 ‰) towards lighter $\delta^{13}C$ values at the splice point between the Kottaphi Hill succession and the Lapatza Hill succession (Figure 5.3.1.1). Following this offset, the $\delta^{13}C_{planktic}$ and $\delta^{13}C_{finefraction}$ records show discrete trends.

A similar offset was recorded in the $\delta^{18}O_{finefraction}$ (Chapter 4.2.1). Possible reasons for this offset were discussed in Chapter 4.3.1 and attributed mainly to the relatively high terrigenous component in the Lapatza Hill succession. The offsets noted for fine fraction stable isotope records at the splice point between the two successions are related to the lithological differences between the two successions. Such lithological differences between the two successions, as well as the settings in which the successions were deposited and the relationship of each succession sampled to the underlying and overlying strata are discussed in Chapter 3.3.

The trend shown in the $\delta^{13}C_{finefraction}$ record is most likely the result of compositional changes in the fine fraction bulk samples, although further chemical analysis would be required to confirm this. Both the $\delta^{18}O_{planktic}$ and $\delta^{13}C_{planktic}$ records do not show a dramatic offset at this splice point. This supports the interpretation that the offset in fine fraction records is due to a difference in the composition of the bulk samples, and not environmental or climatic changes.

As with the $\delta^{18}O$ records (Chapter 4.3.1), the $\delta^{13}C_{planktic}$ and $\delta^{13}C_{finefraction}$ records for the Kottaphi Hill succession show a similar general trend. Therefore, $\delta^{13}C_{finefraction}$ data can be used for palaeoceanographic interpretations where the Kottaphi Hill $\delta^{13}C_{planktic}$ record is incomplete.

A relatively low magnitude shift is noted in the $\delta^{13}C_{planktic}$ record (Figure 5.3.1.1); this shift is likely a result of a small discrepancy between the local $\delta^{13}C_{seawater}$ in each locality. Localised lighter $\delta^{13}C$ values may indicate the demobilisation of isotopically light carbon from a nearby shelf due to sea level changes, or the input of isotopically light carbon from the continent (Vincent *et al.*, 1980, 1985; Kouwenhoven *et al.*, 1999).

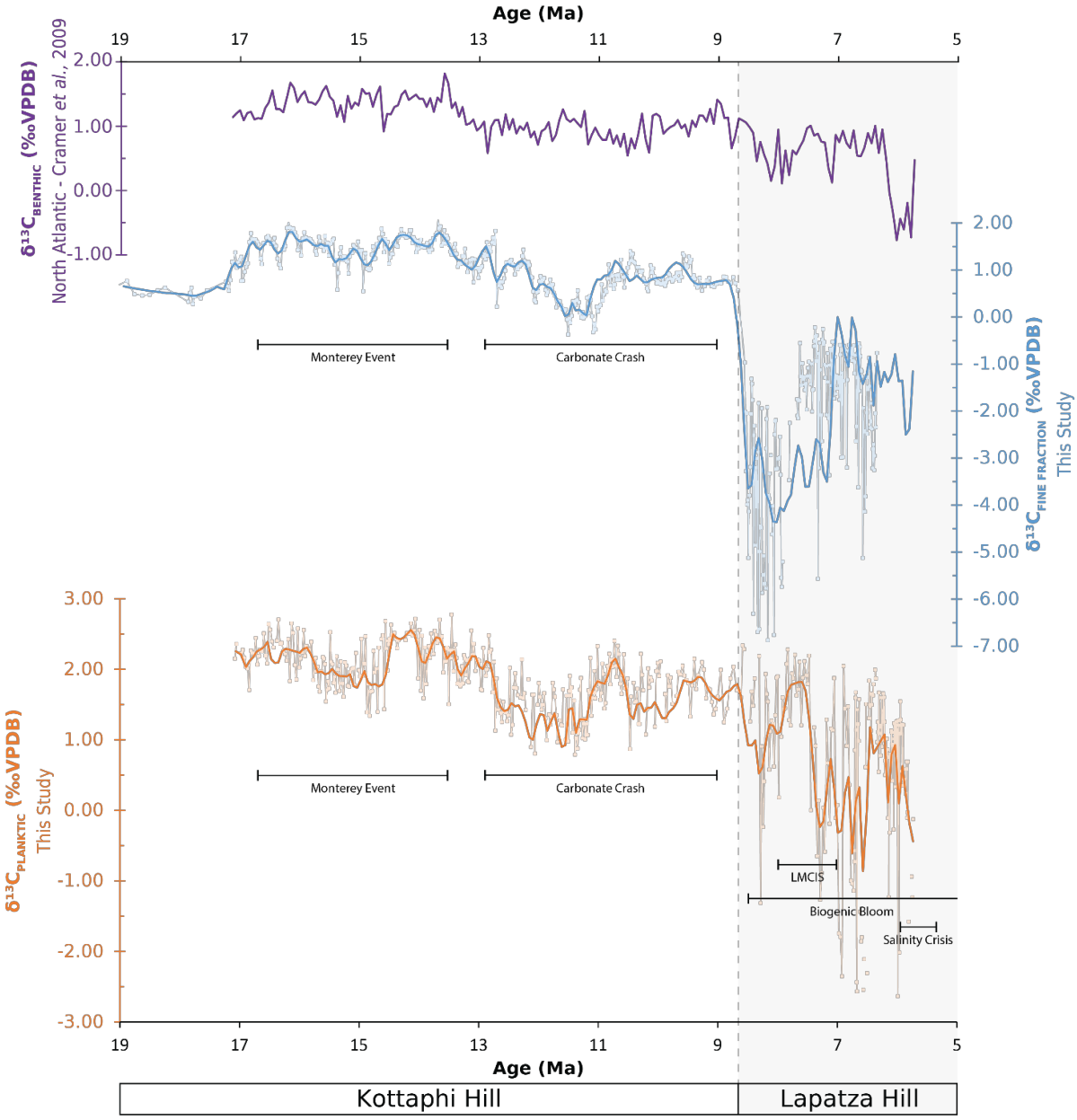


Figure 5.3.1.1 - Plot of $\delta^{13}C_{planktic}$ (orange) and $\delta^{13}C_{finefraction}$ (blue) versus age for the composite temporal record. Measurements are shown relative to VDPB. Both smoothed and calculated data are shown, as in Figure 5.2.1.1 (see Chapter 5.1.4). The open ocean (North Atlantic) benthic foraminifera $\delta^{13}C$ record of Cramer *et al.* (2009) is shown for reference. The timing of several global to regional scale oceanographic events are also shown: (1) The Monterey Event

(Vincent and Berger, 1985; Holbourn *et al.*, 2015); (2) Miocene Carbonate Crash (Lyle *et al.*, 1995; Lübbers *et al.*, 2019); (3) Biogenic Bloom (Dickens and Owen, 1999; Diester-Haass *et al.*, 2004, 2005); (4) Late Miocene Carbon Isotope Shift (LMCIS)(Hodell *et al.*, 1994); (5) The Messinian Salinity Crisis (Krijgsman *et al.*, 1999a).

The $\delta^{13}C_{finefraction}$ record from Kottaphi Hill shows a period of elevated $\delta^{13}C$ values between *c.* 17 Ma and *c.* 13.5 Ma (Figure 5.3.1.1). This period of higher $\delta^{13}C$ is also recorded in the $\delta^{13}C_{planktic}$ record, albeit not as well defined (Figure 5.3.1.1). This interval correlates with the Monterey Event, which is a well-documented global carbon isotope event (Vincent and Berger, 1985; Holbourn *et al.*, 2007, 2015). The Monterey Event is associated with increased biological carbon isotope fractionation under high CO_2 conditions, together with enhanced burial of organic matter on continental shelves as a result of eustatic sea-level rise (Sosdian *et al.*, 2020).

Both the $\delta^{13}C_{finefraction}$ and the $\delta^{13}C_{planktic}$ data for the composite temporal record show a gradual decrease in $\delta^{13}C$ following the Monterey Event (Figure 5.3.1.1). This decrease is also noted in open ocean records (e.g. Cramer *et al.*, 2009), and has been related to increased CO_2 drawdown following the high CO_2 conditions of the Monterey Event (Vincent and Berger, 1985; Flower and Kennett, 1993, 1994; Sosdian *et al.*, 2020). Both the $\delta^{13}C_{finefraction}$ and $\delta^{13}C_{planktic}$ are especially low at *c.* 12 Ma. This trend towards lighter $\delta^{13}C$ may also relate to reduced primary productivity in the oceans due in response to the onset of the Miocene Carbonate Crash (e.g. Holbourn *et al.*, 2018, 2021).

The $\delta^{13}C_{finefraction}$ and $\delta^{13}C_{planktic}$ records both show a shift to heavier values at *c.* 10.8 Ma (Figure 5.3.1.1). This corresponds to the Tortonian Thermal Maximum, which is recorded at a high magnitude in the palaeotemperature records from this succession.

At 7.2 Ma, a dramatic shift (*c.* 2.5 ‰) to lighter carbon isotope values is shown in the $\delta^{13}C_{planktic}$ record (Figure 5.3.1.1). This shift corresponds to the Late Miocene Carbon Isotope shift (LMCIS) (Dickens and Owen, 1999; Diester-Haass *et al.*, 2005; Holbourn *et al.*, 2015, 2018; Tzanova *et al.*, 2015; Herbert *et al.*, 2016; Lyle *et al.*, 2019) and the onset of the Late Miocene-Early Pliocene Biogenic Bloom (Dickens and Owen, 1999; Diester-Haass *et al.*, 2004, 2005). The cause of the LMCIS is unclear (see Chapter 1.2.4). Although the LMCIS is recorded in the new $\delta^{13}C_{planktic}$ record, after this time, the $\delta^{13}C_{planktic}$ record does not appear to reflect the open ocean record from the North Atlantic (Cramer *et al.*, 2009). This indicates that after *c.* 7.2 Ma (early Messinian), the $\delta^{13}C$ composition of seawater in the eastern Mediterranean basins, in which the successions sampled were deposited, was no longer strongly influenced by global $\delta^{13}C$ changes. A change in benthic foraminiferal assemblages and a shift to lighter $\delta^{13}C$ values in the West Alboran Basin (Western Mediterranean) at 7.17 Ma has been related to the restriction of the Mediterranean-Atlantic gateway (Bulian *et al.*, 2022). In the Lapatza Hill succession, a change in the benthic foraminiferal assemblage is noted at 7.23 Ma. Distinguishing between the effects of the LMCIS and the restriction of the Mediterranean-Atlantic gateway is difficult, although, some effect of gateway closure is suggested by the discrete $\delta^{13}C$ trend recorded in the Lapatza Hill succession after *c.* 7.2 Ma. The eastern Mediterranean basins were already at least partially isolated from the open ocean prior to this time, due to the closure of the gateway between the Southern Neotethys and the Indian Ocean during the Early Miocene (see Chapter 1.2.3)

5.3.2 B/Ca – additional insights into carbonate chemistry

The B/Ca record for the composite temporal record provides additional insights into carbonate chemistry. The ratio B/Ca increases from the start of the record until *c.* 13 Ma (Figure 5.3.2.1). The decreasing trend in B/Ca reported by Sosdian *et al.* (2020) at the onset of the Miocene Climate Optimum (MCO) (*c.* 17 Ma) is not observed in the record from Cyprus. It appears that $B(OH)_4^-$/DIC values in the eastern Mediterranean region were already low prior to 17 Ma. At *c.* 16 Ma the B/Ca values of the samples from the Kottaphi Hill succession are similar (50-60 µmol/mol) to those from the Indian Ocean (Sosdian *et al.*, 2020), suggesting that the $B(OH)_4^-$/DIC of the eastern Mediterranean reflected that of the open ocean during this time. It should be noted that the B/Ca record from the Indian Ocean is based on the analysis of *Trilobatus trilobus.* Research into the uptake of B into foraminiferal calcite is relatively new and is ongoing; it is unclear if there are species-specific differences in uptake between *T. trilobus* and *O. universa* (Haynes *et al.*, 2017; Howes *et al.*, 2017; Sosdian *et al.*, 2020). The decreasing trend in the Indian Ocean B/Ca record is attributed to elevated DIC due to volcanic degassing, global warming, and sea-level rise during the MCO (Sosdian *et al.*, 2020). These drivers of elevated DIC can be related to elevated pCO_2 during the Monterey Event (Vincent and Berger, 1985; Holbourn *et al.*, 2007, 2015). It is unclear why this trend is not present in the B/Ca record from Cyprus; however, this apparent discrepancy suggests that there was a difference in seawater chemistry between Cyprus and the Indian Ocean during this interval. This difference in ocean chemistry may have resulted from numerous factors, such as local pH, DIC, salinity, or nutrient concentration (see Chapter 5.1.2). For the Kottaphi Hill succession, it is likely that one, or numerous, controls on B/Ca in foraminiferal calcite (see Chapter

5.1.2) buffered the effects of the Monterey Event on B/Ca values during this time. Apparent cyclicity with a *c.* 0.4 Ma periodicity between *c.* 16.2 Ma to *c.* 14.8 Ma is interpreted to represent oceanographic changes related to eccentricity-forced changes in the carbon cycle. However, a higher resolution record would be required to understand better this apparent cyclicity.

The increasing trend in B/Ca from 17 Ma to 13 Ma in the Kottaphi Hill succession may indicate a rise in surface $B(OH)_4^-$ (and therefore an increase in pH) and/or a fall in surface ocean DIC during this interval. An increasing trend in B/Ca has also been noted at *c.* 13.9 Ma in a succession from Malta (Badger *et al.*, 2013), which was attributed to an increase in pH and a decrease in pCO_2. Analyses of planktic foraminiferal B/Ca in the samples from the Indian Ocean have also revealed an increasing trend throughout this time interval (Sosdian *et al.*, 2020). This increasing B/Ca trend following the MCO can be interpreted as a reduction in surface ocean DIC, driven by a reduction in atmospheric pCO_2. This reduction in atmospheric pCO_2 is related to the climate cooling of the MMCT (Vincent and Berger, 1985; Flower and Kennett, 1993, 1994; Pearson and Palmer, 2000; Sosdian *et al.*, 2020).

Low B/Ca ratios at *c.* 12 Ma occurred at the same time as falls in $\delta^{13}C_{planktic}$ and $\delta^{13}C_{finefraction}$ (Figure 5.3.2.1). It is likely that this corresponds to the Miocene Carbonate Crash (Holbourn *et al.*, 2018, 2021; Lübbers *et al.*, 2019; Preiss-Daimler *et al.*, 2021), which has been related to a reorganisation of ocean circulation patterns as a result of the closure of the Panama Gateway (See Chapter 1.2.3). A small interruption to the increasing B/Ca trend is also noted at *c.* 12 Ma in the Indian Ocean (Sosdian *et al.*, 2020). However, the negative trend in the Indian Ocean record is shorter-lived and at a smaller magnitude than the trend seen in the Kottaphi Hill succession. The timing of

this carbonate chemistry change coincides with a fall in temperatures recorded in both $\delta^{18}O$ and Mg/Ca records.

B/Ca then continued to increase after *c.* 12 Ma until *c.* 9.6 Ma. This increase in B/Ca after *c.* 12 Ma does not appear to relate to $\delta^{13}C$ trends during this time interval. However, the B/Ca increase does again correspond to the trend seen in the Indian Ocean. No high-resolution B/Ca reference data is available for comparison after *c.* 11.5 Ma; however, the increase in B/Ca until *c.* 9.6 Ma is in agreement with low-resolution data from the western tropical Pacific Ocean (Tripati *et al.*, 2009). This increasing B/Ca trend took place during a period of global cooling and glacial expansion which has been related to decreasing atmospheric pCO_2 (Shevenell *et al.*, 2004; Holbourn *et al.*, 2005, 2013; Miller *et al.*, 2020; Westerhold *et al.*, 2020). Therefore, this trend is interpreted to correspond to decreasing atmospheric pCO_2.

No clear trend is seen in the latter part (*c.* 9.6 Ma onwards) of the B/Ca record from both the Kottaphi Hill succession and the Lapatza Hill succession. However, the variability in measured values does appear to increase during this time interval. More data are required in order to interpret the driving force of the apparent increased variability in B/Ca during this interval; however, this may be linked to the partial isolation of the eastern Mediterranean basins as indicated by the Sr isotope data (Chapter 3.3.3). Isolation of a basin is likely to lead to significant changes in seawater chemistry, nutrient supply and other factors, which are known to affect B/Ca in foraminiferal calcite (see Chapter 5.1.2).

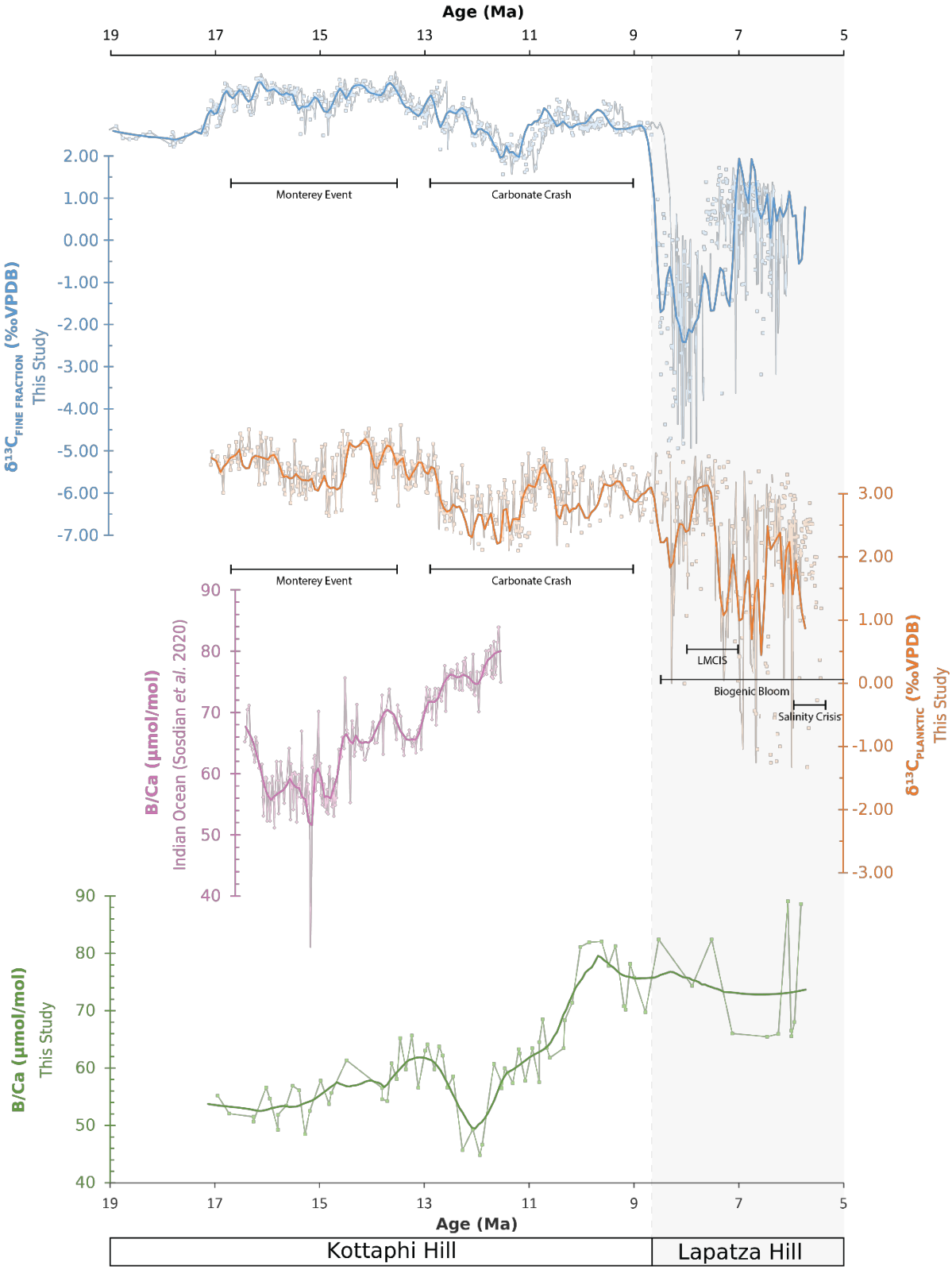


Figure 5.3.2.1 - Plot of B/Ca (green) versus age for the composite temporal record shown relative to the Indian Ocean B/Ca record of Sosdian *et al.* (2020) (pink), together with $\delta^{13}C_{planktic}$ (orange) and $\delta^{13}C_{finefraction}$ (blue) for the composite temporal record. Both smoothed and calculated data are shown, as in Figure 5.2.1.1 (see Chapter 5.1.4). The timing of several global to regional scale climatic and ocean circulation changes are also annotated as in Figure 5.3.1.1.

5.3.3 Salinity ($\delta^{18}O_{sw\text{-}ivc}$)

In this study, $\delta^{18}O_{sw\text{-}ivc}$ is used as a proxy for past changes in salinity. This record is the first long-term palaeo-salinity record of its type for this region and time period. Therefore, few comparisons can be made with pre-existing salinity records. However, the salinity trends recorded can be related to local-to-global, scale oceanographic and climatic events, which are well documented. A weak cyclicity with a 0.4 Ma spacing is present throughout the Kottaphi Hill succession (Figure 5.3.3.1); this pattern is interpreted to represent salinity changes driven by eccentricity-forced climatic changes. Eccentricity-forced climatic changes are expected to have affected the amount of continental run-off, therefore increasing freshwater input into ocean basins and thus salinity.

The start of the $\delta^{18}O_{sw\text{-}ivc}$ record shows that salinity did not change dramatically during the MCO. A drop in salinity is noted at the end of the MCO (*c.* 15 Ma); this was followed by an increasing trend in salinity during the MMCT until *c.* 14 Ma (Figure 5.3.3.1). There is no clear climate-related or global sea level control on this apparent salinity fluctuation. A decrease in salinity may be expected as a result of decreased surface ocean temperatures (Olson *et al.*, 2022), as noted during the MMCT. The controls on the increase in salinity following the initial onset of the MMCT are unclear. By this time, major connectivity between the Southern Neotethys and the Indian Ocean had been lost (see Chapter 1.2.3). It is possible that this salinity trend reflects a local or regional trend in the partially isolated eastern Mediterranean basins. Box modelling studies have suggested that the closure of this gateway resulted in changes to salinity in both the Southern Neotethys and the Indian Ocean (Karami *et al.*, 2009; Hamon *et al.*, 2013). However, better constraints on the timing of ocean gateway closure, together

with more data from Mediterranean and open ocean sites are required in order to assess the geographical extent of this apparent salinity increase.

A long-term reduction in salinity is calculated between *c.* 14 Ma and *c.* 9 Ma (Figure 5.3.3.1). This is consistent with a cooling trend during this interval. The reducing trend in salinity was briefly interrupted by an increase in salinity at *c.* 11 Ma. The timing of this salinity increase coincides with a *c.* 15 m rise in global sea level (Miller *et al.*, 2005, 2020) which precedes the Tortonian Thermal Maximum (Lear *et al.*, 2003; Westerhold *et al.*, 2020), a climatic event which is recorded at a high magnitude in the composite temporal record (see Chapter 4.3).

At *c.* 9 Ma, an increasing trend in salinity began (Figure 5.3.3.1). This increasing trend continued until the end of the record. The longer-term increase in salinity from *c.* 9 Ma is unexpected. Although a salinity increase may be expected for the end of the composite temporal record in relation to the Messinian Salinity Crisis (MSC), this long-term salinity increase appears to have started considerably before the MSC.

Salinity increases related to the MSC are generally believed to have been sudden changes which took place shortly before the onset of the crisis itself (*c.* 5.96 Ma) (Krijgsman *et al.*, 1999a, 2018; Rouchy and Caruso, 2006; Roveri *et al.*, 2014). However, increased salinity and aridity prior to the MSC (sometimes referred to as 'preconditioning') were recently reported to have taken place from *c.* 6.9 Ma, according to $\delta^{18}O_{sw\text{-}ivc}$ based salinity records (Butiseacă *et al.*, 2022; Kontakiotis *et al.*, 2022) and biomarkers (Bulian *et al.*, 2021; Butiseacă *et al.*, 2022).

A steep increasing salinity trend from *c.* 6.3 Ma until the end of the succession sampled is recorded in the composite temporal record (Figure 5.3.3.1). Although this salinity increase took place *c.* 0.4 Ma before the salinity crisis itself, the timing of this increase

in salinity is within the recently suggested time interval salinity and aridity increase prior to the MSC (Bulian *et al.*, 2021; Butiseacă *et al.*, 2022; Kontakiotis *et al.*, 2022).

The steep salinity increase from *c.* 6.3 Ma onwards was briefly interrupted by an apparent fall in salinity at *c.* 6 Ma (Figure 5.3.3.1). The recorded fall in salinity at *c.* 6 Ma may represent a periodic reduction of local salinity due to an abrupt increase in freshwater input into the basin. A similar salinity fluctuation is recorded between *c.* 6.41 Ma and *c.* 5.97 in $\delta^{18}O_{sw\text{-}ivc}$ based salinity records from Zakynthos Island (Greece), and is interpreted to be a result of a climatically controlled increase in freshwater input from the African continent (Vasiliev *et al.*, 2019).

Records from the modern Indian Ocean indicate that a *c.* 1.0 ‰ $\delta^{18}O_{sw\text{-}ivc}$ increase is equivalent to a *c.* 3 PSU increase (Delaygue *et al.*, 2001). By this metric, the *c.* 4.3 ‰ $\delta^{18}O_{sw\text{-}ivc}$ increase noted in the Lapatza Hill succession could represent up to 12.9 PSU increase.

The occurrence of an increasing salinity trend beginning *c.* 2 My prior to any other known preconditioning events is unique to this study and warrants further detailed investigation (with more detailed sampling). The modern Mediterranean Sea has a higher salinity (albeit variable) than the open oceans due to its partial isolation from open ocean circulation patterns (Baringer and Price, 1999; Bethoux and Gentili, 1999). It is possible that the Southern Neotethys became progressively more saline as a result of its transition from an open ocean basin, during the Early Miocene to a more isolated sea after the loss of connection with the Indian Ocean to the east. Such isolation effects could have been exaggerated in the easternmost Mediterranean region. However, the increase in salinity recorded began significantly after the latest estimates of the final closure of the eastern Tethys seaway (*c.* 11 Ma) (Hüsing *et al.*,

2009). Other analyses, such as B/Ca and Sr isotope analyses, have indicated that the Lapatza Hill succession may have been deposited in a partial (or periodically) isolated basin. If this is the case, then it is likely that this early-Late Miocene increase in salinity is a local effect related to the isolation of the basin.

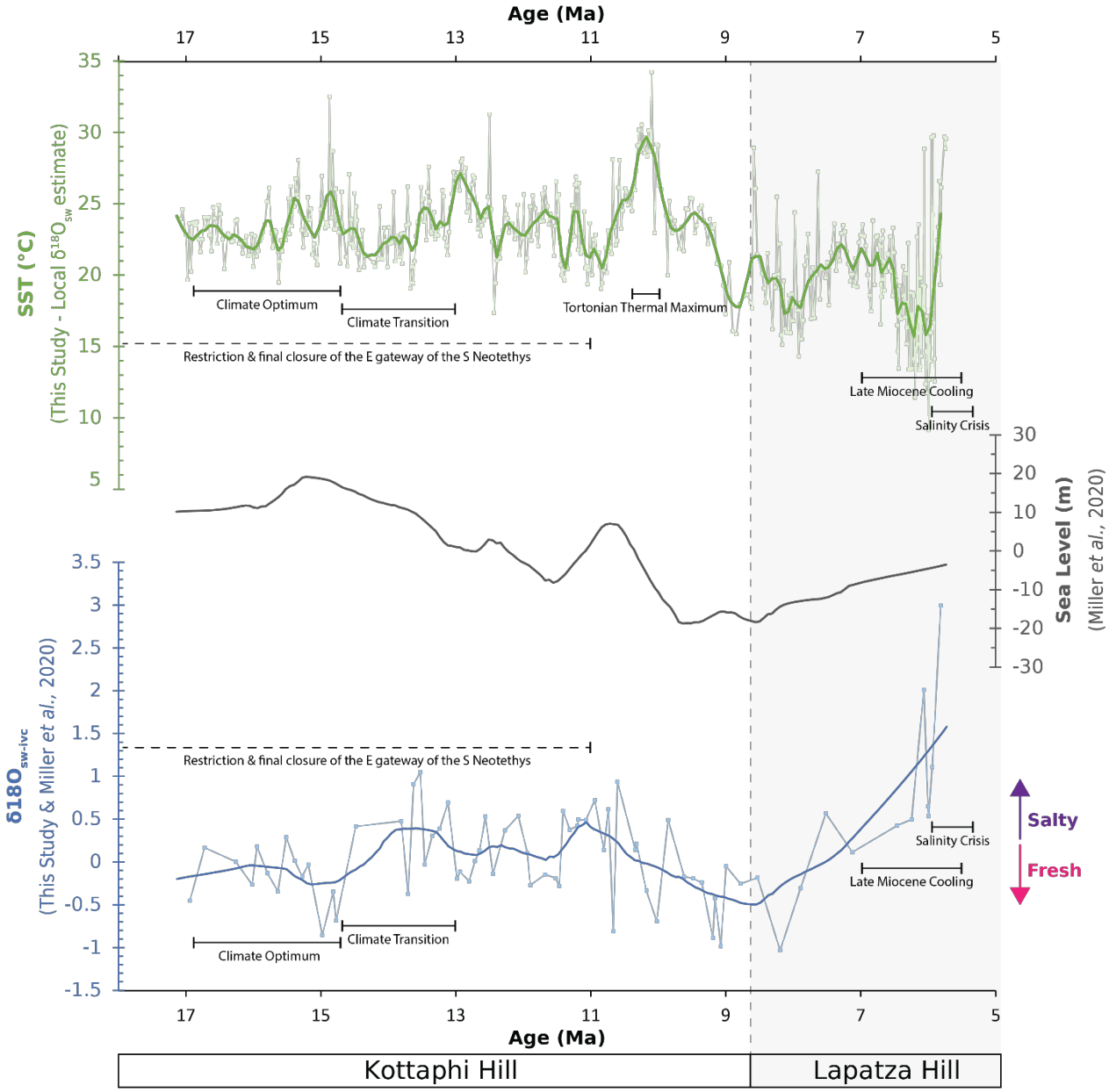


Figure 5.3.3.1 - Plot of $\delta^{18}O_{sw\text{-}ivc}$ (blue) versus age for the composite temporal record. The new temperature record calculated using the local estimation of $\delta^{18}O_{sw}$ (green) (see Chapter 4.2.4) is also shown together with a Miocene sea-level record (grey) (Miller *et al.*, 2020). Both smoothed and calculated data are shown, as in Figure 5.2.1.1 (see Chapter 5.1.4). The timing of several global to regional scale climatic and oceanographic events are also shown: (1) The Miocene Climate Optimum (Zachos *et al.*, 2008; Holbourn *et al.*, 2015; Westerhold *et al.*, 2020); (2) Restriction (from *c.* 20 Ma) and closure of the eastern gateway

of the Southern Neotethys (see Chapter 1.2.3) (Hüsing *et al.*, 2009; Bialik *et al.*, 2019); (3) The Miocene Climate Transition (Holbourn *et al.*, 2005; Westerhold *et al.*, 2020); (4) The Tortonian Thermal Maximum (Westerhold *et al.*, 2020); (5) Late Miocene Cooling (Herbert *et al.*, 2016); (6) The Messinian Salinity Crisis (Krijgsman *et al.*, 1999a).

5.3.4 Additional insights into Local Hydrography

In this study, Ba/Ca and Na/Ca are used as potential proxies for salinity (or the balance of freshwater versus salt water) in the basins. Therefore, the results of the Na/Ca and Ba/Ca analyses are compared to the salinity record produced using the well-established $\delta^{18}O_{sw\text{-}ivc}$ method.

Na/Ca changes in the composite temporal record show a similar overall increasing trend to the $\delta^{18}O_{sw\text{-}ivc}$ record (Figure 5.3.4.1). However, the shorter-term fluctuation and changes recorded in the $\delta^{18}O_{sw\text{-}ivc}$ record are not recorded by the Na/Ca proxy. The Na/Ca proxy does not record the decrease in salinity recorded by $\delta^{18}O_{sw\text{-}ivc}$ between *c.* 14 Ma and *c.* 9 Ma but instead records an increase during this time. A steep increase in Na/Ca is recorded between *c.* 6.3 Ma and the end of the record. This was interrupted by a fall in Na/Ca at *c.* 6 Ma. This Late Messinian fluctuation is similar to the fluctuation seen in the $\delta^{18}O_{sw\text{-}ivc}$ based salinity record.

Although the Na/Ca data for the composite temporal record have some similarities to the $\delta^{18}O_{sw\text{-}ivc}$ based salinity record, there are clear discrepancies between the records produced by these two methods. Whilst it is likely that the Late Messinian Na/Ca increase and fluctuation is related to the MSC, it appears that during other parts of the record, Na/Ca in the planktic foraminiferal samples was driven by factors other than salinity. It is unclear which other factors control the Na/Ca values in the composite temporal record, although it is possible that this record reflects seawater calcium concentration (Zhou *et al.*, 2021). The controls on the incorporation of Na into

foraminiferal calcite are complex and are unlikely to be reliable as a proxy for past salinity changes.

The Ba/Ca record was expected to show changes in freshwater input. At times when the basin was isolated, the Ba/Ca might be expected to have an approximately inverse relationship with salinity, as increased freshwater input would reduce the salinity of seawater. In reality, for the majority of the Kottaphi Hill succession, very few changes are recorded in Ba/Ca and no overall trend is present (Figure 5.3.4.1). This is likely to be a result of this part of the succession representing a relatively open ocean setting, where freshwater input was either consistent or had little effect on the local composition of seawater. Small peaks in this part of the record may represent times when continental runoff was increased, so freshwater input had a greater relative impact on seawater composition.

After *c.* 9.2 Ma, Ba/Ca shows relatively high variability (Figure 5.3.4.1). This high variability is likely to indicate some changes in seawater chemistry or circulation patterns. It is likely that the relative amount of freshwater input increased as the depositional environment became shallower, as indicated by the shallowing-upwards sequence inferred from sedimentological observations (Chapter 0). This may also relate to the inferred partial isolation of the basin in which sediments were deposited, as is suggested based on other analyses (B/Ca and Sr isotopes).

The Ba/Ca record shows an increasing trend for the Lapatza Hill succession between 7.90 Ma and the end of the record (5.82 Ma) (Figure 5.3.4.1). This trend indicates greater freshwater input during a time when the $\delta^{18}O_{sw\text{-}ivc}$ record indicates that salinity was increasing, therefore not showing the inverse relationship between Ba/Ca and salinity that was expected. Recent studies from various locations also suggest that

salinity in the Mediterranean region increased between *c.* 6.9 Ma to *c.* 5.96 Ma as part of the preconditioning of the MSC (Bulian *et al.*, 2021; Butiseacă *et al.*, 2022; Kontakiotis *et al.*, 2022). Increased freshwater input suggested by B/Ca data appears incompatible with increasing salinity. However, it is possible that freshwater input contributed a greater relative proportion of seawater in an isolated basin where there was little to no input of seawater from the open ocean. The results of the Ba/Ca analyses are therefore inconclusive; this indicates that the Ba/Ca method is not suitable for the successions examined in this study.

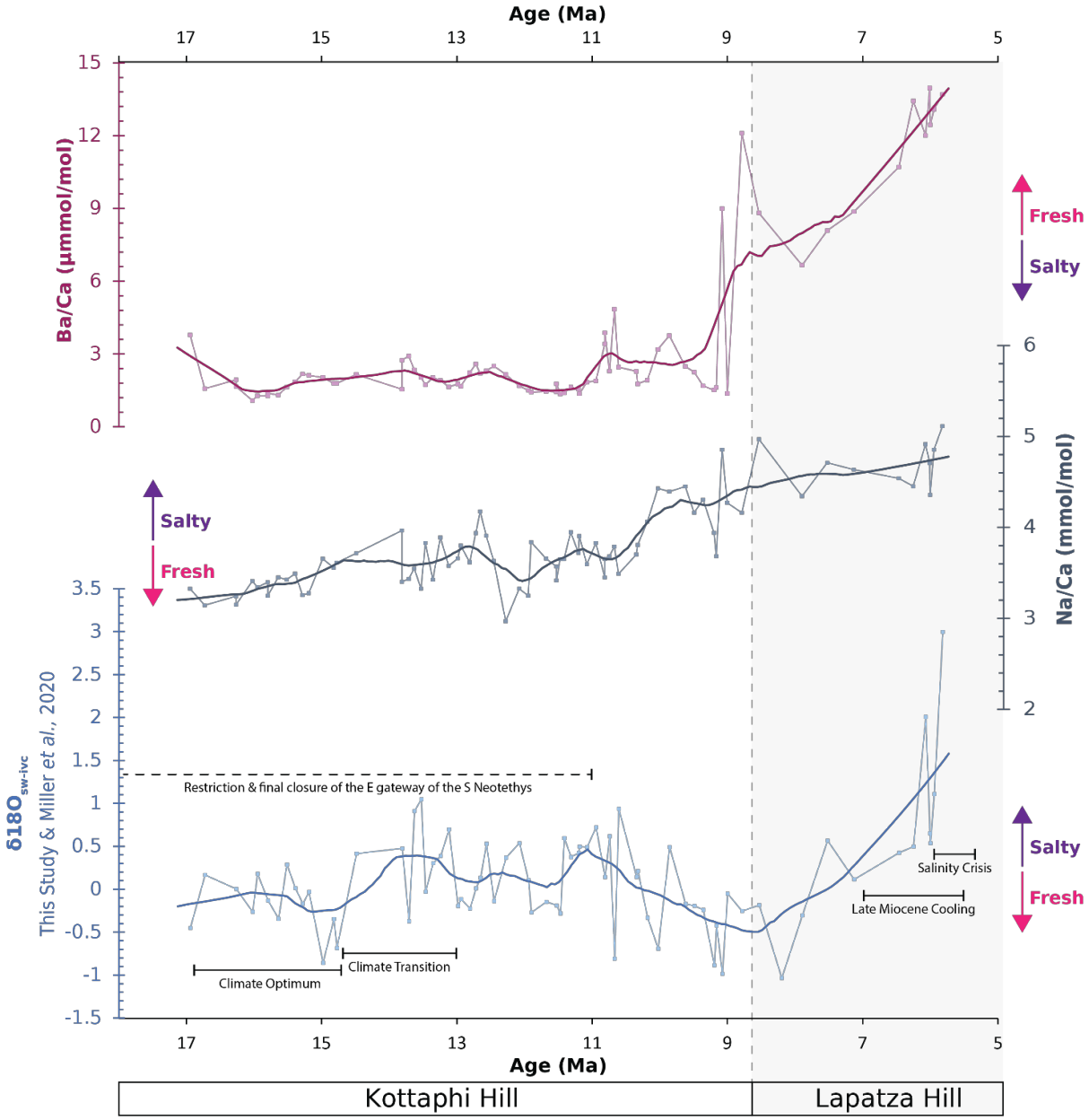


Figure 5.3.4.1- Plot of $\delta^{18}O_{sw\text{-}ivc}$ (blue), Na/Ca (grey) and Ba/Ca (burgundy) versus age for the composite temporal record. Both smoothed and calculated data are shown, as in Figure 5.2.1.1 (see Chapter 5.1.4). The timing of several global to regional scale climatic and ocean circulation changes are also annotated as in Figure 5.3.3.1.

5.4 **Summary of key points**

- A shift in $\delta^{13}C_{finefraction}$ values between the Kottaphi Hill succession and the Lapatza Hill succession is attributed to the larger terrigenous component in samples from the Lapatza Hill succession.

- The Early-Middle Miocene Monterey Event is recorded clearly in the composite temporal record.
- A negative shift in $\delta^{13}C_{planktic}$ values at *c.* 7.2 Ma could correlate to either the global 'Late Miocene Carbon Isotope Shift' or to a regional event due to the partial closure of the Gateway between the proto-Mediterranean Sea and the Atlantic Ocean.
- B/Ca analysis suggests that the $B(OH)_4^-$/DIC of the eastern Mediterranean was similar to that of the open ocean during the Early to Middle Miocene. A long-term increasing B/Ca trend during this interval is inferred to represent decreasing atmospheric pCO_2. An interruption to the long-term increasing B/Ca trend at *c.* 12 Ma corresponds to the Miocene Carbonate Crash.
- $\delta^{18}O_{sw\text{-}ivc}$ data show few changes to salinity during the MCO. Fluctuations in salinity following the MCO are likely to be related to both climatic and ocean circulation changes.
- An increasing salinity trend between *c.* 9 Ma and the end of the composite temporal record (5.74 Ma) is inferred to be a result of partial or periodic isolation of the basin. This is supported by increased variability in $\delta^{13}C$ and B/Ca data during this interval.
- Dramatic salinity fluctuations from 6.3 Ma, which culminated in a steep increase in salinity, are inferred to represent environmental changes prior to the Messinian Salinity Crisis.
- The Na/Ca and Ba/Ca proxies for salinity and freshwater input were not suitable for the successions sampled during this study.

6 Synthesis – Miocene palaeoceanographic evolution of Cyprus in the context of the geological development of the eastern Mediterranean region

This chapter summarises and synthesises the data and interpretations discussed in previous chapters in order to interpret the evolution of palaeoceanographic and climatic conditions during the time span covered by this study. These interpretations also take account of the regional geological and tectonic development of the eastern Mediterranean region. This chapter is organised in chronological order, with discussions separated into geological time periods.

Two summary figures provide context for the discussion made in this chapter. Figure 6.1 shows sketch maps of the regional tectonic setting during the time interval studied in this thesis. Relevant sections and figures from previous chapters are referred to in this chapter, where appropriate. Selected data are displayed in Figure 6.2 which summarises the key data presented in previous chapters.

A series of palaeogeographic reconstructions, which show the inferred evolution of the Mediterranean basins throughout the studied time interval, are also included within the text. These figures are adapted from a recent study on the palaeoceanographic evolution of the Mediterranean area (Cornacchia *et al.*, 2021), which was based on pre-existing data from studies cited earlier in this thesis (e.g. Hüsing *et al.*, 2009; Bialik *et al.*, 2019; Coletti *et al.*, 2019a).

A series of schematic cross-sections, which show the inferred development of the sedimentary basins of Cyprus, are included within the text and summarised in Figure 6.3. These cross-sections focus on the development of the successions studied in this research project in the geological context of Cyprus, and are based on interpretations from this study and pre-existing literature. The majority of these reconstructions are

based on structural and sedimentological field studies (some of which integrate borehole data), supported by biostratigraphic and strontium isotope dating (Robertson and Woodcock, 1986; Robertson *et al.*, 1995; Follows *et al.*, 1996; Lord *et al.*, 2000; Harrison *et al.*, 2004; Kinnaird *et al.*, 2011; McCay, 2011; McCay and Robertson, 2012; McCay *et al.*, 2013). Borehole data (Gass, 1960; Harrison *et al.*, 2004) and seismic studies (Maillard *et al.*, 2011) give additional information on the structural development and provide further context for strata which are not exposed in the field. Two deep boreholes give the most complete known sequences of the Troodos Massif (Kato Lakatamia borehole) and the Kyrenia Range (Lefkoniko borehole) (Harrison *et al.*, 2004 and references cited). A borehole drilled at Xeri (Τσέρι or Tseri) also provides information on the Late Miocene pre-evaporitic and evaporitic sequences beneath the Mesaoria (Mesarya) Basin (Gass, 1960). The nature of the subsurface geology between the Ovgos and Kythrea faults is unclear, as is indicated in these schematic cross-sections. The presence of a buried accretionary wedge beneath the surface in this area has previously been suggested (McCay, 2011; McCay and Robertson, 2012). However, as there is no evidence of this in field study, seismic surveys or borehole data, it is not included in the cross-sections presented in this chapter.

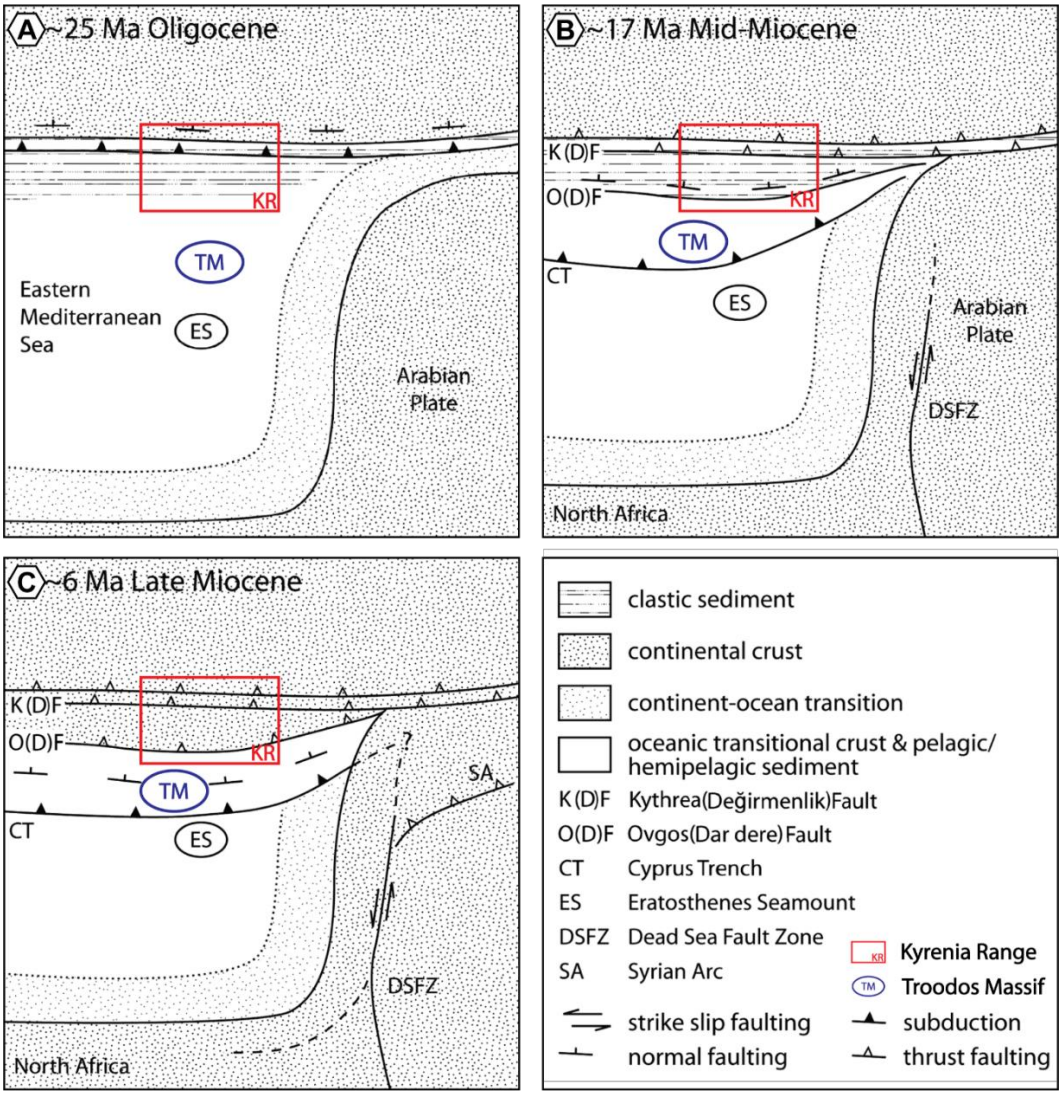


Figure 6.1 – Summary sketch map showing the inferred regional tectonic setting during Late Oligocene to Late Miocene time (modified from McCay and Robertson, 2013). The approximate locations of the Kyrenia Range and Troodos Massif during each time interval are shown.

A) Continental collision between the Tauride allochthons and the Arabian platform had begun during the Late Eocene as indicated by sedimentological evidence of thrusting on the arabic plate in Southeast Turkey (Boulton *et al.*, 2006; Boulton and Robertson, 2008). During the Oligocene, the Kyrenia Range formed the upper plate of a zone of northward convergence, and turbidites accumulated in a deep basin to the south of the range.

B) By the Middle Miocene, the Kythrea (Değirmenlik) Fault had become established. The nature of the Kythrea Fault during this time is not well constrained. The Ovgos (Dar Dere) Fault was also established between the Kyrenia Range and the Troodos Massif by the Middle Miocene.

C) By the late Miocene, suture tightening had resulted in southward thrusting of the Kyrenia Range. The Kyrenia Range was uplifted to form a low-lying island and roll-back-related extension had resulted in normal faulting in the Troodos Massif, leading to the formation of 'half-graben' fault blocks. The Ovgos Fault acted as a 'down-to-the-north' extensional lineament.

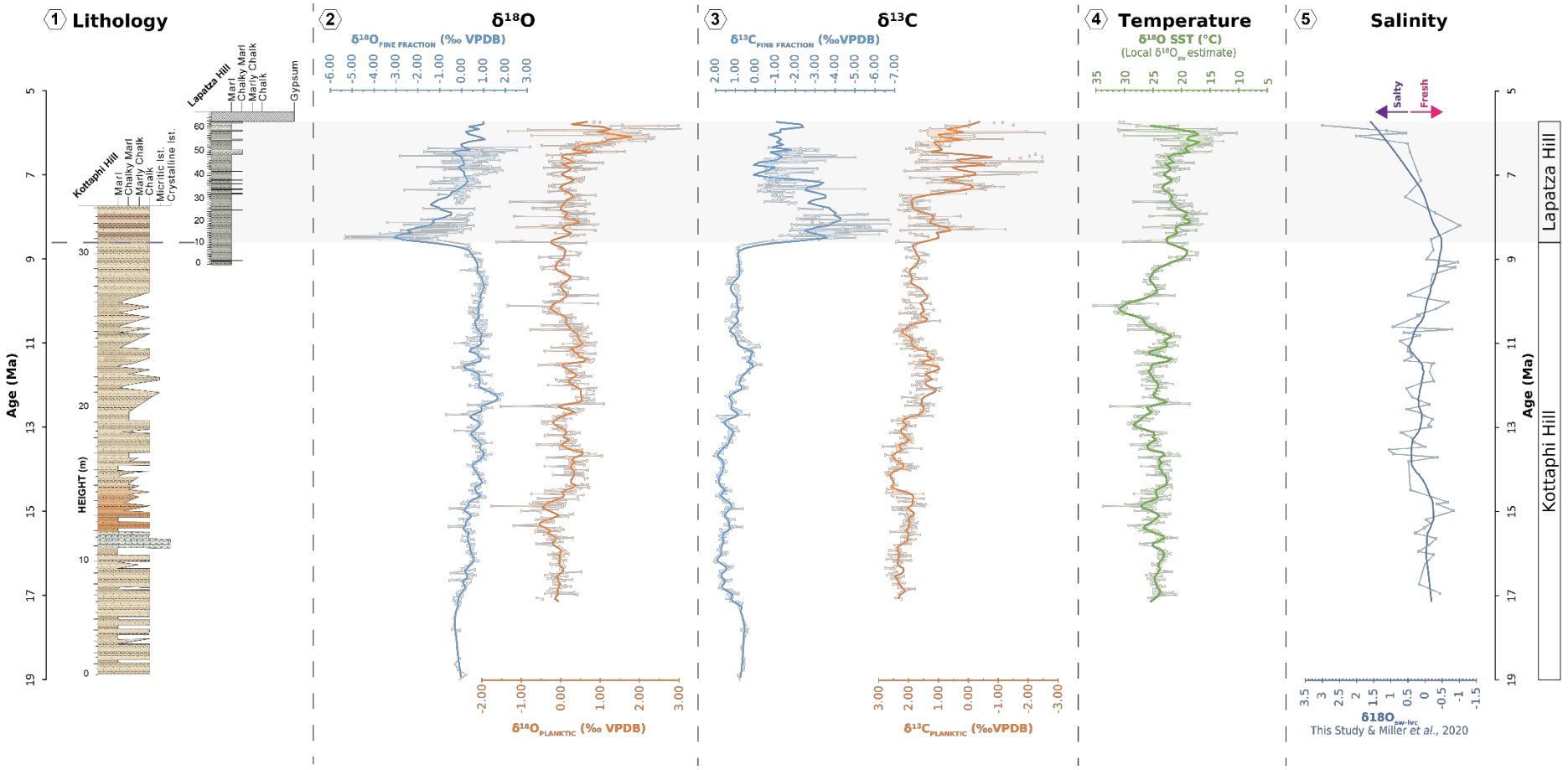


Figure 6.2 – Summary figure showing key data presented in this thesis: (1) Stratigraphic logs of both the Kottaphi Hill succession and the Lapatza Hill succession scaled to age (Chapter 3.2); (2) $\delta^{18}O_{planktic}$ and $\delta^{18}O_{finefraction}$ records for the composite temporal record(Chapter 4.2); (3) $\delta^{13}C_{planktic}$ and $\delta^{13}C_{finefraction}$ records for the composite temporal record(Chapter 5.2); (4) Palaeotemperatures for the composite temporal record, calculated using the Mg/Ca-based local estimation of $\delta^{18}O_{sw}$(Chapter 4.2); (5) $\delta^{18}O_{sw\text{-}ivc}$ salinity record for the composite temporal record (Chapter 5.2). All measured or calculated data are shown with box markers connected by a thin line. Bold lines show these data smoothed by a locally weighted function over 60 kyr.

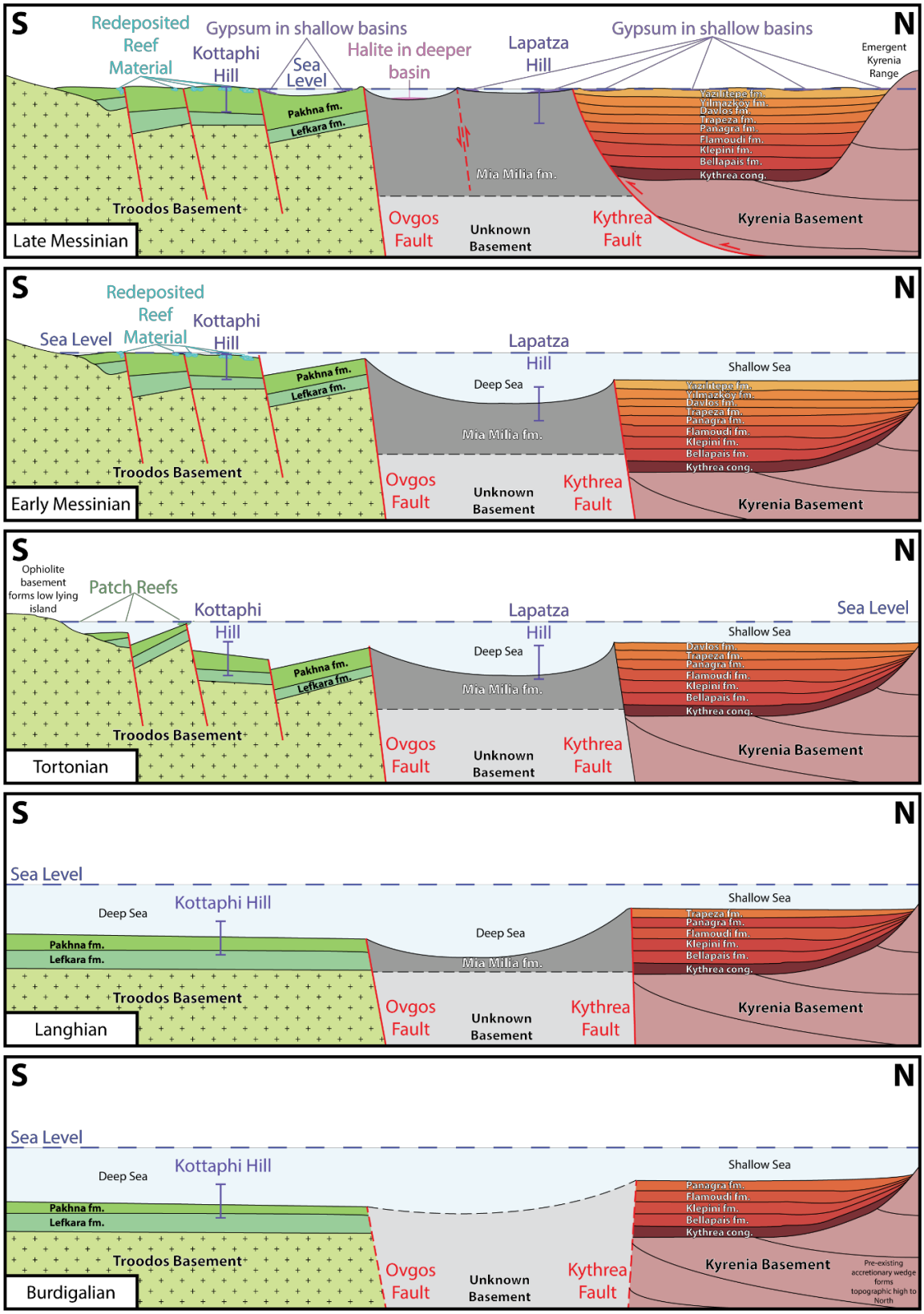


Figure 6.3 – Schematic cross-section of the depositional environments of the sedimentary basins in Cyprus during the Miocene. See introductory text of this chapter and images included in text for information on the basis of interpretations shown.

6.1 **Late Oligocene (Chattian) – 27.82 Ma to 23.03 Ma**

Samples of oyster shell material from Kouroulla Gorge were dated as latest Oligocene (Chapter 3.2.5). This dating supports the existence of an Upper Oligocene shallow-water carbonate shelf in NW Cyprus (Cannings, 2018; Cannings *et al.*, 2020).

The collision of the Arabian and Tauride (Eurasian) plates, which is interpreted to have started during the Eocene (Boulton *et al.*, 2006; Boulton and Robertson, 2007, 2008; Robertson *et al.*, 2016a) continued throughout the Oligocene and into the Early Miocene in this region (Figure 6.1) (McCay and Robertson, 2013). The collision was the result of northward subduction of the Southern Neotethys, which led to a great reduction in the size of the ocean (Şengör and Yilmaz, 1981; Robertson and Dixon, 1984; Şengör *et al.*, 1984; Okay and Tüysüz, 1999; Barrier and Wrielynck, 2008; Robertson *et al.*, 2012a).

In the Kyrenia Range, during the Oligocene, gravity flows resulted in the deposition of the Bellapais (Beylerbeyi) Formation in a basin located above and to the south of deformed Eocene and older units. The Bellapais Formation is rich in ophiolitic lithic fragments (e.g. boninite), which were probably derived from southern and/or southeastern Turkey (McCay, 2011; McCay and Robertson, 2012). In southern Cyprus, the pelagic carbonates of the Upper Lefkara Formation were deposited in a deep basin above older deep-sea sediments, which, in turn, overlie the Troodos ophiolite basement (Robertson and Hudson, 1974; Robertson, 1976). Fossil contourites preserved in the Upper Lefkara Formation in southern Cyprus indicate that bottom water currents were relatively strong and persistent during the Oligocene (Kähler and Stow, 1998; Stow *et al.*, 2002; Miguez-Salas and Rodríguez-Tovar, 2019a; Hüneke *et al.*, 2021; Hernández-Molina *et al.*, 2022). These bottom water currents were likely related to ocean water circulation through the ocean gateway that

linked the Southern Neotethys with the Indian Ocean. This gateway is widely believed to have remained open during the Oligocene (Figure 6.2) (Hüsing *et al.*, 2009; Bialik *et al.*, 2019; Cornacchia *et al.*, 2021). No evidence of such strong bottom water currents is preserved in the Miocene sediments of the Pakhna Formation, possibly because it was deposited following the restriction of the ocean gateway. Strong bottom currents during the Oligocene are a possible explanation for the hiatus in deposition during the Oligocene, noted in locations on the northern margin of the Troodos ophiolite (Davies, 2001). It is likely that the basin in which these Oligocene sediments were deposited formed as a result of ongoing northward plate convergence combined with subduction-related rollback at a trench to the south of Cyprus (Robertson, 1998d; Kinnaird and Robertson, 2013).

6.2 **Early Miocene (Aquitanian and Burdigalian) - 23.03 Ma to 15.97 Ma**

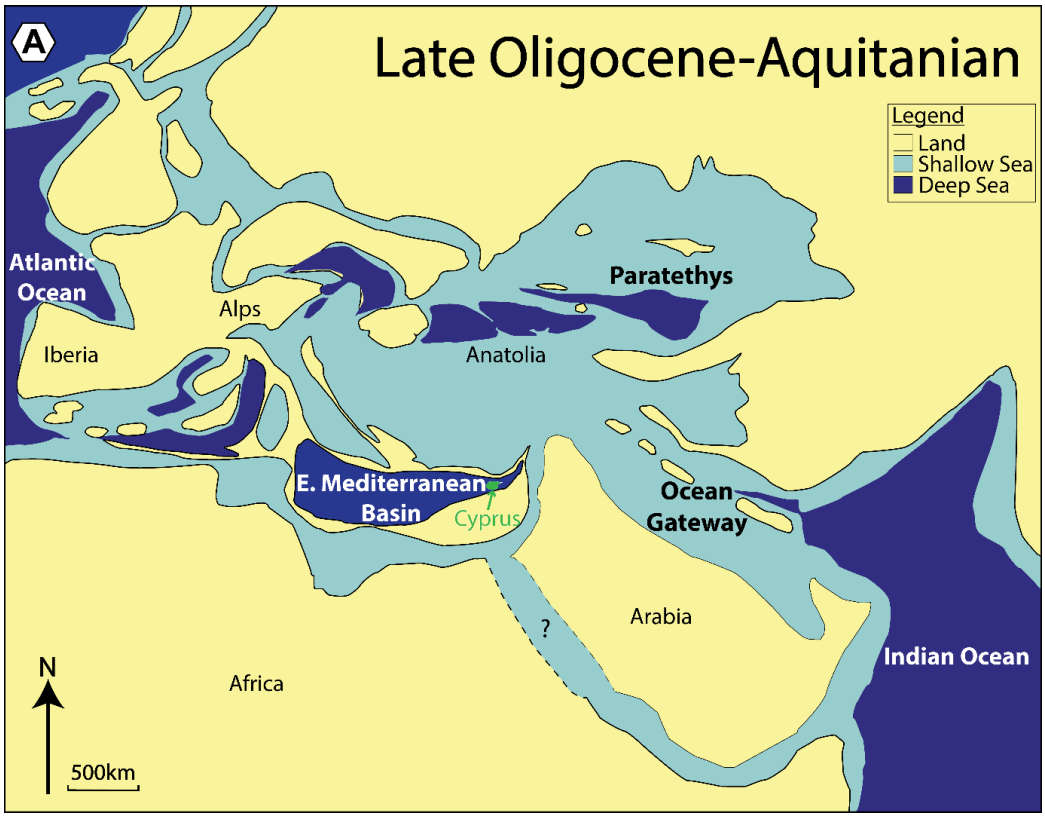


Figure 6.2.1 – Simplified palaeogeographic map of the Southern Neotethys (proto-Mediterranean/Mediterranean) and Paratethys during the Late Oligocene-Aquatanian (Early Miocene). Dark Blue indicates deep basins (modified from Cornacchia *et al.*, 2021).

The *Faviidae sp.* coral sample from the debris-flow deposits at Kouroulla Gorge is dated as Burdigalian (Chapter 3.2.5). This supports an Early Miocene age for the Terra Member reef development phase in NW Cyprus (Follows, 1992; Follows *et al.*, 1996; Cannings *et al.*, 2020; Coletti *et al.*, 2021). The Burdigalian age of this coral sample and the Late Oligocene age of oyster shell deposits in the debris-flow material at Kouroulla Gorge indicate that this material was redeposited *c.* 6-12 My after these organisms had been living. This suggests that the trigger of debris-flow deposition at Kouroulla Gorge was not the same as the trigger that terminated reef development, as had been previously suggested (Cannings, 2018). It is likely that the Early Miocene reef development ended as a result of a complex combination of temperature fall, related glacio-eustatic sea-level changes, regional tectonic subsidence and local tectonic uplift or subsidence (Cannings *et al.*, 2020). More specifically, debris-flow deposition was probably influenced by a combination of global sea level change related to the MMCT, and local-regional-scale tectonics.

There is no evidence of Early Miocene Terra Member reef development along the northern margin of the Troodos Ophiolite. During the Early Miocene, the Kottaphi Hill succession remained in a deep-water setting. The oldest samples collected as part of the composite temporal record in this study are from the Kottaphi Hill succession, the oldest being Burdigalian (18.96 Ma). These samples (facies A in Chapter 3) were not deemed suitable for geochemical analyses of planktic foraminiferal tests, due to the absence and/or poor preservation quality of planktic foraminifera in these samples. Therefore, the samples from 18.96 Ma to 17.08 Ma were only subjected to bulk rock (XRF and XRD) and fine fraction (carbon and oxygen stable isotope) geochemical analysis.

XRF and XRD analyses of a representative chalk sample from within the interval between 18.96 Ma and 17.25 Ma (facies A in Chapter 3) record a relatively small terrigenous component. This is in agreement with the interpretation of a deep marine depositional setting for these sediments, as suggested by field sedimentological observations. The chalk and marl couplets are overlain by a marine firm ground, as reported in previous studies (Davies, 2001; Penttila, 2014). In this study, the units that were deposited between 17.25 and 17.09 Ma, based on the new age model, are interpreted to represent a marine firmground (Chapter 3.3.2). This is because of the relatively low degree of cementation, nodule formation and bioturbation when compared to more fully developed marine hardgrounds (Christ *et al.*, 2015; Cornacchia *et al.*, 2022). It is possible that the reduction in sedimentation rate, which resulted in the formation of the firm ground, was related to regional to global-scale oceanographic changes. The relatively low amount of P_2O_5 identified in a representative sample from the incipient hardground indicates that this is not a phosphatic hardground. Therefore, the upwelling-related phosphogenesis model which has been suggested to have resulted in Burdigalian hardground layers in the central Mediterranean (Cornacchia *et al.*, 2021, 2022) is not compatible with the marine firm ground at Kottaphi Hill. A further possibility, is that a pulse of tectonic uplift inhibited deposition at Kottaphi Hill during this interval, with fine-grained deep-sea sediments being accumulated elsewhere. However, this does not explain the later resumption in pelagic sediment deposition.

Although, as discussed in Chapter 0, the closure of the eastern gateway of the Southern Neotethys may have had an effect on sedimentation in the eastern Mediterranean basins, it is unclear if the formation of the marine firm ground was related to such changes in ocean circulation. It is possible that the formation of the firm ground was related to the onset of the Miocene Climate Optimum (MCO) or the

onset of the Monterey Event. However, further, research (such as in-depth geochemical analysis) on the formation of this firm ground is required to understand the controls on its formation. Coeval firm grounds or hardgrounds are not documented from other locations in Cyprus. The discovery and correlation of other firm grounds (assuming that they exist) could help to better understand the conditions that resulted in firm ground formation.

There is no clear offset in oxygen or carbon stable isotope composition between the lowermost chalk-marl couplets (facies A) and the marine firm ground (facies B in Chapter 3). Bulk fine fraction oxygen stable isotope data record a *c.* 0.3 ‰ decrease between 18.96 Ma and 17.08 Ma, indicating some warming during this interval. $\delta^{18}O_{finefraction}$ values are not suitable for full palaeotemperature calibrations (see Chapter 2.5); however, this *c.* 0.3‰ decrease in $\delta^{18}O_{finefraction}$ may indicate up to 2°C of warming (Chapter 4.3.1). This $\delta^{18}O$ trend is in agreement with a global reference curve (Westerhold *et al.*, 2020). Fine fraction carbon stable isotope data for this interval (18.96 Ma-17.08 Ma) record a slight (*c.* 0.3‰) decrease between 18.96 Ma and 17.73 Ma, followed by a *c.* 0.3‰ increase between 17.73 Ma and 17.08 Ma. This increase is interpreted to represent the beginning of the globally recognised Monterey Event (Vincent and Berger, 1985; Holbourn *et al.*, 2015).

Distinctive reddish marl and chalk couplets (facies C in Chapter 3) overlie the incipient marine firm ground (facies D in Chapter 3) at Kottaphi Hill. Well-preserved planktic foraminifera appear in these reddish marls; therefore, the geochemical record based on the analyses of foraminiferal tests begins at 17.08 Ma.

Palaeotemperature calculations record a warm period (*c.* 23.35°C average) from 17.08 Ma to 14.78 Ma (Langhian). This warm period represents the globally

recognised Middle Miocene Climate Optimum (MCO) (Zachos *et al.*, 2008; Holbourn *et al.*, 2015; Westerhold *et al.*, 2020). The most extreme highs of this warm period took place during the Middle Miocene (Langhian). The warmest interval recorded during the late Miocene was at *c.* 16.15 Ma, when the calculated temperatures reached *c.* 25°C.

The reddish marl and chalk beds contain relatively high levels of terrigenous material (indicated by high levels of Al, Mg, K, Ti, Ba and Si) (Chapter 3.3.2). It is likely that most of this terrigenous material originated in southeastern Turkey, as is inferred from coeval sediments from the Kyrenia Range of northern Cyprus (McCay and Robertson, 2012; Chen and Robertson, 2020; Chen *et al.*, 2022). Some of the terrigenous material could represent enhanced weathering (related to the MCO), including of ultramafic rocks, followed by fluvial run-off from the continental landmasses, resulting from continental collision in southeastern Turkey. It is highly unlikely that much of this terrigenous material was derived from the Troodos ophiolite, as there is no evidence that the adjacent ophiolite was exposed at this time (Follows and Robertson, 1990; Eaton and Robertson, 1993; Penttila, 2014). The reddish colour of the sediments deposited during this time is attributed to high levels of oxidised iron in the sediment. Although the large terrigenous component in these sediments is likely to contribute to Fe_2O_3 levels, some of this Fe_2O_3 is interpreted to represent seawater precipitate. Higher rates of Fe_2O_3 precipitation from seawater may have taken place in strongly oxidising seawaters during an interval of extreme warming (i.e. the MCO). No major trend in salinity changes is indicated by $\delta^{18}O_{sw\text{-}ivc}$ record during the Early Miocene part of the composite temporal record.

An increase in $\delta^{13}C$ values is recorded at *c.* 17 Ma in both the fine fraction and the planktic foraminiferal samples from the Kottaphi Hill succession. This period of high

$\delta^{13}C$ is especially prominent in the $\delta^{13}C_{finefraction}$ record and correlates with the globally recognised Monterey Event. Elevated DIC (due to increased pCO_2) at the onset of the Monterey Event is reported from the Indian Ocean (Sosdian *et al.*, 2020). However, the B/Ca record from the Kottaphi Hill succession does not indicate elevated DIC. This is likely a result of other factors, such as local pH, DIC, salinity or nutrient concentration buffering the effects of the Monterey Event during this time (see Chapter 5.1.2 & 5.3.2).

During the Early Miocene, the collision between the Arabian platform and the Tauride continent reached an advanced stage, with the thrusting of the Tauride allochtons over the Arabian foreland to the south (e.g. Robertson *et al.*, 2016a) (Figure 6.1). This resulted in the elimination of the Southern Neotethys in Southeast Turkey and the termination of the deep water connection to the Indian Ocean, although shallow-marine circulation was still possible (Hüsing *et al.*, 2009; Bialik *et al.*, 2019; Cornacchia *et al.*, 2021) (Figure 6.2.3).

The Kottaphi Hill succession is interpreted to represent a deep marine depositional setting throughout the Early Miocene (Figure 6.2.2). This interpretation is supported by the low sedimentation rates, as calculated using multiple dating methods, the sedimentological information and the indicative benthic foraminiferal assemblages (see Chapter 3.3.2). Sedimentation at Kottaphi Hill does not appear to have been dramatically altered by the ongoing continental collision several hundred kilometres to the east in southeastern Turkey (Figure 6.1). This is mainly because Cyprus remained in a deep-water embayment of the North African continental margin to the east during this time (Robertson *et al.*, 2012a) (Figure 6.1).

In the Kyrenia Range, the Klepini (Arapköy), Flamoudi (Tirmen) and Panagra (Geçitköy) Formations were deposited during the Early Miocene (Figure 6.2.2).

Geochemical and palaeocurrent data indicate that these units contain redeposited material derived from the Tauride allochthons to the northeast and north (McCay and Robertson, 2012). The redeposition of material from the Tauride allochthons was related to the ongoing continental collision.

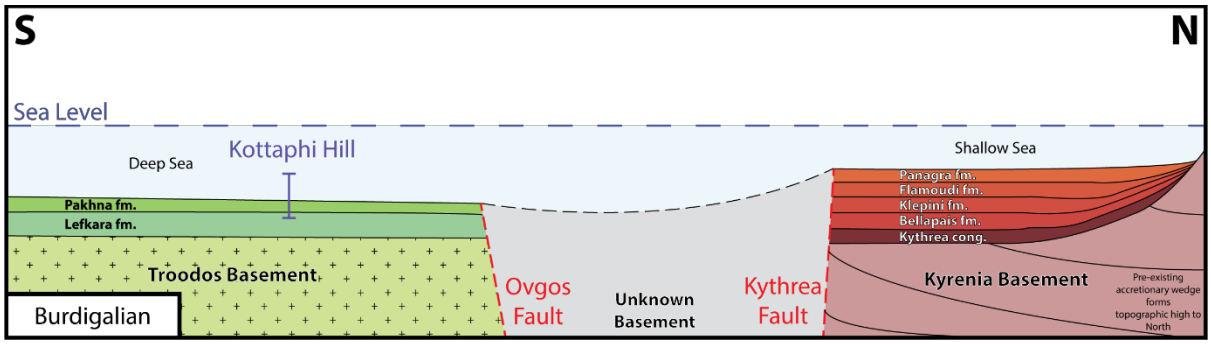


Figure 6.2.2 – Schematic cross-section of the depositional environments of the sedimentary basins in Cyprus during the Burdigalian. Dashed lines indicate faults, contacts or surfaces interpreted with lower levels of confidence. Interpretations of the Ovgos and Kythrea Faults are based on continental drilling studies and subsequent publications (Harrison *et al.*, 2004; Kinnaird and Robertson, 2013). Evidence for the stratigraphy of the Troodos Massif and Kyrenia Range comes from previous field studies supported by continental drilling studies (Robertson, 1976; Follows, 1990; Eaton and Robertson, 1993; Harrison *et al.*, 2004; Kinnaird and Robertson, 2013; McCay *et al.*, 2013). See introductory text to this chapter for additional information about the basis for this schematic model.

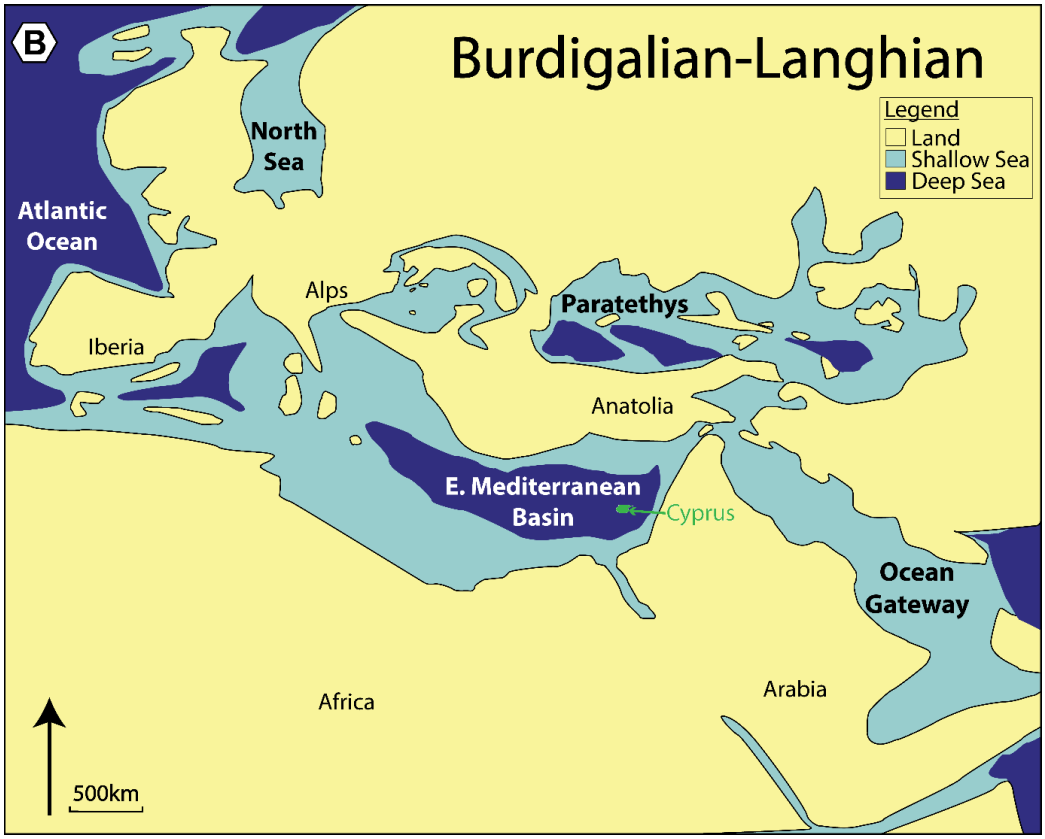


Figure 6.2.3 – Simplified palaeogeographic map of the Southern Neotethys (proto-Mediterranean/Mediterranean) and Paratethys during the Burdigalian-Langhian. Dark Blue indicates deep basins (modified from Cornacchia *et al.*, 2021).

6.3 **Middle Miocene (Langhian and Serravallian) - 15.97 Ma to 11.63 Ma**

The deposition of the reddish marl and chalk couplets in the Kottaphi Hill succession continued during the earliest Middle Miocene. Three extreme warming peaks are recorded in samples from the reddish marl and chalk couplets at the start of the Middle Miocene during the MCO. These three periods of inferred extremely high temperatures at *c.* 15.7 Ma, *c.* 15.3 Ma and *c.* 14.9 Ma correlate with warm peaks on the *c.* 400-kyr eccentricity cycle, as recorded in the Pacific Ocean (Miller *et al.*, 2005, 2020). These peaks are believed to represent times of an ice-free Earth. It has been suggested that the last of these peaks represents the most recent occurrence of an ice-free Earth (Miller *et al.*, 2005, 2020). $\delta^{13}C$ measurements remained high throughout the MCO, although short-lived negative $\delta^{13}C$ excursions are recorded in both fine fraction and

planktic foraminiferal records at *c.* 15.3 Ma and *c.* 14.9 Ma. These negative excursions represent the two latest warming periods of the MCO.

The notable reddish colour of the chalk and marl couplets gradually faded to a buff colour by 14.80 Ma, suggesting a waning in Fe_2O_3 enrichment, potentially indicating less oxidising conditions. XRF and XRD analyses indicate that terrigenous input was also reduced by 14.80 Ma. The small terrigenous component in the chalk and marl couplets deposited between 14.80 Ma and 10.25 Ma (Tortonian) is unlikely to have come from the same North African source as the terrigenous components of the Mamonia Complex (SW Cyprus) or the Troodos Ophiolite. These chalk and marl couplets have high levels of V and low levels of Cr and Zr compared to the other facies at Kottaphi Hill, indicating that the terrigenous component may have come from a different source to the other facies at Kottaphi Hill and the Kyrenia Range sediments (Chapter 3.3.2). It is possible that this terrigenous material came from a more remote source, such as Miocene runoff from the North African Continent (e.g. via the early Nile River). More detailed geochemical analysis would be needed to resolve these alternative possible sources of terrigenous material.

The above lithological change briefly preceded the first step of cooling related to the Middle Miocene Climate Transition (MMCT) (Holbourn *et al.*, 2005; Westerhold *et al.*, 2020) which is recorded at 14.78 Ma in this study. This *c*. 4.5°C inferred fall is indicated by a $\delta^{18}O$ fall, as recorded in both fine fraction and planktic foraminiferal records. This $\delta^{18}O$ fall correlates with Mi3a global $\delta^{18}O$ event (Miller *et al.*, 1991b, 2020). Despite the noted lithological change and the presence of the $\delta^{18}O$ signal of the Mi3a event, no evidence of sea-level fall associated with the start of the MMCT (Miller *et al.*, 1991b, 2020) was identified in the Kottaphi Hill succession. Instead, the basin remained in a deep marine setting throughout the Middle Miocene, deep enough to be relatively

unaffected by sea-level changes. It is likely that the lithological change (i.e. differences in the terrigenous component) is related to the MMCT or the end of high-temperature conditions of the MCO. Global cooling is likely to have altered both continental weathering processes and ocean circulation patterns at this time (Woodruff and Savin, 1989; Wright *et al.*, 1992), resulting in changes in the transport of terrigenous material to the Kottaphi Hill succession. The waning of the source of Fe_2O_3 enrichment is interpreted to be a result of the MMCT with oceanic cooling, resulting in decreased Fe_2O_3 precipitation from seawater. An increase in salinity during this initial cooling step is indicated by $\delta^{18}O_{sw\text{-}ivc}$ calculations. The reason for this increase in salinity is unclear (see Chapter 5.3.3).

Deep-marine sedimentation continued at Kottaphi Hill during the Middle Miocene time interval (Figure 6.3.1). The Kythrea (Değirmenlik) Fault was active during this time and contrasting sedimentary sequences were deposited to the north versus the south of this fault (McCay and Robertson, 2012, 2013). To the south of the Kythrea Fault, the deposition of the Mia Milia (Dağyolu) Formation began in a relatively deep basin that preceded the Pliocene Mesaoria (Mesarya) Basin. To the north of the Kythrea Fault, the clastic Trapeza (Esentepe) Formation, composed of well-organised beds of marl, claystone and fine-grained sandstone, was deposited above claystones, marlstones and rare sandstones of the Panagra Formation (McCay, 2011; McCay and Robertson, 2012) (Figure 6.3.1).

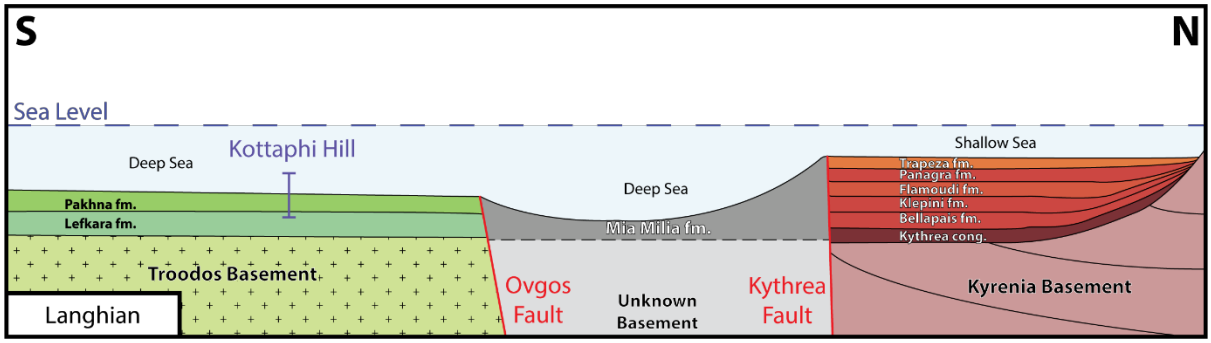


Figure 6.3.1 – Schematic cross-section of the depositional environments of the sedimentary basins in Cyprus during the Langhian. Dashed lines indicate faults, contacts or surfaces interpreted with lower levels of confidence. Interpretations of the structure and stratigraphy are based on previous research cited in the caption of Figure 6.2.2 and the introductory text of this chapter, together with those mentioned in the text of the chapter.

A second step of cooling related to the MMCT is recorded at *c*. 13.7 Ma, corresponding to the Mi3 $\delta^{18}O$ event (Miller *et al.*, 1991b, 2020). This was followed by a distinct warming period until *c.* 12.8 Ma. Although some warming is recorded in open ocean records following the Mi3 $\delta^{18}O$ event (Zachos *et al.*, 1994; Miller *et al.*, 2020; Westerhold *et al.*, 2020), the magnitude of warming recorded in the samples from the Kottaphi Hill succession appears to be unique globally. Analysis of coeval samples elsewhere in the eastern Mediterranean region and elsewhere are required to consider whether this warming represents a regional or local warming event.

At *c.* 13.5 Ma, a gradual decreasing trend in both the $\delta^{13}C_{finefraction}$ and $\delta^{13}C_{planktic}$ records began. This decreasing trend is recorded in several locations globally, related to increased CO_2 drawdown following the high CO_2 conditions of the Monterey Event (Vincent and Berger, 1985; Flower and Kennett, 1993, 1994; Sosdian *et al.*, 2020). An increasing trend in B/Ca during the MMCT indicates a reduction in surface ocean DIC, driven by a reduction in atmospheric pCO_2. This trend is also recorded in Malta (Badger *et al.*, 2013) and the Indian Ocean (Sosdian *et al.*, 2020).

The final step of cooling associated with the MMCT is recorded between 12.8 Ma and 12.42 Ma. This cooling corresponds with the Mi4 $\delta^{18}O$ event. Two micritic limestone firmground layers, separated by the first organic carbon-rich marl layer noted at Kottaphi Hill, were deposited during this time. These lithologies, together with benthic foraminiferal assemblages and low V/Al and Mo/Al ratios suggest extremely low sedimentation rates in a low oxygen environment during this time interval. Stronger oxygen minimum zone conditions related to increased productivity and upwelling have previously been suggested during the MMCT (Nathan and Leckie, 2009; Tian *et al.*, 2014; Hess *et al.*, 2023).

At *c.* 12 Ma, a fall in $\delta^{13}C_{planktic}$ and $\delta^{13}C_{finefraction}$ and B/Ca is recorded in the Kottaphi Hill succession. This event coincided with the Miocene Carbonate Crash (Holbourn *et al.*, 2018, 2021; Lübbers *et al.*, 2019; Preiss-Daimler *et al.*, 2021), a global event which has been related to the reorganisation of global ocean circulation patterns as a result of the formation of the Isthmus of Panama (see Chapter 1.2.3) (Lyle *et al.*, 1995). The deposition of carbonate material continued in the Kottaphi Hill succession throughout the Miocene Carbonate Crash. Towards the top of this part of the Kottaphi Hill succession, darker marl beds were noted (Chapter 3.2.1). The darker colour of these marl beds may indicate that these beds are rich in organic material. However, these marl beds are not as clearly enriched in organic material as the 'ghost sapropels' documented in the overlying units (see below). The oxic decomposition of organic material has previously been related to increased $CaCO_3$ dissolution during the Miocene Carbonate Crash in the Mediterranean (Torfstein and Steinberg, 2020).

Following the Miocene Carbonate Crash, B/Ca began to increase in planktic foraminifera samples from the Kottaphi Hill succession, until the earliest Late Miocene (*c.* 9.6 Ma). This increasing B/Ca trend is interpreted to correspond to decreasing

pCO_2 in relation to global cooling and glacial expansion (see Chapter 5.3.2). Both $\delta^{13}C_{planktic}$ and $\delta^{13}C_{finefraction}$ also rise, following the fall associated with the Miocene Carbonate Crash.

The collision between the Arabian platform and the Tauride continent was complete by the Middle Miocene (Figure 6.1); however, sediment supply to the eastern Mediterranean basins from the Tauride allochtons continued from emergent crust (Robertson *et al.*, 2004, 2006, 2016a; McCay and Robertson, 2013). Connectivity between the eastern Mediterranean basins and the Indian Ocean had effectively ended by this time (Figure 6.3.2) (Robertson *et al.*, 2006; Hüsing *et al.*, 2009; Cornacchia *et al.*, 2021). By the Tortonian, the Southern Neotethys was reduced to the present-day eastern Mediterranean basin; connectivity with the Atlantic Ocean was retained through the western Mediterranean (Figure 6.3.2).

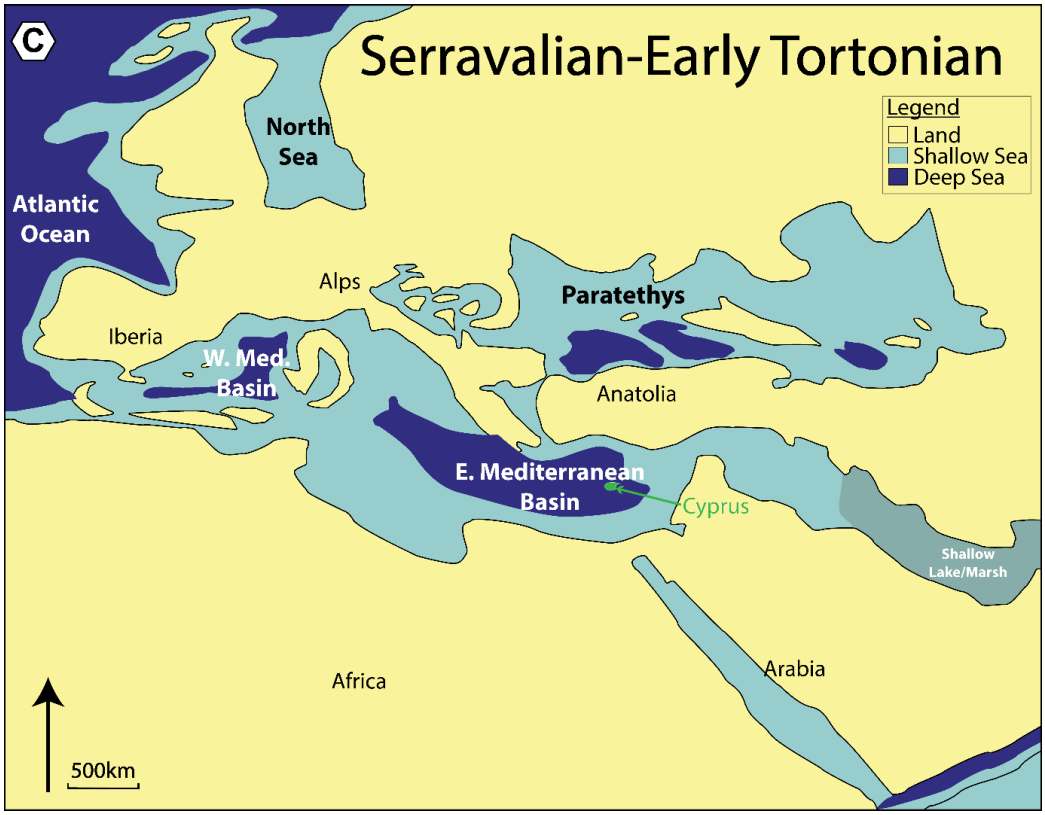


Figure 6.3.2 – Simplified palaeogeographic map of the proto-Mediterranean/Mediterranean and Paratethys during the Serravalian-Early

Tortonian. Dark Blue indicates deep basins (modified from Cornacchia *et al.*, 2021).

6.4 **Late Miocene (Tortonian and Messinian) - 11.63 Ma to 5.33 Ma**

No clear changes in stratigraphic or geochemical records were observed at the boundary between the Middle and Late Miocene (Serravallian-Tortonian boundary).

At 11.4 Ma, a short excursion to colder temperatures is recorded. This event is also documented in both $\delta^{18}O_{planktic}$ and $\delta^{18}O_{finefraction}$, and corresponds with the Mi5 $\delta^{18}O$ event (Miller *et al.*, 1991b). This cooling event was followed at 11.2 Ma by another cooling event, which resulted in the calculated low temperatures of 19.05°C at 10.85 Ma.

At *c.* 10.8 Ma, a dramatic warming event is recorded in samples from the Kottaphi Hill succession. This warming continued until *c.* 10.2 Ma, with the peak temperature estimated as 34.24°C. A small excursion to heavier $\delta^{13}C$ was also recorded in both the fine fraction and the planktic foraminiferal samples during this time. The warming event corresponds to the Tortonian Thermal Maximum (Westerhold *et al.*, 2020). In the composite temporal record of this study, this warming is extreme and relatively long lasting (*c.* 0.6 Ma). The Tortonian Thermal Maximum is recorded in the Pacific Ocean as a transient warming event, which ended after less than 100kyr (Holbourn *et al.*, 2013). A longer-lasting warming event is recorded in the Atlantic Ocean (Lear *et al.*, 2003), which can be correlated with the event observed in the eastern Mediterranean. However, the warming calculated in this study during this interval is more extreme than that recorded in any other records globally. Previous research (Lear *et al.*, 2003) has suggested that, during this time interval, changes in ocean circulation patterns (see Chapter 4.3.3) resulted in the Pacific and Atlantic Oceans experiencing discrete climatic events. The similarity between palaeotemperature

records in the eastern Mediterranean and the Atlantic Ocean is to be expected, as by this time, circulation between the proto-Mediterranean and the Pacific Ocean had been lost (Hüsing *et al.*, 2009; Bialik *et al.*, 2019; Cornacchia *et al.*, 2021). The higher magnitude of the warming event recorded in the eastern Mediterranean and the Atlantic Ocean may be attributed to further changes in ocean circulation patterns. However, more data from surrounding localities in the eastern Mediterranean region together with other Atlantic and Mediterranean sites are required for a complete understanding of the nature of this apparent extreme warming event.

Previous research (Penttila, 2014) indicated that the first occurrence of Troodos ophiolite-derived material is preserved in sediments deposited at *c.* 10.6 Ma. This indicates that by this time the Troodos ophiolite had been uplifted enough to emerge from the seafloor at least locally (discussed further below).

At 10.25 Ma, a change in lithology is recorded in the Kottaphi Hill succession. After this time (until *c.* 7.72 Ma), chalky marl beds are interbedded with thin marl beds. Several of these soft marl beds have a distinctive dark reddish brown colour; these are interpreted as sapropels that have been modified by post-depositional oxidation, also known as ‘ghost sapropels’ (Higgs *et al.*, 1994; Kroon *et al.*, 1998; Penttila, 2014). The presence of neritic to shallow-marine benthic foraminifera (*Elphidium spp.*) within a benthic foraminiferal assemblage that is otherwise indicative of an outer shelf to bathyal depositional environment indicates increased input of material from shallow water settings. The increased presence of shallow water material likely indicates that the Kottaphi Hill succession was relatively close to a shallow water environment by this time. This is consistent with the sedimentological evidence of the beginning of shallowing in the Kottaphi Hill succession (e.g. input of neritic debris) (see Chapter 3.3.2).

Two steps of cooling are recorded in the samples from the Kottaphi Hill succession at *c.* 9.9 and *c.* 9 Ma. This stepped cooling correlates with cooling in the western Pacific, which has been related to Antarctic glacial expansion (Holbourn *et al.*, 2013). Therefore, this cooling event marks an apparent return to a globally controlled climate recorded in the Kottaphi Hill succession, therefore possibly indicating the end of disequilibrium between the Pacific Ocean and the Atlantic Ocean (and by extension the proto-Mediterranean Sea). This stepwise cooling marks the beginning of a longer-term cooling trend in the composite temporal record, which lasted until *c.* 6 Ma.

At *c.* 9 Ma, the $\delta^{18}O_{sw\text{-}ivc}$ record indicates the onset of a long-term increasing salinity trend. This increasing salinity trend began *c.* 2 Ma before any other known evidence of salinity increase prior to the Messinian Salinity Crisis (MSC) (Bulian *et al.*, 2021; Butiseacă *et al.*, 2022; Kontakiotis *et al.*, 2022), and is therefore unexpected. The early onset of this salinity trend may be related to the partial isolation of the eastern Mediterranean basins during the Tortonian (see below). Changes in the seawater chemistry (such as Sr isotope composition) during the Tortonian have previously been related to the partial isolation of Mediterranean basins, especially in marginal basins near land (Flecker and Ellam, 1999, 2006; Flecker *et al.*, 2002; Cornacchia *et al.*, 2021).

After 8.6 Ma (the splice point), the data used in the composite temporal record is taken from the Lapatza Hill succession rather than the Kottaphi Hill succession. Samples deposited after this point at Kottaphi Hill were still collected and examined; however, they are not included in the composite temporal record.

The deposition of chalky marl with intermittent sapropelic beds continued at Kottaphi Hill until 7.72 Ma. After this time, exposure is very limited; however, this interval of

limited exposure is interpreted to represent a time of mainly muddy marl deposition. This, together with occasional calcarenite debris-flow units in patchy exposures, is consistent with upward shallowing. Shallowing during this interval is supported by the presence of a poorly sorted benthic foraminifera and coralline algae-rich calcarenite above the interval of poor exposure. This interval has previously been the subject of in-depth study of neritic biota (i.e. large benthic foraminifera and calcareous algae) (Coletti *et al.*, 2021), and is interpreted to comprise material that was transported downslope from the lowermost photic zone to the outer shelf. This calcarenite is, in turn, overlain by a talus breccia which preserves reef debris from the Koronia Member poritid coral reef. This breccia is interpreted to have been transported a short distance from a nearby patch reef, specifically the *in situ* reef deposit at Kreatos Hill, *c.* 1km to the East of Kottaphi Hill (Follows and Robertson, 1990; Follows *et al.*, 1996). The upper part of the Kottaphi Hill succession is, therefore, interpreted to represent a shallowing-upward sequence. This shallowing is in agreement with previous research which indicated that reef growth during the Tortonian in Cyprus was controlled by uplift related to regional tectonics (Follows, 1990; Follows and Robertson, 1990; Follows *et al.*, 1996; Kinnaird *et al.*, 2011).

During the Tortonian, early uplift of the Troodos ophiolite resulted in the formation of a low-lying island which locally exposed ophiolitic basement (Robertson, 1976) (Figure 6.4.1). Structural studies specifically indicate that ophiolitic basement rocks were locally exposed along the northern margin of the Troodos ophiolite, related to the back-rotation of fault blocks which formed in an extensional tectonic regime (Follows, 1992; Follows *et al.*, 1996; Robertson and Kinnaird, 2016). Patch reefs grew on the uplifted fault blocks of ophiolitic basement on the northern margin of the ophiolite. Talus from

these reefs and reworked shallow water material was redeposited down-slope during Tortonian time (Figure 6.4.1).

In northern Cyprus, deposition of the hemipelagic Mia Milia Formation continued to the south of the Kythrea Fault, while extremely thick-bedded gravity flows of the Davlos (Kaplica) Formation were deposited to the north of the fault (Figure 6.4.1).

In southeastern Turkey, there was an important episode of re-thrusting during the Late Miocene. This thrusting has been explained by suture tightening in the Tauride thrust belt, sometime after the collision of the Tauride continent with the Arabian platform during the Early Miocene (Robertson *et al.*, 2004, 2006). This resulted in increased clastic run-off, as exemplified by the Davlos Formation in the Kyrenia Range (McCay, 2011; McCay and Robertson, 2012, 2013). This convergence also resulted in major Late Miocene thrusting in the Kyrenia Range (see below).

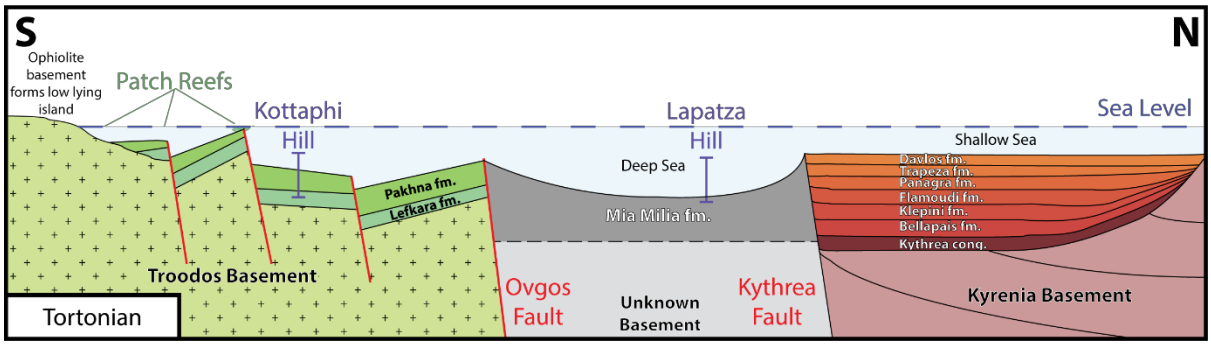


Figure 6.4.1 – Schematic cross-section of the depositional environments of the sedimentary basins in Cyprus during the Tortonian. Dashed lines indicate faults, contacts or surfaces interpreted with lower levels of confidence. Interpretations of the structure and stratigraphy are based on previous research cited in the caption of Figure 6.2.2 and the introductory text of this chapter, together with those mentioned in the text of the chapter. Subduction roll-back-related extension had started to the south of the Ovgos Fault by this time. The uplift, faulted blocks and reef development shown on the Troodos Massif are based on previous studies cited in text (e.g. Robertson, 1976; Follows, 1992; Follows *et al.*, 1996; Robertson and Kinnaird, 2016).

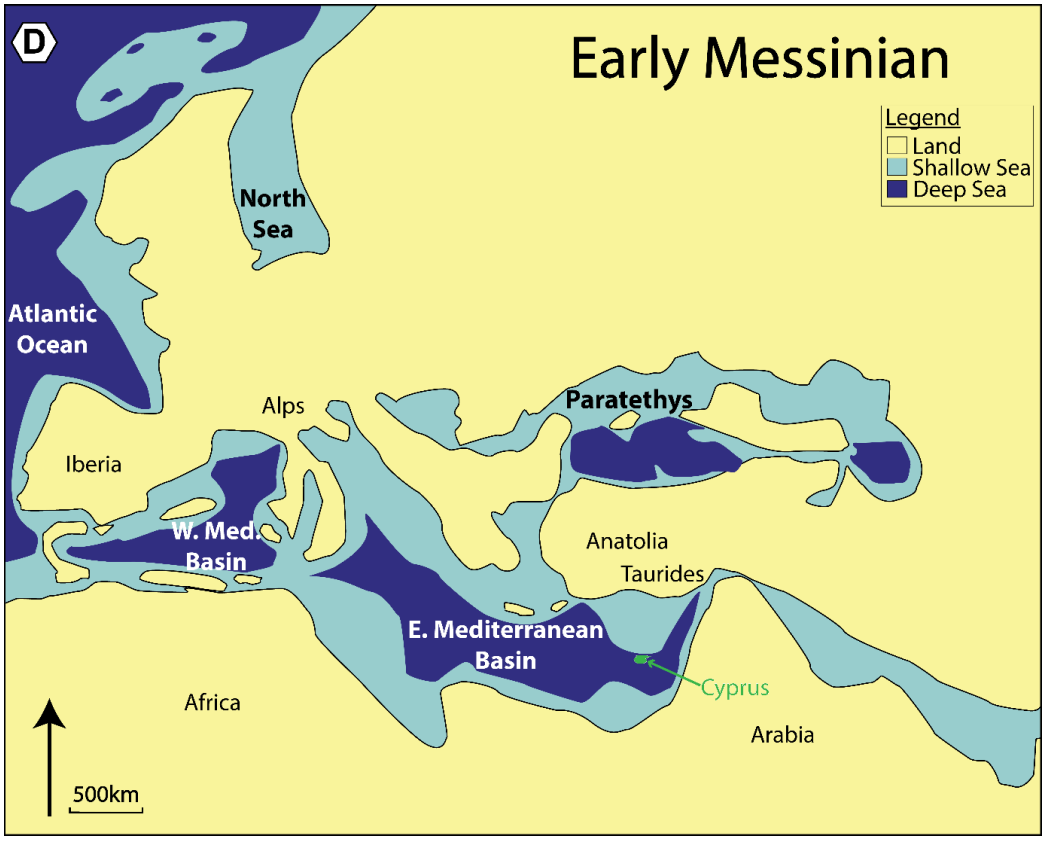


Figure 6.4.2 – Simplified palaeogeographic map of the proto-Mediterranean/Mediterranean and Paratethys during the Early Messinian. Dark Blue indicates deep basins (modified from Cornacchia *et al.*, 2021).

At the splice point (8.6 Ma), a dramatic offset is noted in the fine fraction $\delta^{18}O$ and $\delta^{13}C$ records. This offset is interpreted to be mainly the result of the relatively large terrigenous component in the Lapatza Hill succession compared to the Kottaphi Hill succession (See Chapter 4.3.1 & 5.3.1). A large terrigenous component in the Lapatza Hill succession is indicated by XRD analysis and is supported by the high calculated sedimentation rates. The terrigenous component is especially high near the base of the succession. This difference in terrigenous input highlights the difference in depositional setting between the Kottaphi Hill succession which was relatively isolated from terrigenous input, and the Lapatza Hill succession which had substantial terrigenous input related to ongoing supply to depocentre areas.

Samples were collected and examined from the basal part of the Lapatza Hill succession, which was deposited prior to the splice point (8.6 Ma). However, these samples are not included in the temporal composite record. There is no distinct difference in lithology between the sediments deposited before the splice point at Lapatza Hill and the samples deposited after the splice point. The lowermost samples already have a large terrigenous component.

The relatively high amount of terrigenous material in the oldest part of the Lapatza Hill succession is attributed to the effects of regional tectonics (as discussed above). High levels of sediment input from the Tauride allochthons in southeastern Turkey resulted in turbidite deposition across northern Cyprus and this continued during the Late Miocene (McCay, 2011; McCay and Robertson, 2012).

The large terrigenous component found within the lower part of the Lapatza Hill succession is probably specifically related to the deposition of the Davlos (Kaplica) Formation, which was deposited nearby, to the north of the Kythrea Fault during this time (McCay, 2011; McCay and Robertson, 2012). The gravity-flow deposits of the Davlos Formation are rich in terrigenous material (McCay, 2011; McCay and Robertson, 2012). It is likely that, during this time of high terrigenous input to the north of the Kythrea Fault, an increased amount of terrigenous material was also deposited in adjacent basins, as exemplified in the Lapatza Hill succession.

The source of this terrigenous input is interpreted to have waned during the Late Miocene, resulting in a transition from turbidite deposits to mudrocks and eventually a reduced terrigenous component, as noted in the upper part of the Lapatza Hill succession. It is likely that this reduction in terrigenous supply was caused by the

denudation of the emplaced Tauride thrust belt in southeastern Turkey (Robertson *et al.*, 2013) and/or the early uplift of Cyprus.

The long-term cooling trend recorded from *c.* 10 Ma onwards in the Kottaphi Hill succession is also recorded in the Lapatza Hill succession. The increasing salinity trend recorded from *c.* 9 Ma in the Kottaphi Hill succession also continued in the Lapatza Hill succession.

At 7.2 Ma $\delta^{13}C_{planktic}$ data record a dramatic shift (*c.* 2.5 ‰) to lighter carbon isotope values. This may relate to the Late Miocene Carbon Isotope shift (LMCIS) (Dickens and Owen, 1999; Diester-Haass *et al.*, 2005; Holbourn *et al.*, 2015, 2018; Tzanova *et al.*, 2015; Herbert *et al.*, 2016; Lyle *et al.*, 2019) and the onset of the Late Miocene-Early Pliocene Biogenic Bloom (Dickens and Owen, 1999; Diester-Haass *et al.*, 2004, 2005). However, after this point in time, the $\delta^{13}C_{planktic}$ data from the composite temporal record does not reflect the open ocean record from the North Atlantic (Cramer *et al.*, 2009). This difference suggests that after *c.* 7.2 Ma, the $\delta^{13}C$ composition of seawater in the eastern Mediterranean basins was no longer closely related to global $\delta^{13}C$ changes. A shift to lighter $\delta^{13}C$ values is also recorded in the West Alborian Basin (Western Mediterranean). This shift, at 7.17 Ma, has been related to the restriction of the Mediterranean-Atlantic gateway (Bulian *et al.*, 2022) and is associated with a change in benthic foraminiferal assemblages. Reduced abundance of benthic foraminifera, together with a reduction in species diversity, are recorded at 7.23 Ma in the Lapatza Hill succession. It is possible that the $\delta^{13}C$ shift and benthic foraminifera assemblage changes recorded at Lapatza Hill relate to the changes noted in the Western Mediterranean. It is difficult to distinguish between the effects of the LMCIS and the regional changes recorded in the Mediterranean region during this time (e.g. Mediterranean-Atlantic gateway closure). However, the lack of similarity between

the $\delta^{13}C$ records from the Lapatza Hill succession and the open ocean after this point in time may indicate that regional changes are more likely to have affected the eastern Mediterranean basins during this interval. Ocean chemistry changes recorded in the temporal composite succession in this study appear to have been decoupled from global changes during this time, suggesting that ocean chemistry in the eastern Mediterranean was locally controlled in the latest Late Miocene.

Between 7 Ma and 6 Ma, extreme cooling is recorded in samples from the Lapatza Hill succession. This extreme cooling trend is in agreement with records from several locations around the world, including $U^{K}_{37'}$ records from the central Mediterranean (Tzanova *et al.*, 2015) and the North Atlantic (Herbert *et al.*, 2016). This cooling event has previously been termed 'Late Miocene Cooling' and has been related to reduced atmospheric CO_2 levels (Herbert *et al.*, 2016). This reduction in CO_2 was possibly related to increased drawdown as a result of ocean circulation changes after the closure of the Atlantic-Mediterranean gateway (Herbert *et al.*, 2016; Capella *et al.*, 2019; Tanner *et al.*, 2020). The effects of such a reduction in atmospheric CO_2 are not clear in the B/Ca or $\delta^{13}C$ records from the Lapatza Hill succession; however, this is likely to have been a result of the high variability shown in both records during this time interval. This high variability suggests that local effects (e.g. local hydrography and/or nutrient and sediment supply) had a major control on seawater and carbonate chemistry. Locally controlled oceanographic conditions are consistent with the interpretation of partial isolation of the basin during this time.

Uplift of some parts of the Troodos ophiolite continued into the Messinian, resulting in the local uplift of the ophiolite basement within fault blocks along the northern margin of the ophiolite (Figure 6.4.3). Tortonian reef material was redeposited and underwent subaerial exposure and karstic weathering on these uplifted fault blocks (Follows,

1990; Follows *et al.*, 1996). The Mia Milia Formation continued to be deposited in a relatively deep basin between the Ovgos (Dar Dere) Fault and the Kythrea Fault during the Early Messinian, as preserved in the Lapatza Hill succession (Figure 6.4.3). North of the Kythrea Fault, the relatively fine-grained argillaceous sediments of the Yılmazköy Formation and the overlying Yazılıtepe Formation had been deposited by the Early Messinian. The nature of the original relationship between the Yılmazköy Formation and the Davlos Formation, which lies beneath it, remains poorly understood. Biostratigraphic and strontium isotope dating indicates a hiatus in deposition to the north of the Kythrea Fault during the Early Messinian (McCay, 2011; McCay and Robertson, 2012).

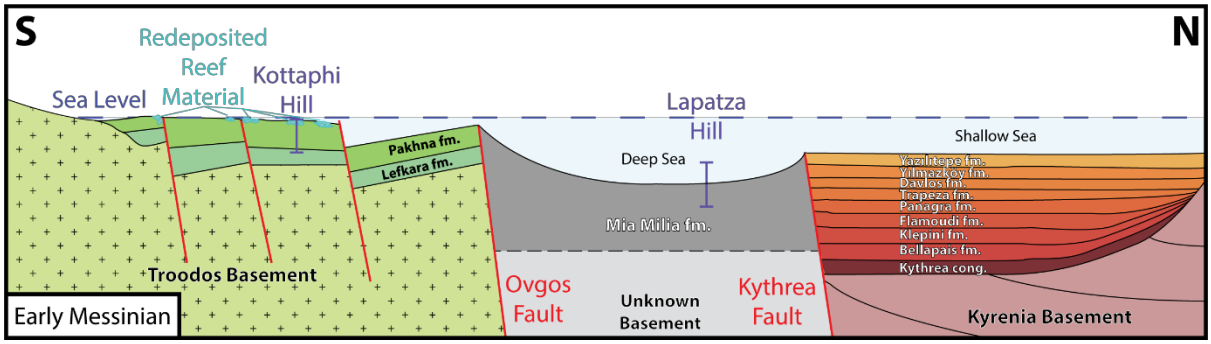


Figure 6.4.3 – Schematic cross-section of the depositional environments of the sedimentary basins in Cyprus during the Early Messinian. Dashed lines indicate faults, contacts or surfaces interpreted with lower levels of confidence. Interpretations of the structure and stratigraphy are based on previous research cited in the caption of Figure 6.2.2 and the introductory text of this chapter, together with those mentioned in the text of the chapter. Reef development on the Troodos Massif had ended by this time, uplifted fault blocks and reef material were uplifted close to, or above sea level (Follows *et al.*, 1996; Kinnaird *et al.*, 2011).

After 6.56 Ma, benthic foraminifera are absent in samples from the Lapatza Hill succession. This is interpreted to be a result of the stratification of the marine water column which resulted in uninhabitable bottom waters. Bottom-water redox changes are also indicated throughout the deposition of the Lapatza Hill succession by the accumulation of manganese oxide-rich layers together with subordinate iron oxide-rich

layers (Chapter 3.3.3). Similar layers accumulated during the same stratigraphic interval in the far northeast of Cyprus in the Karpas Peninsula. There, these layers have been interpreted as the result of manganese run-off from the then-emergent Kyrenia Range into a semi-isolated basin that was subject to fluctuating redox conditions. In outline, dissolved manganese accumulated in low-oxygen water conditions, followed by precipitation during switches to more oxygen-rich conditions (controlled by changing climate and or bottom currents) (Robertson *et al.*, 2019). Partial basin isolation is also indicated by the absence of discoasters and the reduced abundance of planktic foraminifera in the upper part of the Lapatza Hill succession. An absence of discoasters in the Upper Messinian elsewhere in Cyprus has been related to increased salinity and fluctuations in nutrient supply (Wade and Bown, 2006). Taken together, increased salinity and fluctuations in nutrient supply are indicative of basin isolation; the reduction in planktic foraminiferal abundance may also be attributed to these factors.

At 6.3 Ma, the increasing salinity trend indicated by $\delta^{18}O_{sw\text{-}ivc}$ steepened, indicating a period of extreme salinity increase. This extreme increase in salinity is in agreement with the reported timing of salinity increase prior to the MSC ('preconditioning') (Bulian *et al.*, 2021; Butiseacă *et al.*, 2022; Kontakiotis *et al.*, 2022). This increasing salinity trend was briefly interrupted by a trend towards fresher water at *c.* 6 Ma. An approximately coeval decreasing $\delta^{18}O_{sw\text{-}ivc}$ trend is also recorded at this time elsewhere in the Mediterranean (Vasiliev *et al.*, 2019), which can be attributed to increased freshwater input to the eastern Mediterranean basins, mainly from the African continent (i.e. the River Nile). Salinity is then indicated to have increased rapidly towards the end of the composite temporal record.

The salinity increase recorded in the latter part of the composite temporal record culminated in the end of the sequence of hemipelagic sediments which could be sampled and the start of the first thick (*c.* 15 cm) gypsum deposit.

Evaporites were deposited in deep basins around Cyprus during the MSC (Clauzon *et al.*, 1996; Lofi *et al.*, 2005; Roveri *et al.*, 2008). The majority of the evaporite material reported from Cyprus is gypsum, although the composition of evaporite deposits identified through offshore seismic study remains unclear (Maillard *et al.*, 2011).

In Cyprus, generally, the Messinian evaporites are mainly composed of gypsum (Baroz and Bizon, 1974; Robertson, 1977a; Baroz *et al.*, 1978). Sedimentological studies show that this gypsum accumulated in small fault-controlled basins around the Troodos massif (Robertson *et al.*, 1995, 2009). The gypsum succession in the south of Cyprus has recently been correlated with the 'three-stage model' proposed for Messinian evaporite deposition: (1) Primary Lower Gypsum; (2) Re-sedimented Lower Gypsum; (3) Upper Gypsum (Roveri *et al.*, 2014; Manzi *et al.*, 2016; Artiaga *et al.*, 2021). This simple correlation is, however, open to question because it does not take account of the specific tectonic setting of south Cyprus which strongly controlled gypsum deposition.

The evaporitic successions in northern Cyprus are somewhat different from those in southern Cyprus (Varol and Atalar, 2017; Artiaga *et al.*, 2021). Also, the succession preserved in northern Cyprus, including the Lapatza Hill succession studied, does not fit the 'three-stage model'. Specifically, the Upper Gypsum is absent from the evaporitic succession in northern Cyprus (Artiaga *et al.*, 2021).

Messinian-aged halite has been identified through exploration drilling of the Mesaoria Basin in Cyprus. The Xeri borehole (*c.* 10 km south of Nicosia) revealed that 296 m of

halite overlies a sequence of grey marls with anhydrite beneath the centre of the Mesaoria Basin (Gass, 1960; Robertson *et al.*, 1995). A small fault-bounded deep basin has been suggested as the setting for the local halite deposition in Cyprus (Harrison *et al.*, 2004) (Figure 6.4.4). This deep basin was located on the northern side of the Ovgos Fault and is the only locality in Cyprus where the presence of halite is reported. Elsewhere in Cyprus, it appears that shallow basins hosted Gypsum deposition during the MSC, as preserved at the top of the Lapatza Hill succession (Figure 6.4.4).

An apparent warming event is recorded in the latest part of the composite temporal record, shortly before the deposition of gypsum at Lapatza Hill. However, it is unclear if the recorded event represents a real warming event or is an effect of dramatic changes to the local hydrological cycle shortly before evaporite deposition. A similar apparent warming trend recorded in a $U^{K}_{37}{}'$ palaeotemperature record from the central Mediterranean has been attributed to hydrological cycle changes (Tzanova *et al.*, 2015).

The effects of the isolation of the eastern Mediterranean basin are clear in the upper (younger) part of the Lapatza Hill succession, as evidenced by $\delta^{18}O_{sw\text{-}ivc}$ data, together with the unique stable isotope and trace element records. Evidence of basin isolation may be expected during the latest Miocene shortly before the deposition of the evaporite units. However, $\delta^{18}O_{sw\text{-}ivc}$ data from this study, together with the high variability of stable isotope and trace element data indicate that partial isolation of the eastern Mediterranean basins may have taken place as early as *c.* 9.2 Ma. Partial or periodic isolation of eastern Mediterranean basins is supported by the deposition of Mn oxide-rich sediments (implying emergence; see above) and the anomalous Sr isotope values throughout the Lapatza Hill succession (see Chapter 3.3.3).

It is likely that the partial or periodic basin isolation recorded in the Lapatza Hill succession relates to ongoing regional tectonics, resulting from compression between the Arabian platform and the Tauride continent (Figure 6.4.2). Specifically, there was an important phase of southward thrusting in the Kyrenia Range during the Late Miocene-earliest Pliocene (Ducloz, 1972; Baroz, 1979; Robertson and Woodcock, 1986; McCay and Robertson, 2013) which deformed the Mesaoria Basin to the north of the Ovgos Fault. However, there is little or no evidence of this compression further south, including the Kottaphi Hill succession studied. More regionally, during the Late Miocene, the relative motion between the African and Eurasian plates switched from north-south to northwest-southeast, leading to the closure of the ocean gateway between the western Mediterranean and the Atlantic Ocean (Le Pichon *et al.*, 1979; Jolivet and Faccenna, 2000; Nocquet and Calais, 2004; Jolivet *et al.*, 2006).

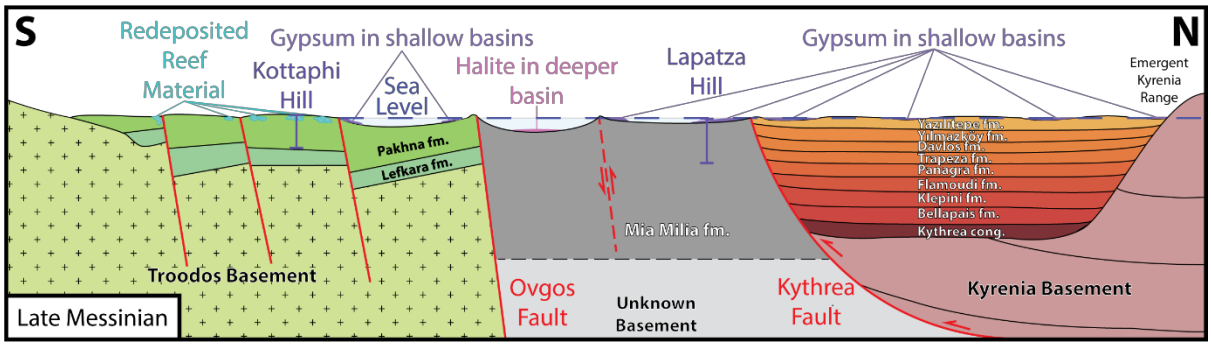


Figure 6.4.4 – Schematic cross-section of the depositional environments of the sedimentary basins in Cyprus during the Late Messinian. Dashed lines indicate faults, contacts or surfaces interpreted with lower levels of confidence. Interpretations of the structure and stratigraphy are based on previous research cited in the caption of Figure 6.2.2 and the introductory text of this chapter, together with those mentioned in the text of the chapter. By this time, the Troodos Massif was exposed subaerially and reef material underwent karstic weathering (Follows, 1990; Follows *et al.*, 1996). Gypsum deposition took place in shallow fault-controlled basins on the Troodos Massif (Baroz and Bizon, 1974; Robertson and Hudson, 1974; Robertson, 1977a; Baroz *et al.*, 1978; Robertson *et al.*, 1995, 2009). Halite deposition took place in a deeper fault-controlled basin to the north of the Ovgos Fault, as indicated by exploration drilling (Gass, 1960; Harrison *et al.*, 2004), this basin was later down-faulted and buried beneath the Mesaoria Basin. To the north, gypsum was deposited locally in small basins (Varol and Atalar, 2017; Artiaga *et al.*, 2021), as preserved at Lapatza Hill.

The end of the MSC resulted from the re-opening of the Atlantic-Mediterranean ocean gateway and the re-flooding of the Mediterranean basins. This re-flooding is marked by Early Pliocene deposition, including in the same part of Cyprus as Miocene sedimentation took place (e.g. Mesaoria Basin).

7 Conclusions & scope for future work

This chapter provides a summary of conclusions, many of which are discussed in more detail in Chapter 6. In addition, a section on the scope for future work in the research area covered by this research project is provided in this chapter.

7.1 Summary Conclusions

The deposition of the Miocene sedimentary sequences of Cyprus was strongly controlled by a combination of local-to-regional scale tectonic and climatic factors. These factors combined to influence a number of variables, such as relative sea level and ocean circulation, which in turn controlled sedimentation in the eastern Mediterranean basins, as studied in this project.

The deposition of the Early to Middle Miocene-aged sediments sampled in this study was relatively free from the major influence of regional-local tectonics. However, the collision of the Tauride continent and the Arabian platform was an important control on the supply of terrigenous material to the Kottaphi Hill succession, and later the Lapatza Hill succession, as suggested for the sediments that were deposited at the same time in the Kyrenia Range.

During the earliest Late Miocene, extensional tectonics resulted in the fault-controlled uplift of the northern margin of the Troodos ophiolite. This fault-controlled uplift is exemplified by the upward shallowing recorded in the Kottaphi Hill succession. Back rotation of uplifted fault blocks exposed the ophiolitic basement rocks, which then acted as a substrate for coral reef growth, such as that preserved as debris in the Kottaphi Hill succession.

Compared to the Kottaphi Hill succession, sedimentological and geochemical data from the Lapatza Hill succession are indicative of high terrigenous input. Similar high

terrigenous input is reported in other Late Miocene sediments from the Kyrenia Range (Davlos and Mia Millia Formations) and has been related (mostly through palaeocurrent data) to post collisional suture tightening in Southeast Turkey. The Late Miocene uplift of Cyprus also influenced sedimentation during this time.

Both post collisional suture tightening in Southeast Turkey and Late Miocene uplift of Cyprus were also important controls on the periodic isolation of an ocean basin during the Late Miocene, as indicated by sedimentological and geochemical data in this study.

Regional tectonics throughout the Miocene resulted in significant changes to connectivity and circulation between ocean basins during the Miocene. The ocean gateway between the Southern Neotethys and the Indian Ocean was significantly restricted and closed to deep-water circulation during the Early Miocene. In this study, a new palaeotemperature record from the eastern Mediterranean region records uniquely high temperatures during the Tortonian Thermal Maximum. This warming event was possibly related to the closure of the eastern gateway of the Southern Neotethys and the resulting disequilibrium between the Atlantic and Pacific Oceans.

Despite ongoing changes to ocean circulation, global carbonate chemistry events such as the Monterey Event and the Miocene Carbonate Crash are present in records from Cyprus.

Global climatic changes are recorded in geochemical records from Cyprus. The Miocene Climate Optimum resulted in peak temperatures *c.* 12 °C warmer than the modern day in the eastern Mediterranean region. Dramatic cooling, related to the Middle Miocene Climate Transition, followed the Miocene Climate Optimum. Cooling

during the Late Miocene, which is reported globally, is also recorded in geochemical records from Cyprus.

During the Late Miocene, the effects of local to regional tectonic events resulted in local isolation of the eastern Mediterranean basins. In this study, both sedimentological and geochemical records provide evidence for the partial, periodical isolation of eastern Mediterranean basins from *c.* 9.2 Ma onwards.

At the end of the Late Miocene, the closure of the gateway between the proto-Mediterranean Sea and the Atlantic Ocean to the west resulted in the isolation of the proto-Mediterranean Sea. The effects of this Mediterranean-wide isolation are recorded from *c.* 7.2 Ma onwards in the geochemical records from this study. Dramatic effects of this isolation are noted from *c.* 6 Ma onwards in these new geochemical records, which include a palaeosalinity proxy method. The Late Miocene isolation of the Mediterranean basins culminated in the deposition of evaporite units during the Messinian Salinity Crisis, as documented in the Lapatza Hill succession, as well as numerous other locations across Cyprus and the Mediterranean region.

7.2 **Future Work**

This research provides a data set that can be further utilised following the refinement and development of new and existing palaeoceanographic proxies. Further development of the Mg/Ca and $\delta^{18}O$ proxies could allow improved palaeotemperature and salinity ($\delta^{18}O_{sw\text{-}ivc}$) records to be developed. Similarly, a better understanding of the controls on B/Ca and $\delta^{13}C$ in foraminiferal calcite could improve interpretations based on seawater carbonate chemistry presented in this thesis. Several additional trace element to calcite ratios in planktic foraminiferal samples were measured during

this project and were not used in this thesis due to the lack of established palaeoceanographic methods based on these measurements. These results are presented in Appendix 8.7 and could be utilised if new proxies/methods are developed in the future.

The geographical extent of several palaeoceanographic changes interpreted in this study is unclear. Research similar to this study on samples from elsewhere in the eastern Mediterranean region and further afield would help to establish if these palaeoceanographic events took place on a local or regional scale.

Further geological and geochemical research on the timing of the restriction and closure of the gateway that once linked the eastern Mediterranean basins with the Indian Ocean could help to settle the discrepancies in timings as currently reported. Whilst geological evidence records the closure of the physical ocean gateway, geochemical evidence documents the termination of circulation between the two ocean basins. Research on the relationship between these two closely related events could help to bring clarity to discussions on the closure of the ocean gateway and ocean circulation. Studies that combine both geological and geochemical evidence as part of an integrated approach could bring together a vast amount of geological and geochemical evidence, which are sometimes previously treated separately. Better constraints on the timing and nature of this restriction and closure, together with the effects on ocean circulation could help to relate the palaeoceanographic changes seen in the composite temporal record with the effects of the closure of this ocean gateway. It is likely that modelling studies will play an important part in resolving these issues.

Additional geochemical analysis on the Miocene sediments of Cyprus and other eastern Mediterranean localities could help to confirm the provenance and therefore

help to resolve the transport pathways of terrigenous material found in Miocene hemipelagic and pelagic sediments. An improved understanding of such transport pathways could give insights into both the tectonic and oceanographic (ocean circulation) settings of the region during Miocene time.

References

Adams, C.G., Benson, R.H., Kidd, R.B., Ryan, W.B.F. and Wright, R.C. (1977) 'The Messinian salinity crisis and evidence of late Miocene eustatic changes in the world ocean', *Nature*, 269(5627). Available at: https://doi.org/10.1038/269383a0.

Adegbie, A.T., Schneider, R.R., Röhl, U. and Wefer, G. (2003) 'Glacial millennial-scale fluctuations in central African precipitation recorded in terrigenous sediment supply and freshwater signals offshore Cameroon', *Palaeogeography, Palaeoclimatology, Palaeoecology*, 197(3), pp. 323–333. Available at: https://doi.org/https://doi.org/10.1016/S0031-0182(03)00474-7.

Agnini, C., Monechi, S. and Raffi, I. (2017) 'Calcareous nannofossil biostratigraphy: historical background and application in Cenozoic chronostratigraphy', in *Lethaia*. Available at: https://doi.org/10.1111/let.12218.

Aharon, P. and Sen Gupta, B.K. (1994) 'Bathymetric reconstructions of the Miocene-age "calcari aLucina" (northern Apennines, Italy) from oxygen isotopes and benthic Foraminifera', *Geo-Marine Letters*, 14(2), pp. 219–230. Available at: https://doi.org/10.1007/BF01203734.

Aksu, A.E., Hall, J. and Yaltırak, C. (2021) 'Miocene–Quaternary tectonic, kinematic and sedimentary evolution of the eastern Mediterranean Sea: A regional synthesis', *Earth-Science Reviews*, 220, p. 103719. Available at: https://doi.org/10.1016/J.EARSCIREV.2021.103719.

Allen, K.A., Hönisch, B., Eggins, S.M., Haynes, L.L., Rosenthal, Y. and Yu, J. (2016) 'Trace element proxies for surface ocean conditions: A synthesis of culture calibrations with planktic foraminifera', *Geochimica et Cosmochimica Acta*, 193, pp. 197–221. Available at: https://doi.org/https://doi.org/10.1016/j.gca.2016.08.015.

Allen, K.A., Hönisch, B., Eggins, S.M. and Rosenthal, Y. (2012) 'Environmental controls on B/Ca in calcite tests of the tropical planktic foraminifer species Globigerinoides ruber and Globigerinoides sacculifer', *Earth and Planetary Science Letters*, 351–352, pp. 270–280. Available at: https://doi.org/https://doi.org/10.1016/j.epsl.2012.07.004.

Allen, K.A., Hönisch, B., Eggins, S.M., Yu, J., Spero, H.J. and Elderfield, H. (2011) 'Controls on boron incorporation in cultured tests of the planktic foraminifer Orbulina universa', *Earth and Planetary Science Letters*, 309(3–4), pp. 291–301. Available at: https://doi.org/10.1016/J.EPSL.2011.07.010.

Allerton, S. and Vine, F.J. (1987) 'Spreading structure of the Troodos ophiolite, Cyprus: some paleomagnetic constraints.', *Geology*, 15(7). Available at: https://doi.org/10.1130/0091-7613(1987)15<593:SSOTTO>2.0.CO;2.

Allouc, J. (1990) 'Quaternary crusts on slopes of the Mediterranean Sea: A tentative explanation for their genesis', *Marine Geology*, 94(3), pp. 205–238. Available at: https://doi.org/https://doi.org/10.1016/0025-3227(90)90070-Z.

Anand, P., Elderfield, H. and Conte, M.H. (2003) 'Calibration of Mg/Ca thermometry in planktonic foraminifera from a sediment trap time series', *Paleoceanography*, 18(2). Available at: https://doi.org/10.1029/2002PA000846.

Anderson, T.F. and Cole, S.A. (1975) 'The stable isotope geochemistry of marine coccoliths; a preliminary comparison with planktonic foraminifera', *Journal of Foraminiferal Research*, 5(3), pp. 188–192. Available at: https://doi.org/10.2113/GSJFR.5.3.188.

Andrew, T. and Robertson, A.H.F. (2002) 'The Beyşehir-Hoyran-Hadim Nappes: Genesis and emplacement of mesozoic marginal and oceanic units of the northern Neotethys in southern Turkey', *Journal of the Geological Society*, 159(5). Available at: https://doi.org/10.1144/0016-764901-157.

Antonarakou, A., Kontakiotis, G., Vasilatos, C., Besiou, E., Zarkogiannis, S.D., Drinia, H., Mortyn, P.G., Tsaparas, N., Makri, P. and Karakitsios, V. (2019) 'Evaluating the Effect of Marine Diagenesis on Late Miocene Pre-Evaporitic Sedimentary Successions of Eastern Mediterranean Sea', *IOP Conference Series: Earth and Environmental Science*, 221, p. 012051. Available at: https://doi.org/10.1088/1755-1315/221/1/012051.

Arbuszewski, J., deMenocal, P., Kaplan, A. and Farmer, E.C. (2010) 'On the fidelity of shell-derived δ18Oseawater estimates', *Earth and Planetary Science Letters*, 300(3–4), pp. 185–196. Available at: https://doi.org/10.1016/J.EPSL.2010.10.035.

Armstrong McKay, D.I., Tyrrell, T., Wilson, P.A. and Foster, G.L. (2014) 'Estimating the impact of the cryptic degassing of Large Igneous Provinces: A mid-Miocene case-study', *Earth and Planetary Science Letters*, 403, pp. 254–262. Available at: https://doi.org/10.1016/j.epsl.2014.06.040.

Armstrong, P.A., Ehlers, T.A., Chapman, D.S., Farley, K.A. and Kamp, P.J.J. (2003) 'Exhumation of the central Wasatch Mountains, Utah: 1. Patterns and timing of exhumation deduced from low-temperature thermochronology data', *Journal of Geophysical Research: Solid Earth*, 108(B3). Available at: https://doi.org/10.1029/2001jb001708.

Artiaga, D., García-Veigas, J., Cendón, D.I., Atalar, C. and Gibert, L. (2021) 'The Messinian evaporites of the Mesaoria basin (North Cyprus): A discrepancy with the current chronostratigraphic understanding', *Palaeogeography, Palaeoclimatology, Palaeoecology*, 584, p. 110681. Available at: https://doi.org/https://doi.org/10.1016/j.palaeo.2021.110681.

Arz, H.W., Pätzold, J. and Wefer, G. (1998) 'Correlated Millennial-Scale Changes in Surface Hydrography and Terrigenous Sediment Yield Inferred from Last-Glacial Marine Deposits off Northeastern Brazil', *Quaternary Research*, 50(2), pp. 157–166. Available at: https://doi.org/https://doi.org/10.1006/qres.1998.1992.

Athanasiou, M., Triantaphyllou, M. V., Dimiza, M.D., Gogou, A., Panagiotopoulos, I., Arabas, A., Skampa, E., Kouli, K., Hatzaki, M. and Tsiolakis, E. (2021) 'Reconstruction of oceanographic and environmental conditions in the eastern Mediterranean (Kottafi Hill section, Cyprus Island) during the middle Miocene Climate Transition', *Revue de Micropaléontologie*, 70, p. 100480. Available at: https://doi.org/10.1016/J.REVMIC.2020.100480.

Aze, T., Ezard, T.H.G., Purvis, A., Coxall, H.K., Stewart, D.R.M., Wade, B.S. and Pearson, P.N. (2011) 'A phylogeny of Cenozoic macroperforate planktonic foraminifera from fossil data', *Biological Reviews*, 86(4), pp. 900–927. Available at: https://doi.org/10.1111/J.1469-185X.2011.00178.X.

Backman, J., Raffi, I., Rio, D., Fornaciari, E. and Pälike, H. (2012) 'Biozonation and biochronology of miocene through pleistocene calcareous nannofossils from low and middle latitudes', *Newsletters on Stratigraphy*, 45(3), pp. 221–244. Available at: https://doi.org/10.1127/0078-0421/2012/0022.

Backman, J. and Shackleton, N.J. (1983) 'Quantitative biochronology of Pliocene and early Pleistocene calcareous nannofossils from the Atlantic, Indian and Pacific oceans', *Marine Micropaleontology*, 8(2), pp. 141–170. Available at: https://doi.org/10.1016/0377-8398(83)90009-9.

Badger, M.P.S., Lear, C.H., Pancost, R.D., Foster, G.L., Bailey, T.R., Leng, M.J. and Abels, H.A. (2013) 'CO2 drawdown following the middle Miocene expansion of the Antarctic Ice Sheet', *Paleoceanography*, 28(1). Available at: https://doi.org/10.1002/palo.20015.

Bagnall, P.S. (1960) *The geology and mineral resources of the Pano Lefkara-Larnaca area*. authority of the Government of Cyprus.

Bahr, A., Schönfeld, J., Hoffmann, J., Voigt, S., Aurahs, R., Kucera, M., Flögel, S., Jentzen, A. and Gerdes, A. (2013) 'Comparison of Ba/Ca and δOWATER18 as freshwater proxies: A multi-species core-top study on planktonic foraminifera from the vicinity of the Orinoco River mouth', *Earth and Planetary Science Letters*, 383, pp. 45–57. Available at: https://doi.org/https://doi.org/10.1016/j.epsl.2013.09.036.

Bailey, T.R., McArthur, J.M., Prince, H. and Thirlwall, M.F. (2000a) 'Dissolution methods for strontium isotope stratigraphy: whole rock analysis', *Chemical Geology*, 167(3–4), pp. 313–319. Available at: https://doi.org/10.1016/S0009-2541(99)00235-1.

Bailey, W.R., Holdsworth, R.E. and Swarbrick, R.E. (2000b) 'Kinematic history of a reactivated oceanic suture: The Mamonia Complex Suture Zone, SW Cyprus', *Journal of the Geological Society*, 157(6), pp. 1107–1126. Available at: https://doi.org/10.1144/jgs.157.6.1107.

Balmer, E.M., Robertson, A.H.F., Raffi, I. and Kroon, D. (2019) 'Pliocene-Pleistocene sedimentary development of the syntectonic Polis graben, NW Cyprus: Evidence from facies analysis, nannofossil biochronology and strontium isotope dating', *Geological Magazine*, 156(5), pp. 889–917. Available at:

https://doi.org/10.1017/S0016756818000286.

Banner, F.T. (1982) 'A classification and introduction to the Globigerinacea BT - Aspects of Micropalaeontology', in F.T. Banner and A.R. Lord (eds). Dordrecht: Springer Netherlands, pp. 142–239. Available at: https://doi.org/10.1007/978-94-011-6841-0_5.

Baringer, M.O. and Price, J.F. (1999) 'A review of the physical oceanography of the Mediterranean outflow', *Marine Geology*, 155(1), pp. 63–82. Available at: https://doi.org/https://doi.org/10.1016/S0025-3227(98)00141-8.

Barker, P.F. and Burrell, J. (1977) 'The opening of Drake Passage', *Marine Geology*, 25(1), pp. 15–34. Available at: https://doi.org/https://doi.org/10.1016/0025-3227(77)90045-7.

Barker, P.F. and Thomas, E. (2004) 'Origin, signature and palaeoclimatic influence of the Antarctic Circumpolar Current', *Earth-Science Reviews*, 66(1), pp. 143–162. Available at: https://doi.org/https://doi.org/10.1016/j.earscirev.2003.10.003.

Barker, S., Greaves, M. and Elderfield, H. (2003) 'A study of cleaning procedures used for foraminiferal Mg/Ca paleothermometry', *Geochemistry, Geophysics, Geosystems*, 4(9). Available at: https://doi.org/10.1029/2003GC000559.

Baroz, F. (1979) *Etude géologique dans le Pentadaktylos et la Mesaoria (Chypre Septentrionale)*. Université de Nancy.

Baroz, F. and Bizon, G. (1974) 'Le néogène de la chaine du Pentadaktylos et de la partie nord de la Mésaoria (Chypre). Etude stratigraphique et micropaléontologique', *Revue de l'Institut Français du Pétrole*, 29(3), pp. 327–360. Available at: https://doi.org/10.2516/ogst:1974015.

Baroz, F., Bizon, G., JJ, B., KO, H., JP, M. and Muller, C. (1978) 'Le Miocene terminal et le Pliocene dans la region de Polemi (Chypre Ouest); Milieux de depot.'

Barrier, E. and Wrielynck, B. (2008) 'Palaeotectonic maps of the Middle East: Tectonono-Sedimentary-Palinspastic maps from Late Norian to Pliocene. Atlas of 14 maps at 1/18 500 000. Publisher CGMW, Paris, France.', *Palaeotectonic maps of the Middle East: Tectonono-Sedimentary-Palinspastic maps from Late Norian to Pliocene. Atlas of 14 maps at 1/18 500 000. Publisher CGMW, Paris, France.*, 53(8–10).

Bé, A.W.H., Morse, J.W. and Harrison, S.M. (1975) 'Progressive dissolution and ultrastructural breakdown of planktonic foraminifera'.

Bemis, B.E., Spero, H.J., Bijma, J. and Lea, D.W. (1998) 'Reevaluation of the oxygen isotopic composition of planktonic foraminifera: Experimental results and revised paleotemperature equations', *Paleoceanography*, 13(2). Available at: https://doi.org/10.1029/98PA00070.

Berger, A. (1988) 'Milankovitch Theory and climate', *Reviews of Geophysics*. Available at: https://doi.org/10.1029/RG026i004p00624.

Berger, A.L. (1977) 'Support for the astronomical theory of climatic change', *Nature*, 269(5623). Available at: https://doi.org/10.1038/269044a0.

Berger, A.L. (1978) 'Long-term variations of caloric insolation resulting from the earth's orbital elements', *Quaternary Research*, 9(2), pp. 139–167. Available at: https://doi.org/https://doi.org/10.1016/0033-5894(78)90064-9.

Berger, W.H. (1970) 'Planktonic Foraminifera: Selective solution and the lysocline', *Marine Geology*, 8(2), pp. 111–138. Available at: https://doi.org/10.1016/0025-3227(70)90001-0.

Bergslien, E.T. (2013) 'X-ray diffraction and field portable X-ray fluorescence analysis and screening of soils: Project design', *Geological Society Special Publication*, 384(1), pp. 27–46. Available at: https://doi.org/10.1144/SP384.14.

Berner, R.A. (2004) 'A model for calcium, magnesium and sulfate in seawater over Phanerozoic time', *American Journal of Science*, 304(5), pp. 438–453. Available at: https://doi.org/10.2475/AJS.304.5.438.

Bethoux, J.P. and Gentili, B. (1999) 'Functioning of the Mediterranean Sea: past and present changes related to freshwater input and climate changes', *Journal of Marine Systems*, 20(1), pp. 33–47.

Available at: https://doi.org/https://doi.org/10.1016/S0924-7963(98)00069-4.

Bialik, O.M., Frank, M., Betzler, C., Zammit, R. and Waldmann, N.D. (2019) 'Two-step closure of the Miocene Indian Ocean Gateway to the Mediterranean', *Scientific Reports*, 9(1), p. 8842. Available at: https://doi.org/10.1038/s41598-019-45308-7.

Bialik, O.M., Reolid, J., Kulhanek, D.K., Hincke, C., Waldmann, N.D. and Betzler, C. (2022) 'Sedimentary response to current and nutrient regime rearrangement in the Eastern Mediterranean during the early to middle Miocene (Southwestern Cyprus)', *Palaeogeography, Palaeoclimatology, Palaeoecology*, 588, p. 110819. Available at: https://doi.org/10.1016/J.PALAEO.2021.110819.

Bijl, P.K. *et al.* (2013) 'Eocene cooling linked to early flow across the Tasmanian Gateway', *Proceedings of the National Academy of Sciences*, 110(24), pp. 9645–9650. Available at: https://doi.org/10.1073/pnas.1220872110.

Birch, H., Coxall, H.K., Pearson, P.N., Kroon, D. and O'Regan, M. (2013) 'Planktonic foraminifera stable isotopes and water column structure: Disentangling ecological signals', *Marine Micropaleontology*, 101, pp. 127–145. Available at: https://doi.org/10.1016/J.MARMICRO.2013.02.002.

Birck, J.L. (1986) 'Precision K□Rb□Sr isotopic analysis: Application to Rb□Sr chronology', *Chemical Geology*, 56(1–2), pp. 73–83. Available at: https://doi.org/10.1016/0009-2541(86)90111-7.

Bish, D.L. and Reynolds, R.C. (1989) 'Sample preparation for X-ray diffraction', *Reviews in Mineralogy and Geochemistry*, 20(1), pp. 73–99.

Bissett, A., Neu, T.R. and de Beer, D. (2011) 'Dissolution of Calcite in the Twilight Zone: Bacterial Control of Dissolution of Sinking Planktonic Carbonates Is Unlikely', *PLOS ONE*, 6(11), p. e26404. Available at: https://doi.org/10.1371/JOURNAL.PONE.0026404.

Blanc, P.L. (2002) 'The opening of the plio-quaternary gibraltar strait: Assessing the size of a cataclysm', *Geodinamica Acta*, 15(5–6), pp. 303–317. Available at: https://doi.org/10.1080/09853111.2002.10510763.

Blow, W.H. (1956) 'Origin and Evolution of the Foraminiferal Genus Orbulina d'Orbigny', *Micropaleontology*, 2(1), p. 57. Available at: https://doi.org/10.2307/1484492.

De Boer, P.L. and Smith, D.G. (1994) 'Orbital forcing and cyclic sequences', *Orbital forcing and cyclic sequences* [Preprint]. Available at: https://doi.org/10.1016/s0264-8172(97)88314-6.

Böhme, M., Ilg, A. and Winklhofer, M. (2008) 'Late Miocene "washhouse" climate in Europe', *Earth and Planetary Science Letters*, 275(3), pp. 393–401. Available at: https://doi.org/https://doi.org/10.1016/j.epsl.2008.09.011.

Bosworth, W. and McClay, K. (2001) 'Structural and stratigraphic evolution of the Gulf of Suez Rift, Egypt: a synthesis', *Mémoires du Muséum national d'histoire naturelle*, 186.

BouDagher-Fadel, M. and Lord, A. (2006) 'Illusory stratigraphy decoded by Oligocene-Miocene autochthonous and allochthonous foraminifera in the Terra Member, Pakhna Formation (Cyprus)', *Stratigraphy*, pp. 217–226.

Boulton, S.J. and Robertson, A.H.F. (2007) 'The Miocene of the Hatay area, S Turkey: Transition from the Arabian passive margin to an underfilled foreland basin related to closure of the Southern Neotethys Ocean', *Sedimentary Geology*, 198(1–2). Available at: https://doi.org/10.1016/j.sedgeo.2006.12.001.

Boulton, S.J. and Robertson, A.H.F. (2008) 'The Neogene–Recent Hatay Graben, South Central Turkey: graben formation in a setting of oblique extension (transtension) related to post-collisional tectonic escape', *Geological Magazine*, 145(6), pp. 800–821. Available at: https://doi.org/10.1017/S0016756808005013.

Boulton, S.J., Robertson, A.H.F. and Ünlügenç, U.C. (2006) 'Tectonic and sedimentary evolution of the Cenozoic Hatay Graben, Southern Turkey: A two-phase model for graben formation', *Geological Society Special Publication*, 260, pp. 613–634. Available at: https://doi.org/10.1144/GSL.SP.2006.260.01.26.

Bouvier-Soumagnac, Y. and Duplessy, J.C. (1985) 'Carbon and oxygen isotopic composition of

planktonic foraminifera from laboratory culture, plankton tows and Recent sediment: implications for the reconstruction of paleoclimatic conditions and of the global carbon-cycle.', *Journal of Foraminiferal Research*, 15(4). Available at: https://doi.org/10.2113/gsjfr.15.4.302.

Bown, P.R. and Young, J.R. (1998) *Techniques in: Calcareous Nannofossil Biostratigraphy*, *Paleoceanography*.

Boyle, E.A. and Keigwin, L.D. (1985) 'Comparison of Atlantic and Pacific paleochemical records for the last 215,000 years: changes in deep ocean circulation and chemical inventories', *Earth and Planetary Science Letters*, 76(1–2). Available at: https://doi.org/10.1016/0012-821X(85)90154-2.

Boyle, J.F. and Robertson, A.H.F. (1984) 'Evolving metallogenesis at the Troodos spreading axis', *Geological Society Special Publication*, 13. Available at: https://doi.org/10.1144/GSL.SP.1984.013.01.15.

Bracciali, L., Marroni, M., Pandolfi, L. and Rocchi, S. (2007) *Geochemistry and petrography of Western Tethys Cretaceous sedimentary covers (Corsica and Northern Apennines): From source areas to configuration of margins*, *Special Paper of the Geological Society of America*. Available at: https://doi.org/10.1130/2006.2420(06).

Bramlette, M.N. and Riede, W.R. (1954) 'Stratigraphic value of discoasters and some other microfossils related to Recent coccolithophores', *Journal of Paleontology*, pp. 385–403.

Brand, U., Azmy, K., Bitner, M.A., Logan, A., Zuschin, M., Came, R. and Ruggiero, E. (2013) 'Oxygen isotopes and MgCO3 in brachiopod calcite and a new paleotemperature equation', *Chemical Geology*, 359. Available at: https://doi.org/10.1016/j.chemgeo.2013.09.014.

Brand, W.A., Coplen, T.B., Vogl, J., Rosner, M. and Prohaska, T. (2014) 'Assessment of international reference materials for isotope-ratio analysis (IUPAC technical report)', *Pure and Applied Chemistry*, 86(3), pp. 425–467. Available at: https://doi.org/10.1515/PAC-2013-1023/MACHINEREADABLECITATION/RIS.

Brass, G.W. (1975) 'The effect of weathering on the distribution of strontium isotopes in weathering profiles', *Geochimica et Cosmochimica Acta*, 39(12), pp. 1647–1653. Available at: https://doi.org/10.1016/0016-7037(75)90086-1.

Brassell, S.C., Eglinton, G., Marlowe, I.T., Pflaumann, U. and Sarnthein, M. (1986) 'Molecular stratigraphy: A new tool for climatic assessment', *Nature*, 320(6058), pp. 129–133. Available at: https://doi.org/10.1038/320129a0.

Brigaud, B., Pucéat, E., Pellenard, P., Vincent, B. and Joachimski, M.M. (2008) 'Climatic fluctuations and seasonality during the Late Jurassic (Oxfordian–Early Kimmeridgian) inferred from δ18O of Paris Basin oyster shells', *Earth and Planetary Science Letters*, 273(1–2), pp. 58–67. Available at: https://doi.org/10.1016/J.EPSL.2008.06.015.

Brown, G. and Brindley, G.W. (1980) 'X-ray Diffraction Procedures for Clay Mineral Identification', *Crystal Structures of Clay Minerals and their X-Ray Identification*, pp. 305–360. Available at: https://doi.org/10.1180/MONO-5.5.

Bulian, F., Kouwenhoven, T.J., Jiménez-Espejo, F.J., Krijgsman, W., Andersen, N. and Sierro, F.J. (2022) 'Impact of the Mediterranean-Atlantic connectivity and the late Miocene carbon shift on deep-sea communities in the Western Alboran Basin', *Palaeogeography, Palaeoclimatology, Palaeoecology*, 589, p. 110841. Available at: https://doi.org/https://doi.org/10.1016/j.palaeo.2022.110841.

Bulian, F., Kouwenhoven, T.J., Sierro, F.J. and Krijgsman, W. (2021) 'Geochemical and micropaleontological evidence of the Messinian Salinity Crisis preconditioning phase in the West Alboran Basin', in *EGU General Assembly Conference Abstracts*, pp. EGU21-2126.

Burbank, D.W., Beck, R.A., Raynolds, R.G.H., Hobbs, R. and Tahirkheli, R.A.K. (1988) 'Thrusting and gravel progradation in foreland basins: a test of post- thrusting gravel dispersal', *Geology*, 16(12). Available at: https://doi.org/10.1130/0091-7613(1988)016<1143:TAGPIF>2.3.CO;2.

Burollet, P.F. (1991) 'Structures and tectonics of Tunisia', *Tectonophysics*, 195(2–4), pp. 359–369. Available at: https://doi.org/10.1016/0040-1951(91)90221-D.

Butiseacă, G.A., van der Meer, M.T.J., Kontakiotis, G., Agiadi, K., Thivaiou, D., Besiou, E., Antonarakou, A., Mulch, A. and Vasiliev, I. (2022) 'Multiple crises preceded the Mediterranean Salinity Crisis: Aridification and vegetation changes revealed by biomarkers and stable isotopes', *Global and Planetary Change*, 217, p. 103951. Available at: https://doi.org/https://doi.org/10.1016/j.gloplacha.2022.103951.

Campani, M., Mulch, A., Kempf, O., Schlunegger, F. and Mancktelow, N. (2012) 'Miocene paleotopography of the Central Alps', *Earth and Planetary Science Letters*, 337–338, pp. 174–185. Available at: https://doi.org/10.1016/J.EPSL.2012.05.017.

Cannings, T. (2018) *Microfossil and strontium isotope constraints on the age and development of the Miocene- Pliocene Polis graben, North West Cyprus*. University of Edinburgh.

Cannings, T., Balmer, E.M., Coletti, G., Ickert, R.B., Kroon, D., Raffi, I. and Robertson, A.H.F. (2020) 'Microfossil and strontium isotope chronology used to identify the controls of Miocene reefs and related facies in NW Cyprus', *Journal of the Geological Society*, 178(2). Available at: https://doi.org/10.1144/JGS2020-081.

Capella, W., Flecker, R., Hernández-Molina, F.J., Simon, D., Meijer, P.T., Rogerson, M., Sierro, F.J. and Krijgsman, W. (2019) 'Mediterranean isolation preconditioning the Earth System for late Miocene climate cooling', *Scientific Reports*, 9(1), pp. 1–8. Available at: https://doi.org/10.1038/s41598-019-40208-2.

Casford, J.S.L., Rohling, E.J., Abu-Zied, R.H., Fontanier, C., Jorissen, F.J., Leng, M.J., Schmiedl, G. and Thomson, J. (2003) 'A dynamic concept for eastern Mediterranean circulation and oxygenation during sapropel formation', *Palaeogeography, Palaeoclimatology, Palaeoecology*, 190, pp. 103–119. Available at: https://doi.org/10.1016/S0031-0182(02)00601-6.

Cerling, T.E., Harris, J.M., MacFadden, B.J., Leakey, M.G., Quade, J., Eisenmann, V. and Ehleringer, J.R. (1997) 'Global vegetation change through the Miocene/Pliocene boundary', *Nature*, 389(6647), pp. 153–158. Available at: https://doi.org/10.1038/38229.

Chappell, J. and Shackleton, N.J. (1986) 'Oxygen isotopes and sea level', *Nature*, 324(6093). Available at: https://doi.org/10.1038/324137a0.

Chen, G. (2018) 'Provenance-related studies of Triassic-Miocene Tethyan sedimentary and igneous rocks from Cyprus'. University of Edinburgh.

Chen, G. and Robertson, A.H.F. (2019) 'Provenance and magmatic-tectonic setting of Campanian-aged volcaniclastic sandstones of the Kannaviou Formation in western Cyprus: Evidence for a South-Neotethyan continental margin volcanic arc', *Sedimentary Geology*, 388. Available at: https://doi.org/10.1016/j.sedgeo.2019.05.002.

Chen, G. and Robertson, A.H.F. (2020) 'User's guide to the interpretation of sandstones using whole-rock chemical data, exemplified by sandstones from Triassic to Miocene passive and active margin settings from the Southern Neotethys in Cyprus', *Sedimentary Geology*, 400, p. 105616. Available at: https://doi.org/https://doi.org/10.1016/j.sedgeo.2020.105616.

Chen, G., Robertson, A.H.F. and Ustaömer, T. (2018) 'U–Pb detrital zircon ages used to infer provenance and tectonic setting of late triassic–miocene sandstones related to the tethyan development of Cyprus', *Journal of the Geological Society*, 176(5). Available at: https://doi.org/10.1144/jgs2018-207.

Chen, G., Robertson, A.H.F. and Wu, F.Y. (2022) 'Detrital zircon geochronology and related evidence from clastic sediments in the Kyrenia Range, N Cyprus: Implications for the Mesozoic-Cenozoic erosional history and tectonics of southern Anatolia', *Earth-Science Reviews*, 233. Available at: https://doi.org/10.1016/J.EARSCIREV.2022.104167.

Chinzei, K. (1995) 'Adaptive significance of the lightweight shell structure in soft bottom oysters', *Neues Jahrbuch für Geologie und Paläontologie - Abhandlungen*, 195(1–3), pp. 217–227. Available at: https://doi.org/10.1127/njgpa/195/1995/217.

Christ, N., Immenhauser, A., Wood, R.A., Darwich, K. and Niedermayr, A. (2015) 'Petrography and environmental controls on the formation of Phanerozoic marine carbonate hardgrounds', *Earth-Science Reviews*, 151, pp. 176–226. Available at:

https://doi.org/https://doi.org/10.1016/j.earscirev.2015.10.002.

Clark, M.K., Schoenbohm, L.M., Royden, L.H., Whipple, K.X., Burchfiel, B.C., Zhang, X., Tang, W., Wang, E. and Chen, L. (2004) 'Surface uplift, tectonics, and erosion of eastern Tibet from large-scale drainage patterns', *Tectonics*, 23(1). Available at: https://doi.org/10.1029/2002TC001402.

Clauzon, G., Suc, J.-P., Gautier, F., Berger, A. and Loutre, M.-F. (1996) 'Alternate interpretation of the Messinian salinity crisis: Controversy resolved?', *Geology*, 24(4), pp. 363–366. Available at: https://doi.org/10.1130/0091-7613(1996)024<0363:AIOTMS>2.3.CO;2.

Cleveland, W.S. (1979) 'Robust Locally Weighted Regression and Smoothing Scatterplots', *Journal of the American Statistical Association*, 74(368), pp. 829–836. Available at: https://doi.org/10.1080/01621459.1979.10481038.

Cleveland, W.S. and Devlin, S.J. (1988) 'Locally Weighted Regression: An Approach to Regression Analysis by Local Fitting', *Journal of the American Statistical Association*, 83(403), pp. 596–610. Available at: https://doi.org/10.1080/01621459.1988.10478639.

Clift, P.D. (2002) 'A brief history of the Indus River', *Geological Society Special Publication*, 195. Available at: https://doi.org/10.1144/GSL.SP.2002.195.01.13.

Clube, T.M.M. and Robertson, A.H.F. (1986) 'The palaeorotation of the troodos microplate, cyprus, in the late mesozoic-early cenozoic plate tectonic framework of the Eastern Mediterranean', *Surveys in Geophysics*, 8(4). Available at: https://doi.org/10.1007/BF01903949.

Coadic, R., Bassinot, F., Dissard, D., Douville, E., Greaves, M. and Michel, E. (2013) 'A core-top study of dissolution effect on B/Ca in Globigerinoides sacculifer from the tropical Atlantic: Potential bias for paleo-reconstruction of seawater carbonate chemistry', *Geochemistry, Geophysics, Geosystems*, 14(4), pp. 1053–1068. Available at: https://doi.org/10.1029/2012GC004296.

Coates, A.G., Collins, L.S., Aubury, M.P. and Berggren, W.A. (2004) 'The geology of the Darien, Panama, and the late Miocene-Pliocene collision of the Panama arc with northwestern South America', *Bulletin of the Geological Society of America*, 116(11–12). Available at: https://doi.org/10.1130/B25275.1.

Coates, A.G. and Stallard, R.F. (2013) 'How old is the Isthmus of Panama?', *Bulletin of Marine Science*, 89(4). Available at: https://doi.org/10.5343/bms.2012.1076.

Coggon, R.M., Teagle, D.A.H., Smith-Duque, C.E., Alt, J.C. and Cooper, M.J. (2010) 'Reconstructing past seawater Mg/Ca and Sr/Ca from mid-ocean ridge flank calcium carbonate veins', *Science*, 327(5969), pp. 1114–1117. Available at: https://doi.org/10.1126/SCIENCE.1182252.

Cohen, K.M., Finney, S.C., Gibbard, P.L. and Fan, J.X. (2013) 'The ICS international chronostratigraphic chart', *Episodes*, 36(3). Available at: https://doi.org/10.18814/epiiugs/2013/v36i3/002.

Coleman, M. and Hodges, K. (1995) 'Evidence for Tibetan plateau uplift before 14 Myr ago from a new minimum age for east-west extension', *Nature*, 374(6517), pp. 49–52. Available at: https://doi.org/10.1038/374049A0.

Coletti, G., Balmer, E.M., Bialik, O.M., Cannings, T., Kroon, D., Robertson, A.H.F. and Basso, D. (2021) 'Microfacies evidence for the evolution of Miocene coral-reef environments in Cyprus', *Palaeogeography, Palaeoclimatology, Palaeoecology*, 584. Available at: https://doi.org/10.1016/j.palaeo.2021.110670.

Coletti, G., Basso, D., Betzler, C., Robertson, A.H.F., Bosio, G., El Kateb, A., Foubert, A., Meilijson, A. and Spezzaferri, S. (2019a) 'Environmental evolution and geological significance of the Miocene carbonates of the Eratosthenes Seamount (ODP Leg 160)', *Palaeogeography, Palaeoclimatology, Palaeoecology*, 530. Available at: https://doi.org/10.1016/j.palaeo.2019.05.009.

Coletti, G., Bosio, G., Collareta, A., Malinverno, E., Bracchi, V.A., Di Celma, C., Basso, D., Stainbank, S., Spezzaferri, S., Cannings, T. and Bianucci, G. (2019b) 'Biostratigraphic, evolutionary, and paleoenvironmental significance of the southernmost lepidocyclinids of the Pacific coast of South America (East Pisco Basin, southern Peru)', *Journal of South American Earth Sciences*, 96. Available at: https://doi.org/10.1016/j.jsames.2019.102372.

Corliss, B.H. (1991) 'Morphology and microhabitat preferences of benthic foraminifera from the northwest Atlantic Ocean', *Marine Micropaleontology*, 17(3–4), pp. 195–236. Available at: https://doi.org/10.1016/0377-8398(91)90014-W.

Cornacchia, I., Brandano, M. and Agostini, S. (2021) 'Miocene paleoceanographic evolution of the Mediterranean area and carbonate production changes: A review', *Earth-Science Reviews*, 221, p. 103785. Available at: https://doi.org/https://doi.org/10.1016/j.earscirev.2021.103785.

Cornacchia, I., Brandano, M., Agostini, S. and Munnecke, A. (2022) 'Neodymium isotopes of central Mediterranean phosphatic hardgrounds reveal Miocene paleoceanography', *Geology*, 50(9), pp. 1023–1027. Available at: https://doi.org/10.1130/G50118.1.

Cramer, B.S., Toggweiler, J.R., Wright, J.D., Katz, M.E. and Miller, K.G. (2009) 'Ocean overturning since the late cretaceous: Inferences from a new benthic foraminiferal isotope compilation', *Paleoceanography*, 24(4). Available at: https://doi.org/10.1029/2008PA001683.

Davies, Q.J. (2001) *Climatic and tectonic controls on deep water sedimentary cyclicity: evidence from the Miocene to Pleistocene of Cyprus*. Open University (United Kingdom).

Dekens, P.S., Lea, D.W., Pak, D.K., Spero, H.J., Dekens, P.S., Lea, D.W. and Pak, D.K. (2002) 'Core top calibration of Mg/Ca in tropical foraminifera: Refining paleotemperature estimation', *Geochemistry, Geophysics, Geosystems*, 3(4), pp. 1–29. Available at: https://doi.org/10.1029/2001GC000200.

Delaney, M.L., W.H.Bé, A. and Boyle, E.A. (1985) 'Li, Sr, Mg, and Na in foraminiferal calcite shells from laboratory culture, sediment traps, and sediment cores', *Geochimica et Cosmochimica Acta*, 49(6), pp. 1327–1341. Available at: https://doi.org/10.1016/0016-7037(85)90284-4.

Delaygue, G., Bard, E., Rollion, C., Jouzel, J., Stiévenard, M., Duplessy, J.C. and Ganssen, G. (2001) 'Oxygen isotope/salinity relationship in the northern Indian Ocean', *Journal of Geophysical Research: Oceans*, 106(C3). Available at: https://doi.org/10.1029/1999jc000061.

deMenocal, P.B. (2004) 'African climate change and faunal evolution during the Pliocene-Pleistocene', *Earth and Planetary Science Letters*, 220(1–2). Available at: https://doi.org/10.1016/S0012-821X(04)00003-2.

Demicco, R. V., Lowenstein, T.K., Hardie, L.A. and Spencer, R.J. (2005) 'Model of seawater composition for the Phanerozoic', *Geology*, 33(11), pp. 877–880. Available at: https://doi.org/10.1130/G21945.1.

Dewey, J. and Bird, J. (1970) 'MOUNTAIN BELTS AND THE NEW GLOBAL TECTONICS', *J Geophys Res*, 75(14), pp. 2625–2647. Available at: https://doi.org/10.1029/jb075i014p02625.

Dewey, J.F., Pitman, W.C., Ryan, W.B.F. and Bonnin, J. (1973) 'Plate Tectonics and the Evolution of the Alpine System', *Bulletin of the Geological Society of America*, 84(10). Available at: https://doi.org/10.1130/0016-7606(1973)84<3137:PTATEO>2.0.CO;2.

Diaz De Gamero, M.L. (1996) 'The changing course of the Orinoco River during the Neogene: a review', *Palaeogeography, Palaeoclimatology, Palaeoecology*, 123, pp. 385–402.

Dickens, G.R. and Owen, R.M. (1999) 'The Latest Miocene-Early Pliocene biogenic bloom: A revised Indian Ocean perspective', in *Marine Geology*. Available at: https://doi.org/10.1016/S0025-3227(99)00057-2.

Dickson, J.A.D. (2004) 'Echinoderm skeletal preservation: Calcite-aragonite seas and the Mg/Ca ratio of Phanerozoic oceans', *Journal of Sedimentary Research*, 74(3), pp. 355–365. Available at: https://doi.org/10.1306/112203740355.

Diester-Haass, L., Billups, K. and Emeis, K.C. (2005) 'In search of the late Miocene-early Pliocene "biogenic bloom" in the Atlantic Ocean (Ocean Drilling Program Sites 982, 925, and 1088)', *Paleoceanography*, 20(4). Available at: https://doi.org/10.1029/2005PA001139.

Diester-Haass, L., Billups, K. and Emeis, K.C. (2006) 'Late Miocene carbon isotope records and marine biological productivity: Was there a (dusty) link?', *Paleoceanography*, 21(4). Available at: https://doi.org/10.1029/2006PA001267.

Diester-Haass, L., Meyers, P.A. and Bickert, T. (2004) 'Carbonate crash and biogenic bloom in the late Miocene: Evidence from ODP Sites 1085, 1086, and 1087 in the Cape Basin, southeast Atlantic Ocean', *Paleoceanography*, 19(1). Available at: https://doi.org/10.1029/2003PA000933.

Dilek, Y., Thy, P., Hacker, B. and Grundvig, S. (1999) 'Structure and petrology of Tauride ophiolites and mafic dike intrusions (Turkey): Implications for the Neotethyan ocean', *Bulletin of the Geological Society of America*, 111(8). Available at: https://doi.org/10.1130/0016-7606(1999)111<1192:SAPOTO>2.3.CO;2.

Ding, L., Spicer, R.A., Yang, J., Xu, Q., Cai, F., Li, S., Lai, Q., Wang, H., Spicer, T.E.V., Yue, Y., Shukla, A., Srivastava, G., Ali Khan, M., Bera, S. and Mehrotra, R. (2017) 'Quantifying the rise of the Himalaya orogen and implications for the South Asian monsoon', *Geology*, 45(3). Available at: https://doi.org/10.1130/G38583.1.

Dobson, D.M., Dickens, G.R. and Rea, D.K. (2001) 'Terrigenous sediment on Ceara Rise: A Cenozoic record of South American orogeny and erosion', *Palaeogeography, Palaeoclimatology, Palaeoecology*, 165(3–4). Available at: https://doi.org/10.1016/S0031-0182(00)00161-9.

Drinia, H., Antonarakou, A., Tsourou, T., Kontakiotis, G., Psychogiou, M. and Anastasakis, G. (2016) 'Foraminifera eco-biostratigraphy of the southern Evoikos outer shelf, central Aegean Sea, during MIS 5 to present', *Continental Shelf Research*, 126, pp. 36–49. Available at: https://doi.org/https://doi.org/10.1016/j.csr.2016.07.009.

Drinia, H., Tsaparas, N., Antonarakou, A. and Goumas, G. (2003) 'Benthic foraminiferal biofacies associated with middle to early late Miocene oxygen deficient conditions in the eastern Mediterranean', in *International Conference on Environmental Science and Technology, Lemnos Island, Greece*, pp. 8–10.

Ducloz, C. (1972) 'The geology of the Bellapais-Kythrea area of the Central Kyrenia Range', *Bulletin-Geological Survey Department*, (6), pp. 1–75.

Dymond, J., Suess, E. and Lyle, M. (1992) 'Barium in Deep-Sea Sediment: A Geochemical Proxy for Paleoproductivity', *Paleoceanography*, 7(2). Available at: https://doi.org/10.1029/92PA00181.

Eaton, S. and Robertson, A.H.F. (1993) 'The Miocene Pakhna Formation, southern Cyprus and its relationship to the Neogene tectonic evolution of the Eastern Mediterranean', *Sedimentary Geology*, 86(3–4). Available at: https://doi.org/10.1016/0037-0738(93)90026-2.

Eggins, S.M., Sadekov, A. and De Deckker, P. (2004) 'Modulation and daily banding of Mg/Ca in Orbulina universa tests by symbiont photosynthesis and respiration: a complication for seawater thermometry?', *Earth and Planetary Science Letters*, 225(3–4), pp. 411–419. Available at: https://doi.org/10.1016/J.EPSL.2004.06.019.

Elderfield, H. (1986) 'Strontium isotope stratigraphy', *Palaeogeography, Palaeoclimatology, Palaeoecology*, 57(1), pp. 71–90. Available at: https://doi.org/10.1016/0031-0182(86)90007-6.

Elderfield, H. and Ganssen, G. (2000) 'Past temperature and δ18O of surface ocean waters inferred from foraminiferal Mg/Ca ratios', *Nature*, 405(6785). Available at: https://doi.org/10.1038/35013033.

Elsom, D.M. (1992) *Earth: the making, shaping, and workings of a planet*. London: Simon and Schuster Limited.

Emeis, K.C., Sakamoto, T., Wehausen, R. and Brumsack, H.J. (2000) 'The sapropel record of the eastern Mediterranean Sea — results of Ocean Drilling Program Leg 160', *Palaeogeography, Palaeoclimatology, Palaeoecology*, 158(3–4), pp. 371–395. Available at: https://doi.org/10.1016/S0031-0182(00)00059-6.

Emiliani, C. (1954) 'Depth habitats of some species of pelagic Foraminifera as indicated by oxygen isotope ratios', *American Journal of Science*, 252(3). Available at: https://doi.org/10.2475/ajs.252.3.149.

Emiliani, C. (1955) 'Pleistocene temperatures', *The Journal of geology*, 63(6), pp. 538–578.

England, P. and Searle, M. (1986) 'The Cretaceous-tertiary deformation of the Lhasa Block and its implications for crustal thickening in Tibet', *Tectonics*, 5(1), pp. 1–14. Available at: https://doi.org/10.1029/TC005I001P00001.

England, P.C. and Houseman, G.A. (1988) 'The mechanics of the Tibetan Plateau', *Philosophical Transactions - Royal Society of London, Series A*, 326(1589), pp. 301–320. Available at: https://doi.org/10.1098/rsta.1988.0089.

Evans, A.D., Teagle, D.A.H., Craw, D., Henstock, T.J. and Falcon-Suarez, I.H. (2021) 'Uplift and Exposure of Serpentinized Massifs: Modeling Differential Serpentinite Diapirism and Exhumation of the Troodos Mantle Sequence, Cyprus', *Journal of Geophysical Research: Solid Earth*, 126(6). Available at: https://doi.org/10.1029/2020JB021079.

Evans, D., Bhatia, R., Stoll, H. and Müller, W. (2015) 'LA-ICPMS Ba/Ca analyses of planktic foraminifera from the Bay of Bengal: Implications for late Pleistocene orbital control on monsoon freshwater flux', *Geochemistry, Geophysics, Geosystems*, 16(8). Available at: https://doi.org/10.1002/2015GC005822.

Evans, D. and Müller, W. (2012) 'Deep time foraminifera Mg/Ca paleothermometry: Nonlinear correction for secular change in seawater Mg/Ca', *Paleoceanography*, 27(4). Available at: https://doi.org/10.1029/2012PA002315.

Evans, D., Wade, B.S., Henehan, M., Erez, J. and Müller, W. (2016) 'Revisiting carbonate chemistry controls on planktic foraminifera Mg / Ca: Implications for sea surface temperature and hydrology shifts over the Paleocene-Eocene Thermal Maximum and Eocene-Oligocene transition', *Climate of the Past*, 12(4), pp. 819–835. Available at: https://doi.org/10.5194/CP-12-819-2016.

Eyal, Y. and Reches, Z. (1983) 'Tectonic analysis of the Dead Sea Rift Region since the Late-Cretaceous based on mesostructures', *Tectonics*, 2(2). Available at: https://doi.org/10.1029/TC002i002p00167.

Farmer, E.C., Kaplan, A., de Menocal, P.B. and Lynch-Stieglitz, J. (2007) 'Corroborating ecological depth preferences of planktonic foraminifera in the tropical Atlantic with the stable oxygen isotope ratios of core top specimens', *Paleoceanography*, 22(3). Available at: https://doi.org/10.1029/2006PA001361.

Farmer, J.R., Keller, K.J., Poirier, R.K., Dwyer, G.S., Schaller, M.F., Coxall, H.K., O'Regan, M. and Cronin, T.M. (2023) 'A 600 kyr reconstruction of deep Arctic seawater δ18O from benthic foraminiferal δ18O and ostracode Mg / Ca paleothermometry', *Clim. Past*, 19(3), pp. 555–578. Available at: https://doi.org/10.5194/cp-19-555-2023.

Ferguson, J.E., Henderson, G.M., Kucera, M. and Rickaby, R.E.M. (2008) 'Systematic change of foraminiferal Mg/Ca ratios across a strong salinity gradient', *Earth and Planetary Science Letters*, 265(1–2). Available at: https://doi.org/10.1016/j.epsl.2007.10.011.

Fielding, C.R. (2001) 'Sedimentation and Tectonics in Rift Basins: Red Sea, Gulf of Aden', *Sedimentology*, 48(3). Available at: https://doi.org/10.1046/j.1365-3091.2001.0394b.x.

Figueiredo, J., Hoorn, C., van der Ven, P. and Soares, E. (2009) 'Late Miocene onset of the Amazon River and the Amazon deep-sea fan: Evidence from the Foz do Amazonas Basin', *Geology*, 37(7), pp. 619–622. Available at: https://doi.org/10.1130/G25567A.1.

Fischer, A.G. and Bottjer, D.J. (1991) 'Orbital Forcing and Sedimentary Sequences', *SEPM Journal of Sedimentary Research*, Vol. 61. Available at: https://doi.org/10.1306/d4267839-2b26-11d7-8648000102c1865d.

Fitton, J.G. and Godard, M. (2004) 'Origin and evolution of magmas on the Ontong Java Plateau', *Geological Society Special Publication*, 229. Available at: https://doi.org/10.1144/GSL.SP.2004.229.01.10.

Fitton, J.G., Saunders, A.D., Norry, M.J., Hardarson, B.S. and Taylor, R.N. (1997) 'Thermal and chemical structure of the Iceland plume', *Earth and Planetary Science Letters*, 153(3–4), pp. 197–208. Available at: https://doi.org/10.1016/S0012-821X(97)00170-2.

Flecker, R. *et al.* (2015) 'Evolution of the Late Miocene Mediterranean–Atlantic gateways and their impact on regional and global environmental change', *Earth-Science Reviews*, 150, pp. 365–392. Available at: https://doi.org/10.1016/J.EARSCIREV.2015.08.007.

Flecker, R. and Ellam, R.M. (1999) 'Distinguishing climatic and tectonic signals in the sedimentary successions of marginal basins using Sr isotopes: An example from the Messinian salinity crisis, Eastern Mediterranean', *Journal of the Geological Society*, 156(4), pp. 847–854. Available at:

https://doi.org/10.1144/GSJGS.156.4.0847.

Flecker, R. and Ellam, R.M. (2006) 'Identifying Late Miocene episodes of connection and isolation in the Mediterranean–Paratethyan realm using Sr isotopes', *Sedimentary Geology*, 188–189, pp. 189–203. Available at: https://doi.org/10.1016/J.SEDGEO.2006.03.005.

Flecker, R., De Villiers, S. and Ellam, R.M. (2002) 'Modelling the effect of evaporation on the salinity-87Sr/86Sr relationship in modern and ancient marginal-marine systems: The Mediterranean Messinian Salinity Crisis', *Earth and Planetary Science Letters*, 203(1), pp. 221–233. Available at: https://doi.org/10.1016/S0012-821X(02)00848-8.

Flower, B.P. and Kennett, J.P. (1993) 'Middle Miocene ocean-climate transition: High-resolution oxygen and carbon isotopic records from Deep Sea Drilling Project Site 588A, southwest Pacific', *Paleoceanography*, 8(6), pp. 811–843. Available at: https://doi.org/10.1029/93PA02196.

Flower, B.P. and Kennett, J.P. (1994) 'The middle Miocene climatic transition: East Antarctic ice sheet development, deep ocean circulation and global carbon cycling', *Palaeogeography, Palaeoclimatology, Palaeoecology*, 108(3–4), pp. 537–555. Available at: https://doi.org/10.1016/0031-0182(94)90251-8.

Follows, E.J. (1990) 'Sedimentology and tectonic setting of Miocene reef and related sediments in Cyprus'. University of Edinburgh.

Follows, E.J. (1992) 'Patterns of reef sedimentation and diagenesis in the Miocene of Cyprus', *Sedimentary Geology*, 79(1–4). Available at: https://doi.org/10.1016/0037-0738(92)90013-H.

Follows, E.J. and Robertson, A.H.F. (1990) 'Sedimentology and structural setting of Miocene reefal limestones in Cyprus', in *Troodos 1987. Symposium*, pp. 207–215.

Follows, E.J., Robertson, A.H.F. and Scoffin, T.P. (1996) 'Tectonic controls on Miocene reefs and related carbonate facies in Cyprus', *Models for carbonate stratigraphy from Miocene reef complexes of Mediterranean regions*, pp. 295–315. Available at: https://doi.org/10.2110/csp.96.01.0295.

Foster, G.L., Lear, C.H. and Rae, J.W.B. (2012) 'The evolution of pCO2, ice volume and climate during the middle Miocene', *Earth and Planetary Science Letters*, 341–344, pp. 243–254. Available at: https://doi.org/https://doi.org/10.1016/j.epsl.2012.06.007.

Fraissinet, C., El Zouine, M., Morel, J.-L., Poisson, A., Andrieux, J. and Faure-Muret, A. (1988) 'Structural evolution of the southern and northern Central High Atlas in paleogene and Mio-Pliocene times', in. Available at: https://doi.org/10.1007/bfb0011597.

Frank, T.D., Arthur, M.A. and Dean, W.E. (1999) 'Diagenesis of lower Cretaceous pelagic carbonates, North Atlantic: Paleoceanographic signals obscured', *Journal of Foraminiferal Research*, 29(4).

Friedrich, O., Schiebel, R., Wilson, P.A., Weldeab, S., Beer, C.J., Cooper, M.J. and Fiebig, J. (2012) 'Influence of test size, water depth, and ecology on Mg/Ca, Sr/Ca, δ18O and δ13C in nine modern species of planktic foraminifers', *Earth and Planetary Science Letters*, 319–320, pp. 133–145. Available at: https://doi.org/10.1016/J.EPSL.2011.12.002.

Frisch, W., Kuhlemann, J., Dunkl, I. and Brügel, A. (1998) 'Palinspastic reconstruction and topographic evolution of the Eastern Alps during late Tertiary tectonic extrusion', *Tectonophysics*, 297(1–4), pp. 1–15. Available at: https://doi.org/10.1016/S0040-1951(98)00160-7.

Frisch, W., Székely, B., Kuhlemann, J. and Dunkl, I. (2000) 'Geomorphologicalevolution of the Eastern Alps in response to Miocene tectonics', *Zeitschrift für Geomorphologie*, 44(1), pp. 103–138. Available at: https://doi.org/10.1127/ZFG/44/2000/103.

Garcés, M., Krijgsman, W. and Agustí, J. (1998) 'Chronology of the late Turolian deposits of the Fortuna basin (SE Spain): implications for the Messinian evolution of the eastern Betics', *Earth and Planetary Science Letters*, 163(1–4), pp. 69–81. Available at: https://doi.org/10.1016/S0012-821X(98)00176-9.

Garcia-Castellanos, D., Estrada, F., Jiménez-Munt, I., Gorini, C., Fernández, M., Vergés, J. and De Vicente, R. (2009) 'Catastrophic flood of the Mediterranean after the Messinian salinity crisis', *Nature*, 462(7274), pp. 778–781. Available at: https://doi.org/10.1038/nature08555.

Garfunkel, Z. and Derin, B. (1984) 'Permian-early Mesozoic tectonism and continental margin formation

in Israel and its implications for the history of the Eastern Mediterranean', *Geological Society Special Publication*, 17, pp. 187–201. Available at: https://doi.org/10.1144/GSL.SP.1984.017.01.12.

Garver, J.I. and Scott, T.J. (1995) 'Trace elements in shale as indicators of crustal provenance and terrane accretion in the southern Canadian Cordillera', *GSA Bulletin*, 107(4), pp. 440–453. Available at: https://doi.org/10.1130/0016-7606(1995)107<0440:TEISAI>2.3.CO;2.

Garzione, C.N., Hoke, G.D., Libarkin, J.C., Withers, S., MacFadden, B., Eiler, J., Ghosh, P. and Mulch, A. (2008) 'Rise of the Andes', *Science*. Available at: https://doi.org/10.1126/science.1148615.

Gaskell, D.E. and Hull, P.M. (2023) 'Technical note: A new online tool for $δ^{18}$O--temperature conversions', *Climate of the Past*, 19(6), pp. 1265–1274. Available at: https://doi.org/10.5194/cp-19-1265-2023.

Gass, I.G. (1960) *The geology and mineral resources of the Dhali area*. authority of the Government of Cyprus.

Gass, I.G., MacLeod, C.J., Murton, B.J., Panayiotou, A., Simonian, K.O. and Xenophontos, C. (1994) *The geological evolution of the Southern Troodos transform fault zone*. Geological Survey Department.

Gass, I.G. and Masson-Smith, D. (1963) 'The geology and gravity anomalies of the Troodos Massif, Cyprus', *Philosophical Transactions of the Royal Society of London. Series A, Mathematical and Physical Sciences*, 255(1060), pp. 417–467.

Ghosh, P., Garzione, C.N. and Eiler, J.M. (2006) 'Rapid uplift of the Altiplano revealed through 13C-18O bonds in paleosol carbonates', *Science*, 311(5760). Available at: https://doi.org/10.1126/science.1119365.

Gilbert, M.F. and Robertson, A.H.F. (2013) 'Field relations, geochemistry and origin of the upper cretaceous volcaniclastic kannaviou formation in western cyprus: Evidence of a southerly neotethyan volcanic arc', *Geological Society Special Publication*, 372(1). Available at: https://doi.org/10.1144/SP372.20.

Glor, R.E. and Warren, D. (2011) 'Testing ecological explanations for biogeographic boundaries', *Evolution*, 65(3). Available at: https://doi.org/10.1111/j.1558-5646.2010.01177.x.

Goff, J.C., Jones, R.W., Horbury, A.D. and Al-Husseini, M.I. (1995) 'Cenozoic basin evolution of the northern part of the Arabian Plate and its control on hydrocarbon habitat', *Middle east petroleum geosciences, GEO*, 94, pp. 402–412.

Goldner, A., Herold, N. and Huber, M. (2014) 'The challenge of simulating the warmth of the mid-Miocene climatic optimum in CESM1', *Climate of the Past*, 10(2), pp. 523–536. Available at: https://doi.org/10.5194/CP-10-523-2014.

Göncüoglu, M.C., Turhan, N. and Tekin, U.K. (2003) 'Evidence for the Triassic rifting and opening of the Neotethyan Izmir-Ankara Ocean and discussion on the presence of Cimmerian events at the northern edge of the Tauride-Anatolide Platform, Turkey', *Bollettino della Societa Geologica Italiana*, 2(1).

Görler, K., Helmdach, F.-F., Gaemers, P., Heißig, K., Hinsch, W., Mädler, K., Schwarzhans, W. and Zucht, M. (2005) 'The uplift of the central High Atlas as deduced from neogene continental sediments of the Ouarzazate province, Morocco', in *The Atlas System of Morocco*. Available at: https://doi.org/10.1007/bfb0011601.

Govin, A., Holzwarth, U., Heslop, D., Ford Keeling, L., Zabel, M., Mulitza, S., Collins, J.A. and Chiessi, C.M. (2012) 'Distribution of major elements in Atlantic surface sediments (36°N-49°S): Imprint of terrigenous input and continental weathering', *Geochemistry, Geophysics, Geosystems*, 13(1). Available at: https://doi.org/10.1029/2011GC003785.

Gradstein, F.M. (2020) 'Chapter 1 - Introduction', in F.M. Gradstein, J.G. Ogg, M.D. Schmitz, and G.M.B.T.-G.T.S. 2020 Ogg (eds). Elsevier, pp. 3–20. Available at: https://doi.org/https://doi.org/10.1016/B978-0-12-824360-2.00001-2.

Gray, W.R. and Evans, D. (2019) 'Nonthermal Influences on Mg/Ca in Planktonic Foraminifera: A Review of Culture Studies and Application to the Last Glacial Maximum', *Paleoceanography and*

Paleoclimatology, 34(3), pp. 306–315. Available at: https://doi.org/10.1029/2018PA003517.

Gray, W.R., Evans, D., Henehan, M., Weldeab, S., Lea, D.W., Müller, W. and Rosenthal, Y. (2023) 'Sodium incorporation in foraminiferal calcite: An evaluation of the Na/Ca salinity proxy and evidence for multiple Na-bearing phases', *Geochimica et Cosmochimica Acta*, 348, pp. 152–164. Available at: https://doi.org/https://doi.org/10.1016/j.gca.2023.03.011.

Gray, W.R., Weldeab, S., Lea, D.W., Rosenthal, Y., Gruber, N., Donner, B. and Fischer, G. (2018) 'The effects of temperature, salinity, and the carbonate system on Mg/Ca in Globigerinoides ruber (white): A global sediment trap calibration', *Earth and Planetary Science Letters*, 482, pp. 607–620. Available at: https://doi.org/10.1016/J.EPSL.2017.11.026.

Groeneveld, J., Filipsson, H.L., Austin, W.E.N., Darling, K., McCarthy, D., Quintana Krupinski, N.B., Bird, C. and Schweizer, M. (2018) 'Assessing proxy signatures of temperature, salinity, and hypoxia in the Baltic Sea through foraminifera-based geochemistry and faunal assemblages', *J. Micropalaeontol.*, 37(2), pp. 403–429. Available at: https://doi.org/10.5194/jm-37-403-2018.

Groeneveld, J., Nürnberg, D., Tiedemann, R., Reichart, G.J., Steph, S., Reuning, L., Crudeli, D. and Mason, P. (2008) 'Foraminiferal Mg/Ca increase in the Caribbean during the Pliocene: Western Atlantic Warm Pool formation, salinity influence, or diagenetic overprint?', *Geochemistry, Geophysics, Geosystems*, 9(1). Available at: https://doi.org/10.1029/2006GC001564.

Grossman, E.L. (2012) 'Applying Oxygen Isotope Paleothermometry in Deep Time', *The Paleontological Society Papers*, 18. Available at: https://doi.org/10.1017/s1089332600002540.

Sen Gupta, B.K. (2003) *Modern Foraminifera*, *Modern Foraminifera*. Available at: https://doi.org/10.1007/0-306-48104-9.

Hakyemez, Y., Turhan, N., Sonmez, I. and Sumengen, M. (2000) 'Kuzey Kıbrıs Turk Cumhuriyeti'nin Jeolojisi [Geology of the Turkish Republic of Northern Cyprus]', *Unpublished report of MTA (Maden Tektik ve Arama), Genel Mudurlugu Jeoloji Etutleri Diaresi, Ankara* [Preprint].

Hamon, N., Sepulchre, P., Lefebvre, V. and Ramstein, G. (2013) 'The role of eastern Tethys seaway closure in the Middle Miocene Climatic Transition (ca. 14 Ma)', *Climate of the Past*, 9(6), pp. 2687–2702. Available at: https://doi.org/10.5194/cp-9-2687-2013.

Hans, U., Kleine, T. and Bourdon, B. (2013) 'Rb–Sr chronology of volatile depletion in differentiated protoplanets: BABI, ADOR and ALL revisited', *Earth and Planetary Science Letters*, 374, pp. 204–214. Available at: https://doi.org/10.1016/J.EPSL.2013.05.029.

Harrison, R.W., Newell, W.L., Batihanli, H., Panayides, I., McGeehin, J.P., Mahan, S.A., Özhür, A., Tsiolakis, E. and Necdet, M. (2004) 'Tectonic framework and Late Cenozoic tectonic history of the northern part of Cyprus: implications for earthquake hazards and regional tectonics', *Journal of Asian Earth Sciences*, 23(2), pp. 191–210. Available at: https://doi.org/10.1016/S1367-9120(03)00095-6.

Harzhauser, M., Piller, W.E. and Steininger, F.F. (2002) 'Circum-Mediterranean Oligo–Miocene biogeographic evolution – the gastropods' point of view', *Palaeogeography, Palaeoclimatology, Palaeoecology*, 183(1–2), pp. 103–133. Available at: https://doi.org/10.1016/S0031-0182(01)00464-3.

Haynes, L.L., Hönisch, B., Dyez, K.A., Holland, K., Rosenthal, Y., Fish, C.R., Subhas, A. V. and Rae, J.W.B. (2017) 'Calibration of the B/Ca proxy in the planktic foraminifer Orbulina universa to Paleocene seawater conditions', *Paleoceanography*, 32(6), pp. 580–599. Available at: https://doi.org/10.1002/2016PA003069.

Hays, J.D., Imbrie, J. and Shackleton, N.J. (1976) 'Variations in the earth's orbit: Pacemaker of the ice ages', *Science*. Available at: https://doi.org/10.1126/science.194.4270.1121.

He, M., Xiao, Y., Jin, Z., Liu, W., Ma, Y., Zhang, Y. and Luo, C. (2013) 'Quantification of boron incorporation into synthetic calcite under controlled pH and temperature conditions using a differential solubility technique', *Chemical Geology*, 337–338, pp. 67–74. Available at: https://doi.org/10.1016/J.CHEMGEO.2012.11.013.

Hemming, N.G. and Hanson, G.N. (1992) 'Boron isotopic composition and concentration in modern marine carbonates', *Geochimica et Cosmochimica Acta*, 56(1), pp. 537–543. Available at: https://doi.org/10.1016/0016-7037(92)90151-8.

Hemming, N.G., Reeder, R.J. and Hanson, G.N. (1995) 'Mineral-fluid partitioning and isotopic fractionation of boron in synthetic calcium carbonate', *Geochimica et Cosmochimica Acta*, 59(2), pp. 371–379. Available at: https://doi.org/10.1016/0016-7037(95)00288-B.

Henehan, M.J., Foster, G.L., Rae, J.W.B., Prentice, K.C., Erez, J., Bostock, H.C., Marshall, B.J. and Wilson, P.A. (2015) 'Evaluating the utility of B/Ca ratios in planktic foraminifera as a proxy for the carbonate system: A case study of Globigerinoides ruber', *Geochemistry, Geophysics, Geosystems*, 16(4), pp. 1052–1069. Available at: https://doi.org/10.1002/2014GC005514.

Henehan, M.J., Rae, J.W.B., Foster, G.L., Erez, J., Prentice, K.C., Kucera, M., Bostock, H.C., Martínez-Botí, M.A., Milton, J.A., Wilson, P.A., Marshall, B.J. and Elliott, T. (2013) 'Calibration of the boron isotope proxy in the planktonic foraminifera Globigerinoides ruber for use in palaeo-CO2 reconstruction', *Earth and Planetary Science Letters*, 364, pp. 111–122. Available at: https://doi.org/10.1016/J.EPSL.2012.12.029.

Henry, C.D. and Aranda-Gomez, J.J. (2000) 'Plate interactions control middle–late Miocene, proto-Gulf and Basin and Range extension in the southern Basin and Range', *Tectonophysics*, 318(1–4), pp. 1–26. Available at: https://doi.org/10.1016/S0040-1951(99)00304-2.

Henson, F.R.S., Browne, R.V. and McGinty, J. (1949) 'A synopsis of the stratigraphy and geological history of Cyprus', *Quarterly Journal of the Geological Society*, 105(1–4), pp. 1–41.

Herbert, T.D., Dalton, C.A., Liu, Z., Salazar, A., Si, W. and Wilson, D.S. (2022) 'Tectonic degassing drove global temperature trends since 20 Ma', *Science*, 377(6601). Available at: https://doi.org/10.1126/science.abl4353.

Herbert, T.D., Lawrence, K.T., Tzanova, A., Peterson, L.C., Caballero-Gill, R. and Kelly, C.S. (2016) 'Late Miocene global cooling and the rise of modern ecosystems', *Nature Geoscience*, 9(11), pp. 843–847. Available at: https://doi.org/10.1038/ngeo2813.

Hernández-Molina, F.J., Hüneke, H., Rodríguez-Tovar, F.J., Ng, Z.L., Llave, E., Mena, A., Gibb, A., Chiarella, D., Sammartino, S. and de la Vara, A. (2022) 'Eocene to middle Miocene contourite deposits in Cyprus: A record of Indian Gateway evolution', *Global and Planetary Change*, 219, p. 103983. Available at: https://doi.org/10.1016/J.GLOPLACHA.2022.103983.

Hershey, J.P., Fernandez, M., Milne, P.J. and Millero, F.J. (1986) 'The ionization of boric acid in NaCl, Na□Ca□Cl and Na□Mg□Cl solutions at 25°C', *Geochimica et Cosmochimica Acta*, 50(1), pp. 143–148. Available at: https://doi.org/10.1016/0016-7037(86)90059-1.

Hess, A. V, Auderset, A., Rosenthal, Y., Miller, K.G., Zhou, X., Sigman, D.M. and Martínez-García, A. (2023) 'A well-oxygenated eastern tropical Pacific during the warm Miocene', *Nature*, 619(7970), pp. 521–525. Available at: https://doi.org/10.1038/s41586-023-06104-6.

Higgs, N.C., Thomson, J., Wilson, T.R.S. and Croudace, I.W. (1994) 'Modification and complete removal of eastern Mediterranean sapropels by postdepositional oxidation', *Geology*, 22(5), pp. 423–426. Available at: https://doi.org/10.1130/0091-7613(1994)022<0423:MACROE>2.3.CO;2.

Hodell, D.A., Benson, R.H., Kent, D. V, Boersma, A. and Rakic-El Bied, K. (1994) 'Magnetostratigraphic, biostratigraphic, and stable isotope stratigraphy of an Upper Miocene drill core from the Salé Briqueterie (northwestern Morocco): A high-resolution chronology for the Messinian stage', *Paleoceanography*, 9(6), pp. 835–855. Available at: https://doi.org/https://doi.org/10.1029/94PA01838.

Hodell, D.A. and Woodruff, F. (1994) 'Variations in the strontium isotopic ratio of seawater during the Miocene: Stratigraphic and geochemical implications', *Paleoceanography*, 9(3). Available at: https://doi.org/10.1029/94PA00292.

Hoffman, A. and Kitchell, J.A. (1984) 'Evolution in a pelagic planktic system: A paleobiologic test of models of multispecies evolution', *Paleobiology*, 1. Available at: https://doi.org/10.1017/S0094837300007995.

Holbourn, A., Kuhnt, W., Clemens, S., Prell, W. and Andersen, N. (2013) 'Middle to late Miocene stepwise climate cooling: Evidence from a high-resolution deep water isotope curve spanning 8 million years', *Paleoceanography*, 28(4). Available at: https://doi.org/10.1002/2013PA002538.

Holbourn, A., Kuhnt, W., Clemens, S.C. and Heslop, D. (2021) 'A ∼12 Myr Miocene Record of East

Asian Monsoon Variability From the South China Sea', *Paleoceanography and Paleoclimatology*, 36(7). Available at: https://doi.org/10.1029/2021PA004267.

Holbourn, A., Kuhnt, W., Kochhann, K.G.D., Andersen, N. and Sebastian Meier, K.J. (2015) 'Global perturbation of the carbon cycle at the onset of the Miocene Climatic Optimum', *Geology*, 43(2), pp. 123–126. Available at: https://doi.org/10.1130/G36317.1.

Holbourn, A., Kuhnt, W., Schulz, M. and Erlenkeuser, H. (2005) 'Impacts of orbital forcing and atmospheric carbon dioxide on Miocene ice-sheet expansion', *Nature*, 438(7067). Available at: https://doi.org/10.1038/nature04123.

Holbourn, A., Kuhnt, W., Schulz, M., Flores, J.-A. and Andersen, N. (2007) 'Orbitally-paced climate evolution during the middle Miocene "Monterey" carbon-isotope excursion', *Earth and Planetary Science Letters*, 261(3), pp. 534–550. Available at: https://doi.org/https://doi.org/10.1016/j.epsl.2007.07.026.

Holbourn, A.E., Kuhnt, W., Clemens, S.C., Kochhann, K.G.D., Jöhnck, J., Lübbers, J. and Andersen, N. (2018) 'Late Miocene climate cooling and intensification of southeast Asian winter monsoon', *Nature Communications*, 9(1). Available at: https://doi.org/10.1038/s41467-018-03950-1.

Hollis, C.J. *et al.* (2019) 'The DeepMIP contribution to PMIP4: Methodologies for selection, compilation and analysis of latest Paleocene and early Eocene climate proxy data, incorporating version 0.1 of the DeepMIP database', *Geoscientific Model Development*, 12(7), pp. 3149–3206. Available at: https://doi.org/10.5194/GMD-12-3149-2019.

Hönisch, B., Allen, K.A., Lea, D.W., Spero, H.J., Eggins, S.M., Arbuszewski, J., deMenocal, P., Rosenthal, Y., Russell, A.D. and Elderfield, H. (2013) 'The influence of salinity on Mg/Ca in planktic foraminifers - Evidence from cultures, core-top sediments and complementary δ18O', *Geochimica et Cosmochimica Acta*, 121. Available at: https://doi.org/10.1016/j.gca.2013.07.028.

Hönisch, B., Allen, K.A., Russell, A.D., Eggins, S.M., Bijma, J., Spero, H.J., Lea, D.W. and Yu, J. (2011) 'Planktic foraminifers as recorders of seawater Ba/Ca', *Marine Micropaleontology*, 79(1), pp. 52–57. Available at: https://doi.org/https://doi.org/10.1016/j.marmicro.2011.01.003.

Hönisch, B. and Hemming, N.G. (2004) 'Ground-truthing the boron isotope-paleo-pH proxy in planktonic foraminifera shells: Partial dissolution and shell size effects', *Paleoceanography*, 19(4), pp. 1–13. Available at: https://doi.org/10.1029/2004PA001026.

Hoogakker, B.A.A., Klinkhammer, G.P., Elderfield, H., Rohling, E.J. and Hayward, C. (2009) 'Mg/Ca paleothermometry in high salinity environments', *Earth and Planetary Science Letters*, 284(3–4), pp. 583–589. Available at: https://doi.org/10.1016/J.EPSL.2009.05.027.

Hooper, P.R. (1982) 'The Columbia River Basalts', *Science*, 215(4539), pp. 1463–1468. Available at: https://doi.org/10.1126/SCIENCE.215.4539.1463.

Horita, J., Zimmermann, H. and Holland, H.D. (2002) 'Chemical evolution of seawater during the Phanerozoic: Implications from the record of marine evaporites', *Geochimica et Cosmochimica Acta*, 66(21), pp. 3733–3756. Available at: https://doi.org/10.1016/S0016-7037(01)00884-5.

Horwitz, E.P., Dietz, M.L. and Fisher, D.E. (1991) 'Separation and Preconcentration of Strontium from Biological, Environmental, and Nuclear Waste Samples by Extraction Chromatography Using a Crown Ether', *Analytical Chemistry*, 63(5). Available at: https://doi.org/10.1021/ac00005a027.

Howes, E.L., Kaczmarek, K., Raitzsch, M., Mewes, A., Bijma, N., Horn, I., Misra, S., Gattuso, J.P. and Bijma, J. (2017) 'Decoupled carbonate chemistry controls on the incorporation of boron into Orbulina universa', *Biogeosciences*, 14(2), pp. 415–430. Available at: https://doi.org/10.5194/BG-14-415-2017.

Hsü, K.J. (1978) 'The messinian salinity crisis - Evidence of Late Miocene eustatic changes in the world ocean', *Naturwissenschaften*, 65(3). Available at: https://doi.org/10.1007/BF00440344.

Hsü, K.J., Cita, M.B. and Ryan, W.B.F. (1973a) '43 . The origin of the Mediterranean evaporites', *Init. Rep. DSDP*, XIII(Part 2).

Hsü, K.J., Ryan, W.B.F. and Cita, M.B. (1973b) 'Late miocene desiccation of the mediterranean', *Nature*, 242(5395), pp. 240–244. Available at: https://doi.org/10.1038/242240a0.

Hüneke, H., Hernández-Molina, F.J., Rodríguez-Tovar, F.J., Llave, E., Chiarella, D., Mena, A. and Stow, D.A.V. (2021) 'Diagnostic criteria using microfacies for calcareous contourites, turbidites and pelagites in the Eocene–Miocene slope succession, southern Cyprus', *Sedimentology*, 68(2), pp. 557–592. Available at: https://doi.org/10.1111/SED.12792.

Hurford, A.J., Hunziker, J.C. and Stöckhert, B. (1991) 'Constraints on the late thermotectonic evolution of the western Alps: Evidence for episodic rapid uplift', *Tectonics*, 10(4). Available at: https://doi.org/10.1029/91TC00167.

Hüsing, S.K., Zachariasse, W.J., Van Hinsbergen, D.J.J., Krijgsman, W., Inceöz, M., Harzhauser, M., Mandic, O. and Kroh, A. (2009) 'Oligocene-miocene basin evolution in se anatolia, turkey: Constraints on the closure of the eastern tethys gateway', *Geological Society Special Publication*, 311(1), pp. 107–132. Available at: https://doi.org/10.1144/SP311.4.

Hut, G. (1987) 'Consultants' group meeting on stable isotope reference samples for geochemical and hydrological investigations', *International Atomic Energy Agency (IAEA)* [Preprint], (September 1985).

Inwood, J., Anderson, M.W., Morris, A. and Robertson, A.H.F. (2009) 'Successive structural events in the Hatay ophiolite of southeast Turkey: Distinguishing oceanic, emplacement and post-emplacement phases of faulting', *Tectonophysics*, 473(1–2). Available at: https://doi.org/10.1016/j.tecto.2008.10.037.

Jacobs, E., Weissert, H., Shields, G. and Stille, P. (1996) 'The Monterey event in the Mediterranean: A record from shelf sediments of Malta', *Paleoceanography*, 11(6). Available at: https://doi.org/10.1029/96PA02230.

Jaeschke, A., Rühlemann, C., Arz, H., Heil, G. and Lohmann, G. (2007) 'Coupling of millennial-scale changes in sea surface temperature and precipitation off northeastern Brazil with high-latitude climate shifts during the last glacial period', *Paleoceanography*, 22(4). Available at: https://doi.org/10.1029/2006PA001391.

Jaffey, N. and Robertson, A.H.F. (2005) 'Non-marine sedimentation associated with Oligocene-Recent exhumation and uplift of the Central Taurus Mountains, S Turkey', *Sedimentary Geology*, 173(1–4), pp. 53–89. Available at: https://doi.org/10.1016/J.SEDGEO.2003.11.025.

Jiménez-Moreno, G., Fauquette, S. and Suc, J.-P. (2008) 'Vegetation, climate and palaeoaltitude reconstructions of the Eastern Alps during the Miocene based on pollen records from Austria, Central Europe', *Journal of Biogeography*, 35(9). Available at: https://doi.org/10.1111/j.1365-2699.2008.01911.x.

John, C.M., Karner, G.D., Browning, E., Leckie, R.M., Mateo, Z., Carson, B. and Lowery, C. (2011) 'Timing and magnitude of Miocene eustasy derived from the mixed siliciclastic-carbonate stratigraphic record of the northeastern Australian margin', *Earth and Planetary Science Letters*, 304(3–4), pp. 455–467. Available at: https://doi.org/10.1016/J.EPSL.2011.02.013.

Jolivet, L., Augier, R., Robin, C., Suc, J.-P. and Rouchy, J.M. (2006) 'Lithospheric-scale geodynamic context of the Messinian salinity crisis', *Sedimentary Geology*, 188–189. Available at: https://doi.org/10.1016/j.sedgeo.2006.02.004.

Jolivet, L. and Faccenna, C. (2000) 'Mediterranean extension and the Africa-Eurasia collision AND FACCENNA- CENOZOIC BASINS AND AFRICA-EURASIA', 19(6), pp. 1095–1106.

Kähler, G. and Stow, D.A.V. (1998) 'Turbidites and contourites of the Palaeogene Lefkara Formation, southern Cyprus', *Sedimentary Geology*, 115(1–4), pp. 215–231. Available at: https://doi.org/10.1016/S0037-0738(97)00094-8.

Kaminski, M.A., Aksu, A., Box, M., Hiscott, R.N., Filipescu, S. and Al-Salameen, M. (2002) 'Late Glacial to Holocene benthic foraminifera in the Marmara Sea: implications for Black Sea–Mediterranean Sea connections following the last deglaciation', *Marine Geology*, 190(1–2), pp. 165–202. Available at: https://doi.org/10.1016/S0025-3227(02)00347-X.

Karami, M.P., Meijer, P.T., Dijkstra, H.A. and Wortel, M.J.R. (2009) 'An oceanic box model of the Miocene Mediterranean Sea with emphasis on the effects of closure of the eastern gateway', *Paleoceanography*, 24(4). Available at: https://doi.org/10.1029/2008PA001679.

Kasbohm, J. and Schoene, B. (2018) 'Rapid eruption of the Columbia River flood basalt and correlation

with the mid-Miocene climate optimum', *Science Advances*, 4(9), p. eaat8223. Available at: https://doi.org/10.1126/sciadv.aat8223.

Katz, M.E. and Miller, K.G. (1996) 'Eocene to Miocene Oceanographic and Provenance Changes in a Sequence Stratigraphic Framework: Benthic Foraminifers of the New Jersey Margin', in *Proceedings of the Ocean Drilling Program, 150 Scientific Results*. Available at: https://doi.org/10.2973/odp.proc.sr.150.003.1996.

Keller, G. and Barron, J.A. (1983) 'Paleoceanographic implications of Miocene deep-sea hiatuses', *GSA Bulletin*, 94(5), pp. 590–613. Available at: https://doi.org/10.1130/0016-7606(1983)94<590:PIOMDH>2.0.CO;2.

Kennett, J.P., Exon, N.F., Kennett, J.P. and Exon, N.F. (2004) 'Paleoceanographic evolution of the Tasmanian Seaway and its climatic implications', *GMS*, 151, pp. 345–367. Available at: https://doi.org/10.1029/151GM19.

Kennett, J.P., Houtz, R.E. and Shackleton, N.J. (1975) 'Paleotemperature History of the Cenozoic and the Initiation of Antarctic Glaciation: Oxygen and Carbon Isotope Analyses in DSDP Sites 277, 279 and 281', in *Initial Reports of the Deep Sea Drilling Project, 29*. U. S. Government Printing Office, pp. 743–756. Available at: https://doi.org/10.2973/dsdp.proc.29.117.1975.

Kennett, J.P. and Shackleton, N.J. (1975) 'Laurentide ice sheet meltwater recorded in gulf of Mexico deep-sea cores', *Science*, 188(4184), pp. 147–150. Available at: https://doi.org/10.1126/science.188.4184.147.

Keul, N., Langer, G., Thoms, S., de Nooijer, L.J., Reichart, G.J. and Bijma, J. (2017) 'Exploring foraminiferal Sr/Ca as a new carbonate system proxy', *Geochimica et Cosmochimica Acta*, 202, pp. 374–386. Available at: https://doi.org/10.1016/J.GCA.2016.11.022.

Kidd, R.G.W. and Cann, J.R. (1974) 'Chilling statistics indicate an ocean-floor spreading origin for the Troodos complex, Cyprus', *Earth and Planetary Science Letters*, 24(1), pp. 151–155. Available at: https://doi.org/10.1016/0012-821X(74)90020-X.

Kim, J.H., Schouten, S., Hopmans, E.C., Donner, B. and Sinninghe Damsté, J.S. (2008) 'Global sediment core-top calibration of the TEX86 paleothermometer in the ocean', *Geochimica et Cosmochimica Acta*, 72(4). Available at: https://doi.org/10.1016/j.gca.2007.12.010.

Kinnaird, T. and Robertson, A.H.F. (2013) 'Tectonic and sedimentary response to subduction and incipient continental collision in southern Cyprus, easternmost Mediterranean region', *Geological Society, London, Special Publications*, 372(1), pp. 585 LP – 614. Available at: https://doi.org/10.1144/SP372.10.

Kinnaird, T.C., Robertson, A.H.F. and Morris, A. (2011) 'Timing of uplift of the Troodos Massif (Cyprus) constrained by sedimentary and magnetic polarity evidence', *Journal of the Geological Society*, 168(2). Available at: https://doi.org/10.1144/0016-76492009-150.

Kisakürek, B., Eisenhauer, A., Böhm, F., Garbe-Schönberg, D. and Erez, J. (2008) 'Controls on shell Mg/Ca and Sr/Ca in cultured planktonic foraminiferan, Globigerinoides ruber (white)', *Earth and Planetary Science Letters*, 273(3–4). Available at: https://doi.org/10.1016/j.epsl.2008.06.026.

Kober, F., Schlunegger, F., Zeilinger, G. and Schneider, H. (2006) 'Surface uplift and climate change: The geomorphic evolution of the Western Escarpment of the Andes of northern Chile between the Miocene and present', *Special Paper of the Geological Society of America*, 398, pp. 75–86. Available at: https://doi.org/10.1130/2006.2398(05).

Kontakiotis, G., Butiseacă, G.A., Antonarakou, A., Agiadi, K., Zarkogiannis, S.D., Krsnik, E., Besiou, E., Zachariasse, W.J., Lourens, L., Thivaiou, D., Koskeridou, E., Moissette, P., Mulch, A., Karakitsios, V. and Vasiliev, I. (2022) 'Hypersalinity accompanies tectonic restriction in the eastern Mediterranean prior to the Messinian Salinity Crisis', *Palaeogeography, Palaeoclimatology, Palaeoecology*, 592, p. 110903. Available at: https://doi.org/https://doi.org/10.1016/j.palaeo.2022.110903.

Kouwenhoven, T.J., Morigi, C., Negri, A., Giunta, S., Krijgsman, W. and Rouchy, J.M. (2006) 'Paleoenvironmental evolution of the eastern Mediterranean during the Messinian: Constraints from integrated microfossil data of the Pissouri Basin (Cyprus)', *Marine Micropaleontology*, 60(1), pp. 17–44.

Available at: https://doi.org/10.1016/j.marmicro.2006.02.005.

Kouwenhoven, T.J., Seidenkrantz, M.S. and Van Der Zwaan, G.J. (1999) 'Deep-water changes: The near-synchronous disappearance of a group of benthic foraminifera from the Late Miocene Mediterranean', *Palaeogeography, Palaeoclimatology, Palaeoecology*, 152(3–4). Available at: https://doi.org/10.1016/S0031-0182(99)00065-6.

Kovac, M., Kral, J., Marton, E., Plasienka, D. and Uher, P. (1994) 'Alpine uplift history of the central western Carpathians: geochronological, paleomagnetic, sedimentary and structural data', *Geologica Carpathica*, 45(2).

Kozdon, R., Kelly, D.C., Kitajima, K., Strickland, A., Fournelle, J.H. and Valley, J.W. (2013) 'In situ δ18O and Mg/Ca analyses of diagenetic and planktic foraminiferal calcite preserved in a deep-sea record of the Paleocene-Eocene thermal maximum', *Paleoceanography*, 28(3). Available at: https://doi.org/10.1002/palo.20048.

Krijgsman, W., Blanc-Valleron, M.-M., Flecker, R., Hilgen, F.J., Kouwenhoven, T.J., Merle, D., Orszag-Sperber, F. and Rouchy, J.M. (2002) 'The onset of the Messinian salinity crisis in the Eastern Mediterranean (Pissouri Basin, Cyprus)', *Earth and Planetary Science Letters*, 194(3), pp. 299–310. Available at: https://doi.org/https://doi.org/10.1016/S0012-821X(01)00574-X.

Krijgsman, W., Capella, W., Simon, D., Hilgen, F.J., Kouwenhoven, T.J., Meijer, P.T., Sierro, F.J., Tulbure, M.A., van den Berg, B.C.J., van der Schee, M. and Flecker, R. (2018) 'The Gibraltar Corridor: Watergate of the Messinian Salinity Crisis', *Marine Geology*, 403, pp. 238–246. Available at: https://doi.org/10.1016/J.MARGEO.2018.06.008.

Krijgsman, W., Hilgen, F.J., Raffi, I., Sierro, F.J. and Wilson, D.S. (1999a) 'Chronology, causes and progression of the Messinian salinity crisis', *Nature*, 400(6745), pp. 652–655. Available at: https://doi.org/10.1038/23231.

Krijgsman, W., Langereis, C.G., Zachariasse, W.J., Boccaletti, M., Moratti, G., Gelati, R., Iaccarino, S., Papani, G. and Villa, G. (1999b) 'Late Neogene evolution of the Taza–Guercif Basin (Rifian Corridor, Morocco) and implications for the Messinian salinity crisis', *Marine Geology*, 153(1–4), pp. 147–160. Available at: https://doi.org/10.1016/S0025-3227(98)00084-X.

Kroon, D., Alexander, I., Little, M., Lourens, L.J., Matthewson, A., Robertson, A.H.F. and Sakamoto, T. (1998) 'Oxygen isotope and Sapropel stratigraphy in the eastern Mediterranean during the last 3.2 million years', *Proceedings of the Ocean Drilling Program: Scientific Results*, 160. Available at: https://doi.org/10.2973/odp.proc.sr.160.071.1998.

Kucera, M. (2007) 'Chapter Six Planktonic Foraminifera as Tracers of Past Oceanic Environments', in C. Hillaire–Marcel and A.B.T.-D. in M.G. De Vernal (eds) *Proxies in Late Cenozoic Paleoceanography*. Elsevier, pp. 213–262. Available at: https://doi.org/https://doi.org/10.1016/S1572-5480(07)01011-1.

Kuhlemann, J. (2007) 'Paleogeographic and paleotopographic evolution of the Swiss and Eastern Alps since the Oligocene', *Global and Planetary Change*, 58(1–4). Available at: https://doi.org/10.1016/j.gloplacha.2007.03.007.

Kuhlemann, J., Frisch, W., Dunkl, I., Székely, B. and Spiegel, C. (2001) 'Miocene shifts of the drainage divide in the alps and their foreland basin', *Zeitschrift fur Geomorphologie*, 45(2). Available at: https://doi.org/10.1127/zfg/45/2001/239.

Kuhnt, W., Holbourn, A., Hall, R., Zuvela, M. and Käse, R. (2004) 'Neogene history of the indonesian throughflow', in *Geophysical Monograph Series*. Available at: https://doi.org/10.1029/149GM16.

Lagabrielle, Y., Goddéris, Y., Donnadieu, Y., Malavieille, J. and Suarez, M. (2009) 'The tectonic history of Drake Passage and its possible impacts on global climate', *Earth and Planetary Science Letters*, 279(3–4). Available at: https://doi.org/10.1016/j.epsl.2008.12.037.

De Lange, G.J., Thomson, J., Reitz, A., Slomp, C.P., Speranza Principato, M., Erba, E. and Corselli, C. (2008) 'Synchronous basin-wide formation and redox-controlled preservation of a Mediterranean sapropel', *Nature Geoscience 2008 1:9*, 1(9), pp. 606–610. Available at: https://doi.org/10.1038/ngeo283.

Lanyon, R., Varne, R. and Crawford, A.J. (1993) 'Tasmanian Tertiary basalts, the Balleny plume, and

opening of the Tasman Sea (southwest Pacific Ocean)', *Geology*, 21(6). Available at: https://doi.org/10.1130/0091-7613(1993)021<0555:TTBTBP>2.3.CO;2.

Lapierre, H. (1972) *Les formations sédimentaires et éruptives des nappes de Mamonia et leurs rélations avec le massif de Troodos (Chypre)*. University of Nancy, France.

Lapierre, H. (1975) 'LES FORMATIONS SEDIMENTAIRES ET ERUPTIVES DES NAPPES DE MAMONIA ET LEURS RELATIONS AVEC LE MASSIF DU TROODOS (CHYPRE OCCIDENTALE).'

Lapierre, H., Bosch, D., Narros, A., Mascle, G.H., Tardy, M. and Demant, A. (2007) 'The Mamonia Complex (SW Cyprus) revisited: remnant of Late Triassic intra-oceanic volcanism along the Tethyan southwestern passive margin', *Geological Magazine*, 144(1), pp. 1–19.

Lavier, L.L., Steckler, M.S. and Brigaud, F. (2001) 'Climatic and tectonic control on the Cenozoic evolution of the West African margin', *Marine Geology*, 178(1–4), pp. 63–80. Available at: https://doi.org/10.1016/S0025-3227(01)00175-X.

Lawver, L.A. and Gahagan, L.M. (2003) 'Evolution of cenozoic seaways in the circum-antarctic region', in *Palaeogeography, Palaeoclimatology, Palaeoecology*. Available at: https://doi.org/10.1016/S0031-0182(03)00392-4.

Lea, D.W., Mashiotta, T.A. and Spero, H.J. (1999) 'Controls on magnesium and strontium uptake in planktonic foraminifera determined by live culturing', *Geochimica et Cosmochimica Acta*, 63(16). Available at: https://doi.org/10.1016/S0016-7037(99)00197-0.

Lear, C.H., Rosenthal, Y. and Slowey, N. (2002) 'Benthic foraminiferal Mg/Ca-paleothermometry: A revised core-top calibration', *Geochimica et Cosmochimica Acta*, 66(19). Available at: https://doi.org/10.1016/S0016-7037(02)00941-9.

Lear, C.H., Rosenthal, Y. and Wright, J.D. (2003) 'The closing of a seaway: Ocean water masses and global climate change', *Earth and Planetary Science Letters*, 210(3–4). Available at: https://doi.org/10.1016/S0012-821X(03)00164-X.

de Leeuw, J.W., v.d. Meer, F.W., Rijpstra, W.I.C. and Schenck, P.A. (1980) 'On the occurrence and structural identification of long chain unsaturated ketones and hydrocarbons in sediments', *Physics and Chemistry of the Earth*, 12(C), pp. 211–217. Available at: https://doi.org/10.1016/0079-1946(79)90105-8.

Lindsay, J.F., Holliday, D.W. and Hulbert, A.G. (1991) 'Sequence Stratigraphy and the Evolution of the Ganges-Brahmaputra Delta Complex1', *AAPG Bulletin*, 75(7), pp. 1233–1254. Available at: https://doi.org/10.1306/0C9B291B-1710-11D7-8645000102C1865D.

Lirer, F., Foresi, L.M., Iaccarino, S.M., Salvatorini, G., Turco, E., Cosentino, C., Sierro, F.J. and Caruso, A. (2019) 'Mediterranean Neogene planktonic foraminifer biozonation and biochronology', *Earth-Science Reviews*, 196(October 2018), p. 102869. Available at: https://doi.org/10.1016/j.earscirev.2019.05.013.

Livermore, R.A. and Smith, A.G. (1985) 'Some Boundary Conditions for the Evolution of the Mediterranean Region', in *Geological Evolution of the Mediterranean Basin*. Available at: https://doi.org/10.1007/978-1-4613-8572-1_5.

Lofi, J., Gorini, C., Berné, S., Clauzon, G., Tadeu Dos Reis, A., Ryan, W.B.F. and Steckler, M.S. (2005) 'Erosional processes and paleo-environmental changes in the Western Gulf of Lions (SW France) during the Messinian Salinity Crisis', *Marine Geology*, 217(1), pp. 1–30. Available at: https://doi.org/https://doi.org/10.1016/j.margeo.2005.02.014.

Lord, A.R., Panayides, I., Urquhart, E., Xenophontos, C. and Malpas, J. (2000) 'A biochronostratigraphical framework for the Late Cretaceous–Recent circum-Troodos sedimentary sequence, Cyprus', in *Proceedings of the Third International Conference on the Geology of the Eastern Mediterranean. Geological Survey Department, Nicosia*, p. 297.

Lourens, L., Hilgen, F.J., Shackleton, N.J., Laskar, J. and Wilson, D. (2005) 'The Neogene period', in *A Geologic Time Scale 2004*. Available at: https://doi.org/10.1017/CBO9780511536045.022.

Lowenstein, T.K., Timofeeff, M.N., Brennan, S.T., Hardie, L.A. and Demicco, R. V. (2001) 'Oscillations

in Phanerozoic seawater chemistry: Evidence from fluid Inclusions', *Science*, 294(5544), pp. 1086–1088. Available at: https://doi.org/10.1126/SCIENCE.1064280.

Lübbers, J., Kuhnt, W., Holbourn, A.E., Bolton, C.T., Gray, E., Usui, Y., Kochhann, K.G.D., Beil, S. and Andersen, N. (2019) 'The Middle to Late Miocene "Carbonate Crash" in the Equatorial Indian Ocean', *Paleoceanography and Paleoclimatology*, 34(5). Available at: https://doi.org/10.1029/2018PA003482.

Luciani, V., R Dickens, G., Backman, J., Fornaciari, E., Giusberti, L., Agnini, C. and D'Onofrio, R. (2016) 'Major perturbations in the global carbon cycle and photosymbiont-bearing planktic foraminifera during the early Eocene', *Climate of the Past*, 12(4). Available at: https://doi.org/10.5194/cp-12-981-2016.

Lyell, C. (1833) *Principles of Geology; Being an Attempt to Explain the Former Changes of the Earth's Surface by Reference to Causes Now in Operation.* Murray, London.

Lyle, M., Dadey, K.A. and Farrell, J.W. (1995) '42. The Late Miocene (11–8 Ma) Eastern Pacific Carbonate Crash: evidence for reorganization of deep-water Circulation by the closure of the Panama Gateway', *Proceedings of the ocean Drilling Program, Scientific Results*, 138.

Lyle, M., Joy Drury, A., Tian, J., Wilkens, R. and Westerhold, T. (2019) 'Late miocene to holocene high-resolution eastern equatorial pacific carbonate records: Stratigraphy linked by dissolution and paleoproductivity', *Climate of the Past*, 15(5). Available at: https://doi.org/10.5194/cp-15-1715-2019.

Mackenzie, G.D., Maguire, P.K.H., Coogan, L.A., Khan, M.A., Eaton, M. and Petrides, G. (2006) 'Geophysical constraints on the crustal architecture of the Troodos ophiolite: Results from the IANGASS project', *Geophysical Journal International*, 167(3). Available at: https://doi.org/10.1111/j.1365-246X.2006.03144.x.

Magyar, I., Radivojević, D., Sztanó, O., Synak, R., Ujszászi, K. and Pócsik, M. (2013) 'Progradation of the paleo-Danube shelf margin across the Pannonian Basin during the Late Miocene and Early Pliocene', *Global and Planetary Change*, 103(1). Available at: https://doi.org/10.1016/j.gloplacha.2012.06.007.

Maillard, A., Hübscher, C., Benkhelil, J. and Tahchi, E. (2011) 'Deformed Messinian markers in the Cyprus Arc: Tectonic and/or Messinian Salinity Crisis indicators?', *Basin Research*, 23(2). Available at: https://doi.org/10.1111/j.1365-2117.2010.00464.x.

Main, C.E., Robertson, A.H.F. and Palamakumbura, R.N. (2016) 'Pleistocene geomorphological and sedimentary development of the Akaki River catchment (northeastern Troodos Massif) in relation to tectonic uplift versus climatic change', *International Journal of Earth Sciences*, 105(1). Available at: https://doi.org/10.1007/s00531-015-1251-6.

Malpas, J., Xenophontos, C. and Williams, D. (1992) 'The Ayia Varvara Formation of SW Cyprus: a product of complex collisional tectonics', *Tectonophysics*, 212(3–4), pp. 193–211.

Mancini, A.M., Gennari, R., Ziveri, P., Mortyn, P.G., Stolwijk, D.J. and Lozar, F. (2020) 'Calcareous nannofossil and foraminiferal trace element records in the Sorbas Basin: A new piece of the Messinian Salinity Crisis onset puzzle', *Palaeogeography, Palaeoclimatology, Palaeoecology*, 554, p. 109796. Available at: https://doi.org/https://doi.org/10.1016/j.palaeo.2020.109796.

Mantis, M. (1970) 'Upper Cretaceous-Tertiary foraminiferal zones in Cyprus', *Sci. Res. Cent. of Cyprus, Epetiris*, 3, pp. 227–241.

Mantis, M. (1972) 'Some Planktonic Foraminifera from South Cyprus'.

Manzi, V., Lugli, S., Roveri, M., Dela Pierre, F., Gennari, R., Lozar, F., Natalicchio, M., Schreiber, B.C., Taviani, M. and Turco, E. (2016) 'The Messinian salinity crisis in Cyprus: a further step towards a new stratigraphic framework for Eastern Mediterranean', *Basin Research*, 28(2), pp. 207–236. Available at: https://doi.org/10.1111/bre.12107.

Marred, M., Naimi, M.N., Djaiz, F., Kherchouche, A. and Boushaba, A. (2022) 'Gastrochaenolites ornatus Kelly and Bromley and other trace fossils on a Middle Miocene omission surface from the Aures Massif, Algeria', *Proceedings of the Geologists' Association*, 133(3), pp. 218–226. Available at: https://doi.org/https://doi.org/10.1016/j.pgeola.2022.04.004.

Marumo, Y. (1986) 'Clay Mineralogical Analysis Using the< 0.05 mm Fraction for Forensic Science

Investigation-Its Application to Volcanic Ash Soils and Yellow Brown Forest Soils', *Jour. Forensic Sci.*, 31, pp. 1039–1049.

Mathien-Blard, E. and Bassinot, F. (2009) 'Salinity bias on the foraminifera Mg/Ca thermometry: Correction procedure and implications for past ocean hydrographic reconstructions', *Geochemistry, Geophysics, Geosystems*, 10(12), p. 12011. Available at: https://doi.org/10.1029/2008GC002353.

Mattinson, J.M. (1972) 'Preparation of hydrofluoric, hydrochloric, and nitric acids at ultralow lead levels', *Analytical Chemistry*, 44(9), pp. 1715–1716.

Mayer, L.A., Shipley, T.H. and Winterer, E.L. (1986) 'Equatorial Pacific Seismic Reflectors as Indicators of Global Oceanographic Events', *Science*, 233(4765), pp. 761–764. Available at: https://doi.org/10.1126/science.233.4765.761.

McArthur, J.M. and Howarth, R.J. (2004) 'Sr-isotope stratigraphy', in F.M. Gradstein, J.G. Ogg, and A.G. Smith (eds) *Geological Timescale 2004*. Cambridge: Cambridge University Press, p. 589.

McArthur, J.M., Howarth, R.J. and Bailey, T.R. (2001) 'Strontium isotope stratigraphy: LOWESS version 3: Best fit to the marine Sr-isotope curve for 0-509 Ma and accompanying look-up table for deriving numerical age', *Journal of Geology*, 109(2), pp. 155–170. Available at: https://doi.org/10.1086/319243/ASSET/IMAGES/LARGE/FG9.JPEG.

McArthur, J.M., Howarth, R.J. and Shields, G.A. (2012) 'Strontium isotope stratigraphy', *The geologic time scale*, 1, pp. 127–144.

McCallum, J.E. and Robertson, A.H.F. (1995a) 'Late Pliocene-early Pleistocene Athalassa Formation, north central Cyprus: carbonate sand bodies in a shallow seaway between two emerging landmasses', *Terra Nova*, 7(2). Available at: https://doi.org/10.1111/j.1365-3121.1995.tb00694.x.

McCallum, J.E. and Robertson, A.H.F. (1995b) 'Sedimentology of two fan-delta systems in the Pliocene-Pleistocene of the Mesaoria Basin, Cyprus', *Sedimentary Geology*, 98(1–4). Available at: https://doi.org/10.1016/0037-0738(95)00034-6.

McCay, G.A. (2011) 'Tectonic-sedimentary evolution of the Girne (Kyrenia) Range and the Mesarya (Mesaoria) Basin, North Cyprus'.

McCay, G.A. and Robertson, A.H.F. (2012) 'Late Eocene-Neogene sedimentary geology of the Girne (Kyrenia) Range, northern Cyprus: A case history of sedimentation related to progressive and diachronous continental collision', *Sedimentary Geology*, 265–266. Available at: https://doi.org/10.1016/j.sedgeo.2012.03.001.

McCay, G.A. and Robertson, A.H.F. (2013) 'Upper miocene-pleistocene deformation of the girne (kyrenia) range and dar dere (Ovgos) lineaments, northern Cyprus: Role in collision and tectonic escape in the easternmost Mediterranean region', *Geological Society Special Publication*, 372(1), pp. 421–445. Available at: https://doi.org/10.1144/SP372.6.

McCay, G.A., Robertson, A.H.F., Kroon, D., Raffi, I., Ellam, R.M. and Necdet, M. (2013) 'Stratigraphy of Cretaceous to Lower Pliocene sediments in the northern part of Cyprus based on comparative 87Sr/86Sr isotopic, nannofossil and planktonic foraminiferal dating', *Geological Magazine*, 150(2), pp. 333–359. Available at: https://doi.org/10.1017/S0016756812000465.

McConnell, M.C. and Thunell, R.C. (2005) 'Calibration of the planktonic foraminiferal Mg/Ca paleothermometer: Sediment trap results from the Guaymas Basin, Gulf of California', *Paleoceanography*, 20(2), pp. 1–18. Available at: https://doi.org/10.1029/2004PA001077.

McQuarrie, N. and Van Hinsbergen, D.J.J. (2013) 'Retrodeforming the Arabia-Eurasia collision zone: Age of collision versus magnitude of continental subduction', *Geology*, 41(3), pp. 315–318. Available at: https://doi.org/10.1130/G33591.1.

Meigs, A.J., Burbank, D.W. and Beck, R.A. (1995) 'Middle-late Miocene (>10 Ma) formation of the Main Boundary Thrust in the western Himalaya', *Geology*, 23(5), pp. 423–426. Available at: https://doi.org/10.1130/0091-7613(1995)023<0423:MLMMFO>2.3.CO;2.

Meijers, M.J.M., Brocard, G.Y., Cosca, M.A., Lüdecke, T., Teyssier, C., Whitney, D.L. and Mulch, A. (2018a) 'Rapid late Miocene surface uplift of the Central Anatolian Plateau margin', *Earth and Planetary*

Science Letters, 497. Available at: https://doi.org/10.1016/j.epsl.2018.05.040.

Meijers, M.J.M., Brocard, G.Y., Whitney, D.L. and Mulch, A. (2020) 'Paleoenvironmental conditions and drainage evolution of the central anatolian lake system (Turkey) during late miocene to pliocene surface uplift', *Geosphere*, 16(2). Available at: https://doi.org/10.1130/GES02135.1.

Meijers, M.J.M., Peynircioğlu, A.A., Cosca, M.A., Brocard, G.Y., Whitney, D.L., Langereis, C.G. and Mulch, A. (2018b) 'Climate stability in central Anatolia during the Messinian Salinity Crisis', *Palaeogeography, Palaeoclimatology, Palaeoecology*, 498. Available at: https://doi.org/10.1016/j.palaeo.2018.03.001.

Melo, V.F., Barbar, L.C., Zamora, P.G.P., Schaefer, C.E. and Cordeiro, G.A. (2008) 'Chemical, physical and mineralogical characterization of soils from the Curitiba Metropolitan Region for forensic purpose', *Forensic Science International*, 179(2–3). Available at: https://doi.org/10.1016/j.forsciint.2008.04.028.

Meulenkamp, J.E. and Sissingh, W. (2003) 'Tertiary palaeogeography and tectonostratigraphic evolution of the Northern and Southern Peri-Tethys platforms and the intermediate domains of the African–Eurasian convergent plate boundary zone', *Palaeogeography, Palaeoclimatology, Palaeoecology*, 196(1–2), pp. 209–228.

Miguez-Salas, O. and Rodríguez-Tovar, F.J. (2019a) 'Ichnofacies distribution in the Eocene-Early Miocene Petra Tou Romiou outcrop, Cyprus: sea level dynamics and palaeoenvironmental implications in a contourite environment', *International Journal of Earth Sciences*, 108(8), pp. 2531–2544. Available at: https://doi.org/10.1007/S00531-019-01775-X/FIGURES/6.

Miguez-Salas, O. and Rodríguez-Tovar, F.J. (2019b) 'Stable deep-sea macrobenthic trace maker associations in disturbed environments from the Eocene Lefkara Formation, Cyprus', *Geobios*, 52, pp. 37–45. Available at: https://doi.org/10.1016/J.GEOBIOS.2018.11.002.

Milankovitch, M. (1941) 'Kanon der Erdbestrahlung und seine Anwendung auf das Eiszeitenproblem', *Königliche Serbische Akademie* [Preprint].

Miller, K.G., Browning, J. V., Schmelz, W.J., Kopp, R.E., Mountain, G.S., Wright, J.D., John Schmelz, W., Kopp, R.E., Mountain, G.S. and Wright, J.D. (2020) 'Cenozoic sea-level and cryospheric evolution from deep-sea geochemical and continental margin records', *Science Advances*, 6(20), p. eaaz1346. Available at: https://doi.org/10.1126/sciadv.aaz1346.

Miller, K.G., Feigenson, M.D., Wright, J.D. and Clement, B.M. (1991a) 'Miocene isotope reference section, Deep Sea Drilling Project Site 608: An evaluation of isotope and biostratigraphic resolution', *Paleoceanography*, 6(1). Available at: https://doi.org/10.1029/90PA01941.

Miller, K.G., Kominz, M.A., Browning, J. V., Wright, J.D., Mountain, G.S., Katz, M.E., Sugarman, P.J., Cramer, B.S., Christie-Blick, N. and Pekar, S.F. (2005) 'The phanerozoic record of global sea-level change', *Science*. Available at: https://doi.org/10.1126/science.1116412.

Miller, K.G., Wright, J.D. and Fairbanks, R.G. (1991b) 'Unlocking the Ice House: Oligocene-Miocene oxygen isotopes, eustasy, and margin erosion', *Journal of Geophysical Research: Solid Earth*, 96(B4), pp. 6829–6848. Available at: https://doi.org/10.1029/90JB02015@10.1002/(ISSN)2169-9356.LTSLC1.

Moissette, P., Cornée, J.-J., Antonarakou, A., Kontakiotis, G., Drinia, H., Koskeridou, E., Tsourou, T., Agiadi, K. and Karakitsios, V. (2018) 'Palaeoenvironmental changes at the Tortonian/Messinian boundary: A deep-sea sedimentary record of the eastern Mediterranean Sea', *Palaeogeography, Palaeoclimatology, Palaeoecology*, 505, pp. 217–233. Available at: https://doi.org/https://doi.org/10.1016/j.palaeo.2018.05.046.

Molinaro, M., Leturmy, P., Guezou, J.C., Frizon de Lamotte, D. and Eshraghi, S.A. (2005) 'The structure and kinematics of the southeastern Zagros fold-thrust belt, Iran: From thin-skinned to thick-skinned tectonics', *Tectonics*, 24(3). Available at: https://doi.org/10.1029/2004TC001633.

Moore, L.J., Murphy, T.J., Barnes, I.L. and Paulsen, P.J. (1982) 'ABSOLUTE ISOTOPIC ABUNDANCE RATIOS AND ATOMIC WEIGHT OF A REFERENCE SAMPLE OF STRONTIUM.', *Journal of Research of the National Bureau of Standards (United States)*, 87(1), pp. 1–8. Available at: https://doi.org/10.6028/JRES.087.001.

Moores, E.M. and Vine, F.J. (1971) 'The Troodos Massif, Cyprus and other ophiolites as oceanic crust:

evaluation and implications', *Philosophical Transactions of the Royal Society of London. Series A, Mathematical and Physical Sciences*, 268(1192), pp. 443–467.

Morag, N., Haviv, I. and Katzir, Y. (2016) 'From ocean depths to mountain tops: Uplift of the Troodos ophiolite (Cyprus) constrained by low-temperature thermochronology and geomorphic analysis', *Tectonics*, 35(3). Available at: https://doi.org/10.1002/2015TC004069.

Morris, A. (1996) 'A review of palaeomagnetic research in the Troodos ophiolite, Cyprus', *Geological Society Special Publication*. Available at: https://doi.org/10.1144/GSL.SP.1996.105.01.27.

Morris, A., Anderson, M.W. and Robertson, A.H.F. (1998) 'Multiple tectonic rotations and transform tectonism in an intraoceanic suture zone, SW Cyprus', *Tectonophysics*, 299(1–3). Available at: https://doi.org/10.1016/S0040-1951(98)00207-8.

Morse, T.J. (1996) 'Biostratigraphical constraints (calcareous nannofossils) on the Late Cretaceous to Late Miocene evolution of SW Cyprus.' Durham University.

Mougenot, D., Recq, M., Virlogeux, P. and Lepvrier, C. (1986) 'Seaward extension of the East African Rift', *Nature 1986 321:6070*, 321(6070), pp. 599–603. Available at: https://doi.org/10.1038/321599a0.

Mukasa, S.B. and Ludden, J.N. (1987) 'Uranium-lead isotopic ages of plagiogranites from the Troodos ophiolite, Cyprus, and their tectonic significance', *Geology*, 15(9), pp. 825–828. Available at: https://doi.org/10.1130/0091-7613(1987)15<825:UIAOPF>2.0.CO;2.

Mulitza, S., Dürkoop, A., Hale, W., Wefer, G. and Stefan Niebler, H. (1997) 'Planktonic foraminifera as recorders of past surface-water stratification', *Geology*, 25(4), pp. 335–338. Available at: https://doi.org/10.1130/0091-7613(1997)025<0335:PFAROP>2.3.CO;2.

Müller, P.J., Kirst, G., Ruhland, G., Von Storch, I. and Rosell-Melé, A. (1998) 'Calibration of the alkenone paleotemperature index U37K based on core-tops from the eastern South Atlantic and the global ocean (60°N-60°S)', *Geochimica et Cosmochimica Acta*, 62(10), pp. 1757–1772. Available at: https://doi.org/10.1016/S0016-7037(98)00097-0.

Murray, H. and Robertson, A.H.F. (2020) 'Pliocene-Pleistocene sedimentary and geomorphologic development of the Vasilikos river catchment, S Cyprus, in relation to uplift of the Troodos ophiolite and climate-related changes', *Geological Magazine*, 157(4). Available at: https://doi.org/10.1017/S0016756819001134.

Mutti, M., Bernoulli, D. and Stille, P. (1997) 'Temperate carbonate platform drowning linked to Miocene oceanographic events: Maiella platform margin, Italy', *Terra Nova*, 9(3), pp. 122–125. Available at: https://doi.org/https://doi.org/10.1046/j.1365-3121.1997.d01-19.x.

Naik, S.S. and Naidu, P.D. (2014) 'Boron/calcium ratios in Globigerinoides ruber from the Arabian Sea: Implications for controls on boron incorporation', *Marine Micropaleontology*, 107, pp. 1–7. Available at: https://doi.org/https://doi.org/10.1016/j.marmicro.2014.01.004.

Nathan, S.A. and Leckie, R.M. (2009) 'Early history of the Western Pacific Warm Pool during the middle to late Miocene (~13.2–5.8 Ma): Role of sea-level change and implications for equatorial circulation', *Palaeogeography, Palaeoclimatology, Palaeoecology*, 274(3), pp. 140–159. Available at: https://doi.org/https://doi.org/10.1016/j.palaeo.2009.01.007.

Neumann, T., Heiser, U., Leosson, M.A. and Kersten, M. (2002) 'Early diagenetic processes during Mn-carbonate formation: evidence from the isotopic composition of authigenic Ca-rhodochrosites of the Baltic Sea', *Geochimica et Cosmochimica Acta*, 66(5), pp. 867–879. Available at: https://doi.org/https://doi.org/10.1016/S0016-7037(01)00819-5.

Neumeister, S., Algeo, T.J., Bechtel, A., Gawlick, H.J., Gratzer, R. and Sachsenhofer, R.F. (2016) 'Redox conditions and depositional environment of the lower Jurassic Bächental bituminous marls (Tyrol, Austria)', *Austrian Journal of Earth Sciences*, 109(2). Available at: https://doi.org/10.17738/ajes.2016.0010.

Ng, Z.L., Hernández-Molina, F.J., Duarte, D., Sierro, F.J., Ledesma, S., Rogerson, M., Llave, E., Roque, C. and Manar, M.A. (2021) 'Latest Miocene restriction of the Mediterranean Outflow Water: a perspective from the Gulf of Cádiz', *Geo-Marine Letters*, 41(2), pp. 1–17. Available at: https://doi.org/10.1007/S00367-021-00693-9/FIGURES/6.

Nicol, S., Pauly, T., Bindoff, N.L., Wright, S., Thiele, D., Hosie, G.W., Strutton, P.G. and Woehler, E. (2000) 'Ocean circulation off east Antarctica affects ecosystem structure and sea-ice extent', *Nature*, 406(6795), pp. 504–507. Available at: https://doi.org/10.1038/35020053.

Nier, A.O. (1938) 'The isotopic constitution of Strontium, Barium, Bismuth, Thallium and Mercury', *Physical Review*, 54(4), pp. 275–278. Available at: https://doi.org/10.1103/PHYSREV.54.275.

Nijenhuis, I.A., Schenau, S.J., Van Der Weijden, C.H., Hilgen, F.J., Lourens, L.J. and Zachariasse, W.J. (1996) 'On the origin of upper Miocene sapropelites: A case study from the Faneromeni section, Crete (Greece)', *Paleoceanography*, 11(5). Available at: https://doi.org/10.1029/96PA01963.

Nocquet, J.M. and Calais, E. (2004) 'Geodetic measurements of crustal deformation in the Western Mediterranean and Europe', *Pure and Applied Geophysics*, 161(3). Available at: https://doi.org/10.1007/s00024-003-2468-z.

Nuber, S., Rae, J.W.B., Zhang, X., Andersen, M.B., Dumont, M.D., Mithan, H.T., Sun, Y., de Boer, B., Hall, I.R. and Barker, S. (2023) 'Indian Ocean salinity build-up primes deglacial ocean circulation recovery', *Nature*, 617(7960), pp. 306–311. Available at: https://doi.org/10.1038/s41586-023-05866-3.

Nürnberg, D., Bijma, J. and Hemleben, C. (1996) 'Assessing the reliability of magnesium in foraminiferal calcite as a proxy for water mass temperatures', *Geochimica et Cosmochimica Acta*, 60(5), pp. 803–814. Available at: https://doi.org/10.1016/0016-7037(95)00446-7.

Okay, A.I., Özcan, E., Cavazza, W., Okay, N. and Less, G. (2010) 'Basement types, Lower Eocene series, Upper Eocene olistostromes and the initiation of the southern Thrace Basin, NW Turkey', *Turkish Journal of Earth Sciences*, 19(1), pp. 1–25.

Okay, A.I. and Tüysüz, O. (1999) 'Tethyan sutures of northern Turkey', *Geological Society Special Publication*, 156. Available at: https://doi.org/10.1144/GSL.SP.1999.156.01.22.

Olson, S., Jansen, M.F., Abbot, D.S., Halevy, I. and Goldblatt, C. (2022) 'The Effect of Ocean Salinity on Climate and Its Implications for Earth's Habitability', *Geophysical Research Letters*, 49(10). Available at: https://doi.org/10.1029/2021GL095748.

Orszag-Sperber, F., Caruso, A., Blanc-Valleron, M.M., Merle, D. and Rouchy, J.M. (2009) 'The onset of the Messinian salinity crisis: Insights from Cyprus sections', *Sedimentary Geology*, 217(1–4), pp. 52–64. Available at: https://doi.org/10.1016/j.sedgeo.2009.03.006.

Orszag-Sperber, F., Rouchy, J.M. and Elion, P. (1989) 'The sedimentary expression of regional tectonic events during the Miocene-Pliocene transition in the southern Cyprus basins', *Geological Magazine*, 126(3), pp. 291–299. Available at: https://doi.org/10.1017/S001675680002238X.

Oslick, J.S., Miller, K.G., Feigenson, M.D. and Wright, J.D. (1994) 'Oligocene-Miocene strontium isotopes: Stratigraphic revisions and correlations to an inferred glacioeustatic record', *Paleoceanography*, 9(3), pp. 427–443. Available at: https://doi.org/10.1029/94PA00249.

Özgül, N. (1984) 'Stratigraphy and tectonic evolution of the Central Taurides.', *Geology of the Taurus Belt. International symposium, 1983, Ankara* [Preprint].

Paillard, D., Labeyrie, L. and Yiou, P. (1996) 'Macintosh Program performs time-series analysis', *Eos, Transactions American Geophysical Union*, 77(39). Available at: https://doi.org/10.1029/96eo00259.

Palamakumbura, R.N. and Robertson, A.H.F. (2016) 'Pleistocene terrace deposition related to tectonically controlled surface uplift: An example of the Kyrenia Range lineament in the northern part of Cyprus', *Sedimentary Geology*, 339. Available at: https://doi.org/10.1016/j.sedgeo.2016.03.022.

Palamakumbura, R.N. and Robertson, A.H.F. (2018) 'Pliocene-Pleistocene sedimentary-tectonic development of the Mesaoria (Mesarya) Basin in an incipient, diachronous collisional setting: facies evidence from the north of Cyprus', *Geological Magazine*, 155(5). Available at: https://doi.org/10.1017/S0016756816001072.

Palamakumbura, R.N., Robertson, A.H.F., Kinnaird, T.C., van Calsteren, P., Kroon, D. and Tait, J.A. (2016a) 'Quantitative dating of pleistocene deposits of the Kyrenia range, Northern Cyprus: Implications for timing, rates of uplift and driving mechanisms', *Journal of the Geological Society*, 173(6), pp. 933–948. Available at: https://doi.org/10.1144/jgs2015-130.

Palamakumbura, R.N., Robertson, A.H.F., Kinnaird, T.C. and Sanderson, D.C.W. (2016b) 'Sedimentary development and correlation of Late Quaternary terraces in the Kyrenia Range, northern Cyprus, using a combination of sedimentology and optical luminescence data', *International Journal of Earth Sciences*, 105(1). Available at: https://doi.org/10.1007/s00531-015-1173-3.

Palmer, M.R. and Elderfield, H. (1985) 'Sr isotope composition of sea water over the past 75 Myr', *Nature*, 314(6011), pp. 526–528.

Pantazis, T.M. (1967) *The geology and mineral resources of the Pharmakas-Kalavasos area*. authority of the Republic of Cyprus.

Parlak, O., Rizaoğlu, T., Bağci, U., Karaoğlan, F. and Höck, V. (2009) 'Tectonic significance of the geochemistry and petrology of ophiolites in southeast Anatolia, Turkey', *Tectonophysics*, 473(1–2). Available at: https://doi.org/10.1016/j.tecto.2008.08.002.

Parlak, O. and Robertson, A.H.F. (2004) 'The ophiolite-related Mersin Melange, southern Turkey: Its role in the tectonic-sedimentary setting of Tethys in the Eastern Mediterranean region', *Geological Magazine*, 141(3). Available at: https://doi.org/10.1017/S0016756804009094.

Partridge, T.C. (1997) 'Late Neogene Uplift in Eastern and Southern Africa and Its Paleoclimatic Implications', in *Tectonic Uplift and Climate Change*. Available at: https://doi.org/10.1007/978-1-4615-5935-1_4.

Payne, A.S. (1995) 'The structural and sedimentary evolution of the Polis graben system, West Cyprus'.

Payne, A.S. and Robertson, A.H.F. (1995) 'Neogene supra-subduction zone extension in the Polis graben system, west Cyprus', *Journal - Geological Society (London)*, 152(4), pp. 613–628. Available at: https://doi.org/10.1144/gsjgs.152.4.0613.

Pazzaglia, F.J. and Gardner, T.W. (1994) 'Late Cenozoic flexural deformation of the middle U.S. Atlantic passive margin', *Journal of Geophysical Research: Solid Earth*, 99(B6), pp. 12143–12157. Available at: https://doi.org/10.1029/93JB03130.

Pearce, J.A., Lippard, S.J. and Roberts, S. (1984) 'Characteristics and tectonic significance of supra-subduction zone ophiolites', *Geological Society Special Publication*, 16. Available at: https://doi.org/10.1144/GSL.SP.1984.016.01.06.

Pearce, J.A. and Robinson, P.T. (2010) 'The Troodos ophiolitic complex probably formed in a subduction initiation, slab edge setting', *Gondwana Research*, 18(1), pp. 60–81. Available at: https://doi.org/https://doi.org/10.1016/j.gr.2009.12.003.

Pearson, P.N. (2012) 'Oxygen Isotopes in Foraminifera: Overview and Historical Review', *The Paleontological Society Papers*, 18. Available at: https://doi.org/10.1017/s1089332600002539.

Pearson, P.N. and Burgess, C.E. (2008) 'Foraminifer test preservation and diagenesis: Comparison of high latitude Eocene sites', *Geological Society Special Publication*, 303, pp. 59–72. Available at: https://doi.org/10.1144/SP303.5/ASSET/740B0874-88EF-444C-A04E-58C8D85D0150/ASSETS/IMAGES/LARGE/1444CH05F04.JPG.

Pearson, P.N., Ditchfield, P.W., Singano, J., Harcourt-Brown, K.G., Nicholas, C.J., Olsson, R.K., Shackleton, N.J. and Hall, M.A. (2001) 'Warm tropical sea surface temperatures in the Late Cretaceous and Eocene epochs', *Nature 2001 413:6855*, 413(6855), pp. 481–487. Available at: https://doi.org/10.1038/35097000.

Pearson, P.N. and Palmer, M.R. (2000) 'Atmospheric carbon dioxide concentrations over the past 60 million years', *Nature*, 406(6797), pp. 695–699. Available at: https://doi.org/10.1038/35021000.

Pearson, P.N., Shackleton, N.J. and Hall, M.A. (1997) 'Stable isotopic evidence for the sympatric divergence of Globigerinoides trilobus and Orbulina universa (planktonic foraminifera)', *Journal of the Geological Society*, 154(2). Available at: https://doi.org/10.1144/gsjgs.154.2.0295.

Pekar, S.F. and Kominz, M.A. (2001) 'Two-Dimensional Paleoslope Modeling: A New Method for Estimating Water Depths of Benthic Foraminiferal Biofacies and Paleoshelf Margins', *Journal of Sedimentary Research*, 71(4), pp. 608–620. Available at: https://doi.org/10.1306/100600710608.

Penttila, A. (2014) *Refining the timing of uplift in the northern margin of the Troodos Massif (Cyprus): Evidence from the Miocene sedimentary record.* University of Edinburgh.

Perkins, M.E., Brown, F.H., Nash, W.P., McIntosh, W. and Williams, S.K. (1998) 'Sequence, age, and source of silicic fallout tuffs in middle to late Miocene basins of the northern Basin and Range province', *Bulletin of the Geological Society of America*, 110(3). Available at: https://doi.org/10.1130/0016-7606(1998)110<0344:SAASOS>2.3.CO;2.

Pfuhl, H.A. and McCave, I.N. (2005) 'Evidence for late Oligocene establishment of the Antarctic Circumpolar Current', *Earth and Planetary Science Letters*, 235(3), pp. 715–728. Available at: https://doi.org/https://doi.org/10.1016/j.epsl.2005.04.025.

Philip Horwitz, E., Dietz, M.L. and Chiarizia, R. (1992) 'A novel strontium-selective extraction chromatographic resin', *Solvent Extraction and Ion Exchange*, 10(2), pp. 313–336. Available at: https://doi.org/10.1080/07366299208918107.

Le Pichon, X., Angelier, J., Aubouin, J., Lyberis, N., Monti, S., Renard, V., Got, H., Hsü, K.J., Mart, Y., Mascle, J., Matthews, D., Mitropoulos, D., Tsoflias, P. and Chronis, G. (1979) 'From subduction to transform motion: a seabeam survey of the Hellenic trench system', *Earth and Planetary Science Letters*, 44(3). Available at: https://doi.org/10.1016/0012-821X(79)90082-7.

Pin, C., Briot, D., Bassin, C. and Poitrasson, F. (1994) 'Concomitant separation of strontium and samarium-neodymium for isotopic analysis in silicate samples, based on specific extraction chromatography', *Analytica Chimica Acta*, 298(2), pp. 209–217. Available at: https://doi.org/10.1016/0003-2670(94)00274-6.

Piqué, A., Tricart, P., Guiraud, R., Laville, E., Bouaziz, S., Amrhar, M. and Ait Ouali, R. (2002) 'The Mesozoic–Cenozoic Atlas belt (North Africa): an overview', *Geodinamica Acta*, 15(3), pp. 185–208. Available at: https://doi.org/10.1016/S0985-3111(02)01088-4.

Pons, J.M. and Vicens, E. (2008) 'The structure of the outer shell layer in radiolitid rudists, a morphoconstructional approach', *Lethaia*, 41(3), pp. 219–234. Available at: https://doi.org/10.1111/J.1502-3931.2007.00048.X/ASSET/389251F6-BC9C-468F-A88B-43C4C4D0A9CB/ASSETS/GRAPHIC/J.1502-3931.2007.00048.X.16.JPG.

Poole, A. and Robertson, A.H.F. (1998) 'Pleistocene fanglomerate deposition related to uplift of the Troodos ophiolite, Cyprus', *Proceedings of the Ocean Drilling Program: Scientific Results*, 160. Available at: https://doi.org/10.2973/odp.proc.sr.160.064.1998.

Poole, A.J. and Robertson, A.H.F. (1991) 'Quaternary uplift and sea-level change at an active plate boundary, Cyprus', *Journal of the Geological Society*, 148(5). Available at: https://doi.org/10.1144/gsjgs.148.5.0909.

Poole, A.J., Shimmield, G.B. and Robertson, A.H.F. (1990) 'Late Quaternary uplift of the Troodos ophiolite, Cyprus: uranium- series dating of Pleistocene coral', *Geology*, 18(9). Available at: https://doi.org/10.1130/0091-7613(1990)018<0894:LQUOTT>2.3.CO;2.

Pound, M.J., Haywood, A.M., Salzmann, U. and Riding, J.B. (2012) 'Global vegetation dynamics and latitudinal temperature gradients during the Mid to Late Miocene (15.97-5.33Ma)', *Earth-Science Reviews*. Elsevier, pp. 1–22. Available at: https://doi.org/10.1016/j.earscirev.2012.02.005.

Preiss-Daimler, I., Zarkogiannis, S.D., Kontakiotis, G., Henrich, R. and Antonarakou, A. (2021) 'Paleoceanographic perturbations and the marine carbonate system during the middle to late miocene carbonate crash— a critical review', *Geosciences (Switzerland)*. Available at: https://doi.org/10.3390/geosciences11020094.

Prentice, M.L. and Matthews, R.K. (1991) 'Tertiary ice sheet dynamics: The Snow Gun Hypothesis', *Journal of Geophysical Research: Solid Earth*, 96(B4), pp. 6811–6827. Available at: https://doi.org/10.1029/90JB01614.

Purser, B.H. and Bosence, D.W.J. (1998) 'Organization and scientific contributions in sedimentation and tectonics of rift basins: Red Sea-Gulf of Aden', in *Sedimentation and Tectonics in Rift Basins Red Sea:- Gulf of Aden*. Available at: https://doi.org/10.1007/978-94-011-4930-3_1.

Rathmann, S., Hess, S., Kuhnert, H. and Mulitza, S. (2004) 'Mg/Ca ratios of the benthic foraminifera

Oridorsalis umbonatus obtained by laser ablation from core top sediments: Relationship to bottom water temperature', *Geochemistry, Geophysics, Geosystems*, 5(12). Available at: https://doi.org/10.1029/2004GC000808.

Raup, D.M. and Sepkoski, J.J. (1984) 'Periodicity of extinctions in the geologic past.', *Proceedings of the National Academy of Sciences of the United States of America*, 81(3). Available at: https://doi.org/10.1073/pnas.81.3.801.

Rautenschlein, M., Jenner, G.A., Hertogen, J., Hofmann, A.W., Kerrich, R., Schmincke, H.-U. and White, W.M. (1985) 'Isotopic and trace element composition of volcanic glasses from the Akaki Canyon, Cyprus: implications for the origin of the Troodos ophiolite', *Earth and Planetary Science Letters*, 75(4), pp. 369–383. Available at: https://doi.org/https://doi.org/10.1016/0012-821X(85)90180-3.

Rawlins, B.G., Kemp, S.J., Hodgkinson, E.H., Riding, J.B., Vane, C.H., Poulton, C. and Freeborough, K. (2006) 'Potential and pitfalls in establishing the provenance of earth-related samples in forensic investigations', *Journal of Forensic Sciences*. Available at: https://doi.org/10.1111/j.1556-4029.2006.00152.x.

Raymo, M.E., Ruddiman, W.F. and Froelich, P.N. (1988) 'Influence of late Cenozoic mountain building on ocean geochemical cycles', *Geology*, 16(7). Available at: https://doi.org/10.1130/0091-7613(1988)016<0649:IOLCMB>2.3.CO;2.

Rea, D.K. (2013) 'Delivery of Himalayan Sediment to the Northern Indian Ocean and Its Relation to Global Climate, Sea Level, Uplift, and Seawater Strontium', in. Available at: https://doi.org/10.1029/gm070p0387.

Read, T.J. (1993) *The sedimentology of the Oligocene to Miocene Transition in the Limassol - Larnaca Area, Southern Cyprus.* University of London.

Reghellin, D., Coxall, H.K., Dickens, G.R. and Backman, J. (2015) 'Carbon and oxygen isotopes of bulk carbonate in sediment deposited beneath the eastern equatorial Pacific over the last 8 million years', *Paleoceanography*, 30(10), pp. 1261–1286. Available at: https://doi.org/10.1002/2015PA002825.

Reghellin, D., Dickens, G.R., Coxall, H.K. and Backman, J. (2019) 'Understanding bulk sediment stable isotope records in the Eastern Equatorial Pacific, from seven million years ago to present-day', *Paleoceanography and Paleoclimatology* [Preprint]. Available at: https://doi.org/10.1029/2019pa003586.

Reidel, S. (2015) 'Igneous Rock Associations 15. The Columbia River Basalt Group: A Flood Basalt Province in the Pacific Northwest, USA', *Geoscience Canada*, 42(1), pp. 151–168.

Reitz, A., Thomson, J., De Lange, G.J. and Hensen, C. (2006) 'Source and development of large manganese enrichments above eastern Mediterranean sapropel S1', *Paleoceanography*, 21(3). Available at: https://doi.org/10.1029/2005PA001169.

Richter, F.M., Rowley, D.B. and DePaolo, D.J. (1992) 'Sr isotope evolution of seawater: the role of tectonics', *Earth and Planetary Science Letters*, 109(1–2), pp. 11–23. Available at: https://doi.org/10.1016/0012-821X(92)90070-C.

Riethdorf, J.R., Max, L., Nürnberg, D., Lembke-Jene, L. and Tiedemann, R. (2013) 'Deglacial development of (sub) sea surface temperature and salinity in the subarctic northwest Pacific: Implications for upper-ocean stratification', *Paleoceanography*, 28(1). Available at: https://doi.org/10.1002/palo.20014.

Ring, U. and Layer, P.W. (2003) 'High-pressure metamorphism in the Aegean, eastern Mediterranean: Underplating and exhumation from the Late Cretaceous until the Miocene to Recent above the retreating Hellenic subduction zone', *Tectonics*, 22(3). Available at: https://doi.org/10.1029/2001TC001350.

Roberts, C.D., Legrande, A.N. and Tripati, A.K. (2011) 'Sensitivity of seawater oxygen isotopes to climatic and tectonic boundary conditions in an early Paleogene simulation with GISS ModelE-R', *Paleoceanography*, 26(4). Available at: https://doi.org/10.1029/2010PA002025.

Robertson, A.H.F. (1975) 'Cyprus umbers: Basalt-sediment relationships on a Mesozoic ocean ridge', *Journal of the Geological Society*, 131(5). Available at: https://doi.org/10.1144/gsjgs.131.5.0511.

Robertson, A.H.F. (1976) 'Pelagic Chalks and Calciturbidites from the Lower Tertiary of the Troodos Massif, Cyprus', *SEPM Journal of Sedimentary Research*, Vol. 46. Available at: https://doi.org/10.1306/212f70bd-2b24-11d7-8648000102c1865d.

Robertson, A.H.F. (1977a) 'Tertiary uplift history of the Troodos massif, Cyprus', *Bulletin of the Geological Society of America*, 88(12), pp. 1763–1772. Available at: https://doi.org/10.1130/0016-7606(1977)88<1763:TUHOTT>2.0.CO;2.

Robertson, A.H.F. (1977b) 'The Kannaviou Formation, Cyprus: Volcaniclastic sedimentation of a probable late Cretaceous volcanic arc', *Journal of the Geological Society*, 134(3), pp. 269–292. Available at: https://doi.org/10.1144/GSJGS.134.3.0269.

Robertson, A.H.F. (1977c) 'The origin and diagenesis of cherts from Cyprus', *Sedimentology*, 24(1). Available at: https://doi.org/10.1111/j.1365-3091.1977.tb00117.x.

Robertson, A.H.F. (1990) 'Tectonic evolution of Cyprus.', in A. Panayiotou (ed.) *Ophiolites and Oceanic Lithosphere. Proceedings of the International Symposium*. Nicosia, Cyprus, pp. 235–250.

Robertson, A.H.F. (1998a) 'Late Miocene paleoenvironments and tectonic setting of the southern margin of Cyprus and the Eratosthenes Seamount', *Proceedings of the Ocean Drilling Program: Scientific Results*, 160. Available at: https://doi.org/10.2973/odp.proc.sr.160.037.1998.

Robertson, A.H.F. (1998b) 'Mesozoic-Tertiary tectonic evolution of the easternmost Mediterranean area: Integration of marine and land evidence', *Proceedings of the Ocean Drilling Program: Scientific Results*, 160. Available at: https://doi.org/10.2973/odp.proc.sr.160.061.1998.

Robertson, A.H.F. (1998c) 'Significance of Lower Pliocene mass-flow deposits for the timing and process of collision of the Eratosthenes Seamount with the Cyprus active margin', *Proceedings of the Ocean Drilling Program: Scientific Results*, 160. Available at: https://doi.org/10.2973/odp.proc.sr.160.038.1998.

Robertson, A.H.F. (1998d) 'Tectonic significance of the Eratosthenes Seamount: A continental fragment in the process of collision with a subduction zone in the eastern Mediterranean (Ocean Drilling Program Leg 160)', *Tectonophysics*, 298(1–3). Available at: https://doi.org/10.1016/S0040-1951(98)00178-4.

Robertson, A.H.F. (2000) 'Mesozoic-Tertiary tectonic-sedimentary evolution of a south Tethyan oceanic basin and its margins in southern Turkey', *Geological Society Special Publication*, 173, pp. 97–138. Available at: https://doi.org/10.1144/GSL.SP.2000.173.01.05.

Robertson, A.H.F., Boulton, S.J., Tasli, K., Yildirim, N., Inan, N., Yildiz, A. and Parlak, O. (2016a) 'Late Cretaceous–Miocene sedimentary development of the Arabian continental margin in SE Turkey (Adıyaman region): Implications for regional palaeogeography and the closure history of Southern Neotethys', *Journal of Asian Earth Sciences*, 115, pp. 571–616. Available at: https://doi.org/10.1016/J.JSEAES.2015.01.025.

Robertson, A.H.F., Boulton, S.J., Taslı, K., Yıldırım, N., İnan, N., Yıldız, A. and Parlak, O. (2016b) 'Late Cretaceous–Miocene sedimentary development of the Arabian continental margin in SE Turkey (Adıyaman region): Implications for regional palaeogeography and the closure history of Southern Neotethys', *Journal of Asian Earth Sciences*, 115, pp. 571–616. Available at: https://doi.org/https://doi.org/10.1016/j.jseaes.2015.01.025.

Robertson, A.H.F., Clift, P.D., Degnan, P.J. and Jones, G. (1991) 'Palaeogeographic and palaeotectonic evolution of the Eastern Mediterranean Neotethys', *Palaeogeography, Palaeoclimatology, Palaeoecology*, 87(1–4). Available at: https://doi.org/10.1016/0031-0182(91)90140-M.

Robertson, A.H.F. and Dixon, J.E. (1984) 'Introduction: Aspects of the geological evolution of the Eastern Mediterranean', *Geological Society Special Publication*, 17. Available at: https://doi.org/10.1144/GSL.SP.1984.017.01.02.

Robertson, A.H.F., Eaton, S., Follows, E.J. and McCallum, J.E. (2009) 'The Role of Local Tectonics Versus Global Sea-Level Change in the Neogene Evolution of the Cyprus Active Margin', *Sedimentation, Tectonics and Eustasy*, pp. 331–369. Available at: https://doi.org/10.1002/9781444303896.CH19.

Robertson, A.H.F., Eaton, S., Follows, E.J. and Payne, A.S. (1995) 'Depositional processes and basin analysis of Messinian evaporites in Cyprus', *Terra Nova*, 7(2), pp. 233–253. Available at: https://doi.org/10.1111/J.1365-3121.1995.TB00692.X.

Robertson, A.H.F. and Hudson, J.D. (1973) 'Cyprus umbers: Chemical precipitates on a Tethyan ocean ridge', *Earth and Planetary Science Letters*, 18(1). Available at: https://doi.org/10.1016/0012-821X(73)90039-3.

Robertson, A.H.F. and Hudson, J.D. (1974) 'Pelagic Sediments in the Cretaceous and Tertiary History of the Troodos Massif, Cyprus', in K.J. Hsü and H.C. Jenkyns (eds) *Pelagic Sediments: On Land and under the Sea, vol. 1, Special Publications International Association Sedimentologists*. Vol. 1, Sp. John Wiley & Sons, Ltd, pp. 403–436. Available at: https://doi.org/10.1002/9781444304855.CH19.

Robertson, A.H.F. and Kinnaird, T.C. (2016) 'Structural development of the central Kyrenia Range (north Cyprus) in its regional setting in the eastern Mediterranean region', *International Journal of Earth Sciences*, 105(1), pp. 417–437. Available at: https://doi.org/10.1007/s00531-015-1215-x.

Robertson, A.H.F., McCay, G.A., Tasli, K. and Yildiz, A. (2014) 'Eocene development of the northerly active continental margin of the Southern Neotethys in the Kyrenia Range, north Cyprus', *Geological Magazine*, 151(4). Available at: https://doi.org/10.1017/S0016756813000563.

Robertson, A.H.F., Necdet, M., Raffi, I. and Chen, G. (2019) 'Early Messinian manganese deposition in NE Cyprus related to cyclical redox changes in a silled hemipelagic basin prior to the Mediterranean salinity crisis', *Sedimentary Geology*, 385, pp. 126–148. Available at: https://doi.org/10.1016/J.SEDGEO.2019.03.009.

Robertson, A.H.F., Parlak, O., Kinnaird, T.C., Taslı, K. and Dumitrica, P. (2020) 'Cambrian-Eocene pre-rift, pulsed rift, passive margin and emplacement processes along the northern margin of the Southern Neotethys: Evidence from the Antalya Complex in the Alanya Window (S Turkey)', *Journal of Asian Earth Sciences: X*, 3, p. 100026. Available at: https://doi.org/10.1016/J.JAESX.2020.100026.

Robertson, A.H.F., Parlak, O. and Ustaömer, T. (2012a) 'Overview of the Palaeozoic-Neogene evolution of Neotethys in the Eastern Mediterranean region (Southern Turkey, Cyprus, Syria)', *Petroleum Geoscience*, 18(4). Available at: https://doi.org/10.1144/petgeo2011-091.

Robertson, A.H.F., Parlak, O. and Ustaömer, T. (2013) 'Late palaeozoic-early cenozoic tectonic development of southern turkey and the easternmost mediterranean region: Evidence from the inter-relations of continental and oceanic units', *Geological Society Special Publication*, 372(1). Available at: https://doi.org/10.1144/SP372.22.

Robertson, A.H.F., Tasli, K. and Inan, N. (2012b) 'Evidence from the Kyrenia Range, Cyprus, of the northerly active margin of the Southern Neotethys during Late Cretaceous-Early Cenozoic time', *Geological Magazine*, 149(2). Available at: https://doi.org/10.1017/S0016756811000677.

Robertson, A.H.F., Unlügenç, Ü.C., Inan, N. and Tasli, K. (2004) 'The Misis–Andırın Complex: a Mid-Tertiary melange related to late-stage subduction of the Southern Neotethys in S Turkey', *Journal of Asian Earth Sciences*, 22(5), pp. 413–453. Available at: https://doi.org/10.1016/S1367-9120(03)00062-2.

Robertson, A.H.F., Ustaömer, T., Parlak, O., Ünlügenç, U.C., Taşlı, K. and İnan, N. (2006) 'The Berit transect of the Tauride thrust belt, S Turkey: Late Cretaceous–Early Cenozoic accretionary/collisional processes related to closure of the Southern Neotethys', *Journal of Asian Earth Sciences*, 27(1), pp. 108–145. Available at: https://doi.org/https://doi.org/10.1016/j.jseaes.2005.02.004.

Robertson, A.H.F. and Woodcock, N.H. (1979) 'Mamonia Complex, southwest Cyprus: Evolution and emplacement of a Mesozoic continental margin', *Bulletin of the Geological Society of America*, 90(7). Available at: https://doi.org/10.1130/0016-7606(1979)90<651:MCSCEA>2.0.CO;2.

Robertson, A.H.F. and Woodcock, N.H. (1986) 'The role of the Kyrenia Range Lineament, Cyprus, in the geological evolution of the eastern Mediterranean area', *Philosophical Transactions of the Royal Society of London. Series A, Mathematical and Physical Sciences*, 317(1539), pp. 141–177. Available at: https://doi.org/10.1098/RSTA.1986.0030.

Robertson, A.H.F. and Xenophontos, C. (1993) 'Development of concepts concerning the Troodos

ophiolite and adjacent units in Cyprus', *Geological Society Special Publication*, 76, pp. 85–119. Available at: https://doi.org/10.1144/GSL.SP.1993.076.01.05.

Rohling, E.J. (1994) 'Review and new aspects concerning the formation of eastern Mediterranean sapropels', *Marine Geology*, 122(1–2), pp. 1–28. Available at: https://doi.org/10.1016/0025-3227(94)90202-X.

Rohling, E.J., Sprovieri, M., Cane, T., Casford, J.S.L., Cooke, S., Bouloubassi, I., Emeis, K.C., Schiebel, R., Rogerson, M., Hayes, A., Jorissen, F.J. and Kroon, D. (2004) 'Reconstructing past planktic foraminiferal habitats using stable isotope data: a case history for Mediterranean sapropel S5', *Marine Micropaleontology*, 50(1–2), pp. 89–123. Available at: https://doi.org/10.1016/S0377-8398(03)00068-9.

Rosenberg, R., Kirby, E., Aslan, A., Karlstrom, K., Heizler, M. and Ouimet, W. (2014) 'Late Miocene erosion and evolution of topography along the western slope of the Colorado Rockies', *Geosphere*, 10(4). Available at: https://doi.org/10.1130/GES00989.1.

Rosenthal, Y., Boyle, E.A. and Slowey, N. (1997) 'Temperature control on the incorporation of magnesium, strontium, fluorine, and cadmium into benthic foraminiferal shells from Little Bahama Bank: Prospects for thermocline paleoceanography', *Geochimica et Cosmochimica Acta*, 61(17), pp. 3633–3643. Available at: https://doi.org/10.1016/S0016-7037(97)00181-6.

Rouchy, J.M. and Caruso, A. (2006) 'The Messinian salinity crisis in the Mediterranean basin: A reassessment of the data and an integrated scenario', *Sedimentary Geology*. Available at: https://doi.org/10.1016/j.sedgeo.2006.02.005.

Rouchy, J.M., Droxler, A.W. and Kameo, K. (2000) 'The Caribbean carbonate crash at the middle to late Miocene transition: Linkage to the establishment of the modern global ocean conveyor', in *Proceedings of the Ocean Drilling Program: Scientific Results*. Available at: https://doi.org/10.2973/odp.proc.sr.165.013.2000.

Rouchy, J.M., Orszag-Sperber, F., Blanc-Valleron, M.M., Pierre, C., Rivière, M., Combourieu-Nebout, N. and Panayides, I. (2001) 'Paleoenvironmental changes at the Messinian-Pliocene boundary in the Eastern Mediterranean (southern Cyprus basins): Significance of the Messinian Lago-Mare', *Sedimentary Geology*, 145(1–2). Available at: https://doi.org/10.1016/S0037-0738(01)00126-9.

Roveri, M., Flecker, R., Krijgsman, W., Lofi, J., Lugli, S., Manzi, V., Sierro, F.J., Bertini, A., Camerlenghi, A., De Lange, G., Govers, R., Hilgen, F.J., Hübscher, C., Meijer, P.T. and Stoica, M. (2014) 'The Messinian Salinity Crisis: Past and future of a great challenge for marine sciences', *Marine Geology*, 352, pp. 25–58. Available at: https://doi.org/10.1016/j.margeo.2014.02.002.

Roveri, M., Lugli, S., Manzi, V. and Schreiber, B.C. (2008) 'The Messinian Sicilian stratigraphy revisited: New insights for the Messinian salinity crisis', *Terra Nova*, 20(6). Available at: https://doi.org/10.1111/j.1365-3121.2008.00842.x.

Rudnick, R.L. and Gao, S. (2003) '3.01 - Composition of the Continental Crust', in H.D. Holland and K.K.B.T.-T. on G. Turekian (eds). Oxford: Pergamon, pp. 1–64. Available at: https://doi.org/https://doi.org/10.1016/B0-08-043751-6/03016-4.

Russell, A.D., Hönisch, B., Spero, H.J. and Lea, D.W. (2004) 'Effects of seawater carbonate ion concentration and temperature on shell U, Mg, and Sr in cultured planktonic foraminifera', *Geochimica et Cosmochimica Acta*, 68(21), pp. 4347–4361. Available at: https://doi.org/10.1016/J.GCA.2004.03.013.

Rutten, A. and de Lange, G.J. (2003) 'Sequential extraction of iron, manganese and related elements in S1 sapropel sediments, eastern Mediterranean', *Palaeogeography, Palaeoclimatology, Palaeoecology*, 190, pp. 79–101. Available at: https://doi.org/https://doi.org/10.1016/S0031-0182(02)00600-4.

Ryan, W.B.F. (1973) 'En: Messinian Events in the Mediterranean (CW Drooger, Ed.)'. North-Holland Publ. Co., Amsterdam, Netherlands.

Sadekov, A., Eggins, S.M., De Deckker, P. and Kroon, D. (2008) 'Uncertainties in seawater thermometry deriving from intratest and intertest Mg/Ca variability in Globigerinoides ruber', *Paleoceanography*, 23(1). Available at: https://doi.org/10.1029/2007PA001452.

Sadekov, A., Eggins, S.M., De Deckker, P., Ninnemann, U., Kuhnt, W. and Bassinot, F. (2009) 'Surface and subsurface seawater temperature reconstruction using Mg/Ca microanalysis of planktonic foraminifera Globigerinoides ruber, Globigerinoides sacculifer, and Pulleniatina obliquiloculata', *Paleoceanography*, 24(3). Available at: https://doi.org/10.1029/2008PA001664.

Sælen, G., Lunde, I.L., Porten, K.W., Braga, J.C., Dundas, S.H., Ninnemann, U.S., Ronen, Y. and Talbot, M.R. (2016) 'Oyster shells as recorders of short-term oscillations of salinity and temperature during deposition of coral bioherms and reefs in the miocene lorca basin, se Spain', *Journal of Sedimentary Research*, 86(6). Available at: https://doi.org/10.2110/jsr.2016.18.

Said, R. (1982) 'The geological evolution of the River Nile in Egypt.', *Zeitschrift fur Geomorphologie*, 26(3). Available at: https://doi.org/10.1007/978-94-010-1563-9_1.

Saraswat, R., Kurtarkar, S.R., Yadav, R., Mackensen, A., Singh, D.P., Bhadra, S., Singh, A.D., Tiwari, M., Prabhukeluskar, S.P., Bandodkar, S.R., Pandey, D.K., Clift, P.D., Kulhanek, D.K., Bhishekar, K. and Nair, S. (2019) 'Inconsistent change in surface hydrography of the eastern Arabian Sea during the last four glacial–interglacial intervals', *Geological Magazine*, 157(6), pp. 989–1000. Available at: https://doi.org/10.1017/S0016756819001122.

Savostin, L.A., Sibuet, J.C., Zonenshain, L.P., Le Pichon, X. and Roulet, M.J. (1986) 'Kinematic evolution of the Tethys belt from the Atlantic ocean to the pamirs since the Triassic', *Tectonophysics*, 123(1–4). Available at: https://doi.org/10.1016/0040-1951(86)90192-7.

Scher, H.D. and Martin, E.E. (2006) 'Timing and climatic consequences of the opening of drake passage', *Science*, 312(5772). Available at: https://doi.org/10.1126/science.1120044.

Schildgen, T.F., Cosentino, D., Bookhagen, B., Niedermann, S., Yildirim, C., Echtler, H., Wittmann, H. and Strecker, M.R. (2012) 'Multi-phased uplift of the southern margin of the Central Anatolian plateau, Turkey: A record of tectonic and upper mantle processes', *Earth and Planetary Science Letters*, 317–318. Available at: https://doi.org/10.1016/j.epsl.2011.12.003.

Schmid, S.M., Pfiffner, O.A., Froitzheim, N., Schönborn, G. and Kissling, E. (1996) 'Geophysical-geological transect and tectonic evolution of the Swiss-Italian Alps', *Tectonics*, 15(5), pp. 1036–1064. Available at: https://doi.org/10.1029/96TC00433.

Schmidt, M.W. and Spero, H.J. (2011) 'Meridional shifts in the marine ITCZ and the tropical hydrologic cycle over the last three glacial cycles', *Paleoceanography*, 26(1). Available at: https://doi.org/10.1029/2010PA001976.

Schmincke, H.U., Rautenschlein, M., Robinson, P.T. and Mehegan, J.M. (1983) 'Troodos extrusive series of Cyprus: a comparison with oceanic crust.', *Geology*, 11(7). Available at: https://doi.org/10.1130/0091-7613(1983)11<405:TESOCA>2.0.CO;2.

Schouten, S., Hopmans, E.C., Schefuß, E. and Sinninghe Damsté, J.S. (2002) 'Distributional variations in marine crenarchaeotal membrane lipids: A new tool for reconstructing ancient sea water temperatures?', *Earth and Planetary Science Letters*, 204(1–2). Available at: https://doi.org/10.1016/S0012-821X(02)00979-2.

Schouten, S., Hopmans, E.C. and Sinninghe Damsté, J.S. (2013) 'The organic geochemistry of glycerol dialkyl glycerol tetraether lipids: A review', *Organic Geochemistry*. Pergamon, pp. 19–61. Available at: https://doi.org/10.1016/j.orggeochem.2012.09.006.

Seilacher, A. (1967) 'Bathymetry of trace fossils', *Marine Geology*, 5(5), pp. 413–428. Available at: https://doi.org/https://doi.org/10.1016/0025-3227(67)90051-5.

Sengor, A.M.C., Gorur, N. and Saroglu, F. (1985) 'Strike-slip faulting and related basin formation in zones of tectonic escape: Turkey as a case study.', *Strike-slip deformation, basin formation, and sedimentation* [Preprint]. Available at: https://doi.org/10.2110/pec.85.37.0227.

Şengör, A.M.C., Tüysüz, O., Imren, C., Sakinç, M., Eyidoğan, H., Görür, N., Le Pichon, X. and Rangin, C. (2005) 'The North Anatolian Fault: A new look', *Annual Review of Earth and Planetary Sciences*. Available at: https://doi.org/10.1146/annurev.earth.32.101802.120415.

Şengör, A.M.C. and Yilmaz, Y. (1981) 'Tethyan evolution of Turkey: A plate tectonic approach', *Tectonophysics*, 75(3–4). Available at: https://doi.org/10.1016/0040-1951(81)90275-4.

Şengör, A.M.C., Yilmaz, Y. and Sungurlu, O. (1984) 'Tectonics of the Mediterranean Cimmerides: Nature and evolution of the western termination of Palaeo-Tethys', *Geological Society Special Publication*, 17. Available at: https://doi.org/10.1144/GSL.SP.1984.017.01.04.

Sepulchre, P., Ramstein, G., Fluteau, F., Schuster, M., Tiercelin, J.J. and Brunet, M. (2006) 'Tectonic uplift and Eastern Africa aridification', *Science*, 313(5792), pp. 1419–1423. Available at: https://doi.org/10.1126/SCIENCE.1129158/SUPPL_FILE/SEPULCHRE_SOM.PDF.

Shackleton, N.J. (1967) 'Oxygen Isotope Analyses and Pleistocene Temperatures Re-assessed', *Nature*, 215(5096), pp. 15–17. Available at: https://doi.org/10.1038/215015a0.

Shackleton, N.J. (1974) 'Attainment of isotopic equilibrium between ocean water and the benthonic foraminifera geuns *Uvigerina*: Isotopic changes in the ocean during the last glacial', *Colloques Internationaux du C.N.R.S.*, 219.

Shackleton, N.J., Hall, M.A., Raffi, I., Tauxe, L. and Zachos, J.C. (2000) 'Astronomical calibration age for the Oligocene-Miocene boundary', *Geology*, 28(5), pp. 447–450. Available at: https://doi.org/10.1130/0091-7613(2000)28<447:acafto>2.0.co;2.

Shackleton, N.J., Imbrie, J. and Hall, M.A. (1983) 'Oxygen and carbon isotope record of East Pacific core V19-30: implications for the formation of deep water in the late Pleistocene North Atlantic', *Earth and Planetary Science Letters*, 65(2), pp. 233–244. Available at: https://doi.org/10.1016/0012-821X(83)90162-0.

Shackleton, N.J. and Opdyke, N.D. (1973) 'Oxygen isotope and palaeomagnetic stratigraphy of Equatorial Pacific core V28-238: Oxygen isotope temperatures and ice volumes on a 105 year and 106 year scale', *Quaternary Research*, 3(1), pp. 39–55. Available at: https://doi.org/10.1016/0033-5894(73)90052-5.

Sharp, Z.D., Masson, H. and Lucchini, R. (2005) 'Stable isotope geochemistry and formation mechanisms of quartz veins; extreme paleoaltitudes of the Central Alps in the Neogene', *American Journal of Science*, 305(3). Available at: https://doi.org/10.2475/ajs.305.3.187.

Shevenell, A.E., Kennett, J.P. and Lea, D.W. (2004) 'Middle Miocene Southern Ocean Cooling and Antarctic Cryosphere Expansion', *Science*, 305(5691), pp. 1766–1770. Available at: https://doi.org/10.1126/science.1100061.

Sissingh, W. (2006) 'Syn-kinematic palaeogeographic evolution of the West European Platform: Correlation with Alpine plate collision and foreland deformation', *Geologie en Mijnbouw/Netherlands Journal of Geosciences*, 85(2), pp. 131–180. Available at: https://doi.org/10.1017/S0016774600077933.

Smith, A.B. and Gale, A.S. (2009) 'The pre-Messinian deep-sea Neogene echinoid fauna of the Mediterranean: Surface productivity controls and biogeographical relationships', *Palaeogeography, Palaeoclimatology, Palaeoecology*, 281(1–2), pp. 115–125. Available at: https://doi.org/10.1016/J.PALAEO.2009.07.016.

Smith, A.G. (1971) 'Alpine deformation and the oceanic areas of the Tethys, Mediterranean, and Atlantic', *Bulletin of the Geological Society of America*, 82(8). Available at: https://doi.org/10.1130/0016-7606(1971)82[2039:ADATOA]2.0.CO;2.

Sosdian, S.M., Babila, T.L., Greenop, R., Foster, G.L. and Lear, C.H. (2020) 'Ocean Carbon Storage across the middle Miocene: a new interpretation for the Monterey Event', *Nature Communications 2020 11:1*, 11(1), pp. 1–11. Available at: https://doi.org/10.1038/s41467-019-13792-0.

Spero, H.J. (1988) 'Ultrastructural examination of chamber morphogenesis and biomineralization in the planktonic foraminifer Orbulina universa', *Marine Biology*, 99(1). Available at: https://doi.org/10.1007/BF00644972.

Spero, H.J., Eggins, S.M., Russell, A.D., Vetter, L., Kilburn, M.R. and Hönisch, B. (2015) 'Timing and mechanism for intratest Mg/Ca variability in a living planktic foraminifer', *Earth and Planetary Science Letters*, 409. Available at: https://doi.org/10.1016/j.epsl.2014.10.030.

Spero, H.J. and Williams, D.F. (1988) 'Extracting environmental information from planktonic foraminiferal δ13C data', *Nature*, 335(6192), pp. 717–719. Available at:

https://doi.org/10.1038/335717a0.

Spezzaferri, S., Kucera, M., Pearson, P.N., Wade, B.S., Rappo, S., Poole, C.R., Morard, R. and Stalder, C. (2015) 'Fossil and Genetic Evidence for the Polyphyletic Nature of the Planktonic Foraminifera "Globigerinoides", and Description of the New Genus Trilobatus', *PLOS ONE*, 10(5), p. e0128108. Available at: https://doi.org/10.1371/JOURNAL.PONE.0128108.

Sprovieri, M., D'Alcalà, M.R., Manta, D.S., Bellanca, A., Neri, R., Lirer, F., Taberner, C., Pueyo, J.J. and Sammartino, S. (2008) 'Ba/Ca evolution in water masses of the Mediterranean late Neogene', *Paleoceanography*, 23(3). Available at: https://doi.org/10.1029/2007PA001469.

Stanley, S.M. and Hardie, L.A. (1998) 'Secular oscillations in the carbonate mineralogy of reef-building and sediment-producing organisms driven by tectonically forced shifts in seawater chemistry', *Palaeogeography, Palaeoclimatology, Palaeoecology*, 144(1–2), pp. 3–19. Available at: https://doi.org/10.1016/S0031-0182(98)00109-6.

Stärz, M., Jokat, W., Knorr, G. and Lohmann, G. (2017) 'Threshold in North Atlantic-Arctic Ocean circulation controlled by the subsidence of the Greenland-Scotland Ridge', *Nature Communications*, 8. Available at: https://doi.org/10.1038/ncomms15681.

Steckler, M.S., Berthelot, F., Lyberis, N. and Le Pichon, X. (1988) 'Subsidence in the gulf of suez: implications for rifting and plate kinematics', *Tectonophysics*, 153(1–4), pp. 249–270. Available at: https://doi.org/10.1016/0040-1951(88)90019-4.

Steiger, R.H. and Jäger, E. (1977) 'Subcommission on geochronology: Convention on the use of decay constants in geo- and cosmochronology', *Earth and Planetary Science Letters*, 36(3), pp. 359–362. Available at: https://doi.org/10.1016/0012-821X(77)90060-7.

Steinke, S., Groeneveld, J., Johnstone, H. and Rendle-Bühring, R. (2010) 'East Asian summer monsoon weakening after 7.5 Ma: Evidence from combined planktonic foraminifera Mg/Ca and δ18O (ODP Site 1146; northern South China Sea)', *Palaeogeography, Palaeoclimatology, Palaeoecology*, 289(1–4), pp. 33–43. Available at: https://doi.org/10.1016/J.PALAEO.2010.02.007.

Steinthorsdottir, M. *et al.* (2021) 'The Miocene: The Future of the Past', *Paleoceanography and Paleoclimatology*, 36(4), p. e2020PA004037. Available at: https://doi.org/10.1029/2020PA004037.

Steuber, T. (1999) 'Isotopic and chemical intra-shell variations in low-Mg calcite of rudist bivalves (Mollusca-Hippuritacea): Disequilibrium fractionations and late Cretaceous seasonality', *International Journal of Earth Sciences*, 88(3), pp. 551–570. Available at: https://doi.org/10.1007/S005310050284/METRICS.

Stewart, J.A. *et al.* (2021) 'NIST RM 8301 Boron Isotopes in Marine Carbonate (Simulated Coral and Foraminifera Solutions): Inter-laboratory δ11B and Trace Element Ratio Value Assignment', *Geostandards and Geoanalytical Research*, 45(1), pp. 77–96. Available at: https://doi.org/10.1111/GGR.12363.

Stow, D.A.V., Kahler, G. and Reeder, M. (2002) 'Fossil contourites: type example from an Oligocene palaeoslope system, Cyprus', *Geological Society Memoir*, 22(1). Available at: https://doi.org/10.1144/GSL.MEM.2002.022.01.31.

Super, J.R., Thomas, E., Pagani, M., Huber, M., O'Brien, C.L. and Hull, P.M. (2020) 'Miocene Evolution of North Atlantic Sea Surface Temperature', *Paleoceanography and Paleoclimatology*, 35(5). Available at: https://doi.org/10.1029/2019pa003748.

Swarbrick, R.E. (1980) 'The Mamonia Complex of SW Cyprus: a Mesozoic continental margin and its relationship to the Troodos Complex'.

Swarbrick, R.E. and Naylor, M.A. (1980) 'The Kathikas melange, SW Cyprus: late Cretaceous submarine debris flows', *Sedimentology*, 27(1), pp. 63–78.

Swarbrick, R.E. and Robertson, A.H.F. (1980) 'Revised stratigraphy of the Mesozoic rocks of southern Cyprus', *Geological Magazine*, 117(6). Available at: https://doi.org/10.1017/S0016756800028892.

Tanner, T., Hernández-Almeida, I., Drury, A.J., Guitián, J. and Stoll, H. (2020) 'Decreasing Atmospheric CO2 During the Late Miocene Cooling', *Paleoceanography and Paleoclimatology*, 35(12). Available at:

https://doi.org/10.1029/2020PA003925.

Tapponnier, P., Zhiqin, X., Roger, F., Meyer, B., Arnaud, N., Wittlinger, G. and Jingsui, Y. (2001) 'Oblique stepwise rise and growth of the tibet plateau', *Science*, 294(5547), pp. 1671–1677. Available at: https://doi.org/10.1126/SCIENCE.105978/ASSET/84D0E785-80A0-4345-AA41-1A1012735A79/ASSETS/GRAPHIC/SE4519967003.JPEG.

Taylforth, J.E., McCay, G.A., Ellam, R., Raffi, I., Kroon, D. and Robertson, A.H.F. (2014) 'Middle Miocene (Langhian) sapropel formation in the easternmost Mediterranean deep-water basin: Evidence from northern Cyprus', *Marine and Petroleum Geology*, 57, pp. 521–536. Available at: https://doi.org/10.1016/j.marpetgeo.2014.04.015.

Taylor, S.R. and McLennan, S.M. (1985) *The Continental Crust: its Composition and Evolution. An Examination of the Geochemical Record Preserved in Sedimentary Rocks.*, *The Continental Crust: its Composition and Evolution. An Examination of the Geochemical Record Preserved in Sedimentary Rocks.*

Techtmann, S.M., Fortney, J.L., Ayers, K.A., Joyner, D.C., Linley, T.D., Pfiffner, S.M. and Hazen, T.C. (2015) 'The unique chemistry of Eastern Mediterranean water masses selects for distinct microbial communities by depth', *PLoS ONE*, 10(3). Available at: https://doi.org/10.1371/journal.pone.0120605.

Thrana, C. and Talbot, M.R. (2006) 'High-frequency carbonate-siliciclastic cycles in the Miocene of the Lorca Basin (Western Mediterranean, SE Spain)', *Geologica Acta*, 4(3).

Thunell, R.C. and Honjo, S. (1981) 'Calcite dissolution and the modification of planktonic foraminiferal assemblages', *Marine Micropaleontology*, 6(2), pp. 169–182. Available at: https://doi.org/10.1016/0377-8398(81)90004-9.

Tian, J., Ma, W., Lyle, M.W. and Shackford, J.K. (2014) 'Synchronous mid-Miocene upper and deep oceanic δ13C changes in the east equatorial Pacific linked to ocean cooling and ice sheet expansion', *Earth and Planetary Science Letters*, 406, pp. 72–80. Available at: https://doi.org/https://doi.org/10.1016/j.epsl.2014.09.013.

Tindall, J., Flecker, R., Valdes, P., Schmidt, D.N., Markwick, P. and Harris, J. (2010) 'Modelling the oxygen isotope distribution of ancient seawater using a coupled ocean–atmosphere GCM: Implications for reconstructing early Eocene climate', *Earth and Planetary Science Letters*, 292(3–4), pp. 265–273. Available at: https://doi.org/10.1016/J.EPSL.2009.12.049.

Torfstein, A. and Steinberg, J. (2020) 'The Oligo–Miocene closure of the Tethys Ocean and evolution of the proto-Mediterranean Sea', *Scientific Reports*, 10(1). Available at: https://doi.org/10.1038/s41598-020-70652-4.

Torley, J.M. and Robertson, A.H.F. (2018) 'New evidence and interpretation of facies, provenance and geochemistry of late Triassic-early Cretaceous Tethyan deep-water passive margin-related sedimentary rocks (Ayios Photios Group), SW Cyprus in the context of eastern Mediterranean geodynamics', *Sedimentary Geology*, 377. Available at: https://doi.org/10.1016/j.sedgeo.2018.09.001.

Tosdal, R.M., Clark, A.H. and Farrar, E. (1984) 'Cenozoic polyphase landscape and tectonic evolution of the Cordillera Occidental, southernmost Peru.', *Geological Society of America Bulletin*, 95(11). Available at: https://doi.org/10.1130/0016-7606(1984)95<1318:CPLATE>2.0.CO;2.

Tribovillard, N., Algeo, T.J., Lyons, T. and Riboulleau, A. (2006) 'Trace metals as paleoredox and paleoproductivity proxies: An update', *Chemical Geology*, 232(1), pp. 12–32. Available at: https://doi.org/https://doi.org/10.1016/j.chemgeo.2006.02.012.

Tripati, A.K., Roberts, C.D. and Eagle, R.A. (2009) 'Coupling of CO2 and Ice Sheet Stability Over Major Climate Transitions of the Last 20 Million Years', *Science*, 326(5958), pp. 1394–1397. Available at: https://doi.org/10.1126/science.1178296.

Tzanova, A., Herbert, T.D. and Peterson, L. (2015) 'Cooling Mediterranean Sea surface temperatures during the Late Miocene provide a climate context for evolutionary transitions in Africa and Eurasia', *Earth and Planetary Science Letters*, 419, pp. 71–80. Available at: https://doi.org/https://doi.org/10.1016/j.epsl.2015.03.016.

Urquhart, E. and Banner, F.T. (1994) 'Biostratigraphy of the supra-ophiolite sediments of the Troodos

Massif, Cyprus: the Cretaceous Perapedhi, Kannaviou, Moni and Kathikas formations', *Geological Magazine*, 131(4), pp. 499–518. Available at: https://doi.org/10.1017/S0016756800012127.

Vaks, A., Woodhead, J., Bar-Matthews, M., Ayalon, A., Cliff, R.A., Zilberman, T., Matthews, A. and Frumkin, A. (2013) 'Pliocene-Pleistocene climate of the northern margin of Saharan-Arabian Desert recorded in speleothems from the Negev Desert, Israel', *Earth and Planetary Science Letters*, 368. Available at: https://doi.org/10.1016/j.epsl.2013.02.027.

Varol, B. and Atalar, C. (2017) 'Messinian evaporites in the Mesaoria Basin, North Cyprus: facies and environmental interpretations', *Carbonates and Evaporites*, 32(3), pp. 349–365. Available at: https://doi.org/10.1007/s13146-016-0311-8.

Vasiliev, I., Karakitsios, V., Bouloubassi, I., Agiadi, K., Kontakiotis, G., Antonarakou, A., Triantaphyllou, M., Gogou, A., Kafousia, N., de Rafélis, M., Zarkogiannis, S.D., Kaczmar, F., Parinos, C. and Pasadakis, N. (2019) 'Large Sea Surface Temperature, Salinity, and Productivity-Preservation Changes Preceding the Onset of the Messinian Salinity Crisis in the Eastern Mediterranean Sea', *Paleoceanography and Paleoclimatology*, 34(2). Available at: https://doi.org/10.1029/2018PA003438.

Vincent, E. and Berger, W.H. (1981) *Planktonic foraminifera and their use in paleoceanography*, *The sea*. Edited by C. Emiliani. New York: Wiley-Interscience.

Vincent, E. and Berger, W.H. (1985) 'Carbon dioxide and polar cooling in the Miocene: the Monterey hypothesis.', *The carbon cycle and atmospheric CO* [Preprint]. Available at: https://doi.org/10.1029/gm032p0455.

Vincent, E., Killingley, J.S. and Berger, W.H. (1980) 'The Magnetic Epoch-6 carbon shift: A change in the ocean's 13C/12C ratio 6.2 million years ago', *Marine Micropaleontology*, 5, pp. 185–203. Available at: https://doi.org/https://doi.org/10.1016/0377-8398(80)90010-9.

Vincent, E., Killingley, J.S. and Berger, W.H. (1985) 'Miocene oxygen and carbon isotope stratigraphy of the tropical Indian Ocean', in *The Miocene Ocean: Paleoceanography and Biogeography*. Geological Society of America Memoir 163, pp. 103–130.

De Vleeschouwer, D., Vahlenkamp, M., Crucifix, M. and Pälike, H. (2017) 'Alternating Southern and Northern Hemisphere climate response to astronomical forcing during the past 35 m.y', *Geology*, 45(4), pp. 375–378. Available at: https://doi.org/10.1130/G38663.1.

Voigt, J., Hathorne, E.C., Frank, M. and Holbourn, A. (2016) 'Minimal influence of recrystallization on middle Miocene benthic foraminiferal stable isotope stratigraphy in the eastern equatorial Pacific', *Paleoceanography*, 31(1). Available at: https://doi.org/10.1002/2015PA002822.

Wade, B. (2001) 'High-resolution stable isotope records as indicators of late middle Eocene climate change'. Available at: http://hdl.handle.net/1842/14620 (Accessed: 25 May 2023).

Wade, B.S. and Bown, P.R. (2006) 'Calcareous nannofossils in extreme environments: The Messinian Salinity Crisis, Polemi Basin, Cyprus', *Palaeogeography, Palaeoclimatology, Palaeoecology*, 233(3–4). Available at: https://doi.org/10.1016/j.palaeo.2005.10.007.

Wade, B.S., Pearson, P.N., Berggren, W.A. and Pälike, H. (2011) 'Review and revision of Cenozoic tropical planktonic foraminiferal biostratigraphy and calibration to the geomagnetic polarity and astronomical time scale', *Earth-Science Reviews*, 104(1–3), pp. 111–142. Available at: https://doi.org/10.1016/j.earscirev.2010.09.003.

Waelbroeck, C., Labeyrie, L., Michel, E., Duplessy, J.C., McManus, J.F., Lambeck, K., Balbon, E. and Labracherie, M. (2002) 'Sea-level and deep water temperature changes derived from benthic foraminifera isotopic records', *Quaternary Science Reviews*, 21(1–3), pp. 295–305. Available at: https://doi.org/10.1016/S0277-3791(01)00101-9.

Walford, H.L., White, N.J. and Sydow, J.C. (2005) 'Solid sediment load history of the Zambezi Delta', *Earth and Planetary Science Letters*, 238(1–2). Available at: https://doi.org/10.1016/j.epsl.2005.07.014.

Wang, C., Dai, J., Zhao, X., Li, Y., Graham, S.A., He, D., Ran, B. and Meng, J. (2014) 'Outward-growth of the Tibetan Plateau during the Cenozoic: A review', *Tectonophysics*, 621, pp. 1–43. Available at: https://doi.org/10.1016/J.TECTO.2014.01.036.

Wang, C., Zhao, X., Liu, Z., Lippert, P.C., Graham, S.A., Coe, R.S., Yi, H., Zhu, L., Liu, S. and Li, Y. (2008) 'Constraints on the early uplift history of the Tibetan Plateau', *Proceedings of the National Academy of Sciences of the United States of America*, 105(13), pp. 4987–4992. Available at: https://doi.org/10.1073/PNAS.0703595105/SUPPL_FILE/03595SUPPAPPENDIX.PDF.

Wang, J.G., Hu, X.M., Garzanti, E. and Wu, F.Y. (2013) 'Upper oligocene-lower miocene gangrinboche conglomerate in the Xigaze Area, Southern Tibet: Implications for Himalayan uplift and Paleo-Yarlung-Zangbo initiation', *Journal of Geology*, 121(4). Available at: https://doi.org/10.1086/670722.

Wara, M.W., Delaney, M.L., Bullen, T.D. and Ravelo, A.C. (2003) 'Possible roles of pH, temperature, and partial dissolution in determining boron concentration and isotopic composition in planktonic foraminifera', *Paleoceanography*, 18(4), p. 1100. Available at: https://doi.org/10.1029/2002PA000797.

Weijermars, R. (1988) 'Neogene tectonics in the Western Mediterranean may have caused the Messinian salinity crisis and an associated glacial event', *Tectonophysics*, 148(3–4), pp. 211–219. Available at: https://doi.org/10.1016/0040-1951(88)90129-1.

Westerhold, T. *et al.* (2020) 'An astronomically dated record of Earth's climate and its predictability over the last 66 million years', *Science*, 369(6509), pp. 1383–1388. Available at: https://doi.org/10.1126/SCIENCE.ABA6853/SUPPL_FILE/ABA6853_TABLES_S8_S34.XLSX.

Westerhold, T., Bickert, T. and Röhl, U. (2005) 'Middle to late Miocene oxygen isotope stratigraphy of ODP site 1085 (SE Atlantic): New constrains on Miocene climate variability and sea-level fluctuations', *Palaeogeography, Palaeoclimatology, Palaeoecology*, 217(3–4), pp. 205–222. Available at: https://doi.org/10.1016/j.palaeo.2004.12.001.

Wickman, F.E. (1948) 'Isotope ratios: a clue to the age of certain marine sediments', *The Journal of Geology*, 56(1), pp. 61–66.

Williams, M., Haywood, A.M., Taylor, S.P., Valdes, P.J., Sellwood, B.W. and Hillenbrand, C.D. (2005) 'Evaluating the efficacy of planktonic foraminifer calcite δ18O data for sea surface temperature reconstruction for the Late Miocene', *Geobios*, 38(6), pp. 843–863. Available at: https://doi.org/10.1016/J.GEOBIOS.2004.12.001.

Wit, J.C., de Nooijer, L.J., Wolthers, M. and Reichart, G.J. (2013) 'A novel salinity proxy based on Na incorporation into foraminiferal calcite', *Biogeosciences*, 10(10), pp. 6375–6387. Available at: https://doi.org/10.5194/bg-10-6375-2013.

Woodruff, F. and Savin, S.M. (1985) 'δ13C values of Miocene Pacific benthic foraminifera: Correlations with sea level and biological productivity', *Geology*, 13(2), pp. 119–122. Available at: https://doi.org/10.1130/0091-7613(1985)13<119:CVOMPB>2.0.CO;2.

Woodruff, F. and Savin, S.M. (1989) 'Miocene deepwater oceanography', *Paleoceanography*, 4(1). Available at: https://doi.org/10.1029/PA004i001p00087.

Woodruff, F. and Savin, S.M. (1991) 'Mid-Miocene isotope stratigraphy in the deep sea: High-resolution correlations, paleoclimatic cycles, and sediment preservation', *Paleoceanography*, 6(6). Available at: https://doi.org/10.1029/91PA02561.

Wright, J.D. (1998) 'Role of the Greenland-Scotland Ridge in Neogene climate changes', *Tectonic Boundary Conditions for Climate Reconstructions*, pp. 192–211. Available at: https://www.scopus.com/inward/record.uri?eid=2-s2.0-0003634893&partnerID=40&md5=c6162186c20dbb191ded8d4f9a565d82.

Wright, J.D. (2013) 'Global Climate Change in Marine Stable Isotope Records', in. Available at: https://doi.org/10.1029/rf004p0427.

Wright, J.D., Miller, K.G. and Fairbanks, R.G. (1992) 'Early and Middle Miocene stable isotopes: Implications for Deepwater circulation and climate', *Paleoceanography*, 7(3). Available at: https://doi.org/10.1029/92PA00760.

Xu, Q., Ding, L., Zhang, L., Cai, F., Lai, Q., Yang, D. and Liu-Zeng, J. (2013) 'Paleogene high elevations in the Qiangtang Terrane, central Tibetan Plateau', *Earth and Planetary Science Letters*, 362, pp. 31–42. Available at: https://doi.org/10.1016/J.EPSL.2012.11.058.

Xu, W., Dong, W.J., Fu, T.T., Gao, W., Lu, C.Q., Yan, F., Wu, Y.H., Jiang, K., Jin, J.Q., Chen, H.M., Zhang, Y.P., Hillis, D.M. and Che, J. (2021) 'Herpetological phylogeographic analyses support a Miocene focal point of Himalayan uplift and biological diversification', *National Science Review*, 8(9). Available at: https://doi.org/10.1093/nsr/nwaa263.

You, Y., Huber, M., Müller, R.D., Poulsen, C.J. and Ribbe, J. (2009) 'Simulation of the Middle Miocene Climate Optimum', *Geophysical Research Letters*, 36(4), p. 4702. Available at: https://doi.org/10.1029/2008GL036571.

Young, D.A., Wright, A.P., Roberts, J.L., Warner, R.C., Young, N.W., Greenbaum, J.S., Schroeder, D.M., Holt, J.W., Sugden, D.E., Blankenship, D.D., van Ommen, T.D. and Siegert, M.J. (2011) 'A dynamic early East Antarctic Ice Sheet suggested by ice-covered fjord landscapes', *Nature*, 474(7349), pp. 72–75. Available at: https://doi.org/10.1038/nature10114.

Yu, J., Elderfield, H., Greaves, M. and Day, J. (2007) 'Preferential dissolution of benthic foraminiferal calcite during laboratory reductive cleaning', *Geochemistry, Geophysics, Geosystems*, 8(6). Available at: https://doi.org/10.1029/2006GC001571.

Zachos, J.C., Dickens, G.R. and Zeebe, R.E. (2008) 'An early Cenozoic perspective on greenhouse warming and carbon-cycle dynamics', *Nature 2008 451:7176*, 451(7176), pp. 279–283. Available at: https://doi.org/10.1038/nature06588.

Zachos, J.C., Pagani, H., Sloan, L., Thomas, E. and Billups, K. (2001a) 'Trends, rhythms, and aberrations in global climate 65 Ma to present', *Science*, pp. 686–693. Available at: https://doi.org/10.1126/science.1059412.

Zachos, J.C., Shackleton, N.J., Revenaugh, J.S., Pälike, H. and Flower, B.P. (2001b) 'Climate response to orbital forcing across the oligocene-miocene boundary', *Science*, 292(5515), pp. 274–278. Available at: https://doi.org/10.1126/science.1058288.

Zachos, J.C., Stott, L.D. and Lohmann, K.C. (1994) 'Evolution of Early Cenozoic marine temperatures', *Paleoceanography*, 9(2). Available at: https://doi.org/10.1029/93PA03266.

Zammit, R. (2022) 'Impacts of gateways and climate on regional hydrology and carbon cycle processes: A view from the Miocene sediments of Malta.' Cardiff University.

Zeebe, R.E. and Tyrrell, T. (2019) 'History of carbonate ion concentration over the last 100 million years II: Revised calculations and new data', *Geochimica et Cosmochimica Acta*, 257, pp. 373–392. Available at: https://doi.org/https://doi.org/10.1016/j.gca.2019.02.041.

Zhang, Y.G., Pagani, M., Liu, Z., Bohaty, S.M. and DeConto, R. (2013) 'A 40-million-year history of atmospheric CO $_2$', *Philosophical Transactions of the Royal Society A: Mathematical, Physical and Engineering Sciences*, 371(2001), p. 20130096. Available at: https://doi.org/10.1098/rsta.2013.0096.

Zhang, Z., Ramstein, G., Schuster, M., Li, C., Contoux, C. and Yan, Q. (2014) 'Aridification of the Sahara desert caused by Tethys Sea shrinkage during the Late Miocene', *Nature 2014 513:7518*, 513(7518), pp. 401–404. Available at: https://doi.org/10.1038/nature13705.

Zheng, H., Powell, C.M.A., Rea, D.K., Wang, J. and Wang, P. (2004) 'Late Miocene and mid-Pliocene enhancement of the East Asian monsoon as viewed from the land and sea', *Global and Planetary Change*, 41(3–4), pp. 147–155. Available at: https://doi.org/10.1016/J.GLOPLACHA.2004.01.003.

Zhisheng, A., Kutzbach, J.E., Prell, W.L. and Porter, S.C. (2001) 'Evolution of Asian monsoons and phased uplift of the Himalaya - Tibetan plateau since Late Miocene times', *Nature*, 411(6833). Available at: https://doi.org/10.1038/35075035.

Zhou, J., Poulsen, C.J., Pollard, D. and White, T.S. (2008) 'Simulation of modern and middle Cretaceous marine δ18O with an ocean-atmosphere general circulation model', *Paleoceanography*, 23(3). Available at: https://doi.org/10.1029/2008PA001596.

Zhou, X., Rosenthal, Y., Haynes, L., Si, W., Evans, D., Huang, K.-F., Hönisch, B. and Erez, J. (2021) 'Planktic foraminiferal Na/Ca: A potential proxy for seawater calcium concentration', *Geochimica et Cosmochimica Acta*, 305, pp. 306–322. Available at: https://doi.org/https://doi.org/10.1016/j.gca.2021.04.012.

Zhu, J., Poulsen, C.J., Otto-Bliesner, B.L., Liu, Z., Brady, E.C. and Noone, D.C. (2020) 'Simulation of early Eocene water isotopes using an Earth system model and its implication for past climate reconstruction', *Earth and Planetary Science Letters*, 537, p. 116164. Available at: https://doi.org/10.1016/J.EPSL.2020.116164.

Zoback, M. Lou and Thompson, G.A. (1978) 'Basin and Range rifting in northern Nevada: Clues from a mid-Miocene rift and its subsequent offsets', *Geology*, 6(2). Available at: https://doi.org/10.1130/0091-7613(1978)6<111:BARRIN>2.0.CO;2.

8 Appendices

8.1 Age and $\delta^{18}O$ and $\delta^{13}C$ (planktic and bulk) composition of samples collected at Kottaphi Hill

This table shows the age, height and depth of all samples from the Kottaphi Hill succession, together with the carbon and oxygen stable isotope compositions measured using the methods outlined in Chapter 2.

8.1 Age and δ18O and δ13C composition of samples collected at Kottaphi Hill

Age (Ma)	Height (m)	Depth (m)	Sample ID		Fine Fraction		Orbulina	
					$\delta^{13}C$ (VPDB)	$\delta^{18}O$ (VPDB)	$\delta^{13}C$ (VPDB)	$\delta^{18}O$ (VPDB)
7.722	32.8	0	TC21	192	0.967	0.360	2.133	0.298
7.775	32.7	0.1	TC21	191	1.123	0.931	1.828	0.027
7.829	32.6	0.2	TC21	190	0.948	0.717	1.599	0.284
7.882	32.5	0.3	TC21	189	1.004	0.948	1.905	0.232
7.935	32.4	0.4	TC21	188	0.880	0.837	1.679	0.609
7.989	32.3	0.5	TC21	187	1.011	0.678	1.738	0.512
8.042	32.2	0.6	TC21	186	0.893	1.123	1.561	0.188
8.095	32.1	0.7	TC21	185	0.709	0.599	1.364	0.192
8.149	32	0.8	TC21	184	0.904	0.902	1.610	-0.029
8.202	31.9	0.9	TC21	183	1.072	1.205	1.659	-0.180
8.256	31.8	1	TC21	182	0.826	1.031	1.873	0.127
8.309	31.7	1.1	TC21	181			1.496	-0.268
8.362	31.6	1.2	TC21	180			1.419	-0.130
8.416	31.5	1.3	TC21	179			1.942	0.385
8.469	31.4	1.4	TC21	178			1.498	-0.047
8.522	31.3	1.5	TC21	177			1.613	0.147
8.576	31.2	1.6	TC21	176			1.618	-0.167
8.629	31.1	1.7	TC21	175	0.560	0.180	1.680	-0.006
8.682	31	1.8	TC21	174	0.722	0.232	1.702	-0.127
8.736	30.9	1.9	TC21	173	0.849	-0.024	2.037	-0.104
8.789	30.8	2	TC21	172	0.716	0.290	1.873	0.012
8.842	30.7	2.1	TC21	171	0.747	0.307	1.443	0.449
8.896	30.6	2.2	TC21	170	0.844	0.733	1.251	0.407
8.949	30.5	2.3	TC21	169	0.857	0.018	1.994	-0.596
9.002	30.4	2.4	TC21	168	0.718	0.163	1.612	0.157
9.035	30.3	2.5	TC21	167	0.724	0.574	1.439	-0.076
9.067	30.2	2.6	TC21	166	0.707	0.804	1.362	-0.175
9.100	30.1	2.7	TC21	165	0.642	0.644	1.540	-0.015
9.132	30	2.8	TC21	164	0.655	0.798	1.712	0.162
9.165	29.9	2.9	TC21	163	0.827	0.770	1.735	-0.221
9.197	29.8	3	TC21	162	0.778	0.765	1.593	-0.565
9.229	29.7	3.1	TC21	161	0.656	0.502	1.999	-0.512
9.262	29.6	3.2	TC21	160	0.558	-0.175	2.104	0.032
9.328	29.5	3.3	TC21	159	0.833	0.903	1.918	0.065
9.360	29.45	3.35	TC21	158	0.658	0.868	1.721	0.026
9.393	29.4	3.4	TC21	157	0.631	0.579	2.151	0.135
9.426	29.35	3.45	TC21	156	0.680	0.800	1.773	0.448
9.459	29.3	3.5	TC21	155	0.812	0.754	1.331	0.631
9.492	29.25	3.55	TC21	154	0.886	0.886	1.809	0.195
9.525	29.2	3.6	TC21	153	0.830	0.653	1.848	-0.031
9.557	29.15	3.65	TC21	152	1.223	1.040	1.914	-0.077
9.590	29.1	3.7	TC21	151	1.157	0.826	2.053	-0.312
9.623	29.05	3.75	TC21	150	1.285	0.967	1.928	0.091
9.656	29	3.8	TC21	149	1.076	0.771	1.968	-0.198
9.689	28.95	3.85	TC21	148	1.049	0.887	1.624	0.188
9.722	28.9	3.9	TC21	147	1.116	0.982		
9.755	28.85	3.95	TC21	146	1.304	0.811	1.511	-0.108
9.787	28.8	4	TC21	145	1.350	1.062	1.884	0.134
9.811	28.75	4.05	TC21	144	0.849	0.467	1.758	-0.037
9.835	28.7	4.1	TC21	143	0.940	0.585	1.917	-0.238
9.859	28.65	4.15	TC21	142	0.765	0.980	1.266	0.890
9.883	28.6	4.2	TC21	141	0.809	0.639	1.650	0.105
9.908	28.55	4.25	TC21	140	0.934	0.618		
9.932	28.5	4.3	TC21	139	0.858	0.668		
9.956	28.45	4.35	TC21	138	0.843	0.939	2.116	-0.018
9.980	28.4	4.4	TC21	137	0.785	0.789	1.907	0.006
10.004	28.35	4.45	TC21	136	0.757	0.728	2.095	-0.489
10.028	28.3	4.5	TC21	135	0.815	0.655	1.977	-0.426
10.052	28.25	4.55	TC21	134	0.897	0.908	1.188	0.898
10.076	28.2	4.6	TC21	133	0.925	0.531		

8.1 Age and δ18O and δ13C composition of samples collected at Kottaphi Hill

Age (Ma)	Height (m)	Depth (m)	Sample ID		Fine Fraction		Orbulina	
					$\delta^{13}C$ (VPDB)	$\delta^{18}O$ (VPDB)	$\delta^{13}C$ (VPDB)	$\delta^{18}O$ (VPDB)
10.100	28.15	4.65	TC21	132	0.803	0.595	1.843	-1.393
10.124	28.1	4.7	TC21	131	0.742	0.559	1.888	-0.215
10.144	28.05	4.75	TC21	130	0.664	0.326	1.743	-0.490
10.164	28	4.8	TC21	129	0.729	0.729	2.013	-0.092
10.185	27.95	4.85	TC21	128	0.830	0.840	1.437	-0.346
10.205	27.9	4.9	TC21	127	0.697	0.732	1.077	-0.099
10.225	27.85	4.95	TC21	126	0.709	0.778		
10.245	27.8	5	TC21	125	0.728	0.671	1.702	-0.489
10.266	27.75	5.05	TC21	124	0.754	0.434	1.922	-0.085
10.286	27.7	5.1	TC21	123	0.712	0.428	2.222	-0.386
10.306	27.65	5.15	TC21	122	0.809	0.438	1.227	-0.142
10.327	27.6	5.2	TC21	121	0.866	0.768	1.229	0.237
10.347	27.55	5.25	TC21	120	1.033	0.758	1.724	0.044
10.367	27.5	5.3	TC21	119	0.943	0.820	1.548	-0.008
10.387	27.45	5.35	TC21	118	1.100	0.800	1.532	0.325
10.408	27.4	5.4	TC21	117	0.792	0.787	1.813	0.068
10.428	27.35	5.45	TC21	116	0.553	0.234		
10.448	27.3	5.5	TC21	115	0.608	0.460	1.616	0.204
10.469	27.25	5.55	TC21	114	0.720	0.651	0.873	0.005
10.489	27.2	5.6	TC21	113	0.754	0.450	1.479	-0.060
10.509	27.15	5.65	TC21	112	0.822	0.184	1.872	0.111
10.530	27.1	5.7	TC21	111	0.981	0.527	1.744	0.240
10.550	27.05	5.75	TC21	110	0.954	0.635	1.732	0.491
10.570	27	5.8	TC21	109	0.969	0.220	2.214	-0.519
10.590	26.95	5.85	TC21	108	1.058	0.646	1.925	-0.131
10.611	26.9	5.9	TC21	107	1.056	0.826	1.653	0.634
10.631	26.85	5.95	TC21	106	0.913	0.380	1.797	0.609
10.651	26.8	6	TC21	105	1.146	0.443	2.219	0.250
10.672	26.75	6.05	TC21	104	1.170	0.531	2.336	-0.816
10.692	26.7	6.1	TC21	103	1.344	0.538	1.891	0.574
10.712	26.65	6.15	TC21	102	1.199	0.665	2.051	0.506
10.729	26.6	6.2	TC21	101	1.397	1.003	2.406	0.346
10.746	26.55	6.25	TC21	100	1.140	0.542	2.141	0.287
10.762	26.5	6.3	TC21	99	1.046	0.954	2.033	0.735
10.779	26.45	6.35	TC21	98	0.870	0.731	2.133	0.201
10.796	26.4	6.4	TC21	97	0.867	0.973	1.788	0.251
10.812	26.35	6.45	TC21	96	0.631	0.411	2.222	0.204
10.829	26.3	6.5	TC21	95	0.842	1.016	1.960	0.471
10.846	26.25	6.55	TC21	94	0.963	0.872	2.048	0.639
10.863	26.2	6.6	TC21	93	1.216	0.996	1.854	0.389
10.879	26.15	6.65	TC21	92	0.789	0.371	1.523	0.274
10.896	26.1	6.7	TC21	91	0.904	0.518	1.447	0.362
10.913	26.05	6.75	TC21	90	0.786	0.726	1.932	0.464
10.929	26	6.8	TC21	89	0.889	0.919	2.083	0.271
10.946	25.95	6.85	TC21	88	0.689	0.774	1.663	0.558
10.963	25.9	6.9	TC21	87	0.591	0.424	1.567	0.380
10.980	25.85	6.95	TC21	86	0.877	0.684	1.787	0.852
10.996	25.8	7	TC21	85	0.983	1.214	1.834	0.449
11.013	25.75	7.05	TC21	84	0.670	0.590	2.330	0.006
11.030	25.7	7.1	TC21	83	1.118	1.148	1.721	0.648
11.046	25.65	7.15	TC21	82	0.818	1.080	1.591	0.808
11.063	25.6	7.2	TC21	81	0.536	0.101	1.980	0.504
11.080	25.55	7.25	TC21	80	0.575	0.519	1.671	0.490
11.097	25.5	7.3	TC21	79	0.478	0.534	1.596	-0.289
11.113	25.45	7.35	TC21	78	0.348	0.192	1.344	0.343
11.130	25.4	7.4	TC21	77	0.692	0.865	2.162	0.323
11.147	25.35	7.45	TC21	76	0.251	0.136	1.670	0.479
11.161	25.3	7.5	TC21	75	0.216	0.253	1.706	0.225
11.175	25.25	7.55	TC21	74	0.118	-0.467	1.070	-0.459
11.189	25.2	7.6	TC21	73	0.222	0.566	1.068	0.559

8.1 Age and δ18O and δ13C composition of samples collected at Kottaphi Hill

Age (Ma)	Height (m)	Depth (m)	Sample ID		Fine Fraction		Orbulina	
					$\delta^{13}C$ (VPDB)	$\delta^{18}O$ (VPDB)	$\delta^{13}C$ (VPDB)	$\delta^{18}O$ (VPDB)
11.203	25.15	7.65	TC21	72	-0.270	0.068	1.230	0.574
11.218	25.1	7.7	TC21	71	-0.140	0.496	1.007	0.240
11.232	25.05	7.75	TC21	70	-0.322	0.261	1.294	0.222
11.246	25	7.8	TC21	69	0.013	0.458	1.231	0.842
11.260	24.95	7.85	TC21	68	0.363	0.838	1.024	0.433
11.274	24.9	7.9	TC21	67	0.443	1.070	1.284	0.122
11.288	24.85	7.95	TC21	66	0.083	0.580	1.879	0.495
11.303	24.8	8	TC21	65	0.407	0.359	1.711	0.236
11.317	24.75	8.05	TC21	64	0.052	0.519	1.142	0.444
11.331	24.7	8.1	TC21	63	0.010	0.663	1.098	0.345
11.345	24.65	8.15	TC21	62	-0.025	0.655	0.877	0.636
11.359	24.6	8.2	TC21	61	0.103	0.523	1.019	0.591
11.373	24.55	8.25	TC21	60	-0.014	0.801	1.034	0.610
11.388	24.5	8.3	TC21	59	0.089	0.700	0.792	0.781
11.402	24.45	8.35	TC21	58	0.311	1.106	1.558	0.732
11.416	24.4	8.4	TC21	57	0.564	1.107	1.367	0.610
11.430	24.35	8.45	TC21	56	0.356	0.688	1.102	0.772
11.444	24.3	8.5	TC21	55	0.246	0.662	1.747	0.706
11.458	24.25	8.55	TC21	54	0.329	0.507	1.628	0.405
11.473	24.2	8.6	TC21	53	0.337	0.602	1.908	-0.153
11.487	24.15	8.65	TC21	52	0.024	-0.076	1.693	0.058
11.501	24.1	8.7	TC21	51	-0.121	-0.124	0.979	-0.286
11.515	24.05	8.75	TC21	50	-0.023	-0.104	1.014	-0.607
11.529	24	8.8	TC21	49	-0.374	0.099	1.625	-0.049
11.543	23.95	8.85	TC21	48	-0.057	0.490	1.001	0.452
11.558	23.9	8.9	TC21	47	0.157	0.046		
11.572	23.85	8.95	TC21	46	0.127	-0.216		
11.586	23.8	9	TC21	45	0.161	-0.526	1.716	0.095
11.600	23.75	9.05	TC21	44	0.186	-0.090	1.201	0.103
11.620	23.7	9.1	TC21	43	0.246	0.383	1.212	0.350
11.640	23.65	9.15	TC21	42	0.335	-0.043	1.277	0.178
11.660	23.6	9.2	TC21	41	0.328	0.423		
11.680	23.55	9.25	TC21	35	0.350	0.924	0.969	0.094
11.700	23.5	9.3	TC21	34	0.206	0.502	1.351	0.539
11.720	23.45	9.35	TC21	33	0.457	0.586	1.611	0.102
11.740	23.4	9.4	TC21	32	0.512	0.338	1.714	0.462
11.760	23.35	9.45	TC21	31	0.693	1.225	1.812	0.318
11.780	23.3	9.5	TC21	30	0.618	0.509	1.333	0.734
11.800	23.25	9.55	TC21	29	0.794	0.760	1.215	0.520
11.820	23.2	9.6	TC21	28	0.664	0.611	1.360	0.107
11.840	23.15	9.65	TC21	27	0.530	0.412		
11.860	23.1	9.7	TC21	26	0.465	0.522	0.998	-0.168
11.880	23.05	9.75	TC21	25	0.574	0.775	1.306	0.442
11.902	23	9.8	TC21	24	0.830	0.763	1.664	-0.098
11.924	22.95	9.85	TC21	23	0.792	0.808	1.499	0.167
11.946	22.9	9.9	TC21	22	0.740	0.741	1.428	0.326
11.968	22.85	9.95	TC21	21	0.869	0.993	1.609	0.644
11.991	22.8	10	TC21	20	0.760	0.541	1.807	-0.370
12.013	22.75	10.05	TC21	19	0.541	0.242	1.500	0.387
12.035	22.7	10.1	TC21	18	0.524	0.590		
12.057	22.65	10.15	TC21	17	0.312	0.503	0.807	0.868
12.079	22.6	10.2	TC21	16	0.356	0.685	1.646	0.248
12.101	22.55	10.25	TC21	15	0.542	1.169	1.643	0.708
12.123	22.5	10.3	TC21	14	0.837	1.032	0.898	0.791
12.145	22.45	10.35	TC21	13	0.860	1.285		
12.167	22.4	10.4	TC21	12	1.102	0.967	1.860	0.610
12.190	22.35	10.45	TC21	11	1.167	1.331		
12.212	22.3	10.5	TC21	10	1.055	1.210	1.427	0.779
12.234	22.25	10.55	TC21	9	1.146	1.710	1.663	0.595
12.256	22.2	10.6	TC21	8	1.194	1.736	1.590	0.552

8.1 Age and δ18O and δ13C composition of samples collected at Kottaphi Hill

Age (Ma)	Height (m)	Depth (m)	Sample ID		Fine Fraction		Orbulina	
					$\delta^{13}C$ (VPDB)	$\delta^{18}O$ (VPDB)	$\delta^{13}C$ (VPDB)	$\delta^{18}O$ (VPDB)
12.278	22.15	10.65	TC21	7	1.429	1.330	2.143	0.324
12.300	22.1	10.7	TC21	6	1.297	1.534	1.603	0.670
12.322	22.05	10.75	TC21	5	1.114	1.547		
12.344	22	10.8	TC21	4	1.084	1.506	1.637	0.798
12.366	21.95	10.85	TC21	3	1.084	1.612	1.733	0.361
12.389	21.9	10.9	TC21	2	1.013	1.619	1.946	0.558
12.411	21.85	10.95	TC21	1	1.098	1.445	1.741	0.748
12.433	21.8	11	TC19	243	0.904	0.847	1.212	1.045
12.455	21.75	11.05	TC19	242	1.099	0.820	1.074	-0.130
12.477	21.7	11.1	TC19	241	1.129	0.873	2.024	-0.393
12.499	21.65	11.15	TC19	240	1.215	0.848	1.353	-1.573
12.522	21.6	11.2	TC19	239	1.186	0.152	1.264	-0.160
12.544	21.55	11.25	TC19	238	1.128	0.727	1.389	0.336
12.566	21.5	11.3	TC19	237	1.129	0.700	1.399	0.525
12.588	21.45	11.35	TC19	236	1.161	1.270	1.543	0.468
12.610	21.4	11.4	TC19	235	0.986	0.973	1.253	0.411
12.632	21.35	11.45	TC19	234	0.820	0.790	1.382	0.437
12.655	21.3	11.5	TC19	233	0.744	0.851	1.562	0.026
12.677	21.25	11.55	TC19	232	0.619	0.568	1.428	0.347
12.699	21.2	11.6	TC19	231	0.753	0.250	1.874	0.127
12.721	21.15	11.65	TC19	230	0.662	0.150	1.130	-0.109
12.743	21.1	11.7	TC19	229	0.832	0.158	2.106	-0.243
12.766	21.05	11.75	TC19	228	0.220	-0.830	1.674	-0.209
12.788	21	11.8	TC19	227	1.833	0.752	2.282	0.221
12.810	20.95	11.85	TC19	226	1.556	0.591	2.249	-0.172
12.832	20.9	11.9	TC19	225	1.689	0.801	2.482	0.060
12.854	20.85	11.95	TC19	224	1.586	0.709	2.002	-0.518
12.876	20.8	12	TC19	223	1.393	0.723	1.911	-0.386
12.899	20.75	12.05	TC19	222	1.486	0.679	2.070	-0.509
12.921	20.7	12.1	TC19	221	1.309	0.659	2.305	-0.403
12.943	20.65	12.15	TC19	220	1.587	0.748	1.705	0.086
12.965	20.6	12.2	TC19	219	1.224	0.815	1.720	-0.083
12.987	20.55	12.25	TC19	218	1.348	0.611	2.119	0.087
13.010	20.5	12.3	TC19	217	1.290	0.792	2.136	0.037
13.032	20.45	12.35	TC19	216	1.081	0.619	2.144	-0.261
13.054	20.4	12.4	TC19	215	1.049	0.301	1.979	-0.072
13.076	20.35	12.45	TC19	214	0.977	0.413	2.365	0.006
13.098	20.3	12.5	TC19	213	0.835	0.154	2.209	0.225
13.120	20.25	12.55	TC19	212	1.039	0.549	2.553	0.433
13.143	20.2	12.6	TC19	211	1.043	0.304	2.153	0.314
13.165	20.15	12.65	TC19	210	1.225	0.473	1.819	0.216
13.181	20.1	12.7	TC19	209	0.742	-0.469	1.831	-0.380
13.197	20.05	12.75	TC19	208	1.241	0.350	2.131	-0.455
13.212	20	12.8	TC19	207	1.104	0.337	1.925	0.028
13.228	19.95	12.85	TC19	206	1.214	0.877	2.157	0.086
13.244	19.9	12.9	TC19	205	1.086	0.572	2.201	0.092
13.260	19.85	12.95	TC19	204	0.955	0.248	1.803	0.247
13.276	19.8	13	TC19	203	1.183	0.620	2.044	0.257
13.292	19.75	13.05	TC19	202	1.450	0.571	1.787	0.192
13.308	19.7	13.1	TC19	201	1.291	0.366	1.761	0.343
13.324	19.65	13.15	TC19	200	1.297	0.801	1.788	-0.040
13.339	19.6	13.2	TC19	199	1.140	0.597	1.966	0.118
13.355	19.55	13.25	TC19	198	1.131	0.417	1.799	0.300
13.371	19.5	13.3	TC19	197	1.128	0.909	2.161	0.272
13.387	19.45	13.35	TC19	196	1.069	0.515	2.354	-0.160
13.403	19.4	13.4	TC19	195	1.340	1.233	2.239	-0.650
13.419	19.35	13.45	TC19	194	1.554	0.861	1.977	-0.273
13.435	19.3	13.5	TC19	193	1.477	0.668	2.273	0.433
13.451	19.25	13.55	TC19	192	1.353	0.747	2.779	0.041
13.466	19.2	13.6	TC19	191	1.330	0.382	2.159	0.181

8.1 Age and δ18O and δ13C composition of samples collected at Kottaphi Hill

Age (Ma)	Height (m)	Depth (m)	Sample ID		Fine Fraction		Orbulina	
					$\delta^{13}C$ (VPDB)	$\delta^{18}O$ (VPDB)	$\delta^{13}C$ (VPDB)	$\delta^{18}O$ (VPDB)
13.482	19.15	13.65	TC19	190	1.390	0.611	2.273	-0.069
13.498	19.1	13.7	TC19	189	1.537	0.550	1.505	0.042
13.514	19.05	13.75	TC19	188	1.668	0.854	2.301	-0.063
13.530	19	13.8	TC19	187	1.726	0.724	2.309	0.488
13.550	18.95	13.85	TC19	186	1.565	0.949	2.113	0.420
13.570	18.9	13.9	TC19	185	1.842	0.917	2.291	0.300
13.591	18.85	13.95	TC19	184	1.571	0.545	1.954	0.393
13.611	18.8	14	TC19	183	1.518	0.771	2.470	0.643
13.631	18.75	14.05	TC19	182	1.929	1.224	2.430	0.844
13.651	18.7	14.1	TC19	181	1.886	1.044	2.704	0.645
13.671	18.65	14.15	TC19	180	2.065	0.848	2.409	1.003
13.691	18.6	14.2	TC19	179	1.788	0.609	2.379	0.103
13.712	18.55	14.25	TC19	178	1.750	0.848	2.489	-0.398
13.732	18.5	14.3	TC19	177	1.641	0.855	2.548	0.136
13.752	18.45	14.35	TC19	176	1.676	0.951	2.221	0.292
13.772	18.4	14.4	TC19	175	1.430	0.594	2.333	0.202
13.792	18.35	14.45	TC19	174	1.607	0.741	2.510	0.614
13.812	18.3	14.5	TC19	173	1.374	0.396	2.168	0.157
13.833	18.25	14.55	TC19	172	1.417	0.565	2.330	0.493
13.853	18.2	14.6	TC19	171	1.570	0.517	2.200	0.286
13.873	18.15	14.65	TC19	170	1.518	0.377	1.793	0.187
13.896	18.1	14.7	TC19	169	1.475	0.126	2.311	0.556
13.919	18.05	14.75	TC19	168	1.518	0.268	1.590	-0.456
13.943	18	14.8	TC19	167	1.489	0.386	2.478	0.279
13.966	17.95	14.85	TC19	166	1.644	0.429	1.699	0.296
13.989	17.9	14.9	TC19	165	1.577	0.544	2.562	0.059
14.012	17.85	14.95	TC19	164	1.450	0.503	1.873	0.637
14.035	17.8	15	TC19	163	1.616	0.450	2.415	0.250
14.059	17.75	15.05	TC19	162	1.376	0.492	2.719	0.067
14.082	17.7	15.1	TC19	161	1.645	0.604	2.554	0.520
14.105	17.65	15.15	TC19	160	1.694	0.721	2.485	0.511
14.128	17.6	15.2	TC19	159	1.582	0.386	2.653	-0.245
14.152	17.55	15.25	TC19	158	1.841	0.840	2.508	0.523
14.175	17.5	15.3	TC19	157	1.842	0.622		
14.198	17.45	15.35	TC19	156	1.748	0.651	2.515	0.630
14.221	17.4	15.4	TC19	155	1.697	0.681	2.417	0.565
14.244	17.35	15.45	TC19	154	1.688	0.675		
14.268	17.3	15.5	TC19	153	1.723	0.862		
14.291	17.25	15.55	TC19	152	1.768	0.839		
14.314	17.2	15.6	TC19	151	1.735	0.845		
14.337	17.15	15.65	TC19	150	1.865	0.943	2.414	0.464
14.361	17.1	15.7	TC19	149	1.746	0.932	2.302	0.637
14.384	17.05	15.75	TC19	148	1.695	0.545	2.434	0.099
14.407	17	15.8	TC19	147	1.500	0.396	2.517	0.245
14.430	16.95	15.85	TC19	146	1.512	0.284	2.485	0.674
14.453	16.9	15.9	TC19	145	1.586	0.429	2.487	0.434
14.465	16.85	15.95	TC19	144	1.567	0.709	2.636	-0.045
14.476	16.8	16	TC19	143	1.336	0.552	2.407	-0.247
14.488	16.75	16.05	TC19	142	1.346	0.633	2.436	0.169
14.499	16.7	16.1	TC19	141	1.263	0.491	2.353	-0.449
14.511	16.65	16.15	TC19	140	1.134	0.220	2.406	0.332
14.522	16.6	16.2	TC19	139	1.595	0.470	1.986	0.286
14.534	16.55	16.25	TC19	138	1.464	0.406		
14.545	16.5	16.3	TC19	137	1.656	0.788	2.296	-0.110
14.557	16.45	16.35	TC19	136	1.376	0.363	2.684	0.237
14.579	16.4	16.4	TC19	135	1.764	0.669	1.435	-0.792
14.601	16.35	16.45	TC19	134	1.873	0.766	2.486	0.530
14.623	16.3	16.5	TC19	133	1.654	0.845	2.431	0.379
14.645	16.25	16.55	TC19	132	1.680	0.949		
14.667	16.2	16.6	TC19	131	1.505	0.618	2.308	-0.039

8.1 Age and δ18O and δ13C composition of samples collected at Kottaphi Hill

Age (Ma)	Height (m)	Depth (m)	Sample ID		Fine Fraction		Orbulina	
					$\delta^{13}C$ (VPDB)	$\delta^{18}O$ (VPDB)	$\delta^{13}C$ (VPDB)	$\delta^{18}O$ (VPDB)
14.689	16.15	16.65	TC19	130	1.549	0.480	1.398	-0.624
14.712	16.1	16.7	TC19	129	1.244	0.360	2.010	0.401
14.734	16.05	16.75	TC19	128	1.231	0.170	1.957	-0.070
14.756	16	16.8	TC19	127	1.502	0.622	2.262	-0.198
14.778	15.95	16.85	TC19	126	1.328	-0.068	1.693	-0.737
14.800	15.9	16.9	TC19	125	1.027	0.127	1.686	0.074
14.822	15.85	16.95	TC19	124	0.995	-0.151	1.343	-0.845
14.845	15.8	17	TC19	123	1.036	0.089	1.796	0.047
14.868	15.75	17.05	TC19	122	1.023	0.473	1.392	-1.801
14.891	15.7	17.1	TC19	121	1.354	0.660	2.470	0.005
14.914	15.65	17.15	TC19	120	1.170	0.140	2.082	-0.129
14.937	15.6	17.2	TC19	119	0.549	-0.680	1.913	-0.130
14.960	15.55	17.25	TC19	118	1.419	-0.053	2.435	-0.527
14.983	15.5	17.3	TC19	117	1.308	-0.030	1.900	-1.051
15.006	15.45	17.35	TC19	116	1.411	-0.019	1.991	-0.559
15.029	15.4	17.4	TC19	115	1.601	-0.047		
15.052	15.35	17.45	TC19	114	1.413	0.154	2.232	0.262
15.075	15.3	17.5	TC19	113	1.457	0.455	1.777	0.162
15.098	15.25	17.55	TC19	112	1.488	0.626	2.018	-0.034
15.121	15.2	17.6	TC19	111	1.528	0.505	2.005	0.132
15.144	15.15	17.65	TC19	110	1.367	0.271	1.964	-0.532
15.167	15.1	17.7	TC19	109	1.420	0.226	1.754	-0.361
15.190	15.05	17.75	TC19	108	1.288	0.154	1.768	-0.684
15.213	15	17.8	TC19	107	0.925	-0.247	2.053	-0.235
15.236	14.95	17.85	TC19	106	1.180	0.019	2.102	-0.562
15.259	14.9	17.9	TC19	105	1.203	0.052	1.613	-0.236
15.282	14.85	17.95	TC19	104	1.282	0.002	1.801	-0.579
15.305	14.8	18	TC19	103	1.282	0.136	2.111	-0.677
15.328	14.75	18.05	TC19	102	1.221	0.155	1.697	-1.239
15.351	14.7	18.1	TC19	101	1.478	0.259	1.997	-0.555
15.374	14.65	18.15	TC19	100	1.348	0.133	2.184	-0.606
15.392	14.6	18.2	TC19	99	0.936	-0.266	1.670	-0.058
15.410	14.55	18.25	TC19	98	0.579	-0.731	1.897	-0.168
15.428	14.5	18.3	TC19	97	1.219	-0.023	1.809	0.020
15.445	14.45	18.35	TC19	96	1.111	0.013	2.074	-0.665
15.463	14.4	18.4	TC19	95	1.665	0.276	2.106	-0.072
15.481	14.35	18.45	TC19	94	1.624	0.208	2.530	-0.698
15.499	14.3	18.5	TC19	93	1.565	0.082	1.729	-0.349
15.517	14.25	18.55	TC19	92	1.550	0.445	1.833	-0.299
15.534	14.2	18.6	TC19	91	1.305	0.079	1.711	-0.392
15.552	14.15	18.65	TC19	90	1.583	0.304	1.544	-0.463
15.570	14.1	18.7	TC19	89	1.470	0.058	2.076	-0.165
15.588	14.05	18.75	TC19	88	1.718	0.146	2.152	-0.333
15.605	14	18.8	TC19	87	1.410	-0.089	2.172	-0.036
15.623	13.95	18.85	TC19	86	1.516	0.189	1.971	0.261
15.641	13.9	18.9	TC19	85	1.503	0.186	1.971	-0.204
15.659	13.85	18.95	TC19	84	1.617	0.208	1.686	-0.412
15.677	13.8	19	TC19	83	1.707	0.429	1.759	-0.373
15.694	13.75	19.05	TC19	82	1.507	-0.138	2.037	-0.093
15.712	13.7	19.1	TC19	81	1.329	0.005	1.971	0.015
15.730	13.65	19.15	TC19	80	1.402	0.188	2.164	-0.137
15.763	13.6	19.2	TC19	79	1.547	0.241	1.850	-0.665
15.796	13.55	19.25	TC19	78	1.602	0.436	2.394	-0.342
15.829	13.5	19.3	TC19	77	1.651	0.121	2.275	-0.085
15.854	13.45	19.35	TC19	76	1.665	0.195	2.284	-0.039
15.878	13.4	19.4	TC19	75	1.642	0.371	2.334	-0.016
15.902	13.35	19.45	TC19	74	1.690	0.256	2.189	-0.034
15.926	13.3	19.5	TC19	73	1.802	0.370	2.559	0.061
15.951	13.25	19.55	TC19	72	1.666	0.176	2.242	0.083
15.975	13.2	19.6	TC19	71	1.307	0.102	2.156	-0.253

8.1 Age and δ18O and δ13C composition of samples collected at Kottaphi Hill

Age (Ma)	Height (m)	Depth (m)	Sample ID		Fine Fraction		Orbulina	
					$\delta^{13}C$ (VPDB)	$\delta^{18}O$ (VPDB)	$\delta^{13}C$ (VPDB)	$\delta^{18}O$ (VPDB)
15.999	13.15	19.65	TC19	70	1.612	0.506	2.027	0.159
16.024	13.1	19.7	TC19	69	1.421	0.244	2.580	-0.350
16.048	13.05	19.75	TC19	68	1.720	0.414	1.856	-0.015
16.075	13	19.8	TC19	67	1.798	0.299	2.062	0.030
16.102	12.95	19.85	TC19	66	1.883	0.378	2.519	-0.230
16.129	12.9	19.9	TC19	65	1.806	0.480	2.654	-0.124
16.157	12.85	19.95	TC19	64	1.904	0.517	1.835	0.085
16.184	12.8	20	TC19	63	2.014	0.606	2.428	-0.028
16.211	12.75	20.05	TC19	62	1.895	0.274	2.123	0.006
16.238	12.7	20.1	TC19	61	1.508	0.268	2.221	-0.310
16.265	12.65	20.15	TC19	60	1.430	0.320	2.257	-0.265
16.293	12.6	20.2	TC19	59	1.431	0.248	2.377	0.036
16.320	12.55	20.25	TC19	58	1.036	0.048	2.364	0.056
16.347	12.5	20.3	TC19	57	1.118	0.068	2.710	-0.034
16.374	12.45	20.35	TC19	56	1.241	-0.129	2.406	-0.055
16.401	12.4	20.4	TC19	55	1.509	0.470		
16.429	12.35	20.45	TC19	54	1.680	0.156	2.312	0.471
16.456	12.3	20.5	TC19	53	1.571	-0.269	2.397	0.044
16.483	12.25	20.55	TC19	52	1.554	-0.638	2.563	-0.319
16.510	12.2	20.6	TC19	51	1.663	0.336	2.644	-0.445
16.537	12.15	20.65	TC19	50	1.718	0.520	2.084	0.130
16.565	12.1	20.7	TC19	49	1.690	0.259	2.196	-0.241
16.592	12.05	20.75	TC19	48	1.573	0.309	2.512	-0.393
16.619	12	20.8	TC19	47	1.571	0.298	2.255	0.251
16.646	11.95	20.85	TC19	46	1.128	-0.250	2.270	0.024
16.657	11.93	20.87	TC19	45	1.254	-0.547	2.282	-0.235
16.674	11.9	20.9	TC19	44	1.240	-0.689	2.188	-0.103
16.701	11.85	20.95	TC19	43	1.543	0.284	2.067	-0.229
16.728	11.8	21	TC19	42	1.602	0.167	2.448	-0.218
16.755	11.75	21.05	TC19	41	1.648	0.121	2.203	0.062
16.782	11.7	21.1	TC19	40	1.656	0.089	2.232	0.204
16.810	11.65	21.15	TC19	39	1.643	-0.099	2.268	-0.020
16.837	11.6	21.2	TC19	38	1.780	0.044	1.707	-0.310
16.864	11.55	21.25	TC19	37	1.595	0.054	2.014	-0.307
16.891	11.5	21.3	TC19	36	1.138	0.029	2.037	-0.378
16.918	11.45	21.35	TC19	35	1.065	-0.135	2.165	0.295
16.946	11.4	21.4	TC19	34	0.960	-0.290	2.280	-0.445
16.973	11.35	21.45	TC19	33	0.772	-0.358	2.231	0.376
17.000	11.3	21.5	TC19	32	0.763	-0.142		
17.000	11.3	21.5	TC19	245	1.277	-0.100	1.421	-0.287
17.025	11.25	21.55	TC19	246	1.222	-0.337		
17.050	11.2	21.6	TC19	247	1.166	-0.072	2.360	-0.653
17.075	11.15	21.65	TC19	248	1.050	-0.507	2.151	-0.511
17.100	11.1	21.7	TC19	249	1.373	-0.180		
17.125	11.05	21.75	TC19	250	1.150	-0.213		
17.150	11	21.8	TC19	251	1.172	-0.498		
17.175	10.95	21.85	TC19	252	0.785	-0.385		
17.200	10.9	21.9	TC19	253	0.556	-0.190		
17.225	10.85	21.95	TC19	254	0.654	-0.413		
17.250	10.8	22	TC19	255	0.751	-0.211		
17.550	10.2	22.6	TC19	269	0.566	-0.515		
17.650	10	22.8	TC19	268	0.394	-0.468		
17.750	9.8	23	TC19	267	0.430	-0.488		
17.771	9.6	23.2	TC19	266	0.275	-0.500		
17.792	9.4	23.4	TC19	265	0.622	-0.577		
17.817	9.2	23.6	TC19	264	0.510	-0.227		
17.842	9	23.8	TC19	263	0.322	-0.386		
18.214	6	26.8	TC19	262	0.623	-0.335		
18.338	5	27.8	TC19	261	0.567	-0.300		
18.462	4	28.8	TC19	260	0.474	-0.225		

8.1 Age and δ18O and δ13C composition of samples collected at Kottaphi Hill

Age (Ma)	Height (m)	Depth (m)	Sample ID	Fine Fraction		Orbulina	
				$\delta^{13}C$ (VPDB)	$\delta^{18}O$ (VPDB)	$\delta^{13}C$ (VPDB)	$\delta^{18}O$ (VPDB)
18.586	3	29.8	TC19 259	0.459	-0.438		
18.711	2	30.8	TC19 258	0.486	-0.304		
18.835	1	31.8	TC19 257	0.766	0.068		
18.959	0	32.8	TC19 256	0.683	-0.270		

8.2 Age and $\delta^{18}O$ and $\delta^{13}C$ (planktic and bulk) composition of samples collected at Lapatza Hill

This table shows the age, height and depth of all samples from the Lapatza Hill succession, together with the carbon and oxygen stable isotope compositions measured using the methods outlined in Chapter 2.

8.2 Age and δ18O and δ13C composition of samples collected at Lapatza Hill

Age (Ma)	Height (m)	Depth (m)	Sample ID		Fine Fraction		Orbulina	
					$\delta^{13}C$ (VPDB)	$\delta^{18}O$ (VPDB)	$\delta^{13}C$ (VPDB)	$\delta^{18}O$ (VPDB)
5.732	62.75	3.25	TC21	470	-0.768	2.992	-0.123	0.804
5.739	62.5	3.5	TC21	469	-1.012	-0.112		
5.745	62.25	3.75	TC21	468	-2.348	1.192	-1.229	0.948
5.751	62	4	TC21	467	-2.050	-1.651		
5.758	61.75	4.25	TC21	466	-2.950	-0.773	-0.937	0.780
5.764	61.5	4.5	TC21	465	-3.259	-0.089		
5.770	61.25	4.75	TC21	464	-2.707	1.314		
5.776	61	5	TC21	463	-2.807	0.894		
5.783	60.75	5.25	TC21	462	-3.214	2.381		
5.789	60.5	5.5	TC21	461	-2.382	1.893		
5.795	60.25	5.75	TC21	460	-1.833	0.679		
5.802	60	6	TC21	459	-2.221	0.524		
5.808	59.75	6.25	TC21	458	-2.356	-1.849	-1.576	1.517
5.814	59.5	6.5	TC21	457	-1.473	0.601		
5.820	59.25	6.75	TC21	456	-0.869	1.813	0.690	2.934
5.827	59	7	TC21	455	-1.542	1.401	-0.029	2.429
5.833	58.75	7.25	TC21	454	-1.490	0.763	-0.103	1.220
5.839	58.5	7.5	TC21	453	-2.485	0.739		
5.846	58.25	7.75	TC21	452	-2.036	-1.373	0.692	2.032
5.852	58	8	TC21	451	-1.281	0.165	0.237	1.585
5.858	57.75	8.25	TC21	450	-3.816	1.497	0.588	1.675
5.864	57.5	8.5	TC21	449	-4.143	1.379		
5.871	57.25	8.75	TC21	448	-2.422	-2.957		
5.877	57	9	TC21	447	-2.444	0.544		
5.883	56.75	9.25	TC21	446	-1.931	1.245	0.442	1.620
5.889	56.5	9.5	TC21	445	-5.126	1.244		
5.896	56.25	9.75	TC21	444	-1.261	0.701	1.212	1.514
5.902	56	10	TC21	443	-1.151	1.363	0.352	3.019
5.908	55.75	10.25	TC21	442	-1.130	0.450	0.450	2.588
5.915	55.5	10.5	TC21	441	-0.836	1.093	0.556	1.963
5.921	55.25	10.75	TC21	440	-0.633	-0.553	1.220	-0.868
5.927	55	11	TC21	431	-1.576	0.971		
5.933	54.75	11.25	TC21	430	-0.560	-0.260	1.086	0.083
5.940	54.5	11.5	TC21	429	-3.624	1.603	1.286	1.223
5.946	54.25	11.75	TC21	428	-0.778	0.537	1.546	1.256
5.952	54	12	TC21	427	-1.287	-1.034	0.416	-1.381
5.959	53.75	12.25	TC21	426	-2.326	0.459		
5.965	53.5	12.5	TC21	425	-2.643	1.048	-2.015	1.201
5.971	53.25	12.75	TC21	424	-0.814	-0.500	1.209	1.483
5.977	53	13	TC21	423	-0.961	0.327	1.092	1.160
5.984	52.75	13.25	TC21	422	-1.199	-0.966	1.277	1.479
5.990	52.5	13.5	TC21	421	-0.611	0.252	-2.634	0.605
5.996	52.25	13.75	TC21	420	-0.799	0.737	1.145	1.951
6.003	52	14	TC21	419	-0.736	-0.170	0.653	0.685
6.009	51.75	14.25	TC21	418	-0.929	-0.158	1.210	0.724
6.015	51.5	14.5	TC21	417	-0.662	-0.184	1.262	0.559
6.021	51.25	14.75	TC21	416	-0.739	-0.200	0.336	1.078
6.028	51	15	TC21	415	-0.789	0.724	0.997	1.989
6.034	50.75	15.25	TC21	414	-0.865	1.197	1.200	1.538
6.040	50.5	15.5	TC21	413	-0.597	1.164	0.849	2.173
6.047	50.25	15.75	TC21	412	-0.721	-2.160	1.014	0.903
6.053	50	16	TC21	411	-1.018	0.185	1.237	1.404
6.059	49.75	16.25	TC21	410	-1.337	1.623	-0.270	-0.787
6.065	49.5	16.5	TC21	409	-3.204	1.519		
6.072	49.25	16.75	TC21	408	-0.914	1.375	0.924	2.069
6.078	49	17	TC21	407	-0.798	-0.806	0.422	1.463
6.084	48.75	17.25	TC21	406	-0.688	-0.933	0.938	2.061
6.091	48.5	17.5	TC21	405	-0.765	0.485	1.107	1.743
6.097	48.25	17.75	TC21	404	-0.616	1.158	1.133	2.333
6.104	48	18	TC21	403	-1.357	1.732	0.750	1.924

8.2 Age and δ18O and δ13C composition of samples collected at Lapatza Hill

Age (Ma)	Height (m)	Depth (m)	Sample ID		Fine Fraction		Orbulina	
					$\delta^{13}C$ (VPDB)	$\delta^{18}O$ (VPDB)	$\delta^{13}C$ (VPDB)	$\delta^{18}O$ (VPDB)
6.111	47.75	18.25	TC21	402	-2.979	1.179	0.717	1.078
6.118	47.5	18.5	TC21	401	-1.191	0.981	0.800	2.305
6.125	47.25	18.75	TC21	400	-1.273	1.255	-0.312	1.131
6.132	47	19	TC21	399	-2.992	1.487	0.755	2.239
6.139	46.75	19.25	TC21	398	-0.803	0.827	-1.229	1.134
6.147	46.5	19.5	TC21	397	-0.596	0.941		
6.154	46.25	19.75	TC21	396	-1.760	1.024	-0.108	1.515
6.161	46	20	TC21	395	-1.284	0.880	0.864	1.625
6.168	45.75	20.25	TC21	394	-1.280	0.654		
6.175	45.5	20.5	TC21	393	-1.522	0.634	1.017	1.561
6.182	45.25	20.75	TC21	392	-1.303	0.506	0.574	1.748
6.189	45	21	TC21	391	-1.246	0.456	0.672	1.479
6.196	44.75	21.25	TC21	390	-1.287	0.000	0.708	2.104
6.203	44.5	21.5	TC21	385	-1.636	0.416	0.503	1.004
6.210	44.25	21.75	TC21	384	-0.850	0.491	1.255	1.422
6.218	44	22	TC21	383	-1.737	0.305	1.607	0.445
6.225	43.75	22.25	TC21	382	-0.646	0.055	1.000	0.347
6.232	43.5	22.5	TC21	381	-0.929	-0.933	1.659	0.843
6.239	43.25	22.75	TC21	380	-0.527	0.476	1.413	1.330
6.246	43	23	TC21	379	-1.205	-0.159	1.309	0.470
6.253	42.75	23.25	TC21	378	-1.462	-0.207	0.904	0.488
6.260	42.5	23.5	TC21	377	-0.716	0.499	1.598	0.447
6.267	42.25	23.75	TC21	376	-0.674	-0.572	1.183	0.127
6.274	42	24	TC21	375	-1.024	0.206	0.779	1.266
6.282	41.75	24.25	TC21	374	-3.366	0.574		
6.289	41.5	24.5	TC21	373	-2.154	-0.560	1.088	1.289
6.296	41.25	24.75	TC21	372	-1.381	-1.469	1.208	-0.533
6.303	41	25	TC21	371	-0.771	-1.524	1.671	0.516
6.310	40.75	25.25	TC21	370			0.547	0.357
6.317	40.5	25.5	TC21	369	-2.085	0.684	1.113	0.737
6.324	40.25	25.75	TC21	368	-1.042	0.501	1.255	0.991
6.331	40	26	TC21	367	-1.293	-1.558	0.969	-0.019
6.338	39.75	26.25	TC21	366	-1.013	0.404		
6.345	39.5	26.5	TC21	365	-0.527	0.268		
6.353	39.25	26.75	TC21	364	-0.574	-0.416	1.871	0.663
6.360	39	27	TC21	363	-0.258	-0.288	1.875	0.363
6.367	38.75	27.25	TC21	362	-0.484	-0.087	1.995	-0.050
6.374	38.5	27.5	TC21	361	-2.640	-0.444		
6.381	38.25	27.75	TC21	360	-2.084	-0.201		
6.388	38	28	TC21	356	-2.827	1.142		
6.395	37.75	28.25	TC21	355	-1.125	0.218	1.791	0.545
6.402	37.5	28.5	TC21	354	-0.551	0.334	1.630	0.788
6.409	37.25	28.75	TC21	353	-3.213	0.699		
6.416	37	29	TC21	352	-0.771	0.336	1.638	0.701
6.424	36.75	29.25	TC21	351	-5.570	-1.123	1.499	0.345
6.431	36.5	29.5	TC21	350	-0.939	-1.509	1.657	0.805
6.438	36.25	29.75	TC21	349	-0.389	0.206	1.130	1.581
6.445	36	30	TC21	348	-0.940	-2.744		
6.452	35.75	30.25	TC21	347	-0.415	0.256	1.471	1.358
6.459	35.5	30.5	TC21	346	-0.222	0.042	1.493	0.993
6.466	35.25	30.75	TC21	345	-0.515	-0.384	1.842	0.634
6.473	35	31	TC21	344	-0.620	0.010	1.307	0.354
6.480	34.75	31.25	TC21	343	-1.538	-0.026		
6.487	34.5	31.5	TC21	342	-1.555	0.020		
6.495	34.25	31.75	TC21	341	-2.010	-0.149		
6.502	34	32	TC21	340	-0.994	-0.201	-2.308	-0.046
6.509	33.75	32.25	TC21	339	-1.431	-0.354		
6.516	33.5	32.5	TC21	338	-1.281	-0.511		
6.523	33.25	32.75	TC21	337	-1.250	-1.195	1.510	-0.407

8.2 Age and δ18O and δ13C composition of samples collected at Lapatza Hill

Age (Ma)	Height (m)	Depth (m)	Sample ID		Fine Fraction		Orbulina	
					$\delta^{13}C$ (VPDB)	$\delta^{18}O$ (VPDB)	$\delta^{13}C$ (VPDB)	$\delta^{18}O$ (VPDB)
6.530	33	33	TC21	336	-0.953	-0.160	0.614	0.589
6.537	32.75	33.25	TC21	335				
6.544	32.5	33.5	TC21	334	-1.082	-0.006		
6.551	32.25	33.75	TC21	333	-1.258	0.090	-2.111	0.234
6.558	32	34	TC21	332	-1.966	-0.246		
6.565	31.75	34.25	TC21	331	-1.409	0.213	-2.542	-0.269
6.572	31.5	34.5	TC21	330	-1.428	0.004		
6.579	31.25	34.75	TC21	329	-1.556	-0.474		
6.586	31	35	TC21	328	-1.283	-0.225		
6.593	30.75	35.25	TC21	327	-1.325	-0.288	-1.798	0.001
6.600	30.5	35.5	TC21	326	-1.272	-0.331	-1.856	-0.014
6.608	30.25	35.75	TC21	325	-0.982	-0.015		
6.615	30	36	TC21	324	-1.454	0.034		
6.622	29.75	36.25	TC21	323			-1.436	0.250
6.629	29.5	36.5	TC21	322	-1.270	-0.060		
6.636	29.25	36.75	TC21	321	-0.555	-0.095	1.578	0.148
6.643	29	37	TC21	320	-1.777	-0.155	0.983	0.226
6.650	28.75	37.25	TC21	317	-1.771	-0.333	1.226	0.529
6.657	28.5	37.5	TC21	316	-2.154	-0.116	0.246	0.188
6.664	28.25	37.75	TC21	315	-2.099	-0.075	1.430	0.102
6.671	28	38	TC21	314	-1.748	-0.362	-2.565	-0.338
6.678	27.75	38.25	TC21	313			-2.436	-0.224
6.685	27.5	38.5	TC21	312			1.141	0.371
6.692	27.25	38.75	TC21	311			1.677	0.629
6.699	27	39	TC21	310			1.597	0.445
6.706	26.75	39.25	TC21	309			0.855	1.027
6.713	26.5	39.5	TC21	308			-0.727	-0.099
6.720	26.25	39.75	TC21	307			-0.568	0.071
6.727	26	40	TC21	306			-1.138	-0.132
6.751	25.75	40.25	TC21	305			-1.038	-0.254
6.774	25.5	40.5	TC21	304			-0.994	-0.231
6.797	25.25	40.75	TC21	303			0.364	0.469
6.820	25	41	TC21	302	-2.254	-1.875	1.475	-0.466
6.846	24.75	41.25	TC21	301	-3.472	0.460	0.916	0.859
6.872	24.5	41.5	TC21	300			1.445	0.635
6.898	24.25	41.75	TC21	299			2.047	0.338
6.924	24	42	TC21	298			-2.352	-0.081
6.950	23.75	42.25	TC21	297			-1.791	-0.215
6.975	23.5	42.5	TC21	296			-1.742	-0.382
7.001	23.25	42.75	TC21	295			0.077	-0.224
7.027	23	43	TC21	294			-0.105	-0.113
7.053	22.75	43.25	TC21	293			1.877	0.539
7.079	22.5	43.5	TC21	292			1.139	0.125
7.105	22.25	43.75	TC21	291			1.160	0.534
7.131	22	44	TC21	290	-5.201	0.248	-0.188	0.364
7.157	21.75	44.25	TC21	289	-5.742	0.313	0.673	0.472
7.183	21.5	44.5	TC21	288	-5.542	0.340	1.289	0.218
7.209	21.25	44.75	TC21	287	-3.354	0.249	-0.585	0.037
7.235	21	45	TC21	286	-2.545	-0.222	0.041	-0.246
7.260	20.75	45.25	TC21	285	-2.992	-0.321	-0.886	-0.341
7.286	20.5	45.5	TC21	284			-1.266	-0.219
7.312	20.25	45.75	TC21	283	-3.017	-0.296	0.142	0.183
7.338	20	46	TC21	282	-3.223	-0.236	-0.646	-0.059
7.364	19.75	46.25	TC21	281	-3.229	-0.377	0.917	0.330
7.390	19.5	46.5	TC21	278	-3.236	0.128	1.178	-0.352
7.417	19.25	46.75	TC21	277	-2.192	-0.615		
7.443	19	47	TC21	276	-2.215	-0.599	0.003	0.070
7.470	18.75	47.25	TC21	275	-2.498	-1.402	2.194	0.841
7.497	18.5	47.5	TC21	274	-6.762	-1.980	1.794	0.220

8.2 Age and δ18O and δ13C composition of samples collected at Lapatza Hill

Age (Ma)	Height (m)	Depth (m)	Sample ID		Fine Fraction		Orbulina	
					$\delta^{13}C$ (VPDB)	$\delta^{18}O$ (VPDB)	$\delta^{13}C$ (VPDB)	$\delta^{18}O$ (VPDB)
7.523	18.25	47.75	TC21	273	-4.232	0.035	1.917	0.445
7.550	18	48	TC21	272	-4.014	0.170	2.116	0.262
7.577	17.75	48.25	TC21	271	-4.621	0.025	1.882	0.189
7.603	17.5	48.5	TC21	270			1.208	0.586
7.630	17.25	48.75	TC21	269	-2.941	-5.687	2.108	-1.331
7.657	17	49	TC21	268			1.716	0.109
7.684	16.75	49.25	TC21	267	-3.329	-3.534	1.630	0.683
7.710	16.5	49.5	TC21	266	-3.866	0.077	2.208	-0.111
7.737	16.25	49.75	TC21	265	-3.793	-0.094	1.872	0.577
7.760	16	50	TC21	264	-6.876	-1.047	1.942	0.025
7.783	15.75	50.25	TC21	263	-1.917	-2.413	1.207	-0.759
7.805	15.5	50.5	TC21	262	-2.168	-2.759	1.283	-0.471
7.828	15.25	50.75	TC21	261	-2.794	-0.629	2.283	-0.403
7.851	15	51	TC21	260	-5.773	0.426	2.077	0.352
7.874	14.75	51.25	TC21	259	-5.670	-0.092	1.450	0.579
7.897	14.5	51.5	TC21	258	-5.079	-1.870	1.433	0.004
7.917	14.25	51.75	TC21	257			1.602	0.799
7.937	14	52	TC21	256	-5.484	-0.267	1.044	0.152
7.958	13.75	52.25	TC21	255	-5.869	-0.426		
7.978	13.5	52.5	TC21	254	-1.942	-2.210	0.186	-1.227
7.998	13.25	52.75	TC21	253	-4.486	-0.105	1.899	0.374
8.018	13	53	TC21	252	-4.446	0.276	1.882	0.005
8.039	12.75	53.25	TC21	251	-4.988	-0.058	1.351	0.595
8.059	12.5	53.5	TC21	250	-6.639	-2.490	0.624	0.064
8.079	12.25	53.75	TC21	249	-1.834	-2.905	1.226	0.319
8.100	12	54	TC21	248	-2.873	-2.042	1.275	0.657
8.120	11.75	54.25	TC21	247	-6.698	-2.277	1.122	0.626
8.140	11.5	54.5	TC21	246	-3.005	-0.320	0.578	-0.050
8.160	11.25	54.75	TC21	245	-4.036	-0.743	1.544	0.900
8.181	11	55	TC21	244	-3.200	-0.114	1.649	0.786
8.201	10.75	55.25	TC21	243	-4.855	-0.458	1.937	-0.524
8.221	10.5	55.5	TC21	242	-2.311	-3.421	0.411	-0.058
8.242	10.25	55.75	TC21	241	-2.516	-3.003	-0.236	-1.162
8.262	10	56	TC21	240	-6.309	-3.869	0.908	0.185
8.282	9.75	56.25	TC21	239	-1.767	-2.692	-1.311	0.025
8.307	9.5	56.5	TC21	238	-1.416	-0.918	2.190	0.838
8.333	9.25	56.75	TC21	237	-1.315	-0.783		
8.358	9	57	TC21	236	-2.058	-3.396		
8.383	8.75	57.25	TC21	235	-3.193	-5.463	1.874	-0.184
8.408	8.5	57.5	TC21	234	-3.794	-1.239	1.482	0.565
8.433	8.25	57.75	TC21	233	-4.134	-1.402	1.687	0.381
8.459	8	58	TC21	232	-5.122	-2.277	1.261	0.197
8.484	7.75	58.25	TC21	231	-3.895	-5.231		
8.509	7.5	58.5	TC21	230	-3.988	-5.486		
8.534	7.25	58.75	TC21	229	-2.048	-1.507		
8.559	7	59	TC21	228	-3.282	-3.907	2.285	-1.021
8.585	6.75	59.25	TC21	227	-2.012	-2.823	2.340	-1.676
8.610	6.5	59.5	TC21	226	-0.966	-1.229	1.602	0.599
8.635	6.25	59.75	TC21	225	-1.696	-0.078	1.942	0.006
8.660	6	60	TC21	224	-1.714	-0.328	1.520	0.542
8.685	5.75	60.25	TC21	223	-2.740	-3.084	1.674	0.440
8.711	5.5	60.5	TC21	222	-1.025	-2.275	1.855	-0.386
8.730	5.25	60.75	TC21	221	-2.121	-0.829	2.490	0.232
8.749	5	61	TC21	220	-2.002	-2.102	0.725	-0.093
8.769	4.75	61.25	TC21	219	-2.185	-1.470	1.253	-0.626
8.788	4.5	61.5	TC21	218	-2.064	-2.364	1.743	-0.098
8.807	4.25	61.75	TC21	217	-1.887	-4.636	1.880	0.257
8.827	4	62	TC21	216	-2.458	-5.500	2.163	-0.161
8.846	3.75	62.25	TC21	215	-0.769	-1.086	2.094	0.450

8.2 Age and δ18O and δ13C composition of samples collected at Lapatza Hill

Age (Ma)	Height (m)	Depth (m)	Sample ID		Fine Fraction		Orbulina	
					$\delta^{13}C$ (VPDB)	$\delta^{18}O$ (VPDB)	$\delta^{13}C$ (VPDB)	$\delta^{18}O$ (VPDB)
8.865	3.5	62.5	TC21	214	-2.835	-1.128	1.678	0.677
8.885	3.25	62.75	TC21	213			0.981	0.439
8.904	3	63	TC21	212	-3.049	-2.248	1.136	0.142
8.923	2.75	63.25	TC21	211	-3.154	-5.806		
8.943	2.5	63.5	TC21	210	-2.846	-5.756		
8.962	2.25	63.75	TC21	209	-2.224	-0.894	1.579	0.336
8.981	2	64	TC21	208	-3.113	-0.391	2.249	0.394
9.001	1.75	64.25	TC21	207	-2.506	-0.985	1.794	-0.129
9.020	1.5	64.5	TC21	206	-4.047	-2.221	1.485	0.068
9.040	1.25	64.75	TC21	205	-3.061	-1.284	1.466	0.203
9.059	1	65	TC21	204	-5.555	-3.206	1.501	-0.441
9.078	0.75	65.25	TC21	203			1.513	-0.635
9.098	0.5	65.5	TC21	202	-2.534	-0.802	1.466	0.765
9.117	0.25	65.75	TC21	201	-4.093	-1.377	0.986	-0.441
9.136	0	66	TC21	200	-4.923	-1.696	1.629	-0.018

8.3 All measurements of the COR1D standard during planktic foraminifera analysis used in this research

This table shows measurements collected from all analyses of the COR1D standard during analysis of planktic foraminifera samples. As described in Chapter 2.5.2.

8.3 All measurements of the COR1D standard during planktic foraminifera analysis used in this research

Date	Run number	Position	1 Cycle Int Samp 44	1 Cycle Int Ref 44	d13C [VPDB]	d18O [VPDB]
14.07.21	Run 1	1			-0.597	-4.850
14.07.21	Run 1	2			-0.619	-4.834
14.07.21	Run 1	3			-0.715	-4.985
14.07.21	Run 1	4			-0.724	-5.022
14.07.21	Run 1	14			-0.586	-4.926
21.07.21	Run 2	1	1752	1799	-0.681	-5.027
21.07.21	Run 2	2	5661	5895	-0.585	-4.768
21.07.21	Run 2	3	4976	5253	-0.534	-4.782
21.07.21	Run 2	4	3809	3924	-0.683	-4.977
21.07.21	Run 2	14	2984	3076	-0.712	-4.909
21.07.21	Run 2	24	1246	1276	-0.681	-4.953
21.07.21	Run 2	25	1477	1502	-0.640	-5.015
21.07.21	Run 2	26	1469	1497	-0.668	-4.956
27.07.21	Run 2b	1			-0.614	-4.943
27.07.21	Run 2b	2			-0.622	-4.861
27.07.21	Run 2b	3			-0.637	-4.946
27.07.21	Run 2b	4			-0.589	-4.843
27.07.21	Run 2b	12			-0.757	-4.941
27.07.21	Run 2b	13			-0.626	-5.008
27.07.21	Run 2b	14			-0.691	-4.922
08.09.21	Run 3	1			-0.683	-4.925
08.09.21	Run 3	2			-0.590	-4.880
08.09.21	Run 3	3			-0.699	-5.005
08.09.21	Run 3	4			-0.665	-4.903
08.09.21	Run 3	22			-0.603	-4.903
17.09.21	Run 4	1	618	625	-0.691	-4.988
17.09.21	Run 4	2	2112	2189	-0.657	-4.944
17.09.21	Run 4	3	2556	2664	-0.599	-4.928
17.09.21	Run 4	4	4476	4634	-0.646	-4.833
29.09.21	Run 4 b	1	5271	5562	-0.608	-4.869
29.09.21	Run 4 b	2	4759	5040	-0.644	-4.877
29.09.21	Run 4 b	3	4330	4545	-0.577	-4.894
29.09.21	Run 4 b	23	4727	4960	-0.691	-4.984
29.09.21	Run 4 b	24	4247	4469	-0.721	-4.990
12.10.21	Run 5 a	1	3139	3204	-0.669	-4.999
12.10.21	Run 5 a	2	4986	5227	-0.683	-4.799
12.10.21	Run 5 a	3	4171	4368	-0.610	-4.890
12.10.21	Run 5 a	4	4121	4232	-0.642	-4.826
13.10.21	Run 5 a	24	4582	4770	-0.634	-4.904
13.10.21	Run 5 a	25	4181	4309	-0.633	-4.984
13.10.21	Run 5 a	26	3693	3795	-0.661	-4.928
13.10.21	Run 5 a	27	3365	3481	-0.653	-5.054
13.10.21	Run 5b	1	3430	3537	-0.705	-4.980
13.10.21	Run 5b	2	2590	2644	-0.616	-4.861
13.10.21	Run 5b	3	4560	4718	-0.599	-4.855
13.10.21	Run 5b	4	3962	4159	-0.615	-4.873
14.10.21	Run 5b	23	2634	2494	-0.744	-5.120
14.10.21	Run 5b	24	4299	4475	-0.608	-4.848
27.10.21	Run 6a	1	1916	1938	-0.676	-4.903
27.10.21	Run 6a	2	1582	1753	-0.701	-4.941
27.10.21	Run 6a	3	1212	1184	-0.669	-4.873
27.10.21	Run 6a	4	1020	983	-0.587	-4.932
27.10.21	Run 6a	5	856	823	-0.606	-4.966
10.11.21	Run 6b	1			-0.648	-4.833
10.11.21	Run 6b	2			-0.653	-4.974
10.11.21	Run 6b	3			-0.607	-4.854
10.11.21	Run 6b	4			-0.717	-5.036
10.11.21	Run 6b	37			-0.615	-4.920
08.12.21	Run 7	1			-0.738	-4.878
08.12.21	Run 7	2			-0.600	-4.809
08.12.21	Run 7	3			-0.592	-4.853
08.12.21	Run 7	15			-0.617	-5.006
08.12.21	Run 7	27			-0.631	-5.028
08.12.21	Run 7	28			-0.700	-4.975
08.12.21	Run 7	29			-0.658	-4.912
10.12.21	Run7 b	2	2824	2968	-0.608	-4.952
10.12.21	Run7 b	3	2880	3083	-0.548	-4.749
11.12.21	Run7 b	29	3966	4126	-0.712	-5.014
11.12.21	Run7 b	30	4428	4774	-0.725	-4.977
17.05.22	Run 1	1	2613	2706	-0.610	-4.904

8.3 All measurements of the COR1D standard during planktic foraminifera analysis used in this research

Date	Run number	Position	1 Cycle Int Samp 44	1 Cycle Int Ref 44	d13C [VPDB]	d18O [VPDB]
17.05.22	Run 1	2	1913	1960	-0.624	-4.912
17.05.22	Run 1	3	1625	1666	-0.664	-4.866
17.05.22	Run 1	4	976	1045	-0.787	-4.938
18.05.22	Run 1	23	1696	1823	-0.695	-5.027
18.05.22	Run 1	24				
18.05.22	Run 1	43	3249	3375	-0.436	-4.856
18.05.22	Run 1	44	1267	1346	-0.745	-4.975
18.05.22	Run 1	45	2949	3094	-0.578	-4.871
18.05.22	Run 1	46	1652	1691	-0.693	-4.958
24.05.22	Run 2	1	1986	2073	-0.741	-4.974
24.05.22	Run 2	2	2503	2673	-0.633	-4.911
24.05.22	Run 2	3	3446	3636	-0.607	-4.908
24.05.22	Run 2	4	3852	4312	-0.657	-4.934
25.05.22	Run 2	23	3417	3735	-0.613	-4.885
25.05.22	Run 2	24	2874	3216	-0.641	-4.916
25.05.22	Run 2	25	4947	5364	-0.644	-4.933
27.05.22	Run 3	1	3449	3713	-0.669	-4.952
27.05.22	Run 3	2	4345	4863	-0.675	-4.929
27.05.22	Run 3	3	2047	2224	-0.757	-4.986
27.05.22	Run 3	4	3450	3844	-0.632	-4.855
28.05.22	Run 3	23	3079	3226	-0.607	-4.916
28.05.22	Run 3	24	2430	2644	-0.578	-4.885
28.05.22	Run 3	25	2276	2378	-0.617	-4.939
18.07.22	Run 4	2	3354	3595	-0.705	-5.019
18.07.22	Run 4	3	2664	2787	-0.593	-4.844
18.07.22	Run 4	4	2740	2918	-0.659	-4.988
19.07.22	Run 4	17	2678	2756	-0.665	-4.921
19.07.22	Run 4	18	2294	2416	-0.641	-4.927
19.07.22	Run 4	31	3744	3934	-0.594	-4.892
19.07.22	Run 4	32	3369	3459	-0.679	-4.873
25.07.22	Run 5	1	2998	3166	-0.620	-4.886
25.07.22	Run 5	2	3502	3688	-0.684	-5.007
25.07.22	Run 5	3	3086	3276	-0.592	-4.958
25.07.22	Run 5	4	2643	2777	-0.642	-5.021
26.07.22	Run 5	17	2549	2729	-0.657	-5.006
26.07.22	Run 5	18	1202	1227	-0.717	-4.673
26.07.22	Run 5	31	3867	4053	-0.625	-4.911
22.08.22	Run 6	1	3810	3956	-0.623	-4.887
22.08.22	Run 6	2	3388	3512	-0.665	-4.873
22.08.22	Run 6	3	2968	3062	-0.626	-4.930
22.08.22	Run 6	4	2600	2829	-0.632	-4.849
23.08.22	Run 6	17	2691	2766	-0.708	-4.965
23.08.22	Run 6	18	2337	2439	-0.656	-4.964
23.08.22	Run 6	31	3801	4012	-0.652	-4.992
23.08.22	Run 6	32	3424	3633	-0.623	-4.923
24.08.22	Run 6b	1	3736	3888	-0.492	-4.915
24.08.22	Run 6b	2	3275	3512	-0.690	-4.933
24.08.22	Run 6b	3	2973	3075	-0.704	-4.979
24.08.22	Run 6b	4	2596	2724	-0.674	-4.868
24.08.22	Run 6b	9	3053	3129	-0.662	-4.937
24.08.22	Run 6b	10	2647	2773	-0.665	-4.905
25.08.22	Run 7a	1	3712	3983	-0.691	-4.874
25.08.22	Run 7a	2	2910	2983	-0.667	-4.986
25.08.22	Run 7a	3	3161	3270	-0.682	-4.922
25.08.22	Run 7a	4	2780	2895	-0.643	-4.899
25.08.22	Run 7a	18	2880	3078	-0.558	-4.934
18.10.22	Run 7b	1	2234	2345	-0.653	-5.147
18.10.22	Run 7b	2	1993	2091	-0.486	-5.070
18.10.22	Run 7b	3	3507	3761	-0.552	-5.041
19.10.22	Run 7b	17	2950	3061	-0.614	-5.104
19.10.22	Run 7b	18	2605	2676	-0.610	-5.026
19.10.22	Run 7b	30	2637	2728	-0.623	-4.959
19.10.22	Run 7b	31	2335	2457	-0.624	-5.130
19.10.22	Run 7b	32	2002	2033	-0.653	-4.995
19.10.22	Run 7b	33	3386	3595	-0.614	-5.052
19.10.22	Run 7b	34	3111	3270	-0.644	-4.971
20.10.22	Run 8	1	3413	3603	-0.631	-4.942
20.10.22	Run 8	2	3082	3206	-0.572	-4.858
20.10.22	Run 8	3	2729	2879	-0.604	-5.021

8.3 All measurements of the COR1D standard during planktic foraminifera analysis used in this research

Date	Run number	Position	1 Cycle Int Samp 44	1 Cycle Int Ref 44	d13C [VPDB]	d18O [VPDB]
20.10.22	Run 8	4	2465	2537	-0.582	-4.911
21.10.22	Run 8	17	1976	2000	-0.615	-5.112
21.10.22	Run 8	18	1738	1701	-0.619	-4.928
27.10.22	Run 9	1	3333	3332	-0.575	-4.853
27.10.22	Run 9	2	3040	3166	-0.680	-4.895
27.10.22	Run 9	3	2666	2819	-0.630	-4.935
27.10.22	Run 9	4	2358	2400	-0.669	-4.966
28.10.22	Run 9	15	2979	3159	-0.696	-4.976
28.10.22	Run 9	16	2718	2781	-0.638	-4.914
28.10.22	Run 10	1	3354	3515	-0.639	-4.855
28.10.22	Run 10	2	3094	3080	-0.657	-4.918
28.10.22	Run 10	3	2669	2787	-0.634	-4.954
28.10.22	Run 10	4	2382	2457	-0.587	-4.848
28.10.22	Run 10	5	2109	2112	-0.689	-5.022
28.10.22	Run 10	6	1806	1831	-0.682	-4.943
31.10.22	Run 11	1	3277	3433	-0.714	-4.908
31.10.22	Run 11	2	2948	3043	-0.631	-4.910
31.10.22	Run 11	3	2649	2683	-0.680	-4.951
31.10.22	Run 11	4	2297	2384	-0.607	-4.854
01.11.22	Run 11	13	3437	3387	-0.635	-4.997
01.11.22	Run 11	14	2903	3053	-0.621	-4.918
02.11.22	Run 12	1	3266	3420	-0.712	-4.877
02.11.22	Run 12	2	2950	3009	-0.640	-4.940
02.11.22	Run 12	3	2563	2650	-0.628	-4.969
02.11.22	Run 12	4	2291	2302	-0.618	-4.960
03.11.22	Run 12	13	3334	3425	-0.630	-4.922
03.11.22	Run 12	14	2985	3050	-0.660	-4.872
04.11.22	Run 13	1	2863	2960	-0.650	-4.924
04.11.22	Run 13	2	2509	2604	-0.603	-4.747
04.11.22	Run 13	3	2232	2331	-0.625	-4.999
04.11.22	Run 13	4	2022	2055	-0.667	-4.868
05.11.22	Run 13	17	1811	1838	-0.737	-5.039
05.11.22	Run 13	18	1616	1558	-0.607	-4.961
07.11.22	Run 14	1	2762	2857	-0.693	-4.869
07.11.22	Run 14	2	2457	2492	-0.646	-4.954
07.11.22	Run 14	3	2145	2194	-0.634	-5.018
07.11.22	Run 14	4	1895	1882	-0.619	-4.851
08.11.22	Run 15	1	2798	2919	-0.693	-4.906
08.11.22	Run 15	2	2532	2643	-0.657	-4.835
08.11.22	Run 15	3	2248	2320	-0.693	-4.908
08.11.22	Run 15	4	1982	2007	-0.633	-4.870
09.11.22	Run 15	18	1759	1711	-0.592	-4.975
09.11.22	Run 15	19	2800	2922	-0.639	-4.940
09.11.22	Run 15	30	1422	1471	-0.708	-4.987
09.11.22	Run 15	31	2772	2935	-0.602	-4.968
09.11.22	Run 15	32	2489	2579	-0.615	-4.921
10.11.22	Run 16	1	2866	2934	-0.650	-4.946
10.11.22	Run 16	2	2501	2606	-0.602	-4.828
10.11.22	Run 16	3	2208	2285	-0.715	-5.030
10.11.22	Run 16	4	1903	1969	-0.625	-4.889
11.11.22	Run 17	1	2827	2860	-0.656	-4.903
11.11.22	Run 17	2	2020	2067	-0.708	-4.957
11.11.22	Run 17	3	1721	1755	-0.623	-4.930
12.11.22	Run 17	26	2325	2323	-0.646	-4.931
12.11.22	Run 17	27	2015	1967	-0.661	-4.878
14.11.22	Run 18	1	2745	2705	-0.697	-5.064
14.11.22	Run 18	2	2343	2384	-0.650	-4.832
14.11.22	Run 18	3	2051	2084	-0.680	-4.942
14.11.22	Run 18	4	1762	1782	-0.656	-4.959
15.11.22	Run 18	17	1607	1596	-0.579	-4.895
15.11.22	Run 18	18	1324	1344	-0.627	-4.848
15.11.22	Run 19	1	2713	2770	-0.666	-4.982
15.11.22	Run 19	2	2362	2443	-0.616	-4.849
15.11.22	Run 19	3	2088	2148	-0.649	-4.969
15.11.22	Run 19	4	1857	1855	-0.661	-4.894
16.11.22	Run 20	1	2705	2772	-0.641	-4.897
16.11.22	Run 20	2	2373	2416	-0.659	-4.867
16.11.22	Run 20	3	2096	2092	-0.712	-4.996
16.11.22	Run 20	4	1765	1794	-0.701	-4.922

8.3 All measurements of the COR1D standard during planktic foraminifera analysis used in this research

Date	Run number	Position	1 Cycle Int Samp 44	1 Cycle Int Ref 44	d13C [VPDB]	d18O [VPDB]
17.11.22	Run 20	15	1984	2020	-0.580	-4.961
17.11.22	Run 20	16	1706	1747	-0.595	-4.895
18.11.22	Run 21	1	2668	2729	-0.675	-4.912
18.11.22	Run 21	2	2350	2394	-0.655	-4.884
18.11.22	Run 21	3	2030	2092	-0.639	-4.905
18.11.22	Run 21	4	1785	1833	-0.732	-4.981
19.11.22	Run 21	15	2107	2136	-0.632	-4.966
19.11.22	Run 21	16	1811	1876	-0.555	-4.890
24.11.22	Run 22	1	2771	2770	-0.681	-4.913
24.11.22	Run 22	2	2407	2412	-0.658	-4.926
24.11.22	Run 22	3	2038	2122	-0.647	-4.949
24.11.22	Run 22	4	1879	1848	-0.668	-4.957
25.11.22	Run 22	15	2071	2108	-0.589	-4.902
25.11.22	Run 22	16	1810	1824	-0.645	-4.894
28.11.22	Run 23	1	2728	2794	-0.652	-4.998
28.11.22	Run 23	2	2436	2521	-0.620	-4.830
28.11.22	Run 23	3	2146	2187	-0.664	-4.926
28.11.22	Run 23	4	1887	1903	-0.676	-4.937
29.11.22	Run 23	15	2261	2276	-0.622	-4.935
29.11.22	Run 23	16	1971	2013	-0.655	-4.915
02.12.22	Run 24	1	2646	2748	-0.640	-4.857
02.12.22	Run 24	2	2380	2428	-0.634	-4.886
02.12.22	Run 24	3	2057	2124	-0.685	-4.994
02.12.22	Run 24	4	1798	1865	-0.646	-4.949
03.12.22	Run 24	15	2261	2318	-0.633	-4.923
03.12.22	Run 24	16	1974	1988	-0.652	-4.929
06.12.22	Run 25	2	2909	3009	-0.652	-4.941
06.12.22	Run 25	3	2624	2687	-0.633	-5.019
06.12.22	Run 25	4	2335	2392	-0.675	-4.932
07.12.22	Run 25	15	2670	2757	-0.658	-4.864
07.12.22	Run 25	16	2398	2427	-0.622	-4.874
07.12.22	Run 25	27	2563	2622	-0.649	-4.907
09.12.22	Run 25 b	1	2474	2598	-0.690	-4.866
09.12.22	Run 25 b	2	2262	2262	-0.681	-4.948
09.12.22	Run 25 b	3	3217	3178	-0.554	-5.021
09.12.22	Run 25 b	4	2804	2867	-0.667	-4.858
06.01.23	Run 26	2	2741	2875	-0.636	-4.918
06.01.23	Run 26	3	2531	2533	-0.712	-4.970
06.01.23	Run 26	4	2163	2215	-0.652	-4.878
07.01.23	Run 26	15	2818	3003	-0.681	-4.841
07.01.23	Run 26	16	2635	2650	-0.611	-4.896
07.01.23	Run 26	27	2792	2880	-0.623	-4.926
07.01.23	Run 26	28	2511	2537	-0.655	-5.007
07.01.23	Run 26	29	2191	2259	-0.617	-4.895
07.01.23	Run 26	30	1928	1965	-0.645	-4.977
09.01.23	Run 27	1	3019	3234	-0.591	-4.825
09.01.23	Run 27	2	2849	2865	-0.659	-4.888
09.01.23	Run 27	3	2459	2572	-0.676	-4.911
09.01.23	Run 27	4	2257	2250	-0.668	-4.969
09.01.23	Run 27	14	2803	2840	-0.626	-4.853
10.01.23	Run 27	15	2484	2468	-0.654	-5.016
10.01.23	Run 27	23	2762	2783	-0.658	-4.916
10.01.23	Run 27	24	2420	2504	-0.594	-4.908

8.4 All measurements of the COR1D standard during fine fraction analysis used in this research

This table shows measurements collected from all analyses of the COR1D standard during analysis of fine fraction foraminifera samples. As described in Chapter 2.5.1.

8.4 All measurements of the COR1D standard during fine fraction analysis used in this research

Date	Run	Height (nA)	$\delta^{13}C$ (Gas)	$\delta^{13}C$ (VPDB)	$\delta^{18}O$ (VPDB)	$\delta^{18}O$ (Gas)
26.01.21	Run 1	22.56		-0.626	-4.931	
26.01.21	Run 1	11.23		-0.616	-4.952	
26.01.21	Run 1	21.49		-0.594	-4.876	
26.01.21	Run 1	18.28		-0.696	-4.992	
26.01.21	Run 1	18.57		-0.620	-4.928	
26.01.21	Run 1	31.21		-0.681	-4.810	
26.01.21	Run 1	17.21		-0.649	-4.936	
26.01.21	Run 1	21.12		-0.629	-4.850	
26.01.21	Run 1	7.91		-0.720	-5.032	
26.01.21	Run 2	9.00		-0.699	-4.999	
26.01.21	Run 2	6.15		-0.562	-4.960	
26.01.21	Run 2	9.99		-0.655	-4.914	
26.01.21	Run 2	7.46		-0.594	-4.985	
26.01.21	Run 2	11.32		-0.737	-4.969	
26.01.21	Run 2	3.12		-0.591	-4.747	
26.01.21	Run 2	9.12		-0.698	-4.888	
25/02/2021	Run 7	2.69	-0.529	-0.704	-4.987	9.785
25/02/2021	Run 7	4.79	-0.460	-0.636	-5.010	9.762
25/02/2021	Run 7	7.85	-0.450	-0.625	-4.873	9.900
25/02/2021	Run 7	7.38	-0.481	-0.656	-4.971	9.802
25/02/2021	Run 7	7.52	-0.553	-0.728	-4.921	9.851
25/02/2021	Run 7	4.69	-0.490	-0.666	-4.644	10.132
25/02/2021	Run 7	1.74	-0.454	-0.630	-4.868	9.906
09/03/2021	Run 9	7.63	-0.519	-0.689	-4.947	9.970
09/03/2021	Run 9	9.56	-0.488	-0.658	-4.923	9.994
09/03/2021	Run 9	10.64	-0.435	-0.605	-4.954	9.963
09/03/2021	Run 9	12.69	-0.462	-0.632	-4.818	10.100
09/03/2021	Run 9	5.97	-0.458	-0.628	-4.972	9.945
09/03/2021	Run 9	9.40	-0.505	-0.675	-4.924	9.993
19/07/2021	Run 10	3.00	-0.338	-0.532	-5.197	10.081
19/07/2021	Run 10	3.38	-0.453	-0.647	-5.069	10.211
19/07/2021	Run 10	2.01	-0.458	-0.652	-5.238	10.039
19/07/2021	Run 10	2.88	-0.426	-0.619	-4.713	10.572
19/07/2021	Run 10	4.34	-0.458	-0.652	-4.662	10.624
19/07/2021	Run 10	5.98	-0.515	-0.709	-5.175	10.103
19/07/2021	Run 10	3.46	-0.396	-0.589	-4.660	10.626
19/07/2021	Run 10	1.99	-0.589	-0.783	-4.670	10.615
17/01/2022	Run 11	4.36	-0.399	-0.624	-5.005	10.734
17/01/2022	Run 11	2.93	-0.389	-0.614	-4.728	11.015
17/01/2022	Run 11	3.17	-0.394	-0.619	-4.828	10.914
17/01/2022	Run 11	4.43	-0.417	-0.642	-5.008	10.731
17/01/2022	Run 11	3.60	-0.515	-0.740	-5.045	10.694
18/01/2022	Run12	11.95	-0.410	-0.719	-5.108	10.380
18/01/2022	Run12	9.94	-0.303	-0.612	-4.985	10.505
18/01/2022	Run12	9.80	-0.270	-0.579	-4.803	10.690
18/01/2022	Run12	12.41	-0.384	-0.693	-5.009	10.481
18/01/2022	Run12	10.88	-0.248	-0.557	-4.797	10.696
18/01/2022	Run12	10.91	-0.443	-0.752	-4.928	10.562
18/01/2022	Run12	11.17	-0.301	-0.610	-4.935	10.556
18/01/2022	Run12	5.96	-0.352	-0.661	-4.817	10.675
19/01/2022	Run 13	6.58	-0.526	-0.757	-4.893	10.719
19/01/2022	Run 13	4.77	-0.460	-0.691	-4.880	10.733
19/01/2022	Run 13	5.17	-0.376	-0.607	-4.814	10.800
19/01/2022	Run 13	6.98	-0.394	-0.624	-4.890	10.723
19/01/2022	Run 13	5.18	-0.293	-0.524	-4.819	10.795
19/01/2022	Run 13	5.45	-0.473	-0.704	-5.011	10.600
19/01/2022	Run 13	10.99	-0.408	-0.639	-5.090	10.520
19/01/2022	Run 13	8.71	-0.407	-0.637	-4.987	10.624
24/02/2022	Run 15	5.75	-0.667	-0.806	-4.876	10.446
24/02/2022	Run 15	5.88	-0.439	-0.578	-4.848	10.475
24/02/2022	Run 15	9.20	-0.450	-0.588	-4.952	10.369
24/02/2022	Run 15	8.82	-0.342	-0.480	-4.884	10.439
24/02/2022	Run 15	6.82	-0.540	-0.679	-4.959	10.363
24/02/2022	Run 15	7.90	-0.429	-0.567	-4.863	10.459
24/02/2022	Run 15	8.11	-0.621	-0.759	-4.985	10.335
24/02/2022	Run 15	8.47	-0.528	-0.667	-4.891	10.431
24/02/2022	Run 15	9.90	-0.331	-0.469	-4.867	10.456
24/02/2022	Run 15	10.47	-0.403	-0.542	-4.949	10.373
24/02/2022	Run 15	11.89	-0.618	-0.757	-5.016	10.305
24/02/2022	Run 15	9.26	-0.469	-0.607	-5.022	10.298

8.4 All measurements of the COR1D standard during fine fraction analysis used in this research

Date	Run	Height (nA)	$\delta^{13}C$ (Gas)	$\delta^{13}C$ (VPDB)	$\delta^{18}O$ (VPDB)	$\delta^{18}O$ (Gas)
24/02/2022	Run 15	9.14	-0.537	-0.676	-4.869	10.454
24/02/2022	Run 15	9.21	-0.759	-0.897	-4.941	10.380
14/03/2022	Run 16	10.97	-0.816	-0.772	-5.015	-5.020
14/03/2022	Run 16	9.86	-0.718	-0.674	-4.952	-4.957
14/03/2022	Run 16	9.90	-0.634	-0.590	-4.941	-4.946
14/03/2022	Run 16	9.89	-0.724	-0.679	-4.938	-4.944
14/03/2022	Run 16	12.98	-0.644	-0.600	-5.011	-5.016
14/03/2022	Run 16	12.92	-0.640	-0.596	-5.023	-5.028
14/03/2022	Run 16	8.72	-0.665	-0.620	-4.727	-4.732
14/03/2022	Run 16	12.53	-0.683	-0.639	-4.946	-4.952
14/03/2022	Run 16	13.01	-0.599	-0.555	-4.871	-4.876
14/03/2022	Run 16	12.08	-0.660	-0.616	-4.843	-4.848
14/03/2022	Run 16	5.83	-0.833	-0.789	-4.827	-4.832
18/03/2022	Run 17	8.16	-0.584	-0.488	-4.770	9.903
18/03/2022	Run 17	3.34	-0.858	-0.762	-5.147	9.520
18/03/2022	Run 17	3.34	-0.723	-0.627	-4.907	9.763
18/03/2022	Run 17	4.82	-0.622	-0.525	-4.630	10.045
18/03/2022	Run 17	3.35	-0.732	-0.636	-4.732	9.940
18/03/2022	Run 17	2.03	-0.798	-0.701	-5.200	9.466
18/03/2022	Run 17	1.98	-1.012	-0.916	-5.319	9.345
18/03/2022	Run 17	2.75	-0.807	-0.710	-4.866	9.804
18/03/2022	Run 17	2.16	-0.607	-0.510	-4.767	9.906
18/03/2022	Run 17	5.67	-0.718	-0.621	-4.769	9.903
18/03/2022	Run 17	1.04	-0.971	-0.875	-5.516	9.145
18/03/2022	Run 17	8.38	-0.500	-0.404	-4.453	10.224
22/08/2022	Run 18		8.081	-0.544	-4.746	
22/08/2022	Run 18		7.725	-0.615	-4.785	
22/08/2022	Run 18		8.164	-0.633	-4.934	
22/08/2022	Run 18		8.361	-0.663	-4.912	
22/08/2022	Run 18		9.183	-0.625	-4.885	
22/08/2022	Run 18		7.135	-0.671	-4.961	
24/08/2022	Run 19	9.46		-0.532	-4.930	
24/08/2022	Run 19	8.23		-0.554	-4.713	
24/08/2022	Run 19	0.25		-0.672	-4.970	
24/08/2022	Run 19	7.91		-0.624	-4.876	
24/08/2022	Run 19	7.62		-0.695	-4.971	
24/08/2022	Run 19	7.68		-0.601	-4.875	
24/08/2022	Run 19	6.33		-0.674	-4.904	
24/08/2022	Run 19	8.06		-0.622	-4.942	
21/09/2022	Run 20 a	8.23		-0.577	-5.048	
21/09/2022	Run 20 a	8.60		-0.703	-4.929	
21/09/2022	Run 20 a	7.04		-0.593	-4.917	
	Run 21	9.65	-1.049	-0.733	-4.952	10.146
	Run 21	7.32	-0.925	-0.608	-4.915	10.184
	Run 21	9.07	-0.919	-0.603	-4.901	10.198
	Run 21	6.94	-1.021	-0.648	-4.923	10.287
	Run 21	9.26	-0.925	-0.648	-4.923	10.087
18/10/2022	Run 22	8.37	-1.064	-0.671	-4.909	10.042
18/10/2022	Run 22	7.71	-1.057	-0.664	-4.821	10.131
18/10/2022	Run 22	9.73	-1.002	-0.609	-5.039	9.910
18/10/2022	Run 22	7.86	-1.027	-0.629	-4.898	10.142
18/10/2022	Run 22	8.87	-1.064	-0.667	-4.948	10.092
18/10/2022	Run 22	9.16	-1.052	-0.622	-4.899	10.050
18/10/2022	Run 22	10.00	-1.105	-0.674	-4.947	10.001
18/10/2022	Run 22	7.58	-1.028	-0.578	-4.793	10.302
18/10/2022	Run 22	7.07	-1.167	-0.718	-5.053	10.038
18/10/2022	Run 22	3.83	-1.112	-0.687	-4.920	10.498
18/10/2022	Run 22	4.03	-1.034	-0.609	-4.926	10.492
19/10/2022	Run 23	8.39	-1.040	-0.629	-4.904	10.138
19/10/2022	Run 23	8.26	-1.083	-0.672	-4.831	10.211
19/10/2022	Run 23	9.61	-1.056	-0.644	-5.034	10.006
19/10/2022	Run 23	8.65	-1.017	-0.564	-4.909	10.166
19/10/2022	Run 23	7.96	-1.184	-0.732	-4.937	10.138
19/10/2022	Run 23	8.40	-1.040	-0.640	-4.902	10.129
19/10/2022	Run 23	9.50	-1.055	-0.656	-4.944	10.087
19/10/2022	Run 23	9.01	-1.089	-0.706	-4.979	10.086
19/10/2022	Run 23	8.83	-0.974	-0.590	-4.867	10.200
19/10/2022	Run 23	3.56	-0.944	-0.648	-4.923	10.378
21/10/2022	Run 24	8.63	-1.024	-0.634	-4.955	10.078

8.4 All measurements of the COR1D standard during fine fraction analysis used in this research

Date	Run	Height (nA)	$\delta^{13}C$ (Gas)	$\delta^{13}C$ (VPDB)	$\delta^{18}O$ (VPDB)	$\delta^{18}O$ (Gas)
21/10/2022	Run 24	8.88	-1.014	-0.624	-4.865	10.169
21/10/2022	Run 24	7.46	-1.077	-0.686	-4.949	10.083
21/10/2022	Run 24	7.03	-0.989	-0.623	-4.862	10.219
21/10/2022	Run 24	7.53	-1.039	-0.673	-4.984	10.096
21/10/2022	Run 24	8.87	-1.087	-0.664	-4.916	10.119
21/10/2022	Run 24	9.10	-1.055	-0.632	-4.930	10.105
21/10/2022	Run 24	8.45	-1.055	-0.674	-4.940	10.015
21/10/2022	Run 24	7.55	-1.003	-0.622	-4.906	10.050
21/10/2022	Run 24	9.08	-1.017	-0.620	-4.924	10.070
21/10/2022	Run 24	8.20	-1.073	-0.676	-4.922	10.073
21/10/2022	Run 25	8.23		-0.648	-4.923	
21/10/2022	Run 25	7.91		-0.648	-4.923	
21/10/2022	Run 25	4.57		-0.694	-4.701	
21/10/2022	Run 25	7.99		-0.602	-5.145	
21/10/2022	Run 25	7.31		-0.741	-5.015	
21/10/2022	Run 25	7.76		-0.555	-4.831	
21/10/2022	Run 25	8.75		-0.589	-4.795	
21/10/2022	Run 25	7.10		-0.707	-5.051	
02/02/2021	Run 3	10.49	-0.513	-0.707	-5.010	9.938
02/02/2021	Run 3	15.55	-0.416	-0.610	-4.803	10.148
02/02/2021	Run 3	11.89	-0.450	-0.644	-5.064	9.883
02/02/2021	Run 3	7.90	-0.433	-0.627	-5.050	9.898
02/02/2021	Run 3	11.90	-0.478	-0.672	-4.851	10.098
02/02/2021	Run 3	13.26	-0.424	-0.618	-4.804	10.146
02/02/2021	Run 3	14.10	-0.463	-0.657	-4.878	10.071
16/02/2021	Run 4	7.80	-0.486	-0.643	-4.894	9.875
16/02/2021	Run 4	2.09	-0.587	-0.743	-5.043	9.724
16/02/2021	Run 4	8.27	-0.423	-0.580	-4.829	9.942
16/02/2021	Run 4	7.78	-0.498	-0.654	-4.956	9.813
16/02/2021	Run 4	4.28	-0.448	-0.605	-4.823	9.948
16/02/2021	Run 4	5.08	-0.500	-0.656	-4.913	9.856
16/02/2021	Run 4	6.05	-0.448	-0.604	-4.979	9.790
16/02/2021	Run 4	9.53	-0.578	-0.735	-4.980	9.788
16/02/2021	Run 4	4.85	-0.453	-0.610	-5.053	9.715
16/02/2021	Run 4	5.57	-0.415	-0.571	-4.906	9.864
16/02/2021	Run 4	4.74	-0.569	-0.726	-4.779	9.992
19/02/2021	Run 5	8.59	-0.381	-0.609	-4.828	9.978
19/02/2021	Run 5	7.51	-0.300	-0.528	-4.832	9.975
19/02/2021	Run 5	4.68	-0.394	-0.622	-5.027	9.777
19/02/2021	Run 5	4.91	-0.425	-0.653	-4.977	9.828
19/02/2021	Run 5	9.17	-0.534	-0.762	-4.883	9.923
19/02/2021	Run 5	6.14	-0.388	-0.617	-4.996	9.808
19/02/2021	Run 5	7.68	-0.516	-0.745	-4.918	9.888
23/02/2021	Run 6	28.68	-0.385	-0.630	-4.962	10.101
23/02/2021	Run 6	11.44	-0.370	-0.614	-5.007	10.056
23/02/2021	Run 6	8.28	-0.426	-0.671	-4.818	10.247
23/02/2021	Run 6	7.02	-0.343	-0.587	-4.852	10.212
23/02/2021	Run 6	14.24	-0.436	-0.681	-4.997	10.066
23/02/2021	Run 6	13.79	-0.476	-0.720	-4.900	10.164
05/03/2021	Run 8	9.32	-0.618	-0.711	-5.027	9.882
05/03/2021	Run 8	5.25	-0.581	-0.674	-4.706	10.207
05/03/2021	Run 8	4.76	-0.484	-0.577	-4.726	10.187
05/03/2021	Run 8	7.38	-0.502	-0.595	-4.976	9.933
05/03/2021	Run 8	2.86	-0.673	-0.766	-5.019	9.889
05/03/2021	Run 8	9.60	-0.509	-0.603	-4.994	9.915
05/03/2021	Run 8	8.54	-0.439	-0.532	-4.928	9.983
05/03/2021	Run 8	2.17	-0.633	-0.726	-5.008	9.901

8.5 Foraminiferal preservation and lithological information for samples collected at Kottaphi Hill

This table shows the information collected on general lithology, collection height and foraminifera preservation for all samples collected from the Kottaphi Hill succession.

8.5 Foraminiferal preservation and lithological information for samples collected at Kottaphi Hill

Height (m)	Sample ID		Lithology	Note	Foraminifera Preservation level
32.9	TC21	**193**	Chalk	Light hard	0
32.8	TC21	**192**	Chalk	Light hard	4
32.7	TC21	**191**	Chalk	Light hard	4
32.6	TC21	**190**	Chalk	Light hard	4
32.5	TC21	**189**	Marl	Dark soft	4
32.4	TC21	**188**	Chalk	Light hard	4
32.3	TC21	**187**	Chalk	Light hard	4
32.2	TC21	**186**	Chalk	Light hard	3
32.1	TC21	**185**	Chalk	Light hard	3
32	TC21	**184**	Marly Chalk	Dark hard	3
31.9	TC21	**183**	Chalk	Light hard	4
31.8	TC21	**182**	Marl	Dark soft	4
31.7	TC21	**181**	Chalk	Light hard	4
31.6	TC21	**180**	Chalk	Light hard	4
31.5	TC21	**179**	Chalk	Light hard	4
31.4	TC21	**178**	Chalk	Light Hard - Fe rich	3
31.3	TC21	**177**	Chalk	Light hard	4
31.2	TC21	**176**	Chalk	Light hard	3
31.1	TC21	**175**	Chalk	Light hard	4
31	TC21	**174**	Chalk	Light hard	4
30.9	TC21	**173**	Marl	Dark soft	3
30.8	TC21	**172**	Chalk	Light hard	4
30.7	TC21	**171**	Chalk	Light hard	4
30.6	TC21	**170**	Chalk	Light hard	4
30.5	TC21	**169**	Chalk	Light hard	4
30.4	TC21	**168**	Marl	Dark soft	3
30.3	TC21	**167**	Chalk	Light hard	4
30.2	TC21	**166**	Chalk	Light hard	4
30.1	TC21	**165**	Chalk	Light hard	3
30	TC21	**164**	Chalk	Light hard	4
29.9	TC21	**163**	Chalk	Light hard	3
29.8	TC21	**162**	Chalk	Light hard	4
29.7	TC21	**161**	Chalk	Light hard	4
29.6	TC21	**160**	Marl	Dark soft	4
29.5	TC21	**159**	Chalk	Light hard	4
29.45	TC21	**158**	Chalk	Light hard	4
29.4	TC21	**157**	Chalk	Light hard	3
29.35	TC21	**156**	Chalk	Light hard	3
29.3	TC21	**155**	Chalk	Light hard	4
29.25	TC21	**154**	Chalk	Light hard	3
29.2	TC21	**153**	Marly Chalk	Light hard	4
29.15	TC21	**152**	Marly Chalk	Light hard	4
29.1	TC21	**151**	Chalk	Light hard	4
29.05	TC21	**150**	Chalk	Light hard	4
29	TC21	**149**	Chalk	Light hard	3
28.95	TC21	**148**	Chalk	Light hard	3
28.9	TC21	**147**	Chalk	Light hard	0
28.85	TC21	**146**	Chalk	Light hard	3
28.8	TC21	**145**	Chalk	Light hard	3
28.75	TC21	**144**	Chalk	Light hard	3
28.7	TC21	**143**	Chalk	Light hard	3
28.65	TC21	**142**	Chalk	Light hard	3
28.6	TC21	**141**	Chalk	Light hard	3
28.55	TC21	**140**	Chalk	Light hard	0
28.5	TC21	**139**	Chalk	Light hard	0
28.45	TC21	**138**	Chalk	Light hard	3
28.4	TC21	**137**	Chalk	Light hard	3
28.35	TC21	**136**	Chalk	Light hard	3
28.3	TC21	**135**	Chalk	Light hard	3
28.25	TC21	**134**	Marl	Dark soft	3
28.2	TC21	**133**	Chalk	Light hard	0
28.15	TC21	**132**	Chalk	Light hard	3
28.1	TC21	**131**	Marl	Dark soft	3
28.05	TC21	**130**	Chalk	Light hard	3
28	TC21	**129**	Chalk	Light hard	2
27.95	TC21	**128**	Chalk	Light hard	3
27.9	TC21	**127**	Chalk	Light hard	3
27.85	TC21	**126**	Chalk	Light hard	0
27.8	TC21	**125**	Chalk	Light hard	3

8.5 Foraminiferal preservation and lithological information for samples collected at Kottaphi Hill

Height (m)	Sample ID	Lithology	Note	Foraminifera Preservation level
27.75	TC21 **124**	Marl	Dark soft	3
27.7	TC21 **123**	Marl	Dark soft	3
27.65	TC21 **122**	Chalk	Light hard	3
27.6	TC21 **121**	Chalk	Light hard	4
27.55	TC21 **120**	Marly Chalk	Light hard	3
27.5	TC21 **119**	Marly Chalk	Light hard	3
27.45	TC21 **118**	Chalk	Light hard	3
27.4	TC21 **117**	Chalk	Light hard	3
27.35	TC21 **116**	Marly Chalk	Light hard	0
27.3	TC21 **115**	Chalky Marl	Dark soft	3
27.25	TC21 **114**	Marly Chalk	Light hard	3
27.2	TC21 **113**	Chalky Marl	Dark soft	3
27.15	TC21 **112**	Chalky Marl	Dark soft	4
27.1	TC21 **111**	Chalky Marl	Dark soft	3
27.05	TC21 **110**	Marly Chalk	Light hard	4
27	TC21 **109**	Chalk	Light hard	4
26.95	TC21 **108**	Marly Chalk	Light hard	3
26.9	TC21 **107**	Marl	Dark soft	4
26.85	TC21 **106**	Marl	Dark soft	4
26.8	TC21 **105**	Chalky Marl	Light soft	3
26.75	TC21 **104**	Chalky Marl	Light hard	4
26.7	TC21 **103**	Chalky Marl	Light hard	4
26.65	TC21 **102**	Marl	Dark soft	4
26.6	TC21 **101**	Marl	Dark soft	4
26.55	TC21 **100**	Marl	Dark soft	4
26.5	TC21 **099**	Marl	Dark soft	4
26.45	TC21 **098**	Marl	Dark soft	4
26.4	TC21 **097**	Marly Chalk	Light hard	4
26.35	TC21 **096**	Marl	Dark soft	4
26.3	TC21 **095**	Marly Chalk	Dark hard	3
26.25	TC21 **094**	Chalky Marl	Dark soft	3
26.2	TC21 **093**	Marly chalk	Dark hard	4
26.15	TC21 **092**	Marl	Dark soft	4
26.1	TC21 **091**	Chalky Marl	Dark hard	4
26.05	TC21 **090**	Chalky Marl	Dark soft	4
26	TC21 **089**	Marl	Dark soft	4
25.95	TC21 **088**	Marl	Dark soft	4
25.9	TC21 **087**	Marl	Dark soft	4
25.85	TC21 **086**	Marl	Dark soft	4
25.8	TC21 **085**	Marl	Dark soft	4
25.75	TC21 **084**	Marly chalk	Dark hard	4
25.7	TC21 **083**	Marl	Dark soft	4
25.65	TC21 **082**	Marl	Dark soft	4
25.6	TC21 **081**	Marly Chalk	Light hard	4
25.55	TC21 **080**	Marly Chalk	Dark hard Fe rich	4
25.5	TC21 **079**	Marl	Dark soft	4
25.45	TC21 **078**	Marl	Dark soft	4
25.4	TC21 **077**	Marl	Dark soft	4
25.35	TC21 **076**	Marl	Dark soft	4
25.3	TC21 **075**	Marl	Dark soft	4
25.25	TC21 **074**	Marl	Dark soft	4
25.2	TC21 **073**	Marl	Dark soft	3
25.15	TC21 **072**	Marl	Dark soft	4
25.1	TC21 **071**	Marly Chalk	Dark soft	4
25.05	TC21 **070**	Chalky Marl	Dark soft	4
25	TC21 **069**	Marly Chalk	Light hard	4
24.95	TC21 **068**	Marly Chalk	Light hard	0
24.9	TC21 **067**	Marly Chalk	Light hard	4
24.85	TC21 **066**	Marly Chalk	Light hard	4
24.8	TC21 **065**	Marl	Dark soft	3
24.75	TC21 **064**	Marl	Dark soft	4
24.7	TC21 **063**	Chalky Marl	Dark soft	4
24.65	TC21 **062**	Marl Chalk	Light hard	4
24.6	TC21 **061**	Marl Chalk	Light hard	4
24.55	TC21 **060**	Chalk	Light hard	4
24.5	TC21 **059**	Chalk	Light hard	4
24.45	TC21 **058**	Chalk	Light hard	4
24.4	TC21 **057**	Marly chalk	Light hard	4

8.5 Foraminiferal preservation and lithological information for samples collected at Kottaphi Hill

Height (m)	Sample ID	Lithology	Note	Foraminifera Preservation level
24.35	TC21 **056**	Marly chalk	Light hard	4
24.3	TC21 **055**	Chalky Marl	Light hard	4
24.25	TC21 **054**	Chalky Marl	Light hard	4
24.2	TC21 **053**	Marl	Dark soft	4
24.15	TC21 **052**	Marl	Dark soft	4
24.1	TC21 **051**	Marl	Dark soft	4
24.05	TC21 **050**	Marl	Dark soft	3
24	TC21 **049**	Marl	Dark soft	3
23.95	TC21 **048**	Marl	Dark soft	3
23.9	TC21 **047**	Marl	Dark soft	0
23.85	TC21 **046**	Marl	Dark soft	0
23.8	TC21 **045**	Marl	Dark soft	3
23.75	TC21 **044**	Marl	Dark soft	4
23.7	TC21 **043**	Marl	Dark soft	3
23.65	TC21 **042**	Chalk	Light hard	3
23.6	TC21 **041**	Chalk	Light hard	0
23.55	TC21 **035**	Chalk	Light hard	2
23.5	TC21 **034**	Chalk	Light hard	2
23.45	TC21 **033**	Chalk	Light hard	2
23.4	TC21 **032**	Marl	Dark soft	3
23.35	TC21 **031**	Marl	Dark soft	2
23.3	TC21 **030**	Marly Chalk	Light hard	3
23.25	TC21 **029**	Chalk	Light hard	3
23.2	TC21 **028**	Chalk	Light hard	3
23.15	TC21 **027**	Chalk	Light hard	3
23.1	TC21 **026**	Chalky Marl	Light hard	2
23.05	TC21 **025**	Chalky Marl	Light hard	3
23	TC21 **024**	Marl	Dark soft	3
22.95	TC21 **023**	Marl	Dark soft	3
22.9	TC21 **022**	Marl	Dark soft	3
22.85	TC21 **021**	Marl	Dark soft	3
22.8	TC21 **020**	Chalky Marl	Light hard	4
22.75	TC21 **019**	Chalky Marl	Light hard	2
22.7	TC21 **018**	Chalky Marl	Light hard	0
22.65	TC21 **017**	Marl	Dark soft	1
22.6	TC21 **016**	Marl	Dark soft	4
22.55	TC21 **015**	Marl	Dark soft	3
22.5	TC21 **014**	Marl	Dark soft	3
22.45	TC21 **013**	Chalk	Light hard	0
22.4	TC21 **012**	Chalk	Light hard	3
22.35	TC21 **011**	Chalk	Light hard	0
22.3	TC21 **010**	Marly Chalk	Light hard	3
22.25	TC21 **009**	Marly Chalk	Light soft	2
22.2	TC21 **008**	Marly Chalk	Light soft	3
22.15	TC21 **007**	Marly Chalk	Light soft	3
22.1	TC21 **006**	Chalky Marl	Light soft	4
22.05	TC21 **005**	Chalky Marl	Light soft	0
22	TC21 **004**	Chalky Marl	Dark soft	3
21.95	TC21 **003**	Marl	Light soft	3
21.9	TC21 **002**	Marl	Light soft	3
21.85	TC21 **001**	Marl	Light soft	4
32.85	TC19 **277**	Marl	Interbedded Marl	4
31.85	TC19 **276**	Marl	Interbedded Marl	4
30.35	TC19 **275**	Sapropel	Surrounded by Marl	3
28.85	TC19 **274**	Sapropel	Surrounded by Marl	4
27.35	TC19 **273**	Sapropel	Surrounded by Marl	4
25.35	TC19 **272**	Sapropel	~10cm thick	4
24.85	TC19 **271**	Marl	Beneath hard layer	4
23.35	TC19 **270**	Sapropel	Above hard layer	2
21.85	TC19 **244**	Harder Limestone	Light	3
21.8	TC19 **243**	Harder Limestone	Light	2
21.75	TC19 **242**	Harder Limestone	Light	3
21.7	TC19 **241**	Harder Limestone	Light	2
21.65	TC19 **240**	Harder Limestone	Light	2
21.6	TC19 **239**	Faint sapropel	Ghost sapropel	2
21.55	TC19 **238**	Harder Limestone	Light	3
21.5	TC19 **237**	Chalky Marl	Light	4
21.45	TC19 **236**	Chalky Marl	Light	3

8.5 Foraminiferal preservation and lithological information for samples collected at Kottaphi Hill

Height (m)	Sample ID	Lithology	Note	Foraminifera Preservation level
21.4	TC19 **235**	Chalky Marl	Light	2
21.35	TC19 **234**	Marl	Dark	4
21.3	TC19 **233**	Marl	Dark	4
21.25	TC19 **232**	Marl	Dark	4
21.2	TC19 **231**	Marl	Dark	4
21.15	TC19 **230**	Marl	Dark	4
21.1	TC19 **229**	Hard Marl	Light	3
21.05	TC19 **228**	Sapropel	Brown	3
21	TC19 **227**	Hard Chalk	Light	4
20.95	TC19 **226**	Hard Chalk	Light	2
20.9	TC19 **225**	Hard Chalk	Light	2
20.85	TC19 **224**	Limestone	Light	2
20.8	TC19 **223**	Chalk	Light	4
20.75	TC19 **222**	Chalk	Light	4
20.7	TC19 **221**	Marl	Dark	3
20.65	TC19 **220**	Marl	Dark	4
20.6	TC19 **219**	Marl	Dark	4
20.55	TC19 **218**	Chalk	Light	4
20.5	TC19 **217**	Chalk	Light	3
20.45	TC19 **216**	Marl	Dark	4
20.4	TC19 **215**	Marl	Dark	4
20.35	TC19 **214**	Marl	Dark	4
20.3	TC19 **213**	Marl	Dark	3
20.25	TC19 **212**	Chalky Marl	Dark	4
20.2	TC19 **211**	Chalky Marl	Dark	3
20.15	TC19 **210**	Marl	Dark	3
20.1	TC19 **209**	Sapropel	Sapropel	4
20.05	TC19 **208**	Chalk	Light	4
20	TC19 **207**	Chalk	Light	4
19.95	TC19 **206**	Chalk	Light	4
19.9	TC19 **205**	Chalk	Light	3
19.85	TC19 **204**	Marl	Dark	4
19.8	TC19 **203**	Marl	Dark	4
19.75	TC19 **202**	Chalk	Light	2
19.7	TC19 **201**	Chalk	Light	2
19.65	TC19 **200**	Marl	Dark	3
19.6	TC19 **199**	Chalk	Light	2
19.55	TC19 **198**	Marl	Dark	3
19.5	TC19 **197**	Marl	Dark	4
19.45	TC19 **196**	Marl	Dark	4
19.4	TC19 **195**	Sapropel	Sapropel	4
19.35	TC19 **194**	Marl	Dark	4
19.3	TC19 **193**	Marl	Dark	4
19.25	TC19 **192**	Marl	Dark	4
19.2	TC19 **191**	Marl	Dark	4
19.15	TC19 **190**	Marl	Dark	4
19.1	TC19 **189**	Chalky Marl	Dark	4
19.05	TC19 **188**	Chalky Marl	Dark	4
19	TC19 **187**	Chalk	Light	4
18.95	TC19 **186**	Marl	Dark	4
18.9	TC19 **185**	Marl	Dark	4
18.85	TC19 **184**	Chalky Marl	Dark	4
18.8	TC19 **183**	Marl	Dark	4
18.75	TC19 **182**	Chalk	Light	3
18.7	TC19 **181**	Chalk	Light	2
18.65	TC19 **180**	Chalk	Light	3
18.6	TC19 **179**	Chalk	Light	2
18.55	TC19 **178**	Chalk	Light	2
18.5	TC19 **177**	Chalk	Light	3
18.45	TC19 **176**	Chalk	Light	2
18.4	TC19 **175**	Marl	Dark	4
18.35	TC19 **174**	Marl (very marly)	Dark	4
18.3	TC19 **173**	Marl	Dark	4
18.25	TC19 **172**	Marl	Dark	2
18.2	TC19 **171**	Marl	Light	2
18.15	TC19 **170**	Chalk	Light	3
18.1	TC19 **169**	Chalky Marl	Light	3
18.05	TC19 **168**	Chalky Marl	Light	3

8.5 Foraminiferal preservation and lithological information for samples collected at Kottaphi Hill

Height (m)	Sample ID	Lithology	Note	Foraminifera Preservation level
18	TC19 **167**	Chalky Marl	Light	4
17.95	TC19 **166**	Chalky Marl	Light	4
17.9	TC19 **165**	Chalky Marl	Light	3
17.85	TC19 **164**	Marl	Dark	3
17.8	TC19 **163**	Marl	Dark	4
17.75	TC19 **162**	Marl	Dark	3
17.7	TC19 **161**	Marl	Dark	4
17.65	TC19 **160**	Chalky Marl	Light	3
17.6	TC19 **159**	Marl	Dark	3
17.55	TC19 **158**	Marl	Dark	2
17.5	TC19 **157**	Chalk	Light	2
17.45	TC19 **156**	Chalky Marl	Transitional	2
17.4	TC19 **155**	Marl	Dark	3
17.35	TC19 **154**	Chalky Marl	Dark	2
17.3	TC19 **153**	Chalk	Light	2
17.25	TC19 **152**	Chalk	Light	2
17.2	TC19 **151**	Chalk	Light	2
17.15	TC19 **150**	Chalk	Light	2
17.1	TC19 **149**	Chalk	Light	2
17.05	TC19 **148**	Chalk	Light	2
17	TC19 **147**	Chalk	Light	4
16.95	TC19 **146**	Chalk	Light	4
16.9	TC19 **145**	Chalky Marl	Dark	2
16.85	TC19 **144**	Chalky Marl	Dark	4
16.8	TC19 **143**	Chalky Marl	Dark	4
16.75	TC19 **142**	Chalky Marl	Dark	4
16.7	TC19 **141**	Chalky Marl	Dark	3
16.65	TC19 **140**	Chalky Marl	Dark	4
16.6	TC19 **139**	Chalky Marl	Light	3
16.55	TC19 **138**	Chalky Marl	Light	4
16.5	TC19 **137**	Chalky Marl	Light	3
16.45	TC19 **136**	Chalky Marl	Light	4
16.4	TC19 **135**	Chalky Marl	Transitional	4
16.35	TC19 **134**	Chalky Marl	Light	2
16.3	TC19 **133**	Chalk	Light	4
16.25	TC19 **132**	Chalk	Light	2
16.2	TC19 **131**	Chalk	Light	2
16.15	TC19 **130**	Chalk	Light	2
16.1	TC19 **129**	Chalky Marl	Transitional	4
16.05	TC19 **128**	Marl	Dark	3
16	TC19 **127**	Marl	Dark	4
15.95	TC19 **126**	Marl	Dark	3
15.9	TC19 **125**	Marl	Dark	4
15.85	TC19 **124**	Marl	Dark	4
15.8	TC19 **123**	Marl	Dark	4
15.75	TC19 **122**	Chalky Marl	Dark	4
15.7	TC19 **121**	Chalk	Light	2
15.65	TC19 **120**	Chalky Marl	Transitional	4
15.6	TC19 **119**	Marl	Dark	4
15.55	TC19 **118**	Marl	Dark	3
15.5	TC19 **117**	Marl	Dark	4
15.45	TC19 **116**	Marl	Dark	4
15.4	TC19 **115**	Marl	Dark	0
15.35	TC19 **114**	Chalky Marl	Light	3
15.3	TC19 **113**	Chalky Marl	Light	2
15.25	TC19 **112**	Chalky Marl	Light	2
15.2	TC19 **111**	Chalky Marl	Light	2
15.15	TC19 **110**	Chalky Marl	Light	2
15.1	TC19 **109**	Chalky Marl	Light	1
15.05	TC19 **108**	Marl	Light	2
15	TC19 **107**	Marl	Light	4
14.95	TC19 **106**	Marl	Light	4
14.9	TC19 **105**	Chalky Marl	Light	3
14.85	TC19 **104**	Marl	Red Band	4
14.8	TC19 **103**	Chalky Marl	Red Band	2
14.75	TC19 **102**	Chalky Marl	Light	3
14.7	TC19 **101**	Chalky Marl	Light	1
14.65	TC19 **100**	Chalky Marl (Harder)	Light	2

8.5 Foraminiferal preservation and lithological information for samples collected at Kottaphi Hill

Height (m)	Sample ID	Lithology	Note	Foraminifera Preservation level
14.6	TC19 **099**	Chalky Marl	Light	4
14.55	TC19 **098**	Chalky Marl	Light	3
14.5	TC19 **097**	Marl	Dark	3
14.45	TC19 **096**	Marl	Dark	4
14.4	TC19 **095**	Marl	Dark	4
14.35	TC19 **094**	Chalk	Light	2
14.3	TC19 **093**	Chalky Marl	Light	3
14.25	TC19 **092**	Chalky Marl	Light	3
14.2	TC19 **091**	Marl	Dark	2
14.15	TC19 **090**	Marl	Dark (possible modern soil contamination)	3
14.1	TC19 **089**	Marl	Dark	3
14.05	TC19 **088**	Chalky Marl	Pinkish Dark	4
14	TC19 **087**	Chalky Marl	Pinkish Dark	3
13.95	TC19 **086**	Marl	Dark	4
13.9	TC19 **085**	Marl	Pinkish Dark	4
13.85	TC19 **084**	Marl	Red Band (Dark)	4
13.8	TC19 **083**	Marl	Dark	3
13.75	TC19 **082**	Marl	Dark	3
13.7	TC19 **081**	Marl	Dark	4
13.65	TC19 **080**	Marl	Dark	3
13.6	TC19 **079**	Marl	Dark	3
13.55	TC19 **078**	Marl	Dark	4
13.5	TC19 **077**	Chalk	Transitional	3
13.45	TC19 **076**	Chalk	Light	2
13.4	TC19 **075**	Chalk	Light	3
13.35	TC19 **074**	Chalk	Light	3
13.3	TC19 **073**	Chalky Marl	Transitional	2
13.25	TC19 **072**	Marl	Dark	4
13.2	TC19 **071**	Marl	Dark	3
13.15	TC19 **070**	Marl	Dark	4
13.1	TC19 **069**	Marl	Dark	4
13.05	TC19 **068**	Marly Chalk	Light	2
13	TC19 **067**	Chalk	Light	2
12.95	TC19 **066**	Chalk	Light	2
12.9	TC19 **065**	Chalk	Light	2
12.85	TC19 **064**	Chalk	Light	2
12.8	TC19 **063**	Chalk	Light	3
12.75	TC19 **062**	Chalk	Light	2
12.7	TC19 **061**	Marl	Dark	4
12.65	TC19 **060**	Marl	Dark	4
12.6	TC19 **059**	Marl	Dark	3
12.55	TC19 **058**	Marl	Dark	3
12.5	TC19 **057**	Marl	Dark	3
12.45	TC19 **056**	Marl	Dark	3
12.4	TC19 **055**	Chalk	Light	2
12.35	TC19 **054**	Chalk	Light	2
12.3	TC19 **053**	Chalk	Light	2
12.25	TC19 **052**	Chalk	Light	2
12.2	TC19 **051**	Chalky Marl	Light	3
12.15	TC19 **050**	Chalky Marl	Light	2
12.1	TC19 **049**	Chalky Marl	Light	2
12.05	TC19 **048**	Chalky Marl	Light	2
12	TC19 **047**	Marl	Dark	4
11.95	TC19 **046**	Marl	Pinkish Dark	4
11.93	TC19 **045**	Marl	Red Band (Possible Sapropel)	4
11.9	TC19 **044**	Marl	Dark	4
11.85	TC19 **043**	Marl	Dark	2
11.8	TC19 **042**	Marl	Dark	4
11.75	TC19 **041**	Marl	Dark	3
11.7	TC19 **040**	Chalk	Light	3
11.65	TC19 **039**	Chalk	Light	2
11.6	TC19 **038**	Chalk	Light	1
11.55	TC19 **037**	Chalk	Light	2
11.5	TC19 **036**	Chalk	Light (Fossiliferous)	4
11.45	TC19 **035**	Chalk	Light	3
11.4	TC19 **034**	Chalk	Light	4
11.35	TC19 **033**	Marl	Dark	3
11.3	TC19 **032**	Limestone	Hard (just above hardground)	1

8.5 Foraminiferal preservation and lithological information for samples collected at Kottaphi Hill

Height (m)	Sample ID		Lithology	Note	Foraminifera Preservation level
11.3	TC19	**245**	Limestone	Hardground	1
11.25	TC19	**246**	Limestone	Hardground	1
11.2	TC19	**247**	Micritic Limestone	Hardground	2
11.15	TC19	**248**	Micritic Limestone	Softer Layer	3
11.1	TC19	**249**	Limestone	Top of hardground	1
11.05	TC19	**250**	Limestone	Top of hardground	2
11	TC19	**251**	Micritic Limestone	Softer Layer	0
10.95	TC19	**252**	Limestone	Hardground	1
10.9	TC19	**253**	Limestone	Softer Layer	3
10.85	TC19	**254**	Limestone	Softer Layer	3
10.8	TC19	**255**	Limestone	Softer Layer	3
10.2	TC19	**269**	Chalk	Light	3
10	TC19	**268**	Chalky Marl	Dark	3
9.8	TC19	**267**	Chalky Marl	Dark	3
9.6	TC19	**266**	Chalky Marl	Dark	3
9.4	TC19	**265**	Chalky Marl	Dark	2
9.2	TC19	**264**	Chalky Marl	Dark	3
9	TC19	**263**	Chalky Marl	Dark	3
6	TC19	**262**	Chalky Marl	Dark	2
5	TC19	**261**	Chalky Marl	Dark	2
4	TC19	**260**	Chalky Marl	Dark	2
3	TC19	**259**	Chalky Marl	Dark	2
2	TC19	**258**	Chalky Marl	Dark	2
1	TC19	**257**	Chalky Marl	Dark	1
0	TC19	**256**	Chalky Marl	Dark	1

8.6 Foraminiferal preservation and lithological information for samples collected at Lapatza Hill

This table shows the information collected on general lithology, collection height and foraminifera preservation for all samples collected from the Lapatza Hill succession.

8.6 Foraminiferal preservation and lithological information for samples collected at Lapatza Hill

Height (m)	Sample ID		Lithology	Note	Foraminifera Preservation level
66	TC21	**483**	Marl	Dark soft	0
65.75	TC21	**482**	Marl	Dark soft	0
65.5	TC21	**481**	Marl	Dark soft	0
65.25	TC21	**480**	Marl	Dark soft	0
65	TC21	**479**	Marl	Dark soft	0
64.75	TC21	**478**	Marl	Dark soft	0
64.5	TC21	**477**	Marl	Dark soft	0
64.25	TC21	**476**	Marl	Dark soft	0
64	TC21	**475**	Marl	Dark soft	0
63.75	TC21	**474**	Marl	Dark soft	0
63.5	TC21	**473**	Marl	Light soft	2
63.25	TC21	**472**	Marl	Dark soft	2
63	TC21	**471**	Chalky Marl	Light hard	0
62.75	TC21	**470**	Marl	Dark soft	0
62.5	TC21	**469**	Marl	Dark soft	2
62.25	TC21	**468**	Marl	Dark soft	2
62	TC21	**467**	Marl	Dark soft	0
61.75	TC21	**466**	Marl	Dark soft	2
61.5	TC21	**465**	Marl	Dark soft	0
61.25	TC21	**464**	Marl	Dark soft	0
61	TC21	**463**	Marl	Dark soft	0
60.75	TC21	**462**	Marl	Dark soft	0
60.5	TC21	**461**	Marl	Dark soft	2
60.25	TC21	**460**	Marl	Dark soft	0
60	TC21	**459**	Marl	Dark soft	2
59.75	TC21	**458**	Marl	Dark soft	4
59.5	TC21	**457**	Marl	Dark soft	4
59.25	TC21	**456**	Chalky Marl	Light soft	4
59	TC21	**455**	Chalky Marl	Light soft	3
58.75	TC21	**454**	Marl	Dark soft	3
58.5	TC21	**453**	Marl	Dark soft	3
58.25	TC21	**452**	Marl	Dark soft	3
58	TC21	**451**	Marl	Dark soft	4
57.75	TC21	**450**	Marl	Dark soft	4
57.5	TC21	**449**	Marl	Dark soft	4
57.25	TC21	**448**	Marl	Dark soft	4
57	TC21	**447**	Marl	Dark soft	4
56.75	TC21	**446**	Marl	Dark soft	4
56.5	TC21	**445**	Marl	Dark soft	4
56.25	TC21	**444**	Marl	Dark soft	2
56	TC21	**443**	Marl	Dark soft	3
55.75	TC21	**442**	Marl	Dark soft	3
55.5	TC21	**441**	Marl	Dark soft	4
55.25	**TC21**	**440**	Chalky Marl	Light soft	3
55	**TC21**	**431**	Chalky Marl	Light soft	4
54.75	TC21	**430**	Marl	Dark soft	3
54.5	TC21	**429**	Marl	Dark soft	4
54.25	TC21	**428**	Marl	Dark soft	4

8.6 Foraminiferal preservation and lithological information for samples collected at Lapatza Hill

Height (m)	Sample ID		Lithology	Note	Foraminifera Preservation level
54	TC21	**427**	Marl	Dark soft	4
53.75	TC21	**426**	Marl	Dark soft	4
53.5	TC21	**425**	Marl	Dark soft	4
53.25	TC21	**424**	Marl	Dark soft	4
53	TC21	**423**	Marl	Dark soft	4
52.75	TC21	**422**	Marl	Dark soft	4
52.5	TC21	**421**	Marl	Dark soft	4
52.25	TC21	**420**	Marl	Dark soft	4
52	TC21	**419**	Marl	Dark soft	4
51.75	TC21	**418**	Marl	Dark soft	4
51.5	TC21	**417**	Marl	Dark soft	4
51.25	TC21	**416**	Marl	Dark soft	4
51	TC21	**415**	Chalky Marl	Light soft	4
50.75	TC21	**414**	Chalky Marl	Light soft	4
50.5	TC21	**413**	Chalky Marl	Light soft	4
50.25	TC21	**412**	Chalky Marl	Light soft	3
50	TC21	**411**	Chalky Marl	Light soft	4
49.75	TC21	**410**	Chalky Marl	Light soft	4
49.5	TC21	**409**	Chalky Marl	Light soft	4
49.25	TC21	**408**	Chalky Marl	Light soft	4
49	TC21	**407**	Marl	Dark soft	4
48.75	TC21	**406**	Marl	Dark soft	3
48.5	TC21	**405**	Marl	Dark soft	4
48.25	TC21	**404**	Marl	Dark soft	4
48	TC21	**403**	Marl	Dark soft	4
47.75	TC21	**402**	Marl	Dark soft	4
47.5	TC21	**401**	Marl	Dark soft	4
47.25	TC21	**400**	Marl	Dark soft	4
47	TC21	**399**	Marl	Dark soft	4
46.75	TC21	**398**	Marl	Dark soft	4
46.5	TC21	**397**	Marl	Dark soft	4
46.25	TC21	**396**	Marl	Dark soft	4
46	TC21	**395**	Marl	Dark soft	4
45.75	TC21	**394**	Marl	Dark soft	4
45.5	TC21	**393**	Marl	Dark soft	4
45.25	TC21	**392**	Marl	Dark soft	4
45	TC21	**391**	Marl	Dark soft	4
44.75	**TC21**	**390**	Marl	Dark soft	4
44.5	**TC21**	**385**	Marl	Dark soft	4
44.25	TC21	**384**	Marl	Dark soft	4
44	TC21	**383**	Marl	Dark soft	3
43.75	TC21	**382**	Marl	Dark soft	3
43.5	TC21	**381**	Marl	Dark soft	3
43.25	TC21	**380**	Marl	Dark soft	2
43	TC21	**379**	Marl	Dark soft	4
42.75	TC21	**378**	Marl	Dark soft	4
42.5	TC21	**377**	Marl	Dark soft	3
42.25	TC21	**376**	Marl	Dark soft	3

8.6 Foraminiferal preservation and lithological information for samples collected at Lapatza Hill

Height (m)	Sample ID		Lithology	Note	Foraminifera Preservation level
42	TC21	**375**	Chalky Marl	Dark soft	3
41.75	TC21	**374**	Marl	Dark soft	3
41.5	TC21	**373**	Marl	Dark soft	3
41.25	TC21	**372**	Marl	Dark soft	3
41	TC21	**371**	Marl	Dark soft	2
40.75	TC21	**370**	Marl	Dark soft	4
40.5	TC21	**369**	Marl	Dark soft	3
40.25	TC21	**368**	Marl	Dark soft	3
40	TC21	**367**	Marl	Dark soft	3
39.75	TC21	**366**	Marl	Dark soft	3
39.5	TC21	**365**	Marl	Dark soft	3
39.25	TC21	**364**	Marl	Dark soft	3
39	TC21	**363**	Marl	Dark soft	3
38.75	TC21	**362**	Marl	Dark soft	3
38.5	TC21	**361**	Marl	Dark soft	2
38.25	**TC21**	**360**	Chalky Marl	Dark soft	3
38	**TC21**	**356**	Marl	Dark soft	3
37.75	TC21	**355**	Marl	Dark soft	3
37.5	TC21	**354**	Marl	Dark soft	3
37.25	TC21	**353**	Marl	Dark soft	3
37	TC21	**352**	Marl	Dark soft	3
36.75	TC21	**351**	Chalky Marl	Dark soft	3
36.5	TC21	**350**	Marl	Dark soft	3
36.25	TC21	**349**	Marl	Dark soft	3
36	TC21	**348**	Marl	Dark soft	0
35.75	TC21	**347**	Marl	Dark soft	3
35.5	TC21	**346**	Marl	Dark soft	4
35.25	TC21	**345**	Marl	Dark soft	4
35	TC21	**344**	Marl	Dark soft	3
34.75	TC21	**343**	Marl	Dark soft	3
34.5	TC21	**342**	Marl	Dark soft	3
34.25	TC21	**341**	Marl	Dark soft	3
34	TC21	**340**	Marl	Dark soft	3
33.75	TC21	**339**	Marl	Dark soft	3
33.5	TC21	**338**	Marl	Dark soft	3
33.25	TC21	**337**	Marl	Dark soft	4
33	TC21	**336**	Marl	Dark soft	4
32.75	TC21	**335**	Marl	Dark soft	4
32.5	TC21	**334**	Chalky Marl	Light soft	4
32.25	TC21	**333**	Marl	Dark soft	4
32	TC21	**332**	Marl	Dark soft	4
31.75	TC21	**331**	Marl	Dark soft	4
31.5	TC21	**330**	Marl	Dark soft	4
31.25	TC21	**329**	Marl	Dark soft	4
31	TC21	**328**	Marl	Dark soft	4
30.75	TC21	**327**	Marl	Dark soft	4
30.5	TC21	**326**	Marl	Dark soft	4
30.25	TC21	**325**	Marl	Dark soft	4

8.6 Foraminiferal preservation and lithological information for samples collected at Lapatza Hill

Height (m)	Sample ID		Lithology	Note	Foraminifera Preservation level
30	TC21	**324**	Marl	Dark soft	4
29.75	TC21	**323**	Marl	Dark soft	4
29.5	TC21	**322**	Marl	Dark soft	4
29.25	TC21	**321**	Marl	Dark soft	4
29	**TC21**	**320**	Marl	Dark soft	4
28.75	**TC21**	**317**	Marl	Dark soft	4
28.5	TC21	**316**	Marl	Dark soft	4
28.25	TC21	**315**	Marl	Dark soft	4
28	TC21	**314**	Marl	Dark soft	4
27.75	TC21	**313**	Marl	Dark soft	4
27.5	TC21	**312**	Marl	Dark soft	4
27.25	TC21	**311**	Marl	Dark soft	4
27	TC21	**310**	Marl	Dark soft	4
26.75	TC21	**309**	Marl	Dark soft	4
26.5	TC21	**308**	Marl	Dark soft	4
26.25	TC21	**307**	Marl	Dark soft	4
26	TC21	**306**	Marl	Dark soft	4
25.75	TC21	**305**	Chalky Marl	Light soft	4
25.5	TC21	**304**	Marl	Dark soft	4
25.25	TC21	**303**	Marl	Dark soft	4
25	TC21	**302**	Marl	Dark soft	4
24.75	TC21	**301**	Marl	Dark soft	4
24.5	TC21	**300**	Marl	Dark soft	4
24.25	TC21	**299**	Marl	Dark soft	4
24	TC21	**298**	Marl	Dark soft	4
23.75	TC21	**297**	Marl	Dark soft	4
23.5	TC21	**296**	Marl	Dark soft	4
23.25	TC21	**295**	Marl	Dark soft	4
23	TC21	**294**	Marl	Dark soft	4
22.75	TC21	**293**	Marl	Dark soft	4
22.5	TC21	**292**	Marl	Dark soft	4
22.25	TC21	**291**	Marl	Dark soft	4
22	TC21	**290**	Marl	Dark soft	4
21.75	TC21	**289**	Marl	Dark soft	4
21.5	TC21	**288**	Marl	Dark soft	4
21.25	TC21	**287**	Marl	Dark soft	4
21	TC21	**286**	Marl	Dark soft	4
20.75	TC21	**285**	Marl	Dark soft	3
20.5	TC21	**284**	Marl	Dark soft	4
20.25	TC21	**283**	Marl	Dark soft	4
20	TC21	**282**	Marl	Dark soft	3
19.75	**TC21**	**281**	Marl	Dark soft	3
19.5	**TC21**	**278**	Marl	Dark soft	3
19.25	**TC21**	**277**	Marl	Dark soft	0
19	**TC21**	**276**	Marl	Dark soft	3
18.75	**TC21**	**275**	Marl	Dark soft	3
18.5	**TC21**	**274**	Marl	Dark soft	3
18.25	TC21	**273**	Marl	Dark soft	4

8.6 Foraminiferal preservation and lithological information for samples collected at Lapatza Hill

Height (m)	Sample ID		Lithology	Note	Foraminifera Preservation level
18	TC21	**272**	Marl	Dark soft	4
17.75	TC21	**271**	Marl	Dark soft	4
17.5	TC21	**270**	Marl	Dark soft	4
17.25	TC21	**269**	Marl	Dark soft	2
17	TC21	**268**	Marl	Dark soft	3
16.75	TC21	**267**	Marl	Dark soft	3
16.5	TC21	**266**	Marl	Dark soft	3
16.25	TC21	**265**	Marl	Dark soft	3
16	TC21	**264**	Marl	Dark soft	4
15.75	TC21	**263**	Marl	Dark soft	4
15.5	TC21	**262**	Marl	Dark soft	2
15.25	TC21	**261**	Marl	Dark soft	3
15	TC21	**260**	Marl	Dark soft	4
14.75	TC21	**259**	Marl	Dark soft	3
14.5	TC21	**258**	Marl	Dark soft	4
14.25	TC21	**257**	Marl	Dark soft	4
14	TC21	**256**	Marl	Dark soft	4
13.75	TC21	**255**	Marl	Dark soft	4
13.5	TC21	**254**	Marl	Dark soft	4
13.25	TC21	**253**	Marl	Dark soft	4
13	TC21	**252**	Marl	Dark soft	4
12.75	TC21	**251**	Marl	Dark soft	3
12.5	TC21	**250**	Marl	Dark soft	4
12.25	TC21	**249**	Marl	Dark soft	4
12	TC21	**248**	Marl	Dark soft	3
11.75	TC21	**247**	Marl	Dark soft	4
11.5	TC21	**246**	Marl	Dark soft	3
11.25	TC21	**245**	Marl	Dark soft	3
11	TC21	**244**	Marl	Dark soft	4
10.75	TC21	**243**	Marl	Dark soft	4
10.5	TC21	**242**	Marl	Dark soft	3
10.25	TC21	**241**	Marl	Dark soft	3
10	TC21	**240**	Marl	Dark soft	4
9.75	TC21	**239**	Marl	Dark soft	4
9.5	TC21	**238**	Marl	Dark soft	4
9.25	TC21	**237**	Marl	Dark soft	0
9	TC21	**236**	Marl	Dark soft	0
8.75	TC21	**235**	Marl	Dark soft	3
8.5	TC21	**234**	Marl	Dark soft	4
8.25	TC21	**233**	Marl	Dark soft	4
8	TC21	**232**	Marl	Dark soft	4
7.75	**TC21**	**231**	Marl	Dark soft	0
7.5	**TC21**	**230**	Marl	Dark soft	0
7.25	TC21	**229**	Marl	Dark soft	4
7	TC21	**228**	Marl	Dark soft	4
6.75	TC21	**227**	Marl	Dark soft	4
6.5	TC21	**226**	Marl	Dark soft	4
6.25	TC21	**225**	Marl	Dark soft	4

8.6 Foraminiferal preservation and lithological information for samples collected at Lapatza Hill

Height (m)	Sample ID		Lithology	Note	Foraminifera Preservation level
6	TC21	**224**	Marl	Dark soft	4
5.75	TC21	**223**	Marl	Dark soft	4
5.5	TC21	**222**	Marl	Dark soft	4
5.25	TC21	**221**	Marl	Dark soft	4
5	TC21	**220**	Marl	Dark soft	4
4.75	TC21	**219**	Marl	Dark soft	3
4.5	TC21	**218**	Marl	Dark soft	4
4.25	TC21	**217**	Marl	Dark soft	3
4	TC21	**216**	Marl	Dark soft	4
3.75	TC21	**215**	Marl	Dark soft	3
3.5	TC21	**214**	Marl	Dark soft	4
3.25	TC21	**213**	Marl	Dark soft	3
3	TC21	**212**	Marl	Dark soft	3
2.75	TC21	**211**	Marl	Dark soft	0
2.5	TC21	**210**	Marl	Dark soft	0
2.25	TC21	**209**	Marl	Dark soft	4
2	TC21	**208**	Marl	Dark soft	4
1.75	TC21	**207**	Marl	Dark soft	4
1.5	TC21	**206**	Marl	Dark soft	3
1.25	TC21	**205**	Marl	Dark soft	3
1	TC21	**204**	Marl	Dark soft	4
0.75	TC21	**203**	Marl	Dark soft	4
0.5	TC21	**202**	Marl	Dark soft	3
0.25	TC21	**201**	Marl	Dark soft	3
0	TC21	**200**	Marl	Dark soft	4

8.7 **Trace element data for planktic foraminifera samples**

This table shows all data collected during trace element analysis of foraminifera samples, as described in Chapter 2.6. Samples which were excluded from use in this thesis are also shown, but indicated as excluded.

8.7 Trace element data for planktic foraminifera samples

Sample ID		Acid for digestion (µl)	Run No.	Age [Ma]	Li7 (µmol/mol)	Li7 (µmol/mol) (EXCLUDED)	B11 (µmol/mol)	B11 (µmol/mol) (EXCLUDED)	Na23 (mmol/mol)	Na23 (mmol/mol) (EXCLUDED)	Mg24 (mmol/mol)	Mg24 (mmol/mol) (EXCLUDED)	Mg25 (mmol/mol)	Mg25 (mmol/mol) (EXCLUDED)
TC21	**456**	35	2	5.820	11.522		88.619		5.114		7.166		7.254	
TC21	**428**	35	4	5.946	11.993		68.023		4.856		6.305		6.376	
TC21	**419**	25	4	6.003	10.370		65.539		4.357		5.024		5.009	
TC21	**418**	45	1	6.009	11.511		66.526		4.708		5.415		5.440	
TC21	**408**	35	2	6.072	11.154		89.081		4.915		5.844		5.919	
TC21	**395**	25	4	6.161		11.970		56.531		3.548		11.997		12.403
TC21	**378**	25	4	6.253	10.333		65.948		4.453		5.979		6.007	
TC21	**364**	45	1	6.353		12.175		76.364		5.103		9.740		10.010
TC21	**364**	45	2	6.353		12.345		78.185		5.283		9.845		9.983
TC21	**345**	25	4	6.466	10.012		65.469		4.540		6.627		6.713	
TC21	**330**	45	4	6.572		8.336		30.653		2.003		10.353		10.618
TC21	**311**	135	1	6.692		10.067		40.568		2.549		11.080		11.427
TC21	**310**	25	4	6.699		9.706		61.306		4.132		5.181		5.174
TC21	**290**	35	2	7.131	10.583		66.024		4.635		7.578		7.803	
TC21	**273**	25	4	7.523	10.690		82.458		4.712		7.434		7.650	
TC21	**263**	35	1	7.783		12.497		53.702		4.352		4.575		4.624
TC21	**258**	25	4	7.897	9.926		74.345		4.343		6.503		6.666	
TC21	**243A**	45	2	8.201		8.047		36.989		2.728		8.890		9.067
TC21	**243B**	55	2	8.201	10.491		34.534		2.324		11.753		11.796	
TC21	**229**	25	4	8.534	10.935		82.425		4.970		8.407		8.713	
TC21	**218**	105	4	8.788	9.789		69.734		4.162		6.969		7.215	
TC21	**216**	25	1	8.827		11.225		69.432		4.566		6.479		6.690
TC21	**168**	25	4	9.002	11.173		75.801		4.271		7.579		7.797	
TC21	**203**	35	2	9.078	11.168		78.178		4.856		8.330		8.539	
TC21	**163**	55	1	9.165	13.366		70.185		3.683		10.829		11.064	
TC21	**162**	35	4	9.197	11.229		70.803		3.939		8.134		8.396	
TC21	**158**	35	2	9.360	12.128		81.275		4.306		11.310		11.480	
TC21	**154**	35	4	9.492	11.973		77.854		4.162		11.902		12.230	
TC21	**150**	25	4	9.623	11.656		82.070		4.449		8.628		8.959	
TC21	**142**	55	1	9.859	15.379		81.955		4.394		12.509		12.655	
TC21	**135**	45	4	10.028	14.782		81.128		4.430		11.813		11.729	
TC21	**128**	25	4	10.185	12.166		71.391		4.063		10.926		11.364	

8.7 Trace element data for planktic foraminifera samples

Sample ID		Acid for digestion (µl)	Run No.	Age [Ma]	Li7 (µmol/mol)	Li7 (µmol/mol) (EXCLUDED)	B11 (µmol/mol)	B11 (µmol/mol) (EXCLUDED)	Na23 (mmol/mol)	Na23 (mmol/mol) (EXCLUDED)	Mg24 (mmol/mol)	Mg24 (mmol/mol) (EXCLUDED)	Mg25 (mmol/mol)	Mg25 (mmol/mol) (EXCLUDED)
TC21	**121**	25	1	10.327	13.160		68.338		3.808		12.543		12.814	
TC21	**120**	25	4	10.347	11.543		63.470		3.703		10.792		11.117	
TC21	**112**	35	2	10.509		9.387		61.876		4.444		6.220		6.330
TC21	**107**	25	4	10.611	10.123		61.799		3.489		9.601		9.888	
TC21	**104**	55	4	10.672	10.989		63.560		3.789		8.985		9.222	
TC21	**100**	25	4	10.746	10.333		68.517		3.683		8.353		8.564	
TC21	**096**	55	1	10.812	13.443		64.550		3.654		9.310		9.580	
TC21	**096A**	45	2	10.812		12.402		69.976		3.897		8.922		8.972
TC21	**096B**	35	2	10.812	13.488		57.550		3.452		9.238		9.454	
TC21	**088**	35	4	10.946	11.289		63.483		3.828		9.715		10.015	
TC21	**080**	25	4	11.080	10.643		57.791		3.595		8.228		8.502	
TC21	**073**	25	4	11.189	11.403		62.574		3.906		7.967		8.193	
TC21	**072**	35	1	11.203	14.928		63.319		3.721		11.206		11.472	
TC21	**064**	35	3	11.317	11.362		57.384		3.948		8.377		8.434	
TC21	**061**	45	3	11.359		24.412		58.068		3.592		13.802		14.406
TC21	**057**	35	3	11.416	12.598		59.220		3.652		9.312		9.622	
TC21	**053**	35	3	11.473	11.695		59.976		3.653		9.032		9.468	
TC21	**049**	95	1	11.529	13.252		56.497		3.417		11.138		11.405	
TC21	**049**	45	2	11.529	14.017		57.427		3.571		9.931		10.007	
TC21	**035**	35	3	11.680	14.811		60.742		3.657		9.030		9.334	
TC21	**024**	35	2	11.902	11.542		46.641		3.838		9.072		9.098	
TC21	**022**	35	1	11.946	10.776		44.809		3.250		8.467		8.727	
TC21	**016**	45	3	12.079	12.874		49.366		3.326		9.023		9.395	
TC21	**07**	35	3	12.278	22.498		45.676		2.969		11.201		11.648	
TC19	**242**	35	3	12.455	17.253		58.569		3.631		9.080		9.481	
TC19	**237**	25	1	12.566	14.420		56.590		3.908		10.659		10.990	
TC19	**233**	45	2	12.655	14.571		62.223		4.174		10.760		10.790	
TC19	**230**	25	3	12.721	20.037		63.779		3.937		11.149		11.615	
TC19	**226**	35	3	12.810	18.207		59.775		3.616		12.027		12.564	
TC19	**220**	35	3	12.943	13.437		64.142		3.800		11.975		12.471	
TC19	**218**	105	1	12.987		14.322		59.877		3.508		16.445		16.672
TC19	**218A**	55	2	12.987		13.715		63.748		3.874		12.295		12.320

8.7 Trace element data for planktic foraminifera samples

Sample ID		Acid for digestion (µl)	Run No.	Age [Ma]	Li7 (µmol/mol)	Li7 (µmol/mol) (EXCLUDED)	B11 (µmol/mol)	B11 (µmol/mol) (EXCLUDED)	Na23 (mmol/mol)	Na23 (mmol/mol) (EXCLUDED)	Mg24 (mmol/mol)	Mg24 (mmol/mol) (EXCLUDED)	Mg25 (mmol/mol)	Mg25 (mmol/mol) (EXCLUDED)
TC19	**218B**	45	2	12.987	16.015		63.066		3.659		13.281		13.180	
TC19	**212**	45	3	13.120	16.306		56.561		3.578		11.227		11.821	
TC19	**205**	45	3	13.244	14.071		65.687		3.890		9.435		9.918	
TC19	**198**	25	3	13.355	16.158		59.783		3.425		9.457		9.888	
TC19	**195**	35	1	13.403		12.979		59.504		3.986		6.024		6.073
TC19	**191**	45	2	13.466	15.246		65.223		3.830		10.936		10.727	
TC19	**187**	45	3	13.530	20.811		58.085		3.326		10.368		10.928	
TC19	**182**	35	3	13.631	13.479		60.833		3.550		7.761		7.810	
TC19	**178**	45	3	13.712	14.580		54.236		3.434		9.894		10.388	
TC19	**173**	75	1	13.812	12.970		54.601		3.403		10.097		10.386	
TC19	**173**	45	2	13.812	12.051		56.541		3.966		8.289		8.401	
TC19	**165**	45	3	13.989		16.103		55.581		3.512		11.235		11.589
TC19	**147**	35	1	14.407		13.621		58.945		3.792		12.075		12.369
TC19	**142**	55	3	14.488	21.924		61.364		3.717		11.626		12.170	
TC19	**126**	55	2	14.778	11.932		55.705		3.612		8.852		8.943	
TC19	**124**	35	1	14.822	12.337		53.735		3.558		10.481		10.917	
TC19	**117**	45	3	14.983	13.518		57.824		3.656		10.629		10.866	
TC19	**108**	45	3	15.190	15.343		52.533		3.277		9.649		9.998	
TC19	**104**	55	1	15.282	10.967		48.438		3.256		9.889		10.120	
TC19	**099**	45	2	15.392	14.704		56.115		3.492		11.253		11.223	
TC19	**092**	45	3	15.517	13.568		56.924		3.427		9.382		9.707	
TC19	**085**	45	3	15.641	12.980		53.411		3.452		9.217		9.589	
TC19	**078**	105	1	15.796	11.470		51.864		3.250		10.113		10.354	
TC19	**078**	35	2	15.796	11.077		49.237		3.398		8.348		8.330	
TC19	**072**	35	3	15.951	12.763		54.683		3.344		9.382		9.870	
TC19	**069**	35	3	16.024	11.589		56.609		3.411		8.290		8.540	
TC19	**060**	105	1	16.265	12.420		50.660		3.151		9.535		9.955	
TC19	**060**	45	2	16.265	11.342		51.509		3.244		9.004		9.038	
TC19	**042**	55	1	16.728	11.879		52.074		3.144		9.227		9.542	
TC19	**034**	25	1	16.946	12.557		55.206		3.326		9.890		10.162	

8.7 Trace element data for planktic foraminifera samples

Sample ID		Acid for digestion (µl)	Run No.	Age [Ma]	Mg26 (mmol/mol)	Mg26 (mmol/mol) (EXCLUDED)	Al27 (µmol/mol)	Al27 (µmol/mol) (EXCLUDED)	Sr88 (mmol/mol)	Sr88 (mmol/mol) (EXCLUDED)	Mo92 (µmol/mol)	Mo92 (µmol/mol) (EXCLUDED)	Cd111 (µmol/mol)	Cd111 (µmol/mol) (EXCLUDED)
TC21	**456**	35	2	5.820	7.259		61.835		1.307		0.035		0.001	
TC21	**428**	35	4	5.946	6.448		18.939		1.294		0.135		0.055	
TC21	**419**	25	4	6.003	5.030		16.410		1.266		0.209		0.049	
TC21	**418**	45	1	6.009	5.633		51.728		1.287		0.196		0.106	
TC21	**408**	35	2	6.072	5.957		39.658		1.287		0.008		0.001	
TC21	**395**	25	4	6.161		12.256		280.175		1.206		2.461		0.015
TC21	**378**	25	4	6.253	6.022		14.260		1.216		0.169		0.030	
TC21	**364**	45	1	6.353		9.953		26.401		1.252		0.024		0.009
TC21	**364**	45	2	6.353		9.839		20.971		1.258		-0.008		0.018
TC21	**345**	25	4	6.466	6.779		10.207		1.213		0.018		0.009	
TC21	**330**	45	4	6.572		10.607		319.376		1.043		0.425		0.009
TC21	**311**	135	1	6.692		11.444		236.777		1.070		0.388		0.022
TC21	**310**	25	4	6.699		5.172		44.431		1.172		0.069		0.015
TC21	**290**	35	2	7.131	7.777		92.344		1.283		0.006		0.013	
TC21	**273**	25	4	7.523	7.544		11.987		1.270		0.093		0.010	
TC21	**263**	35	1	7.783		4.606		167.677		1.254		0.722		0.797
TC21	**258**	25	4	7.897	6.693		15.137		1.266		0.026		0.014	
TC21	**243A**	45	2	8.201		9.064		115.981		1.147		0.131		0.006
TC21	**243B**	55	2	8.201	11.740		583.464		1.129		0.322		0.017	
TC21	**229**	25	4	8.534	8.486		17.313		1.260		0.157		0.008	
TC21	**218**	105	4	8.788	7.183		76.606		1.202		0.106		0.014	
TC21	**216**	25	1	8.827		6.640		66.451		1.279		0.322		0.018
TC21	**168**	25	4	9.002	7.735		35.590		1.326		0.070		0.088	
TC21	**203**	35	2	9.078	8.524		218.555		1.261		0.069		0.015	
TC21	**163**	55	1	9.165	11.096		271.580		1.198		0.426		0.057	
TC21	**162**	35	4	9.197	8.365		51.097		1.233		0.207		0.054	
TC21	**158**	35	2	9.360	11.410		123.432		1.184		0.025		0.063	
TC21	**154**	35	4	9.492	11.945		109.488		1.184		0.200		0.073	
TC21	**150**	25	4	9.623	8.774		31.405		1.269		0.169		0.050	
TC21	**142**	55	1	9.859	12.705		331.902		1.293		0.260		0.114	
TC21	**135**	45	4	10.028	11.720		358.625		1.200		0.213		0.070	
TC21	**128**	25	4	10.185	11.193		104.193		1.149		0.091		0.114	

8.7 Trace element data for planktic foraminifera samples

Sample ID		Acid for digestion (µl)	Run No.	Age [Ma]	Mg26 (mmol/mol)	Mg26 (mmol/mol) (EXCLUDED)	Al27 (µmol/mol)	Al27 (µmol/mol) (EXCLUDED)	Sr88 (mmol/mol)	Sr88 (mmol/mol) (EXCLUDED)	Mo92 (µmol/mol)	Mo92 (µmol/mol) (EXCLUDED)	Cd111 (µmol/mol)	Cd111 (µmol/mol) (EXCLUDED)
TC21	**121**	25	1	10.327	12.893		216.142		1.145		0.177		0.236	
TC21	**120**	25	4	10.347	11.039		198.576		1.133		0.223		0.106	
TC21	**112**	35	2	10.509		6.334		23.526		1.269		-0.006		0.016
TC21	**107**	25	4	10.611	9.795		88.487		1.127		0.115		0.078	
TC21	**104**	55	4	10.672	9.118		65.634		1.131		0.092		0.080	
TC21	**100**	25	4	10.746	8.543		97.518		1.140		0.111		0.081	
TC21	**096**	55	1	10.812	9.503		240.713		1.201		0.269		0.516	
TC21	**096A**	45	2	10.812		8.900		247.854		1.197		0.199		0.375
TC21	**096B**	35	2	10.812	9.400		327.750		1.171		0.315		0.561	
TC21	**088**	35	4	10.946	10.018		92.404		1.211		0.294		0.350	
TC21	**080**	25	4	11.080	8.448		52.393		1.181		1.101		0.165	
TC21	**073**	25	4	11.189	8.081		35.120		1.251		0.233		2.038	
TC21	**072**	35	1	11.203	11.433		487.490		1.213		0.426		2.131	
TC21	**064**	35	3	11.317	8.417		50.390		1.253		0.011		0.483	
TC21	**061**	45	3	11.359		14.284		1568.710		1.179		1.093		0.486
TC21	**057**	35	3	11.416	9.476		185.782		1.168		1.585		0.926	
TC21	**053**	35	3	11.473	9.386		111.052		1.204		1.049		1.503	
TC21	**049**	95	1	11.529	11.328		421.272		1.168		0.256		1.004	
TC21	**049**	45	2	11.529	9.966		858.901		1.153		0.544		0.589	
TC21	**035**	35	3	11.680	9.261		418.306		1.185		1.424		0.751	
TC21	**024**	35	2	11.902	9.173		111.460		1.169		0.089		0.080	
TC21	**022**	35	1	11.946	8.774		131.800		1.142		0.252		0.103	
TC21	**016**	45	3	12.079	9.350		314.602		1.119		0.792		0.080	
TC21	**07**	35	3	12.278	11.488		1735.692		1.078		1.444		0.124	
TC19	**242**	35	3	12.455	9.402		853.363		1.196		1.671		0.191	
TC19	**237**	25	1	12.566	10.884		223.228		1.217		0.281		0.371	
TC19	**233**	45	2	12.655	10.780		411.623		1.187		0.237		0.449	
TC19	**230**	25	3	12.721	11.435		984.212		1.240		1.028		0.900	
TC19	**226**	35	3	12.810	12.298		760.012		1.180		1.144		0.870	
TC19	**220**	35	3	12.943	12.292		190.397		1.202		0.849		0.189	
TC19	**218**	105	1	12.987		16.694		365.213		1.180		0.378		0.235
TC19	**218A**	55	2	12.987		12.313		427.221		1.238		0.238		0.156

8.7 Trace element data for planktic foraminifera samples

Sample ID		Acid for digestion (µl)	Run No.	Age [Ma]	Mg26 (mmol/mol)	Mg26 (mmol/mol) (EXCLUDED)	Al27 (µmol/mol)	Al27 (µmol/mol) (EXCLUDED)	Sr88 (mmol/mol)	Sr88 (mmol/mol) (EXCLUDED)	Mo92 (µmol/mol)	Mo92 (µmol/mol) (EXCLUDED)	Cd111 (µmol/mol)	Cd111 (µmol/mol) (EXCLUDED)
TC19	**218B**	45	2	12.987	13.184		1294.061		1.204		1.067		0.219	
TC19	**212**	45	3	13.120	11.637		605.276		1.216		0.768		0.154	
TC19	**205**	45	3	13.244	9.889		317.011		1.282		0.938		0.517	
TC19	**198**	25	3	13.355	9.706		679.695		1.233		1.046		1.009	
TC19	**195**	35	1	13.403		5.984		217.311		1.369		0.292		4.921
TC19	**191**	45	2	13.466	10.675		767.805		1.267		0.546		0.429	
TC19	**187**	45	3	13.530	10.777		1309.217		1.218		0.897		0.304	
TC19	**182**	35	3	13.631	7.745		309.156		1.272		0.719		0.116	
TC19	**178**	45	3	13.712	10.244		500.892		1.175		0.828		0.113	
TC19	**173**	75	1	13.812	10.336		334.692		1.224		0.207		0.121	
TC19	**173**	45	2	13.812	8.308		133.258		1.224		0.117		0.064	
TC19	**165**	45	3	13.989		11.561		629.538		1.208		1.292		0.104
TC19	**147**	35	1	14.407		12.376		261.358		1.258		0.270		0.173
TC19	**142**	55	3	14.488	12.052		1358.100		1.257		1.287		0.238	
TC19	**126**	55	2	14.778	9.012		181.789		1.222		0.153		0.104	
TC19	**124**	35	1	14.822	10.751		269.267		1.237		0.247		0.145	
TC19	**117**	45	3	14.983	10.718		296.092		1.198		0.768		0.143	
TC19	**108**	45	3	15.190	9.906		714.746		1.169		1.238		0.128	
TC19	**104**	55	1	15.282	10.035		171.927		1.146		0.736		0.133	
TC19	**099**	45	2	15.392	11.288		925.413		1.203		0.783		0.064	
TC19	**092**	45	3	15.517	9.513		411.712		1.201		1.025		0.095	
TC19	**085**	45	3	15.641	9.408		283.679		1.185		1.164		0.117	
TC19	**078**	105	1	15.796	10.321		205.186		1.160		0.362		0.131	
TC19	**078**	35	2	15.796	8.260		108.299		1.192		0.082		0.082	
TC19	**072**	35	3	15.951	9.673		296.848		1.178		1.317		0.126	
TC19	**069**	35	3	16.024	8.533		144.987		1.190		1.295		0.118	
TC19	**060**	105	1	16.265	9.770		325.371		1.178		0.474		0.131	
TC19	**060**	45	2	16.265	9.016		289.809		1.164		0.207		0.095	
TC19	**042**	55	1	16.728	9.432		284.532		1.176		0.298		0.170	
TC19	**034**	25	1	16.946	10.097		174.168		1.164		0.566		0.145	

8.7 Trace element data for planktic foraminifera samples

Sample ID		Acid for digestion (µl)	Run No.	Age [Ma]	Ba138 (µmol/mol)	Ba138 (µmol/mol) (EXCLUDED)	U238 (nmol/mol)	U238 (nmol/mol) (EXCLUDED)	K39_39_H2 (µmol/mol)	K39_39_H2 (µmol/mol) (EXCLUDED)	Mn55_55_H2 (µmol/mol)	Mn55_55_H2 (µmol/mol) (EXCLUDED)	Fe56_56_H2 (µmol/mol)	Fe56_56_H2 (µmol/mol) (EXCLUDED)
TC21	456	35	2	5.820	13.707		17.730		79.506		359.444		84.327	
TC21	428	35	4	5.946	13.088		47.867		32.349		303.074		27.161	
TC21	419	25	4	6.003	12.439		115.109		28.991		358.983		16.180	
TC21	418	45	1	6.009	13.962		213.183		40.080		318.586		107.137	
TC21	408	35	2	6.072	12.007		9.863		166.374		256.704		27.130	
TC21	395	25	4	6.161		28.647		134.347		76.389		7465.372		634.173
TC21	378	25	4	6.253	13.434		98.181		32.509		382.778		37.381	
TC21	364	45	1	6.353		10.608		34.432		43.785		1021.295		137.074
TC21	364	45	2	6.353		9.278		32.018		129.636		549.639		135.705
TC21	345	25	4	6.466	10.706		14.336		33.132		1077.833		64.007	
TC21	330	45	4	6.572		20.326		116.402		91.190		7951.897		2764.637
TC21	311	135	1	6.692		21.340		243.595		108.722		8624.893		3023.758
TC21	310	25	4	6.699		10.199		60.927		37.676		610.741		222.528
TC21	290	35	2	7.131	8.862		89.061		48.273		779.422		273.645	
TC21	273	25	4	7.523	8.088		38.602		32.563		497.012		189.014	
TC21	263	35	1	7.783		8.201		603.876		52.325		199.595		487.355
TC21	258	25	4	7.897	6.656		33.797		27.094		347.839		118.628	
TC21	243A	45	2	8.201		18.887		140.033		71.116		3684.615		2848.456
TC21	243B	55	2	8.201	22.254		186.495		257.979			4600.837		3971.278
TC21	229	25	4	8.534	8.811		33.935		41.857		801.880		156.100	
TC21	218	105	4	8.788	12.106		17.713		42.919			3926.302	928.027	
TC21	216	25	1	8.827		10.520		19.860		39.356		4023.507		246.988
TC21	168	25	4	9.002	1.367		137.303		40.708		46.705		105.540	
TC21	203	35	2	9.078	8.997		24.352		91.184		720.603		429.641	
TC21	163	55	1	9.165	1.624		330.772		102.789		269.506		407.259	
TC21	162	35	4	9.197	1.512		183.445		39.649		126.838		187.217	
TC21	158	35	2	9.360	1.685		208.490		77.986		270.556		514.577	
TC21	154	35	4	9.492	2.255		221.530		71.276		281.484		509.060	
TC21	150	25	4	9.623	2.483		137.655		41.175		136.032		235.239	
TC21	142	55	1	9.859	3.759		240.880		99.626		300.672		616.746	
TC21	135	45	4	10.028	3.192		218.890		461.977		292.032		607.965	
TC21	128	25	4	10.185	1.922		196.701		54.585		302.696		540.886	

8.7 Trace element data for planktic foraminifera samples

Sample ID		Acid for digestion (µl)	Run No.	Age [Ma]	Ba138 (µmol/mol)	Ba138 (µmol/mol) (EXCLUDED)	U238 (nmol/mol)	U238 (nmol/mol) (EXCLUDED)	K39_39_H2 (µmol/mol)	K39_39_H2 (µmol/mol) (EXCLUDED)	Mn55_55_H2 (µmol/mol)	Mn55_55_H2 (µmol/mol) (EXCLUDED)	Fe56_56_H2 (µmol/mol)	Fe56_56_H2 (µmol/mol) (EXCLUDED)
TC21	**121**	25	1	10.327	1.764		280.955		90.779		350.406		933.479	
TC21	**120**	25	4	10.347	2.282		160.219		80.719		303.278		633.705	
TC21	**112**	35	2	10.509		8.361		91.535		30.235		707.419		177.891
TC21	**107**	25	4	10.611	2.458		163.624		51.256		519.889		643.598	
TC21	**104**	55	4	10.672	4.845		178.406		47.391		498.781		497.679	
TC21	**100**	25	4	10.746	2.290		120.698		57.737		322.531		395.989	
TC21	**096**	55	1	10.812	3.873		398.244		83.264		311.663		630.733	
TC21	**096A**	45	2	10.812		2.339		319.519		245.769		268.029		534.795
TC21	**096B**	35	2	10.812	3.413		443.818		143.451		360.859		682.392	
TC21	**088**	35	4	10.946	1.892		247.527		54.748		359.318		400.586	
TC21	**080**	25	4	11.080	1.835		156.856		43.345		372.679		369.132	
TC21	**073**	25	4	11.189	1.359		190.590		40.853		199.519		265.016	
TC21	**072**	35	1	11.203	1.552		317.572		134.216		355.030		731.554	
TC21	**064**	35	3	11.317	1.634		244.527		87.729		252.404		353.079	
TC21	**061**	45	3	11.359		2.013		424.606		306.014		481.718		1191.739
TC21	**057**	35	3	11.416	1.390		223.296		67.140		320.212		508.681	
TC21	**053**	35	3	11.473	1.347		212.348		52.632		280.841		480.380	
TC21	**049**	95	1	11.529	1.773		332.452		110.981		496.862		712.416	
TC21	**049**	45	2	11.529	1.437		263.433		595.710		409.637		730.734	
TC21	**035**	35	3	11.680	1.454		241.068		108.416		436.474		596.433	
TC21	**024**	35	2	11.902	1.427		104.092		749.017		828.677		529.783	
TC21	**022**	35	1	11.946	1.503		136.089		66.722		933.126		620.707	
TC21	**016**	45	3	12.079	1.681		126.490		91.775		841.352		621.467	
TC21	**07**	35	3	12.278	2.153		163.692		313.588		843.483		1286.006	
TC19	**242**	35	3	12.455	2.506		215.845		180.768		563.531		841.877	
TC19	**237**	25	1	12.566	2.304		371.921		90.706		508.434		671.697	
TC19	**233**	45	2	12.655	2.196		290.807		498.167		508.073		790.601	
TC19	**230**	25	3	12.721	2.588		299.116		175.982		415.221		962.253	
TC19	**226**	35	3	12.810	2.232		268.400		156.482		450.347		1032.632	
TC19	**220**	35	3	12.943	1.669		119.483		61.934		333.932		671.385	
TC19	**218**	105	1	12.987		11.226		176.892		129.377		473.826		1155.046
TC19	**218A**	55	2	12.987		1.494		112.346		255.433		328.263		816.276

8.7 Trace element data for planktic foraminifera samples

Sample ID		Acid for digestion (µl)	Run No.	Age [Ma]	Ba138 (µmol/mol)	Ba138 (µmol/mol) (EXCLUDED)	U238 (nmol/mol)	U238 (nmol/mol) (EXCLUDED)	K39_39_H2 (µmol/mol)	K39_39_H2 (µmol/mol) (EXCLUDED)	Mn55_55_H2 (µmol/mol)	Mn55_55_H2 (µmol/mol) (EXCLUDED)	Fe56_56_H2 (µmol/mol)	Fe56_56_H2 (µmol/mol) (EXCLUDED)
TC19	**218B**	45	2	12.987	1.760		142.887		385.141		366.932		1139.545	
TC19	**212**	45	3	13.120	1.642		158.367		123.579		503.125		1046.863	
TC19	**205**	45	3	13.244	1.907		202.568		147.922		327.002		714.523	
TC19	**198**	25	3	13.355	2.026		172.620		143.724		408.965		969.464	
TC19	**195**	35	1	13.403		8.636		382.469		69.088		114.074		333.116
TC19	**191**	45	2	13.466	1.729		176.930		239.461		463.855		1012.823	
TC19	**187**	45	3	13.530	2.030		157.915		215.416		662.691		1553.887	
TC19	**182**	35	3	13.631	2.342		76.251		101.377		510.813		678.013	
TC19	**178**	45	3	13.712	2.915		90.812		114.052		615.195		1077.130	
TC19	**173**	75	1	13.812	2.742		138.286		112.997		531.910		1111.482	
TC19	**173**	45	2	13.812	1.545		97.846		777.801		398.983		779.917	
TC19	**165**	45	3	13.989		18.162		110.439		148.168		586.184		1261.780
TC19	**147**	35	1	14.407		1.842		93.835		138.117		750.738		1058.298
TC19	**142**	55	3	14.488	2.154		104.548		238.089		686.112		1312.536	
TC19	**126**	55	2	14.778	1.787		26.947		155.278		668.377		650.555	
TC19	**124**	35	1	14.822	1.788		32.705		94.779		890.756		828.808	
TC19	**117**	45	3	14.983	2.036		32.520		83.857		957.490		749.066	
TC19	**108**	45	3	15.190	2.117		43.525		170.651		801.539		800.705	
TC19	**104**	55	1	15.282	2.173		46.138		87.069		959.001		678.604	
TC19	**099**	45	2	15.392	1.850		35.924		298.160		793.918		1150.216	
TC19	**092**	45	3	15.517	1.632		37.625		98.771		684.391		708.848	
TC19	**085**	45	3	15.641	1.303		29.547		80.462		767.824		584.449	
TC19	**078**	105	1	15.796	1.378		41.585		85.236		1191.684		808.770	
TC19	**078**	35	2	15.796	1.272		27.811		130.230		924.956		544.899	
TC19	**072**	35	3	15.951	1.274		36.052		89.116		984.391		642.151	
TC19	**069**	35	3	16.024	1.079		37.386		60.764		809.765		521.185	
TC19	**060**	105	1	16.265	1.656		61.745		101.518		990.762		803.887	
TC19	**060**	45	2	16.265	1.936		42.325		109.547		856.494		674.151	
TC19	**042**	55	1	16.728	1.567		67.368		99.752		693.098		768.021	
TC19	**034**	25	1	16.946	3.783		75.799		71.605		1792.005		680.572	

8.7 Trace element data for planktic foraminifera samples

Sample ID		Acid for digestion (µl)	Run No.	Age [Ma]	Ni58_58_H2 (µmol/mol)	Ni58_58_H2 (µmol/mol) (EXCLUDED)	Cu63_63_H2 (µmol/mol)	Cu63_63_H2 (µmol/mol) (EXCLUDED)	Zn64_64_H2 (µmol/mol)	Zn64_64_H2 (µmol/mol) (EXCLUDED)	Rb85_85_H2 (µmol/mol)	Rb85_85_H2 (µmol/mol) (EXCLUDED)	P31_47_O2 (µmol/mol)	P31_47_O2 (µmol/mol) (EXCLUDED)
TC21	**456**	35	2	5.820	1.666		0.334		82.827		0.066		70.469	
TC21	**428**	35	4	5.946	0.607		0.460		3.227		0.013		69.254	
TC21	**419**	25	4	6.003	0.537		0.857		4.483		0.012		78.055	
TC21	**418**	45	1	6.009		119.465		159.108	29.893		0.026		87.957	
TC21	**408**	35	2	6.072	1.443		0.246			135.452	0.046		64.637	
TC21	**395**	25	4	6.161		6.296		1.845		5.458		0.175		174.154
TC21	**378**	25	4	6.253	0.874		0.615		4.018		0.007		75.125	
TC21	**364**	45	1	6.353		2.279		2.266		4.716		0.014		97.501
TC21	**364**	45	2	6.353		1.863		0.353		10.685		0.028		92.349
TC21	**345**	25	4	6.466	0.675		0.784		4.561		0.007		94.212	
TC21	**330**	45	4	6.572		21.804		3.663		8.267		0.228		175.853
TC21	**311**	135	1	6.692		13.189		7.819		23.708		0.204		180.866
TC21	**310**	25	4	6.699		2.435		0.860		6.281		0.030		86.643
TC21	**290**	35	2	7.131	2.427		0.240		4.513		0.057		114.144	
TC21	**273**	25	4	7.523	1.543		0.529		4.177		0.007		94.286	
TC21	**263**	35	1	7.783		7.241		34.086		30.449		0.078		137.838
TC21	**258**	25	4	7.897	1.113		0.623		5.749		0.012		83.866	
TC21	**243A**	45	2	8.201		11.706		0.747		28.750		0.119		160.435
TC21	**243B**	55	2	8.201	16.655		4.040			132.735	0.389		219.364	
TC21	**229**	25	4	8.534	1.594		0.583		5.682		0.011		98.138	
TC21	**218**	105	4	8.788	8.837		2.128		6.530		0.055		116.882	
TC21	**216**	25	1	8.827		3.366		37.663		42.853		0.041		130.273
TC21	**168**	25	4	9.002	1.282		1.249		4.666		0.023		86.323	
TC21	**203**	35	2	9.078	3.329		1.332		9.878		0.170		124.802	
TC21	**163**	55	1	9.165	3.945		4.091		9.030		0.264		239.818	
TC21	**162**	35	4	9.197	1.820		1.088		4.541		0.040		122.588	
TC21	**158**	35	2	9.360	3.682		0.681		6.378		0.123		191.283	
TC21	**154**	35	4	9.492	4.626		1.670		6.548		0.080		199.204	
TC21	**150**	25	4	9.623	2.389		1.264		4.006		0.021		119.789	
TC21	**142**	55	1	9.859	4.831		10.496		19.977		0.216		302.129	
TC21	**135**	45	4	10.028	4.243		1.188			380.805	0.388		217.135	
TC21	**128**	25	4	10.185	4.887		1.919		5.771		0.075		201.959	

8.7 Trace element data for planktic foraminifera samples

Sample ID		Acid for digestion (µl)	Run No.	Age [Ma]	Ni58_58_H2 (µmol/mol)	Ni58_58_H2 (µmol/mol) (EXCLUDED)	Cu63_63_H2 (µmol/mol)	Cu63_63_H2 (µmol/mol) (EXCLUDED)	Zn64_64_H2 (µmol/mol)	Zn64_64_H2 (µmol/mol) (EXCLUDED)	Rb85_85_H2 (µmol/mol)	Rb85_85_H2 (µmol/mol) (EXCLUDED)	P31_47_O2 (µmol/mol)	P31_47_O2 (µmol/mol) (EXCLUDED)
TC21	**121**	25	1	10.327	5.535		1.821		7.248		0.213		271.018	
TC21	**120**	25	4	10.347	5.708		2.105		6.276		0.165		203.395	
TC21	**112**	35	2	10.509		1.970		0.221		4.258		0.017		99.245
TC21	**107**	25	4	10.611	6.220		1.645		6.820		0.098		176.649	
TC21	**104**	55	4	10.672	4.184		1.511		5.282		0.058		163.362	
TC21	**100**	25	4	10.746	3.456		1.738		7.939		0.070		131.203	
TC21	**096**	55	1	10.812	4.620		4.779		9.469		0.196		187.503	
TC21	**096A**	45	2	10.812		4.025		1.362		143.674		0.223		148.157
TC21	**096B**	35	2	10.812	5.068		5.478		59.427		0.315		228.944	
TC21	**088**	35	4	10.946	3.654		1.666		5.510		0.096		184.759	
TC21	**080**	25	4	11.080	3.234		1.909		4.862		0.055		131.989	
TC21	**073**	25	4	11.189	2.702		1.326		4.609		0.034		115.263	
TC21	**072**	35	1	11.203	5.421		11.579		18.698		0.371		268.003	
TC21	**064**	35	3	11.317	2.885		0.860		43.531		0.053		158.796	
TC21	**061**	45	3	11.359		19.554		4.866		13.460		0.737		495.429
TC21	**057**	35	3	11.416	5.428			36.791	19.738		0.100		113.790	
TC21	**053**	35	3	11.473	4.607		1.057		4.218		0.051		106.921	
TC21	**049**	95	1	11.529	4.894		8.398		15.303		0.250		226.257	
TC21	**049**	45	2	11.529	4.965		1.145			532.012	0.497		190.817	
TC21	**035**	35	3	11.680	8.152		1.533		5.809		0.216		252.121	
TC21	**024**	35	2	11.902	3.570		1.465			528.294	0.180		184.212	
TC21	**022**	35	1	11.946	4.394		3.528		8.143		0.152		225.676	
TC21	**016**	45	3	12.079	7.085		3.852		5.058		0.203		170.401	
TC21	**07**	35	3	12.278	21.225		16.818		15.000		0.896		270.664	
TC19	**242**	35	3	12.455	12.072		3.714		7.165		0.423		203.867	
TC19	**237**	25	1	12.566	4.489		3.287		7.006		0.206		221.765	
TC19	**233**	45	2	12.655	4.931		1.278		94.899		0.477		170.115	
TC19	**230**	25	3	12.721	16.165		6.293		8.786		0.437		196.236	
TC19	**226**	35	3	12.810	14.201		4.075		8.685		0.385		214.190	
TC19	**220**	35	3	12.943	6.440		1.327		2.969		0.086		137.454	
TC19	**218**	105	1	12.987		6.642		12.125		26.630		0.331		237.216
TC19	**218A**	55	2	12.987		4.794		0.887		159.532		0.302		177.381

8.7 Trace element data for planktic foraminifera samples

Sample ID		Acid for digestion (µl)	Run No.	Age [Ma]	Ni58_58_H2 (µmol/mol)	Ni58_58_H2 (µmol/mol) (EXCLUDED)	Cu63_63_H2 (µmol/mol)	Cu63_63_H2 (µmol/mol) (EXCLUDED)	Zn64_64_H2 (µmol/mol)	Zn64_64_H2 (µmol/mol) (EXCLUDED)	Rb85_85_H2 (µmol/mol)	Rb85_85_H2 (µmol/mol) (EXCLUDED)	P31_47_O2 (µmol/mol)	P31_47_O2 (µmol/mol) (EXCLUDED)
TC19	**218B**	45	2	12.987	6.858		5.491		93.150		0.690		210.960	
TC19	**212**	45	3	13.120	12.182		2.838		6.473		0.266		150.822	
TC19	**205**	45	3	13.244	8.092		2.757		9.737		0.161		137.656	
TC19	**198**	25	3	13.355	12.707		3.603		9.671		0.344		172.952	
TC19	**195**	35	1	13.403		4.159		10.022		10.556		0.132		77.819
TC19	**191**	45	2	13.466	6.218		1.412		75.384		0.453		169.050	
TC19	**187**	45	3	13.530	21.090		8.594		14.297		0.559		211.458	
TC19	**182**	35	3	13.631	7.550		2.366		13.055		0.184		126.406	
TC19	**178**	45	3	13.712	12.182		3.036		6.606		0.233		157.082	
TC19	**173**	75	1	13.812	6.808		9.609		21.261		0.282		210.042	
TC19	**173**	45	2	13.812	4.644		1.537			397.910	0.148		122.166	
TC19	**165**	45	3	13.989		15.183		3.877		8.940		0.338		173.078
TC19	**147**	35	1	14.407		7.366		2.954		17.267		0.249		232.048
TC19	**142**	55	3	14.488	23.052		8.497		13.862		0.583		233.063	
TC19	**126**	55	2	14.778	4.263		2.390		82.995		0.138		165.455	
TC19	**124**	35	1	14.822	5.857		2.793		9.528		0.216		208.224	
TC19	**117**	45	3	14.983	8.030		3.206		5.733		0.144		161.584	
TC19	**108**	45	3	15.190	10.689		4.220		9.791		0.404		192.325	
TC19	**104**	55	1	15.282	4.586		3.096		8.508		0.175		213.999	
TC19	**099**	45	2	15.392	7.190		2.330		7.677		0.646		200.891	
TC19	**092**	45	3	15.517	8.161		2.773		5.838		0.190		161.239	
TC19	**085**	45	3	15.641	6.189		3.128		6.236		0.129		178.306	
TC19	**078**	105	1	15.796	5.012		7.614		15.039		0.182		179.079	
TC19	**078**	35	2	15.796	3.659		2.471		24.925		0.117		136.299	
TC19	**072**	35	3	15.951	6.817		3.984		7.966		0.161		172.014	
TC19	**069**	35	3	16.024	5.011		2.614		4.643		0.070		155.081	
TC19	**060**	105	1	16.265	5.352		6.003		14.059		0.257		214.735	
TC19	**060**	45	2	16.265	4.285		2.027		15.945		0.251		173.318	
TC19	**042**	55	1	16.728	4.890		4.123		10.461		0.258		192.701	
TC19	**034**	25	1	16.946	5.134		2.236		6.429		0.163		190.744	

8.7 Trace element data for planktic foraminifera samples

Sample ID		Acid for digestion (µl)	Run No.	Age [Ma]	S32_48_O2 (mmol/mol)	S32_48_O2 (mmol/mol) (EXCLUDED)	Co59_75_O2 (µmol/mol)	Co59_75_O2 (µmol/mol) (EXCLUDED)	Nd146_162_O2 (µmol/mol)	Nd146_162_O2 (µmol/mol) (EXCLUDED)
TC21	**456**	35	2	5.820	1.739		0.336		0.213	
TC21	**428**	35	4	5.946	1.641		0.732		0.510	
TC21	**419**	25	4	6.003	1.125		0.651		0.709	
TC21	**418**	45	1	6.009	1.449		0.396			
TC21	**408**	35	2	6.072	1.616		0.261		0.291	
TC21	**395**	25	4	6.161		1.161		0.789		2.285
TC21	**378**	25	4	6.253	1.141		0.662		0.366	
TC21	**364**	45	1	6.353		1.499		0.174		
TC21	**364**	45	2	6.353		1.439		0.410		0.933
TC21	**345**	25	4	6.466	1.561		0.602		1.215	
TC21	**330**	45	4	6.572		0.463		0.659		4.940
TC21	**311**	135	1	6.692		0.724		1.178		
TC21	**310**	25	4	6.699		1.086		0.900		1.356
TC21	**290**	35	2	7.131	1.042		0.325		0.865	
TC21	**273**	25	4	7.523	1.300		0.533		1.005	
TC21	**263**	35	1	7.783		14.714		3.719		
TC21	**258**	25	4	7.897	1.104		0.653		0.692	
TC21	**243A**	45	2	8.201		0.552		0.348		4.173
TC21	**243B**	55	2	8.201	0.566		0.885			5.014
TC21	**229**	25	4	8.534	1.426		0.643		0.904	
TC21	**218**	105	4	8.788	1.158		0.744		2.025	
TC21	**216**	25	1	8.827		0.896		0.430		
TC21	**168**	25	4	9.002	1.403		0.653		0.696	
TC21	**203**	35	2	9.078	0.937		0.252		1.964	
TC21	**163**	55	1	9.165	1.285		2.906			
TC21	**162**	35	4	9.197	1.255		0.729		0.872	
TC21	**158**	35	2	9.360	1.314		0.205		0.808	
TC21	**154**	35	4	9.492	1.328		0.638		1.160	
TC21	**150**	25	4	9.623	1.398		0.693		0.575	
TC21	**142**	55	1	9.859	1.361		1.839			
TC21	**135**	45	4	10.028	1.276		0.497		1.034	
TC21	**128**	25	4	10.185	1.321		0.676		1.214	

8.7 Trace element data for planktic foraminifera samples

Sample ID		Acid for digestion (µl)	Run No.	Age [Ma]	S32_48_O2 (mmol/mol)	S32_48_O2 (mmol/mol) (EXCLUDED)	Co59_75_O2 (µmol/mol)	Co59_75_O2 (µmol/mol) (EXCLUDED)	Nd146_162_O2 (µmol/mol)	Nd146_162_O2 (µmol/mol) (EXCLUDED)
TC21	**121**	25	1	10.327	1.327		4.248			
TC21	**120**	25	4	10.347	1.349		0.755		1.398	
TC21	**112**	35	2	10.509		1.025		0.298		0.815
TC21	**107**	25	4	10.611	1.222		0.696		1.128	
TC21	**104**	55	4	10.672	1.181		0.637		1.416	
TC21	**100**	25	4	10.746	1.259		0.648		1.001	
TC21	**096**	55	1	10.812	1.255		0.453			
TC21	**096A**	45	2	10.812		1.305		0.642		0.869
TC21	**096B**	35	2	10.812	1.375		1.505		1.352	
TC21	**088**	35	4	10.946	1.189		0.700		1.344	
TC21	**080**	25	4	11.080	1.216		0.613		1.345	
TC21	**073**	25	4	11.189	1.186		0.586		0.577	
TC21	**072**	35	1	11.203	1.192		0.228			
TC21	**064**	35	3	11.317	1.176		0.578		0.714	
TC21	**061**	45	3	11.359		1.145		1.272		1.143
TC21	**057**	35	3	11.416	1.133		0.598		0.837	
TC21	**053**	35	3	11.473	1.164		0.362		0.823	
TC21	**049**	95	1	11.529	1.138		0.358			
TC21	**049**	45	2	11.529	1.198		0.863		0.874	
TC21	**035**	35	3	11.680	1.184		0.610		1.161	
TC21	**024**	35	2	11.902	1.528		0.517		1.933	
TC21	**022**	35	1	11.946	1.282		1.227			
TC21	**016**	45	3	12.079	1.137		1.057		1.719	
TC21	**07**	35	3	12.278	1.067		1.367		2.056	
TC19	**242**	35	3	12.455	1.127		1.942		1.687	
TC19	**237**	25	1	12.566	1.417		0.331			
TC19	**233**	45	2	12.655	1.416		0.541		1.285	
TC19	**230**	25	3	12.721	1.367		1.760		1.649	
TC19	**226**	35	3	12.810	1.328		0.734		1.606	
TC19	**220**	35	3	12.943	1.305		0.438		1.295	
TC19	**218**	105	1	12.987		1.395		0.231		
TC19	**218A**	55	2	12.987		1.405		0.669		1.241

8.7 Trace element data for planktic foraminifera samples

Sample ID		Acid for digestion (µl)	Run No.	Age [Ma]	S32_48_O2 (mmol/mol)	S32_48_O2 (mmol/mol) (EXCLUDED)	Co59_75_O2 (µmol/mol)	Co59_75_O2 (µmol/mol) (EXCLUDED)	Nd146_162_O2 (µmol/mol)	Nd146_162_O2 (µmol/mol) (EXCLUDED)
TC19	**218B**	45	2	12.987	1.375		0.732		1.434	
TC19	**212**	45	3	13.120	1.300		0.622		1.001	
TC19	**205**	45	3	13.244	1.274		0.682		0.874	
TC19	**198**	25	3	13.355	1.294		0.600		1.113	
TC19	**195**	35	1	13.403		1.140		-1.037		
TC19	**191**	45	2	13.466	1.336		0.960		1.243	
TC19	**187**	45	3	13.530	1.166		1.184		1.753	
TC19	**182**	35	3	13.631	1.236		0.736		1.102	
TC19	**178**	45	3	13.712	1.273		0.768		1.278	
TC19	**173**	75	1	13.812	1.344		0.834			
TC19	**173**	45	2	13.812	1.465		0.436		1.034	
TC19	**165**	45	3	13.989		1.232		1.929		1.472
TC19	**147**	35	1	14.407		1.171		3.072		
TC19	**142**	55	3	14.488	1.271		3.715		1.337	
TC19	**126**	55	2	14.778	1.201		0.604		1.812	
TC19	**124**	35	1	14.822	1.238		1.610			
TC19	**117**	45	3	14.983	1.276		0.803		1.653	
TC19	**108**	45	3	15.190	1.220		1.087		1.914	
TC19	**104**	55	1	15.282	1.332		0.768			
TC19	**099**	45	2	15.392	1.309		0.900		1.557	
TC19	**092**	45	3	15.517	1.278		0.826		1.564	
TC19	**085**	45	3	15.641	1.267		0.889		1.590	
TC19	**078**	105	1	15.796	1.362		0.890			
TC19	**078**	35	2	15.796	1.401		0.344		1.482	
TC19	**072**	35	3	15.951	1.363		0.910		1.638	
TC19	**069**	35	3	16.024	1.325		0.754		1.585	
TC19	**060**	105	1	16.265	1.310		1.078			
TC19	**060**	45	2	16.265	1.265		0.647		1.902	
TC19	**042**	55	1	16.728	1.192		0.465			
TC19	**034**	25	1	16.946	1.206		0.747			

8.8 All measurements of the NITS RM 8301F standard during analysis used in this research

This table shows all measurements of the NITS RM 8301F standard (Stewart *et al.*, 2021) during the trace element analysis of planktic foraminifera samples, as described in Chapter 2.6. Interlab mean values from Stewart *et al.* (2021) are shown, together with mean values from the St Andrews Isotope Geochemistry lab where analysis took place.

8.8 All measurements of the NITS RM 8301F standard during analysis used in this research

Run No	Li7	B11	Na23	Mg24	Mg25	Mg26	Al27	Sr88	Mo92	Cd111	Ba138	U238	K39_39_H2	Mn55_55_H2	Fe56_56_H2	Ni58_58_H2
	µmol/mol	µmol/mol	mmol/mol	mmol/mol	mmol/mol	mmol/mol	µmol/mol	mmol/mol	µmol/mol	µmol/mol	µmol/mol	nmol/mol	µmol/mol	µmol/mol	µmol/mol	µmol/mol
1	9.841	151.302	3.025	2.638	2.676	2.671	101.282	1.358	0.065	0.619	3.978	70.707	-1.131	52.193	26.228	5.214
1	9.443	146.535	2.992	2.619	2.626	2.632	98.984	1.339	0.061	0.600	3.945	66.827	-1.126	52.427	25.876	5.251
1	9.281	146.202	2.993	2.615	2.634	2.628	98.599	1.333	0.062	0.630	3.947	67.522	-1.090	52.360	25.962	5.249
1	9.494	144.434	2.989	2.611	2.629	2.627	98.854	1.351	0.066	0.592	3.965	68.395	-1.106	52.774	28.021	5.330
2	9.505	147.103	3.008	2.610	2.619	2.633	100.124	1.336	0.073	0.572	3.930	67.338	-0.450	50.627	26.055	4.818
2	9.468	144.874	2.997	2.598	2.588	2.606	98.101	1.338	0.071	0.607	3.950	66.885	-0.528	50.869	26.072	4.803
2	9.482	147.266	3.010	2.639	2.627	2.643	98.850	1.339	0.073	0.591	3.978	70.475	-0.601	50.228	25.720	4.810
2	9.336	146.061	3.007	2.611	2.625	2.627	98.736	1.342	0.074	0.599	3.980	68.623	-0.556	50.402	26.164	4.855
3	9.121	143.927	2.990	2.617	2.634	2.620	100.772	1.339	0.083	0.561	4.010	66.907	1.764	50.450	23.443	6.131
3	9.371	145.893	2.974	2.598	2.629	2.626	101.321	1.337	0.083	0.647	4.005	66.562	1.713	50.064	23.302	6.130
3	9.345	147.035	3.017	2.621	2.636	2.644	101.401	1.341	0.089	0.594	4.039	70.496	1.759	50.717	23.631	6.173
3	9.216	143.069	2.957	2.588	2.609	2.616	100.176	1.340	0.087	0.599	4.003	66.331	1.923	50.469	23.558	6.265
4	9.182	143.380	2.962	2.605	2.613	2.602	100.831	1.325	0.092	0.586	4.008	67.639	1.134	50.826	23.944	6.256
4	9.181	142.377	2.935	2.592	2.621	2.618	100.958	1.343	0.094	0.610	4.009	66.648	1.126	50.931	24.194	6.357
4	9.120	140.695	2.947	2.586	2.602	2.604	100.896	1.336	0.086	0.589	4.021	67.296	1.164	50.678	23.876	6.197
4	9.274	143.135	2.954	2.594	2.592	2.601	100.347	1.325	0.087	0.622	4.029	66.671	1.112	51.195	23.961	6.219
Mean (TC)	9.354	145.206	2.987	2.609	2.622	2.625	98.960	1.339	0.078	0.600	3.971	67.912	0.319	50.880	25.000	5.629
Mean (StAiG)	9.450	144.500	3.010	2.630	2.550		95.000	1.331	3.890	0.605	3.890	69.000		49.100		
Mean (Inter lab)	9.000	139.000	3.050	2.630	2.620		91.000	1.340	3.900	0.580	3.910	68.000		50.200		
STDEV	0.186	2.519	0.027	0.016	0.020	0.018	1.136	0.008	0.011	0.021	0.033	1.491	1.224	0.864	1.410	0.630
RSTDEV	1.986	1.735	0.901	0.617	0.776	0.693	1.148	0.608	14.175	3.572	0.832	2.195	383.480	1.698	5.641	11.195

8.8 All measurements of the NITS RM 8301F standard during analysis used in this research

Run No	Cu63_63_H2	Zn64_64_H2	Rb85_85_H2	P31_47_O2	S32_48_O2	Co59_75_O2	Nd146_162_O2
	µmol/mol	µmol/mol	µmol/mol	µmol/mol	mmol/mol	µmol/mol	µmol/mol
1	5.782	9.299	0.071	31.521	0.048	0.667	
1	5.739	9.334	0.078	32.098	0.048	0.691	
1	5.900	9.417	0.077	31.316	0.047	0.698	
1	5.810	9.594	0.078	31.765	0.048	0.792	
2	5.849	9.792	0.078	32.289	0.049	0.881	5.407
2	5.819	9.660	0.078	31.439	0.050	0.686	4.944
2	5.690	9.732	0.076	32.083	0.051	0.792	5.222
2	5.840	9.765	0.078	31.832	0.050	0.738	5.229
3	5.389	8.278	0.084	28.882	0.093	0.897	5.079
3	5.478	8.276	0.085	31.030	0.091	0.759	5.005
3	5.401	8.133	0.080	30.607	0.093	0.779	4.835
3	5.368	8.307	0.083	31.596	0.093	0.877	5.071
4	5.257	8.931	0.081	30.307	0.093	0.909	5.100
4	5.395	9.045	0.080	31.109	0.095	1.014	5.101
4	5.393	8.959	0.085	30.152	0.092	0.969	5.057
4	5.456	9.118	0.081	30.446	0.092	0.935	5.376
Mean (TC)	5.598	9.102	0.080	31.155	0.071	0.818	5.119
Mean (StAiG)							
Mean (Inter lab)							
STDEV	0.222	0.580	0.004	0.895	0.023	0.110	0.166
RSTDEV	3.966	6.370	4.480	2.873	32.128	13.404	3.248

8.9 **Temperatures calculated from Mg/Ca and $\delta^{18}O_{planktic}$ data**

This table shows the temperatures calculated using both Mg/Ca and $\delta^{18}O_{planktic}$ data (see Chapter 4.1). $\delta^{18}O_{planktic}$ data was collected using the method outlined in Chapter 2.5.2, temperatures were calculated using the method outlined in Chapter 4.1. Temperatures using $\delta^{18}O_{planktic}$ data are shown calculated using a latitude based estimation of $\delta^{18}O_{seawater}$ (Zachos *et al.*, 1994) and a local estimation of $\delta^{18}O_{seawater}$ as discussed in Chapter 4.1. Mg/Ca data was collected using the method outlined in Chapter 2.6 and temperatures were calculated using the method outlined in Chapter 4.1.

8.9 Temperatures calculated from Mg/Ca and δ18Oplanktic data

Sample ID	Age (Ma)	Temperature (°C) based on $\delta^{18}O$ (Bemis *et al.,* 1998) - Latitude based $\delta^{18}O$ seawater estimate (Zachos *et al.,* 1994)	Temperature based on Mg/Ca (Gray & Evans, 2019)	Temperature (°C) based on $\delta^{18}O$ (Bemis et al., 1998) - Local $\delta^{18}O$ seawater estimate using Mg/Ca data
TC19 248	17.075	21.180		23.935
TC19 247	17.050	21.861		24.616
TC19 245	17.000	20.104		22.858
TC19 33	16.973	16.914		19.668
TC19 34	16.946	20.865	23.620	23.620
TC19 35	16.918	17.305		20.248
TC19 36	16.891	20.543		23.676
TC19 37	16.864	20.199		23.521
TC19 38	16.837	20.215		23.727
TC19 39	16.810	18.817		22.518
TC19 40	16.782	17.743		21.633
TC19 41	16.755	18.426		22.506
TC19 42	16.728	19.773	22.695	24.042
TC19 43	16.701	19.822		24.065
TC19 44	16.674	19.216		23.433
TC19 45	16.657	19.853		24.054
TC19 46	16.646	18.605		22.795
TC19 47	16.619	17.516		21.680
TC19 48	16.592	20.612		24.749
TC19 49	16.565	19.881		23.992
TC19 50	16.537	18.098		22.182
TC19 51	16.510	20.864		24.922
TC19 52	16.483	20.257		24.289
TC19 53	16.456	18.510		22.515
TC19 54	16.429	16.458		20.437
TC19 56	16.374	18.987		22.913
TC19 57	16.347	18.884		22.784
TC19 58	16.320	18.452		22.325
TC19 59	16.293	18.549		22.396
TC19 60	16.265	19.998	22.369	23.818
TC19 61	16.238	20.214		23.883
TC19 62	16.211	18.692		22.209
TC19 63	16.184	18.858		22.224
TC19 64	16.157	18.313		21.527
TC19 65	16.129	19.317		22.380
TC19 66	16.102	19.827		22.738
TC19 67	16.075	18.579		21.339
TC19 68	16.048	18.795		21.403
TC19 69	16.024	20.405	21.268	22.878
TC19 70	15.999	17.957		20.599
TC19 71	15.975	19.939		22.749
TC19 72	15.951	18.326	22.918	21.305
TC19 73	15.926	18.430		21.693
TC19 74	15.902	18.885		22.432
TC19 75	15.878	18.799		22.629
TC19 76	15.854	18.909		23.023
TC19 77	15.829	19.131		23.529
TC19 78	15.796	20.370	23.917	25.156
TC19 79	15.763	21.922		26.108
TC19 80	15.730	19.381		22.966
TC19 81	15.712	18.652		21.915
TC19 82	15.694	19.168		22.109
TC19 83	15.677	20.519		23.138
TC19 84	15.659	20.706		23.003
TC19 85	15.641	19.702	22.681	21.676
TC19 86	15.623	17.466		19.488
TC19 87	15.605	18.894		20.964
TC19 88	15.588	20.325		22.442
TC19 89	15.570	19.515		21.679
TC19 90	15.552	20.951		23.162
TC19 91	15.534	20.610		22.869
TC19 92	15.517	20.163	22.917	22.470
TC19 93	15.499	20.403		23.210
TC19 94	15.481	22.078		25.385
TC19 95	15.463	19.067		22.875
TC19 96	15.445	21.919		26.227
TC19 97	15.428	18.626		23.434

8.9 Temperatures calculated from Mg/Ca and δ18Oplanktic data

Sample ID	Age (Ma)	Temperature (°C) based on $\delta^{18}O$ (Bemis *et al.,* 1998) - Latitude based $\delta^{18}O$ seawater estimate (Zachos *et al.,* 1994)	Temperature based on Mg/Ca (Gray & Evans, 2019)	Temperature (°C) based on $\delta^{18}O$ (Bemis et al., 1998) - Local $\delta^{18}O$ seawater estimate using Mg/Ca data
TC19 98	15.410	19.532		24.841
TC19 99	15.392	19.000	25.342	24.810
TC19 100	15.374	21.636		26.770
TC19 101	15.351	21.393		25.654
TC19 102	15.328	24.682		28.070
TC19 103	15.305	21.977		24.492
TC19 104	15.282	21.507	23.618	23.148
TC19 105	15.259	19.857		21.948
TC19 106	15.236	21.428		23.968
TC19 107	15.213	19.852		22.842
TC19 108	15.190	22.013	23.291	25.452
TC19 109	15.167	20.461		23.870
TC19 110	15.144	21.282		24.661
TC19 111	15.121	18.088		21.437
TC19 112	15.098	18.888		22.207
TC19 113	15.075	17.941		21.229
TC19 114	15.052	17.464		20.722
TC19 116	15.006	21.414		24.611
TC19 117	14.983	23.778	24.581	26.945
TC19 118	14.960	21.258		24.815
TC19 119	14.937	19.346		23.293
TC19 120	14.914	19.342		23.679
TC19 121	14.891	18.700		23.427
TC19 122	14.868	27.387		32.503
TC19 123	14.845	18.497		24.004
TC19 124	14.822	22.785	24.394	28.682
TC19 125	14.800	18.366		23.202
TC19 126	14.778	22.268	22.142	26.044
TC19 127	14.756	19.677		23.538
TC19 128	14.734	19.058		23.004
TC19 129	14.712	16.794		20.825
TC19 130	14.689	21.726		25.843
TC19 131	14.667	18.913		23.114
TC19 133	14.623	16.900		21.272
TC19 134	14.601	16.172		20.630
TC19 135	14.579	22.531		27.074
TC19 136	14.557	17.581		22.209
TC19 137	14.545	19.254		23.926
TC19 139	14.522	17.348		22.108
TC19 140	14.511	17.125		21.930
TC19 141	14.499	20.882		25.732
TC19 142	14.488	17.910	25.776	22.804
TC19 143	14.476	19.911		24.805
TC19 144	14.465	18.939		23.834
TC19 145	14.453	16.635		21.530
TC19 146	14.430	15.481		20.377
TC19 147	14.407	17.544		22.441
TC19 148	14.384	18.249		23.146
TC19 149	14.361	15.659		20.557
TC19 150	14.337	16.491		21.390
TC19 155	14.221	16.005		20.908
TC19 156	14.198	15.692		20.596
TC19 158	14.152	16.207		21.112
TC19 159	14.128	19.901		24.807
TC19 160	14.105	16.265		21.171
TC19 161	14.082	16.222		21.129
TC19 162	14.059	18.400		23.309
TC19 163	14.035	17.520		22.429
TC19 164	14.012	15.657		20.567
TC19 165	13.989	18.438		23.349
TC19 166	13.966	17.298		22.209
TC19 167	13.943	17.383		22.295
TC19 168	13.919	20.915		25.828
TC19 169	13.896	16.046		20.960
TC19 170	13.873	17.824		22.738
TC19 171	13.853	17.346		22.261

8.9 Temperatures calculated from Mg/Ca and δ18Oplanktic data

Sample ID	Age (Ma)	Temperature (°C) based on $\delta^{18}O$ (Bemis *et al.,* 1998) - Latitude based $\delta^{18}O$ seawater estimate (Zachos *et al.,* 1994)	Temperature based on Mg/Ca (Gray & Evans, 2019)	Temperature (°C) based on $\delta^{18}O$ (Bemis et al., 1998) - Local $\delta^{18}O$ seawater estimate using Mg/Ca data
TC19 172	13.833	16.350		21.266
TC19 173	13.812	17.967	21.267	22.884
TC19 174	13.792	15.768		20.813
TC19 175	13.772	17.752		22.925
TC19 176	13.752	17.317		22.619
TC19 177	13.732	18.067		23.497
TC19 178	13.712	20.639	23.626	26.198
TC19 179	13.691	18.229		23.590
TC19 180	13.671	13.898		19.061
TC19 181	13.651	15.621		20.587
TC19 182	13.631	14.664	20.389	19.432
TC19 183	13.611	15.628		20.952
TC19 184	13.591	16.832		22.712
TC19 185	13.570	17.279		23.714
TC19 186	13.550	16.704		23.695
TC19 187	13.530	16.373	24.250	23.920
TC19 188	13.514	19.028		26.164
TC19 189	13.498	18.519		25.245
TC19 190	13.482	19.057		25.371
TC19 191	13.466	17.851	24.961	23.755
TC19 192	13.451	18.527		24.389
TC19 193	13.435	16.640		22.461
TC19 194	13.419	20.037		25.816
TC19 195	13.403	21.851		27.588
TC19 196	13.387	19.491		25.186
TC19 197	13.371	17.413		23.066
TC19 198	13.355	17.279	23.024	22.890
TC19 199	13.339	18.153		23.704
TC19 200	13.324	18.917		24.409
TC19 201	13.308	17.072		22.503
TC19 202	13.292	17.800		23.172
TC19 203	13.276	17.485		22.797
TC19 204	13.260	17.536		22.788
TC19 205	13.244	18.281	22.993	23.473
TC19 206	13.228	18.310		23.446
TC19 207	13.212	18.586		23.667
TC19 208	13.197	20.910		25.935
TC19 209	13.181	20.553		25.522
TC19 210	13.165	17.684		22.598
TC19 211	13.143	17.212		22.049
TC19 212	13.120	16.638	25.311	21.396
TC19 213	13.098	17.642		23.020
TC19 214	13.076	18.693		24.693
TC19 215	13.054	19.070		25.690
TC19 216	13.032	19.978		27.217
TC19 217	13.010	18.547		26.407
TC19 218	12.987	18.306	27.551	26.786
TC19 219	12.965	19.121		27.173
TC19 220	12.943	18.311	26.170	25.935
TC19 221	12.921	20.663		27.958
TC19 222	12.899	21.172		28.138
TC19 223	12.876	20.578		27.215
TC19 224	12.854	21.214		27.523
TC19 225	12.832	18.434		24.414
TC19 226	12.810	19.550	26.229	25.201
TC19 227	12.788	17.662		23.789
TC19 228	12.766	19.727		26.331
TC19 229	12.743	19.893		26.973
TC19 230	12.721	19.245	25.218	26.801
TC19 231	12.699	18.111		24.981
TC19 232	12.677	17.051		23.236
TC19 233	12.655	18.599	24.745	24.099
TC19 234	12.632	16.622		22.746
TC19 235	12.610	16.746		23.494
TC19 236	12.588	16.469		23.842
TC19 237	12.566	16.197	24.619	24.194

8.9 Temperatures calculated from Mg/Ca and δ18Oplanktic data

Sample ID	Age (Ma)	Temperature (°C) based on $\delta^{18}O$ (Bemis *et al.,* 1998) - Latitude based $\delta^{18}O$ seawater estimate (Zachos *et al.,* 1994)	Temperature based on Mg/Ca (Gray & Evans, 2019)	Temperature (°C) based on $\delta^{18}O$ (Bemis et al., 1998) - Local $\delta^{18}O$ seawater estimate using Mg/Ca data
TC19 238	12.544	17.107		24.103
TC19 239	12.522	19.490		25.485
TC19 240	12.499	26.291		31.284
TC19 241	12.477	20.615		24.608
TC19 242	12.455	19.349	22.481	22.340
TC19 243	12.433	13.694		17.350
TC21 1	12.411	15.127		19.445
TC21 2	12.389	16.039		21.020
TC21 3	12.366	16.986		22.629
TC21 4	12.344	14.885		21.191
TC21 6	12.300	15.501		23.133
TC21 7	12.278	17.163	25.280	25.457
TC21 8	12.256	16.069		24.266
TC21 9	12.234	15.862		23.962
TC21 10	12.212	14.975		22.978
TC21 12	12.167	15.788		23.597
TC21 14	12.123	14.917		22.532
TC21 15	12.101	15.319		22.837
TC21 16	12.079	17.529	22.396	24.951
TC21 17	12.057	14.550		21.405
TC21 19	12.013	16.863		22.584
TC21 20	11.991	20.502		25.656
TC21 21	11.968	15.626		20.214
TC21 22	11.946	17.156	21.549	21.176
TC21 23	11.924	17.918		22.731
TC21 24	11.902	19.195	22.470	24.802
TC21 25	11.880	16.596		22.427
TC21 26	11.860	19.530		25.564
TC21 28	11.820	18.209		24.648
TC21 29	11.800	16.224		22.866
TC21 30	11.780	15.190		22.035
TC21 31	11.760	17.193		24.241
TC21 32	11.740	16.499		23.749
TC21 33	11.720	18.232		25.684
TC21 34	11.700	16.130		23.785
TC21 35	11.680	18.273	22.408	26.131
TC21 42	11.640	17.868		24.830
TC21 43	11.620	17.039		23.553
TC21 44	11.600	18.228		24.294
TC21 45	11.586	18.268		24.017
TC21 48	11.543	16.550		21.348
TC21 49	11.529	18.960	23.676	23.441
TC21 50	11.515	21.640		26.547
TC21 51	11.501	20.099		25.432
TC21 52	11.487	18.444		24.204
TC21 53	11.473	19.458	22.410	25.644
TC21 54	11.458	16.773		22.559
TC21 55	11.444	15.329		20.715
TC21 56	11.430	15.010		19.996
TC21 57	11.416	15.788	22.818	20.374
TC21 58	11.402	15.203		19.827
TC21 59	11.388	14.964		19.627
TC21 60	11.373	15.790		20.492
TC21 61	11.359	15.881		20.622
TC21 62	11.345	15.663		20.442
TC21 63	11.331	17.062		21.879
TC21 64	11.317	16.585	21.407	21.442
TC21 65	11.303	17.588		23.082
TC21 66	11.288	16.342		22.474
TC21 67	11.274	18.137		24.907
TC21 68	11.260	16.640		24.047
TC21 69	11.246	14.674		22.719
TC21 70	11.232	17.656		26.338
TC21 71	11.218	17.566		26.886
TC21 72	11.203	15.960	25.287	25.918
TC21 73	11.189	16.036	20.737	21.763

8.9 Temperatures calculated from Mg/Ca and δ18Oplanktic data

Sample ID	Age (Ma)	Temperature (°C) based on $\delta^{18}O$ (Bemis *et al.,* 1998) - Latitude based $\delta^{18}O$ seawater estimate (Zachos *et al.,* 1994)	Temperature based on Mg/Ca (Gray & Evans, 2019)	Temperature (°C) based on $\delta^{18}O$ (Bemis et al., 1998) - Local $\delta^{18}O$ seawater estimate using Mg/Ca data
TC21 74	11.175	20.928		26.445
TC21 75	11.161	17.641		22.948
TC21 76	11.147	16.417		21.514
TC21 77	11.130	17.168		22.018
TC21 78	11.113	17.074		21.675
TC21 79	11.097	20.115		24.468
TC21 80	11.080	16.364	21.168	20.470
TC21 81	11.063	16.300		20.619
TC21 82	11.046	14.837		19.370
TC21 83	11.030	15.604		20.351
TC21 84	11.013	18.692		23.652
TC21 85	10.996	16.563		21.738
TC21 86	10.980	14.627		20.015
TC21 87	10.963	16.893		22.495
TC21 88	10.946	16.037	23.382	21.852
TC21 89	10.929	17.418		22.831
TC21 90	10.913	16.492		21.503
TC21 91	10.896	16.983		21.592
TC21 92	10.879	17.406		21.613
TC21 93	10.863	16.851		20.655
TC21 94	10.846	15.649		19.051
TC21 95	10.829	16.457		19.456
TC21 96	10.812	17.741	22.712	20.338
TC21 97	10.796	17.515		20.904
TC21 98	10.779	17.754		21.935
TC21 99	10.762	15.186		20.159
TC21 100	10.746	17.340	21.368	23.104
TC21 101	10.729	17.058		22.751
TC21 102	10.712	16.289		21.911
TC21 103	10.692	15.960		21.495
TC21 104	10.672	22.649	22.341	28.097
TC21 105	10.651	17.519		23.395
TC21 106	10.631	15.796		22.100
TC21 107	10.611	15.674	23.224	22.407
TC21 108	10.590	19.351		26.138
TC21 109	10.570	21.217		28.059
TC21 110	10.550	16.363		23.260
TC21 111	10.530	17.567		24.519
TC21 112	10.509	18.190		25.196
TC21 113	10.489	19.009		26.070
TC21 114	10.469	18.698		25.814
TC21 115	10.448	17.740		24.910
TC21 117	10.408	18.396		25.676
TC21 118	10.387	17.161		24.495
TC21 119	10.367	18.760		26.149
TC21 120	10.347	18.510	24.784	25.954
TC21 121	10.327	17.583	26.789	27.313
TC21 122	10.306	19.406		29.071
TC21 123	10.286	20.579		30.179
TC21 124	10.266	19.132		28.667
TC21 125	10.245	21.075		30.545
TC21 127	10.205	19.199		28.538
TC21 128	10.185	20.387	24.948	29.661
TC21 129	10.164	19.165		28.329
TC21 130	10.144	21.080		30.134
TC21 131	10.124	19.757		28.701
TC21 132	10.100	25.425		34.238
TC21 134	10.052	14.406		22.958
TC21 135	10.028	20.772	25.989	29.194
TC21 136	10.004	21.075		29.084
TC21 137	9.980	18.692		26.289
TC21 138	9.956	18.811		25.996
TC21 141	9.883	18.218		24.165
TC21 142	9.859	14.443	26.752	19.979
TC21 143	9.835	19.867		25.186
TC21 144	9.811	18.903		24.005

8.9 Temperatures calculated from Mg/Ca and δ18Oplanktic data

Sample ID	Age (Ma)	Temperature (°C) based on $\delta^{18}O$ (Bemis *et al.,* 1998) - Latitude based $\delta^{18}O$ seawater estimate (Zachos *et al.,* 1994)	Temperature based on Mg/Ca (Gray & Evans, 2019)	Temperature (°C) based on $\delta^{18}O$ (Bemis et al., 1998) - Local $\delta^{18}O$ seawater estimate using Mg/Ca data
TC21 145	9.787	18.080		22.966
TC21 146	9.755	19.242		23.831
TC21 148	9.689	17.818		21.815
TC21 149	9.656	19.675		23.375
TC21 150	9.623	18.285	21.800	21.689
TC21 151	9.590	20.223		24.671
TC21 152	9.557	19.093		24.585
TC21 153	9.525	18.872		25.407
TC21 154	9.492	17.785	26.090	25.364
TC21 155	9.459	15.688		22.942
TC21 156	9.426	16.567		23.496
TC21 157	9.393	18.075		24.678
TC21 158	9.360	18.600	25.410	24.878
TC21 159	9.328	18.409		23.797
TC21 160	9.262	18.570		22.177
TC21 161	9.229	21.184		23.911
TC21 162	9.197	21.440	21.014	23.288
TC21 163	9.165	19.785	24.829	23.534
TC21 164	9.132	17.945		20.805
TC21 165	9.100	18.796		20.765
TC21 166	9.067	19.565		20.644
TC21 167	9.035	19.088		19.278
TC21 168	9.002	17.968	20.071	17.267
TC21 169	8.949	21.588		20.887
TC21 170	8.896	16.766		16.065
TC21 171	8.842	16.564		15.863
TC21 172	8.789	18.664		17.963
TC21 173	8.736	19.224		18.523
TC21 174	8.682	19.332		18.631
TC21 175	8.629	18.754		18.053
TC21 226	8.610	15.841		17.687
TC21 227	8.585	26.784		28.924
TC21 228	8.559	23.633		26.069
TC21 229	8.534		21.453	21.453
TC21 232	8.459	17.774		20.102
TC21 233	8.433	16.892		19.086
TC21 234	8.408	16.004		18.064
TC21 235	8.383	19.610		21.535
TC21 238	8.307	14.690		16.213
TC21 239	8.282	18.602		19.991
TC21 240	8.262	17.834		19.115
TC21 241	8.242	24.313		25.486
TC21 242	8.221	19.001		20.066
TC21 243	8.201	21.243	22.200	22.200
TC21 244	8.181	14.943		15.791
TC21 245	8.160	14.393		15.132
TC21 246	8.140	18.964		19.595
TC21 247	8.120	15.713		16.235
TC21 248	8.100	15.562		15.976
TC21 249	8.079	17.187		17.492
TC21 250	8.059	18.416		18.612
TC21 251	8.039	15.860		15.948
TC21 252	8.018	18.698		18.677
TC21 253	7.998	16.924		16.795
TC21 254	7.978	24.623		24.385
TC21 256	7.937	17.991		17.536
TC21 257	7.917	14.881		14.318
TC21 258	7.897	18.703	18.031	18.031
TC21 259	7.874	15.939		15.506
TC21 260	7.851	17.029		16.834
TC21 261	7.828	20.661		20.705
TC21 262	7.805	20.988		21.271
TC21 263	7.783	22.374		22.895
TC21 264	7.760	18.602		19.361
TC21 265	7.737	15.948		16.946
TC21 266	7.710	19.254		20.531

8.9 Temperatures calculated from Mg/Ca and δ18Oplanktic data

Sample ID	Age (Ma)	Temperature (°C) based on $\delta^{18}O$ (Bemis *et al.,* 1998) - Latitude based $\delta^{18}O$ seawater estimate (Zachos *et al.,* 1994)	Temperature based on Mg/Ca (Gray & Evans, 2019)	Temperature (°C) based on $\delta^{18}O$ (Bemis et al., 1998) - Local $\delta^{18}O$ seawater estimate using Mg/Ca data
TC21 267	7.684	15.435		16.991
TC21 268	7.657	18.200		20.035
TC21 269	7.630	25.123		27.236
TC21 270	7.603	15.903		18.296
TC21 271	7.577	17.812		20.483
TC21 272	7.550	17.462		20.413
TC21 273	7.523	16.584	19.814	19.814
TC21 274	7.497	17.666		20.887
TC21 275	7.470	14.675		17.887
TC21 276	7.443	18.385		21.587
TC21 278	7.390	20.414		23.599
TC21 281	7.364	17.133		20.308
TC21 282	7.338	19.005		22.172
TC21 283	7.312	17.843		21.001
TC21 284	7.286	19.775		22.924
TC21 285	7.260	20.361		23.501
TC21 286	7.235	19.908		23.039
TC21 287	7.209	18.544		21.666
TC21 288	7.183	17.676		20.790
TC21 289	7.157	16.452		19.557
TC21 290	7.131	16.973	20.069	20.069
TC21 291	7.105	16.153		19.230
TC21 292	7.079	18.122		21.180
TC21 293	7.053	16.131		19.170
TC21 294	7.027	19.266		22.287
TC21 295	7.001	19.803		22.804
TC21 296	6.975	20.559		23.541
TC21 297	6.950	19.759		22.723
TC21 298	6.924	19.113		22.058
TC21 299	6.898	17.095		20.020
TC21 300	6.872	15.668		18.575
TC21 301	6.846	14.589		17.477
TC21 302	6.820	20.962		23.830
TC21 303	6.797	16.468		19.320
TC21 304	6.774	19.834		22.669
TC21 305	6.751	19.945		22.762
TC21 306	6.727	19.358		22.158
TC21 307	6.720	18.381		21.176
TC21 308	6.713	19.201		21.991
TC21 309	6.706	13.782		16.567
TC21 310	6.699	16.582		19.362
TC21 311	6.692	15.697		18.471
TC21 312	6.685	16.937		19.706
TC21 313	6.678	19.798		22.562
TC21 314	6.671	20.349		23.108
TC21 315	6.664	18.230		20.984
TC21 316	6.657	17.819		20.568
TC21 317	6.650	16.177		18.921
TC21 320	6.643	17.634		20.372
TC21 321	6.636	18.010		20.744
TC21 323	6.622	17.519		20.242
TC21 326	6.600	18.790		21.498
TC21 327	6.593	18.718		21.421
TC21 331	6.565	20.016		22.698
TC21 333	6.551	17.599		20.270
TC21 336	6.530	15.888		18.543
TC21 337	6.523	20.678		23.329
TC21 340	6.502	18.946		21.581
TC21 344	6.473	17.021		19.635
TC21 345	6.466	15.673	18.282	18.282
TC21 346	6.459	13.946		16.486
TC21 347	6.452	12.193		14.664
TC21 349	6.438	11.120		13.453
TC21 350	6.431	14.853		17.116
TC21 351	6.424	17.061		19.256
TC21 352	6.416	15.353		17.478

8.9 Temperatures calculated from Mg/Ca and δ18Oplanktic data

Sample ID	Age (Ma)	Temperature (°C) based on $\delta^{18}O$ (Bemis *et al.,* 1998) - Latitude based $\delta^{18}O$ seawater estimate (Zachos *et al.,* 1994)	Temperature based on Mg/Ca (Gray & Evans, 2019)	Temperature (°C) based on $\delta^{18}O$ (Bemis et al., 1998) - Local $\delta^{18}O$ seawater estimate using Mg/Ca data
TC21 354	6.402	14.934		16.921
TC21 355	6.395	16.101		18.019
TC21 362	6.367	18.965		20.607
TC21 363	6.360	16.978		18.550
TC21 364	6.353	15.534		17.037
TC21 367	6.331	18.814		20.110
TC21 368	6.324	13.954		15.180
TC21 369	6.317	15.177		16.334
TC21 370	6.310	17.005		18.093
TC21 371	6.303	16.240		17.259
TC21 372	6.296	21.287		22.237
TC21 373	6.289	12.522		13.403
TC21 375	6.274	12.633		13.375
TC21 376	6.267	18.112		18.785
TC21 377	6.260	16.575		17.179
TC21 378	6.253	16.375	16.911	16.911
TC21 379	6.246	16.461		17.282
TC21 380	6.239	12.326		13.433
TC21 381	6.232	14.668		16.061
TC21 382	6.225	17.055		18.733
TC21 383	6.218	16.584		18.548
TC21 384	6.210	11.881		14.131
TC21 385	6.203	13.892		16.427
TC21 390	6.196	8.602		11.423
TC21 391	6.189	11.611		14.718
TC21 392	6.182	10.315		13.708
TC21 393	6.175	11.215		14.893
TC21 394	6.168			22.687
TC21 395	6.161	10.905		15.155
TC21 396	6.154	11.435		15.971
TC21 397	6.147			23.544
TC21 398	6.139	13.268		18.376
TC21 399	6.132	7.952		13.345
TC21 400	6.125	13.282		18.961
TC21 401	6.118	7.635		13.600
TC21 402	6.111	13.538		19.789
TC21 403	6.104	9.469		16.006
TC21 404	6.097	7.499		14.321
TC21 405	6.091	10.340		17.415
TC21 407	6.078	11.686		19.267
TC21 408	6.072	8.773	16.606	16.606
TC21 410	6.059	22.509		28.845
TC21 411	6.053	11.968		17.555
TC21 412	6.047	14.378		19.216
TC21 413	6.040	8.270		12.360
TC21 414	6.034	11.327		14.668
TC21 415	6.028	9.158		11.750
TC21 416	6.021	13.538		15.382
TC21 417	6.015	16.032		17.127
TC21 418	6.009	15.242	15.588	15.588
TC21 419	6.003	15.429	14.590	14.590
TC21 420	5.996	9.337		9.140
TC21 421	5.990	15.812		16.256
TC21 422	5.984	11.607		12.693
TC21 423	5.977	13.141		14.869
TC21 424	5.971	11.592		13.961
TC21 425	5.965	12.945		15.955
TC21 427	5.952	25.366		29.660
TC21 428	5.946	12.683	17.619	17.619
TC21 429	5.940	12.842		18.266
TC21 430	5.933	18.323		24.236
TC21 440	5.921	22.896		29.787
TC21 441	5.915	9.281		16.661
TC21 442	5.908	6.275		14.144
TC21 443	5.902	4.203		12.561
TC21 444	5.896	11.440		20.286

8.9 Temperatures calculated from Mg/Ca and δ18Oplanktic data

Sample ID	Age (Ma)	Temperature (°C) based on $\delta^{18}O$ (Bemis *et al.,* 1998) - Latitude based $\delta^{18}O$ seawater estimate (Zachos *et al.,* 1994)	Temperature based on Mg/Ca (Gray & Evans, 2019)	Temperature (°C) based on $\delta^{18}O$ (Bemis et al., 1998) - Local $\delta^{18}O$ seawater estimate using Mg/Ca data
TC21 446	5.883	10.931		20.756
TC21 450	5.858	10.668		22.448
TC21 451	5.852	11.098		23.367
TC21 452	5.846	8.947		21.706
TC21 454	5.833	12.853		26.589
TC21 455	5.827	7.041		21.266
TC21 456	5.820	4.611	19.326	19.326
TC21 458	5.808	11.428		26.142
TC21 466	5.758	14.973		29.687
TC21 468	5.745	14.161		28.876
TC21 470	5.732	14.854		29.568

8.10 $\delta^{18}O_{seawater}$ and $\delta^{18}O_{sw\text{-}ivc}$ calculated from Mg/Ca and $\delta^{18}O_{planktic}$ data

This table shows estimates of local $\delta^{18}O_{seawater}$ and $\delta^{18}O_{sw\text{-}ivc}$ relative to time (Ma) for the composite temporal record. $\delta^{18}O_{seawater}$ was calculated from Mg/Ca and $\delta^{18}O_{planktic}$ data using the method outline in Chapter 4.1(Equation 4.1.4.1). $\delta^{18}O_{sw\text{-}ivc}$ was calculated from Mg/Ca, $\delta^{18}O_{planktic}$ and $\delta^{18}O_{benthic}$ data from Miller *et al.* (2020) using the method outline in Chapter 5.1.3 (Equation 5.1.3.2).

8.10 δ18Oseawater and δ18Osw-ivc calculated from Mg/Ca and δ18Oplanktic data

Sample ID	Age (Ma)	δ18Osw (VPDB)	δ18Osw (VSMOW)	δ18Osw Local (Salinity) (VPDB)	δ18Osw Local (Salinity) (VSMOW)
TC21 456	5.820	3.521	34.550	2.995	34.008
TC21 428	5.946	1.488	32.454	1.110	32.065
TC21 419	6.003	0.288	31.217	0.537	31.474
TC21 418	6.009	0.534	31.471	0.651	31.591
TC21 408	6.072	2.091	33.075	2.009	32.991
TC21 378	6.253	0.573	31.511	0.497	31.433
TC21 345	6.466	1.005	31.956	0.425	31.358
TC21 290	7.131	1.106	32.060	0.114	31.038
TC21 273	7.523	1.133	32.089	0.567	31.504
TC21 258	7.897	0.322	31.252	-0.304	30.606
TC21 243	8.201	0.661	31.601	-1.034	29.854
TC21 229	8.534	1.030	31.982	-0.184	30.730
TC21 218	8.788	0.412	31.345	-0.254	30.658
TC21 168	9.002	0.316	31.246	-0.050	30.868
TC21 203	9.078	0.370	31.301	-0.985	29.905
TC21 163	9.165	1.242	32.200	-0.422	30.485
TC21 162	9.197	0.846	31.793	-0.887	30.005
TC21 158	9.360	1.767	32.742	-0.240	30.673
TC21 154	9.492	2.038	33.021	-0.194	30.720
TC21 150	9.623	1.170	32.126	-0.171	30.744
TC21 142	9.859	1.613	32.583	0.491	31.426
TC21 135	10.028	2.213	33.201	-0.693	30.206
TC21 128	10.185	2.390	33.384	-0.332	30.577
TC21 121	10.327	2.485	33.482	0.214	31.141
TC21 120	10.347	2.010	32.992	0.141	31.066
TC21 107	10.611	1.862	32.839	0.937	31.886
TC21 104	10.672	1.595	32.564	-0.810	30.085
TC21 100	10.746	1.660	32.632	0.618	31.557
TC21 96	10.812	1.002	31.953	0.140	31.064
TC21 88	10.946	1.671	32.643	0.722	31.664
TC21 80	11.080	1.316	32.276	0.490	31.425
TC21 73	11.189	1.653	32.624	0.496	31.432
TC21 72	11.203	2.532	33.531	0.423	31.356
TC21 64	11.317	1.472	32.437	0.375	31.307
TC21 57	11.416	1.416	32.379	0.597	31.535
TC21 53	11.473	1.748	32.722	-0.282	30.630
TC21 49	11.529	1.394	32.357	-0.188	30.726
TC21 35	11.680	2.096	33.081	-0.146	30.769
TC21 24	11.902	1.628	32.598	-0.270	30.641
TC21 22	11.946	1.298	32.258	0.106	31.029
TC21 16	12.079	2.005	32.987	0.538	31.475
TC21 7	12.278	2.186	33.174	0.367	31.299
TC19 242	12.455	1.084	32.037	-0.139	30.777
TC19 237	12.566	2.125	33.110	0.531	31.467
TC19 233	12.655	1.605	32.575	0.134	31.058
TC19 230	12.721	2.033	33.016	0.011	30.931
TC19 226	12.810	1.637	32.608	-0.225	30.688
TC19 220	12.943	2.047	33.030	-0.115	30.802
TC19 218	12.987	2.225	33.214	-0.196	30.718
TC19 212	13.120	1.451	32.416	0.697	31.639

8.10 δ18Oseawater and δ18Osw-ivc calculated from Mg/Ca and δ18Oplanktic data

Sample ID	Age (Ma)	δ18Osw (VPDB)	δ18Osw (VSMOW)	δ18Osw Local (Salinity) (VPDB)	δ18Osw Local (Salinity) (VSMOW)
TC19 205	13.244	1.542	32.509	0.387	31.319
TC19 198	13.355	1.629	32.599	0.304	31.234
TC19 191	13.466	1.690	32.662	-0.029	30.891
TC19 187	13.530	2.031	33.014	1.048	32.001
TC19 182	13.631	1.453	32.418	0.910	31.858
TC19 178	13.712	1.618	32.588	-0.373	30.535
TC19 173	13.812	1.484	32.450	0.476	31.411
TC19 142	14.488	1.480	32.445	0.415	31.348
TC19 126	14.778	1.247	32.206	-0.685	30.214
TC19 124	14.822	1.688	32.660	-0.347	30.563
TC19 117	14.983	1.121	32.075	-0.856	30.037
TC19 108	15.190	1.177	32.134	-0.030	30.889
TC19 104	15.282	0.803	31.748	-0.170	30.745
TC19 99	15.392	1.670	32.642	0.012	30.933
TC19 92	15.517	0.942	31.891	0.288	31.217
TC19 85	15.641	0.873	31.820	-0.344	30.566
TC19 78	15.796	1.457	32.422	-0.132	30.784
TC19 72	15.951	1.081	32.035	0.180	31.106
TC19 69	16.024	0.976	31.926	-0.264	30.648
TC19 60	16.265	1.256	32.215	0.003	30.923
TC19 42	16.728	1.350	32.311	0.166	31.092
TC19 34	16.946	1.035	31.987	-0.452	30.454

8.11 All data collected during strontium isotope analysis, including ages calculated

This table shows all data collected during strontium isotope analysis during this study relative to age (Ma) for the composite temporal record using the method outlined in Chapter 2.4. Strontium isotopic ages were calculated using the LOWESS Sr isotope Look-Up Table (Version 4: 08/04) (McArthur *et al.*, 2001; McArthur and Howarth, 2004). The total combined errors were then calculated from a combination of the uncertainties of the Sr isotopic analyses, and the error (upper and lower age range) of the LOWESS Sr isotope Look-Up Table (Version 4: 08/04) (McArthur *et al.*, 2001; McArthur and Howarth, 2004).

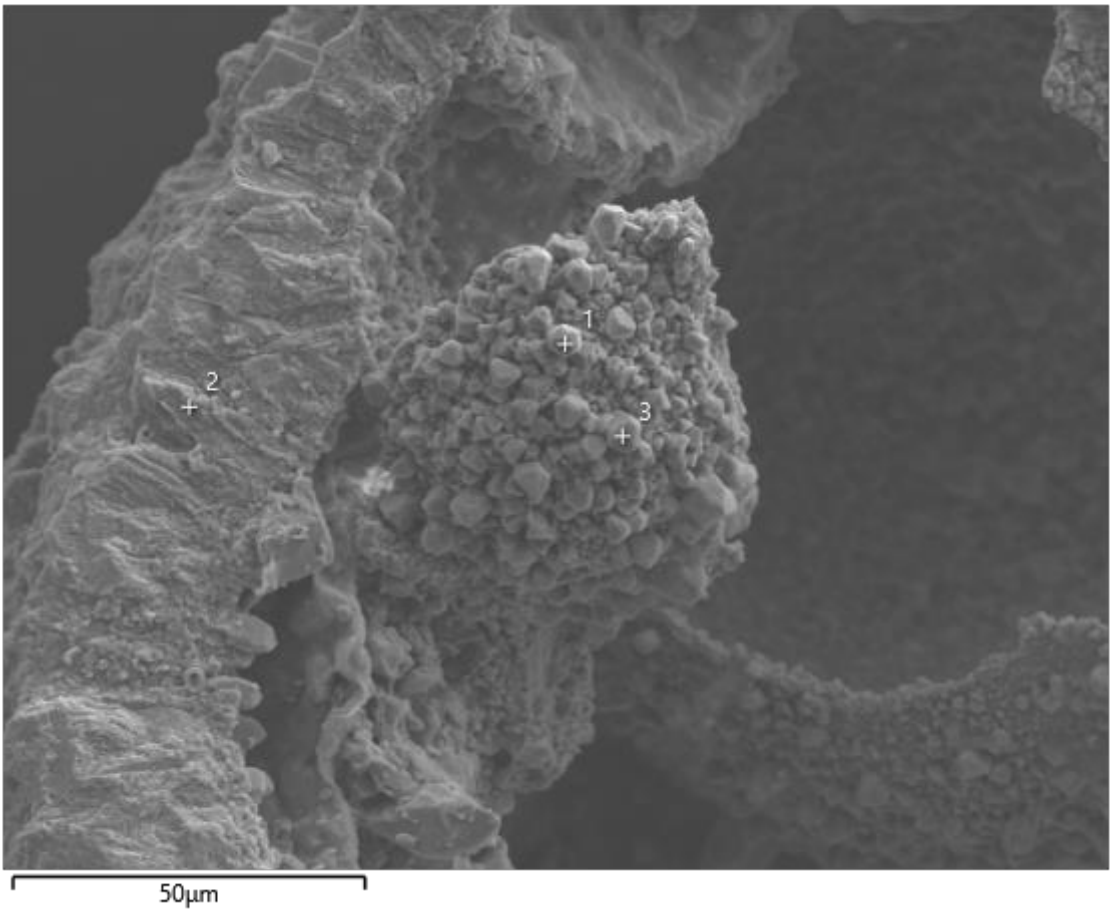
8.11 All data collected during strontium isotope analysis, including ages calculated

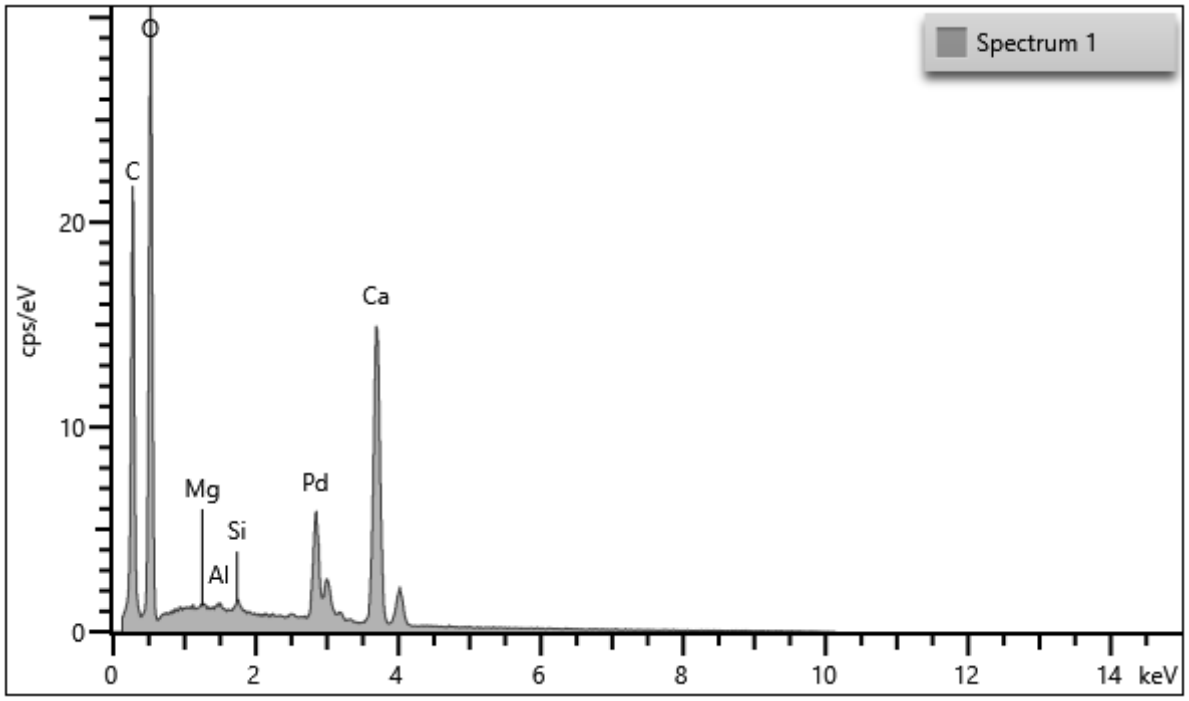
TC Sample Number	Sample Type	Target Reasoning	87Sr/86Sr	% Std Err	2 σ abs	SRM897 2 σ abs	87Sr/86Sr - SRM897 2 σ abs	87Sr/86Sr + SRM897 2 σ abs	Age (from LOOKUP Table)	Min Age (+)	Max Age (-)	Age -	Age +
TCKG02L	Oyster Shell	Oyster Shell 1 - light band	0.708221	0.0012	1.69973E-05	0.000007	0.708214	0.708228	23.63	23.33	23.93	0.3	0.3
TCKG02D	Oyster Shell	Oyster Shell 1 - dark band	0.708182	0.001	1.41636E-05	0.000007	0.708175	0.708189	24.37	24.07	24.72	0.3	0.35
TCKG03L	Oyster Shell	Oyster Shell 2 - light band	0.708256	0.0011	1.55816E-05	0.000007	0.708249	0.708263	22.96	22.71	23.24	0.25	0.28
TCKG03D	Oyster Shell	Oyster Shell 2 - dark band	0.708133	0.0013	1.84115E-05	0.000007	0.708126	0.70814	25.62	25.16	26.1	0.46	0.48
TCKG06	Coral	Coral/Carbonate Material	0.708461	0.0012	1.70031E-05	0.000007	0.708454	0.708468	19.68	19.5	19.86	0.18	0.18
TC19040	Planktic Foraminifera	KH 21.65m	0.708706	0.0013	1.84264E-05	0.000007	0.708699	0.708713	16.22	16.01	16.46	0.21	0.24
TC19136	Planktic Foraminifera	KH 15.825m	0.708784	0.0012	1.70108E-05	0.000007	0.708777	0.708791	14.92	14.48	15.21	0.44	0.29
TC21006	Planktic Foraminifera	KH 10.55m	0.708827	0.0013	1.84295E-05	0.000007	0.70882	0.708834	12.45	11.76	13.03	0.69	0.58
TC21115	Planktic Foraminifera	KH 5.275m	0.70892	0.0013	1.84319E-05	0.000007	0.708913	0.708927	8.84	7.85	9.43	0.99	0.59
TC21191	Planktic Foraminifera	KH 0m	0.708948	0.0013	1.84326E-05	0.000007	0.708941	0.708955	7.25	6.86	7.82	0.39	0.57
TC22203	Planktic Foraminifera	LH 62.75m	0.70901	0.0014	1.98523E-05	0.000007	0.709003	0.709017	5.71	5.5	5.89	0.21	0.18
TC22264	Planktic Foraminifera	LH 47.0625m	0.709022	0.002	2.83609E-05	0.000007	0.709015	0.709029	5.44	5.139	5.66	0.301	0.22
TC22330	Planktic Foraminifera	LH 31.375m	0.708845	0.0012	1.70123E-05	0.000007	0.708838	0.708852	11.45	10.9	12.24	0.55	0.79
TC22399	Planktic Foraminifera	LH 15.6875m	0.708989	0.0014	1.98517E-05	0.000007	0.708982	0.708996	6.07	5.92	6.25	0.15	0.18
TC22470	Planktic Foraminifera	LH 0m	0.709241	0.0012	1.70218E-05	0.000007	0.709234	0.709248	N/A	N/A	N/A	N/A	N/A

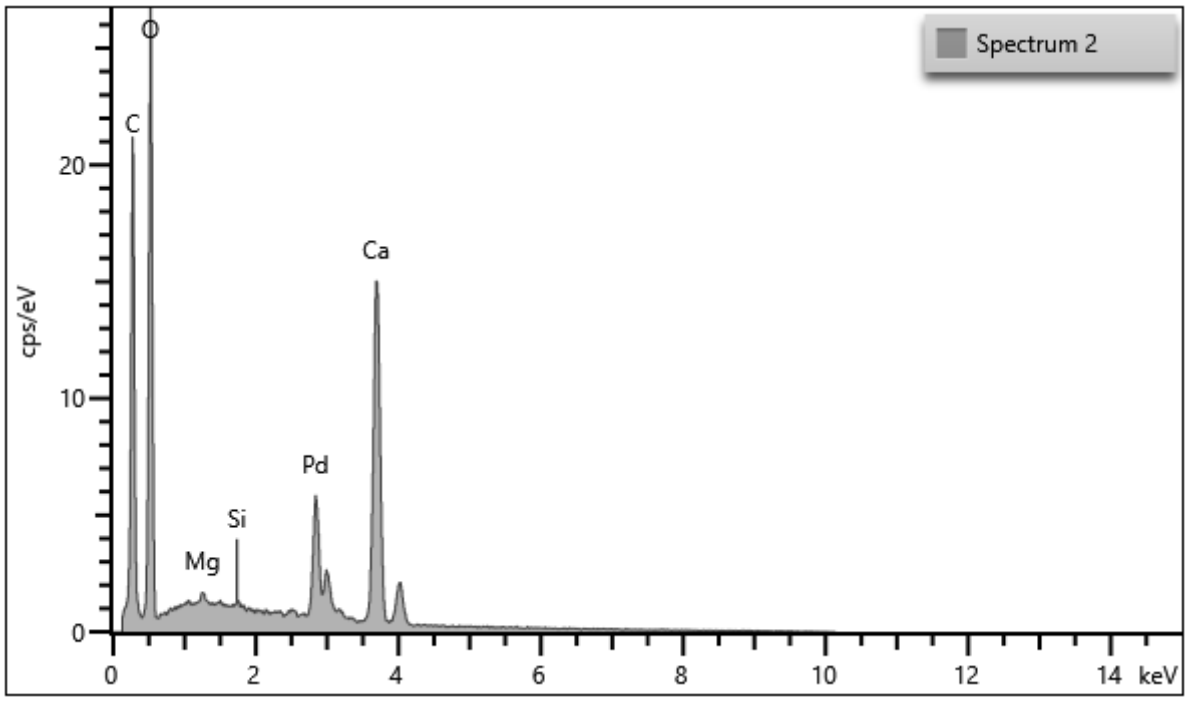
8.12 Energy dispersive X-ray spectrometry data for planktic foraminifera samples

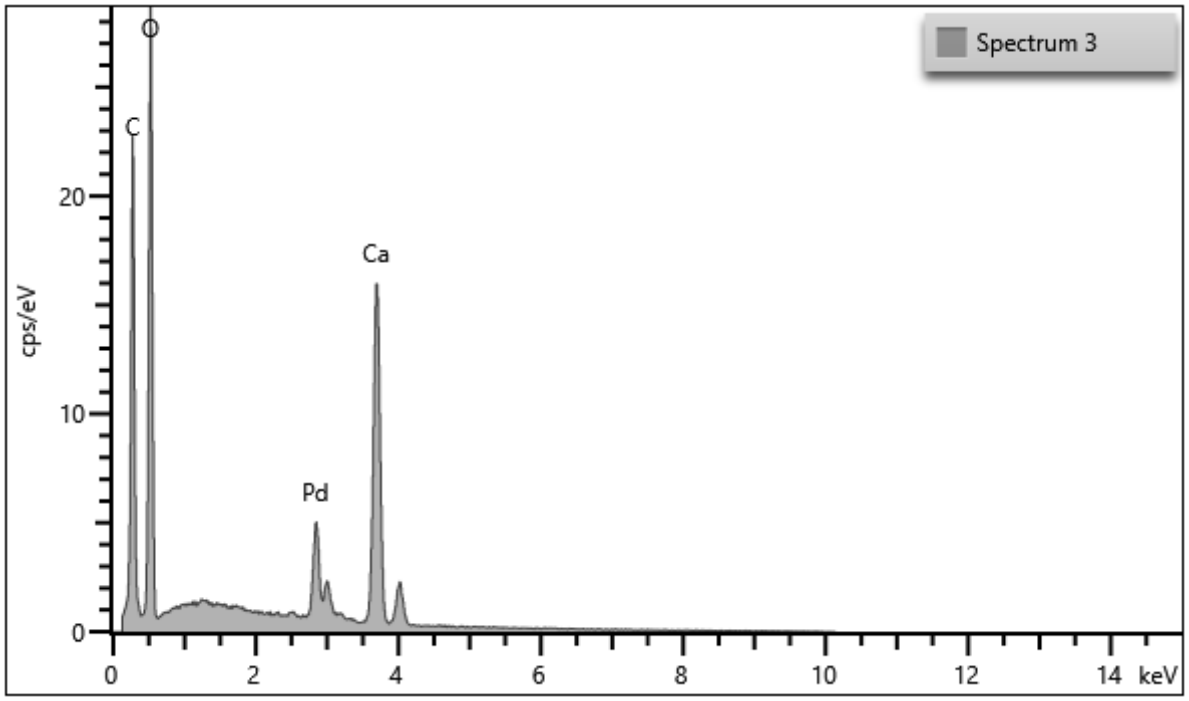
Energy dispersive X-ray spectrometry data is provided in this appendix. Spectra for each sample are numbered and labelled on the scanning electron micrographs shown. Spectra are shown in cps/eV (counts per second per electron-volt).

8.12.1 Sample TC19 214 (cleaned and broken)

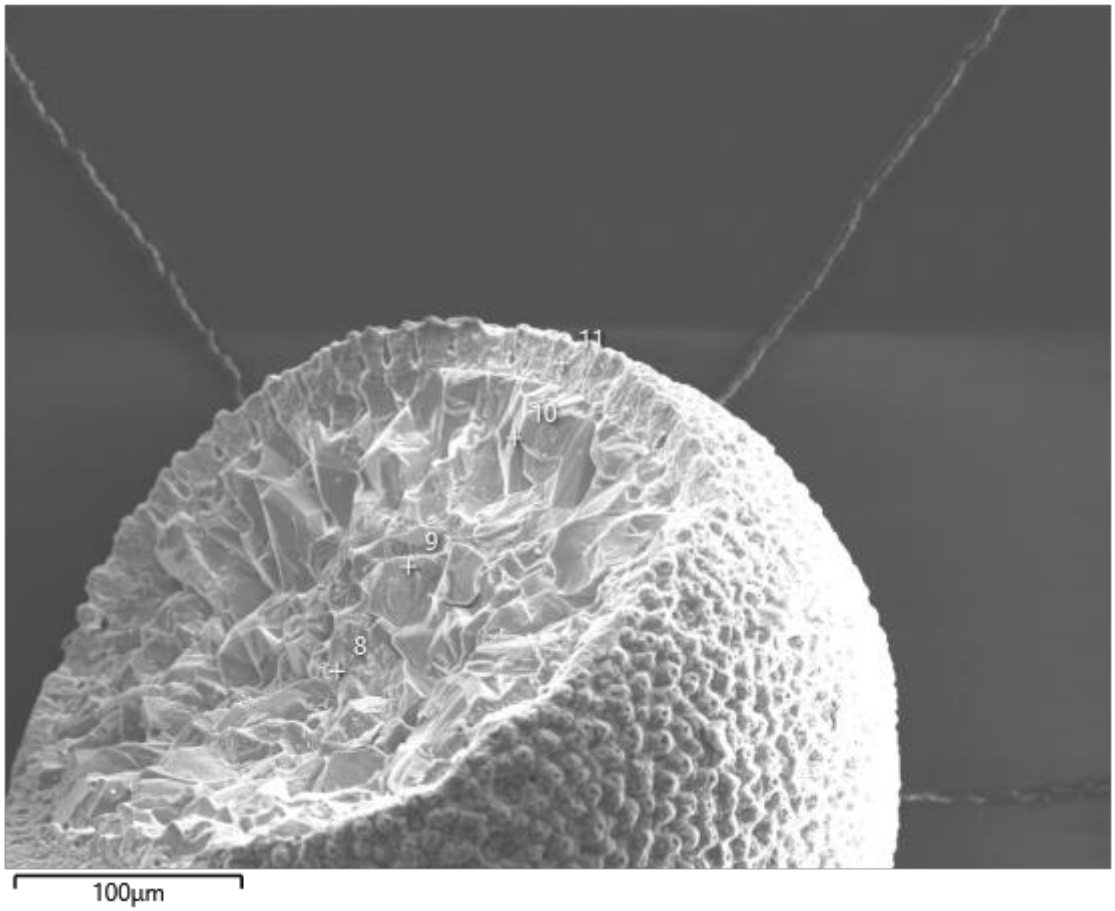


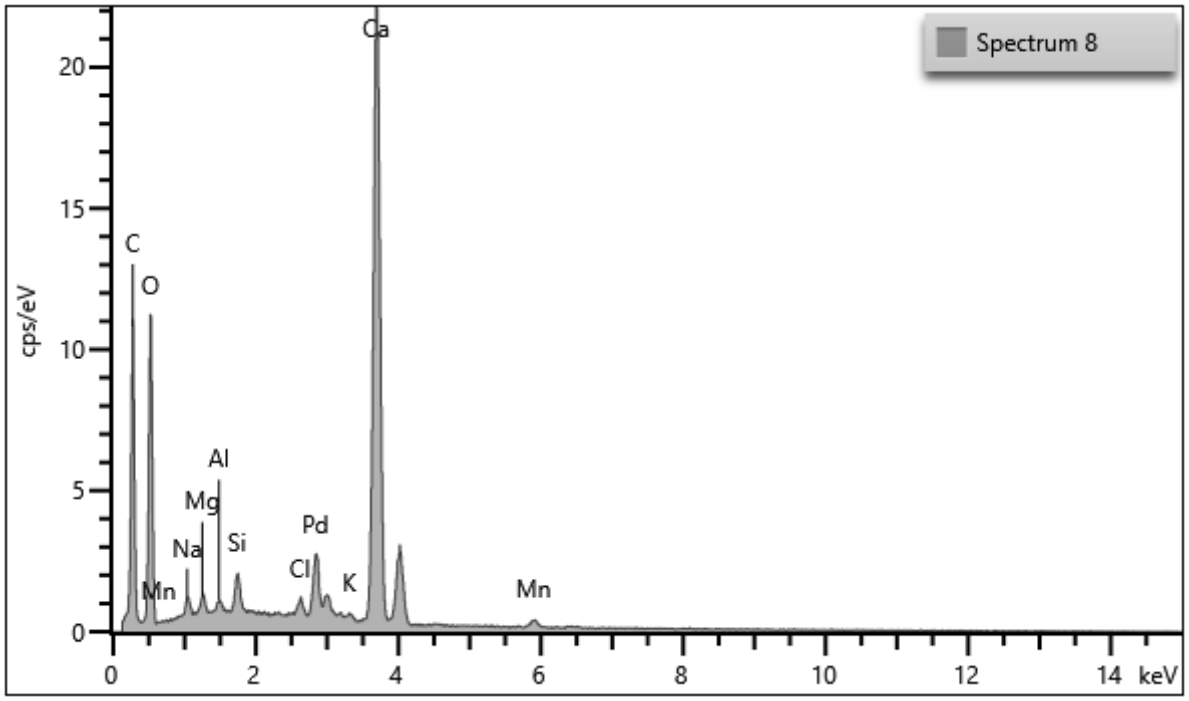

Spectrum 1
O
C
Ca
Mg
Pd
Si
Al
cps/eV
0
10
20
0
2
4
6
8
10
12
14
keV

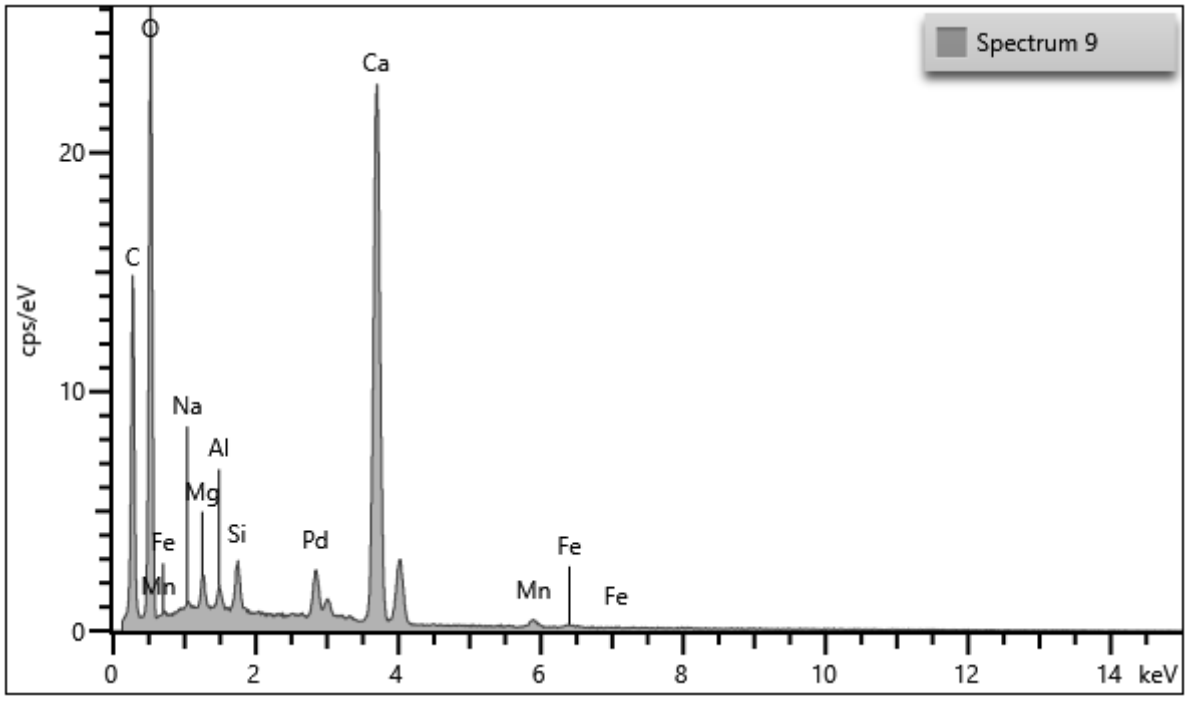

Spectrum 2
O
C
Ca
Pd
Si
Mg
cps/eV
0
10
20
0
2
4
6
8
10
12
14
keV

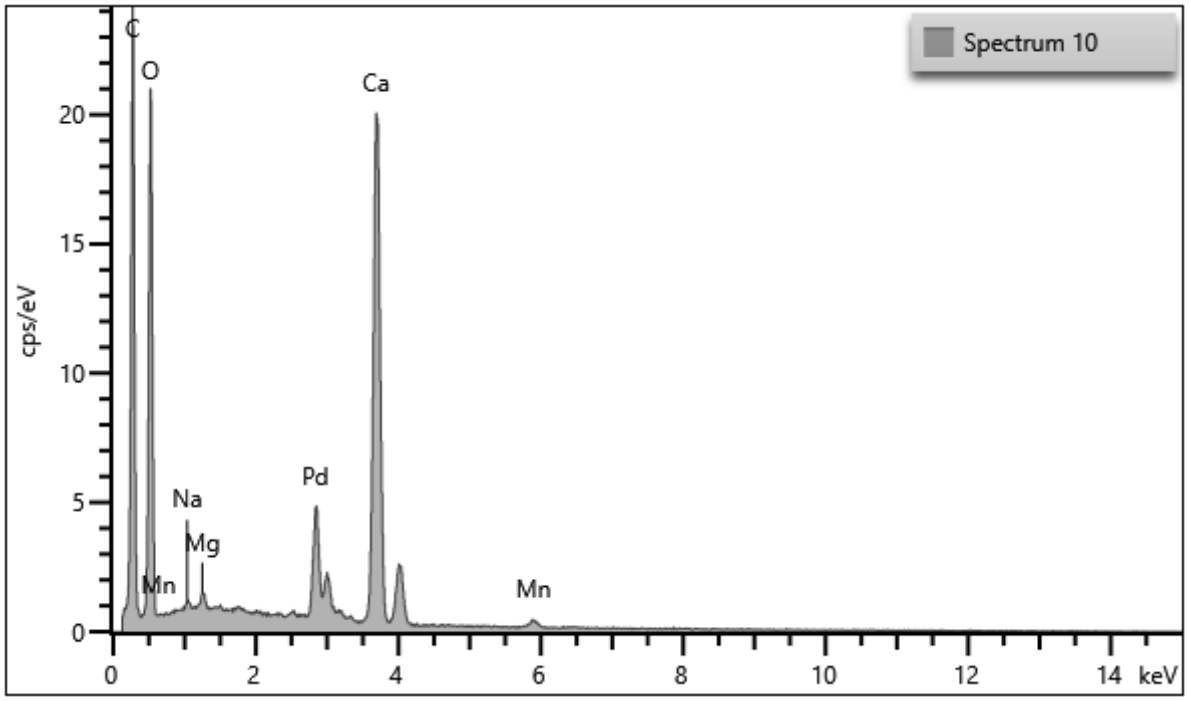


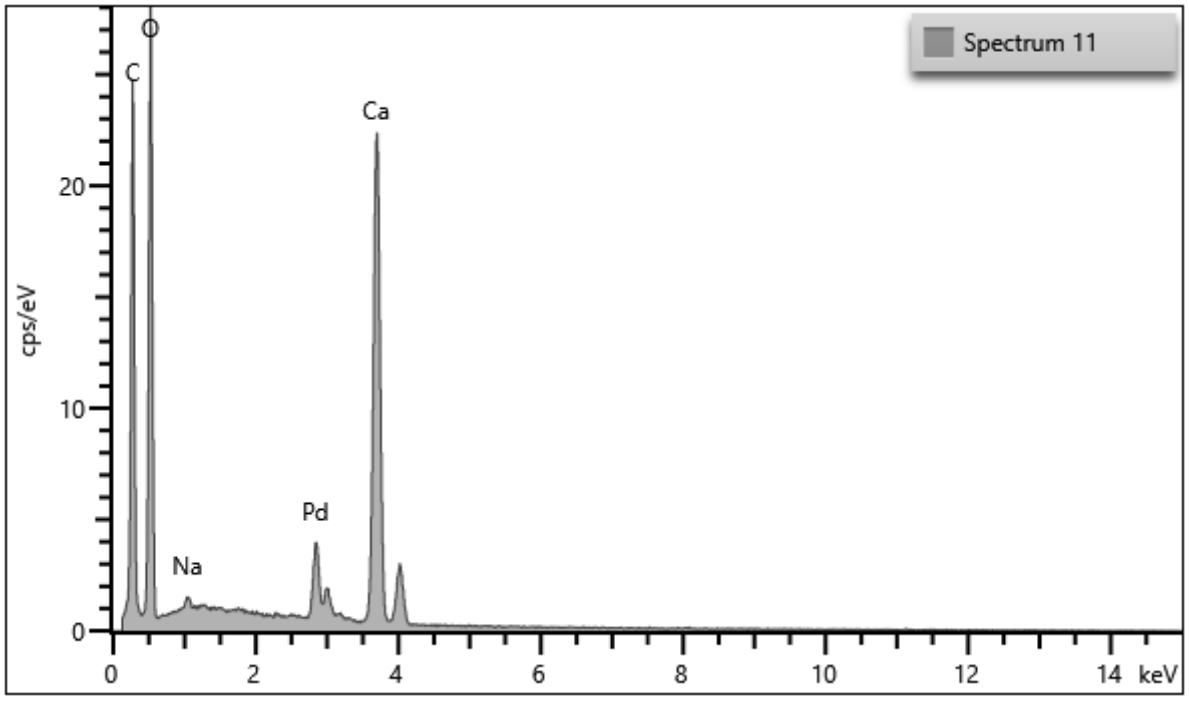
8.12.2 Sample TC21 426 (cleaned and broken)



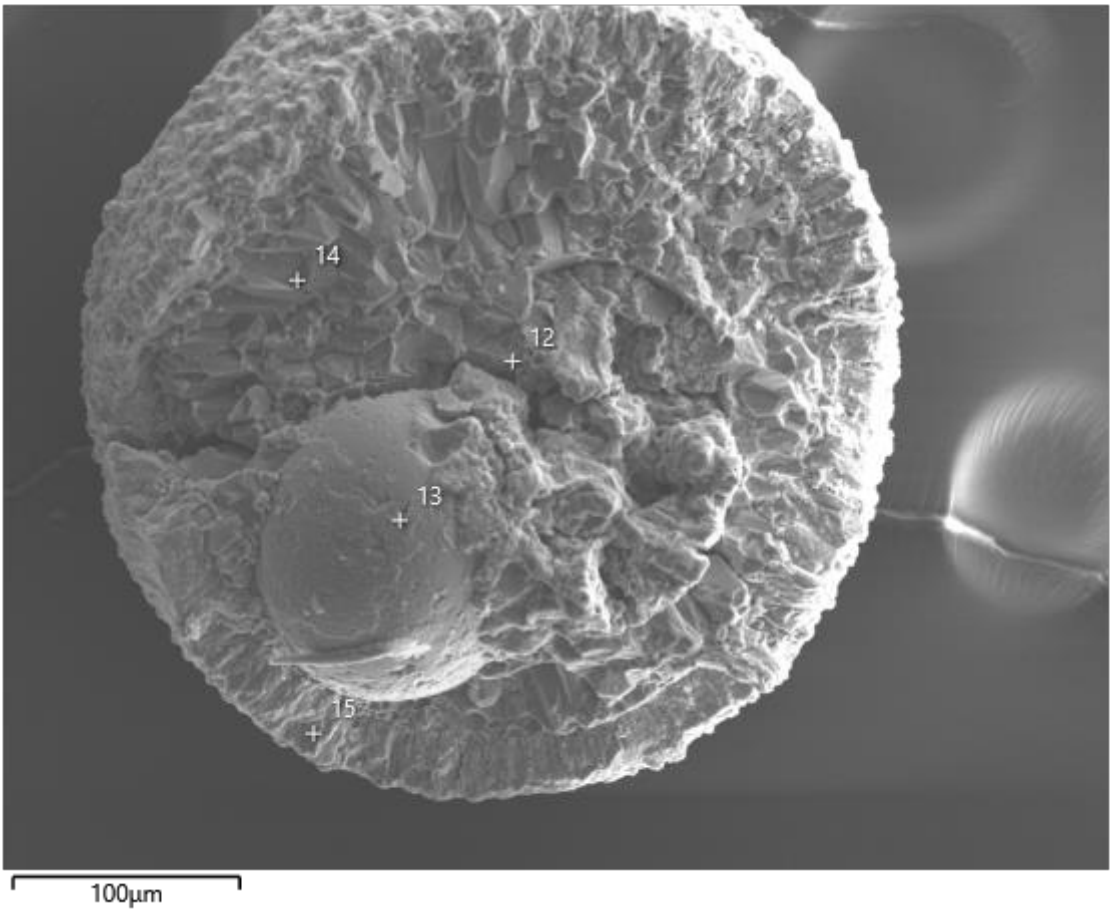

Spectrum 8
cps/eV
keV
C
O
Na
Mg
Al
Si
Mn
Cl
K
Pd
Ca
Mn

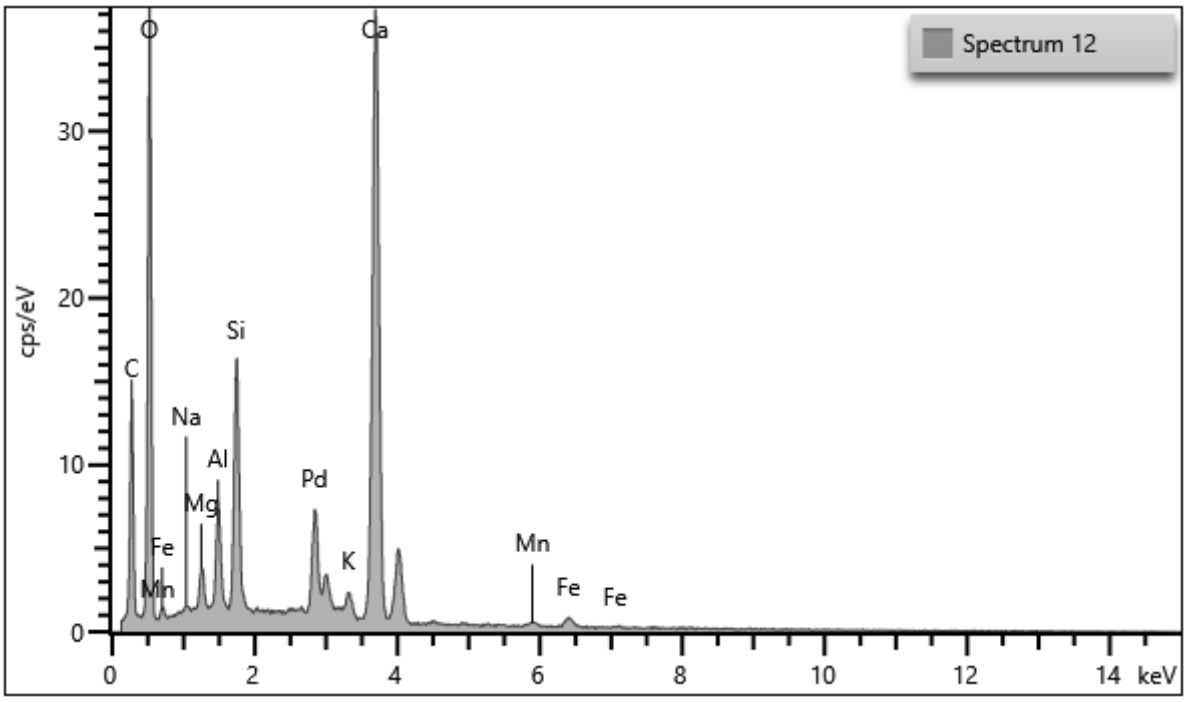

Spectrum 9
cps/eV
keV
O
C
Na
Mg
Al
Si
Fe
Mn
Pd
Ca
Mn
Fe
Fe

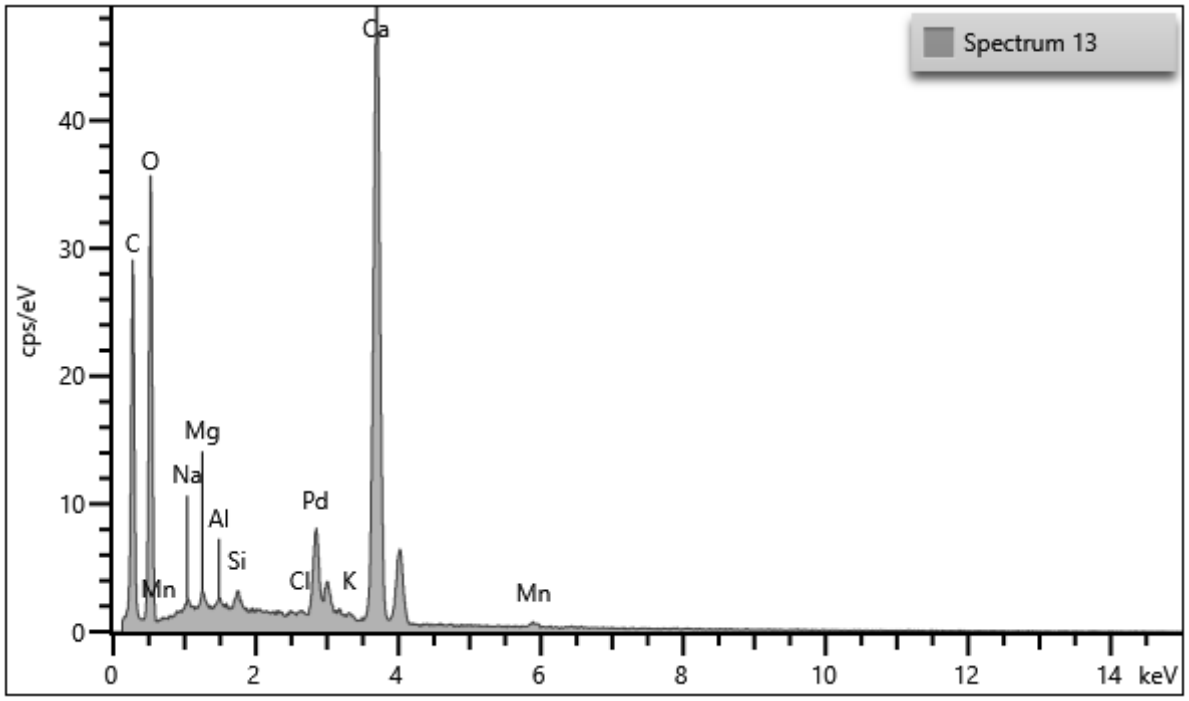

Spectrum 10
C
O
Ca
Na
Mg
Pd
Mn
Mn
cps/eV
0
5
10
15
20
0
2
4
6
8
10
12
14
keV

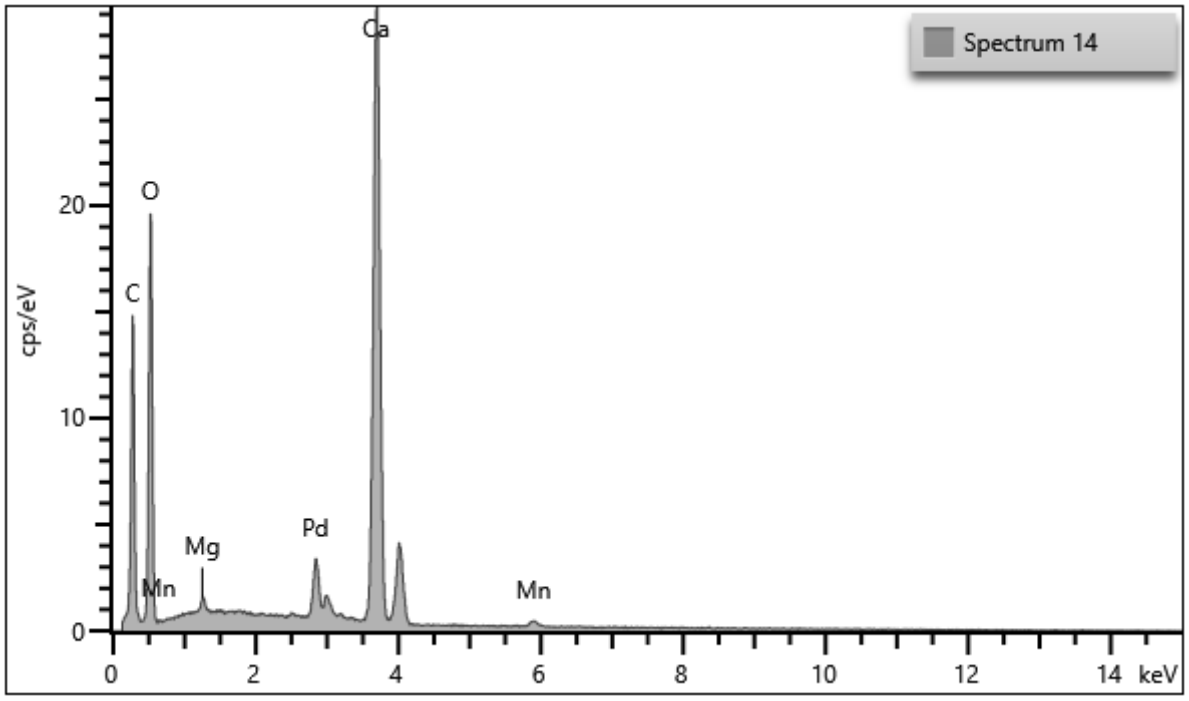

Spectrum 11
O
C
Ca
Pd
Na
cps/eV
0
10
20
0
2
4
6
8
10
12
14
keV

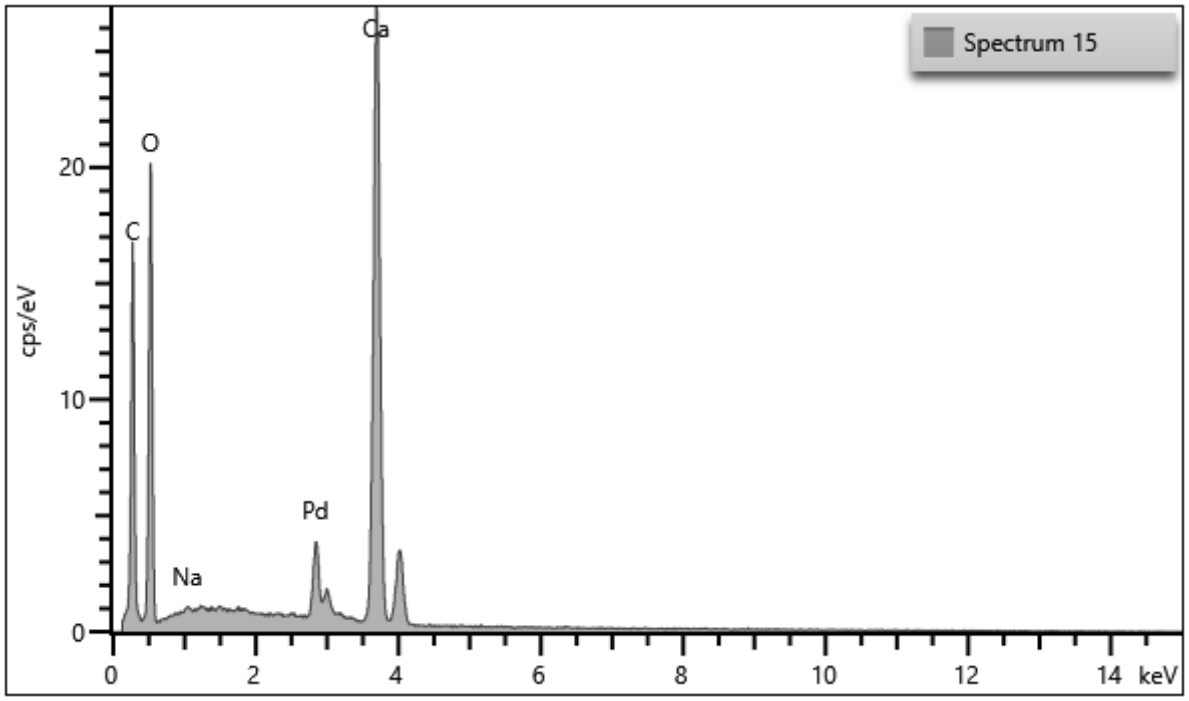
8.12.3 Sample TC21 341 (cleaned and broken)





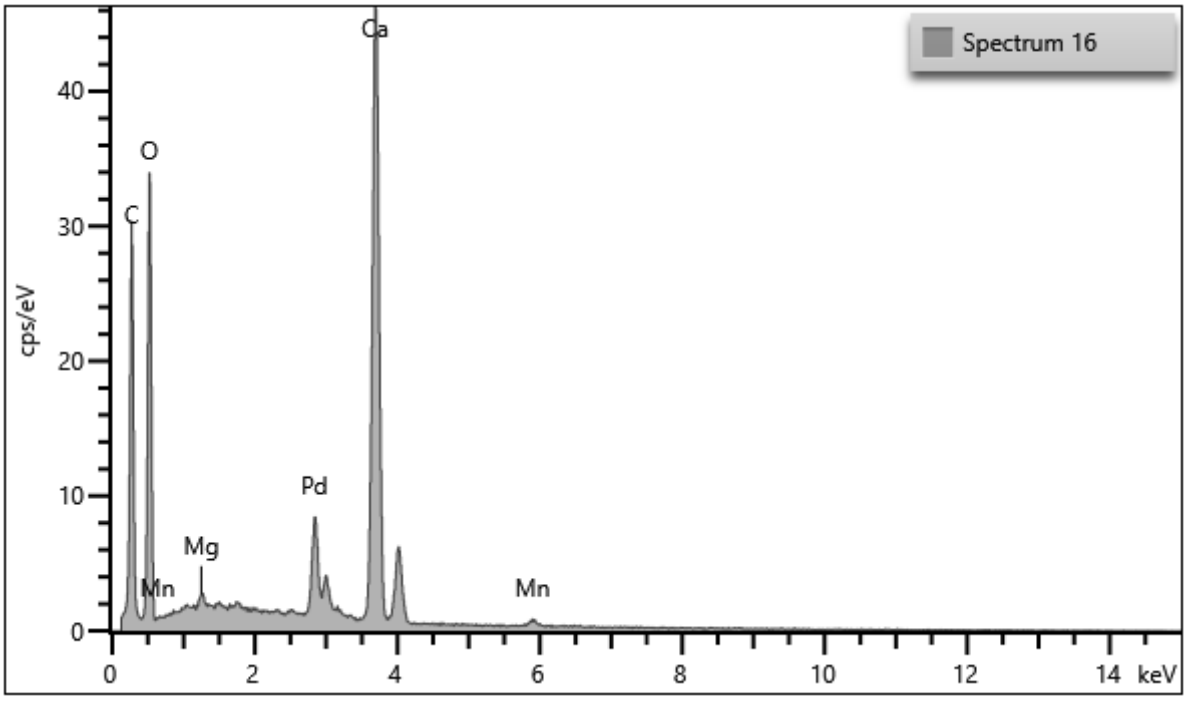

Spectrum 13
Ca
O
C
Mg
Na
Al
Si
Pd
Cl
K
Mn
Mn
cps/eV
0
10
20
30
40
0
2
4
6
8
10
12
14
keV

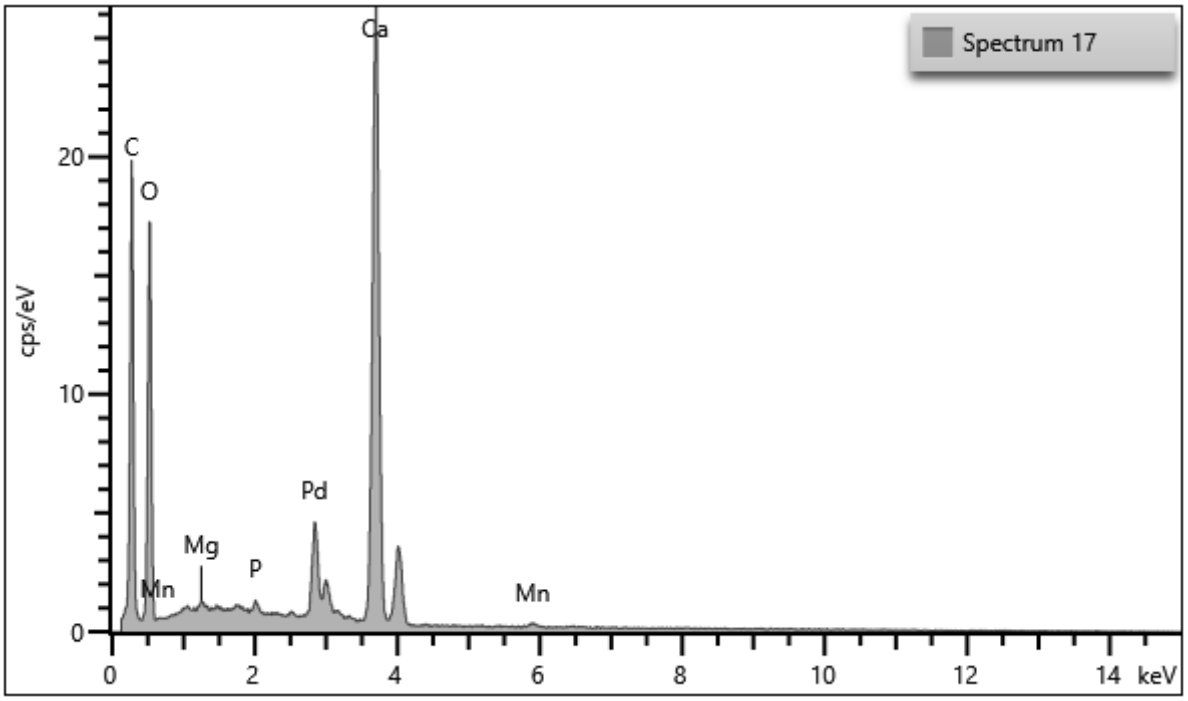

Spectrum 14
Ca
O
C
Mg
Pd
Mn
Mn
cps/eV
0
10
20
0
2
4
6
8
10
12
14
keV

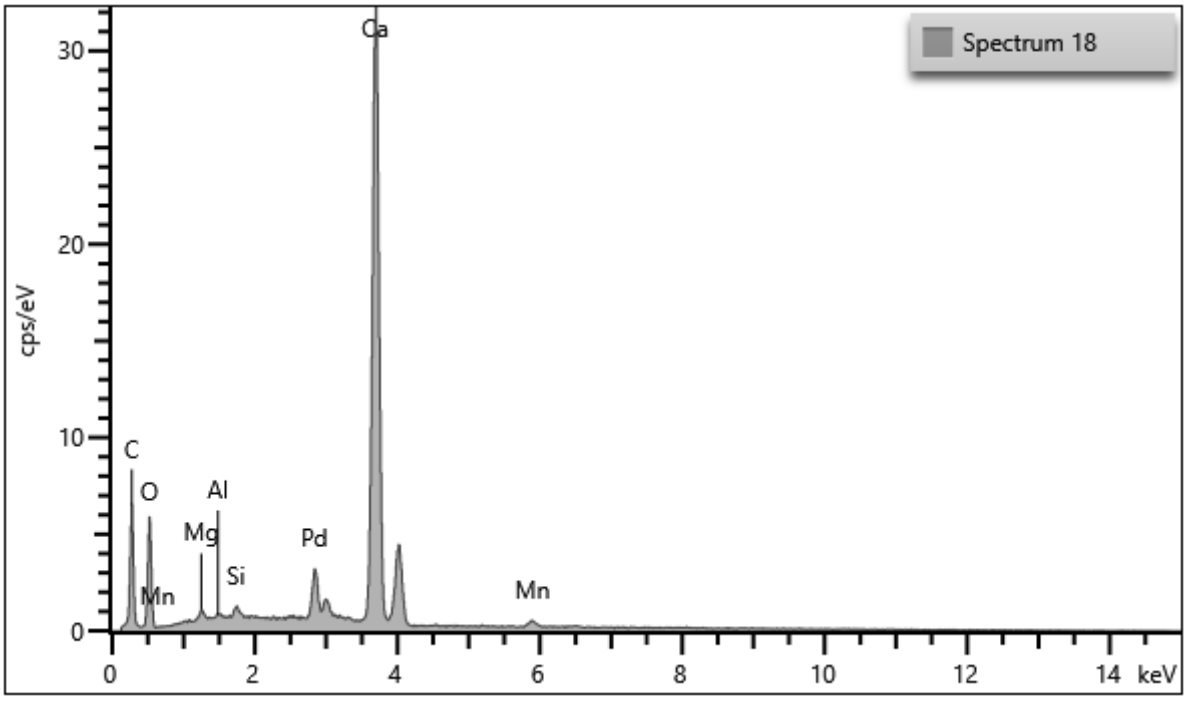

Spectrum 15
Ca
O
C
Na
Pd
cps/eV
20
10
0
0
2
4
6
8
10
12
14
keV

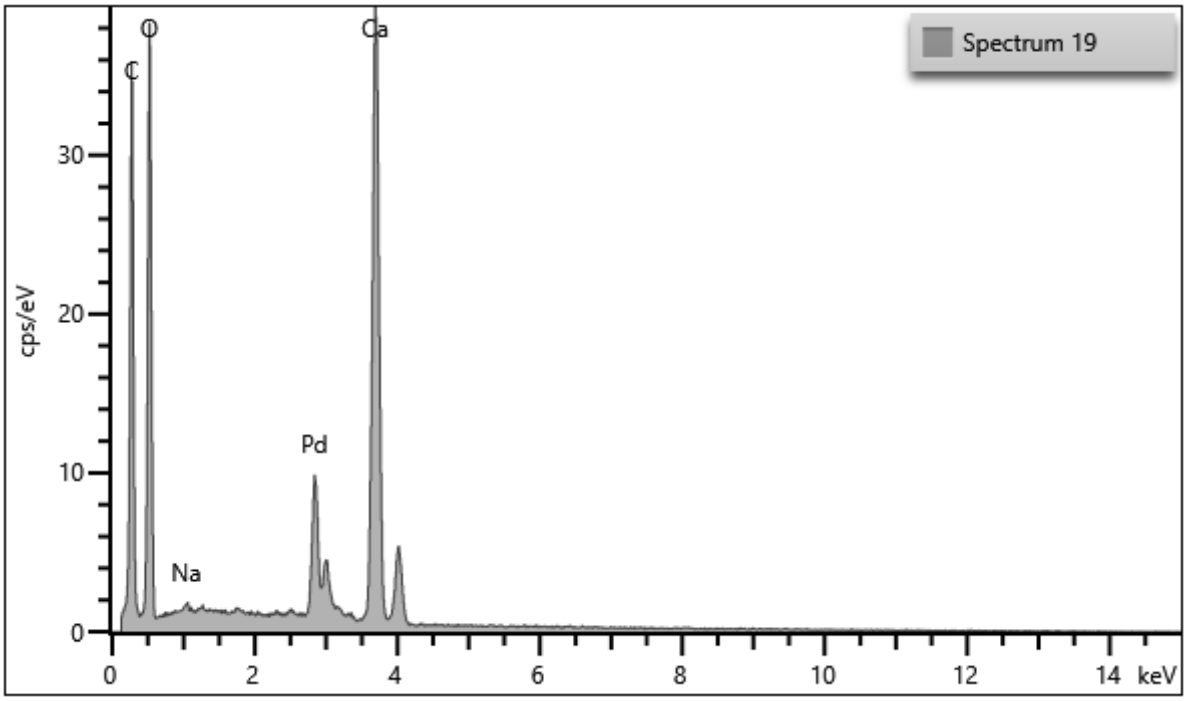
8.12.4 Sample TC21 341 (cleaned and broken)

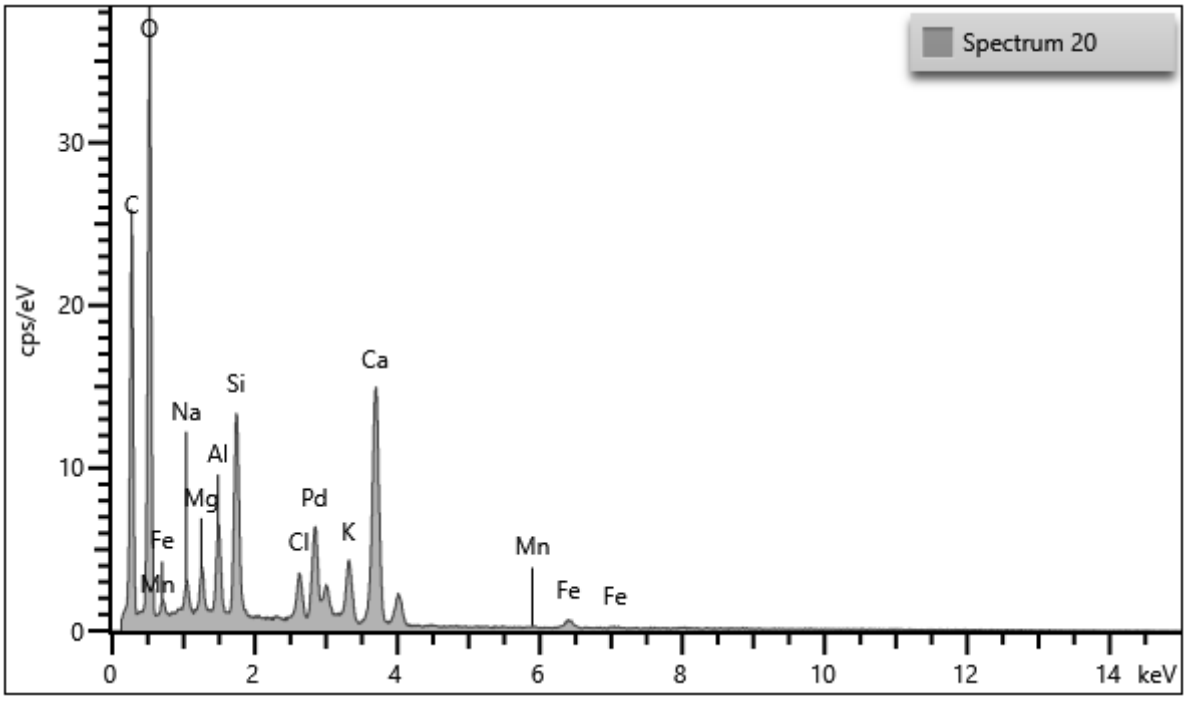




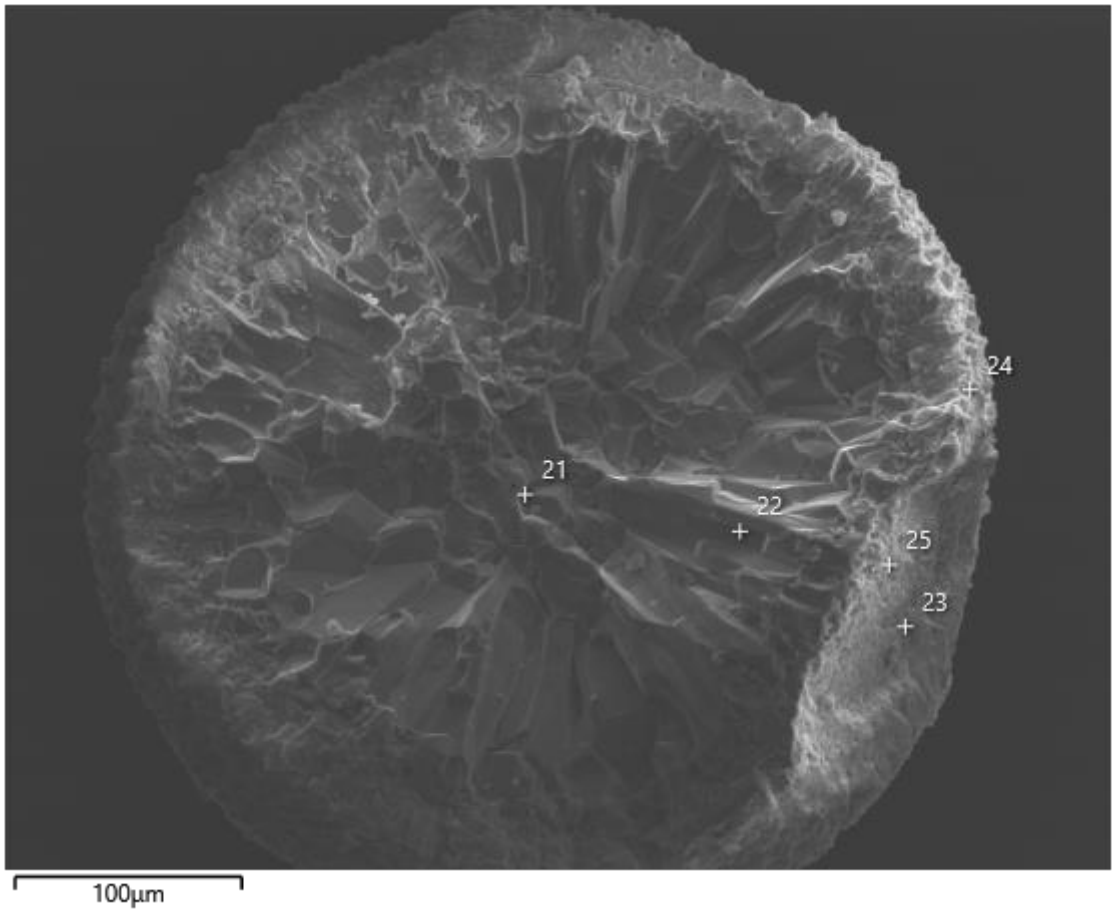

Spectrum 17
Ca
C
O
Mg
P
Pd
Mn
Mn
cps/eV
0
10
20
0
2
4
6
8
10
12
14
keV

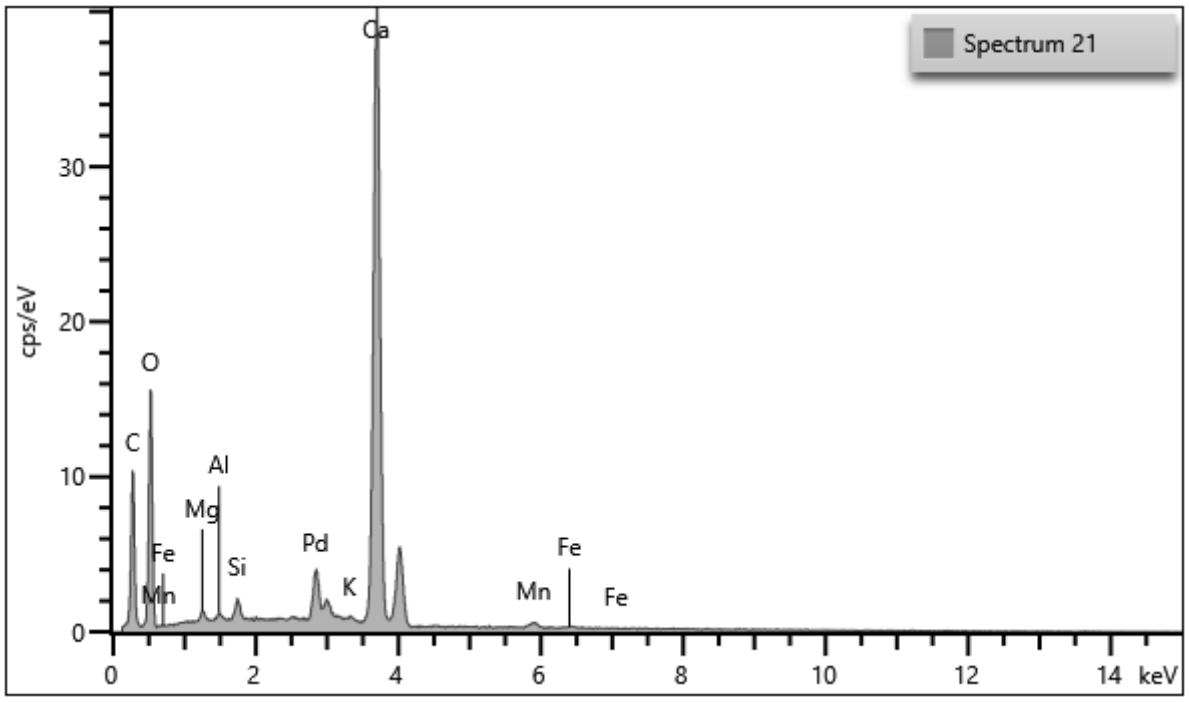

Spectrum 18
Ca
C
O
Al
Mg
Si
Pd
Mn
Mn
cps/eV
0
10
20
30
0
2
4
6
8
10
12
14
keV

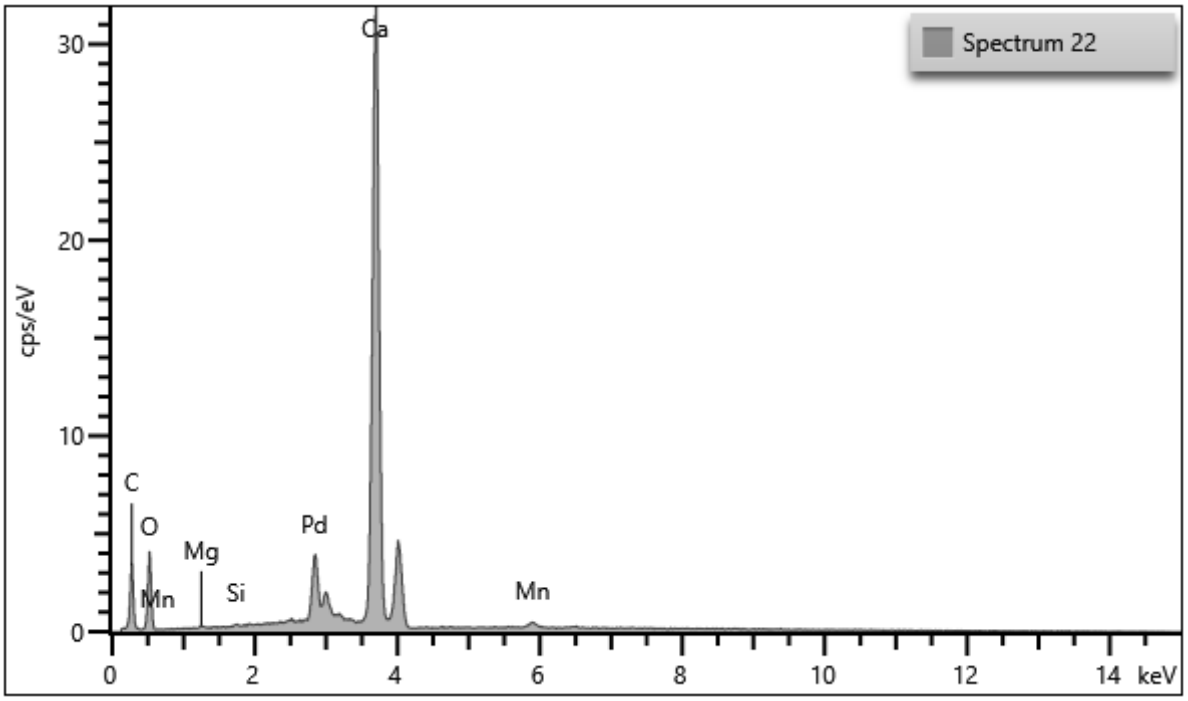

Spectrum 19
O
C
Ca
Pd
Na
cps/eV
0
10
20
30
0
2
4
6
8
10
12
14
keV

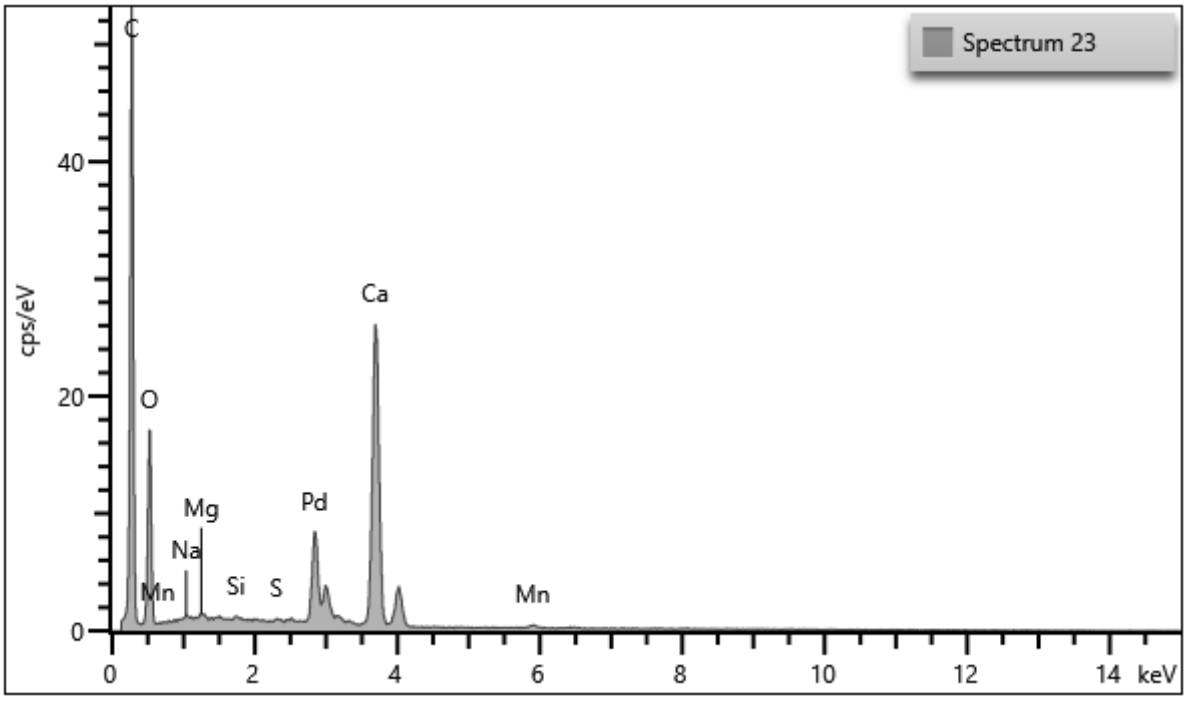

Spectrum 20
O
C
Ca
Si
Na
Al
Mg
Pd
Cl
K
Fe
Mn
Mn
Fe
Fe
cps/eV
0
10
20
30
0
2
4
6
8
10
12
14
keV

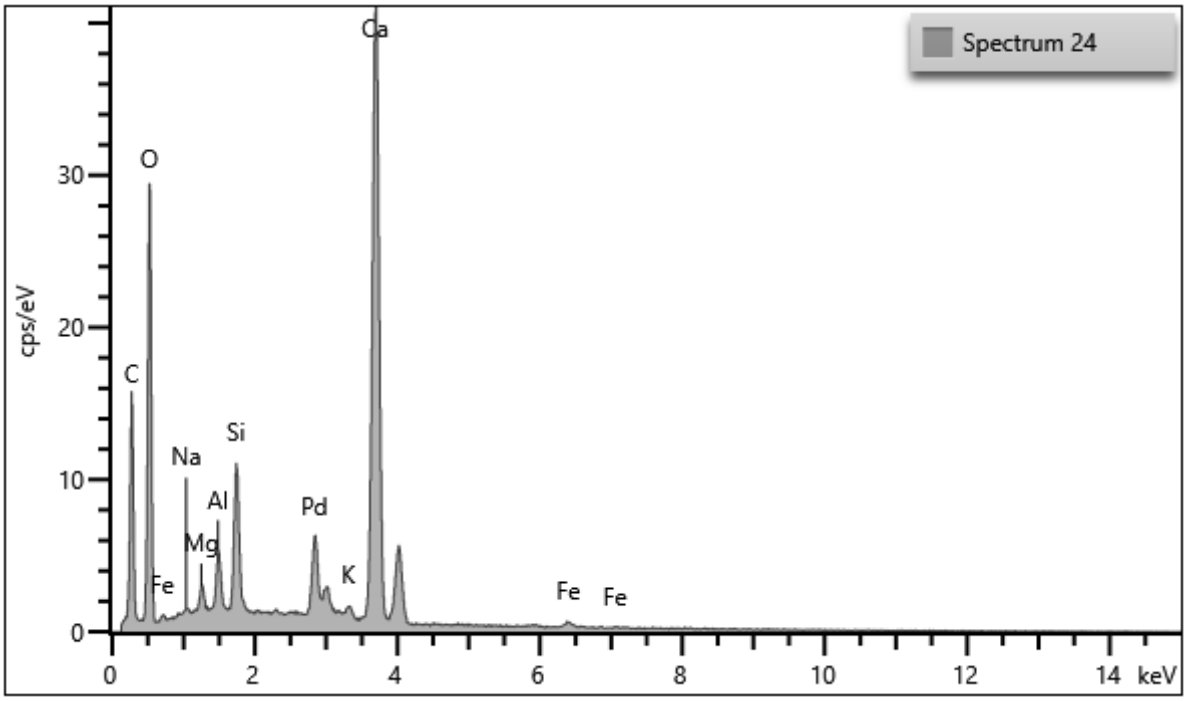
8.12.5 Sample TC21 341 (uncleaned and broken)

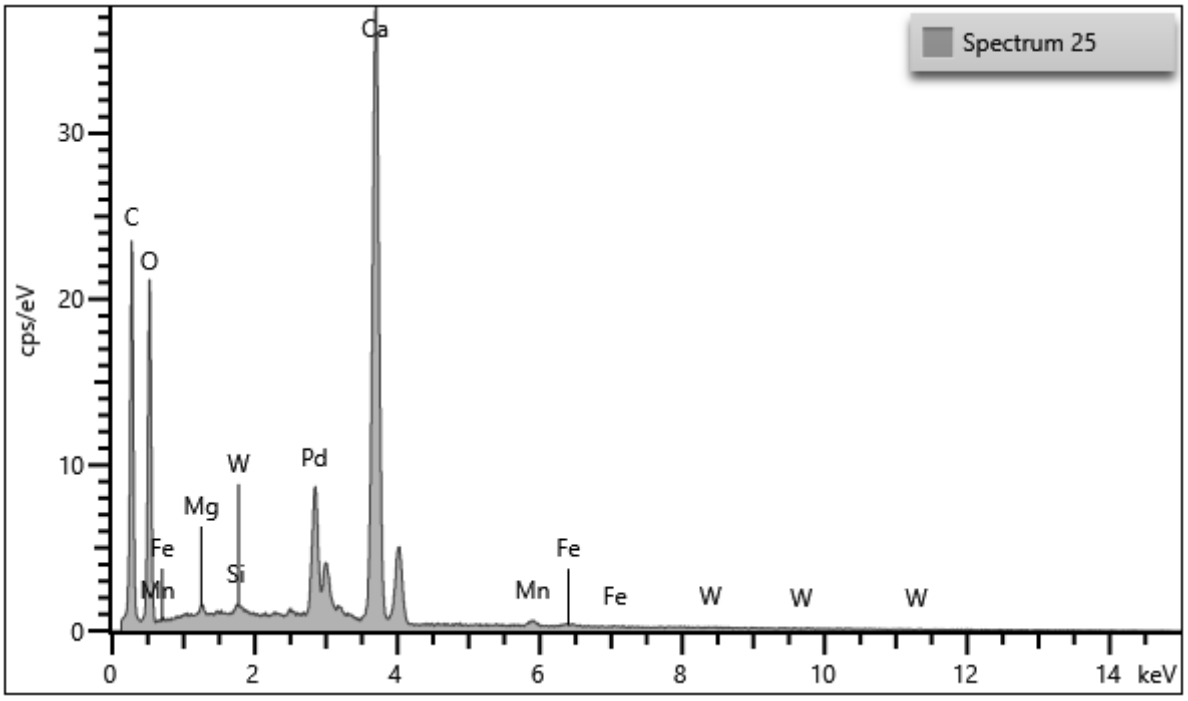




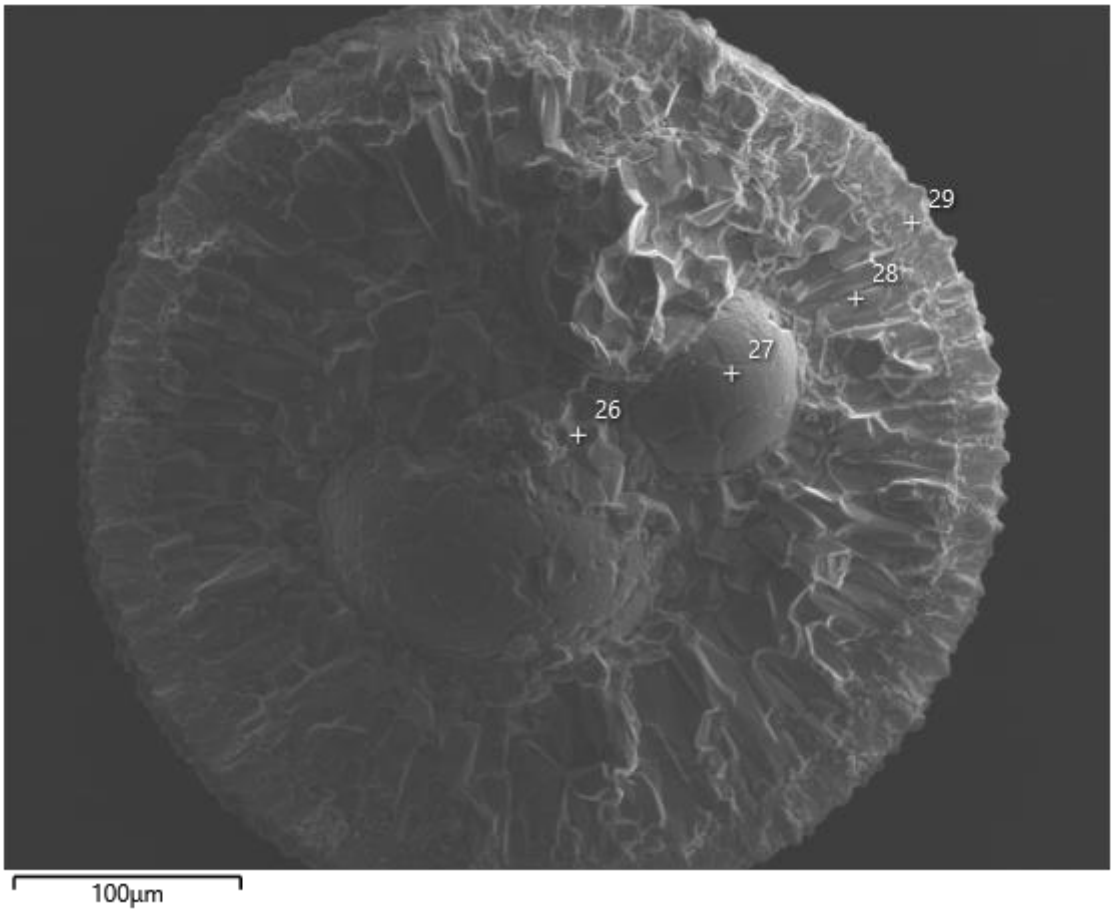

Spectrum 22
cps/eV
30
20
10
0
Ca
C
O
Mg
Mn
Si
Pd
Mn
0
2
4
6
8
10
12
14 keV

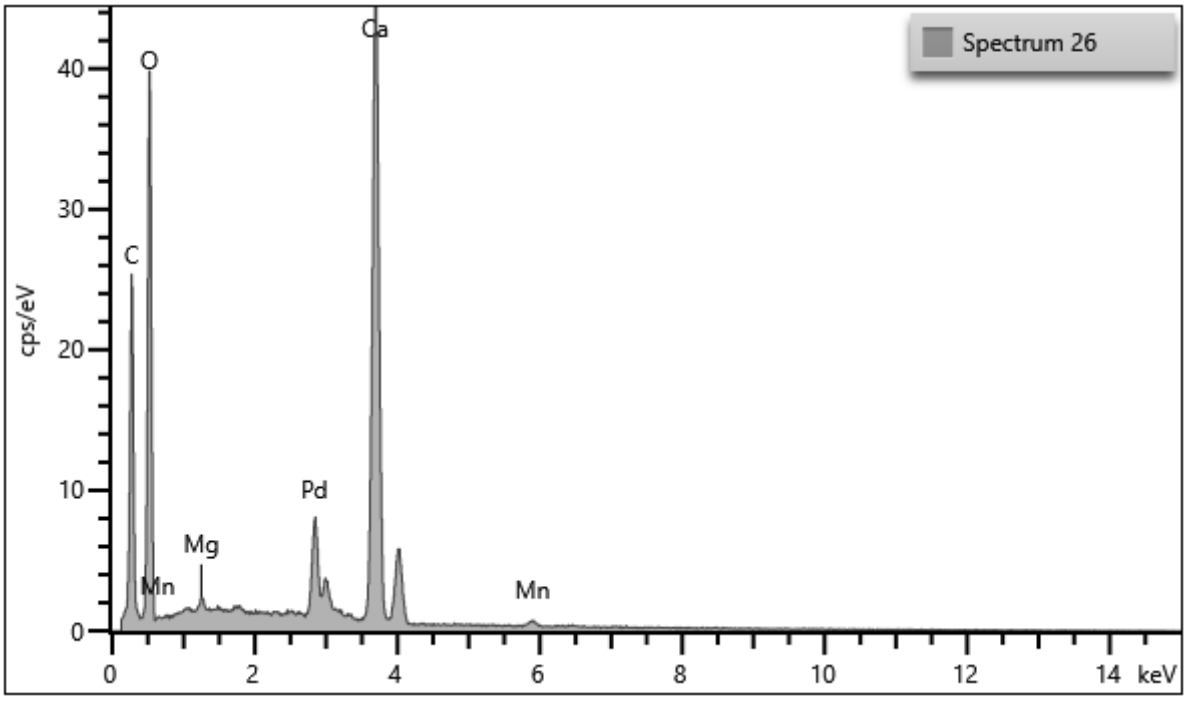

Spectrum 23
cps/eV
40
20
0
C
Ca
O
Mg
Pd
Na
Mn
Si
S
Mn
0
2
4
6
8
10
12
14 keV

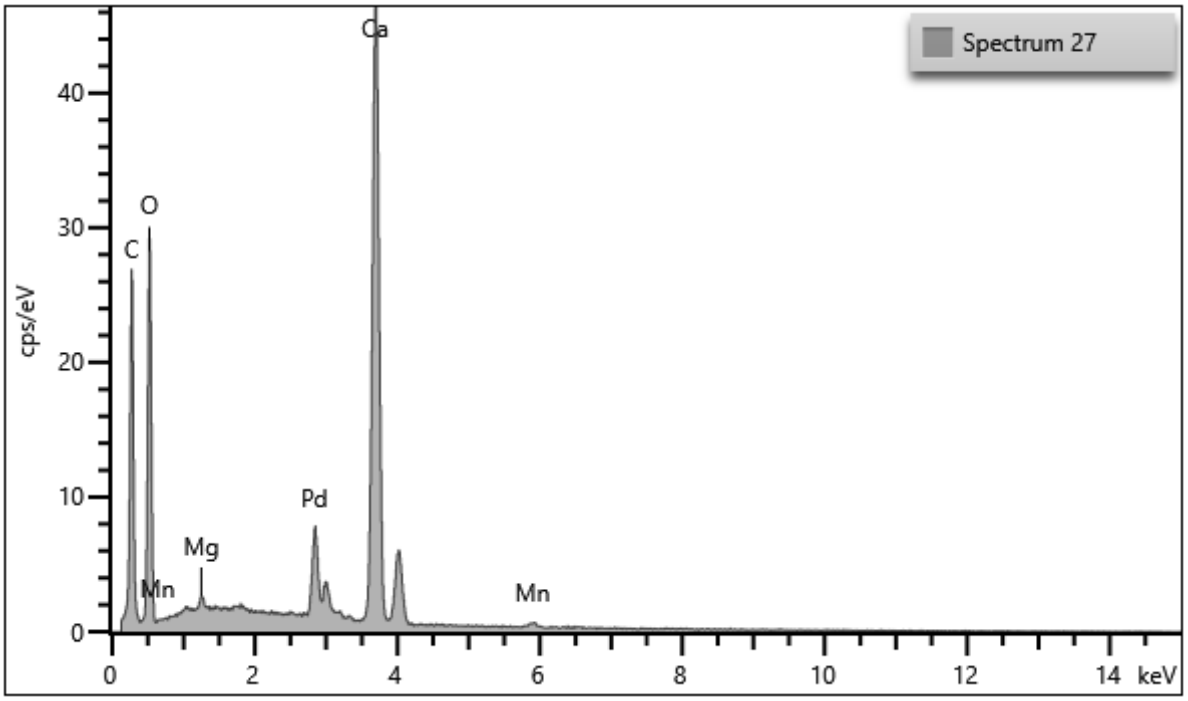

Spectrum 24
Ca
O
C
Na
Si
Al
Mg
Pd
Fe
K
Fe
Fe
cps/eV
0
10
20
30
0
2
4
6
8
10
12
14
keV

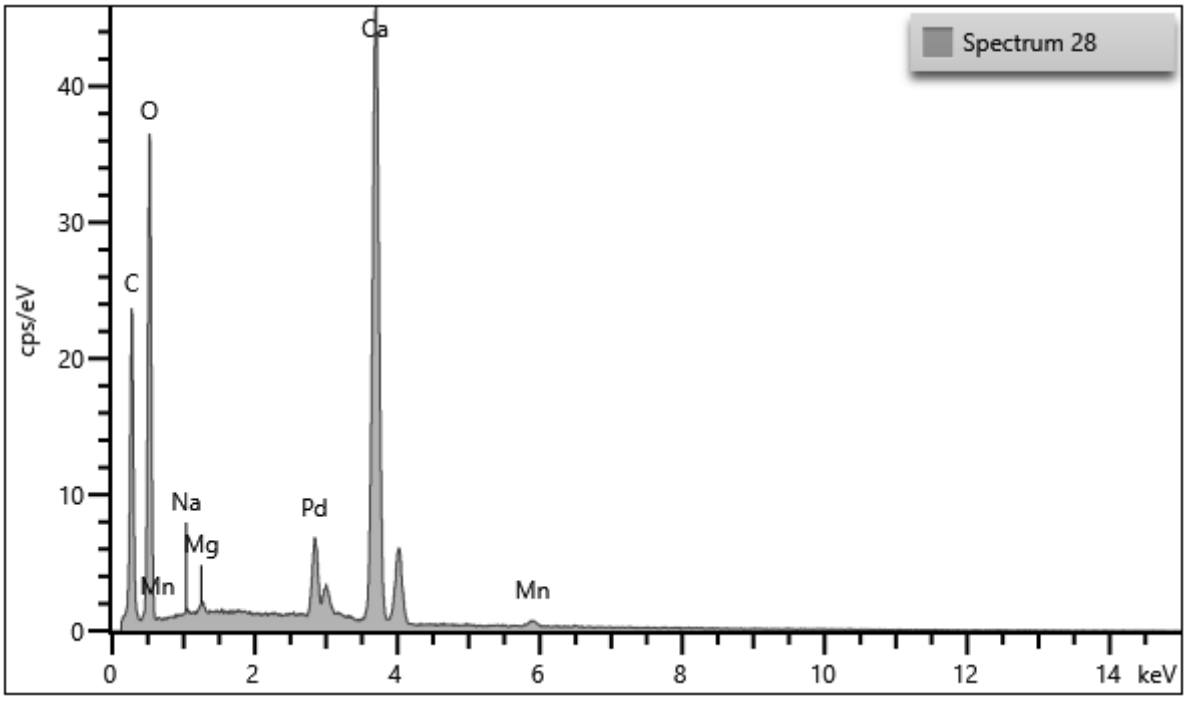

Spectrum 25
Ca
C
O
W
Pd
Mg
Fe
Si
Mn
Mn
Fe
Fe
W
W
W
cps/eV
0
10
20
30
0
2
4
6
8
10
12
14
keV

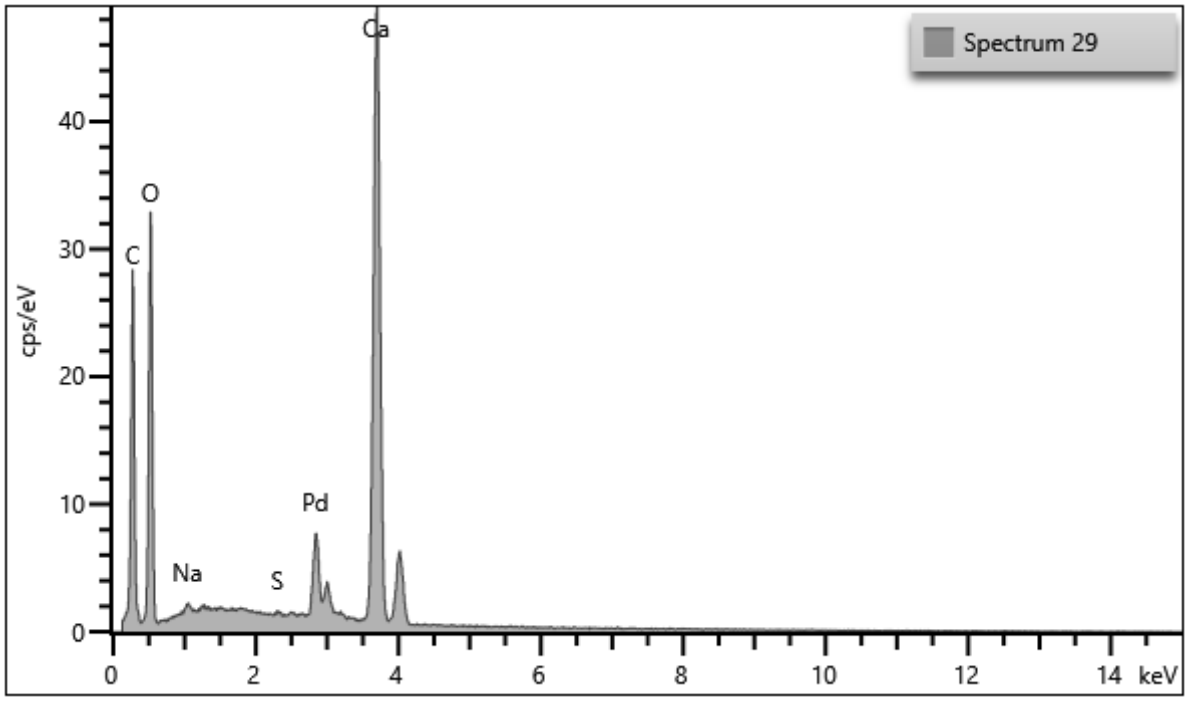
8.12.6 Sample TC21 341 (uncleaned and broken)






Spectrum 27
Ca
O
C
Mg
Mn
Pd
Mn
cps/eV
0
10
20
30
40
0
2
4
6
8
10
12
14
keV


Spectrum 28
Ca
O
C
Na
Mg
Mn
Pd
Mn
cps/eV
0
10
20
30
40
0
2
4
6
8
10
12
14
keV


Spectrum 29
Ca
O
C
Pd
Na
S
cps/eV
40
30
20
10
0
0
2
4
6
8
10
12
14
keV

8.13 X-ray Fluorescence Data for samples collected at Kottaphi Hill

			(ppm)														
Height (m)	**Sample Number**	**Lithology note**	**V**	**Cr**	**Ni**	**Cu**	**Zn**	**Br**	**Rb**	**Sr**	**Zr**	**Mo**	**I**	**Ba**	**Y**	**Sc**	**Nb**
1	TC19 257	Facies A- Chalk	47.3	87.9	59.2	25.1	34.8	9.3	11	1058.8	18.5	1.6	12.2	571.3	11.1	14.5	4
11.25	TC19 246	Facies B - Crystalline limestone	32.1	56	70.4	20.1	38.4	12.8	20.6	1063.4	14.6	1.7	30.1	770	18	46.4	1.9
11.35	TC19 033	Facies C - Reddish Marl	43.9	141.6	146.2	69.3	67	5.4	40.6	797.8	66.5	1.5	18.2	97.2	12	4.5	6.4
18.75	TC19 182	Facies D - Chalk	93.4	10.1	78	27.9	19.9	4.4	23.5	1120.4	20.9	2.8	22.6	61.7	6.8	30.8	7.4
32.85	TC19 277	Facies E - Calcareous Marl	70.7	66.3	74.9	22.4	36.7	12	22.4	894.8	33	2.4	5.6	62.2	1.9	1	9.5

			%										
Height (m)	**Sample Number**	**Lithology note**	**Na_2O**	**Al_2O_3**	**CaO**	**Fe_2O_3**	**K_2O**	**MgO**	**MnO**	**P_2O_5**	**SiO_2**	**TiO_2**	**Total**	**LOI**
1	TC19 257	Facies A- Chalk	0.09	2.39	50.3	1.34	0.45	1.32	0.06	0.09	8.16	0.14	63.34	35.48
11.25	TC19 246	Facies B - Crystalline limestone	0.16	3.3	48.45	1.53	0.61	2.09	0.08	0.15	9.96	0.21	66.54	33.22
11.35	TC19 033	Facies C - Reddish Marl	0.25	7.01	35.54	4.14	1.34	3.62	0.09	0.13	23.78	0.44	76.34	23.05
18.75	TC19 182	Facies D - Chalk	0.09	3.83	47.55	1.77	0.69	1.95	0.11	0.08	11.02	0.2	67.39	32.55
32.85	TC19 277	Facies E - Calcareous Marl	0.08	5.33	45.9	2.31	0.85	2.67	0.06	0.14	16.12	0.27	73.73	26.13

8.14 **X-ray Diffraction Data for samples collected at Kottaphi Hill**

Height (m)	Sample Number	Lithology note	Calcite (%)	Quartz (%)	Dolomite (%)	illite_90144 (%)	Kaolinite (BISH) (%)	Chlorite IIb (%)	Ankerite Fe0.7 (%)	Aragonite (%)	Halite (%)	Rhodochrosite (%)	Gypsum (%)	Calcite Magnesian (%)	Ankerite Fe0.2 (%)	Ankerite Fe0.55 (%)
1	TC19257	Facies A Chalk	94	0.7	0.29	1.88	0.5	0.81	BD	BD	0.23	0.16	BD	0.82	0.1	BD
11.25	TC19246	Facies B Crystalline limestone	84	3.2	1.34	2.5	0.16	0.07	1.52	1	0.25	0.6	0.55	1.14	3.5	BD
11.35	TC19033	Facies C Reddish Marl	68	8.8	1.6	6.6	1	1.5	4.9	BD	0.22	0.4	0.51	1.2	4	1
18.75	TC19182	Facies D Chalk	87	1.66	0.49	2.29	0.72	1.29	1.57	1	0.13	0.47	0.3	0.91	2.2	0.52
32.85	TC19277	Facies E Calcareous Marl	83	2.6	1.64	4	0.34	1.4	2.9	BD	0.55	0.63	0.06	0.79	1.1	0.81

8.15 **X-ray Diffraction Data for samples collected at Lapatza Hill**

Height (m)	Sample Number	Lithology note	Calcite (%)	Quartz (%)	Dolomite (%)	illite_90144 (%)	Kaolinite (BISH) (%)	Chlorite IIb (%)	Siderite (%)	Gypsum (%)	Microcline maximum (%)	Muscovite 2m1 (%)	Ankerite Fe0.55 (%)	Pyrite (%)	Albite (%)	Anorthite (%)	Montmorillonite (%)	Birnessite(%)
4.85	K19-2	Grey marl	52.36	14.82	2.03	5.63	1.30	3.00	0.32	1.05	4.59	2.24	3.98	0.22	4.17	4.28	BD	ND
7.25	K19-3	Dark grey marl	25.79	13.90	3.04	9.18	5.43	7.07	0.07	0.78	4.01	11.71	2.90	0.40	10.24	4.56	0.93	ND
9.7	K19-4	Dark grey/brown marl	28.28	13.49	1.97	8.29	5.06	7.81	BD	1.23	3.93	10.96	2.59	0.45	9.43	5.17	1.34	ND
9.75	K19-6	Dark muddy marl	33.61	5.46	19.60	3.50	1.41	5.40	BD	2.19	3.95	3.81	14.30	0.23	4.50	2.03	BD	ND
12.15	K19-7	Grey Marl	46.07	10.59	3.70	5.89	6.34	4.96	BD	0.75	3.53	7.52	2.10	0.21	3.62	2.66	2.08	ND
14.6	K19-8	Grey Marl	36.27	9.45	9.19	7.06	5.69	5.28	BD	1.04	4.57	6.48	4.90	0.18	4.46	2.51	2.93	ND
15.95	K19-9	Dark Marl	33.33	8.65	1.57	8.27	5.94	6.15	0.01	9.09	5.09	10.22	2.55	0.75	3.79	3.20	1.38	ND
18.4	k19-10	Grey Marl	41.07	8.18	3.90	7.97	5.90	6.80	BD	2.91	5.13	7.33	3.30	0.20	5.32	1.41	0.59	BD
18.7	K19-11	Reddish Marl	52.51	7.50	2.50	5.48	4.50	4.35	BD	0.60	3.94	6.81	3.84	0.14	3.66	1.57	2.59	BD
50.75	K19-32	Chalky Marl	78.25	4.59	BD	3.58	2.64	1.56	0.08	0.82	2.49	2.44	BD	0.24	2.09	BD	1.21	ND
53.15	K19-34	Finely laminated marl	74.03	4.25	0.16	3.74	2.45	2.29	0.02	0.55	2.83	4.13	BD	0.37	2.62	1.71	0.84	ND
56.8	K19-36	Reddish Marl	40.10	5.71	BD	6.32	5.01	2.81	0.27	16.04	10.13	2.41	BD	0.46	5.21	4.01	1.52	BD
57.4	K19-37	Reddish Marl	45.27	11.87	0.29	6.66	5.36	3.36	0.28	1.56	3.51	9.12	BD	0.23	3.95	3.03	3.14	2.35
57.7	K19-38	Grey Marl	62.61	7.14	0.30	6.54	3.15	2.85	0.12	1.84	3.93	5.37	BD	0.07	2.87	2.30	0.91	BD
60.7	K19-39	Grey Marl	73.45	4.20	BD	5.25	1.99	1.89	BD	0.73	3.15	4.20	BD	0.10	2.20	1.78	1.05	BD
61.25	K19-40	Pale brown finely laminated marl	69.24	4.66	0.46	4.51	3.20	2.30	BD	1.35	3.25	4.60	BD	0.21	3.11	1.54	1.58	BD
62.85	K19-41	Brown marl topped by base of fine-grained gypsum	50.21	4.45	0.08	3.32	2.68	2.96	BD	21.97	2.28	5.79	0.52	0.18	2.53	3.04	BD	BD